Transactions of the ASME®

Journal of Turbomachinery

Published Quarterly by The American Society of Mechanical Engineers

VOLUME 114 • NUMBER 4 • OCTOBER 1992

Transactions of the ASME, Journal of Turbomachinery (ISSN 0889-504X) is published quarterly (Jan., Apr., July, Oct.) for $130.00 per year by The American Society of Mechanical Engineers, 345 East 47th Street, New York, NY 10017. Second class postage paid at New York, NY and additional mailing offices. POSTMASTER: Send address change to Transactions of the ASME, Journal of Turbomachinery, c/o THE AMERICAN SOCIETY OF MECHANICAL ENGINEERS, 22 Law Drive, Box 2300, Fairfield, NJ 07007-2300.
CHANGES OF ADDRESS must be received at Society headquarters seven weeks before they are to be effective. Please send old label and new address.
PRICES: To members, $40.00, annually; to nonmembers, $130.00.
Add $24.00 for postage to countries outside the United States and Canada.
STATEMENT from By-Laws. The Society shall not be responsible for statements or opinions advanced in papers or . . . printed in its publications (B7.1, Par. 3).

INDEXED by Applied Mechanics Reviews and Engineering Information, Inc.
Canadian Goods & Services Tax Registration #126148048

TECHNICAL PAPERS

(Contents Continued on p. 715)

(Contents Continued)

Heat Transfer, Adiabatic Effectiveness, and Injectant Distributions Downstream of a Single Row and Two Staggered Rows of Compound Angle Film-Cooling Holes

P. M. Ligrani
Department of Mechanical Engineering,
University of Utah,
Salt Lake City, UT 84112

S. Ciriello

D. T. Bishop

Department of Mechanical Engineering,
Naval Postgraduate School,
Monterey, CA 93943

Experimental results are presented that describe the development and structure of flow downstream of one row and downstream of two staggered rows of film-cooling holes with compound angle orientations. With the compound angle configuration, holes are inclined at 35 deg with respect to the test surface when projected into the streamwise/normal plane, and 30 deg with respect to the test surface when projected into the spanwise/normal plane. Within each row, holes are spaced 7.8 hole diameters apart, which gives 3.9d spacing between adjacent holes for the staggered row arrangement. Results presented include disributions of iso-energetic Stanton numbers, and adiabatic film cooling effectiveness deduced from Stanton numbers using superpositiion. Also presented are plots showing the streamwise development of injectant distributions and streamwise development of mean velocity distributions. Spanwise-averaged values of the adiabatic film cooling effectivenss, $\overline{\eta}$, measured downstream of two staggered rows of holes are highest with a blowing ratio m of 0.5, and decrease with blowing ratio because of injection lift-off effects for $x/d < 20$. However, as the boundary layers convect farther downstream, $\overline{\eta}$ values for $m = 0.5$ are lower than values for $m = 1.0$, 1.5, and 1.74 since smaller amounts of injectant are spread along the test surface. These differences also result because injectant from the upstream row of holes eventually merges and coalesces with the injectant from the downstream row of holes (of the two staggered rows) at the higher m. With one row of holes, local effectivenss variations are spanwise periodic, where higher values correspond to locations where injectant is plentiful near the test surface. Local St_f/St_o data also show spanwise periodicity, with local St_f/St_o maxima corresponding to regions of higher mixing between streamwise velocity deficits. Spanwise-averaged iso-energetic Stanton number ratios downstream of both the one-row and two-row arrangements generally range between 1.0 and 1.25, and show little variation with x/d for each value of m tested. However, for each x/d St_f/St_o values increase with m. Additional discussion of these results is presented along with comparisons to ones obtained downstream of film cooling holes with simple angles in which holes are inclined at 35 deg with respect to the test surface in the streamwise/normal plane.

Introduction

Current turbine inlet temperatures of gas turbines are approaching 2000 K. These extreme temperatures, in combination with the high rotational speeds, result in large stress magnitudes on component materials, especially on the blades of the first turbine stage. An efficient means of cooling these components is thus a necessity if such stresses are to be minimized, and the safety, reliability, and operating lifetimes of gas turbines are to be maximized. Film cooling is one method of thermal protection of gas turbine component surfaces that is used extensively in commercial and military applications, particularly on turbine blades, turbine endwalls, combustion chamber linings,

Contributed by the International Gas Turbine Institute and presented at the ASME Winter Annual Meeting, Atlanta, Georgia, December 1–6, 1991. Manuscript received by the International Gas Turbine Institute February 20, 1992. Associate Technical Editor: L. S. Langston.

and afterburner linings. In the past, the most common film cooling arrangement employed holes with simple angle orientations. Simple angle injection refers to situations in which the film is injected from holes inclined to the test surface such that injectant is issued from the holes at an angle with respect to the test surface when viewed in the streamwise/normal plane but approximately in the direction of the mainstream flow when viewed in the streamwise/spanwise plane.

More recently, gas turbine components include film holes with compound angle orientations, which are believed to produce injectant distributions over surfaces giving better protection and higher film effectivnesses than injectant from holes with simple angle orientations. Compound angle orientations are ones in which the film is injected with holes inclined to the test surface such that the injectant is issued with a spanwise velocity component relative to the mainstream flow (when viewed in the streamwise/spanwise plane). Although film cooling from compound angle holes is now quite common on gas turbine components, few data are available in the archival literature on heat transfer and boundary layer behavior downstream of film cooling holes with compound angle orientations.

Experimental results are presented that describe the development and structure of flow downstream of film-cooling holes with compound angle orientations. Results are given that were measured both downstream of one row of holes and downstream of two staggered rows of holes. Holes are inclined at 35 deg with respect to the test surface when projected into the streamwise/normal plane, and 30 deg with respect to the test surface when projected into the spanwise/normal plane. Within each row, holes are spaced $7.8d$ apart, where d is the hole diameter. This gives $3.9d$ spacing between adjacent holes when two staggered rows are employed. Results presented include distributions of surface Stanton numbers, adiabatic film cooling effectiveness deduced from Stanton numbers using superposition, iso-energetic Stanton numbers, and injectant distributions. The Stanton number data are presented for θ values ranging from 0 to 3.0 at x/d ratios from 6.7 to 96.6. Blowing ratios m range from 0.5 to 1.74. Also presented are plots showing the streamwise development of distributions of mean streamwise velocity. Of particular interest are comparisons of these results to ones obtained downstream of film cooling holes with simple angle orientations. With this arrangement, the holes are inclined 35 deg with respect to the test surface in the streamwise/normal plane.

Experimental Apparatus and Procedures

Wind Tunnel and Coordinate System. The wind tunnel is the same one used in the experiments of Ligrani et al. (1989, 1991a). The facility is open-circuit, subsonic, and located in the laboratories of the Department of Mechanical Engineering of the Naval Postgraduate School. A centrifugal blower is located at the upstream end, followed by a diffuser, a header containing a honeycomb and three screens, and then a 16 to 1 contraction ratio nozzle. The nozzle leads to the test section, which is rectangular duct 3.05 m long and 0.61 m wide, with a topwall having adjustable height to permit a zero pressure gradient to be set along the length of the test section (without the film cooling) to within 0.01 inches of water differential pressure. The initial duct height at the nozzle exit is 0.203 m. The free-stream velocity is 10 m/s and the free-stream turbulence intensity is approximately 0.13 percent based on the same velocity. The boundary layer is tripped using a 2-mm-high spanwise uniform strip of tape near the nozzle exit 1.072 m upstream of the constant heat flux transfer surface for the compound angle injection system.

A schematic showing the test section and coordinate system is presented in Fig. 1. Locations of the boundary layer trip, film cooling holes, heat transfer surface, and thermocouple rows along this test surface are evident. Dimensional values of distance labeled in Fig. 1 are given in Table 1. These are given for the compound angle film hole arrangement (configuration 1) as well as for the simple angle film hole arrangement (hereafter referred to as configuration 2). With both arrangements, an unheated starting length exists when the heat transfer surface is at elevated temperature. Thus, the direction of heat transfer is from the wall to the gas. In regard to the coordinate system, Z is the spanwise coordinate measured from the test section spanwise centerline, X is measured from the upstream edge of the boundary layer trip, and Y is measured normal to the test surface. x is measured from the downstream edge of the injection holes and generally presented as x/d.

Figures 2(a) and 2(b) show some boundary layer characteristics measured just downstream of the injection holes at x/d

Nomenclature

A = heat transfer surface area
c = specific heat
d = injection hole diameter
h = heat transfer coefficient with film injection
h_o = baseline heat transfer coefficient, no film injection
h_f = iso-energetic heat transfer coefficient with film injection
I = momentum flux ratio $= \rho_c U_c^2/\rho_\infty U_\infty^2$
k = thermal conductivity
m = blowing ratio $= \rho_c U_c/\rho_\infty U_\infty$
q = wall heat flux
Re_d = injection Reynolds number, $= dU_c/\nu$
s = equivalent slot width
St = Stanton number with film injection
St_o = baseline Stanton number, no film injection
St_f = iso-energetic Stanton number with film injection
$\overline{\mathrm{St}_f}$ = spanwise-averaged iso-energetic Stanton number with film injection
T = static temperature
U = streamwise mean (time-averaged) velocity
u' = streamwise velocity fluctuation
X, x = streamwise distance
Y, y = distance normal to the surface
Z, z = spanwise distance from test surface centerline
α = thermal diffusivity $= k/\rho c$
β = injection hole angle with respect to the test surface as projected into the spanwise/normal plane.
η = adiabatic film cooling effectiveness $= (T_{aw} - T_{r,\infty})/(T_{r,c} - T_{r,\infty})$
$\overline{\eta}$ = spanwise-averaged adiabatic film cooling effectiveness
θ = nondimensional injection temperature $= (T_{r,c} - T_{r,\infty})/(T_w - T_{r,\infty})$
ν = kinematic viscosity
ξ = unheated starting length
ρ = density
Ω = injection hole angles with respect to the test surface as projected into the streamwise/normal plane

Subscripts

aw = adiabatic wall
c = injectant at exits of injection holes
cond = conduction heat transfer
o = stagnation
r = recovery condition
rad = radiation heat transfer
w = wall
∞ = free stream

Superscripts

$\overline{\ }$ = time-average

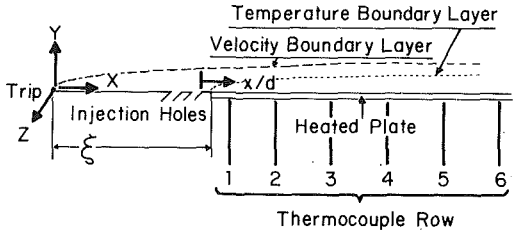

Fig. 1 Coordinate system and schematic of wind tunnel test section

Table 1 Test section geometry characteristics for injection configurations 1 and 2

	Compound angle configuration 1		
	X (m)	x/d	x (m)
Downstream edge of injection holes	1.059	0.00	0.000
Unheated starting length, ξ	1.072	1.38	0.013
Row 1*	1.122	6.67	0.063
Row 2*	1.222	17.25	0.163
Row 3*	1.372	33.12	0.313
Row 4*	1.572	54.29	0.513
Row 5*	1.772	75.45	0.713
Row 6*	1.972	96.61	0.913
	Simple angle configuration 2		
Downstream edge of injection holes	1.083	0.00	0.000
Unheated starting length, ξ	1.097	1.48	0.014
Row 1*	1.147	6.77	0.064
Row 2*	1.247	17.35	0.164
Row 3*	1.397	33.23	0.314
Row 4*	1.597	54.39	0.514
Row 5*	1.797	75.56	0.714
Row 6*	1.997	96.72	0.914

*Refers to thermocouple row locations.

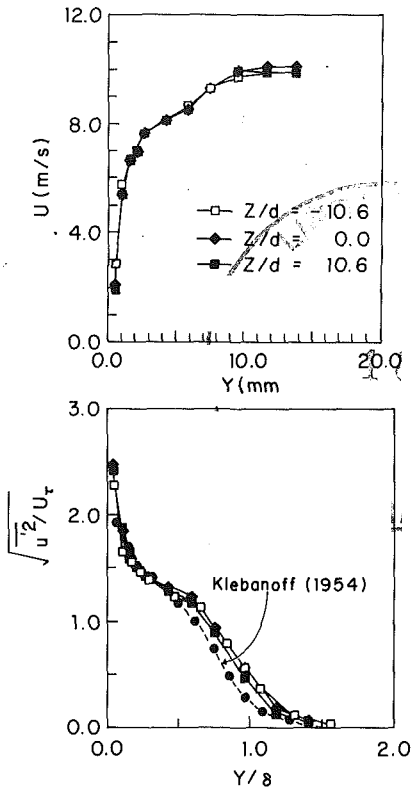

Fig. 2 Boundary layer properties as measured at x/d = 2.75, for three different spanwise locations: (*a*) mean streamwise velocity; (*b*) normalized longitudinal turbulence intensity

= 2.75 with the holes taped closed and no film cooling. In the first of these figures, three mean velocity profiles are presented in dimensional form that illustrate the spanwise uniformity of the mean flow field. When the same profiles are plotted in near-wall or boundary layer coordinates, appropriate portions show agreement with the law of the wall when a Clauser plot is used to determine the local skin friction coefficient (Bishop, 1990). The total boundary layer thickness at this location is 0.973 cm, giving a thickness to hole diameter ratio of 1.03. The ratios of momentum thickness to hole diameter and displacement thickness to hole diameter are 0.13 and 0.22, repsectively. Longitudinal turbulence intensity profiles in Fig. 2(*b*) are normalized using the friction velocity determined from log-law regions of mean velocity profiles. These data show agreement with the data of Klebanoff (1954) except for some small differences in the outer portions of the boundary layer, probably as a result of different free-stream turbulence levels in the two studies. The longitudinal turbulence intensity data also show spanwise unformity, which further evidences a high degree of boundary layer regularity across the span of the wind tunnel test surface.

Injection System. The injection system is described by Ligrani et al. (1991a). Air for the injection system originates in two 1.5 hp DR513 Rotron Blowers capable of producting 30 cfm at 2.5 psig. From the blowers, air flows through a regulating valve, a Fisher and Porter rotometer, a diffuser, and finally into the injection heat exchanger and plenum chamber. The changer provides means to heat the injectant above ambient temperature. With this system and test plate heating, the nondimensional injection temperature parameter θ is maintained at values ranging from 0.0 to 3.0, which includes values within the range of gas turbine component operation. The upper surface of the plenum chamber is connected to the injection configuration, where each tube is 7.6 cm long, giving a length-to-diameter ratio of about 8.

Injection system performance was checked by measuring discharge coefficients at different Reynolds numbers based on injection hole diameter and mean injectant velocity. These values compare favorably with earlier measurements (Ligrani et al., 1989). Procedures to measure discharge coefficients and blowing ratios are described by Ligrani et al. (1989).

Experimental Approach. The present experiment is designed to match a number of operating parameters existing in the first turbine stages of gas turbine engines. These include (range of values are indicated in parentheses): (1) compound angle injection geometry including centerline-to-centerline spacing of injection holes (3.9) as well as spanwise spacing of holes along the test surface (7.8) and elliptical coverage of the film holes in the plane of the test surface, (2) x/d range (6.7–96.7), (3) blowing ratio range (0.5–1.74), (4) momentum flux ratio range (0.25–3.03), (5) injection hole Reynolds number range (3200–26,000), (6) Reynolds numbers based on length along the test surface (7.4×10^5–12.8×10^5), (7) ratio of boundary layer thickness to injection hole diameter (1.03), and (8) nondimensional injection temperatures (θ = 0.0–3.0). Other effects present in operating high-temperature engines (i.e., curvature, high free-stream turbulence, variable properties, stator/blade wake interactions, shock waves, compressibility,

rotation, viscous dissipation, injectant to free-stream density ratio) are left out of our experiment since these may obscure and complicate the interaction of interest. Of these, one of the more important pertains to variable properties: All temperature differences are maintained at levels less than 30°C so that fluid properties are maintained approximately constant. Without this, *linear* superposition of Stanton numbers at different injection temperatures cannot be used to determine magnitudes of the adiabatic film cooling effectivness and iso-energetic Stanton number. Other investigators (Loftus and Jones, 1983; Ligrani and Camci, 1985) use superposition in variable property flows. In the former case, ρ_c/ρ_∞ is maintained constant as θ is varied because θ is altered by changing the wall temperature. In the latter study, the nonlinearity of St/St_o versus θ data in variable property flow is demonstrated.

Streamwise Mean Velocity. The streamwise mean velocity was measured using a five-hole pressure probe with a conical tip manufactured by United Sensors Corporation. Celesco transducers and Carrier Demodulators are used to sense pressures when connected to probe output ports. The same automated traverse used for injectant surveys was used to obtain these surveys. With this device, the pressure probe was traversed over 1.02 cm by 20.3 cm spanwise/normal planes at 800 locations spaced 0.51 cm apart in each direction. At each location, 50 samples of the output from each of the five pressure ports are aquisitioned for later processing. These devices, measurement procedures employed, as well as data acquisition equipment and procedures used are further detailed by Ligrani et al. (1989, 1991a), Bishop (1990), and Ciriello (1991).

Stanton Number Measurements. The heat transfer surface is designed to provide a constant heat flux over its area. The surface next to the airstream is stainless steel foil painted flat black. Immediately beneath this is a liner containing 126 thermocouples, which is just above an Electrofilm Corp. etched foil heater rated at 120 V and 1500 W. Located below the heater are several layers of insulating materials including Lexan sheets, foam insulation, styrofoam, and balsa wood. Surface temperature levels and convective heat transfer rates are controlled by adjusting power into the heater using a Standard Electric Co. Variac, type 3000B. To determine the heat loss by conduction, an energy balance was performed. This was accomplished by insulating the top of the test surface (which is nominally exposed to the airstream) and measuring conduction loss from the bottom as it is dependent upon the difference in temperature between the test surface and surrounding ambient air. Radiation losses from the top of the test surface were analytically estimated. The thermal contact resistance between thermocouples and the foil top surface was estimated on the basis of outputs of the thermocouples and measurements from calibrated liquid crystals on the surface of the foil. This difference was then correlated as a function of heat flux through the foil. Local Stanton numbers are corrected to account for spanwise and streamwise conduction along the foil test surface using procedures described by Wigle (1991). Data presented in the 1991 WAM version of this paper (Ligrani et al., 1991b) are different since they are *not* corrected for spanwise and streamwise conduction along the test surface.

After the surface was completed, a variety of qualification tests were conducted to check the performance of the heat transfer test surface. These are described in detail by Ligrani et al. (1989), Bishop (1990), and Ciriello (1991), along with additional details on the measurement of local Stanton numbers.

Mean Temperature Measurements. Copper-constantan thermocouples were used to measure temperatures along the surface of the test plate, the free-stream temperature, as well as temperature distributions that are correlated to injection distributions. For the distributions, a thermocouple was traversed over spanwise/normal planes (800 probe locations) using an automated two-dimensional traversing system, which could be placed at different streamwise locations. Voltages from thermocouples and the Carrier Demodulators (used for the mean velocity measurements) are digitally sampled and read using a Hewlett-Packard 3497A Data Acquisition Control Unit with a 3498A Extender. These units are controlled by a Hewlett-Packard Series 9000 Model 310 computer.

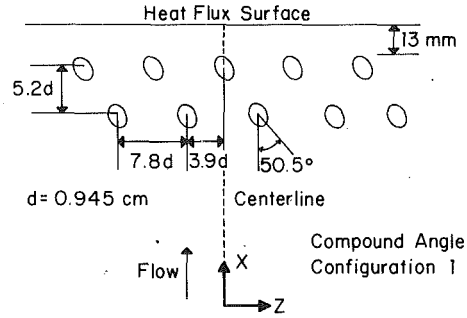

Fig. 3 Compound angle configuration 1 film cooling injection geometry on the test surface

Baseline Data Checks. Repeated measurements of spanwise-averaged Stanton numbers show good agreement (maximum deviation is 4 percent) with the correlation from Kays and Crawford (1980) for turbulent heat transfer to a flat plate with unheated starting length and constant heat flux boundary condition. Ciriello (1991) provides additional details.

Experimental Uncertainties. Uncertainty estimates are based upon 95 percent confidence levels, and determined following procedures described by Kline and McClintock (1953) and Moffat (1982). Typical nominal values of free-stream recovery temperature and wall temperature are 18.0 and 40.0 °C, with respective uncertainties of 0.13 and 0.21°C. The free-stream density, free-stream velocity, and specific heat uncertainties are 0.009 kg/m^3 (1.23 kg/m^3), 0.06 m/s (10.0 m/s), and 1 J/kgK (1006 J/kgK), where typical nominal values are given in parentheses. For convective heat transfer, heat transfer coefficient, and heat transfer area, 10.5 W (270 W), 1.03 W/m^2 K (24.2 W/m^{2}K), and 0.0065 m^2 (0.558 m^2) are typical uncertainties. The uncertainties of St, St/St_0, m, and x/d are 0.000086 (0.00196), 0.058 (1.05), 0.025 (0.50), and 0.36 (41.9). Uncertainties of η and $\overline{St_F/St_o}$ are dependent upon the linear superposition technique employed. The uncertainty of $\overline{St_f/St_0}$ is the same as for $\overline{St/St_0}$. The uncertainty of $\overline{\eta}$ varies between 0.02 and 0.04 effectiveness units where higher values in this range apply when $\overline{\eta}$ is less than about 0.15.

In percentages, uncertainties of these quantities are as follows: free-stream recovery temperature: 0.7; wall temperature: 0.5; free-stream density: 0.7; free-stream velocity: 0.6; specific heat: 0.1; convective heat transfer: 3.9; heat transfer coefficient: 4.3; heat transfer area: 1.2; St: 4.4; St/St_0: 5.5; m: 5.0; and x/d: 0.9.

Injection Configuration

A schematic showing the compound angle film hole geometry (configuration 1) along the test surface is shown in Fig. 3. Here, holes are arranged in two rows, which are staggered with respect to each other, with spanwise spacings between adjacent holes of 3.9d. Centerlines of holes in separate rows are separated by 5.2d in the streamwise direction. When only one row of holes is employed, it is the downstream one located closest to the heat flux surface. With this arrangement, spanwise hole spacing is 7.8d. Each row of holes contains five injection cooling holes with a nominal inside diameter of 0.945

cm. The centerline of the middle hole of the downstream row is located on the spanwise centerline (Z = 0.0 cm) of the test surface. The compound angle holes are employed with $\Omega = 35$ deg and β = 30 deg, where Ω is the angle of the injection holes with respect to the test surface as projected into the streamwise/normal plane, and β is the angle of the injection holes with respect to the test surface as projected into the spanwise/normal plane. Thus, as shown in Fig. 3, holes are oriented so that the spanwise components of injectant velocity are directed in the negative-Z direction. The plane of each injection hole is angled at 50.5 deg from the streamwise/normal (X-Y) plane. Within the plane of each hole, hole centerlines are oriented at angles of 24 deg from the plane of the test surface (X-Z).

In some cases, compound angle results are compared to ones obtained downstream of film holes with simple angle orientations. This simple angle arrangement is denoted configuration 2, and contains holes with Ω = 35 deg and β = 90 deg. Thus, the plane of each injection hole is within the streamwise/normal (X-Y) plane. Within this plane, holes are inclined at an angle of 35 deg with respect to the test surface. The holes are in two staggered rows with a spanwise hole spacing of 3.0d, and separation of centerlines of holes in separate rows of 4.0d in the streamwise direction. When one row is employed, spanwise hole spacing is 6.0d.

Adiabatic Film Cooling Effectiveness Determination

Adiabatic film cooling effectiveness values are determined using linear superposition theory applied to Stanton number ratios measured at different injection temperatures. This is possible since the three-dimensional energy equation that describes the flow field is linear and homogeneous in its dependent variable, temperature, for constant property flow.

The technique of superposition was first applied to film cooling by Metzger et al. (1968). In a comment on this paper, E.R.G. Eckert showed how local heat transfer coefficient ratios for different injection temperatures can be used to deduce the adiabatic wall temperature, T_{aw}, and the iso-energetic heat transfer coefficient, h_f. With these parameters, the heat flux with film cooling is given by

$$q = h_f(T_w - T_{aw}) \tag{1}$$

The same heat flux may also be expressed in terms of the difference between the actual wall temperature and the free-stream recovery temperature using the equation given by

$$q = h(T_w - T_{r,\infty}) \tag{2}$$

Equating these two then produces an equation having the form

$$h = h_f(T_w - T_{aw})/(T_w - T_{r,\infty}) \tag{3}$$

or, after rearrangement,

$$h = h_f[1 - (T_{aw} - T_{r,\infty})/(T_w - T_{r,\infty})]$$

This equation is then equivalent to

$$h = h_f(1 - \theta\ \eta) \tag{4}$$

where $\theta = (T_{r,c} - T_{r,\infty})/(T_w - T_{r,\infty})$ and $\eta = (T_{aw} - T_{r,\infty})/(T_{r,c} - T_{r,\infty})$. Dividing each side of Eq. (4) by h_o, the heat transfer coefficient without film cooling, and then expressing heat transfer coefficients in terms of Stanton numbers produces the form of this equation employed in the present study:

$$\mathrm{St}/\mathrm{St}_o = \mathrm{St}_f/\mathrm{St}_o(1 - \theta\ \eta) \tag{5}$$

A plot of $\mathrm{St}/\mathrm{St}_o$ versus θ, where θ is varied by changing the injection temperature, thus gives a straight line with a vertical axis intercept of $\mathrm{St}_f/\mathrm{St}_o$, and a horizontal axis intercept of $1/\eta$. This approach applies only so long as temperature variations are small enough that fluid properties are reasonably invariant as θ is changed, and as long as fluid properties are reasonably invariant with respect to all three coordinate directions (Ligrani and Camci, 1985; Ligrani, 1990).

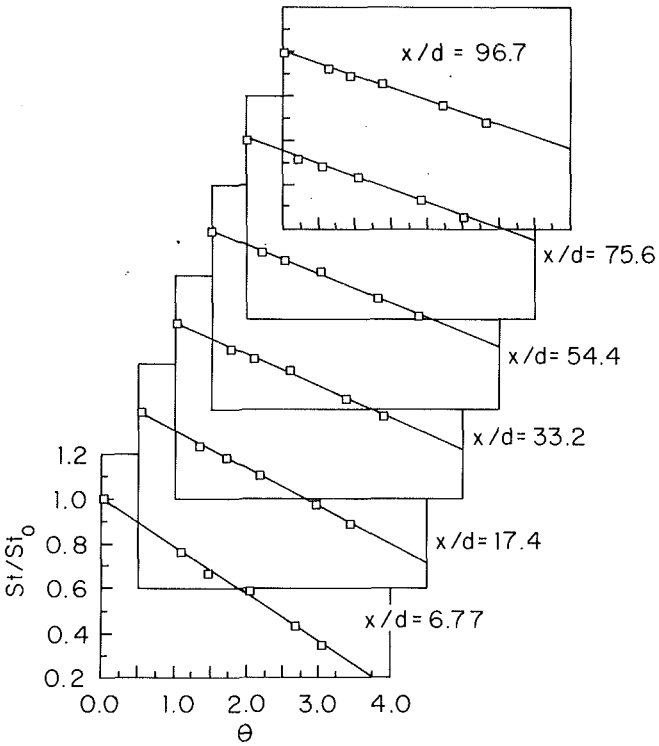

Fig. 4 St/St$_o$ values illustrating the linearity of these data with respect of θ for different streamwise locations. These data are obtained downstream of two staggered rows of simple angle (configuration 2) holes with m = 0.5 at z/d = 0.0.

Figure 4 shows $\mathrm{St}/\mathrm{St}_o$ experimental data obtained at different θ obtained downstream of two rows of film cooling holes with simple angle orientations producing injectant at a blowing ratio of 0.5. As θ is varied from 0.0 to values near 3.0, the blowing ratio is maintained constant and the density ratio changes from 1.0 to about 0.9. In spite of these variations, the linearity of data in Fig. 4 is evident for all six values of x/d along the spanwise centerline of the test surface (Z/d = 0.0). Lines through each set of data also illustrate some of the horizontal axis intercepts and vertical axis intercepts, which give $1/\eta$ and $\mathrm{St}_f/\mathrm{St}_o$, respectively. To obtain local variations of these quantities, the method of linear superposition is applied for each measurement location. In most cases, no extrapolation is needed to determine $\mathrm{St}_f/\mathrm{St}_o$ because $\mathrm{St}/\mathrm{St}_o$ is measured directly at θ = 0 ($T_{r,c} = T_{r,\infty}$). η and $\mathrm{St}_f/\mathrm{St}_o$ data determined using the same approach but for other locations and different experimental conditions are discussed later in the paper.

St_f is the Stanton number based on the iso-energetic heat transfer coefficient h_f. This coefficient is obtained under iso-energetic conditions in which the free-stream and injectant recovery temperatures are the same ($T_{r,c} = T_{r,\infty}$). With this situation, the recovery free-stream temperature is the same as the adiabatic wall temperature, and $h = h_f$.

To check the technique of linear superposition for the determination of η, the adiabatic film cooling effectiveness was also measured using a near-adiabatic condition on the test plate. This was done downstream of one row of holes with simple angle orientations at blowing ratios of 0.5, 1.0, and 1.5. To set the near-adiabatic condition, no power is applied to the test plate. Conduction and radiation losses from the test plate are then taken into account so that plate surface temperatures may be corrected to account for deviations from an exact adiabatic condition. This approach is similar to procedures described by Mick and Mayle (1988) (also see Mehendale

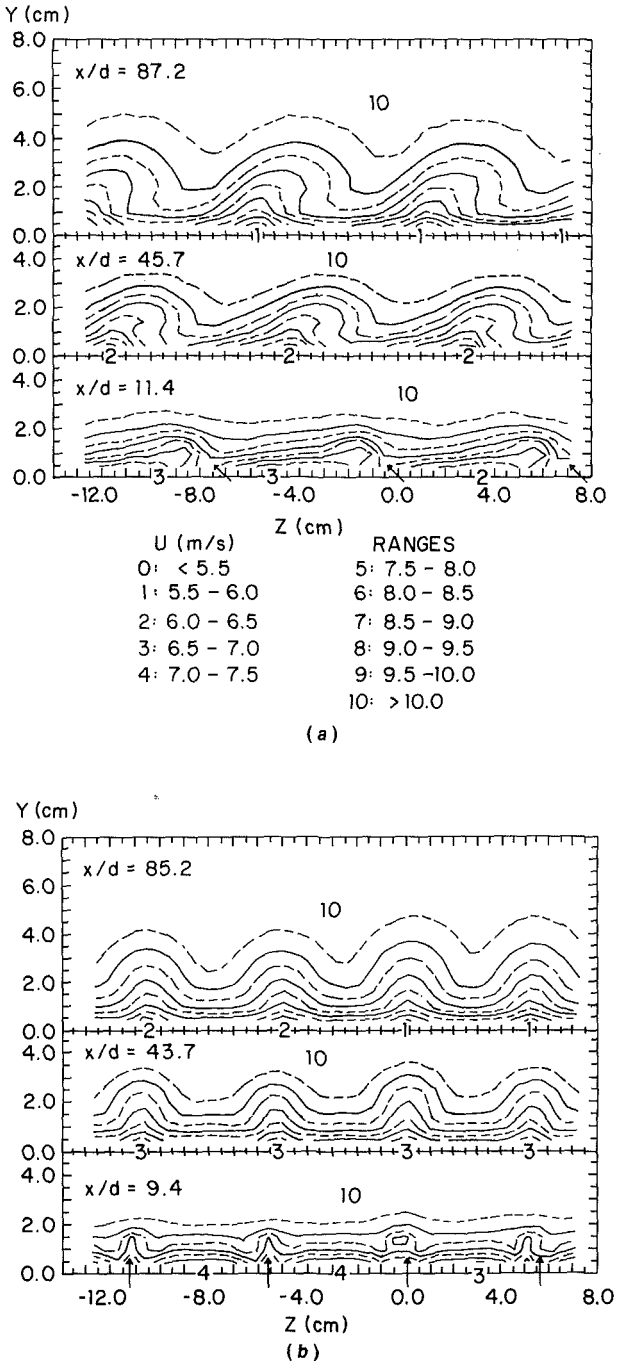

Fig. 5 Streamwise mean velocity development with streamwise distance, as measured downstream of one row of holes with $m = 1.0$: (*a*) compound angle configuration 1; (*b*) simple angle configuration 2

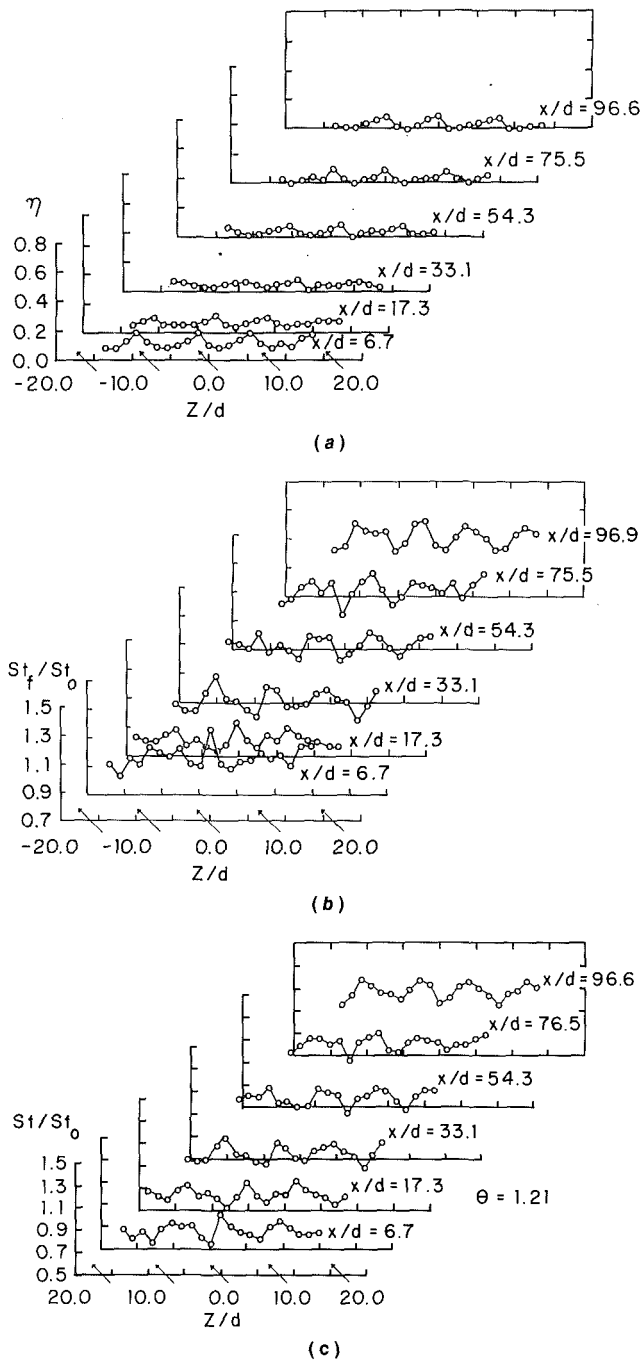

Fig. 6 Streamwise development of: (*a*) local adiabatic film cooling effectiveness, (*b*) local iso-energetic Stanton number ratios, and (*c*) local Stanton number ratios for $\theta = 1.21$, downstream of one row of compound angle configuration 1 film cooling holes with $m = 1.0$

and Han, 1992) wherein direct measurement of the adiabatic film cooling effectiveness relies on equations given by

$$\eta = (T_{aw} - T_{r,\infty})/(T_{r,c} - T_{r,\infty}) \quad (6)$$

and

$$\eta = (T_w - T_{r,\infty})/(T_{r,c} - T_{r,\infty}) + (q_{\text{rad}} + q_{\text{cond}})/h(T_{r,c} - T_{r,\infty}) \quad (7)$$

The second term on the right-hand side of Eq. (7) is thus employed because measured wall temperatures T_w are not exactly the same as the adiabatic wall temperatures T_{aw}. Here, h is the local heat transfer coefficient when the plate is heated. Spanwise-averaged effectiveness values from this direct approach match ones determined using linear superposition of St/St_o versus θ data for the same conditions within the uncertainty ranges of the present data. In most cases, deviations are 7–15 percent. Such agreement validates the linear superposition approach.

Compound Angle Injection From One Row of Holes

Boundary layer behavior downstream of a single row of compound angle film injection holes is discussed in this section. These results are important as they provide insight into the behavior and influences of injectant trajectories from individual holes. This is possible because the relatively large spacing between holes ($7.8d$) results in minimal coalescence of injectant fluid from adjacent holes until fairly large x/d.

Mean Velocity Surveys. Surveys of mean velocity measured downstream of one row of compound angle holes with

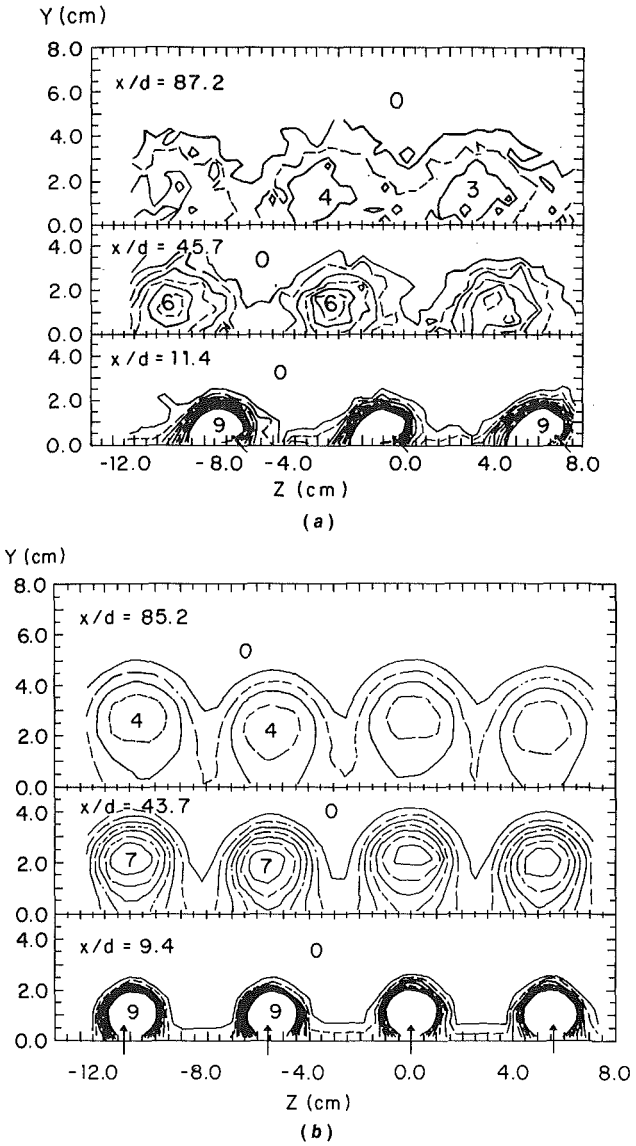

Fig. 7 Mean temperature field showing distributions of film injectant downstream of one row of film cooling holes with m = 1.0: (*a*) compound angle configuration 1; (*b*) simple angle configuration 2

a blowing ratio of 1.0 are presented in Fig. 5(*a*). Locations of film holes are denoted by arrows on the abscissa of this figure as well as on the one which follows. At x/d = 11.4, different velocity deficits are quite similar. Each one is skewed and flattened with the largest gradients in the direction that film is ejected from the surface at Y ranging from 0.5 cm to 2.0 cm. Because of the negative spanwise components of velocity at the exits of the film holes, deficits are also displaced about −1.8 cm by the time they reach x/d = 11.4. As the film-cooled boundary layer convects downstream to x/d of 45.7 and 87.2, the deficits are convected to even smaller Z locations.

Mean velocity surveys measured downstream of holes with simple angle orientations (configuration 2) also producing injectant at a blowing ratio of 1.0 are given in Fig. 5(*b*). At x/d = 9.4, high-velocity regions are present on either sides of velocity deficits. Similar distributions near injection holes are presented by Subramanian et al. (1990), who measured streamwise velocities downstream of a single simple angle injection hole (Ω = 30 deg and β = 90 deg) with m = 1.5. Mean vorticity distributions measured in conjunction indicate that variations such as the ones shown at x/d = 9.4 in Fig. 5(*b*) are due to vortex-like structures that form around the injectant as it leaves the holes. After comparing these results to the ones in the previous figure, it is apparent that velocity deficits are symmetric about streamwise/normal planes, and not skewed and flattened. Because the injectant emerges from the holes in the streamwise direction with no spanwise velocity component, the deficits in Fig. 5(*b*) are at the same spanwise locations as the injection holes as the film-cooled boundary layer convects downstream to x/d = 43.7 and x/d = 85.2.

Local Adiabatic Effectiveness, Injectant, and Stanton Number Ratio Distributions. Adiabatic film cooling effectiveness distributions, iso-energetic Stanton number ratios, Stanton numbers for θ values near 1.21, and injectant distribution surveys measured downstream of one row of compound angle holes are discussed in this section. Where possible, these are compared to results obtained downstream of simple angle holes.

Spanwise distributions of the adiabatic film cooling effectiveness η are presented in Fig. 6(*a*) at x/d of 6.7, 17.3, 33.1, 54.3, 75.5, and 96.6 for m = 1.0. At each streamwise location, η variations are spanwise periodic with Z/d, where higher values correspond to locations where injectant is plentiful. The spanwise periodicity is more pronounced at smaller x/d (6.7) and larger x/d (96.6). In the former case, this is due to accumulations of injectant such as the ones shown in Fig. 7(*a*) for x/d = 11.4. In the latter case, injectant accumulations are again important, however, perturbations to the velocity boundary layer such as the ones for x/d = 87.2 in Fig. 5(*a*) also play an important role.

Local St_f/St_o data, and St/St_o data for θ = 1.21 in Figs. 6(*b*) and 6(*c*) also show spanwise periodicity; however, this periodicity is somewhat out of phase with the η distributions. Here, higher values correspond to regions of higher mixing, which occur just to the left of injectant accumulations (at smaller Z/d), especially for St_f/St_o., These local maxima also correspond to high-velocity regions, which exist near the wall between the streamwise velocity deficits evident in Fig. 5(*a*).

Injection distribution surveys also measured downstream of one row of compound angle injection holes (configuration 1) with m = 1.0 are given in Fig. 7(*a*). These distributions are obtained using procedures described by Ligrani et al. (1989, 1991) in which the injectant is heated without providing any heat to the test plate. With this approach, the injectant is the only source of thermal energy relative to the free-stream flow. Distributions of $(T_o - T_{r,\infty})$ such as the ones in Fig. 7(*a*) thus show how injectant accumulates and is rearranged in the boundary layer, mostly as a result of convective processes including the influences of any secondary flows which may be present. Thus, the temperature field is employed to show injectant distributions in spanwise/normal planes at different streamwise locations.

As for the velocity surveys, arrows along the abscissa in Fig. 7(*a*) indicate film hole locations. Skewed and lop-sided injectant concentrations are evident in the spanwise/normal plane at x/d = 11.4 between regions where injectant is almost nonexistent. With streamwise convection to x/d of 45.7 and 87.2, these accumulations become more diffuse and dissipated. Injectant accumulations for all three x/d show close correspondence to streamwise velocity deficits in Fig. 5(*a*) and to local η maxima in Fig. 6(*a*), and approximate correspondence to locally lower St_f/St_o in Fig. 6(*b*). The distributions in Fig. 7(*a*) are significantly different from the ones in Fig. 7(*b*) measured at the same m downstream of one row of simple angle configuration 2 holes. Injection distributions in this latter figure represent circular or oval concentrations of injectant in spanwise/normal planes, which are present for all three x/d values.

Results showing the influences of blowing ratio on local η in the spanwise/normal plane at x/d = 6.7 are presented in Fig. 8(*a*). These data, which were obtained downstream of one row of compound angle holes, are presented for m of 0.5, 1.0, and 1.3, which are equivalent to momentum flux ratios of 0.25, 1.0, and 1.69. Spanwise periodic variations of η are

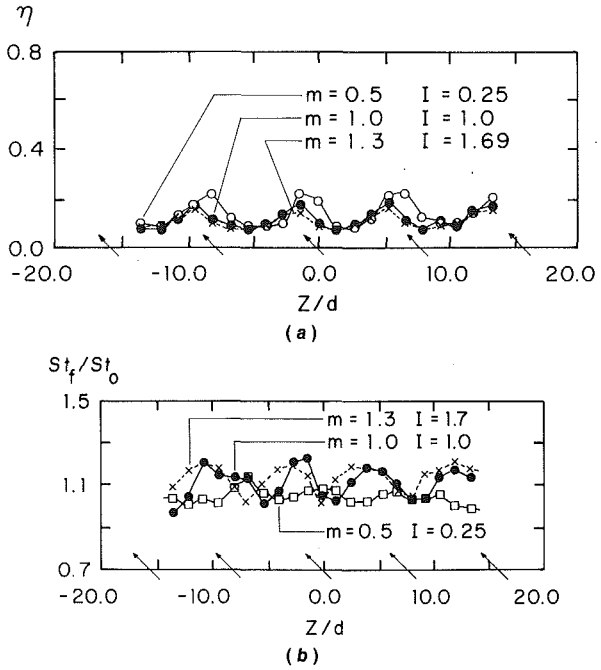

Fig. 8 Local variations of: (*a*) adiabatic film cooling effectivenss for *x/d* = 6.7 and (*b*) iso-energetic Stanton number ratio for *x/d* = 96.6, shown as dependent upon momentum flux ratio and blowing ratio, as measured downstream of one row of configuration 1 compound angle holes

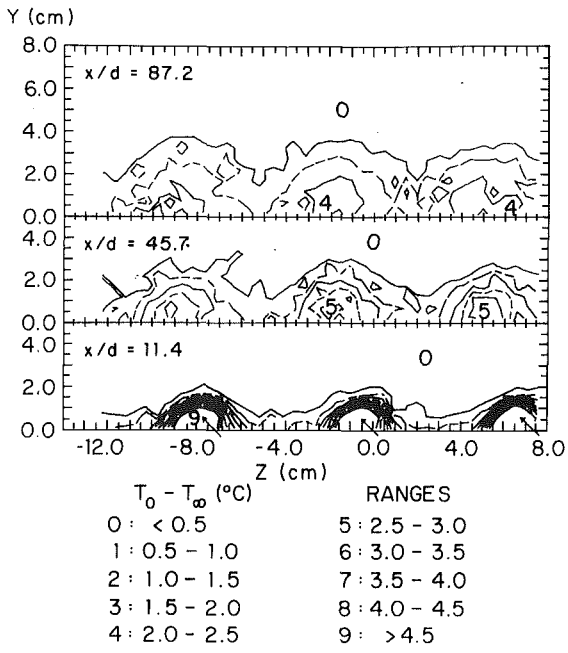

Fig. 9 Mean temperature field showing distributions of film injectant downstream of one row of compound angle configuration 1 film cooling holes with *m* = 0.5

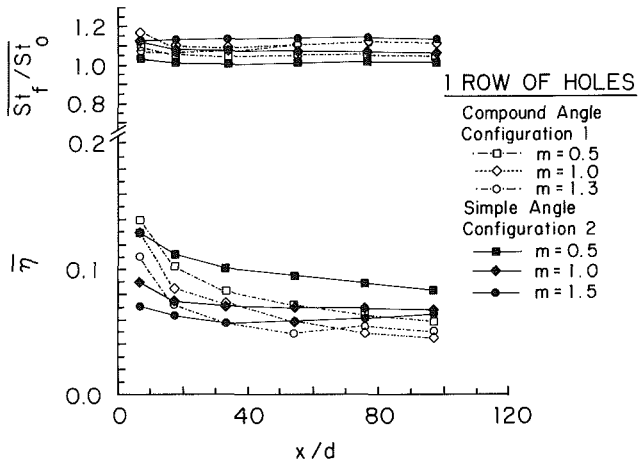

Fig. 10 Spanwise-averaged magnitudes of adiabatic film cooling effectiveness and iso-energetic Stanton number ratio, shown as dependent upon normalized streamwise distance downstream of one row of compound angle configuration 1 film cooling holes. Results are compared to ones measured downstream of one row of simple angle configuration 2 film-cooling holes.

evident for all three m, where the highest local maxima exist at the lowest blowing ratio because jet lift-off is more pronounced at the higher m. These local maxima shift to smaller Z/d as m increases because of injectant momentum, which causes injectant to move in the spanwise direction as it is convected downstream. This spanwise shift with streamwise convection is also evident in Fig. 9 for $m = 0.5$, which also shows significant accumulations of injectant at $x/d = 11.4$ located just to the left of the spanwise centerlines of the injection holes.

Results showing the influences of blowing ratio on local St_f/St_o for the spanwise/normal plane at $x/d = 96.6$ are presented in Fig. 8(*b*). Distributions for $m = 0.5$ show almost no spanwise periodicity. This is because of the diffuse distribution of injectant near this x/d, as illustrated by the $x/d = 87.2$ results in Fig. 9. However, for m of 1.0 and 1.3, significant local increases of St_f/St_o are evident in Fig. 8(*b*) as a result of disturbances to the boundary layer caused farther upstream by the injectant. As for the η distributions in the previous figure, these local maxima also shift to smaller Z/d as m increases because of spanwise convection of the injectant.

Spanwise-Averaged Adiabatic Film Cooling Effectiveness and Stanton Number Ratio Distributions. Spanwise-averaged magnitudes of the adiabatic film effectiveness, and of the iso-energetic Stanton number ratio, are presented in Fig. 10 as measured downstream of one row of compound angle holes. These are determined from averages (arithmetic means) of local distributions, such as the ones shown in Figs. 6(*a*) and 6(*b*). Referring to the spanwise-averaged effectiveness data for compound angle configuration 1, $\bar{\eta}$ decreases with x/d for each blowing ratio as injectant is diffused and convected downstream. For each x/d, $\bar{\eta}$ decreases with blowing ratio because of lift-off of the injectant from the surface.

Data for turbulent injection into a turbulent boundary layer from Goldstein and Yoshida (1982) show a similar trend since their $m = 0.5$ data are higher than their $m = 0.99$ data. Their results were obtained with simple angle holes ($\Omega = 30$ deg, $\beta = 90$ deg) spaced $3d$ apart. Lift-off becomes more severe as injectant momentum increases, and results in accumulation of free-stream and boundary layer fluid between the film and the surface. This diminishes the insulating characteristics of the film as well as the accompanying thermal protection ordinarily provided by it at lower m. $\bar{\eta}$ data from simple angle configuration 2 are also included on Fig. 10 for comparison, and generally cover about the same range of $\bar{\eta}$ as the compound angle data. This is important because the spanwise spacing between holes for the former case is $6.0d$, whereas for the latter case, it is $7.8d$. With the same spanwise hole spacing, the compound angle $\bar{\eta}$ data in Fig. 10 would be shifted about 30 percent higher, provided the magnitude of the effectiveness is solely tied to the amount of injectant issued from the injection holes per unit area of test surface. Even though the actual flow is more complicated, this provides some illustration of the improvements provided by compound angle injection over simple angle injection, especially for smaller x/d.

The spanwise-averaged iso-energetic Stanton number ratios

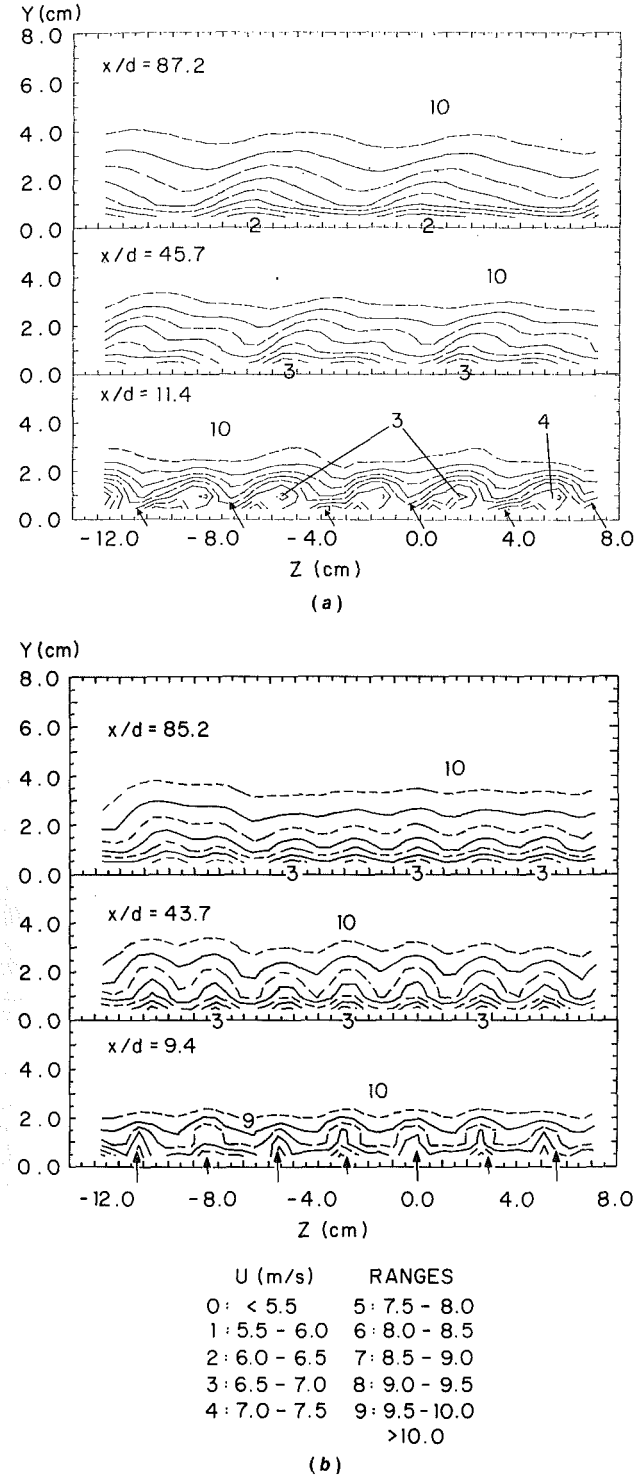

Fig. 11 Streamwise mean velocity development with streamwise distance, as measured downstream of two staggered rows of holes with m = 1.0: (*a*) compound angle configuration 1; (*b*) simple angle configuration 2

in Fig. 10 show little variation with x/d for each m. The compound angle data cover approximately the same range of values as the simple angle data, and show roughly the same trends, increasing with m at each x/d.

Compound Angle Injection From Two Staggered Rows of Holes

Boundary layer behavior downstream of two staggered rows of holes is different from behavior downstream of one row of holes (with twice the spanwise hole spacing) for two important reasons. First of all, because twice as many injection holes are present, twice as much injectant is spread over the same amount of test plate surface area. Second, injectant from adjacent holes merges and coalesces in ways that are not possible when one row of holes is employed because the injectant emerges from holes spaced more closely together. Such interactions are evident in the local distributions of mean velocity, injectant, effectiveness and Stanton number, as well as in the spanwise-averaged distributions of effectiveness and Stanton number described in this section.

Mean Velocity Surveys. Surveys of mean velocity measured downstream of two staggered rows of compound angle film holes with a blowing ratio of 1.0 are presented in Fig. 11(*a*). Locations of film holes are denoted by arrows on the abscissa, where large arrows denote holes in the downstream row and small arrows denote holes in the upstream row. At x/d = 11.4, velocity deficits are skewed and flattened with velocity gradients at Y ranging from 0.5 cm to 2.0 cm, which appear to be largest in the direction that film is ejected from the surface. Because of the negative spanwise components of velocity at the exits of the film holes, deficits are also displaced about −2.5 cm by the time they reach x/d = 11.4. Here, adjacent deficits appear to be quite similar even though they result from injectant that issues from staggered holes in two different rows. However, as the film-cooled boundary layer convects downstream, deficits resulting from injection from the downstream row of holes persist, whereas injectant deficits from the upstream row of holes become less apparent. This occurs because injectant from upstream holes eventually merges and coalesces with injectant that originated from holes in the downstream row. Consequently, half as many velocity deficits are eventually present across the measurement plane (with 7.8d spacing) at x/d of 87.2 compared to the x/d = 11.4 location.

The simple angle results in Fig. 11(*b*) for the same blowing ratio show considerably different qualitative and quantitative behavior. The x/d = 11.4 results in Fig. 11(*a*) show velocity deficits that are skewed and flattened with nonsymmetric velocity gradients. The x/d = 9.4 simple angle results in Fig. 11(*b*) show periodic velocity deficits across the span of the measurement plane. Because the injectant emerges from the holes in the streamwise direction with no spanwise velocity component, these deficits are at the same spanwise locations as the injection holes. In addition, the qualitative and quantitative characteristics of the different deficits are very similar even though adjacent film injection holes are staggered at different streamwise locations. As the film-cooled boundary layer then develops downstream, results at x/d = 43.7 and x/d = 85.2 show velocity deficits that continue to be spanwise periodic at the same spanwise locations as the results at x/d = 9.4. Adjacent deficits are spanwise similar at these far downstream locations, except for outer boundary layer regions at Z values less than −7.0 cm. Here, some spanwise nonuniformity is evident because these locations correspond to the spanwise edge of the rows of film holes. As for Fig. 11(*a*), spanwise locations of the film holes are indicated by arrows on the abscissa in Fig. 11(*b*), where large arrows denote holes in the downstream row and small arrows denote holes in the upstream row.

Local Adiabatic Effectiveness, Injectant, and Stanton Number Ratio Distributions. Adiabatic film cooling effectiveness distributions, iso-energetic Stanton number ratios, Stanton numbers for θ values near 1.44, and injectant distribution surveys are discussed in this section. Where possible, results are compared to measurements made downstream of two staggered rows of simple angle holes (configuration 2). Some influences of blowing ratio are also discussed.

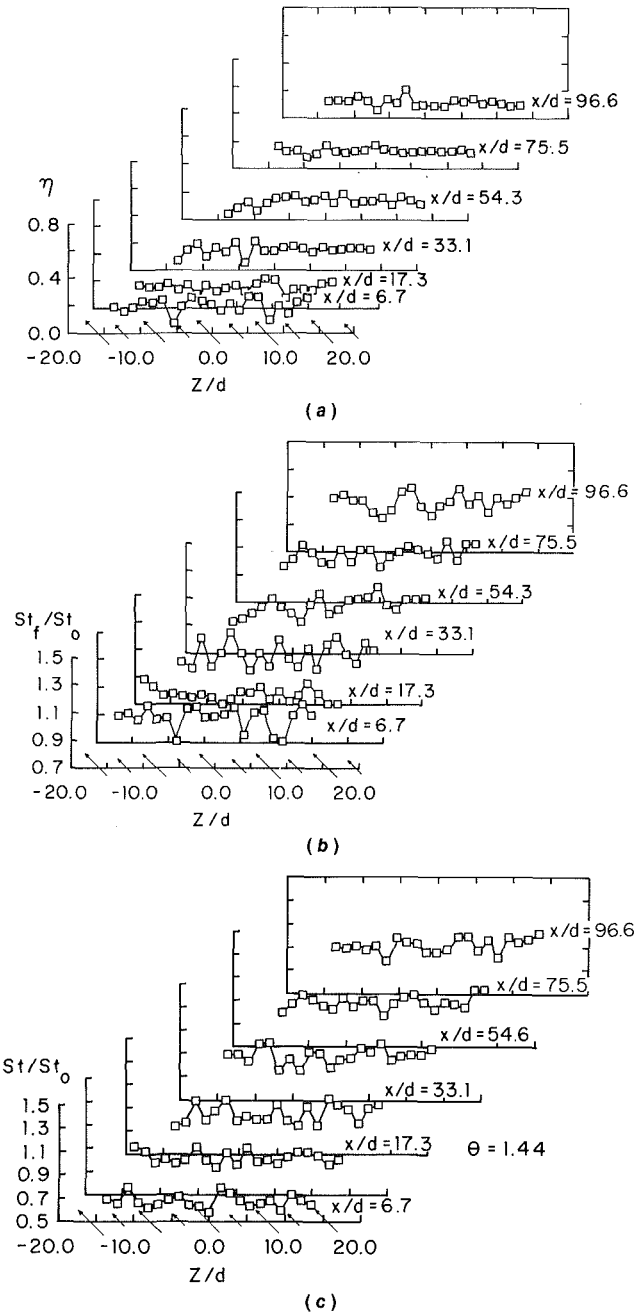

Fig. 12 Streamwise development of: (*a*) local adiabatic film cooling effectiveness, (*b*) local iso-energetic Stanton number ratios, and (*c*) local Stanton number ratios for $\theta = 1.44$, downstream of two staggered rows of compound angle configuration 1 film cooling holes with $m = 1.0$

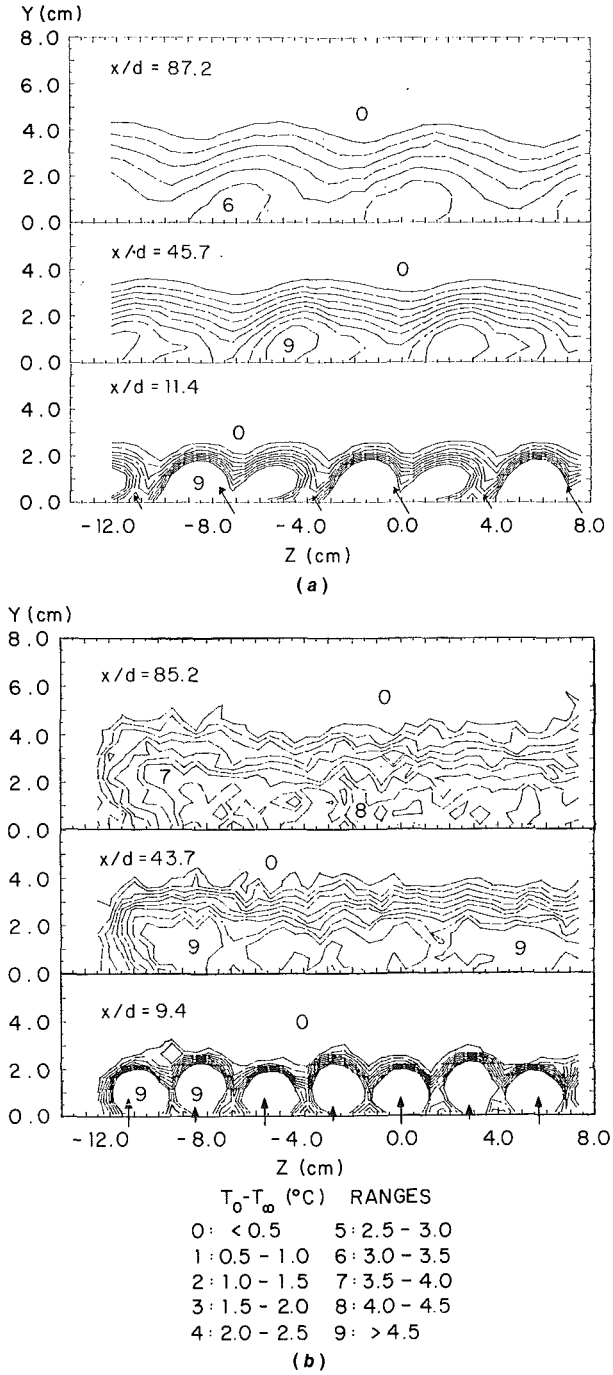

Fig. 13 Mean temperature field showing distributions of film injectant downstream of two staggered rows of film cooling holes with $m = 1.0$: (*a*) compound angle configuration 1; (*b*) simple angle configuration 2

Spanwise distributions of the adiabatic film cooling effectiveness η are presented in Fig. 12(*a*) at x/d of 6.7, 17.3, 33.1, 54.3, 75.5, and 96.6 downstream of the compound angle (configuration 1) holes with $m = 1.0$. Except for some small variations at $x/d = 6.7$, these data show spanwise unformity with Z/d for all six streamwise locations. Local St_f/St_o data, and St/St_o data for $\theta = 1.44$ in Figs. 12(*b*) and 12(*c*) show spanwise uniformity (with some scatter) for $x/d \leq 17.2$. However, in contrast to the η results, periodic St_f/St_o and St/St_o variations are present across the span of the test surface at larger x/d. These are particularly evident in the St_f/St_o data in Fig. 12(*b*) at x/d of 33.1, 54.3, 75.4, and 96.6. At $x/d = 33.1$, alternately large and small St_f/St_o peaks exist. These local maxima correspond to high velocity reigons that exist near the wall between the alternately large and small streamwise velocity deficits evident in Fig. 11(*a*) for $x/d = 45.7$. At $x/d = 87.2$, Fig. 11(*a*) then shows evidence only of the larger streamwise velocity deficits spaced about $7.8d$ apart. Between these deficits, high-velocity regions near the wall correspond to areas where St_f/St_o show local maxima at locations such as $x/d = 96.6$ in Fig. 12(*b*).

Local η, St_f/St_o, and St/St_o data for $\theta = 1.5$ measured downstream of the simple angle configuration 2 are different from the compound angle results because they show spanwise uniformity for Z/d from -10.0 to 10.0 for x/d from 6.8 to 96.7 (Bishop, 1990; Ciriello, 1991). Such behavior evidences spanwise uniform injectant coverage along the test surface even though the film issues from discrete holes, and even though spanwise periodic velocity deficits such as the ones shown in Fig. 11(*b*) are present.

Injection distribution surveys corresponding to the same

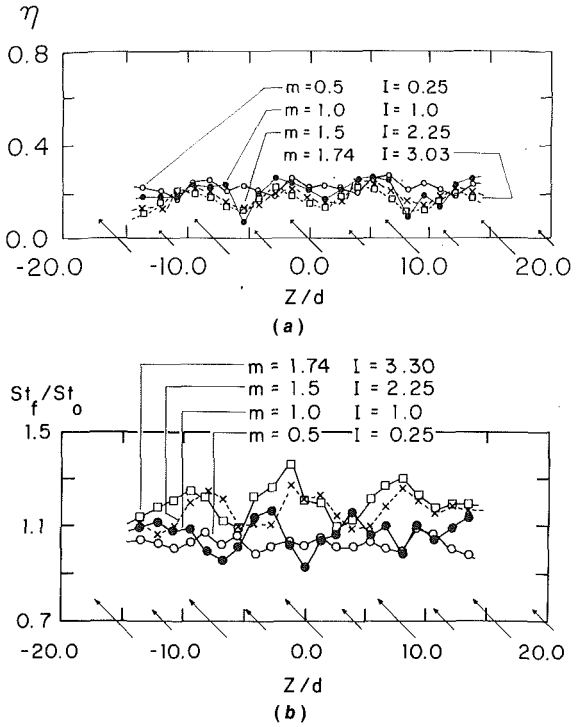

Fig. 14 Local variations of : (*a*) adiabatic film cooling effectiveness for x/d = 6.7 and (*b*) iso-energetic Stanton number ratio for x/d = 96.6, shown as dependent upon momentum flux ratio and blowing ratio, as measured downstream of two staggered rows of configuration 1 compound angle holes

experimental conditions as the results in Figs. 11(*a*) and 12 are given in Fig. 13(*a*) (m = 1.0 with compound angle configuration 1). Large and small arrows along the abscissa indicate film hole locations in downstream and upstream rows, as before. Significant injectant concentrations are evident at x/d = 11.4 where accumulations from the downstream row of holes cover larger portions of the measurement plane than accumulations from the upstream row of holes. With streamwise convection to x/d of 45.7 and 87.2, half as many injectant accumulations are present in the spanwise direction since injectant from the upstream row of holes has merged with the injectant from the downstream row of holes. This behavior is completely consistent with the velocity survey of Fig. 11(*a*), since injectant accumulations for all three x/d show close correspondence to streamwise velocity deficits. Streamwise velocity deficits at x/d of 45.7 and 87.2 also closely correspond to locally lower St_f/St_o in Fig. 12(*b*) for x/d of 54.3, 75.4, and 96.6. St_f/St_o increases most often seem to occur at locations where streamwise velocities are locally higher, which sometimes also correspond to regions where turbulent mixing is locally higher.

Injection distribution surveys are presented in Fig. 13(*b*) measured downstream of two staggered rows of simple angle configuration 2 holes with a blowing ratio m of 1.0. Injectant distributions in this figure are significantly different from the ones in Fig. 13(*a*). At x/d = 9.4, large circular concentrations of injectant are seen across the span of the measurement plane. Every other accumulation is qualitatively similar and adjacent distributions are different since injectant from the downstream row of holes is located slightly closer to the wall than injectant from the upstream row of holes. However, in spite of this spanwise periodicity, η, St/St_o and St_f/St_o data measured downstream of the simple angle holes show little spanwise variations at slightly lower (6.7) and slightly higher (17.2) values of x/d. With downstream development, results for x/d = 43.7 and 85.2 in Fig. 13(*b*) indicate that injectant accumulations from neighboring holes eventually merge together to form a spanwise uniform layer across the span of the test surface. This layer discontinues for Z values less than -13 cm since no injection holes are located at $Z < -11.3$ cm.

Results showing the influences of blowing ratio on local η for x/d = 6.7 and on local St_f/St_o for x/d = 96.6 are presented in Figs. 14(*a*) and 14(*b*), respectively. These data, which were obtained downstream of two staggered rows of compound angle holes, are presented for m of 0.5, 1.0, 1.5, and 1.74, which are equivalent to momentum flux ratios of 0.25, 1.0, 2.25, and 3.03. Figure 14(*a*) shows spanwise periodic variations of η at m = 1.0, m = 1.5, and m = 1.74 with minima that become lower as the blowing ratio increases. Significant η decreases with m are also evident just to the left of these minima (at smaller Z/d). η for these conditions are generally lower than when the blowing ratio is 0.5 because of injectant jet lift-off from the test surface at the higher m.

St_f/St_o distributions for x/d = 96.6 in Fig. 14(*b*) show almost no spanwise periodicity for m = 0.5. However, as m increases to 1.0 and greater, spanwise periodicity develops with amplitude variations that become large with blowing ratio. Corresponding local maxima are tied to higher streamwise velocities and to higher levels of turbulence near the wall. Turbulence levels are believed to increase as injectant with greater amounts of momentum is injected into the boundary layer, and as larger amounts of injectant from the upstream row of holes coalesce with injectant from the downstream row of holes. The consequences of this coalescence seem to be more pronounced as m increases, partly because the merging occurs at locations that are farther upstream as the blowing ratio increases (Ciriello, 1991). In any case, the magnitudes of the St_f/St_o variations at x/d = 96.6 show how persistent such disturbances are in turbulent boundary layers as they retain their history over a very large range of x/d.

Of the blowing ratios tested, m = 0.5 appears to be optimal because of greater spanwise uniformity of local η and St_f/St_o data, and because of higher η magnitudes at x/d = 6.7. Corresponding injectant distributions in Fig. 15 for x/d = 45.7 and x/d = 87.2 are consistent since they show fairly good uniformity across the span of the measurement plane. Thus, spanwise uniform coverage is provided that is not present at x/d = 45.7 and 87.2 with higher blowing ratios (i.e., m = 1 data in Fig. 13*a*). At x/d = 11.4, injectant accumulations in Fig. 15 are spanwise periodic. Every other one of these accumulations is qualitatively similar just like the results in Fig. 13(*a*) at the same x/d (11.4).

Spanwise-Averaged Adiabatic Film-Cooling Effectiveness and Stanton Number Ratio Distributions. Spanwise-averaged values of the adiabatic film cooling effectiveness measured downstream of two staggered rows of compound angle holes (configuration 1) are presented in Fig. 16. Data at x/d less than 20 decrease with blowing ratio because of injection lift-off effects. However, as the boundary layers convect farther downstream, $\bar{\eta}$ values for m = 0.5 are lower than values for m = 1.0, 1.5, and 1.74 since a smaller amount of film is spread along the test surface. These differences also result partially because of the different ways in which the injectant spreads along the test surface. When m = 0.5, the injectant is fairly uniform along the test surface, especially for $x/d \geq 45.7$ (Fig. 15). However, at the higher blowing ratios ($m \geq 1.0$), injectant from the upstream row of holes coalesces with injectant from the downstream row of holes (Figs. 11*a* and 13*a*) resulting in distributions that are spatially nonuniform across the test surface span at x/d even as large as 96.6. This is probably one reason why spanwise-averaged effectiveness values for the three highest m collapse along the same curve for $x/d \geq 40 - 50$.

The $\bar{\eta}$ data from the simple angle two-row arrangement are included on Fig. 16 for comparison. These lie above the compound angle data, especially for $x/d \geq 40 - 50$. However, if one

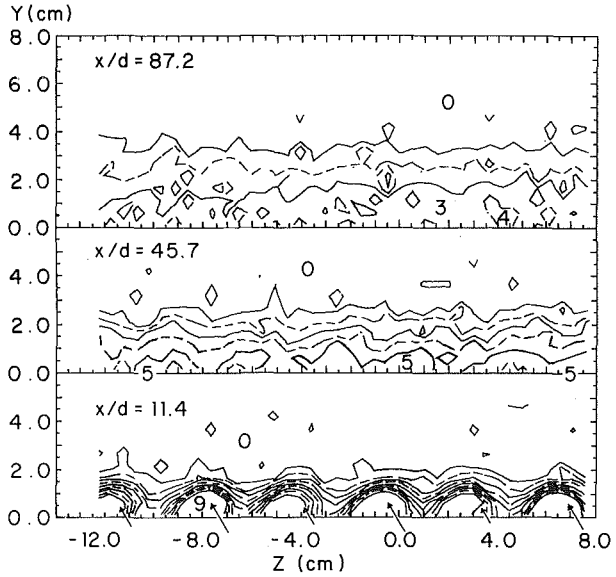

Fig. 15 Mean temperature field showing distributions of film injectant downstream of two staggered rows of compound angle configuration 1 film cooling holes with m = 0.5

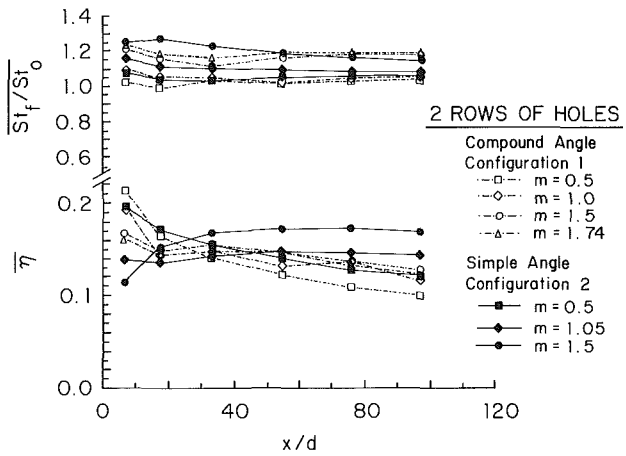

Fig. 16 Spanwise-averaged magnitudes of adiabatic film cooling effectiveness and iso-energetic Stanton number ratio, shown as dependent upon normalized streamwise distance downstream of two staggered rows of compound angle configuration 1 film cooling holes. Results are compared to ones measured downstream of two staggered rows of simple angle configuration 2 film-cooling holes.

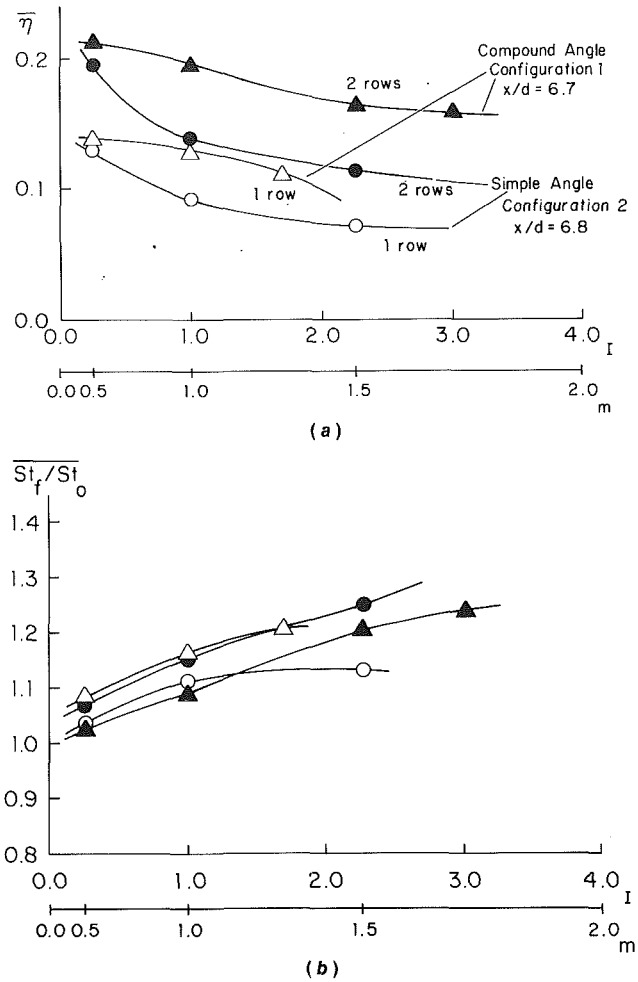

Fig. 17 (*a*) Spanwise-averaged magnitudes of adiabatic film cooling effectiveness and (*b*) spanwise-averaged magnitudes of iso-energetic Stanton number ratio, shown as dependent upon momentum flux ratio and blowing ratio for x/d = 6.7-6.8

accounts for the fact that the spanwise hole spacing is larger for the compound angle case (3.9*d* compared to 3.0*d*), then these data would be shifted about 30 percent higher (with 3.0*d* spanwise hole spacing) if the magnitude of the effectiveness is tied solely to the amount of injectant issued from the injection holes per unit area of test surface. Of course, the actual physical processes are more complicated. A 30 percent shift would move the compound angle data in Fig. 16 over the same range as the simple angle data at $x/d \geq 40-50$. At smaller x/d, the compound angle data would then be higher after the shift, which indicates improved protection for the same spanwise hole spacing.

Jabbari and Goldstein (1978) measured the adiabatic film cooling effectiveness downstream of two staggered rows of simple angle holes having geometries similar to the simple angle holes used in the present study. Because their spanwise hole spacings are half as much (1.5*d*), their $\bar{\eta}$ data are 60-80 percent higher when compared at $m = 0.5$.

The trends of the present simple angle data in Fig. 16 are fairly complex at $x/d \leq 30-40$. Complicated lift-off behavior is evidenced by $\bar{\eta}$ values, which decrease with m at x/d = 6.8 but change from this trend at x/d = 17.4, and x/d = 33.2. The qualitative trends shown by these data for m = 0.5 and m = 1.0 are similar to trends measured by Goldstein and Yoshida (1982) downstream of a single row of simple angle holes (turbulent injection, turbulent free stream, 3*d* spacing, $\Omega = 30$ deg and $\beta = 90$ deg) with the same m. At larger x/d (> 50-60), simple angle $\bar{\eta}$ values in the present study (Fig. 16) increase with blowing ratio, which is consistent with the fact that more injectant is present along the test surface to provide better heat sink characteristics and improved thermal protection. In addition, effectiveness, Stanton number ratios, and injectant distributions for the same x/d indicate that this injectant is spread fairly uniformly over the test surface for all three m tested.

The Goldstein and Yoshida (in this paragraph referred to as G & Y) data for m = 0.5 are in approximate agreement with the $m = 0.5$ compound angle data in Fig. 16. When compared to our simple angle data for m = 0.5, the G & Y data are in approximate agreement for $x/d < 20$. However, for $20 < x/d < 50$, the G & Y data are 15-30 percent lower than the present simple angle results. Some of these differences are because G & Y employ a single row of holes instead of two staggered rows (even though the adjacent spanwise hole spacing is the same, 3.0*d*), and because G & Y use a different injection to free-stream density ratio (theirs is 0.85, ours is near 1.0). Some of the differences are also probably because of the different thermal boundary conditions imposed in the two investigations. However, after accounting for these differences,

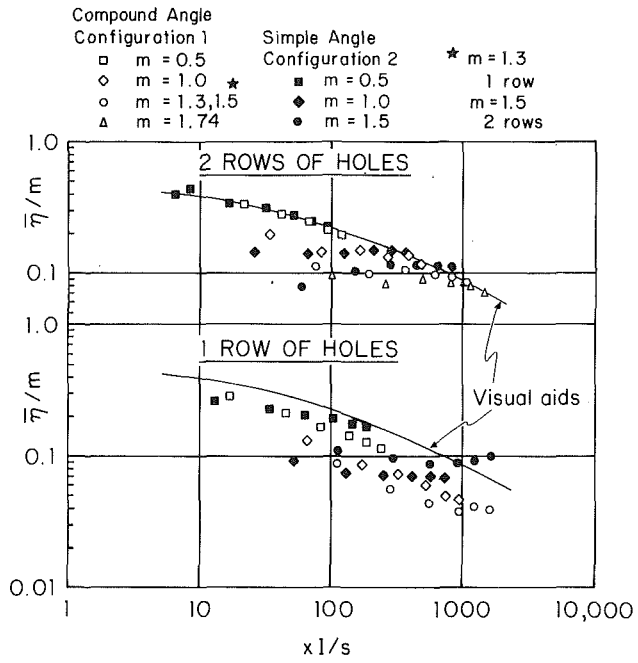

Fig. 18 Adiabatic film-cooling effectiveness data at different blowing ratios, simple angle configuration 2 and compound angle configuration 1: (*a*) downstream of two staggered rows of holes; (*b*) data downstream of one row of holes

the present results may still be 0.01–0.03 effectiveness units higher than G & Y at the same x/d and m.

Spanwise-averaged iso-energetic Stanton number ratios in Fig. 16 show trends similar to ones observed for injection from one row of holes: (1) little $\overline{St_f/St_o}$ variation with x/d is evident for each value of m, (2) compound angle data cover approximately the same range of values as the simple angle data, and (3) for each x/d, $\overline{St_f/St_o}$ values increase with m. Data for $m = 0.5$ show agreement with data from Goldstein and Yoshida (1982) for turbulent injectant into a turbulent boundary layer at the same blowing ratio m.

Influences of Blowing Ratio and Momentum Flux Ratio

Influences of blowing ratio and momentum flux ratio are discussed in reference to Figs. 17(*a*) and 17(*b*), which present data measured at $x/d = 6.7-6.8$. Spanwise-averaged film effectiveness values are presented in the first of these figures for compound angle configuration 1 and for simple angle configuration 2. The compound angle $\bar{\eta}$ data show only a gradual decrease as the momentum flux ratio I increases from 0.25 to 3.0, especially for the two-row case. With two rows, lift-off of the injectant from the test surface is probably occurring at momentum flux ratios between 1.0 and 2.0. In contrast, $\bar{\eta}$ data measured downstream of the simple angle configuration show significant decreases as I increases from 0.25 to 1.0, indicating lift-off at a lower value of momentum flux. These differences result for two principal reasons. First, the lateral component of momentum of the injectant from the compound angle holes causes the injectant to spread out much more in the lateral direction as it is convected downstream and penetrates into the mainstream. Second, the hole angles with respect to the test surface are 24 deg for the compound angle arrangement compared to 35 deg for the simple angle arrangement. Although it is not so apparent from the data presented in Fig. 17(*a*), comparison of Figs. 10 and 16 reveals that injection lift-off is more likely to occur with one row of holes (with $7.8d$ spacing) than with two staggered rows (with $3.9d$ spacing). Because the present density ratio in the present study is near 1, the variation of momentum flux ratio is larger than if the density ratio is near 2 for the range of blowing ratios shown in Fig. 17(*a*). Consequently, our data are more likely to show lift-off effects at a given m than if a higher density ratio is used.

The present spanwise-averaged film effectiveness data are also plotted in Fig. 18 using $\bar{\eta}/m$ versus XI/s coordinates. The amount of scatter shown is about the same in $\bar{\eta}/I$ versus XI/s coordinates. However, in both cases, the data show better collapse than if $\bar{\eta}$ versus Xm/s, η versus X/ms, or η versus $(X/ms)\mathrm{Re}_d - 0.25$ coordinates are employed (Ciriello, 1991). At a particular x/d, Pedersen et al. (1977) used coordinates similar to the ones employed in Fig. 18 (η/m versus I) to collapse data with different injectant to free-stream density ratios together.

In Fig. 17(*b*), $\overline{St_f/St_o}$ data for $x/d = 6.7-6.8$, are seen to increase with m and I because mixing levels in the boundary layer increase with injectant momentum flux. Values measured downstream of 2 rows of simple angle holes and downstream of 1 row of compound angle holes are slightly higher than the other data at each m and I. However, generally, the data for both injection configurations show about the same trend regardless of whether one or two rows of holes is employed. Jabbari and Goldstein (1978) also observed increases of $\overline{h_f/h_o}$ with m in their study of flow downstream of two staggered rows of simple angle holes. Their data are in reasonable agreement with the results in Fig. 17(*b*). For $m > 0.5$, they attribute these increases to "agitation of flow due to the injection at higher velocities."

Summary and Conclusions

Experimental results are presented that describe the development and structure of flow downstream of a single row and two staggered rows of film-cooling holes with compound angle orientations. With this configuration, holes are inclined at 35 deg with respect to the test surface when projected into the streamwise/normal plane, and 30 deg with respect to the test surface when projected into the spanwise/normal plane. Within each row, holes are spaced 7.8 hole diameters apart, which gives $3.9d$ spacing between holes with two staggered rows. Results are presented for an injectant to free-stream density ratio near 1.0, x/d ranging from 6.7 to 96.7, injectant blowing ratios from 0.5 to 1.74, and momentum flux ratios from 0.25 to 3.03.

Spanwise-averaged values of the adiabatic film cooling effectiveness measured downstream of two staggered rows of compound angle holes are highest with a blowing ratio of 0.5, and decrease with blowing ratio because of injection jet lift-off effects for $x/d < 20$. However, as the boundary layers convect farther downstream, $\bar{\eta}$ values for $m = 0.5$ are lower than values for $m = 1.0$, 1.5, and 1.74 since a smaller amount of film is spread along the test surface. Local and spanwise-averaged variations at higher m result, in part, because injectant from the upstream row of holes eventually merges and coalesces with the injectant from the downstream row of holes. This is evident from velocity and injectant surveys, which show half as many velocity deficits and injectant accumulations across spanwise/normal planes (with $7.8d$ spacing) at x/d of 87.2 compared to $x/d = 11.4$. In contrast, the injectant with $m = 0.5$ is fairly uniform along the span of the test surface, especially for $x/d \geq 45.7$.

The results obtained downstream of the single row of compared angle injection holes (with $7.8d$ spacing) are important since the behavior of injectant trajectories from individual holes is apparent. This is because there is minimal coalescence of injectant fluid from adjacent holes until larger x/d. Such coalescence often delays lift-off, especially when two rows of holes are employed. With the one-row arrangement, local η variations are spanwise periodic with Z/d, where higher values correspond to locations where injectant is plentiful near the test surface. Local St_f/St_o data also show spanwise periodicity.

However, for $x/d \geq 33.1$, this periodicity is somewhat out of phase with the η distributions, with local St_f/St_o maxima that correspond to high velocity (and often high mixing) regions near the wall. These exist between streamwise velocity deficits, which are skewed and flattened in spanwise/normal planes with the largest gradients in the direction that film is ejected from the surface. For each x/d, $\overline{\eta}$ is highest for $m \simeq 0.5$, and generally decreases with blowing ratio because of increased lift-off of the injectant from the surface. Lift-off influences are also evident in local η distributions that show local maxima, which also decrease significantly with blowing ratio.

For measurements downstream of both one row of holes and downstream of two rows of holes, spanwise-averaged isoenergetic Stanton number ratios range between 1.0 and 1.25, and show little variation with x/d for each value of m tested. However, for each x/d, $\overline{St_f/St_o}$ values increase with m.

η and $\overline{St_f/St_o}$ data from the compound angle arrangements are compared to results obtained downstream of film holes with simple angle orientations. Because the spanwise hole spacing is larger for the compound angle case ($3.9d$ compared to $3.0d$ for two rows, and $7.8d$ compared to $6.0d$ for one row), an $\overline{\eta}$ increase of about 30 percent is required to compare the two sets for the same spanwise hole spacing. After accounting for this, measurements downstream of two rows of compound angle holes would lie over the same range as the simple angle data at $x/d \geq 40$–50. At smaller x/d, the compound angle data would then be higher, which indicates improved protection for the same spanwise hole spacing. With one row of holes, the compound angle arrangement would provide improvements over the entire range of x/d studied (6.7–96.6), especially for smaller values. Compound angle $\overline{St_f/St_o}$ data cover approximately the same range of values and show roughly the same trends as the simple angle data.

Injectant lift-off downstream of two rows of compound angle holes is occurring at momentum flux ratios between 1.0 and 2.0. In contrast, $\overline{\eta}$ data from the two-row simple angle arrangement evidence lift-off as I increases from 0.25 to 1.0. These differences result because: (1) the lateral component of momentum of the injectant from the compound angle holes causes the injectant to spread out much more in the lateral direction as it is convected downstream, and (2) injectant from the compound angle holes emerges at smaller angles with respect to the plate surface (24 deg instead of 35 deg) even though hole projections in the streamwise/normal planes are the same. Because less coalescence of injectant distributions is occurring downstream of the one-row arrangements, lift-off occurs at slightly lower I compared to the two hole arrangements for simple and compound angle holes. Except for the most severe lift-off situations ($m = 1.0$ and $m = 1.5$ for two rows of simple angle holes), spanwise-averaged effectiveness values are highest at low x/d values, and decrease with increasing x/d (at a particular m) as diffusion of the injectant occurs with downstream convection.

In summary, variations of effectiveness data are mostly due to four parameters: number of rows of injection holes, angular configuration of the film injection holes (simple or compound), blowing ratio/momentum flux ratio, and spanwise spacing of holes in individual rows. Because the spanwise spacing of adjacent holes is half as much for the two staggered hole arrangement ($3.9d$) compared to the one row arrangement ($7.8d$), spanwise-averaged adiabatic effectiveness values are about twice as high. Comparing compound angle injection results to ones from simple angle holes reveals significant differences related to the spanwise component of velocity which results from the compound angle holes. The momentum flux ratio has important consequences in regard to injectant lift-off, and the blowing ratio is important in regard to injectant coverage. Spanwise-hole spacing with either one row or two rows of holes is important in regard to injection coalescence and injectant coverage along the test surface.

Acknowledgments

All of the results presented were obtained at the Naval Postgraduate School. This study was supported, in part, by the Aero-Propulsion Laboratory of Wright Patterson Air Force Base, MIPR Number FY 1455-89-N0670. Dr. Bill Troha was program monitor. Some of the facilities used were purchased using funds from the Naval Postgraduate School Foundation Research Program. Mr. D. M. Kercher, Mr. S. W. Mitchell, Mr. S. M. Jackson, and Professor C. S. Subramanian are also acknowledged for useful discussions of the experiment and results, and/or assistance in obtaining some of the data.

References

Bishop, D. T., 1990, "Heat Transfer, Adiabatic Effectiveness and Injectant Distributions Downstream of Single and Double Rows of Film-Cooling Holes With Compound Angles," M. S. Thesis, Department of Mechanical Engineering, Naval Postgraduate School, Monterey, CA.

Ciriello, S. 1991, "Heat Transfer, Adiabatic Effectiveness and Injectant Distributions Downstream of Single and Double Rows of Film-Cooling Holes With Simple and Compound Angles," M. S. Thesis, Department of Mechanical Engineering, Naval Postgraduate School, Monterey, CA.

Goldstein, R.J., 1971, "Film Cooling," *Advances in Heat Transfer*, Vol. 7, Academic Press, pp. 321–379.

Goldstein, R. J., and Yoshida, T., 1982, "The Influence of a Laminar Boundary Layer and Laminar Injection on Film Cooling Performance," ASME *Journal of Heat Transfer*, Vol. 104, pp. 355–362.

Ito, S., Goldstein, R. J., and Eckert, E. R. G., 1978, "Film Cooling of a Gas Turbine Blade," ASME *Journal of Engineering for Power*, Vol. 100, pp. 476–481.

Jabbari, M. Y., and Goldstein, R. J., 1978, "Adiabatic Wall Temperature and Heat Transfer Downstream of Injection Through Two Rows of Holes," ASME *Journal of Engineering for Power*, Vol. 100, pp. 303–307.

Kays, W. M., and Crawford, M. E., 1980, *Convective Heat and Mass Transfer*, 2nd ed., McGraw-Hill, New York.

Klebanoff, P. S., 1954, "Characteristics of Turbulence in a Boundary Layer With Zero Pressure Gradient," NACA Technical Note 3178.

Kline, S. J., and McClintock, F. A., 1953, "Describing Uncertainties in Single-Sample Experiments," *Mechanical Engineering*, Vol. 75, pp. 3–8.

Ligrani, P. M., and Camci, C., 1985, "Adiabatic Film Cooling Effectiveness From Heat Transfer Measurements in Compressible, Variable Property Flow," ASME *Journal of Heat Transfer*, Vol. 107, pp. 313–320.

Ligrani, P. M., Ortiz, A., Joseph, S. L., and Evans, D. L., 1989, "Effects of Embedded Vortices on Film-Cooled Turbulent Boundary Layers," ASME JOURNAL OF TURBOMACHINERY, Vol. 111, pp. 71–77.

Ligrani, P. M., 1990, "Comment on 'Behavior of a Coolant Film With Two Rows of Holes Along the Pressure Side of a High Pressure Nozzle Guide Vane'," ASME JOURNAL OF TURBOMACHINERY, Vol. 112, pp. 520–521.

Ligrani, P. M., Subramanian, C. S., Craig, D. W., and Kaisuwan, P., 1991a, "Effect of Vortices With Different Circulations on Heat Transfer and Injectant Downstream of a Row of Film-Cooling Holes in a Turbulent Boundary Layer," ASME *Journal of Heat Transfer*, Vol. 113, pp. 79–90.

Ligrani, P. M., Ciriello, S., and Bishop, D. T., 1991b, "Heat Transfer, Adiabatic Effectiveness and Injectant Distributions Downstream of a Single Row and Two Staggered Rows of Compound Angle Film-Cooling Holes," *Heat Transfer in Gas Turbine Engines*, ASME HTD-Vol. 188, pp. 37–51.

Loftus, P. J., and Jones, T. V., 1983, "The Effect of Temperature Ratios on the Film-Cooling Process," ASME *Journal of Engineering for Power*, Vol. 105.

Mehendale, A. B., and Han, J. C., 1992, "Influence of High Mainstream Turbulence on Leading Edge Film Cooling Heat Transfer," ASME JOURNAL OF TURBOMACHINERY, Vol. 114, this issue, pp. 707–715.

Metzger, D. E., Carper, H. J., and Swank, L. R., 1968, "Heat Transfer With Film Cooling Near Nontangential Injection Slots," ASME *Journal of Engineering for Power*, Vol. 90, pp. 157–163.

Mick, W. J., and Mayle, R. E., 1988, "Stagnation Film Cooling and Heat Transfer, Including Its Effect Within the Hole Pattern," ASME JOURNAL OF TURBOMACHINERY, Vol. 110, pp. 66–72.

Moffat, R. J., 1982, "Contributions to the Theory of Single-Sample Uncertainty Analysis," ASME *Journal of Fluids Engineering*, Vol. 104, pp. 250–260.

Pedersen, D. R., Eckert, E. R. G., and Goldstein, R. J., 1977, "Film Cooling With Large Density Differences Between the Mainstream and the Secondary Fluid Measured by the Heat-Mass Transfer Analogy," ASME *Journal of Heat Transfer*, Vol. 99, pp. 620–627.

Subramanian, C. S., Ligrani, P. M., Green, J. G., and Doner, W. D., 1990, "Development and Structure of a Film-Cooling Jet in a Turbulent Boundary Layer With Heat Transfer," *Third International Symposium on Transport Phenomena and Dynamics of Rotating Machinery (ISROMAC-3), Vol. 1: Transport Phenomena*, pp. 49–64, Honolulu, HI.

Wigle, J. M., 1991, "Heat Transfer Adiabatic Effectiveness and Injectant Distributions Downstream of Single and Double Rows of Film Cooling Holes With Compound Angles," M.S. Thesis, Department of Mechanical Engineering, Naval Postgraduate School, Monterey, CA.

Discharge Coefficients of Cooling Holes With Radiused and Chamfered Inlets

N. Hay

A. Spencer[1]

Department of Mechanical Engineering,
University of Nottingham,
Nottingham, NG7 2RD, United Kingdom

The flow of cooling air within the internal passages of gas turbines is controlled and metered using orifices formed of holes in disks and casings. The effects of inlet radiusing and chamfering of these holes on the discharge coefficients forms the subject of this paper. Experimental results for a range of radiusing and chamfering ratios for holes of different length-to-diameter ratios are presented covering the range of pressure ratios of practical interest. The results indicate that radiusing and chamfering are both beneficial in increasing the discharge coefficient. Increases of 10–30 percent are possible. Chamfered holes give the more desirable performance characteristics in addition to being easier to produce than radiused holes.

1 Introduction

Gas turbine engines incorporate a multiplicity of internal passages, which serve to channel the cooling air tapped from the compressors to the various components to be cooled (Fig. 1). These internal flows need to be metered and the pressure drop associated with the metering needs to be as low as possible.

Metering is effected by holes in casings, disks, and blades, which could have a wide range of length-to-diameter ratios and which will operate at an equally wide range of pressure ratios. In the design of the air distribution system, knowledge of the value of the discharge coefficient C_d for these holes is required for the whole range of operating conditions envisaged.

The usual method of keeping the pressure drop associated with metering as low as possible is to use rounded instead of sharp edges at entry to the metering hole or orifice. For short orifices, rounding, or more precisely radiusing helps to reduce or suppress the vena contracta associated with the sharp edge, as shown in Fig. 2. Thus the discharge coefficient rises above the value of 0.61 associated with sharp-edged short orifices. For a given flow this means that metering can be effected with a smaller pressure drop penalty.

If a sharp-edged orifice is long enough ($L/D > 2.0$) the flow reattaches downstream, as shown in Fig. 3, and produces a measure of pressure recovery. Thus the coefficient of discharge will be higher than for the corresponding short orifice. Radiusing is still beneficial but not to the same extent as for short orifices. The improvement in the case of the short as well as the long orifice is a function of the extent of radiusing expressed as the ratio R/D. The discharge coefficient will also be a function of the Reynolds number, although for this particular application, the Reynolds number is high enough ($>2\times10^4$) for its effect to be negligible.

Radiusing and the control of the degree of radiusing present manufacturing difficulties and hence increased cost. Chamfering is much easier and cheaper to produce. Thus if chamfering can approach radiusing in the extent of the improvement of C_d, it could prove to be a preferable alternative.

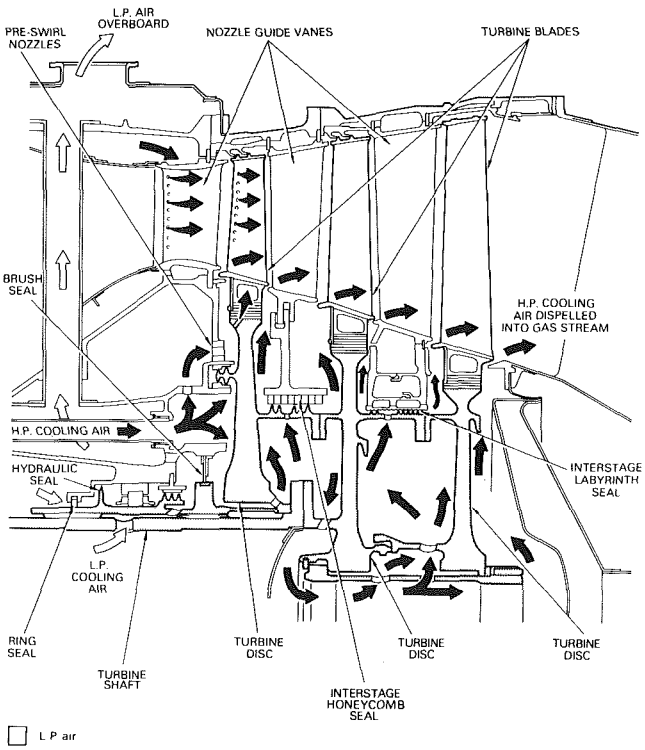

Fig. 1 Internal air cooling in an aero-engine [8]

[1]Present address: Rolls Royce plc, P.O. Box 31, Derby, DE2 8BJ, United Kingdom.

Contributed by the International Gas Turbine Institute and presented at the 36th International Gas Turbine and Aeroengine Congress and Exposition, Orlando, Florida, June 3–6, 1991. Manuscript received at ASME Headquarters March 4, 1991. Paper No. 91-GT-269. Associate Technical Editor: L. A. Riekert.

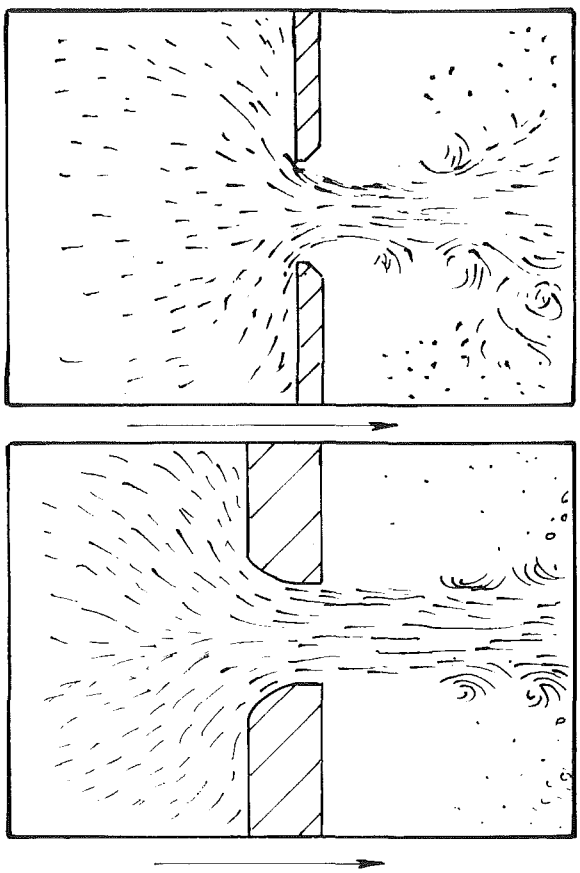

Fig. 2 Flows through sharp-edged and radiused holes (based on flow visualization [9])

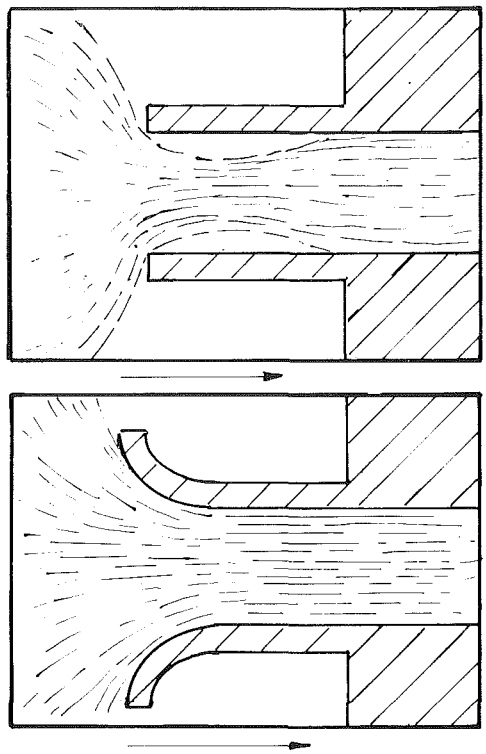

Fig. 3 Reattachment in a long orifice and the effect of inlet radiusing (based on flow visualization, [9])

This paper presents results of experimental measurements of C_d for a range of the parameters L/D and pressure ratio, for sharp-edged orifices, radiused orifices at various R/D ratios and for 45 deg chamfered holes and some 30 deg chamfered holes for a range of chamfering ratios W/D.

2 Previous Work

Deckker and Chang [1] investigated the compressible flow through thick orifices. They compiled data for sharp-edged orifices with length-to-diameter ratios of 0.0, 0.5, 1.0, and 2.0. Their findings showed that there was little dependence of the discharge coefficient on the pressure ratio above a pressure ratio of 2 when the flow chokes. They draw the conclusion that the length-to-diameter ratio is important because of the possibility of jet reattachment, and the behavior of the orifice can be explained on this basis. They also draw attention to marginal attachment/separation that can exist in some cases and that form an unstable area of operation that should be avoided since C_d may vary significantly. This was also noted by Ward-Smith [2].

Lichtarowicz et al. [3] investigated noncompressible flow through long orifices. They gave details of the dependence of the discharge coefficient on the hole Reynolds number, as did Deckker and Chang [1], showing this to be negligible for $\mathrm{Re} > 2 \times 10^4$. They found that C_d can be somewhat unpredictable for length-to-diameter ratios between 0.5 and 2.0 due to the effects of jet reattachment. Length-to-diameter ratios of up to 10 were tested.

Hay et al. [4] studied the combined effects of inlet radiusing and crossflows on long orifices with length-to-diameter ratios of up to 6. They proceeded by producing a baseline set of results with no crossflow, and then compared results with crossflow by relating the two by an additive loss coefficient. This baseline set of results provides a further source for comparison.

McGreehan and Schotsch [5] presented a method for calculating the discharge coefficient of long orifices with rotation and corner radiusing in terms of the discharge coefficients produced by each of these effects individually. They conclude that this method produces quite accurate results. Although the method is tedious to calculate by hand it is well suited to computer coding. Here length-to-diameter ratios up to 10 are considered.

Briggs [6] investigated the effect of inlet radiusing on the discharge coefficient for length-to-diameter ratios of 0.25, 0.5, 1, and 2 on the same rig as used for the present chamfered holes investigation. These results, which are also presented here, provide the basis on which the comparisons between inlet radiusing and inlet chamfering are made.

3 The Test Rig

The rig, shown in Fig. 4, consisted of a 100-mm-dia plenum, which was designed to sit on existing ducting fed with air from a screw compressor through a control valve. The lid of the

Nomenclature

C_d = ratio of actual to theoretical mass flow through hole based on p_1^+/p_2
D = diameter of hole*
L = length of hole*
p_1^+ = upstream stagnation pressure
p_2 = downstream static pressure
R = radius of inlet rounding*
Re = hole Reynolds number $= vD/\nu$
v = velocity through the hole
W = chamfer depth*
θ = chamfer half cone angle*
* = See Fig. 5

Table 1 Representative results for three pressure ratios

Pressure ratio p^+_1/p_2		Radiused Inlet					Chamfer angle 45°					Chamfer angle 30°				
		R/D	L/D				W/D	L/D				W/D	L/D			
			0.25	0.5	1.0	2.0		0.25	0.5	1.0	2.0		0.25	0.5	1.0	2.0
	1.2	0.00	0.62	0.68	0.79	0.75	0.00	0.62	0.71	0.74	0.83	0.00				
		0.04	0.68	0.74	0.76	0.79	0.04	0.73	0.85	0.86	0.87	0.04				
		0.08	0.79	0.83	0.83		0.08	0.73	0.86	0.88	0.86	0.08	0.90	0.94	0.94	0.95
		0.16	0.80		0.86	0.86	0.16	0.74	0.86	0.88	0.88	0.16	0.90	0.94		
		0.20	0.78	0.83		0.84	0.20	0.75	0.86	0.88	0.88	0.20				
	1.6	0.00	0.70	0.73	0.80	0.79	0.00	0.68	0.74	0.77	0.83	0.00				
		0.04	0.76	0.81	0.83	0.86	0.04	0.82	0.87	0.88	0.88	0.04				
		0.08	0.81	0.88	0.88		0.08	0.83	0.88	0.88	0.88	0.08	0.90	0.95	0.94	0.95
		0.16	0.89		0.94	0.88	0.16	0.82	0.88	0.88	0.88	0.16	0.90	0.94		
		0.20	0.87	0.90		0.90	0.20	0.81	0.87	0.88	0.89	0.20				
	2.2	0.00	0.75	0.76	0.84	0.86	0.00	0.74	0.79	0.82	0.85	0.00				
		0.04	0.84	0.86	0.88	0.88	0.04	0.87	0.88	0.89	0.89	0.04				
		0.08	0.89	0.92	0.89		0.08	0.87	0.89	0.89	0.88	0.08	0.93	0.95	0.94	0.95
		0.16	0.91		0.96	0.96	0.16	0.87	0.92	0.89	0.88	0.16	0.92	0.94		
		0.20	0.94	0.95		0.94	0.20	0.86	0.88	0.88	0.89	0.20				
Range of Cd for $1.2 < p^+_1/p_2 < 2.2$		0.00	0.13	0.08	0.05	0.11	0.00	0.12	0.08	0.08	0.02	0.00				
		0.04	0.16	0.12	0.12	0.09	0.04	0.14	0.03	0.03	0.02	0.04				
		0.08	0.10	0.09	0.06		0.08	0.14	0.03	0.01	0.02	0.08	0.03	0.01	0.00	0.00
		0.16	0.11		0.10	0.10	0.16	0.13	0.08	0.01	0.00	0.16	0.02	0.00		
		0.20	0.16	0.12		0.10	0.20	0.11	0.02	0.00	0.01	0.20				

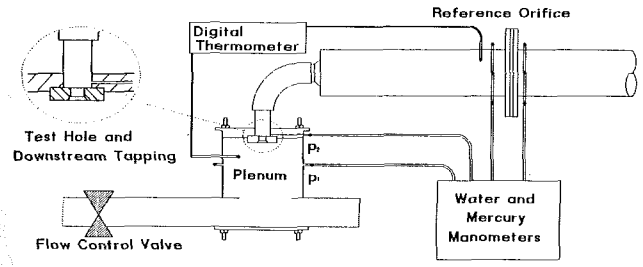

Fig. 4 General arrangement of the test rig

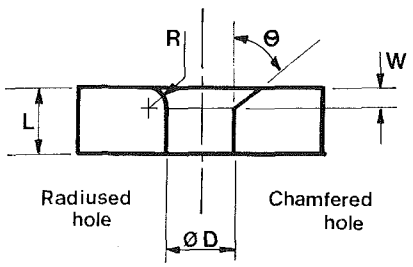

Fig. 5 Hole geometries

plenum housed the test orifices, which were secured by four smoothed countersunk screws. The air from the test orifice was then ducted to an orifice meter designed to BS 1042 and then vented to the atmosphere. The pressure ratio across the test orifice was varied using the control valve to give the range of 1 to 2.2. Pressures were measured using appropriate manometers. The data from the rig were fed to a computer for immediate analysis.

The test orifices were made to a diameter of 10 mm, as previously used by Briggs [6]. This diameter was sufficiently small to achieve the minimum specified Reynolds number of 2×10^4 with the available flow, ensuring that the discharge coefficient is independent of the Reynolds number. Figure 5 shows a drawing of a test orifice on which the radiused and chamfered geometries are shown. A range of values of R and L, and W and L were specified on the basic diameter of 10 mm to give the ranges of R/D, W/D, and L/D of 0–0.2, 0–0.2, and 0–2, respectively. After manufacture each orifice was checked to ensure that there were no burrs and that the dimensions were correct.

4 Results

Measurements of C_d were made at six or seven pressure ratios between 0 and 2.2 for the range of geometries listed above. Representative results can be seen in Table 1. This table shows the discharge coefficient for only three pressure ratios, chosen to straddle the whole range, and for each combination of length-to-diameter ratio and chamfering (and radiusing) to diameter ratio. Also shown in the table is the extent of variation of C_d in the range of pressure ratios between 1.2 and 2.2.

We will look at representative results in more detail first and then comment on the general trends as exhibited by the whole set of data.

4.1 Comparison With Other Results in the Literature. The results for the sharp-edged holes ($R/D=0$, $W/D=0$) were compared with those of Deckker and Chang [1]. A typical comparison is shown in Fig. 6 for $L/D=0.25$. It can be seen that all the data fall within a band of ±5 percent. The same spread was found to apply for the other L/D ratios. Thus the results can be taken to have an uncertainty of ±5 percent.

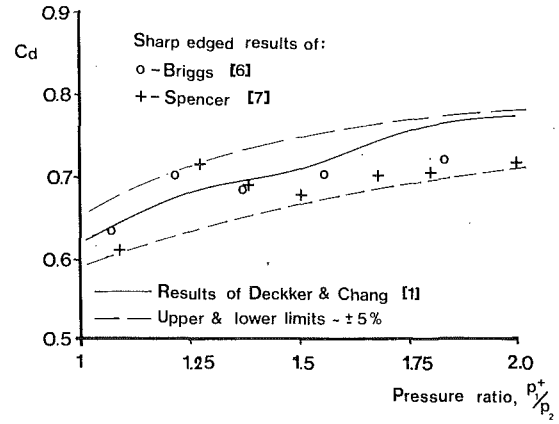

Fig. 6 Comparison of sharp edged results $L/D = 0.25$

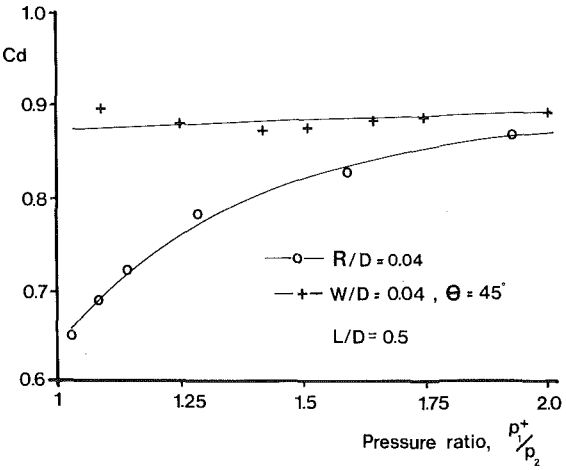

Fig. 7 Dependence of C_d on pressure ratio for inlet radiused and chamfered holes

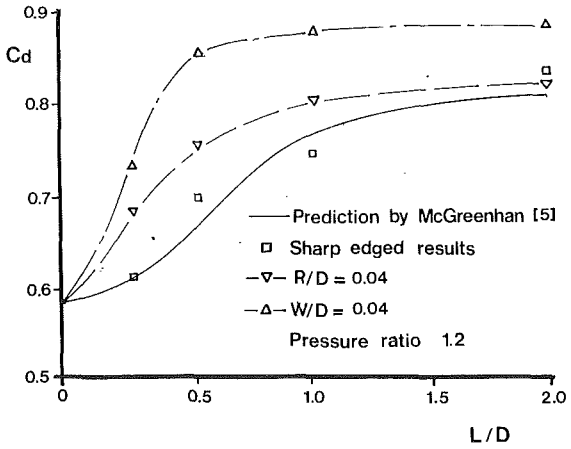

Fig. 8 Dependence of C_d on length-to-diameter ratio

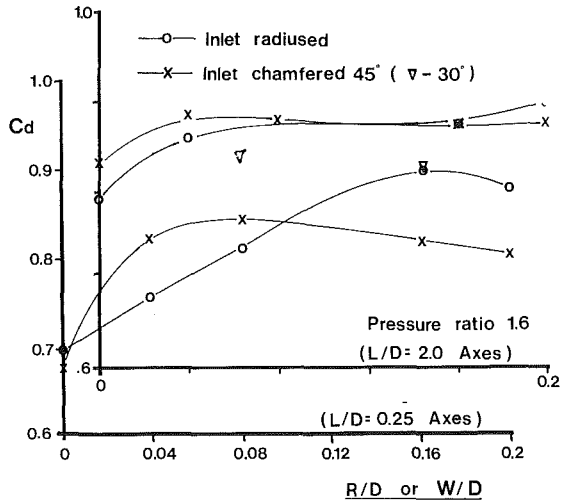

Fig. 9 Effect of inlet radiusing and chamfering on C_d at two length-to-diameter ratios

For the length-to-diameter ratio of 0.25 there is good agreement between all three sets of data. For length-to-diameter ratios of 0.5 and 1.0, the results of this experimental investigation and those of Briggs [6] are consistently 5 percent less than those of Deckker and Chang [1]. However, Lichtarowicz et al. [3] in their investigation of long orifices concluded that below $L/D = 1.5$, the discharge coefficient varies rapidly with L/D. This could account for the difference in this unstable region where marginal re-attachment occurs. Finally for the length-to-diameter ratio of 2 the three sets of data again correlate well except for Briggs' [6] results at low pressure ratios. From this comparison it is concluded that the results obtained in this investigation are sufficiently reliable and show the trends well.

4.2 The Effect of Pressure Ratio. The variation of the discharge coefficient with the pressure ratio can be seen in Fig. 7. This is typical of all geometries tested. It can be seen from Fig. 7 and from Table 1 that by increasing the pressure ratio, the discharge coefficient is increased, the amount of increase depending on the hole geometry. This increase levels off at a pressure ratio of around 2 when the flow chokes. This is in line with the results of Deckker and Chang [1]. The general trends of the effect of pressure ratio on C_d can be gleaned from the "range of C_d" section of Table 1. The thin holes, $L/D = 0.25$, can be seen to have the strongest dependence on the pressure ratio for all W/D and R/D ratios with variations in C_d of about 10 to 15 percent. For chamfered holes this dependence almost disappears as L/D and W/D are increased. Hence, if a hole is required where the discharge coefficient is to vary little with the pressure ratio, then the hole should have a $L/D > 1.0$, and incorporate some inlet chamfering. For inlet radiusing the results show a dependence on the pressure ratio for every radiusing ratio with variations of about 15 percent. For this reason inlet chamfering would be more desirable.

4.3 The Effect of Length-to-Diameter Ratio. The effect of the parameter L/D has been the subject of past publications and formulae have been derived to model the effect with good accuracy. McGreehan and Schotsch [5] were able to derive an empirical expression for sharp-edged holes that fitted the C_d results of Lichtarowicz et al. [3] to within 0.02. The shape of this curve is shown in Fig. 8. The effect of chamfering or radiusing is to cause the plateau of maximum discharge coefficient to start at a lower value of L/D. Therefore using a chamfered or radiused inlet reduces the length of a hole required to avoid a strong dependence of the discharge coefficient on L/D. With a sharp-edged hole Lichtarowicz et al. [3] suggested L/D should be greater than 1.5 to avoid this strong dependence. Now this can be reduced to between 0.5 and 1.0 if required by using a small chamfer. This is because the flow will re-attach to the wall closer to the inlet of the hole when the hole is chamfered. Lichtarowicz et al. [3] found that for the sharp-edged hole C_d dropped linearly from the maximum to 0.74 at $L/D = 10$. The peak in C_d is not obvious in Fig. 7 because the hole is short and the frictional effects that lead to the subsequent drop in C_d are not manifested.

4.4 The Effect of Inlet Radiusing. Inlet radiusing in-

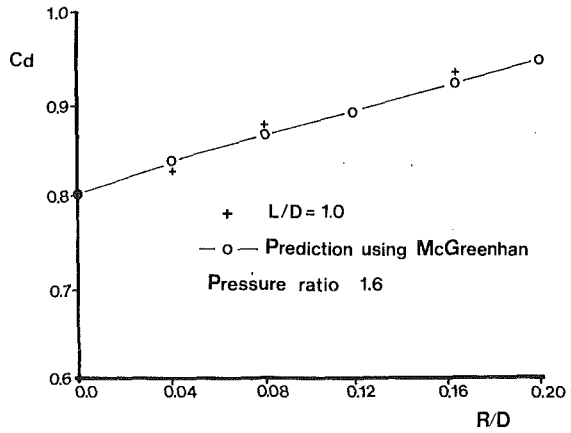

Fig. 10 Comparison of experimental results and prediction for radiused inlet holes

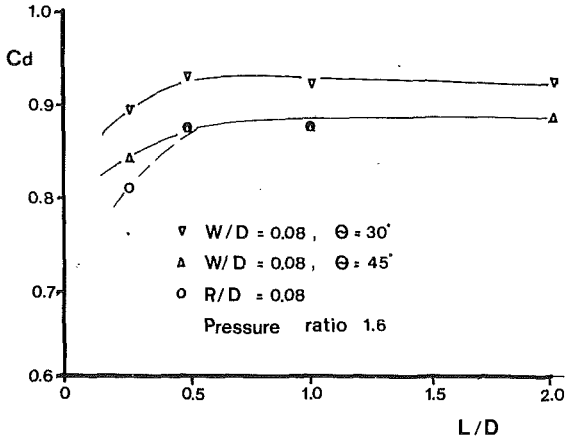

Fig. 11 Dependence of C_d on chamfering angle

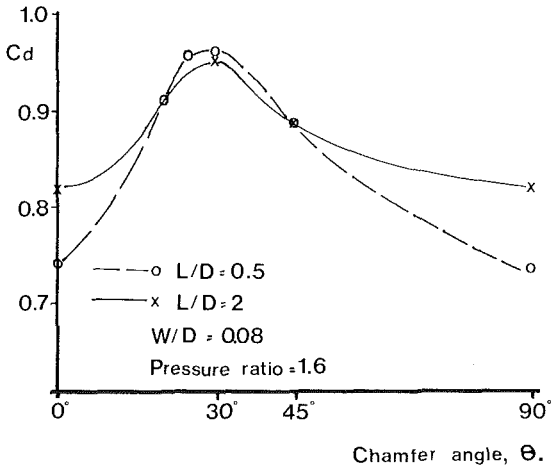

Fig. 12 Predicted variation of C_d with chamfering angle

creases the discharge coefficient (Fig. 9). At a pressure ratio of 1.6 (Table 1) maximum increases of 27, 19, 17, and 14 percent were found for length-to-diameter ratios of 0.25, 0.5, 1.0, and 2.0, respectively. The effects of inlet radiusing have been the subject of past investigations and again McGreehan and Schotsch [5] have produced a correlation to model this effect. A comparison between this correlation and Briggs' [6] results can be seen Fig. 10. It can be seen that there is a good correlation between the experimental and the predicted results.

The increase in C_d with increasing R/D occurs in view of the fact that as the radius becomes larger the local acceleration of the fluid around the periphery drops and separation becomes less likely.

4.5 The Effect of Inlet Chamfering. It is clear from the results (Table 1) that inlet chamfering significantly increases the discharge coefficient. At a pressure ratio of 1.6 the discharge coefficient could be improved by 22, 19, 14, and 6 percent for length-to-diameter ratios of 0.25, 0.5, 1.0, and 2.0 respectively. At least 95 percent of this increase had been achieved at a chamfer ratio of 0.04. These trends can be seen in Fig. 9. The reason for this increase is that the chamfer reduces the size of the vena contracta by encouraging the flow to enter the hole axially. Some separation at the inlet is still expected but to a much lesser degree than for the sharp-edged hole. It appears that the size of the vena contracta remains constant as the chamfer ratio is increased above 0.08, i.e., increasing W/D gives no further benefit. Figure 9 also shows that for $L/D = 0.25$, the discharge coefficient drops fractionally as the chamfer ratio is increased beyond 0.08. A similar behavior was observed with $L/D = 0.5$ and 1.0. The reason for this drop is that in this range of L/D the flow is marginally reattached, and as the chamfer depth is increased there is less pressure recovery within the hole, which leads to a reduced C_d. This phenomenon does not occur when the hole $L/D = 2.0$. Here the flow always re-attaches within the hole and so no drop in C_d occurs with increase in W/D (Fig. 9). A much deeper chamfer would be required before the flow could become separated at exit. Therefore we see that there is a distinct limit to the improvement that can be made by increasing the chamfering ratio for thin holes. Also for holes with $L/D > 2.0$, C_d is virtually independent of the chamfering ratio. This allows designers to specify broader tolerances on the chamfering depth, thereby easing manufacturing difficulty and cost.

4.6 The Effect of the Chamfer Angle. The holes tested were predominantly chamfered at 45 deg. However, it was thought important to test a different angle to see how much of an effect this had. From the results (Table 1) it is evident that chamfering at 30 deg gives a considerable increase in C_d over chamfering at 45 deg. More importantly there is an even smaller dependence on the pressure ratio. This is a desirable feature when designing the holes to control the flow as it means that the discharge coefficient is much more predictable.

Figure 11 shows a comparison between the two chamfering angles for $W/D = 0.08$. We see from Fig. 11 that altering the chamfer angle to 30 deg does not affect the way in which C_d varies with L/D but increases its value by about 0.07. Figure 12 shows the dependence of C_d on the chamfer angle. Results for chamfer angles of 20 and 25 deg (not reported in this paper) are also included in this figure. The value at 90 deg is deduced from the fact that at 90 deg the hole will again be sharp edged but shorter by the depth of the chamfer and can then be predicted from Fig. 8. The chamfer angle that gives the maximum C_d is seen from Fig. 12 to be in the range 25 to 30 deg.

4.7 Comparison Between Inlet Radiusing and Chamfering. Figure 9 shows the effects of increasing W/D and R/D for $L/D = 0.25$ (similar trends are shown at other L/D ratios). It is evident that at small chamfering or radiusing ratios the chamfered hole has a higher C_d. At a ratio of about 0.08 the graphs cross over and above this ratio the radiused hole has the higher C_d. However, by using a 30 deg chamfer instead of a 45 deg chamfer C_d increases to the same level as the maximum achieved by radiusing (Fig. 9). It is seen from Fig. 7 that for chamfered holes the dependence of C_d on pressure ratio is small, which is beneficial. Another advantage of chamfering is that for a given variation in W/D or R/D imposed by manufacturing tolerance bands, C_d for the chamfered holes would vary less than that for radiused holes (Fig. 9). The conclusion

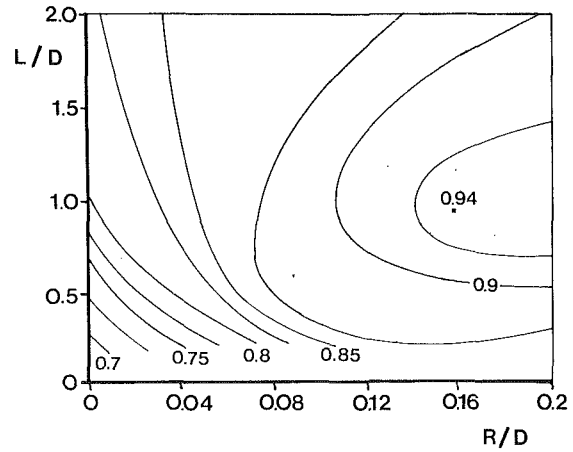

Radiused holes

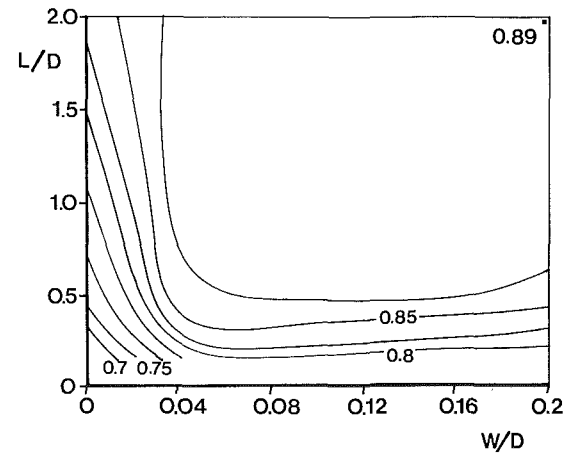

Chamfered holes $\theta = 45°$

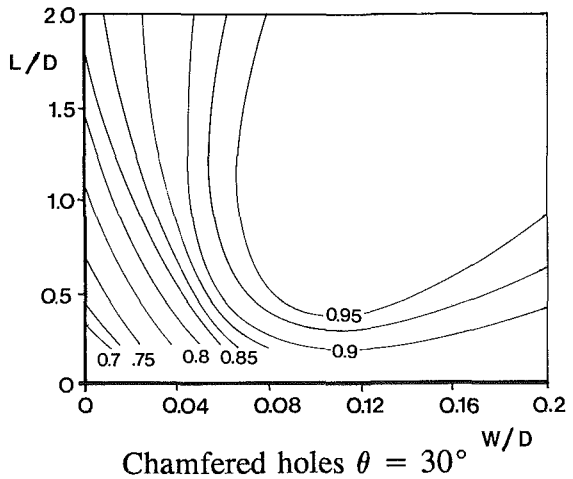

Chamfered holes $\theta = 30°$

Fig. 13 Discharge coefficient contours at a pressure ratio of 1.6

here must be that the advantages of inlet chamfering far outweigh those of inlet radiusing in the range tested.

To put the results into a more useful form for design purposes, contour plots of C_d have been generated for the ranges of L/D, W/D, and R/D tested. The plots for the pressure ratio of 1.6 are shown in Fig. 13. In an attempt to complete the picture, contour plots for the holes chamfered at 30 deg are also given, interpolated from the rather limited experimental data gathered for this chamfering angle. Similar plots were generated for a pressure ratio of 2.2 and may be found from Spencer [7].

5 Conclusions

1 It can be concluded that inlet radiusing and chamfering have a beneficial effect on the value of the discharge coefficient and on the way it varies with the length-to-diameter ratio and the pressure ratio across the hole.

2 Inlet radiusing gave a maximum increase in C_d of 27 percent at a pressure ratio of 1.6. The maximum increase produced by chamfering at the same pressure ratio was 22 percent for the 45 deg chamfer angle and 33 percent for the 30 deg chamfer (all of these at $L/D = 0.25$).

3 All of the benefit of inlet chamfering is achieved within $W/D = 0.08$. For thin holes, $L/D < 2.0$, further increase in the chamfering ratio will fractionally reduce the discharge coeffient.

4 Increasing both L/D and W/D decreases the dependence of C_d on the pressure ratio across the hole.

5 In order to avoid a strong dependence of C_d on L/D, it has been suggested [3] that $L/D > 1.5$. By using a chamfer ratio of 0.04 this limit can be reduced to $L/D > 0.5$.

6 The discharge coefficient is affected noticeably by the chamfer angle. A 30 deg angle gave an increase in C_d of 9 percent over the 45 deg chamfer. There was also a reduction in the dependence of C_d on the pressure ratio.

7 Chamfered holes give the more desirable performance characteristic, in addition to being easier to produce than radiused holes.

8 Of the range of hole geometries tested, the best geometry to give a high discharge coefficient and low dependence on pressure ratio was found to be the hole with a 30 deg chamfer.

Acknowledgments

The authors wish to thank Mr. D. Campbell of Rolls Royce plc for suggesting this investigation, and Miss Pauline Briggs for her work on the radiused holes.

References

1 Deckker, B. E. L., and Chang, U. F., "An Investigation of Steady Compressible Flow Through Thick Orifices," Proc. *IMechE*, Vol. 180, part 3J, 1965/1966.

2 Ward-Smith, A. J., *Pressure Losses in Duct Flows*, Butterworths, United Kingdom, 1971.

3 Lichtarowicz, A., Duggins, R. K., and Markland, E., "Discharge Coefficients for Incompressible, Noncavitating Flow Through Long Orifices," *Journal of Mechanical Engineering Science*, Vol. 7, No. 2, 1965, pp. 210–219.

4 Hay, N., Khaldi, A., and Lampard, D., "Effect of Crossflows on the Discharge Coefficients of Film Cooling Holes With Rounded Entries or Exits," *Proceedings of the 2nd AMSE-JSME Thermal Engineering Joint Conference*, Honolulu, HI, Vol. 3, 1987, pp. 369–374.

5 McGreehan, W. F., and Schotsch, M. J., "Flow Characteristics of Long Orifices With Rotation and Corner Radiusing," ASME JOURNAL OF TURBOMACHINERY, Vol. 110, pp. 213–217.

6 Briggs, P. A., "The Effects of Inlet Rounding on Orifice Discharge Coefficients," Third Year project report, Department of Mechanical Engineering, University of Nottingham, United Kingdom, 1988–1989.

7 Spencer, A., "Discharge Coefficient of Cooling Holes in Gas Turbine Components," Third Year project report, Department of Mechanical Engineering, Univerity of Nottingham, United Kingdom, 1989–90.

8 *The Jet Engine*, Rolls-Royce plc publication, 4th ed., 1986.

9 *Visualised Flow*, The Japan Society of Mechanical Engineers, Pergamon Press, 1988.

Influence of High Mainstream Turbulence on Leading Edge Film Cooling Heat Transfer

A. B. Mehendale
Research Assistant.

J. C. Han
Professor.
Fellow ASME

Turbine Heat Transfer Laboratory,
Mechanical Engineering Department,
Texas A&M University,
College Station, TX 77843

The influence of high mainstream turbulence on leading edge film effectiveness and heat transfer coefficient was studied. High mainstream turbulence was produced by a passive grid and a jet grid. Experiments were performed using a blunt body with a semicylinder leading edge with a flat afterbody. The mainstream Reynolds number based on leading edge diameter was about 100,000. Spanwise and streamwise distributions of film effectiveness and heat transfer coefficient in the leading edge and on the flat sidewall were obtained for three blowing ratios, through rows of holes located at ±15 and ±40 deg from stagnation. The holes in each row were spaced three hole diameters apart and were angled 30 and 90 deg to the surface in the spanwise and streamwise directions, respectively. The results indicate that the film effectiveness decreases with increasing blowing ratio, but the reverse is true for the heat transfer coefficient. The leading edge film effectiveness for low blowing ratio ($B = 0.4$) is significantly reduced by high mainstream turbulence ($Tu = 9.67$ and 12.9 percent). The mainstream turbulence effect is diminished in the leading edge for higher blowing ratios ($B = 0.8$ and 1.2) but still exists on the flat sidewall region. Also, the leading edge heat transfer coefficient for blowing ratio of 0.8 increases with increasing mainstream turbulence; but the effect for other blowing ratios ($B = 0.4$ and 1.2) is not as systematic as for $B = 0.8$. Surface heat load is significantly reduced with leading edge film cooling.

Introduction

For high thermal efficiency and high power density, the trend in advanced aeroengine design is toward high entry gas temperature (1400 °–1500 °C), far above the allowable metal temperature. Highly sophisticated cooling technologies such as film cooling, impingement cooling, and rib/pin augmented cooling are employed for airfoils of advanced gas turbine engines. In film cooling, relatively cool air is injected through the airfoil's surface to form a protective layer between the surface and the hot mainstream gas. Film cooling has been extensively applied to the gas turbine airfoils around the leading edge and on both the pressure and suction surfaces. Film cooling around the leading edge not only protects this region but also affects the aerodynamics and heat transfer over the entire airfoil surface. This investigation focuses on the influence of high mainstream turbulence on leading edge film cooling and heat transfer.

Consider pure heat transfer (without film holes) in the case of flow over a flat plate. Simonich and Bradshaw (1978), Hancock and Bradshaw (1983), and Blair (1983a, 1983b) reported that the heat transfer coefficient increases with increasing grid-generated turbulent intensity. Consider pure heat transfer (without film holes) in the case of flow over a cylinder. O'Brien and VanFossen (1985) studied the effect of turbulence produced by a grid with jet injection (jet-grid) on heat transfer from the leading edge of a circular cylinder. With this jet-grid they were able to produce higher turbulence intensity of up to 12 percent. At turbulence intensity of 10–12 percent, the heat transfer coefficient increased by 37–53 percent over the zero turbulence intensity case for Reynolds number of 48,000–180,000. Young et al. (1992) studied the effect of jet-grid turbulence on flat plate heat transfer and reported that for a turbulence intensity of 15 percent, the heat transfer coefficient increases by 45 percent as compared to the zero turbulence correlation in the fully turbulent region.

There have been many investigations concerning film cooling of flat or mildly curved surfaces with varying blowing ratios and injection geometries, for a low mainstream turbulence intensity of about 0.5 percent (Goldstein, 1971; Eriksen and Goldstein, 1974; Mayle et al., 1977; Ito et al., 1977; Han and Mehendale, 1986). However, there are not many studies on film cooling with injection around the leading edge region of an airfoil. Luckey and L'Ecuyer (1981) and Bonnice and L'Ecuyer (1983) used a circular cylinder with one to five rows of spanwise injection holes to model the leading edge region for various blowing ratios. For a low mainstream turbulence intensity of about 0.5 percent, they reported that the surface heat flux varied in both spanwise and streamwise directions, depending upon the injection geometry and blowing ratio. For

Contributed by the International Gas Turbine Institute and presented at the 35th International Gas Turbine and Aeroengine Congress and Exposition, Brussels, Belgium, June 11–14, 1990. Manuscript received by the International Gas Turbine Institute January 5, 1991. Paper No. 90-GT-9. Associate Technical Editor: S. A. Mosier.

a low mainstream turbulence intensity of about 0.45 percent, Karni and Goldstein (1990) used the naphthalene sublimation technique to study the effect of surface injection from a circular cylinder in crossflow with one row of inclined holes on the local mass transfer. They reported that, with spanwise injection, the mass transfer distribution is extremely sensitive to small changes in the injection hole location relative to stagnation.

Mick and Mayle (1988) used a blunt body with a circular leading edge and a flat afterbody to study the detailed film effectiveness and surface heat transfer for secondary air injection through two rows of inclined holes into the stagnation region of an incident mainstream flow. For a low mainstream turbulence intensity of about 0.5 percent, they found large spanwise variations exist in both film effectiveness and heat transfer coefficient and that the highest values of each do not correspond. The film effectiveness is as high as 0.7–0.8 near the film cooling holes, while the heat transfer coefficient with film cooling is as high as three times those without film cooling. The film effectiveness decays to only 0.1 downstream, while the heat transfer coefficient remains about 10 percent higher than that without injection. They reported also that for typical turbine temperatures, leading edge injection reduces the surface heat load everywhere for all but the highest blowing ratio of 0.97.

Some effort has been made to study the effect of leading edge injection on the film effectiveness and heat transfer coefficient around the film holes and downstream. Most film cooling and heat transfer results are based on very low mainstream turbulence levels. However, the turbulence intensity at the leading edge of the airfoil (after the combustor) can be as high as 15–20 percent in engine operating conditions. High mainstream turbulence has significant impact on leading edge (cylinder) and flat plate heat transfer without film cooling (O'Brien and VanFossen, 1985; Han and Young, 1988). It is of interest whether the high mainstream turbulence has significant impact on leading edge film effectiveness and leading edge heat transfer coefficient with film injection.

This study focuses on the effect of high mainstream turbulence on leading edge film cooling and heat transfer. High mainstream turbulence is produced by a passive grid with turbulence intensity of about 9.67 percent and a jet-grid (similar to that used by Young et al., 1992) with turbulence intensity of about 12.9 percent. The mainstream Reynolds number based on cylinder diameter is about 100,000. Spanwise and streamwise distributions of local heat transfer coefficient and local film cooling effectiveness are obtained by secondary air injection through rows of holes into the stagnation region of incident mainstream flow. Experiments are performed using a blunt body with a semicylinder leading edge with a flat afterbody, similar to that used by Mick and Mayle (1988). Rows of holes are located at ±15 and ±40 deg from stagnation. The holes in each row are spaced three hole diameters apart and are angled 30 deg to the surface in the spanwise direction. Additional information on the present investigation may be found from Mehendale (1991) and Mehendale et al. (1991).

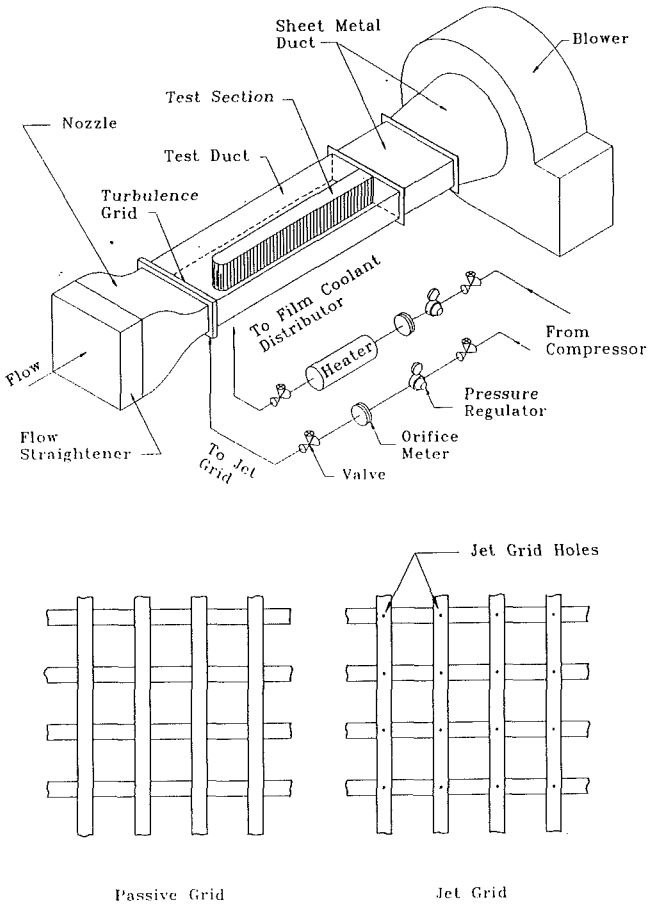

Fig. 1 Schematic of the test rig

Test Apparatus and Instrumentation

A schematic of the low-speed wind tunnel used is shown in Fig. 1. The test apparatus was designed as a suction-type wind tunnel to avoid uncontrolled turbulence in the discharge of the 7.5 kW (10 hp) blower. A flow straightener was followed by

Nomenclature

b = passive grid (or jet grid) width
B = blowing ratio (average secondary-to-mainstream mass flux ratio)
d = film hole diameter
D = leading edge diameter
h = convective heat transfer coefficient
h_o = convective heat transfer coefficient without film holes
L = length of injection hole
Nu_D = Nusselt number based on leading edge diameter
P = pitch of holes in a row
q'' = convective heat flux
q_o'' = convective heat flux without film holes
q_{cond}'' = conduction heat loss flux
q_{gen}'' = generated surface heat flux
q_{rad}'' = radiation heat loss flux
Re_D = Reynolds number based on the incident mainstream velocity (U_∞) and leading edge diameter
T_{aw} = adiabatic wall temperature
T_s = secondary or injected air temperature
Tu = streamwise turbulence intensity = $(\overline{U'^2})^{1/2}/U$
T_w = measured wall (foil) temperature
T_∞ = mainstream or incident air temperature
U = local mainstream velocity
U_∞ = incident mainstream velocity at $X/b = 20$ with no grid
u' = local streamwise fluctuating velocity
X = axial distance measured from grid
x = streamwise distance measured from stagnation
Z = spanwise distance
η = adiabatic film effectiveness
ϕ = overall cooling effectiveness

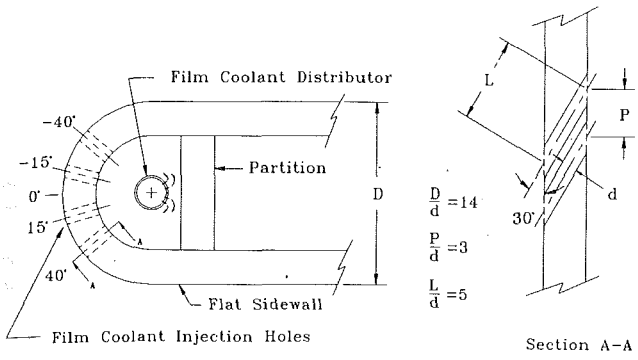

Fig. 2 Schematic of leading edge with film holes

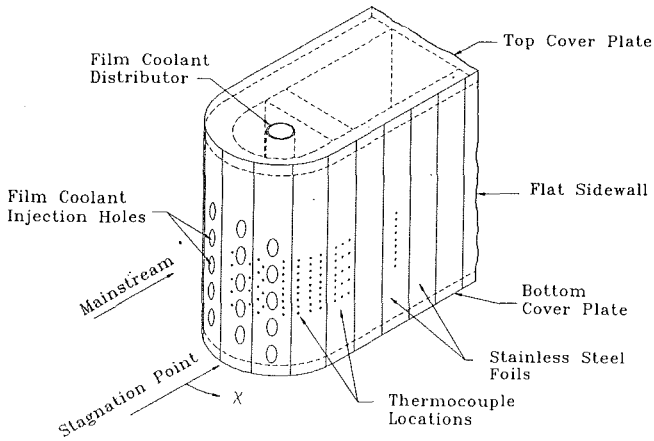

Fig. 3 Leading edge with detailed thermocouple distributions

a contraction inlet nozzle, which was followed by a turbulence grid and then the test channel. The nozzle had a contraction ratio of 3:1. The test channel was 25.4 cm × 76.2 cm in cross section and 183 cm long. The test model was placed in the test channel 47.6 cm downstream of the grid for uniform flow and turbulence.

Two turbulence grids were fabricated to generate different values of turbulence intensities. The first was a passive grid and the second a jet-grid (Fig. 1). The passive grid was made of hollow brass tubes 1.3 cm square in cross section and 4.8 cm apart. This passive grid also served as the jet grid as it had 96 holes, each 0.1 cm in diameter and drilled at points 4.8 cm apart. The holes coincided with the grid nodes. Compressed air flowing inside the hollow tubes was oriented to inject uniformly through these holes in the coflow (downstream) direction with a 2.5 percent injection ratio (injection mass flow rate/mainstream mass flow rate). The jet grid produced a higher turbulence level than the passive grid (Han and Young, 1988).

The test model shown in Fig. 2 simulates a turbine vane. It had a semicylinder leading edge with a radius of 7.6 cm and a height of 25.4 cm. At ± 90 deg from the stagnation line, the leading edge profile merged with 157.5-cm-long flat walls that ran parallel to the end of the test section. The test model was made of high quality laminated wood pieces. The wood thickness was 2.8 cm throughout. Four rows of circular holes were located at ±15 and ± 40 deg from the stagnation line. Each hole had a diameter of 1.1 cm and was angled at 30 and 90 deg to the surface in the spanwise and streamwise directions, respectively. There were five holes in each row, which were spaced three hole diameters apart. The hole to leading edge diameter ratio (d/D) was 0.072 and the hole length to hole diameter ratio (L/d) was 5.1.

The secondary system supplied hot air to the leading edge film holes. The secondary hot air temperature (~ 50°C) was measured by two thermocouples centrally located in two of the film holes at +15 and + 40 deg from the stagnation line. The secondary hot air mass flow rate was measured using a calibrated orifice meter at the end of the heater section.

Forty-five strips of 0.005-cm-thick stainless steel foils were cemented vertically on the outer surface of the test model. Each strip was 25.4 cm long, 3.8 cm wide, and separated from each other by 0.08 cm. The foils were electrically connected by copper bus bars in series, in a serpentine manner. The gaps were filled and made flush with the foil surface by silicone caulk to make the flow surface smooth, and reduce the risk of accidental electrical contact between foils. Holes were cut in the foils to match the film cooling holes in the wood. This surface acted as a constant heat flux test surface when heated (except near film hole region), and an adiabatic surface when unheated. One hundred and six calibrated, 36 gage copper-constantan thermocouples were cemented on the underside of the foils; 77 were distributed in the leading edge region as shown in Fig. 3. Some thermocouples were attached on the inner wall to estimate conduction heat loss through the wood. The thermocouples were wired to a Fluke 2280A dataloger, which was interfaced with an IBM PC. When steady state was reached, five sets of readings were taken at each thermocouple location and averaged to eliminate the minor surface temperature fluctuations.

A TSI IFA 100 constant temperature anemometer (CTA) and a TSI IFA 200 high-speed digitizer were connected to an IBM PC through a TSI DMA connector for recording hot wire data. A calibrated single hot wire measured mainstream velocity and turbulence intensity distributions. The single component streamwise rms calculations were based on 1032 readings from the CTA. The local streamwise turbulence intensity was based on the average of five sets of rms values normalized by the local streamwise velocity. The maximum uncertainty of the streamwise turbulence intensity downstream of turbulence grid was about 10 percent.

Test Conditions and Data Analysis

Tests were conducted in a low turbulence wind tunnel for a Reynolds number of 100,000 based on the leading edge diameter and incident mainstream air velocity. Higher turbulence could be generated by inserting passive or jet grid. Tests were conducted on two test sections: one without film holes in foil for pure heat transfer tests, and one with film holes in foil for film effectiveness and heat transfer with film injection tests. Pure heat transfer tests were performed for mainstream turbulence intensities of 0.75 percent (without grid), 9.67 percent (with passive grid), and 12.9 percent (with jet grid). Film effectiveness and heat transfer with film injection tests were performed for mainstream turbulence intensities of 0.75, 9.67, and 12.9 percent; and for blowing ratios of 0.4, 0.8, and 1.2. Turbulence intensity was based on hot-wire measurement 30 grid diameters downstream of grid, i.e., about 10 cm upstream of the leading edge. Blowing ratio was based on the average mass flux coming out of all film holes and mainstream mass flux. Pitot probe measurements of the centerline velocity at the exit of each film hole indicated that the flow through all holes in a row was the same to within ± 5 percent for the row at 15 deg and ± 4 percent for the row at 40 deg. The ratio of the flow in the row at 40 deg to that at 15 deg was found to be 2.0, 1.5, and 1.2 for M = 0.4, 0.8, and 1.2, respectively. With the single hot-wire probe perpendicular to the injection flow, the turbulence intensity (the rms fluctuations normalized by the incident mainstream velocity when mainstream flow was on) at the exit of each hole was found to be 3–5 percent, 7–12 percent, and 25–30 percent for B = 0.4, 0.8, and 1.2, respectively. Turbulence intensity was fairly uniform at the exit of each film hole in the rows at 15 and 40 deg.

Secondary air temperature was maintained at 25°C above

the mainstream temperature for film cooling. This resulted in a secondary to mainstream density ratio of 0.9; the corresponding momentum flux ratios were 0.18, 0.71, and 1.6 for blowing ratios of 0.4, 0.8, and 1.2. The secondary air temperature for heat transfer with film injection tests was about equal to the mainstream temperature. The corresponding momentum flux ratios were 0.16, 0.64, and 1.44. Note that the density ratio should have an important impact on the film effectiveness and heat transfer for intermediate and higher blowing ratios. This investigation is focused on the high mainstream turbulence effect at a constant density ratio. The density ratio effect will be studied separately. About 3½ to 4 hours were required to reach steady state for each test case. Data for each test case were recorded after 4 hours.

The heat transfer tests were conducted by injecting air through the film holes while power was being supplied to the surface foils. The temperature of the injection air was the same as the mainstream flow. The local heat transfer coefficient was calculated as

$$h = q'' / (T_w - T_\infty) = (q''_{\text{gen}} - q''_{\text{cond}} - q''_{\text{rad}}) / (T_w - T_\infty) \quad (1)$$

where q'' is the convective heat flux from the foil surface, q''_{gen} is the measured generated surface heat flux, q''_{cond} and q''_{rad} are surface conduction through the wood model and surface radiation to the channel walls. The generated heat flux was about 400 W/m^2 and the measured foil temperatures (T_w) ranged from 45 to 50° C. A constant heat flux boundary condition existed everywhere except on the foils with the film holes. The conduction heat loss through the wood model was about 3 percent of the generated heat flux, while the radiation heat loss to the channel walls was about 10 percent of q''_{gen}. Heat loss through thermocouple wires was estimated to be very small when compared to the generated heat flux (less than 0.1 percent); axial and lateral conduction effect between thermocouples through thin foils was also found to be negligible (less than 0.1 percent).

The generated heat flux for foils with film holes was highly nonuniform in both spanwise and streamwise directions. The variation of the generated heat flux, in the foils with the film holes, was determined by comparing the data with film holes to that obtained without film holes. The heat transfer coefficients without film holes were determined by accurate measurement of $(q''_{\text{gen}} - q''_{\text{cond}} - q''_{\text{rad}})/(T_w - T_\infty)$ as presented by Mehendale et al. (1991). The heat transfer coefficients with film holes could be calculated by measuring $(q''_{\text{gen}} - q''_{\text{cond}} - q''_{\text{rad}})/(T_w - T_\infty)$ if q''_{gen} were known. Since the heat transfer coefficients near the stagnation line (before film holes) have to be the same for the cases both with and without film holes, the local heat flux generated q''_{gen} with film holes could be determined by equating $(q''_{\text{gen}} - q''_{\text{cond}} - q''_{\text{rad}})/(T_w - T_\infty)$ for the case without film holes to that with film holes. This method is the same as used by Mick and Mayle (1988). These calculated values of q''_{gen} were used in Eq. (1)) for determining the heat transfer coefficients with film injection. Another method used to estimate the local q''_{gen} was foil resistance. Comparing foil resistance without film holes to that with film holes by knowing hole shape and distribution, the local q''_{gen} with film holes was determined. It was found that these two methods give about the same q''_{gen} for the Eq. (1) calculation.

The film effectiveness tests were conducted by injecting heated air through the film holes without power being supplied to the surface foils. The temperature of the injected heated air was about 25°C higher than that of the mainstream flow. The local film effectiveness was calculated as

$$\eta = \frac{T_{aw} - T_\infty}{T_s - T_\infty} = \frac{T_w - T_\infty}{T_s - T_\infty} + \frac{q''_{\text{rad}} - q''_{\text{cond}}}{h(T_s - T_\infty)} \quad (2)$$

where T_{aw} is the adiabatic wall temperature, T_s is the secondary (heated) air temperature, and T_∞ is the mainstream temperature. Since the test surface was not perfectly adiabatic, some corrections were applied to the measured wall temperature (T_w) in order to obtain the adiabatic film effectiveness. These corrections included the effect of heat transfer by conduction through the wood model (q''_{cond}) and heat loss by radiation to the channel walls (q''_{rad}). h is the local heat transfer coefficient with film injection as calculated from Eq. (1).

Note that the secondary air heated the inside of the leading edge model. Heat was actually transferred to the surface by conduction as seen from Eq. (2). This caused a conduction gain for the locations on the leading edge region. Conduction gain from inside the leading edge to the surface was found using a one-dimensional conduction model. Locations near the film holes also had an additional conduction gain from the hot film passing the injection holes. To estimate this additional conduction gain from the film holes, a model was used based on the assumption that film effectiveness near the stagnation line is very small (~0.05). Using this film effectiveness near the stagnation line, the value of local conduction gain per unit distance from film hole was found. These values were then used to estimate the conduction gain for the locations near film holes. The local film effectiveness was therefore determined using Eq. (2).

An uncertainty analysis was carried out for both the film effectiveness and heat transfer coefficients with film injection. The uncertainty around the film holes is up to 15 percent (primarily due to q''_{gen} estimation) whereas the uncertainty downstream of the leading edge is less than 5 percent (due to T_w measurement).

Results and Discussion

Flow Field Measurements. Velocity and turbulence intensity distributions in the test channel were measured to check the mainstream flow conditions. The velocity profiles at position 1.5 leading edge diameter upstream of leading edge model were measured by traveling a pitot tube probe across the Y-Z midplane. At this location the results showed that the oncoming mainstream flows were fairly uniform over the entire Y-Z midplane (Mehendale, 1991). The local velocity and turbulence intensity distributions along the centerline and right-side line of the test channel for three upstream turbulence conditions are shown in Fig. 4. The ratio of local mainstream velocity to incident mainstream velocity (U/U_∞) along the centerline and right-side line is approximately at a constant value of 1.0 up to 20 grid diameter downstream of grid (i.e., X/b = 20, or 1.5 leading edge diameter upstream of leading edge model). The incident mainstream velocity (U_∞) is 10 m/s at X/b = 20 with no grid condition. The local mainstream velocity along the centerline decreases sharply after X/b = 20 because of approaching leading edge. The local mainstream velocity along the right-side line increases gradually because of the leading edge blockage effect, and then reaches a constant value toward the end of the test model.

Although the mainstream velocity distributions are about the same regardless of upstream turbulence conditions, the mainstream turbulence distributions are quite different as shown in Fig. 4. The streamwise single-component turbulence intensity distribution (local streamwise rms fluctuation divided by local mainstream velocity) for the case without turbulence grid is included for comparison. The results show that, for the cases of passive and jet grids, the streamwise turbulence intensity along the right-side line decreases monotonically with increasing distance from the grids. The streamwise turbulence intensity along the centerline decreases. It then increases due to reduced velocity when the flow approaches the leading edge. At X/b = 30 (i.e., 0.65 leading edge diameter upstream of leading edge model), the centerline turbulence intensity reaches its minimum of 12.9 percent for the jet grid and 9.67 percent for the passive grid. The corresponding dissipation length scales at the same location are estimated to be about 1.7 cm and 1.2

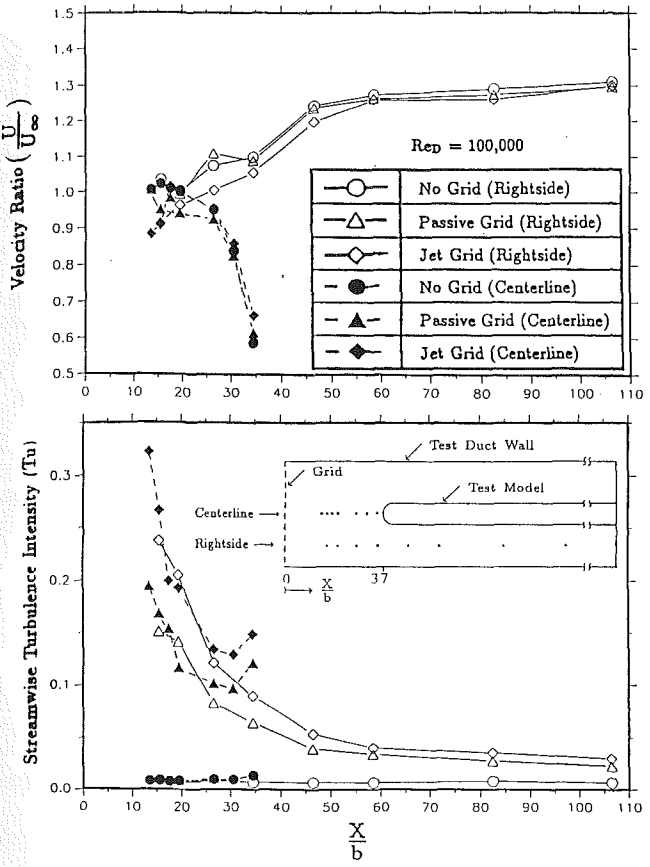

Fig. 4 Streamwise distributions of normalized mainstream velocity and turbulence intensity

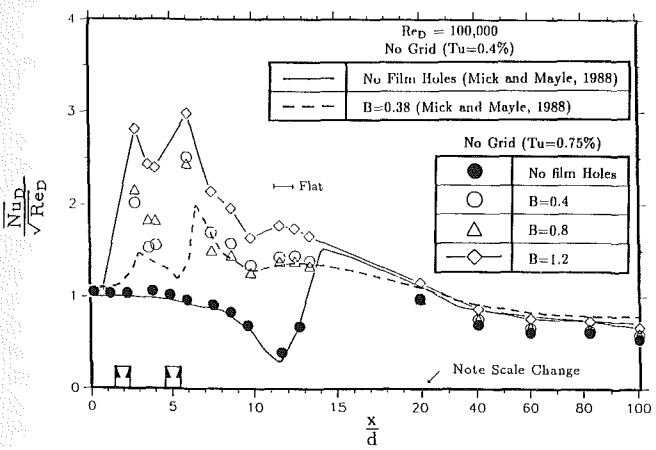

Fig. 5 Spanwise averaged Nusselt number distributions for low mainstream turbulence

cm, respectively (Mehendale, 1991). The objective of this investigation is to study the influence of these oncoming minimum mainstream turbulences (Tu = 9.67 and 12.9 percent based on measurements at X/b = 30) on the leading edge film effectiveness and heat transfer with film injection.

Pure Heat Transfer (Without Film Holes). Pure heat transfer tests on the smooth model (without film holes) were conducted to calibrate the leading edge, and then compared to the published data for low mainstream turbulence level (i.e., without turbulence grid). Detailed results for three Reynolds numbers and four turbulence levels are given by Mehendale et al. (1991). Some of these results are shown in Fig. 5 as a spanwise-averaged Nusselt number $\overline{Nu}_D$ (based on the leading edge diameter), scaled by the square root of the Reynolds number versus the ratio of the streamwise distance to the film hole diameter (x/d). Even though there were no film holes the abscissa is x/d for uniform comparisons. As seen from Fig. 5, the smooth model heat transfer data follow those obtained by Mick and Mayle (1988). Bellows and Mayle (1986) measured detailed velocity profiles in the region where the semicylinder leading edge merges with the flat afterbody and found the existence of a separation bubble. As discussed in Mick and Mayle (1988), the decrease and rapid rise in heat transfer around x/d = 10 is the result of a separating leading edge laminar boundary layer followed by a turbulent reattachment. The present data are slightly higher in the leading edge region and lower on the flat portion of the test model. The wind tunnel in the present study has an inherent turbulent intensity of about 0.75 percent, which is higher than the 0.4 percent in Mick and Mayle's. This is why our data in the leading edge region appear slightly higher. Also, for the same approaching Reynolds number flow, the mainstream velocity on the flat sidewall portion in the present study is 20 percent lower than in Mick and Mayles's case. Thus the boundary layer is thicker, which results in lower heat transfer.

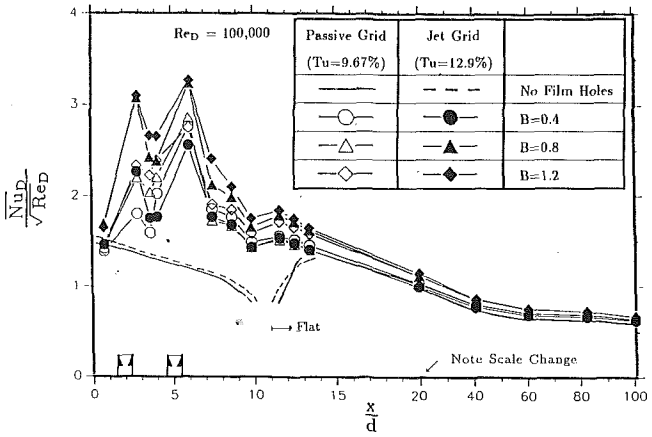

Fig. 6 Spanwise-averaged Nusselt number distributions for high mainstream turbulence

Table 1 Local $Nu_D/(Re_D)^{1/2}$ distributions for B = 0.8

(a) Tu = 0.75%

1.1		2.3	1.9		1.8	2.3		1.6	1.4	1.3		1.3	1.3	1.3									
1.1		2.0			1.9	2.6		1.3	1.4	1.2		1.3											
1.0		2.0	1.9			2.7		1.5	1.5	1.3		1.3	1.3	1.3									
1.1		2.2			1.7	2.7		1.6	1.6	1.4		1.6											
			1.7			2.4		1.6	1.5	1.3		1.6	1.6	1.5									
		2.2			1.9	2.3		1.4	1.3	1.3		1.4											
			1.6			2.4		1.5	1.4	1.2		1.3	1.3	1.3									
						2.5		1.6	1.5	1.3		1.3											
						2.1		1.6	1.5	1.2		1.3	1.3	1.3									

(b) Tu = 12.9%

1.8		3.4	2.5		2.4	3.3		2.2	1.9	1.7		1.7	1.7	1.6									
1.8			2.9			3.3		1.9	2.1	1.7		1.7											
1.6		3.0	2.4		2.6	3.5		2.1	2.1	1.7		1.8	1.7	1.6									
						3.6		2.2	2.2	1.8		1.9											
1.7		3.0	2.3		2.2	3.3		2.3	2.1	1.7		2.0	1.9	1.7									
						3.1		2.0	1.9	1.6		1.9											
		2.9	2.3		2.4	3.0		2.2	1.8	1.6		1.7	1.6	1.6									
1.6			2.1			3.3		2.2	1.9	1.6		1.7											
						2.8		2.2	1.9	1.6		1.7	1.6	1.5									

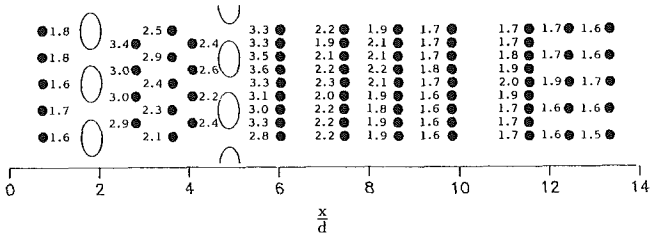

Heat Transfer With Film Injection. Also shown in Fig. 5 is the spanwise-averaged heat transfer with film injection for three blowing ratios at low mainstream turbulence level (no grid). Note that from Fig. 3 thermocouple row numbers 2, 3,

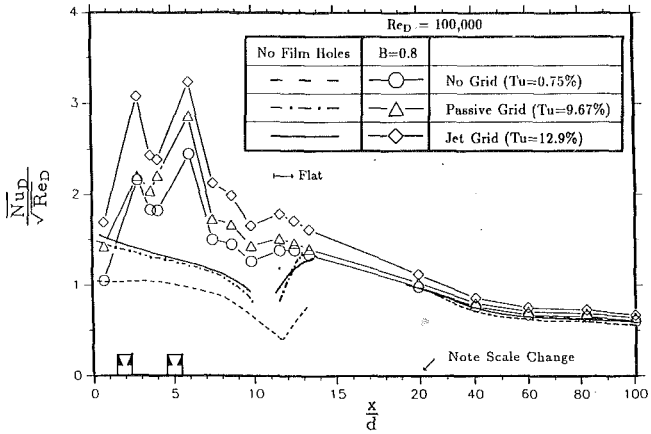

Fig. 7 Effect of mainstream turbulence on spanwise averaged Nusselt number distributions for B = 0.8

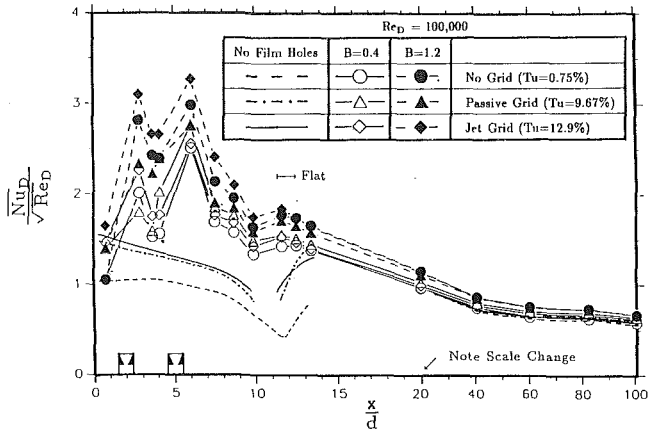

Fig. 8 Effect of mainstream turbulence on spanwise-averaged Nusselt number distributions for B = 0.4 and B = 1.2

and 4 have 4, 5, and 4 thermocouples, respectively, as against for row numbers 5, 6, 7, 8, and 9, which have 9 thermocouples each representing strategic spanwise locations. As seen from Fig. 5, the present data for blowing ratio B = 0.4 follow those by Mick and Mayle (1988) for B = 0.38. Both show a peak in heat transfer after the first row of injection holes. The second peak of Mick and Mayle's data is delayed because the second row of injection holes is located at 44 deg instead of 40 deg as in our case. The present data are higher on the leading edge region but lower on the flat sidewall. The sidewall values are lower because of thicker boundary layer. The film hole spacing in the present study is $3d$ as compared to $4d$ in Mick and Mayle's and the film hole diameter is 1.1 cm as compared to 1.52 cm in their case. For the same blowing ratio there is more flow interaction around the downstream of the injection holes because the film holes are closer and smaller, thus causing higher heat transfer in the leading edge region. As indicated earlier, the turbulence intensities at the exit of the film holes are 3–5 percent, 7–12 percent, and 25–30 percent for B = 0.4, 0.8, and 1.2, respectively. It is seen that the heat transfer between the first and second row increases as the blowing ratio increases. But B = 0.8 has the lowest heat transfer after the second row. For all blowing ratios there is a lower heat transfer region between the two rows of injection holes. The effect of separation bubble, as discussed by Bellows and Mayle (1986) and Mick and Mayle (1988), is shown by the small bump in the curves after the second row of holes.

Data for passive grid (Tu = 9.67 percent) and for jet grid (Tu = 12.9 percent) are shown in Fig. 6 for B = 0.4, 0.8, and 1.2. For comparison, pure heat transfer data (without film injection) for Tu = 9.67 percent and Tu = 12.9 percent are also shown. The trend of two peaks and a separation bubble effect is apparent. As before, the heat transfer is higher with increasing blowing ratio. All the curves merge far downstream of the injection holes.

Table 1 shows the effect of the high mainstream turbulence (Tu = 12.9 percent as compared to Tu = 0.75 percent) on the local heat transfer distributions for an intermediate blowing ratio B = 0.8. The effect of high mainstream turbulence is generally to increase heat transfer at all locations. The local heat transfer variation in the spanwise direction is not so significant as that in the streamwise direction for both high and low turbulence cases. The effect of mainstream turbulence on the spanwise-averaged heat transfer results for a given blowing ratio of B = 0.8 is seen in Fig. 7. The corresponding pure heat transfer data (without film injection) are also included. Before the first row of injection holes, there is an increase of 36 and 61 percent respectively in heat transfer for Tu = 9.67 and 12.9 percent compared to that for Tu = 0.75 percent.

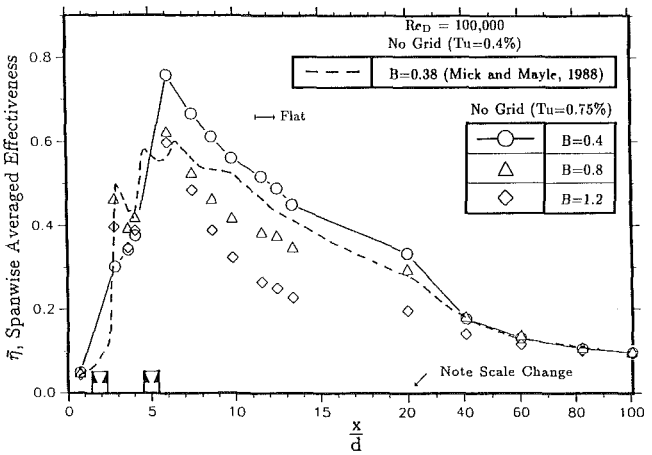

Fig. 9 Spanwise-averaged film effectiveness distributions for low mainstream turbulence

The increases are 20 and 42 percent after the first row of film holes, and after the second row of film holes, the corresponding increases are 17 and 32 percent. The effect of mainstream turbulence on the spanwise-averaged heat transfer for B = 0.4 and 1.2 are also shown for reference in Fig. 8, but the effects for these cases are not so systematic as that for B = 0.8.

Film Cooling Effectiveness. Spanwise-averaged film effectiveness $\bar{\eta}$ distributions for Re_D = 100,000 and B = 0.4, 0.8, 1.2 at Tu = 0.75 percent are shown in Fig. 9. Data by Mick and Mayle (1988) for Re_D = 100,000 and B = 0.38 at Tu = 0.4 percent are also shown for comparison. It can be seen from Mick and Mayle's data that the effectiveness downstream of film holes reaches a peak after the film comes out. A similar trend is seen in the present study. The values of film effectiveness are higher for the present study than the published results. This is because the pitch between the holes is $3d$ as compared to $4d$ in the published results. This provides better film coverage. As indicated earlier, the ratio of the flow in the row at 40 deg to that at 15 deg was measured to be 2 for B = 0.4. Because of this, for B = 0.4, film effectiveness prior to the second row of film holes is the lowest while film effectiveness after the second row of film holes is the highest. The effectiveness for B = 1.2 is the lowest because of the highest penetration of jet in the mainstream. In spite of having highest mass injection, too much penetration and subsequent mixing cause dilution of the secondary air. The trend remains the same for Tu = 9.67 percent and Tu = 12.9 percent for all blowing ratios as in the case of Tu = 0.75 percent as seen from Fig. 10.

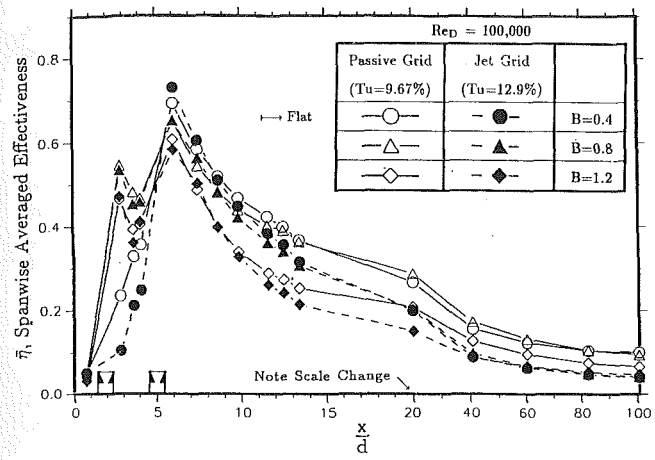

Fig. 10 Spanwise-averaged film effectiveness distributions for high mainstream turbulence

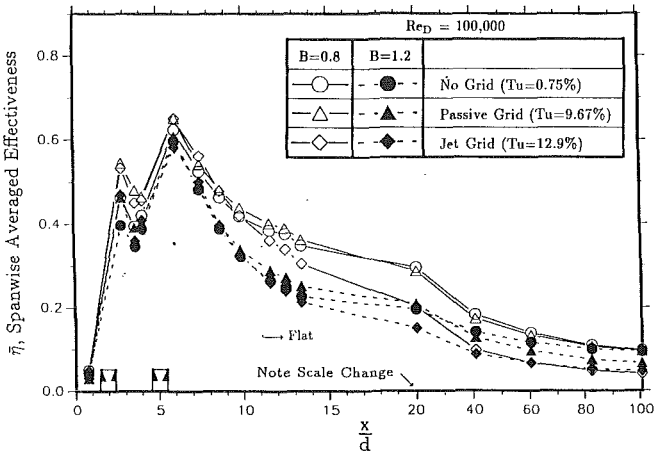

Fig. 11 Effect of mainstream turbulence on spanwise-averaged film effectiveness distributions for B = 0.8 and B = 1.2

Table 2 Local film effectiveness distributions for B = 0.8

(a) Tu = 0.75%

.04	.56	.19	.42	.62	.63	.57	.48	.36	.35	.32	
.06		.48		.48	.41	.42	.47	.46			
.05	.25	.42	.35	.61	.39	.31	.33	.41	.42	.40	
.04	.63	.36	.52	.78	.52	.38	.33	.30			
.06	.43	.52	.39	.57	.66	.57	.44	.35	.34	.31	
				.48	.43	.46	.51	.45			
				.69	.45	.37	.36	.42	.43	.40	
				.81	.59	.49	.37	.34			
				.59	.65	.62	.50	.37	.35	.33	

(b) Tu = 12.9%

.07	.63	.30	.46	.60	.63	.56	.47	.34	.32	.28	
.07		.57		.50	.45	.44	.45	.41			
.03	.38	.49	.43	.66	.42	.33	.34	.37	.37	.33	
	.64			.80	.55	.39	.33	.29			
.03		.42	.51	.67	.68	.55	.41	.30	.28	.26	
	.49		.43	.56	.57	.54	.50	.38			
.04		.47		.71	.52	.43	.43	.42	.39	.33	
				.80	.59	.49	.39	.38			
				.57	.65	.58	.46	.37	.35	.33	

0 2 4 6 8 10 12 14

x/d

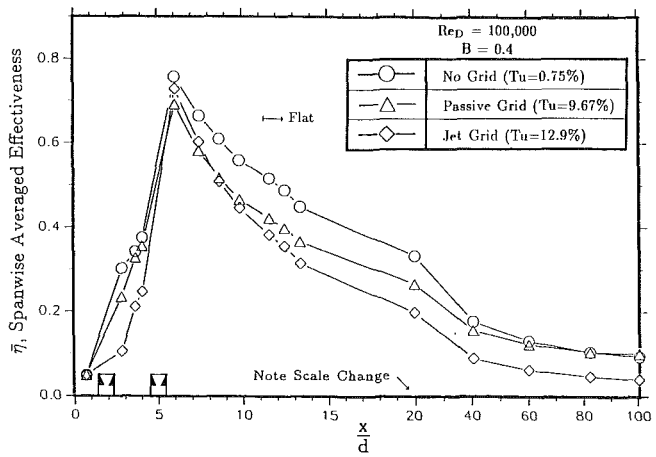

Fig. 12 Effect of mainstream turbulence on spanwise-averaged film effectiveness distributions for B = 0.4

The effects of high mainstream turbulence (Tu = 12.9 percent as compared to Tu = 0.75 percent) on the local film effectiveness distributions for blowing ratio B = 0.8 are listed in Table 2 for reference. The local film effectiveness variation in the spanwise direction is as significant as that in the streamwise direction for both high and low turbulence cases. The spanwise variation is due to the 30 deg spanwise film injection. Figure 11 shows the effect of turbulence intensity on the film effectiveness distributions for a given blowing ratio of 0.8 and 1.2. A study of Tu = 0.75, 9.67, and 12.9 percent indicates that the higher mainstream turbulence flows do not significantly affect film effectiveness for most of leading edge. For B = 0.8 and 1.2, as indicated earlier, the secondary air penetrates the mainstream flow and produces high turbulence intensity at the exit of the film holes (Tu = 7–12 percent for B = 0.8, Tu = 25–30 percent for B = 12). This implies that the film injection already increases high enough turbulence near film holes and hence higher mainstream turbulence flows cannot disturb the film layer in the leading edge region. Once the film-generated turbulence has started reducing toward the end of leading edge and on the flat sidewall (as shown in Fig. 11, but not listed in Table 2), higher mainstream turbulence flows end up reducing the film effectiveness by disturbing the film layer. However, as indicated before, for B = 0.4, the film-generated turbulence near film holes is much lower (Tu = 3–5 percent). The effects of high mainstream turbulence are detrimental to the film layer and cause significantly lower film effectiveness. This can be clearly seen from Fig. 12.

Film Cooling Heat Transfer Performance. It is important to study the combined effect of film effectiveness and heat transfer coefficient to determine the performance of a film-cooled airfoil for a given condition. As shown by Mick and Mayle (1988), the effect of film cooling on the surface heat load can be given by

$$\frac{\bar{q}''}{q_o''} = \frac{1}{n}\sum_{i=1}^{n}\left(\frac{h(x, z_i)}{h_o}\right)\left(1-\frac{\eta(x, z_i)}{\phi}\right) \tag{3}$$

where q_o'' is the heat flux for pure heat transfer (without film holes) at any streamwise location; $\bar{q}''$ is the spanwise-averaged heat flux for heat transfer with film injection at the same streamwise location; n is the number of thermocouples in a row to obtain the spanwise-averaged film effectiveness and heat transfer coefficient; and ϕ is the overall cooling effectiveness given by $\phi = (T_w - T_\infty)/(T_s - T_\infty)$.

ϕ is usually 0.5–0.6 for gas turbines. Using ϕ = 0.6, comparison of overall performance due to film cooling is made. As seen from Fig. 13 for Tu = 0.75 percent, the heat load has the minimum for B = 0.4 from the second row of film holes to the end of leading edge. B = 0.8 shows the best performance before the second row of film holes. This is because for B = 0.4, as observed before, a very small amount of film comes out through the first row of film holes as compared to the

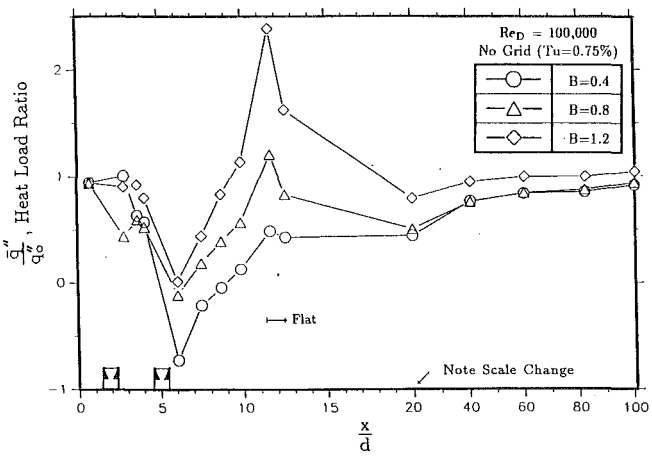

Fig. 13 Effect of film cooling on the surface heat load for ϕ = 0.6 and low mainstream turbulence

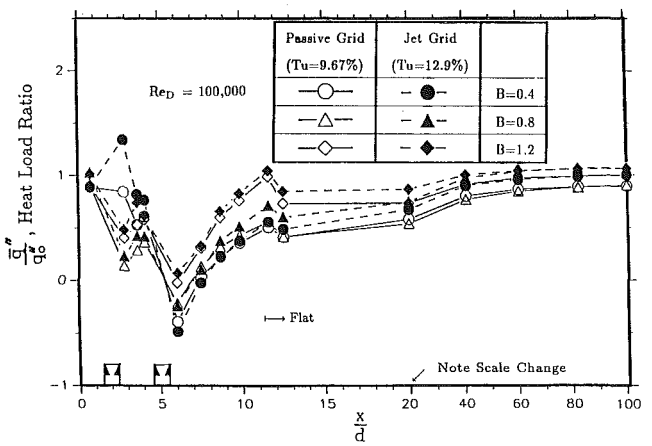

Fig. 14 Effect of film cooling on the surface heat load for ϕ = 0.6 and high mainstream turbulence

second row of film holes. There is an increase in heat load for B = 0.8 and B = 1.2 toward the end of leading edge, more so for B = 1.2 thus reducing the performance. The effect of film cooling is to reduce the heat load for all blowing ratios (except B = 1.2 near separation region). This confirms the results observed by Mick and Mayle (1988). It is also observed that there is a negative heat load for B = 0.4 and 0.8 just after the second row of film holes, which means there is heat flow from the surface to the film. It can be concluded from this that B = 0.4 has the best performance downstream of the second row of film holes, B = 0.8 does better from the first row up to the second row of film holes, and B = 1.2 is not as good as B = 0.8. Head load results for Tu = 9.67 percent and Tu = 12.9 percent flows can be seen in Fig. 14. The trends remain similar to the Tu = 0.75 percent flow case except, in these cases, the spreads are considerably less, due to the blowing ratio.

Concluding Remarks

The influence of high mainstream turbulence on leading edge film effectiveness and heat transfer coefficient with film injection has been investigated. The main findings of the study are:

1 The surface heat load is significantly reduced with leading edge film cooling. Surface heat load for low mainstream turbulence flow (Tu = 0.75 percent) increases with increasing blowing ratio except between row one and row two of the film holes, where the heat load is lowest for B = 0.8. Surface heat load for high mainstream turbulence flows (Tu = 9.67 and 12.9 percent) follows the same trends, but in these cases the spreads are considerably less, due to the blowing ratio.

2 The film effectiveness decreases with increasing blowing ratio, except between row one and row two of film holes, where film effectiveness is highest for B = 0.8 and lowest for B = 0.4. Film effectiveness for low blowing ratio (B = 0.4) in the leading edge region decreases drastically with increasing mainstream turbulence. The film effectiveness for high blowing ratios (B = 0.8 and B = 1.2) on the leading edge region is not significantly affected by higher mainstream turbulence, but the film effectiveness on the flat sidewall region decreases with increasing higher mainstream turbulence.

3 The leading edge heat transfer coefficient with film injection generally increases with increasing blowing ratio, but the effect diminishes at the end of the flat sidewall. For B = 0.8, the leading edge heat transfer coefficient increases with increasing mainstream turbulence. For B = 0.4 and 1.2, however, the mainstream turbulence effect is not so systematic as for B = 0.8.

4 Heat transfer coefficient in the leading edge region with no film holes increases significantly with increasing mainstream turbulence level. The effect diminishes at the end of the flat sidewall due to the decay of mainstream turbulence.

Acknowledgments

The turbulence portion was supported through Dr. Richard B. Rivir of the U.S. Air Force, Wright-Patterson AFB under Contract #F33615-86-2723. The test model portion was associated with the Film Cooling Project sponsored by Textron Lycoming through Contract #H164150. Their support is gratefully acknowledged.

References

Bellows, W. J., and Mayle, R. E., 1986, "Heat Transfer Downstream of a Leading Edge Separation Bubble," ASME JOURNAL OF TURBOMACHINERY, Vol. 198, p. 131-136.

Blair, M. F., 1983a, "Influence of Free-Stream Turbulence on Turbulent Boundary Layer Heat Transfer and Mean Profile Development, Part I—Experimental Data," ASME *Journal of Heat Transfer*, Vol. 105, p. 33-40.

Blair, M. F., 1983b, "Influence of Free-Stream Turbulence on Turbulent Boundary Layer Heat Transfer and Mean Profile Development, Part II—Analysis of Results," ASME *Journal of Heat Transfer*, Vol. 105, pp. 41-47.

Bonnice, M. A., and L'Ecuyer, M. R., 1983, "Stagnation Region Gas Film Cooling—Effects of Dimensionless Coolant Temperature," NASA CR-168197.

Eriksen, V. L., and Goldstein, R. J., 1974, "Heat Transfer and Film Cooling Following Injection Through Inclined Circular Tubes," ASME *Journal of Heat Transfer*, Vol. 96, pp. 239-245.

Goldstein, R. J., 1971, "Film Cooling," *Advances in Heat Transfer*, Academic Press, New York, Vol. 7, pp 321-379.

Han, J. C., and Mehendale, A. B., 1986, "Flat-Plate Film Cooling With Steam Injection Through One Row and Two Rows of Inclined Holes," ASME JOURNAL OF TURBOMACHINERY, Vol. 108, pp. 137-144.

Han, J. C., and Young, C. D., 1988, "The Influence of Jet-Grid Turbulence on Turbulent Boundary Layer Flow and Heat Transfer," *Transport Phenomena in Turbulent Flow*, M. Hirata and N. Kasagi, eds., Hemisphere Publishing Corporation, New York, pp. 501-514.

Hancock, P. E., and Bradshaw, P., 1983, "The Effect of Free-Stream Turbulence on Turbulence Boundary Layers," ASME *Journal of Fluids Engineering*, Vol. 105, pp. 284-289.

Ito, S., Goldstein, R. J., and Eckert, E. R. G., 1977, "Film Cooling of a Gas Turbine Blade," Tokyo Joint Gas Turbine Congress, Paper No. 03.

Karni, J., and Goldstein, R. J., 1990, "Surface Injection Effect on Mass Transfer From a Cylinder in Crossflow: A Simulation of Film Cooling in the Leading Edge Region of a Turbine Blade," ASME JOURNAL OF TURBOMACHINERY, Vol. 112, pp. 418-427.

Luckey, D. W., and L'Ecuyer, M. R., 1981, "Stagnation Region Gas Film Cooling—Spanwise Angled Injection From Multiple Rows of Holes," NASA CR-165333.

Mayle, R. E., Kopper, F. C., Blair, M. F., and Bailey, D. A., 1977, "Effect of Streamline Curvature on Film Cooling," ASME *Journal of Engineering for Power*, Vol. 99, pp. 77-82.

Mehendale, A. B., 1991, "Effect of High Mainstream Turbulence on Leading Edge Heat Transfer and Film Cooling," Ph.D. Dissertation, Texas A&M University.

Mehendale, A. B., Han, J. C., and Ou, S., 1991, "Influence of High Mainstream Turbulence on Leading Edge Heat Transfer," ASME *Journal of Heat Transfer*, Vol. 113, pp. 843-850.

Mick, W. J., and Mayle, R. E., 1988, "Stagnation Film Cooling and Heat Transfer, Including Its Effect Within the Hole Pattern," ASME JOURNAL OF TURBOMACHINERY, Vol. 110, pp. 66–72.

O'Brien, J. E., and VanFossen, G. J., 1985, "The Influence of Jet-Grid Turbulence on Heat Transfer From the Stagnation Region of a Cylinder in Crossflow," ASME Paper No. 85-HT-58.

Simonich, J. C., and Bradshaw, P., 1978, "Effect of Free-Stream Turbulence on Heat Transfer Through a Turbulent Boundary Layer," ASME *Journal of Heat Transfer*, Vol. 100, pp. 671–677.

Young, C. D., Han, J. C., Huang, Y., and Rivir, R. B., 1992, "Influence of Jet-Grid Turbulence on Flat Plate Turbulent Boundary Layer Flow and Heat Transfer," ASME *Journal of Heat Transfer*, Vol. 114, pp. 65–72.

Influence of High Mainstream Turbulence on Leading Edge Film Cooling Heat Transfer: Effect of Film Hole Row Location

S. Ou
Research Assistant.

A. B. Mehendale
Research Assistant.

J. C. Han
Professor.
Fellow ASME

Turbine Heat Transfer Laboratory,
Mechanical Engineering Department,
Texas A&M University,
College Station, TX 77843

The effect of film hole row location on leading edge film cooling effectiveness and heat transfer coefficient under high mainstream turbulence conditions was experimentally determined for flow over a blunt body with semicylinder leading edge and a flat afterbody. Two separate cases of film injection film holes located only at ±15 or ±40 deg were studied. The holes were spaced three hole diameters apart in the spanwise direction and inclined 30 and 90 deg to the surface in the spanwise and streamwise directions, respectively. A bar grid (Tu = 5.07 percent), a passive grid (Tu = 9.67 percent), and a jet grid (Tu = 12.9 percent) produced high mainstream turbulence. The incident mainstream Reynolds number based on cylinder diameter was 100,000. Spanwise and streamwise distributions of film effectiveness and heat transfer coefficient in the leading edge and the flat sidewall were obtained for three blowing ratios. The results show mainstream turbulence adversely affects leading edge film effectiveness for the low blowing ratio (B = 0.4), but the effect reduces for higher blowing ratios (B = 0.8 and 1.2). The leading edge heat transfer coefficient increases with mainstream turbulence level for B = 0.4 and 0.8, but the effect is not systematic for B = 1.2. Mainstream turbulence effect is more severe for ±15 deg one-row injection than for ± 40 deg one-row injection. The surface heat load reduction for ±15 deg one-row injection or ±40 deg one-row injection is smaller than that for two-row injection.

Introduction

To get higher thermal efficiency and higher power output, advanced aeroengines operate at high entry gas temperatures (1400–1500°C), far above the allowable metal temperatures. To operate under such extreme conditions without failure, highly sophisticated cooling techniques such as film cooling, impingement cooling, and rib/pin augmented cooling are employed. In film cooling, a relatively cooler gas is injected through the airfoil surface to form a protective layer between the surface and hot mainstream gases. This technique is extensively applied to gas turbine airfoils, around the leading edge, and on both pressure and suction sides. Film injection at the leading edge of an airfoil affects flow and heat transfer characteristics over the entire airfoil. Film cooling effectiveness and heat transfer distributions over the entire airfoil depend strongly on the location of film holes from stagnation. This investigation focuses on the effect of film hole row location on leading edge film cooling and heat transfer under grid-generated high mainstream turbulence conditions.

Contributed by the International Gas Turbine Division and presented at the ASME Winter Annual Meeting, Dallas, Texas, November 25–30, 1990. Manuscript received by the International Gas Turbine Division April 28, 1990. Paper No. 90-WA/HT-5. Associate Technical Editor: L. A. Riekert.

To model the leading edge region, Luckey and L'Ecuyer (1981) and Bonnice and L'Ecuyer (1983) used a circular cylinder with one to five rows of spanwise injection holes with various blowing ratios. They reported that for a low mainstream turbulence intensity of about 0.5 percent, the surface heat flux varied in both spanwise and streamwise directions depending upon the injection geometry and blowing ratio. Karni and Goldstein (1990) used the naphthalene sublimation technique to study the effect of surface injection from a circular cylinder in crossflow with one row of inclined holes on local mass transfer for a low mainstream turbulence intensity of about 0.45 percent. They reported that for spanwise injection, the mass transfer distribution is extremely sensitive to small changes in the injection row location relative to stagnation. Nirmalan and Hylton (1990) studied the effects of exit Mach number, exit Reynolds number, coolant-to-gas temperature ratio, and coolant-to-gas pressure ratio on turbine vane heat transfer with leading edge and downstream film cooling. They reported that considerable cooling benefits can be achieved by utilizing downstream film cooling.

Mick and Mayle (1988) used a blunt body with a circular leading edge and a flat afterbody to study film effectiveness and surface heat transfer for secondary air injection through

two rows of inclined holes into the stagnation region of an incident mainstream airflow. They found that for a low mainstream turbulence of about 0.5 percent, large spanwise variations exist in film effectiveness and heat transfer and that the highest and lowest values of each do not correspond. The film effectiveness is as high as 0.7–0.8 near the film cooling holes, while the heat transfer with film cooling is three times that without film cooling. The film effectiveness decays to only 0.1 downstream, while the heat transfer remains about 10 percent higher than that without injection. They also reported that for typical turbine temperatures, leading edge injection reduces the surface heat load everywhere for all blowing ratios except the highest one of 0.97.

Mehendale and Han (1992) studied the effect of high mainstream turbulence on leading edge film cooling and heat transfer for the case of flow over a similar test surface. Turbulence was generated by a passive grid ($Tu = 9.67$ percent) and a jet grid ($Tu = 12.9$ percent) at Reynolds number of 100,000. Film injection was through two rows of film holes at ± 15 and ± 40 deg, with blowing ratios of 0.4, 0.8, and 1.2. They found that mainstream turbulence adversely affects leading edge film cooling at a blowing ratio of 0.4. This effect on the leading edge is reduced at higher blowing ratios but the effect still exists on the flat sidewall region. The leading edge heat transfer increases with increasing mainstream turbulence for blowing ratio of 0.8, but the results are not so systematic for other blowing ratios.

This study focuses on the effect of film hole row location on leading edge film cooling, and heat transfer under high mainstream turbulence conditions for flow over a blunt body with a semicylinder leading edge and a flat afterbody. Two separate cases of film injection—film holes only at ± 15 or ± 40deg—are studied. The holes are three hole diameters apart in the spanwise direction and inclined 30 and 90 deg to the surface in the spanwise and streamwise directions, respectively. A bar grid ($Tu = 5.07$ percent), a passive grid ($Tu = 9.67$ percent), and a jet grid ($Tu = 12.9$ percent) produce high mainstream turbulence. Incident mainstream Reynolds number based on cylinder diameter is 100,000. Injecting secondary air through film holes into the stagnation region of the mainstream flow provides film cooling. Spanwise and streamwise distributions of local heat transfer coefficient (with film injection) and local film effectiveness are obtained from the leading edge to the end of the flat afterbody. The main concerns are: (*a*) to document the leading edge film effectiveness and heat transfer data for film holes only at ± 15 and ± 40 deg and (*b*) whether a single row injection can produce a comparable reduced heat load as a two-row injection over most of the leading edge surface.

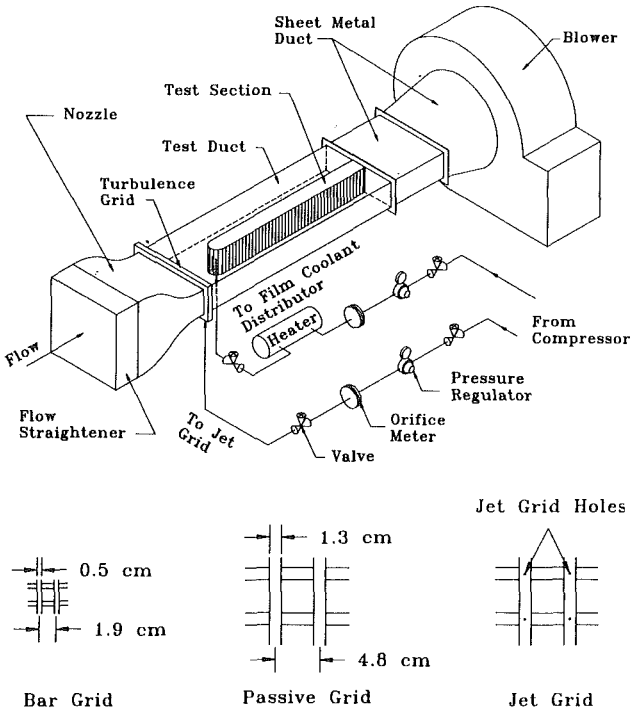

Fig. 1 Schematic of the film cooling test rig

Additonal information on the present investigation is given by Mehendale (1991), Mehendale and Han (1992), and Mehendale et al. (1991).

Test Apparatus and Instrumentation

Figure 1 shows a schematic of the low-speed open circuit wind tunnel used. The test apparatus is a suction type wind tunnel with a 7.5 kW (10 hp) blower. The test channel was 25.4 cm high × 76.2 cm wide in cross section and was 183 cm in length. The two-dimensional inlet nozzle had a 3:1 contraction ratio. Three turbulence grids—a relatively low turbulence bar grid, a high turbulence passive grid, and an even higher turbulence jet grid—produced different levels of turbulence. The bar grid was of stainless steel bars, 0.5 cm square

Nomenclature

b = passive/jet grid tube width
B = blowing ratio (average secondary-to-mainstream mass flux ratio)
d = film hole diameter
D = leading edge diameter
h = convective heat transfer coefficient
h_o = convective heat transfer coefficient without film holes
L = length of injection hole
Nu_D = Nusselt number based on leading edge diameter
P = pitch of holes in a row
q'' = convective heat flux
q''_o = convective heat flux without film holes
q''_{cond} = conduction heat loss flux
q''_{gen} = generated surface heat flux
q''_{rad} = radiation heat loss flux
Re_D = Reynolds number based on the incident mainstream velocity (U_∞) and leading edge diameter
T_{aw} = local adiabatic wall temperature
T_s = secondary or injected air temperature
Tu = streamwise turbulence intensity $= (\overline{u'^2})^{1/2}/U_\infty$
T_w = local measured wall (foil) temperature
T_∞ = mainstream or incident air temperature
U = local mainstream velocity
U_∞ = incident mainstream velocity at $X/b = 20$ with no grid
u' = local streamwise fluctuating velocity
X = axial distance measured from grid
x = streamwise distance measured from stagnation
Z = spanwise dimension
η = adiabatic film effectiveness
ϕ = overall cooling effectiveness

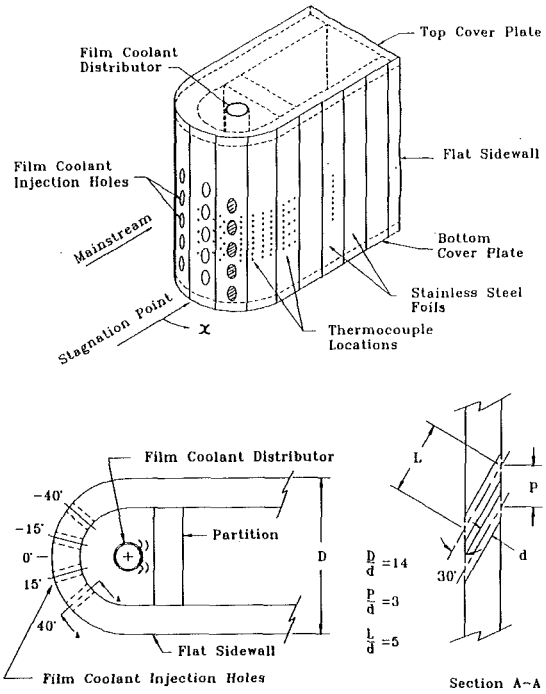

Fig. 2 Schematic of the leading edge with film holes and thermocouples

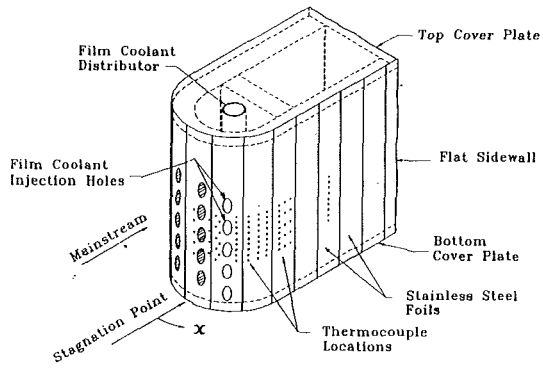

in cross section and 1.92 cm apart. The passive grid was hollow brass tubes, 1.3 cm square in cross section and 4.8 cm apart. Small holes, 0.05 cm in diameter, were drilled in the passive grid at grid nodes as seen in Fig. 1. Compressed air was supplied to the passive grid for use as the jet grid. The air was then injected in the coflow direction to produce higher levels of mainstream turbulence. All the turbulence grids had an open area of 54 percent.

As seen in Fig. 2, the test model was a blunt body with a semicylinder leading edge and a flat afterbody. For uniform approaching flow and turbulence, the leading edge of the test model was positioned at a distance of 47.6 cm downstream of the grid in the test channel ($X/b=37$). The test model was fabricated by laminating 2.8-cm-thick pieces of high-quality oak wood. The test model was 25.4 cm in height. The leading edge diameter was 15.2 cm, creating a flow blockage of 20 percent. Film holes were located at ± 15 and ± 40 deg from stagnation and spaced 3 film hole diameters in the spanwise direction. Each film hole was 1.1 cm in diameter. All film holes inclined 30 and 90 deg to the test surface in the spanwise and streamwise directions, respectively. The hole diameter to leading edge diameter ratio (d/D) was 0.072 and the hole length to hole diameter ratio (L/d) was 5.1. Forty-five strips of 0.05-mm-thick stainless steel foil were cemented vertically on the outer surface of the test model. Each strip was 25.4 cm long, 3.8 cm wide, and they were separated from each other by 0.8 mm. These gaps were filled with silicone caulk and made flush with the foil surface. Holes were cut in the foils to match the film cooling holes in the test model. All foils were connected in series by copper bus bars. The test surface acted as a constant heat flux surface (expect for the foils with film holes) when heated, otherwise it acted as an adiabatic surface. The test model had one inlet port from below for the film coolant.

A secondary system supplied hot air to the leading edge film holes. To run the ± 15 deg tests, film holes at ± 40 deg were plugged with silicone caulk to make the surface flush with the test surface. For ± 40 deg tests, a similar procedure was repeated with the holes at ± 15 deg.

Eighty-eight calibrated thermocouples of 36 gage copper-constantan were cemented on the underside of the foils (73 in the leading edge region and 15 on the flat sidewall) to measure local temperature distribution. Thermocouples were also attached on the inner wall for heat loss estimation. Four thermocouples were centrally located in the bottom holes of each row to measure the secondary hot air temperature. All thermocouples were connected to a Fluke 2280A datalogger that interfaced with an IBM PC. A digital multimeter and an autoranging current clamp were used to measure circuit voltage and current, respectively.

A TSI IFA 100 constant temperature anemometer (CTA) with a TSI IFA 200 high-speed digitizer measured turbulence and velocity data from a calibrated single hot wire. The single component streamwise rms calculations were based on 1032 readings from the CTA. The local streamwise turbulence intensity was based on the average of five sets of rms values normalized by the local streamwise velocity. Pitot probes, 2 mm in diameter, measured velocity profiles, set desired Reynolds number flow, and constantly monitored the flow velocity. These probes connected to a micromanometer. An orifice meter prior to the heater measured the secondary mass flow rate.

Test Conditions and Data Analysis

Before conducting heat transfer or film cooling tests for the first time, it was made sure that corresponding free-stream flow velocities on the left and right sides were the same. This assured that the test model was centrally located within the test channel, i.e., flow symmetry existed and the only pressure gradient on the flat sidewall was because of the growing boundary layer.

Tests were conducted in the low-turbulence wind tunnel for Reynolds number of 100,000 based on leading edge diameter (D) and incident mainstream velocity ($U_\infty = 10$ m/s). Mainstream streamwise turbulence intensity in the test duct without the insertion of any turbulence grid (no grid case) was about 0.75 percent. Higher streamwise turbulence intensities were generated by inserting the appropriate turbulence grid in the mainstream flow at the nozzle exit. Heat transfer and film cooling tests were performed at the reference turbulence intensities of 5.07 percent (bar grid), 9.67 percent (passive grid), and 12.9 percent (jet grid). These reference turbulence intensities were measured at 25–30 grid diameters downstream of each grid, i.e., about 10 cm upstream of the leading edge. The corresponding dissipation length scales at the same location were estimated to be about 1.0 cm, 1.2 cm, and 1.7 cm, respectively. Blowing ratios of 0.4, 0.8, and 1.2 (typical for a real engine) were used. The variation in centerline flow velocity at the exit of each film hole was within ± 5 percent for ± 15 deg tests and ± 4 percent for ± 40 deg tests. The turbulence intensity at the exit of each hole (the rms fluctuations in coolant flow normalized by the incident mainstream velocity) was 3–5 percent, 7–12 percent, and 25–30 percent for blowing ratios of 0.4, 0.8, and 1.2, respectively. The turbulence intensity at the exit of the film holes in any row was uniform.

Secondary air temperature was maintained at 25°C above the mainstream temperature for film effectiveness tests. This resulted in a secondary to mainstream density ratio of 0.9. For heat transfer tests, the secondary air temperature was about the same as the mainstream temperature. For blowing ratios of 0.4, 0.8, and 1.2 the corresponding momentum ratios were 0.18, 0.71, and 1.6 for film effectiveness tests and 0.16, 0.64, and 1.44 for heat transfer tests. Note that the density ratio should have an important impact on film effectiveness and heat transfer for blowing ratios of 0.8 and higher. This investigation focuses on the high mainstream turbulence effect at a constant density ratio. The density ratio effect will be considered separately. It took about 3-1/2 to 4 hours to reach steady state for each test case. Data (surface temperature distribution, power input, and ambient and flow conditions) were recorded when steady state was reached. Five such sets of data were recorded at one minute intervals. An average was made to minimize the effect of fluctuations in operating conditions.

Heat transfer tests were conducted by injecting ambient air through the film holes while power was supplied to the surface foils. The local heat transfer coefficient was calculated as:

$$h = \frac{q''}{T_w - T_{aw}} = \frac{q''_{gen} - q''_{cond} - q''_{rad}}{T_w - T_{aw}} \quad (1)$$

where q'' is the convective heat flux from the foil surface, T_w is the local steady-state foil temperature, T_{aw} is the local adiabatic wall temperature, q''_{gen} is the generated surface heat flux from voltage current calculations, q''_{cond} is the conduction loss flux through the test model and to the surroundings, and q''_{rad} is the radiation loss flux to the test duct walls.

Local radiation and conduction losses were estimated using $\epsilon = 0.22$ and from loss tests, respectively. For the foils without any film holes, there was no spanwise variation in q''_{gen} and so it could be easily calculated. For foils with film holes, the generated surface heat flux varied considerably in the spanwise direction. By comparing the local Nusselt number for a foil without film holes to that for a foil with film holes, the values of local q''_{gen} were estimated. A complete discussion about estimating this nonuniform flux is given by Mehendale and Han (1992). The conduction and radiation losses were about 3 and 10 percent of the generated surface heat, respectively. Heat loss through thermocouple wires was very small when compared to the generated surface heat (less than 0.1 percent). Axial and lateral conduction through the thin foil was also negligible (less than 0.1 percent).

Film effectiveness tests were conducted by injecting hot air through the film holes without power supplied to the surface foils. The temperature of the injected air was about 25°C higher than that of the mainstream flow. The local film effectiveness was calculated as

$$\eta = \frac{T_{aw} - T_\infty}{T_s - T_\infty} = \frac{T_w - T_\infty}{T_s - T_\infty} + \frac{q''_{rad} - q''_{cond}}{h(T_s - T_\infty)} \quad (2)$$

where T_{aw} is the local adiabatic wall temperature, T_s is the secondary (hot) air temperature, and T_∞ is the mainstream temperature. Since the test surface was not perfectly adiabatic, some corrections were applied to the measured wall temperature (T_w) to obtain the adiabatic film effectiveness. These corrections included the effect of heat transfer by conduction through the wood model (q''_{cond}), heat loss by radiation to the wind tunnel walls (q''_{rad}), and the local film cooled heat transfer coefficient (h) as obtained from Eq. (1).

Note that for film effectiveness tests, heat actually was transferred from inside the test model to the test surface for the locations on the leading edge region, i.e., there was a conduction heat gain, as seen from Eq. (2). This gain was estimated by a one-dimensional conduction model. Also, thermocouple locations near the film holes had an additional conduction gain from the hot air passing through the film holes. This additional conduction gain was estimated, as discussed by Mehendale and Han (1992). These additional conduction gain values were then used to estimate the total conduction gain for the thermocouple locations near film holes. The local effectiveness was determined using Eq. (2).

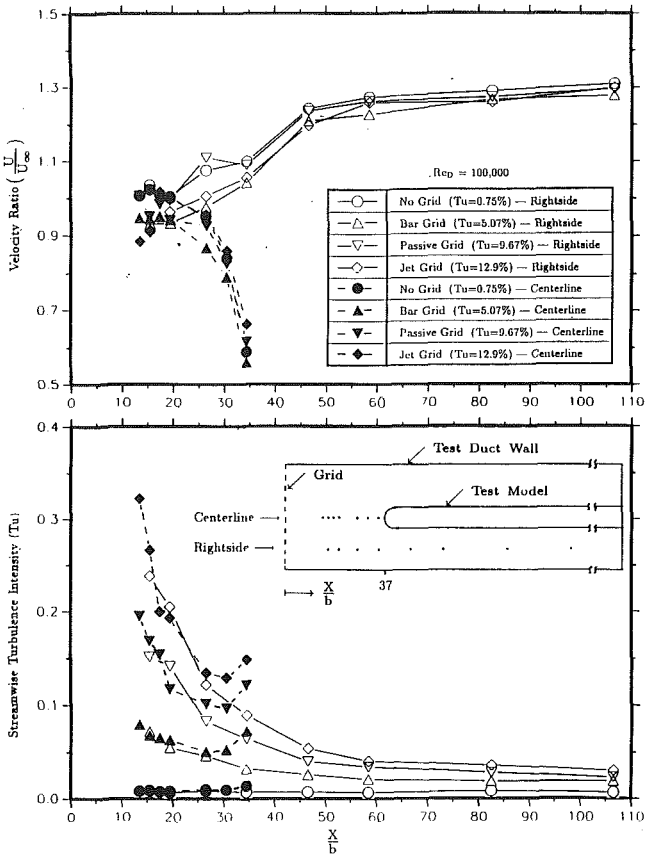

Fig. 3 Streamwise distributions of normalized mainstream velocity and turbulence intensity

An uncertainty analysis based on the method of Kline and McClintock (1953) was carried out for both the film effectiveness and heat transfer with film injection. Based on 20:1 odds, the uncertainty around the film holes was about 15 percent (primarily due to q''_{gen} estimate), whereas the uncertainty downstream of the leading edge is less than 5 percent.

Results and Discussion

Velocity measurements were made at a cross plane 1.5 leading edge diameters upstream of stagnation. Velocities were fairly uniform over the entire plane. The local velocity and turbulence intensity distribution along the centerline and right-side line for all four upstream conditions are shown in Fig. 3. The ratio of local mainstream velocity to incident mainstream velocity (U/U_∞) along the centerline and right-side line is about 1.0 up to 20 grid diameters downstream of grid (i.e., $X/b = 20$, or 1.5 leading edge diameters upstream of stagnation). The incident mainstream velocity (U_∞) is 10 m/s at $X/b = 20$ for no grid case. Local mainstream velocity along centerline decreases sharply after $X/b = 20$ because of stagnation. Due to the blockage effect of the test model, the right-side velocity gradually increases and then attains a constant value. The effect of mainstream turbulence on both velocity profiles is not significant.

As expected, the local turbulence intensity decreases with distance. This decay continues to the end of the test model for locations along the right-side line. However, for locations along the centerline, as we approach stagnation, the turbulence intensity starts increasing. This increase in turbulence intensity

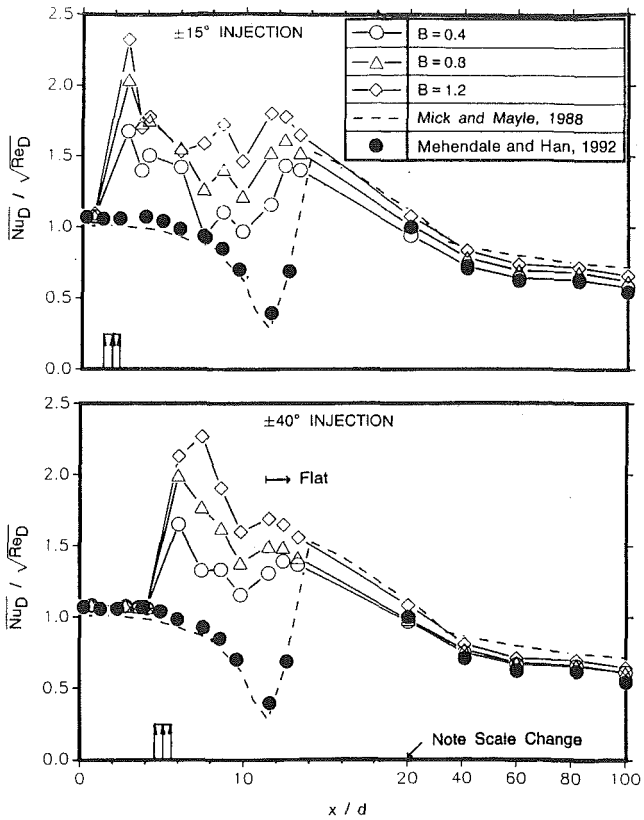

Fig. 4 Effect of blowing ratio on spanwise-averaged Nusselt number distributions for low mainstream turbulence for ±15 and ±40 deg injection

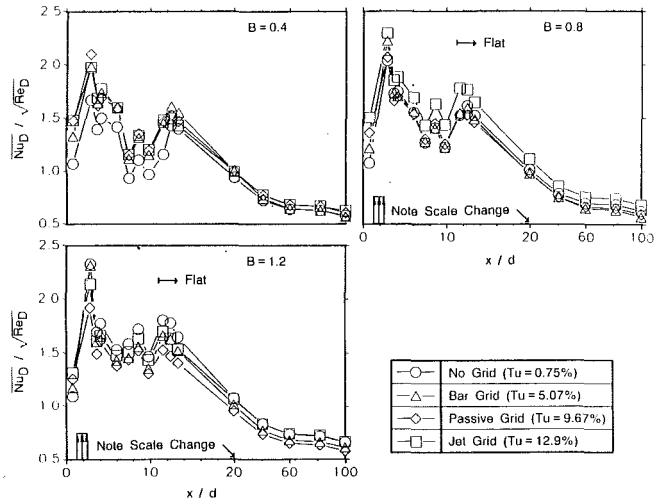

Fig. 5 Effect of mainstream turbulence on spanwise-averaged Nusselt number distributions for $B = 0.4$, 0.8, and 1.2 at ±15 deg injection

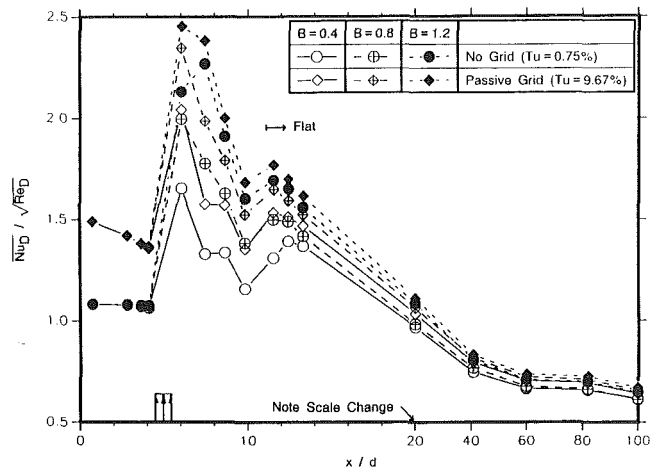

Fig. 6 Effect of mainstream turbulence on spanwise averaged Nusselt number distributions for $B = 0.4$, 0.8, and 1.2 at ±40 deg injection

is due to a decrease in the average local velocity and not an increase in the fluctuating component. For a given upstream turbulence condition, the minimum value of the corresponding turbulence intensity curve was chosen as the reference turbulence intensity for that condition. The reference turbulence intensities for bar grid, passive grid, and jet grid were 5.07, 9.67, and 12.9 percent, respectively. The corresponding dissipation length scales at the same location were estimated to be about 1.0 cm, 1.2 cm, and 1.7 cm.

Heat transfer tests were conducted on a smooth leading edge model without film holes (pure heat transfer) to calibrate the leading edge and the data were compared to the published results for low mainstream turbulence, i.e., for the no grid case. Detailed pure heat transfer data for three Reynolds numbers and four turbulence levels are given by Mehendale et al. (1991).

The heat transfer data for ±15 or ±40 deg injections for the no-grid case are shown in Fig. 4 along with the pure heat transfer data from this investigation and published results. The pure heat transfer data follow the published results. Heat transfer decreases from stagnation, reaches a minimum at separation ($x/d \simeq 12.0$), and then reaches a maximum at reattachment ($x/d \simeq 14.0$). Since an increase in blowing ratio causes an increase in the turbulence at the exit of the film holes, the heat transfer at all locations is higher for the higher blowing ratios for both ±15 and ±40 deg injection cases. This effect of blowing ratio, due to the secondary flow turbulence, decreases considerably on the flat sidewall region for both injection cases, where the data are very close to pure heat transfer data. The increase in heat transfer is most severe on the leading edge downstream of the corresponding row of film holes.

The effect of mainstream turbulence on heat transfer is seen in Fig. 5 for three cases of blowing ratios of 0.4, 0.8 and 1.2 from ±15 deg film holes. For blowing ratios $B = 0.4$, 0.8, and 1.2, the turbulence intensity at the exit of the film holes is about 3–5 percent, 7–12 percent, and 25–30 percent, respectively. The effect of this turbulence is severe for the no-grid case since the mainstream turbulence is low, and the severity increases with increasing blowing ratio. Hence, for blowing ratios of 0.8 and 1.2, the heat transfer for the no-grid case is similar to or even higher than for higher mainstream turbulence cases. With increasing blowing ratio, the secondary flow turbulence dominates the mainstream turbulence. Hence, for higher blowing ratios, the spread in heat transfer due to mainstream turbulence is reduced. It is also seen that increasing blowing ratio causes higher heat transfer for all mainstream turbulence cases.

The effect of mainstream turbulence for the case of ±40 deg injection and three blowing ratios is seen in Fig. 6. Heat transfer for the passive grid is always higher than for no grid for all blowing ratios. The effect of mainstream turbulence is most prominent on the leading edge downstream of 40 deg holes, for the lowest blowing ratio of $B = 0.4$. For higher blowing ratios, however, this effect is reduced. An increase in blowing ratio causes higher heat transfer even for the higher mainstream turbulence case.

The effect of mainstream turbulence on film effectiveness for ±15 deg film injection is shown in Fig. 7 for the three

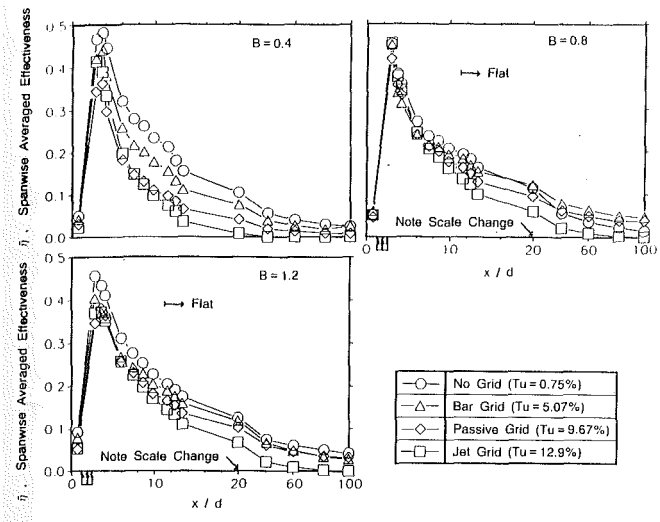

Fig. 7 Effect of mainstream turbulence on spanwise-averaged film effectiveness distributions for $B = 0.4$, 0.8, and 1.2 at ± 15 deg injection

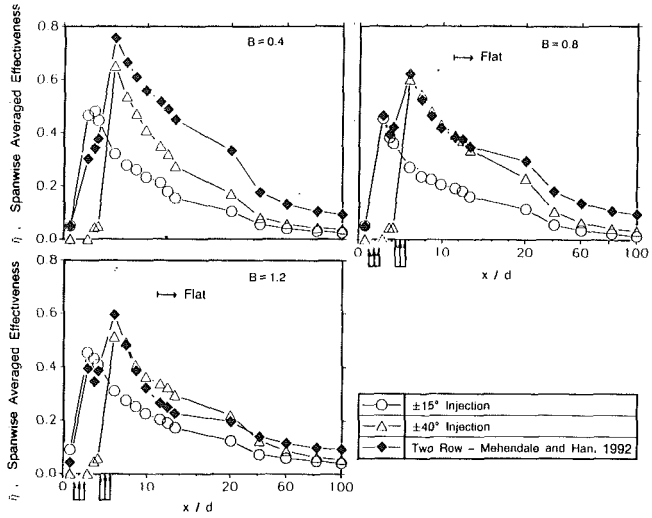

Fig. 9 Effect of film hole row location on spanwise-averaged film effectiveness distributions and comparison with two row data for no-grid case

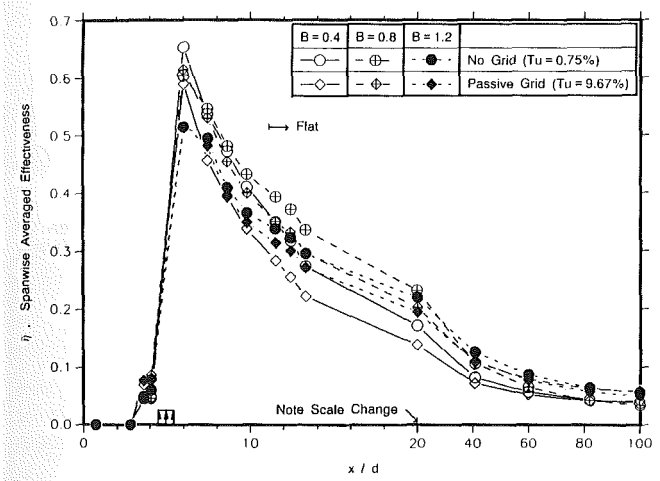

Fig. 8 Effect of mainstream turbulence on spanwise-averaged film effectiveness distributions for $B = 0.4$, 0.8, and 1.2 at ± 40 deg injection

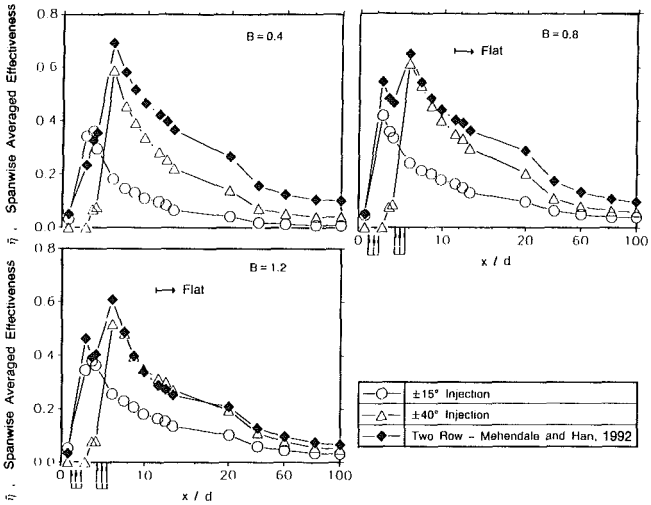

Fig. 10 Effect of film hole row location on spanwise-averaged film effectiveness distributions and comparison with two-row data for passive grid case

blowing ratios. As in the case of heat transfer, for lowest blowing ratio of $B = 0.4$, the mainstream turbulence dominates. The turbulence penetrates the film layer. Thus, higher mainstream turbulence causes lower film effectiveness. As previously discussed, for higher blowing ratios of $B = 0.8$ and 1.2, the secondary turbulence dominates the mainstream turbulence. Thus, the spread in film effectiveness due to mainstream turbulence is reduced. The effectiveness distributions due to mainstream turbulence for the case of ± 40 deg injection at the three blowing ratios are in Fig. 8. The trends are similar to Fig. 7. The effect of mainstream turbulence in reducing film effectiveness is similar, but smaller when compared to the ± 15 deg injection case.

In Fig. 9, film effectiveness for ± 15 or ± 40 deg injections is presented with the data for two row injection from Mehendale and Han (1992). The two row data between 15 and 40 deg should be comparable with ± 15 deg data at similar locations. This is not so because in the case of two-row injection (Mehendale and Han, 1992), $\dot{m}_{40°}/\dot{m}_{15°}$ was 2.0, 1.5, and 1.2 for average blowing ratios of $B = 0.4$, 0.8, and 1.2, respectively. This means that for average blowing ratios of 0.4, 0.8, and 1.2, through two rows combined, the apparent blowing ratios through the row at 15 deg were 0.27, 0.67 and 1.09; whereas the apparent blowing ratios through the row at 40 deg were 0.53, 0.96, and 1.31. This results in an increase of 48, 25, and 10 percent for blowing ratios of 0.4, 0.8, and 1.2, respectively, in the flow coming out of 15 deg holes for $\pm$ 15 deg injection as compared to that for the two-row case. Therefore, we find that ± 15 deg data are usually higher than two-row data between 15 and 40 deg. This difference in film effectiveness is largest for $B = 0.4$. As the blowing ratio increases, the differences decreases. Alternately, there is a corresponding decrease in flow coming out of 40 deg holes for ± 40 deg injection as compared to that for the two-row case. For blowing ratios of 0.4, 0.8, and 1.2, the corresponding reductions are 25, 17, and 8 percent. This is seen in Fig. 9, that while the blowing ratio increases, the ± 40 deg data and the two-row data approach each other. The ± 15, ± 40 deg and two-row film effectiveness data for the passive grid case are shown in Fig. 10. The data have the same trend as for the no-grid case except the effectiveness values are lower. Increasing blowing ratio results is reducing the difference between single-row and two-row data.

The best cooling design should give minimum heat load as compared to the pure heat transfer case. Therefore, it is important to study the overall effect of film cooling. The parameter heat load ratio (Mick and Mayle, 1988) is defined as

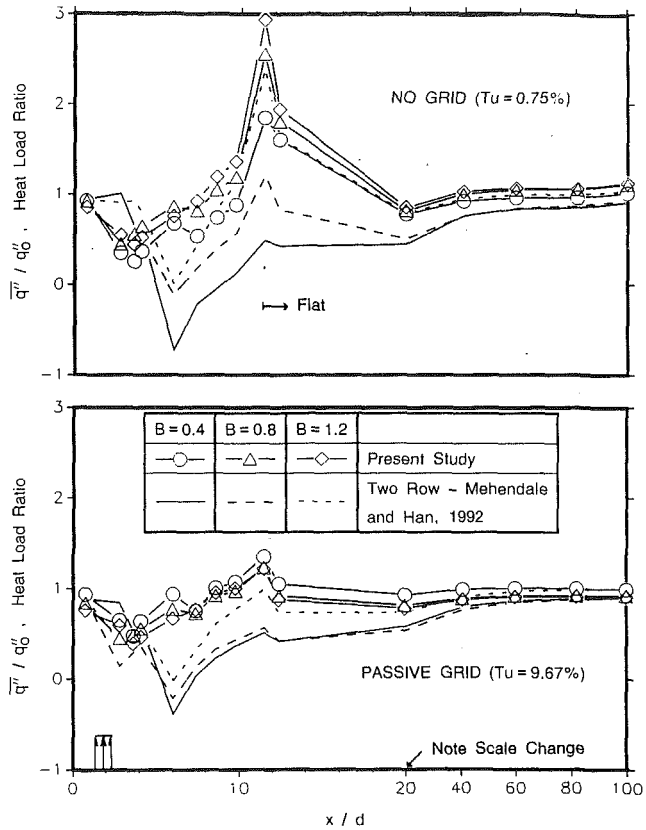

Fig. 11 Effect of blowing ratio, through film holes at ±15 deg, on surface heat load and comparison with two row data for $\phi = 0.6$: no-grid case and passive grid case

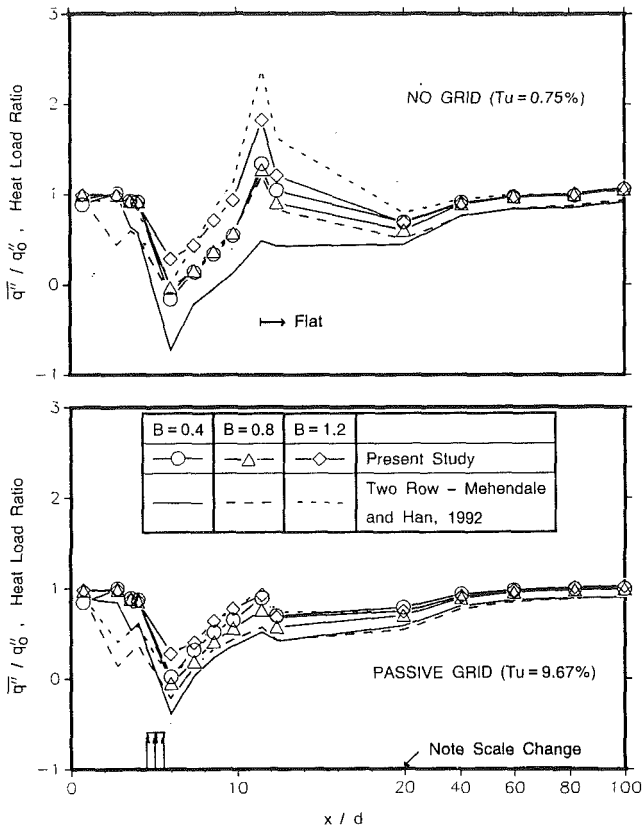

Fig. 12 Effect of blowing ratio, through film holes at ±40 deg, on surface heat load and comparison with two row data for $\phi = 0.6$: no-grid case and passive grid case

$$\frac{\overline{q''}}{q_0''} = \frac{1}{n}\sum_{i=1}^{n}\left(\frac{h(x, z_i)}{h_o}\right)\left(1 - \frac{\eta(x, z_i)}{\phi}\right) \tag{3}$$

where q_o'' is the heat flux for pure heat transfer without film holes at any streamwise location, $\overline{q}''$ is the spanwise-averaged heat flux for film cooled heat transfer at the same streamwise location, n is the number of thermocouples in a row to obtain the spanwise-averaged film effectiveness and heat transfer coefficient, and ϕ is the overall cooling effectiveness given by $\phi = (T_w - T_\infty)/(T_s - T_\infty)$.

The value of ϕ is usually 0.5–0.6 for gas turbines. Using $\phi = 0.6$, comparison of overall performance due to film cooling was made. The heat load ratio for ±15 deg injection under no-grid and passive grid conditions and for three blowing ratios is given in Fig. 11. Also shown for comparison are the two-row data from Mehendale and Han (1992). For the no-grid case, where the secondary turbulence effect is dominant, an increase in blowing ratio results in an increase in heat load, i.e., $B = 0.4$ shows the best performance. Significantly higher heat load is observed near reattachment. The data for the passive grid case for all three blowing ratios are very close and about 1.0 for most of the region. The performance for ±15 deg for $B = 0.4$ is the lowest due to high mainstream turbulence. Unlike the two-row case, no region has a negative heat load. As seen from Fig. 12, for the case of ±40 deg injection under no-grid conditions, the trend is similar to that of ±15 deg injection under similar conditions except there is not much difference between $B = 0.4$ and 0.8, and the heat load is considerably reduced. As before, $B = 1.2$ gives the worst performance. There are some areas with negative heat load. High mainstream turbulence reduces the spread and reduces the heat load near the separation and reattachment region. Unlike the ±15 deg injection case, ±40 deg injection is effective over most of the leading edge region.

Concluding Remarks

The influence of high mainstream turbulence on leading edge film effectiveness and heat transfer with ±15 deg one-row or ±40 deg one-row injection has been investigated. The main findings of the study are:

1 For ±15 deg one-row injection, the film effectiveness decreases with increasing mainstream turbulence level, although the mainstream turbulence effect decreases with increasing blowing ratio. A similar trend is seen for ±40 deg one-row injection, but the effect is not as severe as for ±15 deg injection.

2 For ±15 deg one-row or ±40 deg one-row injection, the leading edge heat transfer coefficient with film injection increases with increasing blowing ratio, but the effect diminishes toward the end of the flat sidewall. For ±15 deg one-row injection, the leading edge heat transfer generally increases with increasing mainstream turbulence level, although the effect is not so systematic for the higher blowing ratio of $B = 1.2$. For ±40 deg one-row injection, clearly higher mainstream turbulence produces higher heat transfer and this effect disappears toward the end of the flat sidewall.

3 For ±15 deg one-row or ±40 deg one-row injection, surface heat load decreases with decreasing blowing ratio for the low mainstream turbulence flow ($Tu = 0.75$ percent). This trend is the same as that found in the previous study of two-row injection. Surface heat load trend for the high mainstream turbulence flow ($Tu = 9.67$ percent) is the same, but the spread due to blowing ratio is considerably less. In general, two-row injection provides more heat load reduction than the corresponding one-row injection.

Acknowledgments

Dr. Richard B. Rivir of the U.S. Air Force Wright Patterson

AFB supported the turbulence portion under contract #F33615-86-2723. The test model portion was associated with the Film Cooling Project sponsored by Textron Lycoming through Contract #H164150. Their support is gratefully acknowledged.

References

Bonnice, M. A., and L'Ecuyer, M. R., 1983, "Stagnation Region Gas Film Cooling—Effects of Dimensionless Coolant Temperature," NASA CR-168197.

Karni, J., and Goldstein, R. J., 1990, "Surface Injection Effect on Mass Transfer From a Cylinder in Crossflow: A Simulation of Film Cooling in the Leading Edge Region of a Turbine Blade," ASME JOURNAL OF TURBOMACHINERY, Vol. 112, pp. 418–427.

Kline, S. J., and McClintock, F. A., 1953, "Describing Uncertainties in Single-Sample Experiments," *Mechanical Engineering*, Vol. 75, pp. 3–8.

Luckey, D. W., and L'Ecuyer, M. R., 1981, "Stagnation Region Gas Film Cooling—Spanwise Angled Injection From Multiple Rows of Holes," NASA CR-165333.

Mehendale, A. B., 1991, "Effect of High Mainstream Turbulence on Leading Edge Heat Transfer and Film Cooling," Ph.D. Dissertation, Texas A&M University.

Mehendale, A. B., Han, J. C., and Ou, S., 1991, "Influence of High Mainstream Turbulence on Leading Edge Heat Transfer," ASME *Journal of Heat Transfer*, Vol. 113, pp. 843–850.

Mehendale, A. B., and Han, J. C., 1992, "Influence of High Mainstream Turbulence on Leading Edge Film Cooling Heat Transfer," ASME JOURNAL OF TURBOMACHINERY, Vol. 114, this issue, pp. 707–715.

Mick, W. J., and Mayle, R. E., 1988, "Stagnation Film Cooling and Heat Transfer, Including Its Effect Within the Hole Pattern," ASME JOURNAL OF TURBOMACHINERY, Vol. 110, pp. 66–72.

Nirmalan, V., and Hylton, L. D., 1990, "An Experimental Study of Turbine Vane Heat Transfer With Leading Edge and Downstream Film Cooling," ASME JOURNAL OF TURBOMACHINERY, Vol. 112, pp. 477–487.

Influence of Mainstream Turbulence on Leading Edge Film Cooling Heat Transfer Through Two Rows of Inclined Film Slots

S. Ou
Research Assistant.

J. C. Han
Professor.
Fellow ASME

Turbine Heat Transfer Laboratory,
Mechanical Engineering Department,
Texas A&M University,
College Station, TX 77843

The effect of film slot injection on leading edge heat transfer coefficient and film cooling effectiveness under high mainstream turbulence conditions was experimentally studied for flow across a blunt body with a semicylinder leading edge and a flat afterbody. High mainstream turbulence levels were generated by a bar grid (Tu = 5.07 percent) and a passive grid (Tu = 9.67 percent). The indicent mainstream Reynolds number based on the cylinder diameter was about 100,000. The spanwise and streamwise distributions of the heat transfer coefficient and film effectiveness in the leading edge and on the flat sidewall were obtained for three blowing ratios (B = 0.4, 0.8, and 1.2) with two rows of film slots located at ±15 and ±40 deg from the stagnation line. The cross-sectional slot length-to-width ratio was two. The slots in each row were spaced three cross-sectional slot lengths apart and were angled 30 and 90 deg to the surface in the spanwise and streamwise directions, respectively. The results show that heat transfer coefficient increases with increasing blowing ratio, but the film effectiveness reaches a maximum at an intermediate blowing ratio of B = 0.8 for both low (Tu = 0.75 percent) and high (Tu = 9.67 percent) mainstream turbulence conditions. The leading edge heat transfer coefficient increases and the film effectiveness decreases with mainstream turbulence level for the low blowing ratio; however, the mainstream turbulence effect decreases for the high blowing ratio. The leading edge heat load is significantly reduced with two rows of film slot injection. The blowing ratio of B = 0.4 provides the lowest heat load in the leading edge region for the low mainstream turbulence, but B = 0.8 gives the lowest heat load for the high mainstream turbulence conditions.

Introduction

The performance of a gas turbine engine is strongly influenced by turbine inlet temperature as shown from the analysis of thermodynamics. The continuing trend toward higher inlet temperatures in gas turbine engine development has resulted in increasing heat loads to turbine components. Modern gas turbine engines are designed to operate at high turbine inlet temperatures (1400°–1500°C), which are far beyond the allowable metal temperatures. Therefore, in order to maintain acceptable life and safety requirements under such extreme operating conditions, highly sophisticated cooling techniques such as film cooling and augmented internal cooling have to be employed. In film cooling, relatively cooler air is injected onto the surface of the blade to form a protective layer between the surface and hot mainstream gases. Film injection around the leading edge of an airfoil affects the film cooling effectiveness and heat transfer coefficient distributions over the entire airfoil. This investigation focuses on the effect of film slot injection on the leading edge film effectiveness and heat transfer coefficient under grid-generated high mainstream turbulence conditions.

Sasaki et al. (1976) studied film cooling in the stagnation region of a circular cylinder with two rows of spanwise angled holes. One row was located at 15 deg and the other at 45 deg from stagnation. They reported that downstream from the second row of holes the adiabatic effectiveness increased with increasing blowing ratio until an optimum blowing ratio of 0.5 to 0.6 was reached. The film effectiveness continually decreased as the blowing ratio increased passed the optimum value. Luckey and L'Ecuyer (1976) used a circular cylinder to model the leading edge region with film holes angled 20, 30, and 40 deg to the surface in the spanwise direction. They detected large spanwise variations in the surface heat flux. They also found that the variations varied with both the injection geometry and blowing ratios. Luckey and L'Ecuyer (1981) and Bonnice and L'Ecuyer (1983) used a circular cylinder with one to five rows of spanwise injection holes with

Contributed by the International Gas Turbine Institute and presented at the 36th International Gas Turbine and Aeroengine Congress and Exposition, Orlando, Florida, June 3–6, 1991. Manuscript received at ASME Headquarters March 4, 1991. Paper No. 91-GT-254. Associate Technical Editor: L. A. Riekert.

various blowing ratios. For a low mainstream turbulence intensity of about 0.5 percent, they found that the surface heat flux varied in both spanwise and streamwise directions depending on the injection geometry and blowing ratio. Karni and Goldstein (1990) used the naphthalene sublimation technique to study the effect of surface injection from a circular cylinder in crossflow with one row of inclined holes on local mass transfer at a low mainstream turbulence intensity of about 0.45 percent. They reported that for spanwise injection, the mass transfer distribution is extremely sensitive to small changes in the injection hole location relative to stagnation line. Nirmalan and Hylton (1990) reported the effects of exit Mach number, exit Reynolds number, coolant-to-gas temperature ratio, and coolant-to-gas pressure ratio on turbine vane heat transfer with leading edge and downstream film cooling. They found that considerable cooling benefits can be obtained by using downstream film cooling.

Mick and Mayle (1988) used a blunt body with a circular leading edge and a flat afterbody to study the film cooling effectiveness and surface heat transfer coefficient in the stagnation region of an incident mainstream flow with secondary air injection through two rows of inclined holes. Under the conditions of a low mainstream turbulence intensity of 0.4 percent and a Reynolds number of 100,000, they found large spanwise variations existed in both film effectiveness and heat transfer coefficient and that the highest values of each do not in general correspond. The film effectiveness near the injection holes was as high as 0.7–0.8, while the heat transfer coefficient with film injection was as high as three times those without film cooling. The film effectiveness decayed to values near 0.1 far downstream, and the heat transfer coefficient remained about 10 percent higher than that without film injection. They also reported that for typical turbine temperatures, leading edge injection reduced the surface heat load everywhere for blowing ratios of 0.38 and 0.64. An exception was an increase in heat load somewhere within the injection region for blowing ratios of 0.97.

Mehendale and Han (1992) used a test model similar to that of Mick and Mayle (1988) to study the effect of high mainstream turbulence on leading edge film cooling and heat transfer. Two turbulence levels (Tu = 9.67 percent and Tu = 12.9 percent) were generated by a passive grid and a jet grid at a leading edge Reynolds number of 100,000. Film coolant was injected through two rows of film holes at ±15 and ±40 deg from stagnation with three blowing ratios of 0.4, 0.8, and 1.2. They found that the leading edge film effectiveness for a blowing ratio of 0.4 was significantly reduced by high mainstream turbulence. For blowing ratios of 0.8 and 1.2, the mainstream turbulence effect was diminished in the leading edge but still existed on the flat sidewall region. They also pointed out that the leading edge heat transfer coefficient for a blowing ratio of 0.8 increased with increasing mainstream turbulence, but the effect is not consistent for blowing ratios of 0.4 and 1.2.

Ou et al. (1992) used the test model of Mehendale and Han (1992) to study the effect of film hole row location on leading edge film cooling effectiveness and heat transfer under high mainsteram turbulence levels (Tu = 5.07–12.9 percent). They investigated two separate cases of film injection: (*a*) the film holes located ±15 deg from stagnation and (*b*) the film holes located at ±40 deg from stagnation. With a Reynolds number of 100,000 and three blowing ratios (B = 0.4, 0.8, and 1.2), the results showed that the mainstream turbulence adversely affected the leading edge film effectiveness for a blowing ratio of 0.4 but the effect was reduced for blowing ratios of 0.8 and 1.2. The leading edge heat transfer coefficient increased with mainstream turbulence levels for B = 0.4 and B = 0.8 but the effect was not consistent for B = 1.2. The results also showed that the effect of mainstream turbulence was more pronounced for ±15 deg one row injection than for ±40 deg one row injection.

There is a long history of film cooling application around the leading edge region of turbine airfoils. However, a review of the literature reveals that previous studies are limited to circular film holes in the leading edge of a cylinder. The shape of film openings could be an important parameter in affecting film cooling performance. This study focuses on the effect of film slot injection, instead of film hole injection, on leading edge film cooling and heat transfer under high mainstream turbulence conditions for flow across a blunt body with a semicylinder leading edge and a flat afterbody. The cross-sectional slot length-to-width ratio is 2. Two rows of film slots are located at ±15 and ±40 deg from stagnation line. The main concerns are: (*a*) to document the leading edge film effectiveness and heat transfer coefficient data under high mainstream turbulence levels, (*b*) to determine the leading edge heat load reduction with two rows of film slot injection and, (*c*) to obtain film cooling contours by using liquid crystals thermal visualization technique.

Nomenclature

b = passive grid width
B = blowing ratio (average secondary-to-mainstream mass flux ratio)
D = leading edge diameter (cylinder diameter)
h = local heat transfer coefficient with film injection
$\overline{h}_o$ = spanwise-averaged heat transfer coefficient without film slots
L = length of injection slot
L_e^u = dissipation length scale
l = cross-sectional length of film slot
Nu_D = Nusselt number based on leading edge diameter
P = pitch of slots in a row
q'' = convective heat flux
$\overline{q}_o''$ = spanwise-averaged heat flux without film slots
$\overline{q}''$ = spanwise-averaged heat flux with film injection
q''_{cond} = conduction heat loss flux
q''_{gen} = foil-generated surface heat flux
q''_{rad} = radiation heat loss flux
Re_D = Reynolds number based on the incident mainstream velocity (U_∞) and leading edge diameter (D)
T_{aw} = adiabatic wall temperature
T_s = secondary or injected air temperature
Tu = streamwise turbulence intensity = $(\overline{u'^2})^{1/2}/U$
T_w = measured wall (foil) temperature
T_∞ = mainstream or incident air temperature
U = local mainstream velocity
U_∞ = incident mainstream velocity at X/b = 20 with no grid
U_s = velocity of secondary flow
u' = local streamwise fluctuating velocity
w = cross-sectional width of film slot
X = axial distance measured from grid
x = streamwise distance measured from stagnation
Z = spanwise distance
η = adiabatic film effectiveness
ρ_∞ = density of mainstream flow
ρ_s = density of secondary flow
ϕ = overall cooling effectiveness

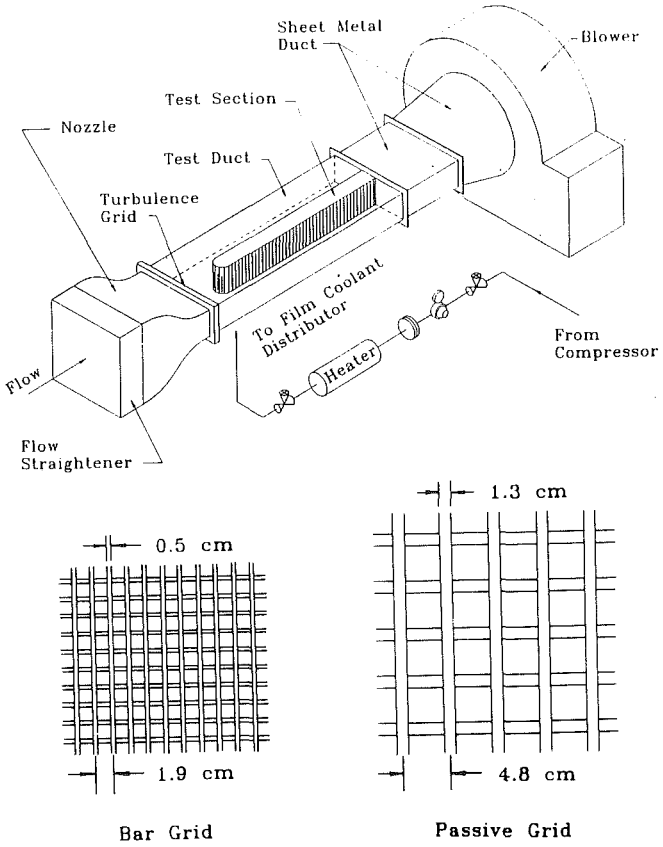

Fig. 1 Schematic of the film cooling test rig

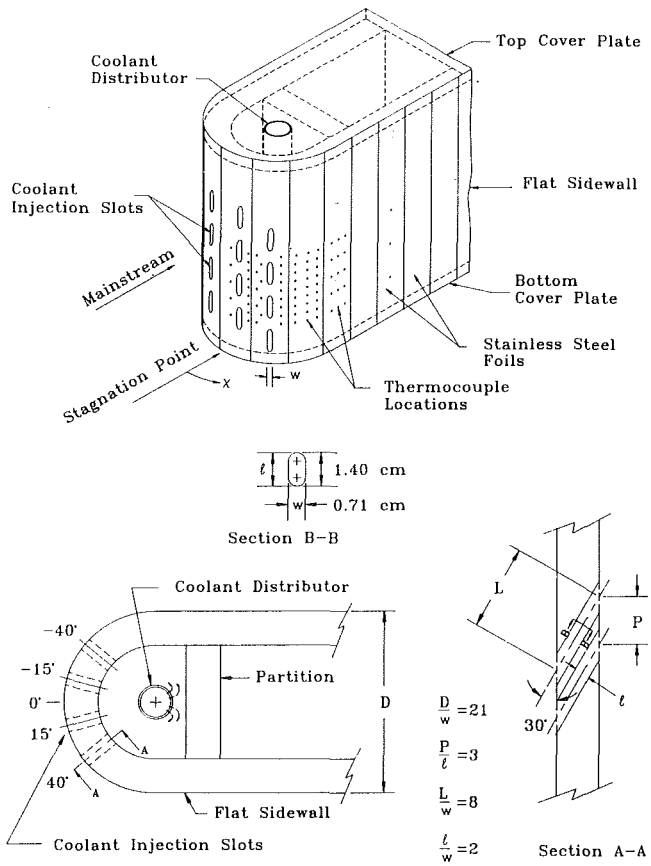

Fig. 2 Schematic of the leading edge with film slots and thermocouples

Test Apparatus and Instrumentation

Test Apparatus. The schematic of the low-speed wind tunnel used in the present study is shown in Fig. 1. The test apparatus was designed as a suction-type wind tunnel to eliminate uncontrollable turbulence from the discharge of a 7.5 kW blower. A flow straightener was placed in front of a nozzle that contracted from 76.2 cm × 76.2 cm at the inlet to 76.2 cm × 25.4 cm at the outlet. The outlet of the nozzle was followed by a turbulence grid and then a test duct. The cross section of the test duct was 25.4 cm in height, 76.2 cm in width, and 183 cm in length. For uniform approaching mainstream flow and turbulence, the leading edge of the test model was placed in the test duct 47.6 cm downstream from the grid.

Figure 1 shows two types of turbulence grid—a bar grid and a passive grid—used to generate two levels of mainstream turbulence intensity. The bar grid was made of stainless steel bars, 0.5 cm square in cross section and 1.9 cm in pitch. The passive grid was made of hollow brass tubes, 1.3 cm square in cross section and 4.8 cm in pitch. The cross section of the turbulence grid was the same as that of the test duct. Both turbulence grids had an open area of 54 percent.

The test model, shown in Fig. 2, simulated the leading edge of a gas turbine vane. It was a blunt body with a semicylinder leading edge and a flat afterbody. High-quality pieces of 2.8-cm-thick thick oak wood were laminated together to form the test model. The leading edge was 15.2 cm in diameter and 25.4 cm in height and created a 20 percent flow blockage in the test duct. For ease of fabrication, the film slots had a semicircle at each end and a rectangle in between. The cross-sectional area of each slot was equal to a circular hole in previous studies (Mehendale and Han, 1922; Ou et al., 1992). Each film slot was 0.70 cm wide and 1.40 cm long in cross section. The cross-sectional slot length-to-width ratio (l/w) was 2. The ratio of cross-sectional slot width-to-leading edge diameter (w/D) was 0.047. Film slots were located at ±15 and ±40 deg from stagnation with a pitch of three cross-sectional slot lengths ($P = 3l$) in the spanwise direction. All film slots were angled 30 and 90 deg to the test surface in the spanwise and streamwise direction, respectively. Forty-five stainless steel strips were cemented vertically on the outer surface of the test model. Each strip of foil was 25.4 cm long, 3.8 cm wide, and 0.005 cm thick. A gap of 0.8 mm separated any two foils. These gaps were filled with wood filler and made flush with the foil surface for electrical insulation. Slots were cut in the foils to match the film cooling slots in the test model. All foils were connected in series by copper bus bars. The test surface, when heated, was used as a constant heat flux (except for foils with film slots) for the heat transfer test. It was used as an adiabatic surface, when unheated, in the film cooling test. An injection system supplied hot air through a heater to the leading edge film slots. Two thermocouples located in the plenum measured the hot film temperature. The mass flow rate of injected hot air was measured by a calibrated orifice meter located before the heater.

Instrumentation. The local surface temperature distribution was measured by 88 calibrated thermocouples of 36 gage copper-constantan (74 in the leading edge region and 14 on the flat sidewall). The thermocouples were soldered on the underside of the foils with a total of 16 rows in the streamwise direction. A thermocouple for each row was attached on the inner wall to estimate conduction heat loss through the wood. All thermocouples were connected to a Fluke 2280A data logger. The measured temperatures were recorded by an IBM PC that interfaced with the Fluke data logger. The voltage and power current input through the foils were measured by a digital multimeter and an autoranging current clamp, respectively. A calibrated single hot-wire anemometer TSI IFA 100

and TSI IFA 200 multichannel digitizer interfaced with an IBM PC and measured the streamwise velocity and turbulence intensity distributions. The local streamwise root mean square (rms) calculations of velocity fluctuations were based on 1032 readings from the hot-wire anemometer. The local streamwise turbulence intensity was then based on the average of five sets of rms values (5160 readings) normalized by the local streamwise velocity. A pitot probe connected to a micromanometer was used to set the incident leading edge Reynolds number at 100,000 and constantly monitor the flow velocity during the experiment.

Test Conditions and Data Analysis

Test Conditions. Flow symmetry was confirmed by measuring the corresponding mainstream velocities on both sides of the test model. This assured that the test model was centrally placed in the test duct. The turbulence levels for the no-grid, bar gird, and passive grid were determined at the leading edge Reynolds number of 100,000. The turbulence intensity distributions were measured with a single hot-wire anemometer downstream of each grid. All heat transfer and film cooling test were conducted under these turbulence intensities for nominal blowing ratios ($\rho_s U_s/\rho_\infty U_\infty$) of $B = 0.4$, 0.8, and 1.2. These blowing ratios were based on the average total mass flow injected through all films slots. Pitot probe measurements of the centerline velocity at the exit of each film slot showed that the flows through all slots in a row were the same to within ± 10 percent for the row at 15 deg and ± 7 percent for the row at 40 deg. The ratio of the flow in the row at 40 deg to that at 15 deg was found to be 5.0, 1.5, and 1.2 for $B = 0.4$, 0.8, and 1.2, respectively. This means that the actual (local) blowing ratio from the 15 deg row and the 40 deg row was 0.13 and 0.67, 0.64 and 0.96,and 1.09 and 1.31 for the (average) blowing ratio of 0.4, 0.8, and 1.2, respectively. Using a single hot-wire probe perpendicular to the injection flow, the turbulence intensity (rms fluctuations normalized by the incident mainstream velocity when mainstream flow was on) at the exit of each slot was 4–5 percent, 6–9 percent, and 22–30 percent for $B = 0.4$, 0.8, and 1.2, respectively. Turbulence intensity was fairly uniform at the exit of each film slot in the rows at ± 15 and ± 40 deg.

The temperature of the injection flow for the heat transfer tests was about the same as that of the mainstream (24°C). However, the injected hot air was kept 25°C higher than the mainstream temperature for film heating tests. This temperature difference resulted in a secondary-to-mainstream density ratio of 0.92. The effect of density ratio is an important parameter. This report focused on the effect of high mainstream turbulence under the condition of constant density ratio. It took about 3.5 to 4 hours for both heat transfer and film cooling test to reach steady state. Relevant data, including surface temperature distribution, power input, and ambient and flow conditions were recorded when steady state was reached. Five sets of data were taken at one minute intervals for the purpose of obtaining the average values and eliminating fluctuations in operating conditions.

Data Analysis. The heat transfer tests were performed by injecting the ambient air (24°C) through the film slots and supplying power to the surface foils. The local heat transfer coefficient was calculated as

$$h = \frac{q''}{T_w - T_{aw}} = \frac{q''_{\text{gen}} - q''_{\text{cond}} - q''_{\text{rad}}}{T_w - T_{aw}} \tag{1}$$

where q'' is the convective heat flux from the foil surface, T_w is the local steady-state foil temperature, T_{aw} is the local adiabatic wall temperature, q''_{gen} is the generated surface heat flux from voltage current measurements, q''_{cond} is the conduction loss flux through the test model to the surroundings, and q''_{rad} is the radiation loss flux to the test duct walls. The generated heat flux was about 920 W/m^2. The highest T_w was kept below 52°C by the power input to avoid damaging the foils during the experiment. Loss tests were performed to determine total heat loss from the test model for a no flow condition. The loss calibration was performed by supplying power to the test model for steady state. This was done for several different power inputs to obtain the relation between the total heat loss and the foil temperature. Local radiation loss was estimated using a foil emissivity of 0.22 at 45°C. By knowing the two, conduction loss was estimated. The conduction and radiation losses were about 3 and 10 percent of the generated surface heat, respectively. Heat losses through thermocouple wires were estimated to be less than 0.1 percent when compared to the generated heat flux; both streamwise and spanwise conductions between thermocouples through thin foils were also found to be negligible (less than 0.1 percent).

It was easy to calculate the uniform q''_{gen} for those foils without films slots. The generated surface heat flux for foils with film slots was nonuniform in both the streamwise and spanwise directions. The local generated heat flux in the foils with film slots was determined by comparing the heat transfer coefficients for a foil with film slots to that for a foil without film slots. The heat transfer coefficients without film slots could be calculated by measurement of $(q''_{\text{gen}} - q''_{\text{cond}} - q''_{\text{rad}})/(T_w - T_{aw})$ where q''_{gen} could be accurately measured. Similarly, the heat transfer coefficients with film slots could be determined by measuring $(q''_{\text{gen}} - q''_{\text{cond}} - q''_{\text{rad}})/(T_w - T_{aw})$ if q''_{gen} were known. Since the heat transfer coefficients near the stagnation line (before the first row of film slots) have the same values for both with and without film slots cases, the local generated heat flux with film slots (q''_{gen}) could be determined by equating $(q''_{\text{gen}} - q''_{\text{cond}} - q''_{\text{rad}})/(T_w - T_{aw})$ for the case without film slots to that for the case with film slots. This is the same method used by Mick and Mayle (1988) and Mehendale and Han (1992). Foil resistance is another method used to estimate the local generated heat flux. By knowing slot shape and pitch and comparing foil resistance with film slots to the without film slots, the local generated heat flux with film slots was determined. Note that these two methods provide about the same local generated heat flux (q''_{gen}) for the Eq. (1) calculation.

The film cooling tests were conducted by injecting hot air through the film slots without supplying power to the surface foils. The temperature of the injected hot air in the leading edge plenum was kept at 50°C, which was 25°C higher than the approximate mainstream temperature. The local adiabatic film effectiveness was calculated as

$$\eta = \frac{T_{aw} - T_\infty}{T_s - T_\infty} = \frac{T_w - T_\infty}{T_s - T_\infty} + \frac{q''_{\text{rad}} - q''_{\text{cond}}}{h(T_s - T_\infty)} \tag{2}$$

where T_{aw} is the local adiabatic wall temperature, T_s the secondary (heated) air temperature, T_∞ the mainstream temperature. Since the test surface was mainly wood and not perfectly adiabatic, some corrections had to be applied to the measured temperatures in order to obtain the adiabatic film effectiveness. These corrections included the effect of heat transfer by conduction through the wood model (q''_{cond}), heat loss by radiation to the test duct walls (q''_{rad}), and the local film-cooled heat transfer coefficient (h) as calculated from Eq. (1). For the film heating tests, heat was actually transferred by conduction from inside the test model to the outer test surface for the locations on the leading edge region. In other words, there existed a conduction heat gain to be considered in Eq. (2). This heat gain was evaluated based on a one-dimensional conduction model. Note that thermocouple locations near the film slots received additional conduction gain from the hot air passing through the film slots. The values for these two conduction heat gains were then used to estimate the total conduction gain for the thermocouple locations near the film slots. Both stream-

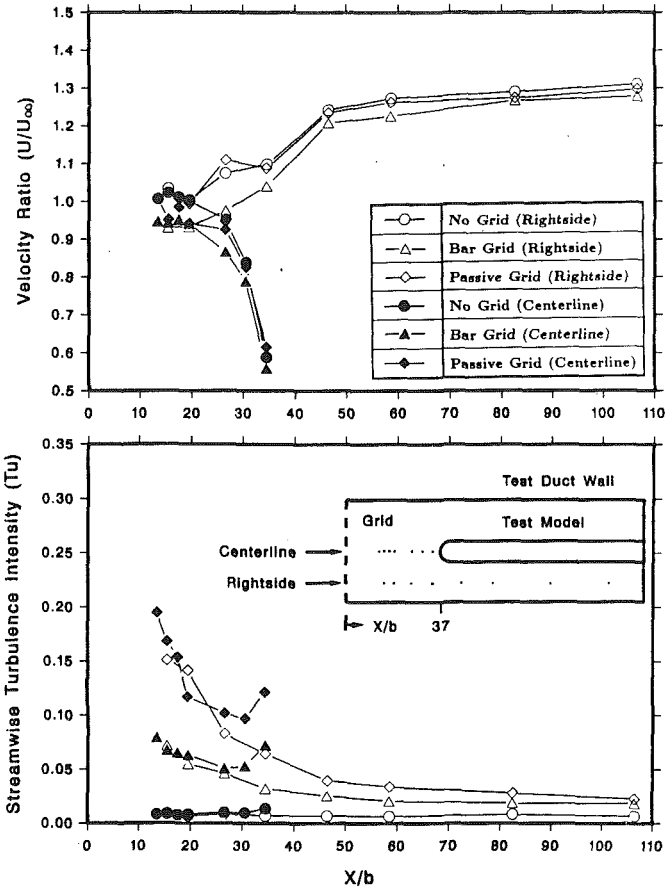

Fig. 3 Streamwise distributions of normalized mainstream velocity and turbulence intensity

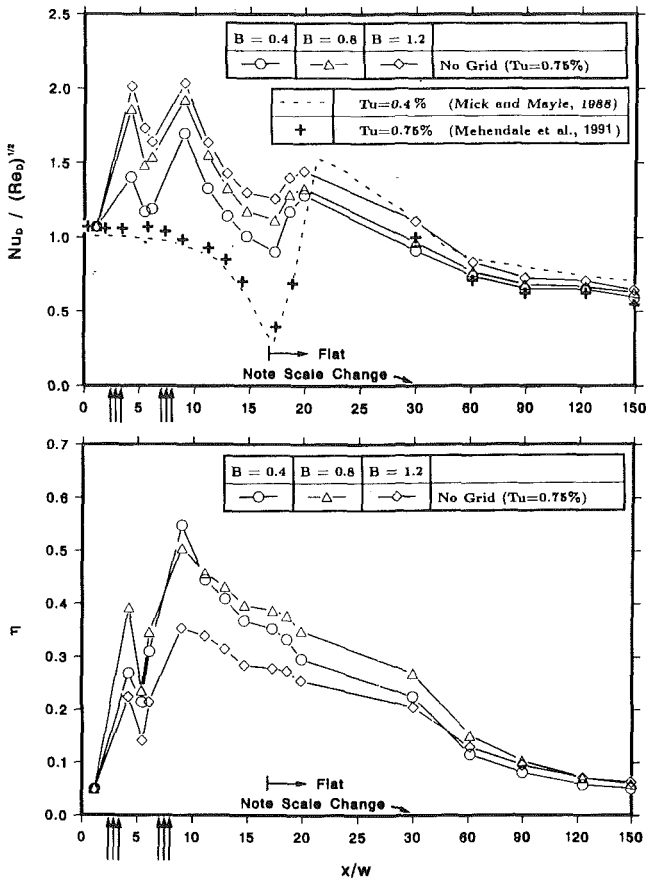

Fig. 4 Effect of blowing ratio on spanwise-averaged distributions of Nusselt number and film effectiveness for Tu = 0.75 percent

wise and spanwise conductions between thermocouples through thin foils were not considered because they were estimated to be less than 0.1 percent of the generated heat flux. The local adiabatic film effectiveness was then calculated by Eq. (2). This method is the same as that used by Mehendale and Han (1992).

An uncertainty analysis based on the method of Kline and McClintock (1953) was carried out for both film effectiveness and heat transfer coefficient with film injection. The uncertainty of heat transfer coefficient around the film slots is about 15 percent, primarily due to q''_{gen} estimation, whereas the uncertainty downstream of the leading edge is less than 5 percent due to T_w measurements. The uncertainty of film effectiveness is about 8 percent near the film slots and less than 5 percent at downstream.

Results and Discussions

Flow Field. Velocity distributions for the no-grid case were measured with a pitot probe across the YZ midplane (perpendicular to the streamwise direction) 1.5 leading edge diameters upstream of stagnation. These velocity profile measurements confirmed that the mainstream approached uniformly over the entire plane. The local velocity and turbulence intensity distributions along both the centerline and right-side line for all three upstream turbulence conditions are shown in Fig. 3. The incident mainstream velocity (U_∞) is 10 m/s at X/b = 20 (or 1.5 leading edge diameters) for the no-grid case. Within $x/b \leq 20$, the ratios of local mainstream velocity to incident mainstream velocity (U/U_∞) along the centerline and right-side line are 2 percent higher than unity for the no-grid case and 5 percent lower than unity for the bar grid and passive grid cases. The local mainstream velocities along the centerline decrease drastically after X/b = 20 due to the leading edge approach. However, due to the blockage effect of the test model, the local mainstream velocities along the right-side line gradually increase and nearly reach a constant value toward the end of the test model. The influence of mainstream turbulence level on these velocity distributions is not significant.

Figure 3 also shows that, as expected, the local turbulence intensity decays with distance from the grid. This decay continues toward the end of the test model for locations along the right-side line. However, the local turbulence intensity begins increasing when the flow approaches stagnation for locations along the centerline. This increase in turbulence intensity is caused by a decrease in the local mainstream velocity and not by an increase in the fluctuating component. It is seen from Fig. 3 that the centerline minimum turbulence intensities occurred at X/b around 30 for grid generated turbulence flows. These minimum turbulence intensities are quoted as the reference turbulence intensities in this study. Therefore, the reference turbulence intensity for the bar grid and passive grid are 5.07 and 9.67 percent, respectively. The corresponding dissipation length scales at the same location are about 1.0 cm (L^u_e/D = 0.066) and 1.5 cm (L^u_e/D = 0.099), respectively. These dissipation length scales are calculated from the method proposed by Hancock and Bradshaw (1983) as $L^u_e = -(\overline{u'^2})^{3/2}/(U\, d\overline{u'^2}/dX)$ and the local mean and fluctuating velocity distributions shown in Fig. 3.

Heat Transfer Coefficient and Film Effectiveness.

Heat transfer tests were conducted separately on a smooth leading edge model without film shots (no film heat transfer)

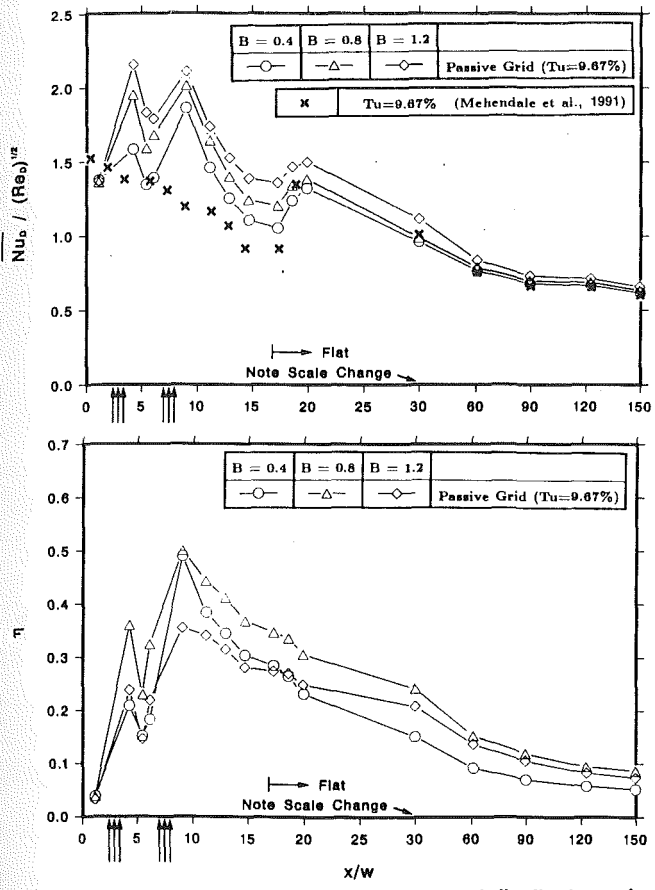

Fig. 5 Effect of blowing ratio on spanwise-averaged distributions of Nusselt number and film effectiveness for Tu = 9.67 percent

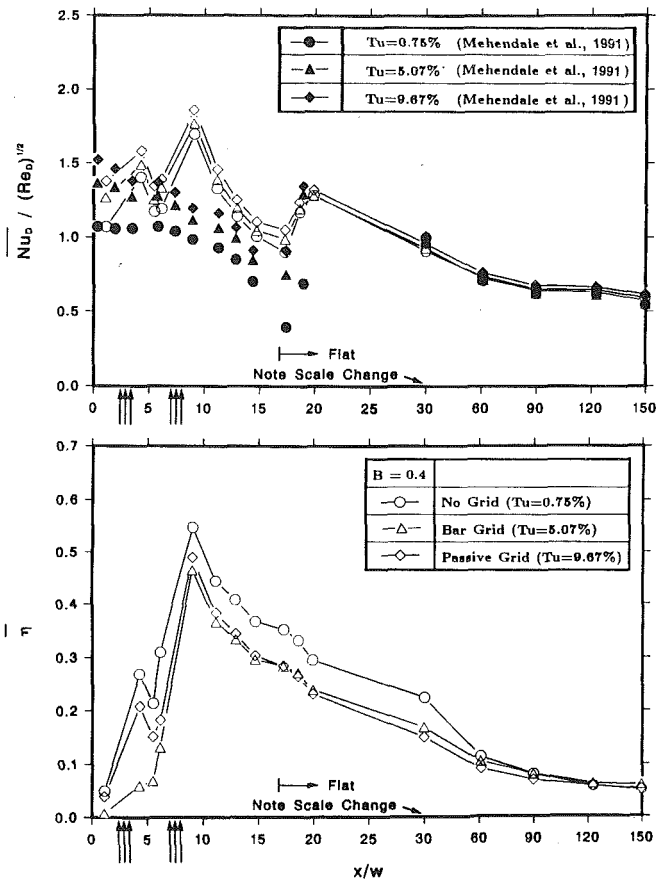

Fig. 6 Effect of mainstream turbulence on spanwise averaged distributions of Nusselt number and film effectiveness for blowing ratio of 0.4

to calibrate the leading edge. The no-film heat transfer data compared well to the published results (Mick and Mayle, 1988) for the no-grid low mainstream turbulence case. Detailed no-film heat transfer data for three Reynolds numbers (Re_D = 25,000, 40,000, and 100,000) and four turbulence levels (Tu = 0.75, 5.07, 9.67, and 12.9 percent) are given by Mehendale et al. (1992). The spanwise-averaged heat transfer coefficients have been converted into the spanwise-averaged Nusselt numbers normalized by a square root of the Reynolds number. Figure 4 shows the normalized Nusselt number distributions for two rows of film slots for the no-grid low mainstream turbulence case (Tu = 0.75 percent) along with the no-film Nusselt number data (without film slots) from this investigation (Mehendale et al., 1991) and published results (Mick and Mayle, 1988). The no-film Nusselt number data of this study follow the published results for the no-grid case. The no-film heat transfer coefficient (normalized Nusselt number) decreases from stagnation, reaches a minimum at separation (x/w = 17) and a maximum at reattachment (x/w = 20). Figure 4 shows the effect of blowing ratio on the leading edge heat transfer coefficient. The results show that the leading edge heat transfer coefficient increases with increasing blowing ratio. This is because an increase in blowing ratio causes more interactions between film jet and mainstream flow and creates an increase in the turbulence at the exit of the film slots as indicated earlier. The increase in heat transfer coefficient is most severe immediately downstream from each row of film slots (two peak regions at x/w = 4 and 9). There are two lower heat transfer coefficient regions for all blowing ratios: one between the first and second film row (x/w = 6) and the other near the separation region (x/w = 17). Heat transfer coefficient increases slightly at the reattachment region (x/w = 20). The blowing ratio effect diminishes on the flat sidewall region. Figure 4 alos shows the effect of blowing ratio on the spanwise-averaged film effectiveness for the no-grid low mainstream turbulent case (Tu = 0.75 percent). In general, for each blowing ratio, the highest film effectiveness is immediately downstream from the second row film slots (x/w = 9) and after that the film effectiveness decreases monotonically toward the end of the flat sidewall. The second peak is immediately downstream from the first row of film slots (x/w = 4) but there exists a low film effectiveness region between the first and second film row (x/w = 6). The film effectiveness for a blowing ratio of 0.8 is better than that of 0.4 because of more film coverage on the surface. However, the film effectiveness for a blowing ratio of 1.2 is much lower than that of 0.4 and 0.8 because too high a blowing ratio causes more jet penetration into the mainstream and results in less film coverage on the surface.

Figure 5 shows the effect of blowing ratio for two rows of film slots on the distributions of spanwise-averaged heat transfer coefficient and film effectiveness for the passive grid high mainstream turbulence case (Tu = 9.67 percent). The no-film heat transfer coefficients (without film slots) under the passive grid high mainstream turbulence condition from this investigation (Mehendale et al., 1991) are also included for comparison. The trends of heat transfer coefficient are similar to Fig. 4 in which the higher blowing ratio causes higher heat transfer coefficient. However, the heat transfer coefficients under high mainstream turbulence conditions (Fig. 5) are higher than those under low mainstream turbulence conditions (Fig. 4). Similarly, the film effectiveness under high mainstream turbulence conditions (Fig. 5) shows a similar trend to that under low mainstream turbulence condition (Fig. 4) in that the blowing ratio of 0.8 provides the best film effectiveness. The film effectivenesses under high mainstream turbulence (Fig. 5) are relatively lower due to mainstream turbulence effect.

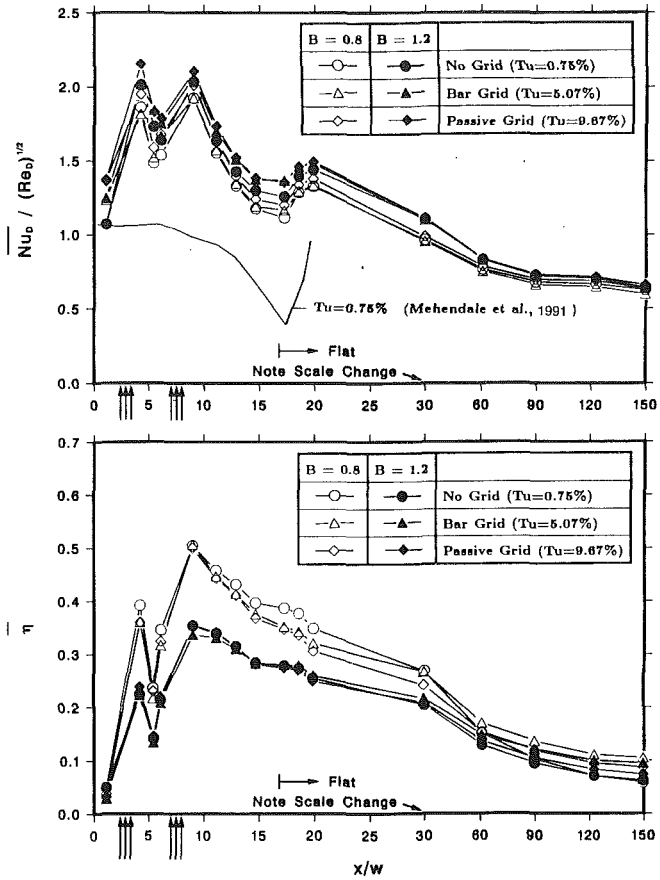

Fig. 7 Effect of mainstream turbulence on spanwise-averaged distributions of Nusselt number and film effectiveness for blowing ratios of 0.8 and 1.2

Table 1 (*a*) Local $Nu_D/(Re_D)^{1/2}$ distributions for $B = 0.8$

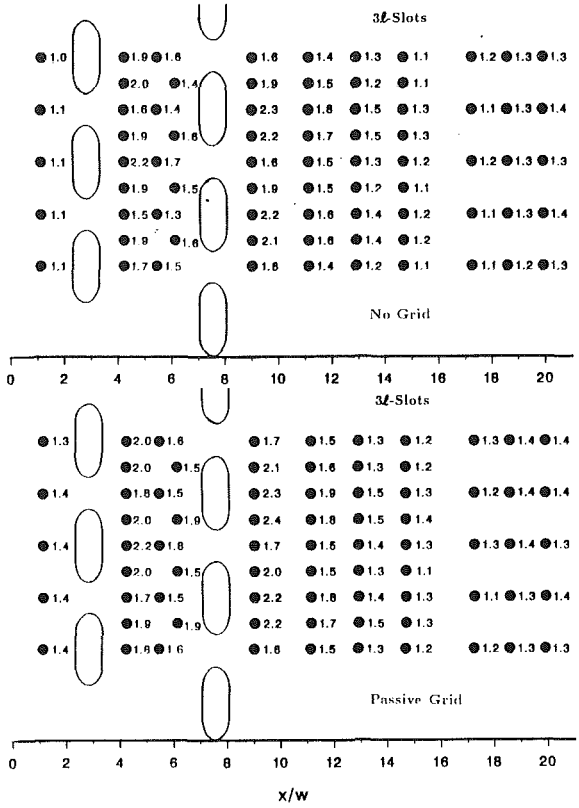

(*b*) Local film effectiveness distributions for $B = 0.8$

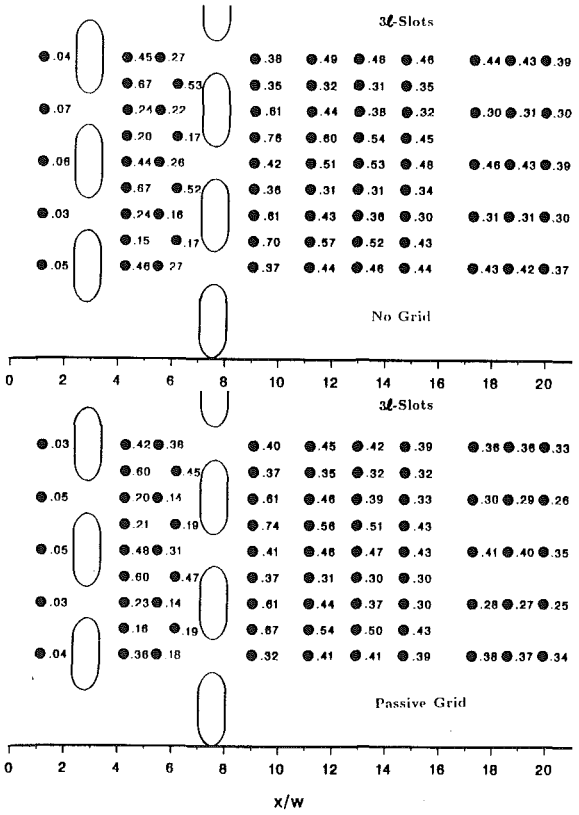

In order to see clearly the effect of mainstream turbulence, Figure 6 shows the results for the case of the lowest blowing ratio of $B = 0.4$. The no-film heat transfer coefficients (without film slots) under three different mainstream turbulence levels from this investigation (Mehendale et al., 1991) are also included for comparison. As expected, the heat transfer coefficient increases with increasing mainstream turbulence level for both with and without film injection cases. However, unlike the heat transfer coefficient for the lowest blowing ratio of $B = 0.4$, the film effectiveness decreases with high mainstream turbulence conditions. As indicated earlier, for the lowest blowing ratio of $B = 0.4$, the jet-induced turbulence intensity at the exit of the film slots is only about 4–5 percent. This means that the mainstream turbulence level is higher than the jet turbulence and dominates the flow field around the leading edge. The higher mainstream turbulence penetrates and disturbs the film layer. Thus, higher mainstream turbulence causes lower film effectiveness and higher heat transfer coefficient.

Figure 7 shows the effect of mainstream turbulence on the heat transfer coefficient and film effectiveness for the blowing ratios of $B = 0.8$ and 1.2. Again, the heat transfer coefficient increases and the film effectiveness decreases with increasing mainstream turbulence level. However, the mainstream turbulence effect is dramatically reduced. As previously indicated, for the blowing ratios of $B = 0.8$ and 1.2, the jet-induced turbulence intensity at the exit of the film slots is about 6–9 percent 22–30 percent, respectively. This means that the jet turbulence level is comparable with (for $B = 0.8$) or even higher than (for $B = 1.2$) the mainstream turbulence and dominates the flow field around the leading edge. The higher jet turbulence protects the film from penetration and disturbance of mainstream turbulence level. Thus, higher mainstream turbulence only slightly alters the film effectiveness and heat transfer coefficient. By comparing Fig. 7 to Fig. 6 it can be

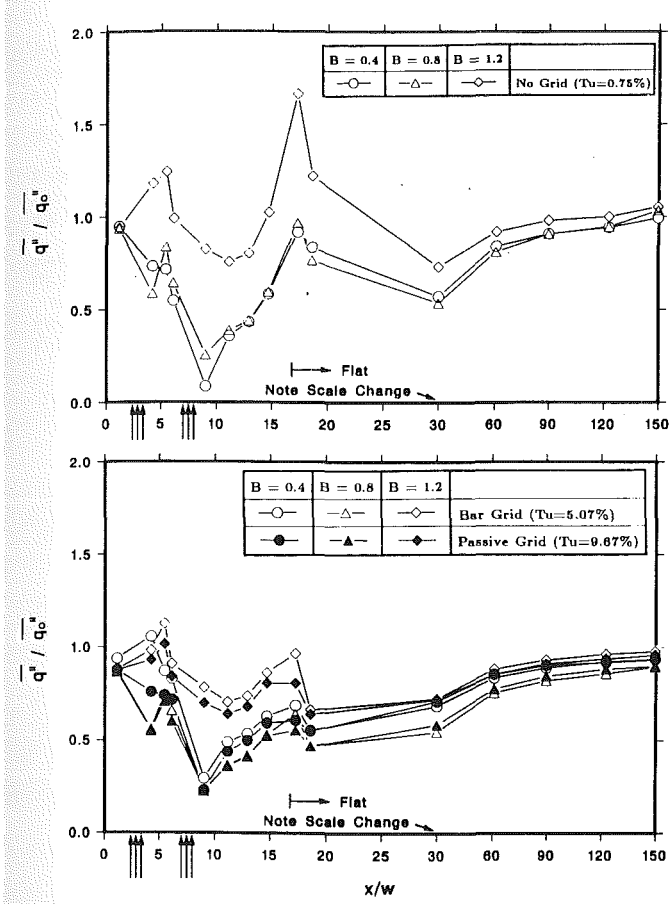

Fig. 8 Effect of blowing ratio on surface heat load ratio for Tu = 0.75, 5.07, and 9.67 percent for ϕ = 0.6

seen that the spread in film effectiveness is relatively small for B = 0.8 and 1.2.

The effect of mainstream turbulence (Tu = 9.67 percent as compared to Tu = 0.75 percent) on the local heat transfer coefficient and film effectiveness distributions for the blowing ratio of B = 0.8 is listed in Table 1 for reference. The local heat transfer coefficient variation in the spanwise direction is not as significant as that in the streamwise direction for both high and low mainstream turbulence cases. However, the spanwise film effectiveness variation is as significant as the streamwise variation.

Film Cooling Heat Transfer Performance. The film injection provides the film coverage on the surface but increases the surface heat transfer coefficient. It is necessary to study the combined effect of these two factors in order to determine the advantages and disadvantages due to film injection. A minimum heat flux should be obtained for the optimum design in film cooling of turbine airfoils compared with the no-film heat flux (with no film slots). The heat load ratio, defined as follows, can be used to evaluate the performance of film cooling (Mick and Mayle, 1988):

$$\frac{\overline{q''}}{\overline{q_o''}} = \frac{1}{n}\sum_{i=0}^{n}\left[\frac{h(x, z_i)}{\overline{h}_o}\right]\left[1-\frac{\eta(x, z_i)}{\phi}\right] \quad (3)$$

where $\overline{q}_o''$ is the spanwise-averaged heat flux with no film slots, $\overline{q}''$ is the spanwise-averaged heat flux with film injection, n is the number of thermocouples in a row to obtain the spanwise-averaged film effectiveness and heat transfer coefficient, and ϕ is the overall cooling effectiveness given by $\phi = (T_w - T_\infty)/(T_s - T_\infty)$. Typically, the value of ϕ ranges from 0.5 to 0.6 for the film cooling of gas turbine airfoils. A value of 0.6 for ϕ is used in this study to compare the overall performance due to film cooling.

As seen in Fig. 8 for Tu = 0.75 percent, the heat load ratio increases with increasing blowing ratio except immediately downstream from the first row of film slots where a blowing ratio of B = 0.8 is the lowest. It implies that B = 0.4 provides the best cooling performance but B = 1.2 is the worst. The application of film injection can be expected to reduce the heat load for B = 0.4 and B = 0.8 (i.e., heat load ratio is less than unity). However, this is not the case for B = 1.2 (i.e., heat load ratio is greater than unity in some regions). As discussed earlier, this is because the higher blowing ratio injects too much film into the mainstream flow and causes higher heat transfer coefficient and lower film effectiveness. This confirms the results observed by Mick and Mayle (1988) and Mehendale and Han (1992). The results also show that the heat load reductions for B = 0.4 and B = 0.8 are about the same for two-row injection under no-grid low mainstream turbulence conditions.

The heat load ratio results for Tu = 5.07 and 9.67 percent flows can also be seen in Fig. 8. The spreads of heat load ratio for all three blowing ratios decrease under higher mainstream turbulence conditions. This is because the denominator $\overline{q}_o''$ (the spanwise-averaged heat flux without film slots) is larger under higher mainstream turbulence levels. In general, the heat load ratio for all three blowing ratios under higher mainstream turbulence conditions is less than unity. However, unlike the low mainstream turbulence case, the heat load ratio for B = 0.8 is the lowest compared to B = 0.4 and 1.2. This is because, as indicated earlier, the higher mainstream turbulence adversely affects the leading edge film effectiveness for the lowest blowing ratio of B = 0.4. Therefore, a blowing ratio of B = 0.8 performs better than B = 0.4. Again, a blowing ratio of B = 1.2 is the worst because of lifting too much film into the mainstream flow.

Liquid Crystals Thermal Visualization. The liquid crystal technique was used for film cooling thermal visualization on a cylinder in cross flow (Hippensteele et al., 1981). A piece of liquid crystal sheet (25.4 cm × 25.4 cm × 0.04 cm) was calibrated with color changes in a temperature controlled water bath. It was then tightly placed against the foils in the leading edge region of the test model. The sheet was firmly glued to the surface foils along its edges. Slots were cut in the liquid crystal to match the slots in the foils and test model. The investigation was conducted only for the film heating test case to observe the effects of mainstream turbulence and blowing ratio. The hot film temperature was kept at 57°C under the same Reynolds number condition used previously.

Figure 9 shows the comparison of hot film thermal visualization for the no-grid (Tu = 0.75 percent) and passive grid (Tu = 9.67 percent) at corresponding blowing ratios of 0.4, 0.6, 0.8, 1.2, and 1.5. The pictures taken for film visualization were originally printed in color. The pictures clearly show different colors representing various temperatures of hot film sensed by the liquid crystal. Unfortunately, they turned blurry when photocopies were made. Therefore, lines were traced accordingly to represent the boundaries of color zones as they were shown in the original color pictures. From the outmost location, each contour stands for the boundary of red, yellow, green, blue, and black for each film slot. These color zones represent the temperatures 40.6°, 41.1°, 41.7°, 46.1°, and 51.7°C according to temperature calibration. As seen in the figure for the no-grid low turbulence case, the blowing ratios between 0.4 and 0.8 provide more film coverage than the higher blowing ratios. For the passive grid high-turbulence case, a blowing ratio of B = 0.8 provides more film coverage than other blowing ratios. These thermal visualization results are reasonably consistent with the film effectiveness presented in

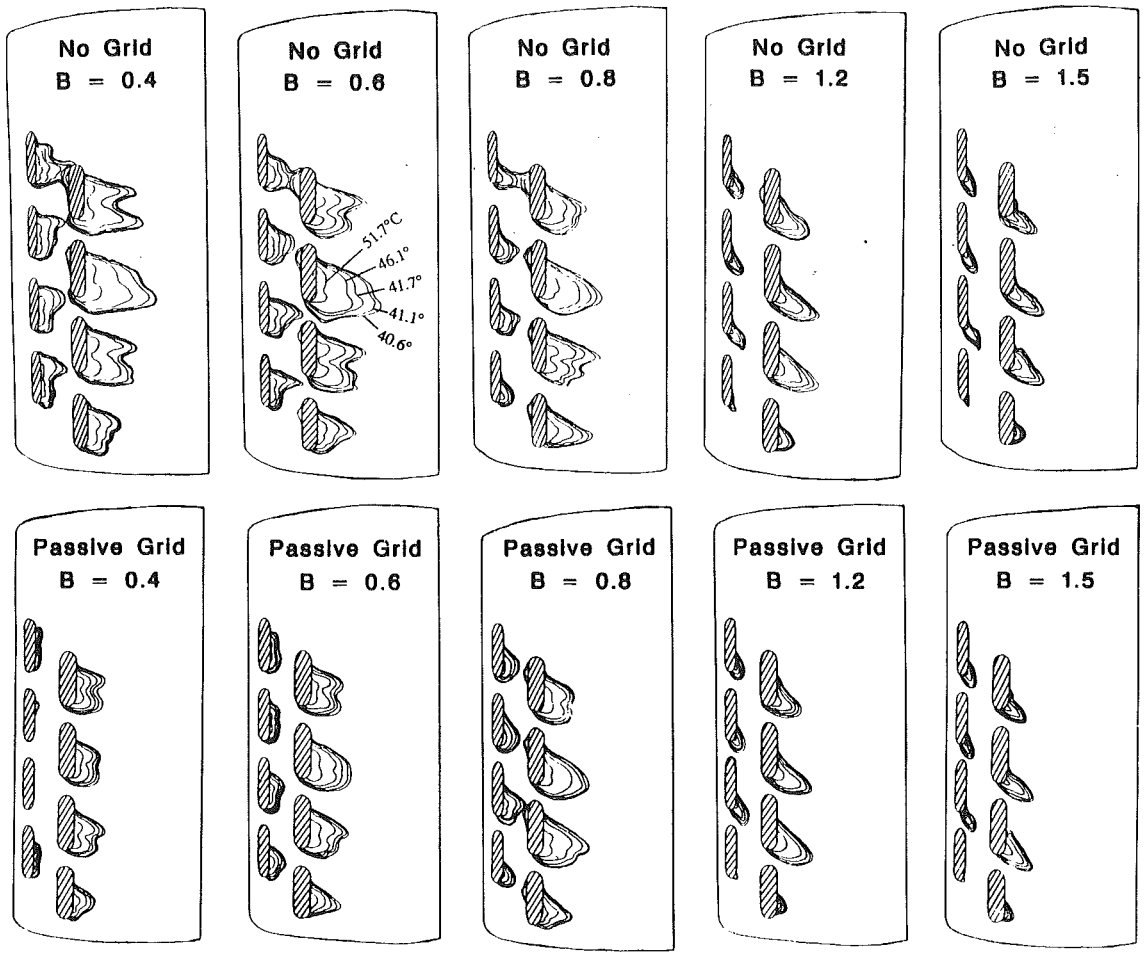

Fig. 9 Comparison of film thermal visualization at blowing ratios of 0.4, 0.6, 0.8, 1.2, and 1.5 for Tu = 0.75 and 9.67 percent

Figs. 4 and 5. The film coverage toward the spanwise direction becomes thinner with increasing blowing ratio. As seen in Fig. 9, the film coverage for the no-grid low turbulence case is always larger than for the passive grid high-turbulence case at a blowing ratio of less than 0.8. The film coverage is about the same at a blowing ratio greater than 0.8. This evidence can also be checked with Fig. 6, which shows that the film effectiveness for the no-grid case is higher than for the passive grid case at low blowing ratios. The mainstream turbulence effect diminishes at the high blowing ratios.

Concluding Remarks

The influence of mainstream turbulence on leading edge heat transfer coefficient and film effectiveness was experimentally studied with two rows of film slots located at ±15 and ±40 deg from stangation line. The main findings of the study include:

1 The leading edge heat transfer coefficient increases by increasing the blowing ratio (from B = 0.4 to 1.2). The leading edge heat transfer coefficient increases with increasing the mainstream turbulence level (from Tu = 0.75 to 9.67 percent) but the effect reduces with increasing blowing ratio.

2 The leading edge film effectiveness for the lowest blowing ratio of B = 0.4 decreases with increasing mainstream turbulence (from Tu = 0.75 to 9.67 percent). However, the mainstream turbulence effect diminishes with increasing blowing ratio. A blowing ratio of B = 0.8 provides better film effectiveness for three different mainstream turbulence intensities of Tu = 0.75, 5.07, and 9.67 percent than other blowing ratios of B = 0.4 and 1.2.

3 The peak heat transfer coefficient with film injection is about two times higher than that without film injection, whereas the corresponding peak film effectiveness is about 0.5.

4 For a low mainstream turbulence intensity of Tu = 0.75 percent, a blowing ratio of B = 0.4 provides the lowest heat load ratio although the difference between B = 0.4 and 0.8 is small. For a high mainstream turbulence intensity of Tu = 9.67 percent, a blowing ratio of B = 0.8 performs better than B = 0.4 and 1.2.

5 The liquid crystal thermal visualization results are reasonably consistent with the film effectiveness data presented in this paper.

Acknowledgments

The project was supported by the Textron Lycoming through contract #H164150. Their support is greatly appreciated.

References

Bonnice, M. A., and L'Ecuyer, W. R., 1983, "Stagnation Region Gas Cooling—Effects of Dimensionless Coolant Temperature," NASA CR-168197.

Hancock, P. E., and Bradshaw, P., 1983, "The Effect of Free-Stream Turbulence on Turbulent Boundary Layers," ASME *Journal of Fluids Engineering*, Vol. 105, pp. 284–289.

Hippensteele, S. A., Russell, L. M., and Stepka, F. S., 1981, "Evaluation of a Method for Heat Transfer Measurements and Thermal Visualization Using a Composite of a Heater Element and Liquid Crystals," NASA Technical Memorandum 81639, Lewis Research Center, Cleveland, OH.

Karni, J., and Goldstein, R. J., 1990, "Surface Injection Effect on Mass Transfer From a Cylinder in Crossflow: A Simulation of Film Cooling in the Leading Edge Region of a Turbine Blade," ASME JOURNAL OF TURBOMACHINERY, Vol. 112, pp. 418–427.

Kline, S. J., and McClintock, F. A., 1953, "Describing Uncertainties in Single-Sample Experiments," *Mechanical Engineering*, Vol. 75, pp. 3–8.

Luckey, D. W., and L'Ecuyer, M. R., 1976, "Stagnation Region Gas Film Cooling—Spanwise Angled Coolant Injection," Thermal Sciences and Propulsion Center, Purdue University, W. Lafayette, IN, Technical Report No. TSPC-TR-76-2.

Luckey, D. W., and L'Ecuyer, M. R., 1981, "Stagnation Region Gas Film Cooling—Spanwise Angled Injection From Multiple Rows of Holes," NASA CR-165333.

Mehendale, A. B., Han, J. C., and Ou, S., 1991, "Influence of High Mainstream Turbulence on Leading Edge Heat Transfer," ASME *Journal of Heat Transfer*, Vol. 113, pp. 843–850.

Mehendale, A. B., and Han, J. C., 1992, "Influence of High Mainstream Turbulence on Leading Edge Film Cooling Heat Transfer," ASME JOURNAL OF TURBOMACHINERY, Vol. 114, this issue, pp. 707-715.

Mick, W. J., and Mayle, R. E., 1988, "Stagnation Film Cooling and Heat Transfer, Including Its Effect Within the Hole Pattern," ASME JOURNAL OF TURBOMACHINERY, Vol. 110, pp. 66–72.

Nirmalan, V., and Hylton, L. O., 1990, "An Experimental Study of Turbine Vane Heat Transfer With Leading Edge and Downstream Film Cooling," ASME JOURNAL OF TURBOMACHINERY, Vol. 112, pp. 477–487.

Ou, S., Mehendale, A. B., and Han, J. C., 1992, "Influence of High Mainstream Turbulence on Leading Edge Film Cooling Heat Transfer: Effect of Film Hole Row Location," ASME JOURNAL OF TURBOMACHINERY, Vol. 114, this issue, pp. 716-723.

Sasaki, M., Takahara, K., Sakata, K., and Kumagai, T., 1976, "Study on Film Cooling of Turbine Blades," *Bulletin of the JSME*, Vol. 19, No. 137, pp. 1344–1352.

Film Cooling Research on the Endwall of a Turbine Nozzle Guide Vane in a Short Duration Annular Cascade: Part 1—Experimental Technique and Results

S. P. Harasgama

C. D. Burton

Royal Aerospace Establishment,
Propulsion Department,
Pyestock, Farnborough,
Hampshire, GU14 OLS, United Kingdom

Heat transfer and aerodynamic measurements have been made on the endwalls of an annular cascade of turbine nozzle guide vanes in the presence of film cooling. The results indicate that high levels of cooling effectiveness can be achieved on the endwalls of turbine nozzle guide vanes (NGV). The NGV were operated at the correct engine nondimensional conditions of Reynolds number, Mach number, gas-to-wall temperature ratio, and gas-to-coolant density ratio. The results show that the secondary flow and horseshoe vortex act on the coolant, which is convected toward the suction side of the NGV endwall passage. Consequently the coolant does not quite reach the pressure side/casing trailing edge, leading to diminished cooling in this region. Increasing the blowing rate from 0.52 to 1.1 results in significant reductions in heat transfer to the endwall. Similar trends are evident when the coolant temperature is reduced. Measured heat transfer rates indicate that over most of the endwall region the film cooling reduces the Nusselt number by 50 to 75 percent.

Introduction

Film cooling is a very effective means of reducing the heat transfer to turbine component surfaces. It generally requires less coolant flow compared to other means of cooling, such as internal convection cooling and impingement cooling. Several authors, e.g., Goldstein (1971), Jones (1986), Eckert et al. (1961), and Crawford et al. (1980), among others, have made detailed studies of film cooling on flat and curved surfaces with and without pressure gradient. The use of film cooling is now widespread in turbine applications and detailed data exist for heat transfer rates with and without film cooling on turbine aerofoils. The situation is quite different where turbine endwalls (platforms) are concerned. To date only four publications exist on film cooling to turbine vane platforms and only one is on a fully annular cascade.

Early work by Blair (1974) on a large-scale, low-speed linear turbine indicated that the secondary flow in the vane passage would modify the cooling effectiveness leading to diminished cooling near the pressure side of the platform. Although qualitatively the results showed good agreement with endwall flow visualizations, the accuracy of the data was not sufficiently good to form a data base for methods development. Blair's work also used a cold air facility with a heated turbine model and did not simulate the essential nondimensional parameters affecting heat transfer in the presence of film cooling. Bourguignon (1985) tested a linear cascade of turbine NGV in a short duration piston tunnel with and without film cooling. Unfortunately no quantitative data have been published on this work and, so far, the results presented have been purely qualitative.

Takeishi et al. (1990) have investigated the heat transfer to turbine vane aerofoils and platforms with and without film cooling. The experimental work was performed on a fully annular vane ring mounted within a low-speed cascade wind tunnel operating with ambient air. The vanes and platforms were heated with thin foil heaters and instrumented with thermocouples for heat transfer measurements. The coolant flow was heated and injected into the vane passage and the thermocouples used to obtain adiabatic wall effectiveness data. The experimental program did not correctly simulate the aerothermal environment of the real turbine; however, the secondary flow field was shown to modify the cooling effectiveness on the platform significantly. The coolant was convected toward the suction side of the platform, leaving the pressure side trailing edge region relatively unprotected.

Granser and Schulenberg (1990) have performed tests on the shroud of a turbine vane with and without film cooling. It was shown that with slot injection the coolant tends to re-energize the endwall boundary layer leading to a reduction in secondary flow. They show that high levels of cooling effectiveness are achieved close to coolant injection with a rapid fall off further downstream. The test facility used a linear vane cascade operating with ambient air and hot gas for the coolant.

Contributed by the International Gas Turbine Institute and presented at the 36th International Gas Turbine and Aeroengine Congress and Exposition, Orlando, Florida, June 3–6, 1991. Manuscript received at ASME Headquarters March 4, 1991. Paper No. 91-GT-252. Associate Technical Editor: L. A. Riekert.

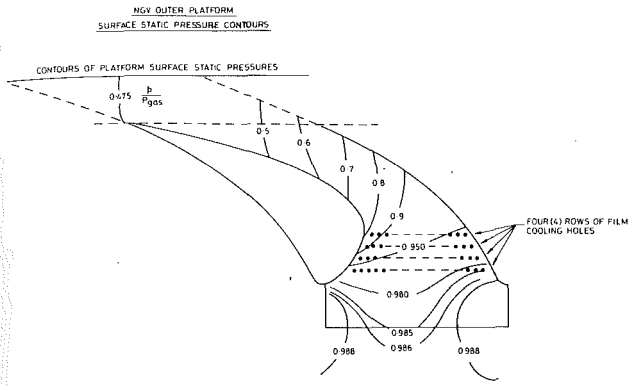

Fig. 1 Typical engine endwall cooling configuration

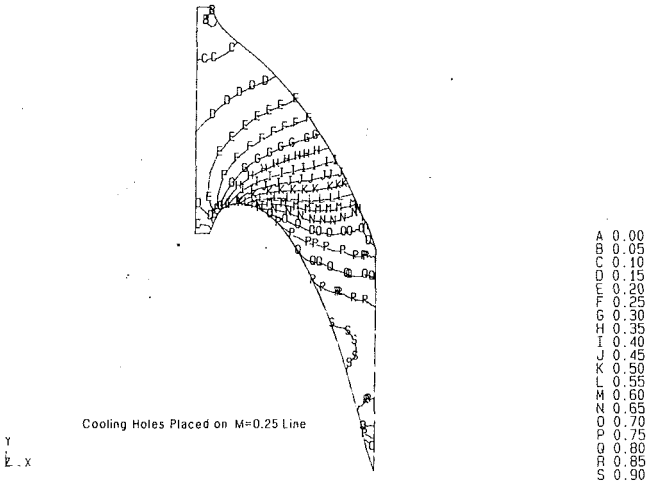

Fig. 2 Predicted Mach number contours on outer platform using inviscid code

It is clear therefore that a requirement exists for detailed data on film cooling on turbine vane platforms. This paper presents data for discrete hole, single-row film cooling on the outer platform of a turbine vane in a fully annular cascade. The NGV were operated at engine values of Reynolds number and Mach number for aerodynamic similarity. Heat transfer similarity was achieved by simulating the engine values of gas-to-wall temperature ratio and coolant-to-gas density ratio. Results include the variation of heat transfer on the vane platform with changing blowing rate and temperature difference ratio, θ.

Similarity Considerations

Similarity of Reynolds number and Mach number is achieved in the ILPC for approximately 0.5 second when operating at a compression ratio of 4:1. The NGV were operated at the following design conditions:

Reynolds number	=	2.55E6	(based on exit conditions)
Mach number	=	0.93	(based on exit conditions)
T_g/T_w	=	1.30	
ρ_i/ρ_g	=	1.80	
θ	=	1.75	

In order to simulate the correct thermal environment, it is required that the coolant-to-gas density ratio and the gas-to-wall temperature ratio both be close to the design values. The fully annular configuration of the ILPC precluded heating/cooling of the NGV, in order to achieve variation of θ. It was therefore necessary to vary the coolant temperature in order to obtain a sufficient range of θ values.

Variation of the coolant temperature will cause changes in the coolant-to-gas density ratio. It was therefore necessary to use foreign gas mixtures with air to maintain the density ratio constant while changing θ. The present experiments used carbon dioxide (CO_2) and air mixtures as the coolant while the main gas stream was air. A system utilizing CO_2 and air mixtures is considered to be an acceptable approach because previous data by Teekaram et al. (1989) have shown that CO_2 behaves in an identical manner to air when used in film cooling. The different thermophysical properties of CO_2 have a negligible effect on the film cooling process itself.

The use of CO_2/air mixtures has an added attraction in that simulation of high values of coolant-to-gas density ratio ($\simeq 1.8$) will require a coolant temperature around 255 K when the gas temperature is 375 K and the wall temperature is ambient (290 K) because of the higher molecular weight of CO_2. If air is used as the coolant, its temperature would need to be around 195 K in order to achieve the correct density ratio. Such cryogenic temperatures would lead to severe icing problems and associated difficulties in manufacture of special valve gear in dispensing the coolant.

Cooling Design

A typical aircraft engine platform film cooling configuration is shown in Fig. 1. The configuration utilizes four rows of cooling holes placed in the blade-to-blade direction. Figure 2 shows computational results of the outer endwall Mach number distribution for the present vane row as depicted in Fig. 3. It is clear that placing the cooling holes directly from the suction side to the pressure side, as in Fig. 1, causes the coolant to emerge into a nonuniform Mach number field, and hence a nonuniform static pressure field. This will generally result in nonuniform blowing rates and possibly lead to jet lift-off. The present cooling design philosophy was to place the cooling holes along an iso-Mach line, thereby ensuring a uniform blowing rate and momentum flux ratio as the coolant emerges into the mainstream.

The momentum flux ratio (I) can be written as

$$I=\frac{\rho_i U_i^2}{\rho_g U_g^2}=\frac{P_{ti}-P_{si}}{P_{tg}-P_{sg}},$$

since the coolant is usually supplied at constant pressure and the free-stream total pressure is nearly constant, then a uniform

Nomenclature

C_t = vane true chord
d = cooling hole diameter
G = blowing rate $=(\rho_i U_i/\rho_g U_g)$
h = heat transfer coefficient
I = momentum flux ratio $=(\rho_i U_i^2/\rho_g U_g^2)$
K = thermal conductivity of air
M = Mach number
Nu = Nusselt number $= h\,C_t/K$
P = pressure
Re = Reynolds number
T = total temperature
U = velocity
X = distance downstream of cooling holes
θ = temperature difference ratio $=(T_g-T_i)/(T_g-T_w)$
ρ = density

Subscripts

g = gas path value
i = injectant value
o = datum uncooled value
s = static value
t = total (stagnation) value
w = wall value

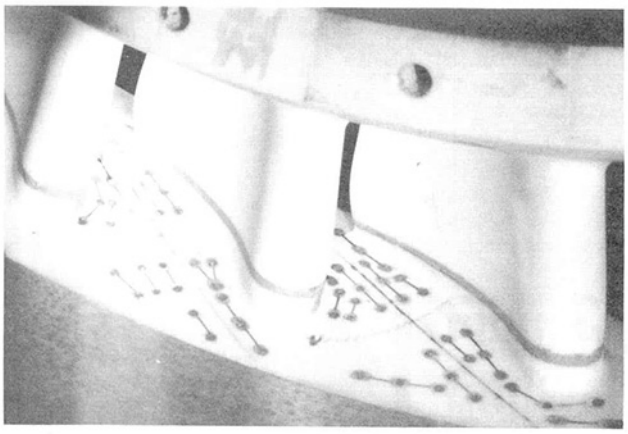

Fig. 3 Heat transfer/cooling NGV hardware

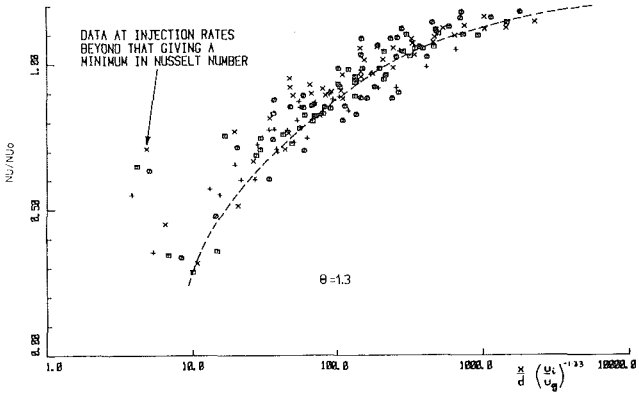

Fig. 4 Correlation of single row cooling holes with zero pressure gradient on flat plate (Forth, 1985)

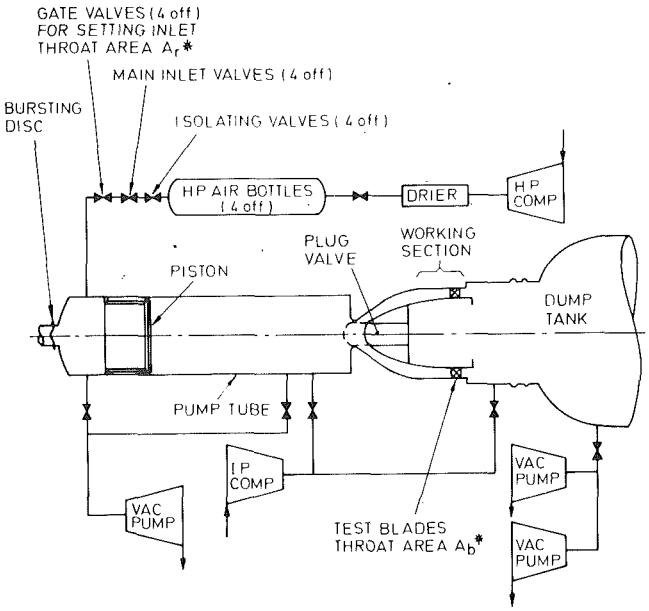

Fig. 5 The ILPC test facility

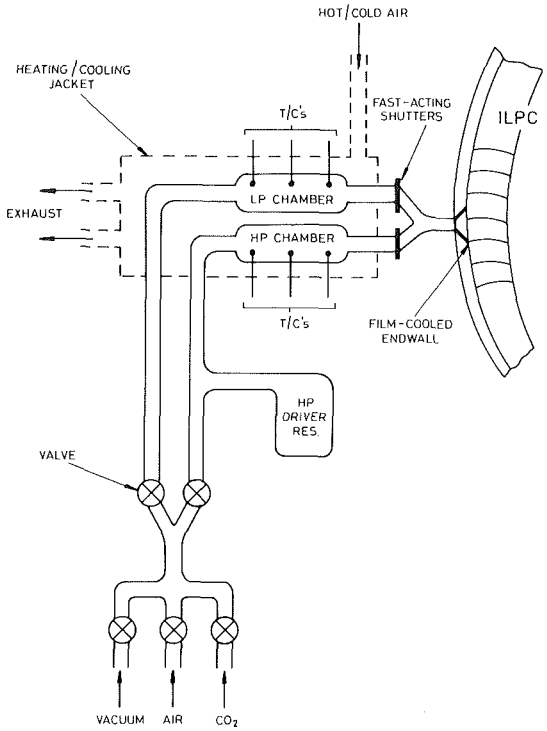

Fig. 6 Injection arrangement

value of I can be obtained right across the platform if P_{sg} is constant. This criterion is satisfied along an iso-Mach line. Once the momentum flux ratio is constant, then the blowing rate (G) is also constant for any fixed value of density ratio.

This design utilizes coolant holes placed along the 0.25 iso-Mach line (Fig. 2) as determined by a three-dimensional inviscid time marching code. The computations were performed on a 19 (radial) × 83 (axial) × 19 (pitchwise) grid using the Denton (1976) code. Previous experience with this code has yielded extremely good agreement between numerical and experimental results on the Mach number distribution on turbine vane platforms (cf. Kingcombe et al., 1989; Harasgama and Wedlake, 1991).

The present design used circular sectioned holes on the outer platform inclined at 30 deg to the local surface and aligned such that the jet axis lies normal to the local iso-Mach line. The cooling hole diameters have been chosen using the correlation shown on Fig. 4 after Forth (1985). The coolant-to-gas density ratio for this vane type is approximately 1.8. Using this density ratio and a modest blowing rate (G) of 0.5 shows that the coolant will persist for approximately 20 coolant hole diameters downstream of the injection plane. The coolant hole diameter is fixed at 1.0 mm. For the present design 19 coolant holes were placed across the platform giving a distance between hole centers of 1.75 mm.

Experimental Facility and Test Program

The film cooling tests were performed in the Isentropic Light Piston Cascade (ILPC). A detailed description of the test facility is given by Brooks et al. (1985). The facility (Fig. 5) operates by utilizing a light piston to compress and heat the test gas (air) rapidly prior to discharging it over a fully annular set of nozzle guide vanes.

In the present film cooling experiments the CO_2/air coolant mixture was contained in two separate reservoirs (Fig. 6), one at low pressure (LP) and one at high pressure (HP). These reservoirs are first evacuated and then filled with CO_2 and air to achieve the correct coolant density. The reservoirs are enclosed within a jacket through which either hot or cold air is circulated in order to obtain the desired value of θ for a particular run. On initiating the ILPC run, the LP coolant is released 50 ms prior to the establishment of the mainstream flow in order to purge the cooling circuit, cooling plenum, and coolant holes of any air. The HP coolant is then released

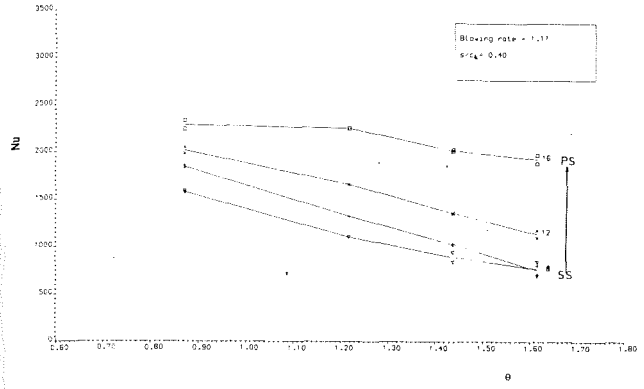

Fig. 7 Variation of Nusselt number with θ

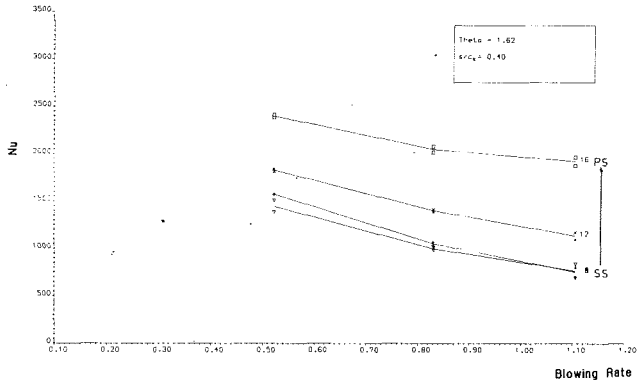

Fig. 8 Variation of Nusselt number with blowing rate

synchronously with the onset of mainstream flow and generates a constant, predetermined blowing rate for the 0.5 s duration of the ILPC run. Release of LP and HP cooling flows is via fast-acting shutter valves.

For the heat transfer tests, two adjacent vane platforms were blown. A total of 68 thin-film heat transfer gages were deposited on the platforms (Fig. 3) to give detailed measurements of heat transfer. The vanes were manufactured using machinable glass ceramic (MACOR[1]) and the unsteady one-dimensional temperature equation utilized to evaluate surface heat transfer (Shultz and Jones, 1973).

The platform static pressure distribution was also measured on a set of aluminum vanes. These were identical to the heat transfer vanes but the instrumentation consisted of surface static pressure tappings at the same geometric positions as the thin film gages. On both sets of vanes the coolant delivery pressure and temperature were measured with static pressure tappings and fast-acting thermocouples placed in the coolant injection plenum.

The vanes were operated at an exit Mach number of 0.93 and Reynolds number based on true chord of 2.55×10^6. The free-stream gas-to-wall temperature ratio was set to 1.3 and the coolant-to-gas density ratio to 1.8 for all tests. Film cooling tests were done at blowing rates of 0.52, 0.83, and 1.11. For all blowing rates results were obtained for θ's of 0.87, 1.22, 1.44, and 1.62. The aluminum vanes used for obtaining platform aerodynamics (static pressures/Mach numbers) were tested with $\theta = 1.0$ for all the blowing rates. The platform heat transfer and aerodynamics were also measured without any cooling flows.

The inlet total pressure and total temperature were measured for all test cases. All experimental results are presented for isothermal wall temperature conditions. Uncertainties on Nusselt number are quantified at ± 7 percent and pressure readings are to within ± 5 percent. The inlet turbulence level was measured at around 6 percent using a hot-wire anemometer. The turbulence was generated by a bar grid placed 4.5 axial chords upstream of the vane leading edge. Detailed velocity and temperature boundary layer traverses were made at inlet to the vanes on both inner and outer annuli.

Results and Discussion

Heat Transfer. All data are presented in the form of Nusselt numbers based on true chord. Initially, data are presented at fixed axial locations downstream of the plane of cooling, indicating the blade-to-blade variations for various blowing rates and θ's. Thereafter platform Nusselt number contours are presented for all cases.

The variation of Nusselt number with θ is presented in

[1]MACOR is a trademark of Corning Glass, USA.

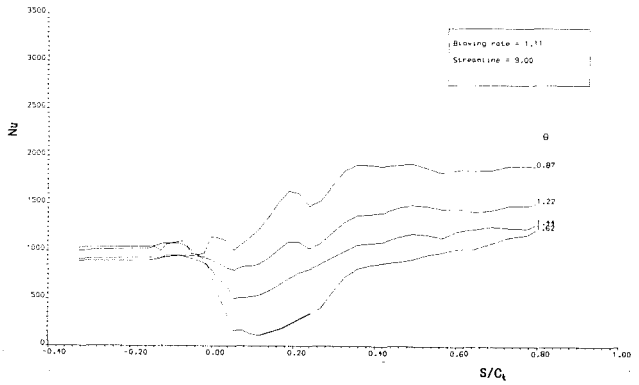

Fig. 9 Streamwise variation of Nusselt number midpassage grid line

Fig. 7 for a blowing rate of 1.1 at a distance of 0.4 chords (C_l) downstream of the cooling plane. These results indicate that Nusselt number decreases with increasing θ as expected. Also shown is the blade-to-blade variation, which indicates that the suction side is receiving more cooling than the pressure side. This also is as expected because the secondary flow will tend to convect the coolant toward the suction side.

A similar trend is evident in Fig. 8, which shows Nusselt number variation with blowing rates. As blowing rate is increased, the surface heat transfer rates decrease. Also evident is that the suction side of the platform is receiving more cooling than the pressure side. The data are for 0.4 chords downstream of the plane of cooling and at a fixed θ of 1.62.

Figure 9 shows the variation of Nu with distance downstream of the cooling holes. The results are for a midpassage streamline and blowing rate of 1.1. It is clear that very little cooling is taking place for $\theta = 0.87$. For θ's of 1.22, 1.44, and 1.62, the Nusselt number is greatly reduced immediately downstream of the injection plane. In the case of $\theta = 1.62$, it can be seen that sufficient cooling is taking place along the midpassage streamline to limit the exit Nusselt number to a value close to the inlet one.

Full area Nusselt number distributions on the outer platform are presented on Fig. 10. These data are for $\theta = 1.62$ at all blowing rates; also included is the datum uncooled Nusselt number distribution. The results show that increasing blowing rate causes a reduction in heat transfer to the platform in all cases. Also evident is the cross-passage variation in cooling. This is most clear for $G = 0.52$ where the coolant is convected toward the suction surface, leaving a patch of high heat transfer near the pressure side trailing edge region. This region tends to receive very little cooling for all blowing rates, although some cooling is evident at the highest blowing rate. The blade-to-blade variation is generated by the cross-passage pressure gradient, which gives rise to the passage secondary flow. The high heat transfer at the pressure side trailing edge is caused

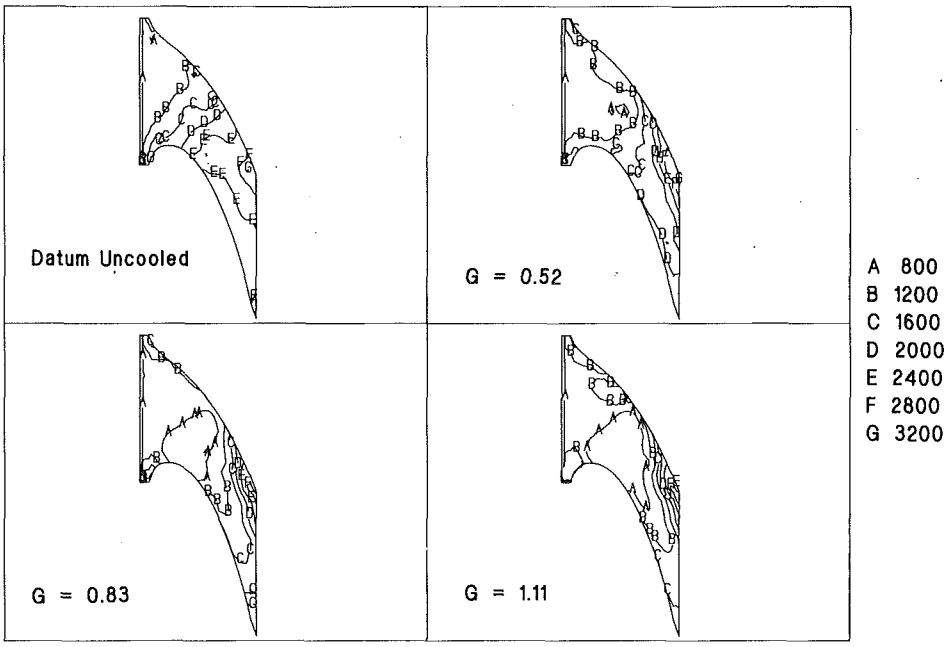

Fig. 10 Endwall Nusselt number distribution for $\theta = 1.62$, all blowing rates

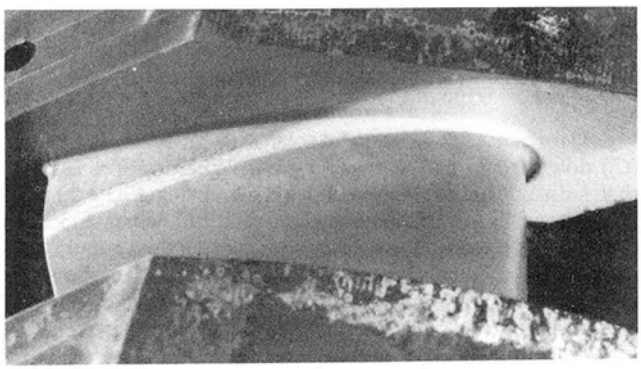

Fig. 11 Suction surface and outer platform flow visualizations

by the passage of the horseshoe vortex, which strips off the inlet boundary layer and thereby some of the coolant as well; this initiates the start of a thin new boundary layer with high heat transfer.

Flow visualizations have been performed on this configuration in the absence of cooling flow. Figure 11 shows the nature of the endwall flow field. It is clear that there is significant migration of flow from the pressure to suction side of the passage. This subsequently reaches the vane suction side midheight plane at the trailing edge, implying that some of the platform cooling air is migrating over the vane suction surface. These flow visualizations lend support to the endwall Nusselt number distributions, which also indicate similar trends. The injection of cooling air will generally tend to re-energize the endwall boundary layer leading to lower secondary flows, but in the present case the fairly low blowing rates used and the discrete hole configuration indicate that such an effect is very minimal.

Further endwall Nusselt number distributions are shown on Figs. 12–14. These show the variation of film cooled Nusselt number for $G = 0.52$, 0.83, and 1.11, respectively, for all the θ conditions. All figures indicate that increasing θ leads to reductions in the heat load to the platform, the largest reduction being at the highest θ. The most cooling occurs for $G = 1.11$ at $\theta = 1.62$ as expected (Fig. 14). Finally, Fig. 15 shows the ratio of cooled-to-uncooled Nusselt number for $G = 1.11$ and $\theta = 1.44$. It is clear that over most of the platform the heat transfer is reduced by 50–75 percent, except near the pressure side trailing edge corner, where the reduction is around 20 percent.

Aerodynamics. The predicted and experimental Mach number distributions on the outer endwall are shown in Fig. 16. Figure 16(*a*) shows the inviscid prediction used in the film cooling design process along with the uncooled Mach number distribution in Fig. 16(*b*), while Fig. 16(*c*) illustrates the platform Mach numbers for the cooled case with $G = 1.11$ and $\theta = 1.0$.

It can be seen that the predicted Mach numbers (Fig. 16*a*) are in excellent agreement with the Mach numbers for the uncooled case (Fig. 16*b*), the iso-Mach line for 0.25 being in an almost identical position in both cases. The only discrepancy is at the crown of the suction surface where, in the experimental case, the contours are erroneous due to the lack of data points, which causes the contours to be linearly extrapolated to the suction surface/platform intersection. The Mach number contours on Fig. 16(*c*) are also in good agreement with the other cases. However, there are very few measurements near the cooling holes due to difficulties in instrumenting this area with static pressure tappings. These results all appear to indicate that the cooling holes do indeed operate with uniform blowing rate across the entire platform.

Conclusions

Heat transfer measurements have been made on the outer platform of a fully annular set of nozzle guide vanes with and without discrete hole film cooling. The salient features of the experimental program are as follows:

- The original design concept of placing film cooling holes along an iso-Mach line has resulted in a very effective method of cooling a nozzle guide vane platform.
- The Nusselt numbers over the platform have been reduced by up to 75 percent in areas closest to the plane of injection. In most other areas the coolant reduces the Nusselt numbers

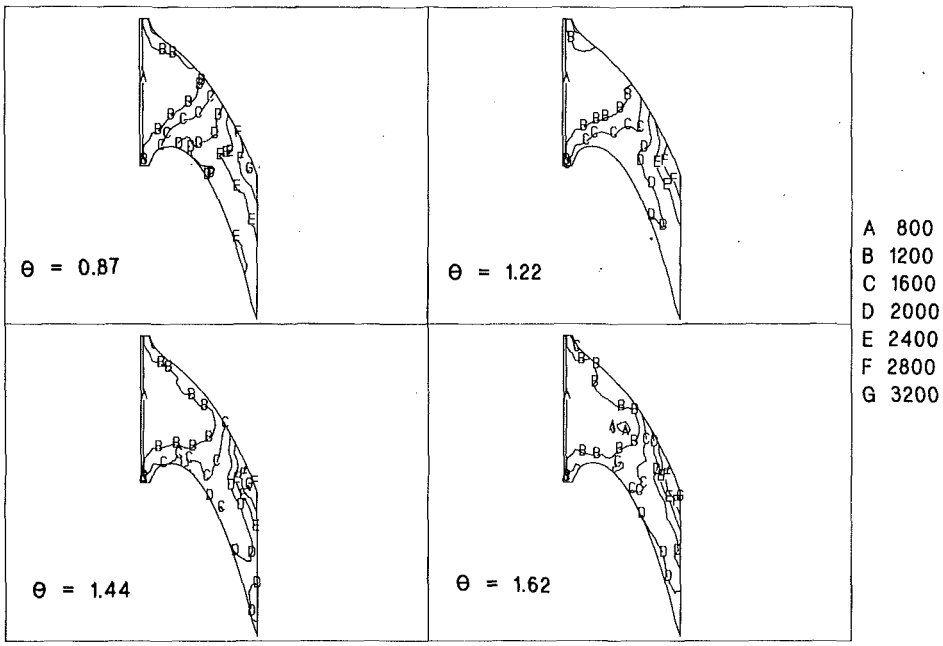

Fig. 12 Endwall Nusselt number distributions for $G = 0.52$: all θ

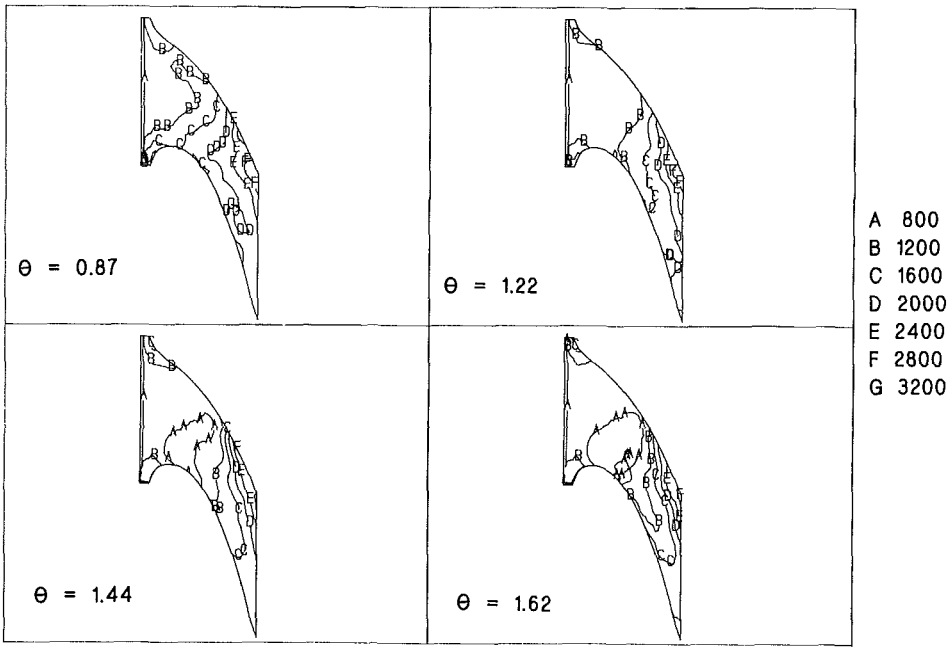

Fig. 13 Endwall Nusselt number distributions for $G = 0.83$: all θ

by around 50 percent, the coolant mass flow being 1.45 percent of throat mass flow for the highest blowing rate.

- The secondary flow in the NGV passage convects the coolant toward the suction side and this results in a relatively high heat load area at the pressure side trailing edge region. In this area, cooling only reduces the Nusselt number by 20 percent for a blowing rate of 1.11 and $\theta = 1.62$.
- The present experiments have covered blowing rates between 0.52 to 1.11 with θ being varied from 0.87 to 1.62. All results indicate that the heat transfer to the platform is reduced with increasing blowing rate and temperature difference ratio (θ).

It is considered that the detailed nature of these data can be utilized for development and validation of computational methods for heat transfer prediction in the presence of film cooling on NGV platforms. The data are further analyzed in a companion paper by Harasgama and Burton (1992).

Acknowledgments

The support of the turbine heat transfer group at Oxford University headed by Professor Terry Jones is greatly appreciated. Thanks are also due to Neil Harvey of Rolls Royce plc, who performed the flow visualizations.

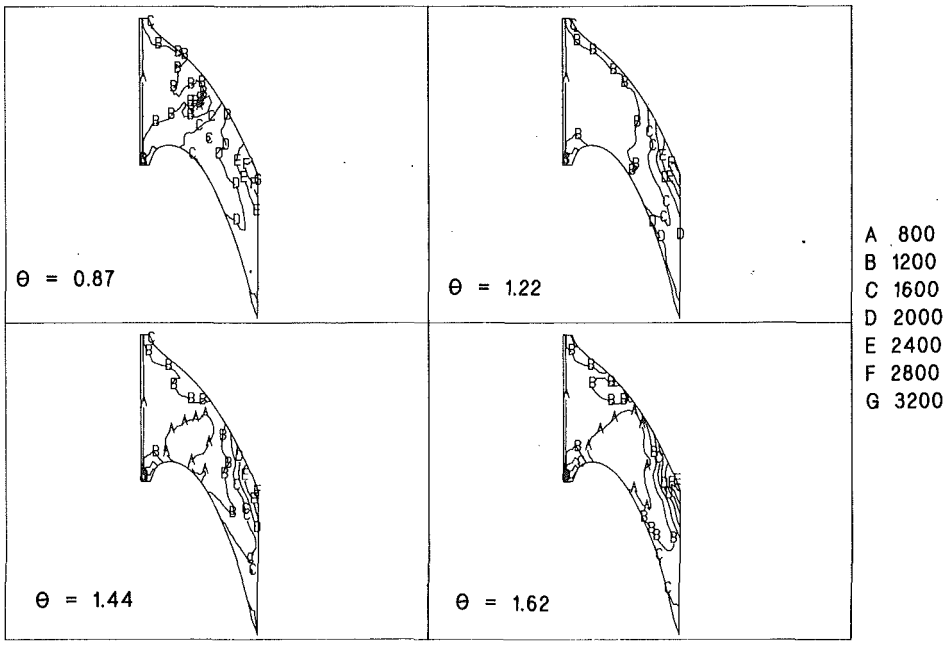

Fig. 14 Endwall Nusselt number distributions for $G = 1.11$: all θ

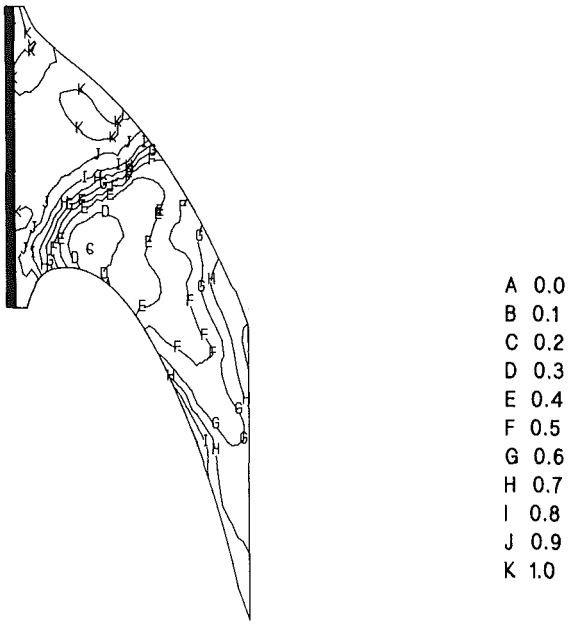

Fig. 15 Ratio of cooled to uncooled Nusselt number for $G = 1.11$ and $\theta = 1.44$

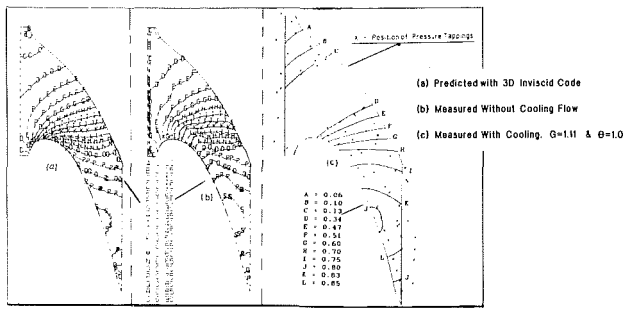

Fig. 16 Mach number distributions on outer platform

References

Blair, M. F., 1974, "An Experimental Study of Heat Transfer and Film Cooling on a Large Scale Turbine Endwall," ASME Paper No. 74-GT-33.

Bourguignon, A. E., 1985, "Etudes des transferts thermiques sur les plates-formes de distribution de turbines avec et sans film refroidissement," in: *Heat Transfer and Cooling in Gas Turbines*, AGARD-CP-390.

Brooks, A. J., Colbourne, D. E., Wedlake, E. T., Jones, T. V., Oldfield, M. L. G., Schultz, D. L., and Loftus, P. J., 1985, "The Isentropic Light Piston Annular Cascade at RAE Pyestock," in: *Heat Transfer and Cooling in Gas Turbines*, AGARD-CP390, Paper No. 31.

Crawford, M. E., Kays, W. M., and Moffat, R. J., 1980, "Full Coverage Film Cooling on Flat, Isothermal Surfaces: A Summary Report on Data and Predictions," NASA-CR-3219, Jan.

Denton, J. D., 1976, "Extension of the Finite Area Time Marching Method to Three Dimensions," VKI-LS-84.

Eckert, E. R. G., Birkbak, R. C., and Hartnett, J. P., 1961, "Velocity tributions, Temperature Distributions, Effectiveness and Heat Transfer in Cooling of a Surface With Pressure Gradient," presented at the International Heat Transfer Conference, Aug.-Sept.; *ASME Conference Proceedings*, 1963.

Forth, C. J. P., 1985, "An Investigation of Scaling Parameters Governing Film Cooling," D. Phil thesis, Department of Engineering Science, Oxford University, United Kingdom.

Goldstein, R. J., 1971, "Film Cooling," in: *Advances in Heat Transfer*, Vol. 7, pp. XX-00.

Granser, D., and Schulenberg, T., 1990, "Prediction and Measurement of Film Cooling Effectiveness for a First Stage Turbine Vane Shroud," ASME Paper No. 90-GT-95.

Harasgama, S. P., and Wedlake, E. T., 1991, "Heat Transfer and Aerodynamics of a High Rim-Speed Turbine Nozzle Guide Vane Tested in the RAE Isentropic Light-Piston Cascade (ILPC)," ASME JOURNAL OF TURBOMACHINERY, Vol. 113, pp. 384-391.

Harasgama, S. P., and Burton, C. D., 1992, "Film Cooling Research on the Endwalls of a Turbine Nozzle Guide Vane in a Short Duration Annular Cascade: 1991, Part 2—Analysis and Correlation of Results," ASME JOURNAL OF TURBOMACHINERY, Vol. 114, this issue, pp. 741-746.

Jones, T. V., 1986, "The Scaling of Film Cooling, Theoretical and Experimental Results," VKI-LS-1986-06.

Kingcombe, R. C., Harasgama, S. P., Wedlake, E. T., and Leversuch, N. P., 1989, "Aerodynamic and Heat Transfer Measurements on Blading for a High Rim-Speed Transonic Turbine," ASME Paper No. 89-GT-228.

Schultz, D. L., and Jones, T. V., 1973, "Heat Transfer Measurements in Short-Duration Hypersonic Facilities," AGARD-AG-165.

Takeishi, K., Matsuura, M., Aoki, S., and Sato, T., 1990, "An Experimental Study of Heat Transfer and Film Cooling on Low Aspect Ratio Turbine Nozzles," ASME JOURNAL OF TURBOMACHINERY, Vol. 112, pp. 488-496.

Teekaram, A., Jones, T. V., and Forth, C. J. P., 1989, "Use of Foreign Gas to Simulate the Effects of Density Ratios in Film Cooling," ASME JOURNAL OF TURBOMACHINERY, Vol. 111, p. 57.

Film Cooling Research on the Endwall of a Turbine Nozzle Guide Vane in a Short Duration Annular Cascade: Part 2—Analysis and Correlation of Results

S. P. Harasgama

C. D. Burton

Royal Aerospace Establishment,
Propulsion Department,
Pyestock, Farnborough,
Hampshire, GU14 OLS, United Kingdom

Results have been presented on the heat transfer characteristics of the film cooled endwall (platform) of a turbine nozzle guide vane in an annular cascade at engine representative conditions in a companion paper by Harasgama and Burton (1992). The present paper reports on the analysis of these measurements. The experimental results are well represented by the superposition theory of film cooling. It is shown that high cooling effectiveness can be achieved when the data are corrected for axial pressure gradients. The data are correlated against both the slot-wall jet parameter and the discrete hole injection function for flat-plate, zero pressure gradient cases. The pressure gradient correction brings the present data to within ±11 percent of the discrete hole correlation. Preliminary predictions of heat transfer reduction have been carried out using the STANCOOL program. These indicate that the code can predict the magnitude of heat transfer reduction correctly, although the absolute values are not in good agreement. This is attributed to the three-dimensional nature of the flow at the endwall.

Introduction

The quest for increased gas turbine efficiency and performance requires that the turbine entry temperatures be maximized. Current engine turbine entry temperatures are significantly greater than the allowable metal temperatures and future technology is targeted at obtaining stoichiometric conditions in the gas turbine combustor. These high temperatures have led to the first-stage high-pressure (HP) turbine being heavily cooled by air bled from the compressor.

Film cooling is an established method by which the turbine is protected from the adverse effects of the hot gas. A large data base exists for the design of film cooling configurations on turbine aerofoils. Goldstein (1971), Jones et al. (1986), and Crawford et al. (1980) have all investigated film cooling of flat and curved surfaces with and without pressure gradients. Several important parameters have been identified that affect the film cooling process. The main parameters are the blowing rate (G) and the temperature difference ratio (θ), which have a first-order effect on the heat transfer coefficient under the film. The injection geometry also has a significant effect and several authors have shown that coolant holes inclined at 30–35 deg to the local surface offer the largest practical reduction in heat transfer for turbine components.

The influence of density ratio on the film cooling process has been investigated by Forth et al. (1985), Ammari et al. (1990), and Pietrzyk et al. (1990). In general the conclusions are that increasing coolant-to-gas density ratio causes a reduction in heat transfer under the film, leading to increased cooling effectiveness. Axial pressure gradients do not appear to have a significant effect on film cooling effectiveness when slot injection is used, as reported by Teekaram et al. (1991). However, when injection is through discrete holes, favorable axial pressure gradients cause an improvement in the film cooling effectiveness when high blowing rates ($G = 0.6$–1.4) are used.

Ligrani and Williams (1990) and Ligrani et al. (1991) have investigated the effects of a single vortex on the heat transfer and hydrodynamic behavior of the coolant injection from a single hole onto a flat plate at zero pressure gradient. They show that the coolant is swept into the vortex and this can lead to reductions or enhancement of the cooling effectiveness depending on the position of the vortex. When the coolant emerges into an upwash region of the vortex, film cooling effectiveness is decreased. The converse is true in the downwash region.

The endwall film cooling configuration in engines contains

Contributed by the International Gas Turbine Institute and presented at the 36th International Gas Turbine and Aeroengine Congress and Exposition, Orlando, Florida, June 3-6, 1991. Manuscript received at ASME Headquarters March 4, 1991. Paper No. 91-GT-253. Associate Technical Editor: L. A. Riekert.

all the physical elements in the above discussion. The features of pressure gradient, secondary flows, and interaction of the horseshoe vortex with the cooling jet all contribute to the complexity of film cooling on NGV platforms. The companion paper by Harasgama and Burton (1992) has presented data on a film cooled endwall in a fully annular vane cascade at engine representative aerothermal conditions. This paper contains an analysis of those data. The superposition theory of film cooling is utilized on the endwall data and the resulting cooling effectiveness is correlated with flat plate data. A preliminary analysis using the STANCOOL program (Crawford et al., 1980) is also presented.

Scaling Parameters

The superposition theory of film cooling has been used in the analysis of the present data. The theory, originally proposed by Metzger et al. (1968) and formalized by Choe et al. (1974), uses the linearity of the energy equation in posing a solution of the form:

$$\frac{\mathrm{Nu}}{\mathrm{Nu}_o} = A + B\theta \tag{1}$$

In the analysis of the present data, this is taken a step further by correcting the Nusselt numbers for property variations in the boundary layer with respect to the gas-to-wall temperature ratio:

$$\left(\frac{\mathrm{Nu}}{\mathrm{Nu}_o}\right)_{cp} = \frac{\mathrm{Nu}}{\mathrm{Nu}_o}\left(\frac{T_w}{T_g}\right)^n = A + B\theta \tag{2}$$

where $n = -0.07$ for a laminar boundary layer and $n = -0.25$ for a turbulent boundary layer.

In the present work a value of -0.25 is used for n because the endwall inlet boundary layer is turbulent within the vane passage (Harvey, 1991). The relationship in Eq. (2) has been verified experimentally by Jones et al. (1986) and numerically by Bose (1979). The ability to use such a relationship in the analysis of film cooling data greatly simplifies scaling of experimental data and extrapolation to other engine operating conditions.

In the present case the boundary layer on the endwall is three dimensional, hence:

$$\left(\frac{\mathrm{Nu}}{\mathrm{Nu}_o}\right)_{cp}(x, y) = A(x, y) + B(x, y)\theta \tag{3}$$

and the values of A and B are unique to any position on the endwall. The parameter A takes the value of heat transfer coefficient when the coolant and gas temperatures are the same and there is unit difference between these and the wall temperature. It therefore represents the extra heat transfer due to jet mixing and will generally exceed a value of unity. The parameter B indicates the cooling effect when the gas and wall temperatures are the same but with varying coolant temperatures. The classical manner of categorizing the usefulness of film cooling is through the adiabatic wall effectiveness (Goldstein, 1971). The relationship between effectiveness and the parameters A and B is well established and is expressed as:

$$\eta = -B/A \tag{4}$$

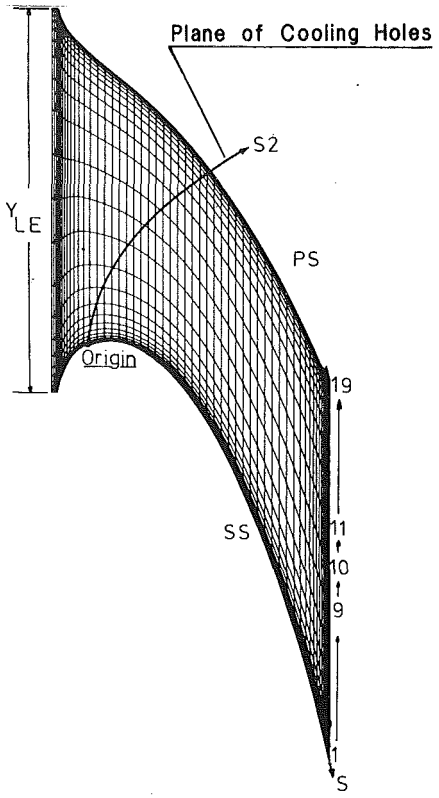

Fig. 1 Grid notation showing streamwise and cross-passage dimensions

Results and Discussion

Effectiveness and Superposition Results. The results are presented in the form of the cooling effectiveness parameter, B/A (η), and also the cooled-to-uncooled Nusselt number ratio corrected for property variations, $(\mathrm{Nu}/\mathrm{Nu}_o)_{cp}$. Figure 1 indicates the form of presentation. Streamlines are numbered 1–19 from suction to pressure side. The nondimensional length along such a streamline is S/C_t. Results are also presented along cross-passage grid lines parallel to the plane of film cooling, the nondimensional length in this case being S_2/Y_{LE}. All heat transfer data presented below have a maximum uncertainty of ± 7 percent.

Nomenclature

A = film cooling superposition parameter
B = film cooling superposition parameter
C_t = vane true chord
d = coolant hole diameter
G = blowing rate = $(\rho_i U_i/\rho_g U_g)$
h = heat transfer coefficient
I = momentum flux ratio = $(\rho_i U_i^2/\rho_g U_g^2)$
K = thermal conductivity of air
M = Mach number
Nu = Nusselt number, based on vane true chord = (hC_t/K)
S = dimension along streamwise (gridline) direction
$S2$ = dimension along gridline parallel to cooling plane
U = free-stream velocity
x = axial distance
y = blade-to-blade (tangential) distance
Y_{LE} = blade-to-blade distance at leading edge, on casing
η = cooling effectiveness
θ = temperature difference ratio = $(T_g - T_i)/(T_g - T_w)$
ρ = density
Φ, Ψ = functional relationship

Subscripts

cp = corrected for property variations
g = gas path value
i = injectant (coolant) value
o = zero coolant case (datum)

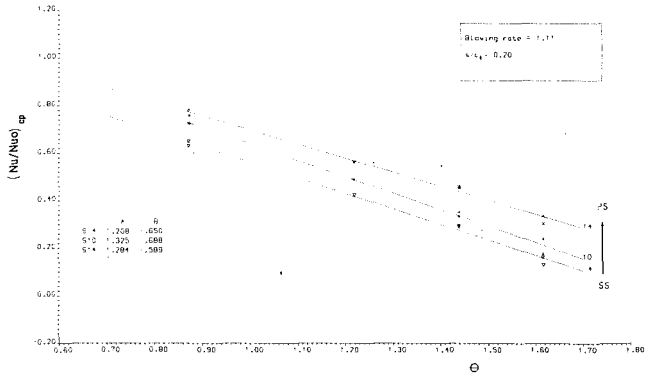

Fig. 2 Variation of Nu/Nu_o with θ

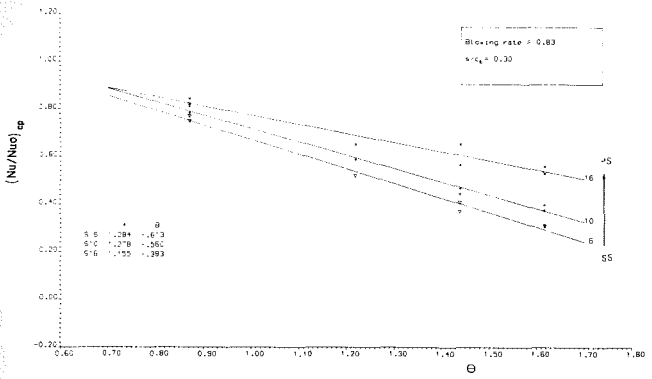

Fig. 3 Variation of Nu/Nu_o with θ

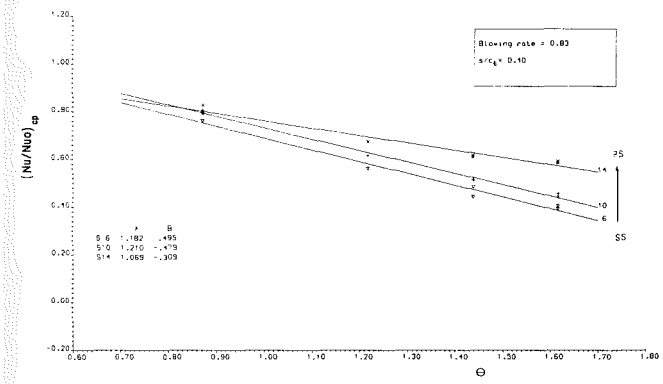

Fig. 4 Variation of Nu/Nu_o with θ

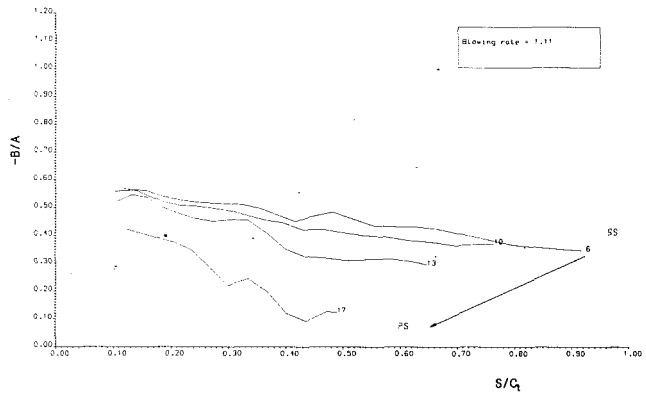

Fig. 5 Streamwise variation of $-B/A$ (effectiveness)

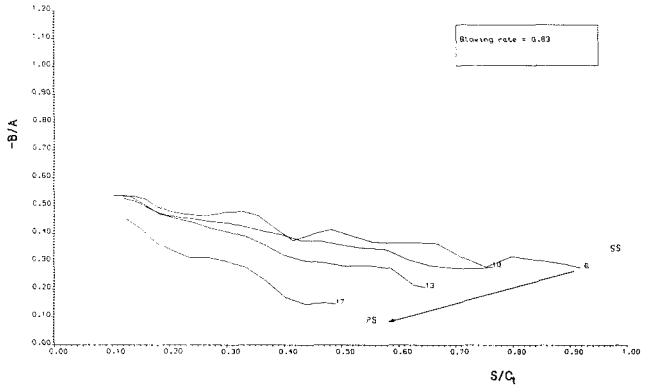

Fig. 6 Streamwise variation of $-B/A$ (effectiveness)

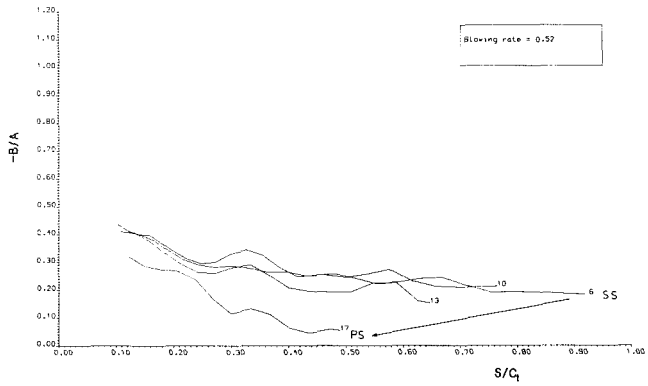

Fig. 7 Streamwise variation of $-B/A$ (effectiveness)

The results in Fig. 2 indicate the variations of $(Nu/Nu_o)_{cp}$ with θ for $S/C_t = 0.2$ from suction to pressure side for a blowing rate of 1.11. It can be seen that the results are well represented by the superposition model of film cooling. As θ is increased $(Nu/Nu_o)_{cp}$ decreases monotonically. This occurs for all streamline positions from suction to pressure side. It may also be seen that the value of A is greater than unity, indicating that mixing will enhance the wall heat transfer for all cases where the injectant and gas temperature are equal. The value of $-B$ is seen to decrease from suction to pressure side of the platform. This may be explained by the secondary flow convecting coolant toward the suction side, thereby reducing the cooling effectiveness near the pressure side (cf. Harasgama and Burton, 1992).

Similar results for a blowing rate of 0.83 are presented in Figs. 3 and 4, at S/C_t of 0.3 and 0.4, respectively. These indicate similar trends to those shown in Fig. 2. Also indicated is that as S/C_t increases from a value of 0.3 to 0.4, there is a reduction in cooling effectiveness, as evidenced from the decrease in the value of $-B$. This axial (streamwise) variation of effectiveness may be seen more clearly in Figs. 5, 6, and 7. These show that for all blowing rates the effectiveness decays with distance from the location of coolant injection. It should also be noted that the decay near the pressure side is more rapid than in other locations. This is obviously quite dissimilar to the two-dimensional flat plate case and is again attributed to the severely three-dimensional nature of the secondary flow at the vane platform. The blade-to-blade variation of effectiveness is more explicitly presented in Fig. 8. This shows the cross-passage variation of $-B/A$ at various locations downstream of the injection plane ($S/C_t = 0.1$, 0.3, 0.5, and 0.7); again the pressure side of the platform has lower cooling effectiveness in comparison to the suction side.

Correlation of Results. Correlation of the present effectiveness results is essential if they are to be of use to the designer of endwall film cooling configurations. Since a large body of data exists for flat-plate zero pressure gradient configurations, it was decided to attempt to correlate the present effectiveness and superposition results with the slot-wall jet parameter (Forth and Jones, 1986) and the discrete hole injection parameter

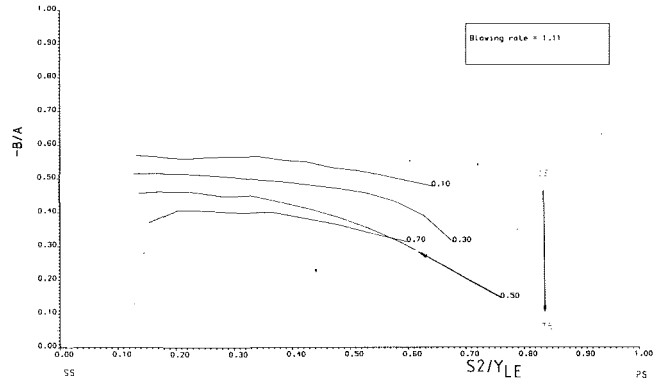

Fig. 8 Cross-passage variation of $-B/A$ (effectiveness)

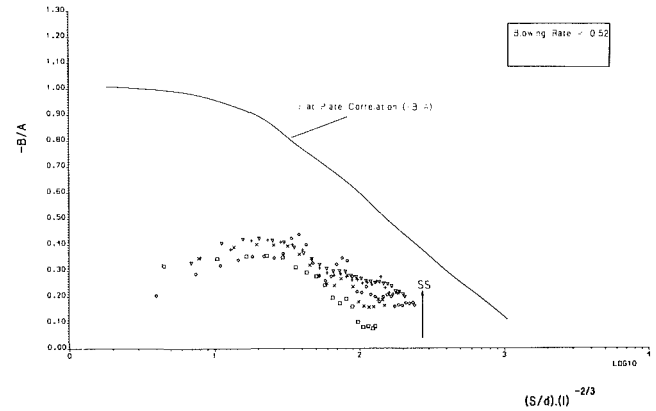

Fig. 9 Comparison of present endwall data with correlation for slot injection of a flat plate and zero pressure gradient

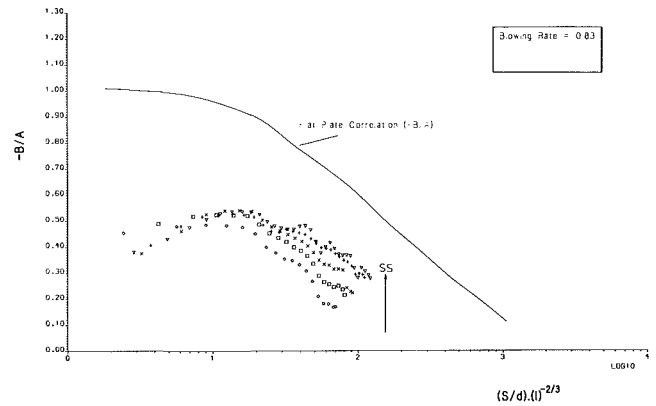

Fig. 10 Comparison of present endwall data with correlation for slot injection on a flat plate and zero pressure gradient

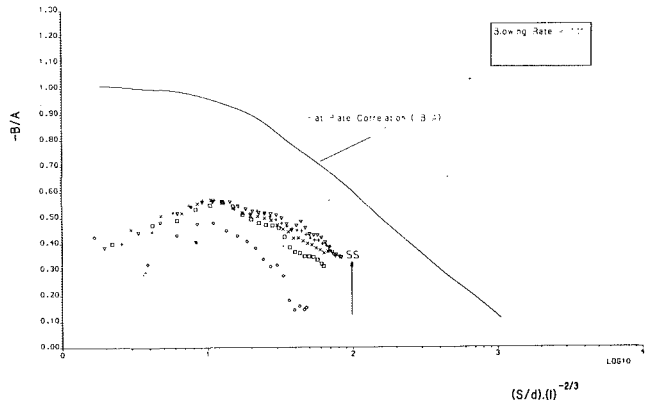

Fig. 11 Comparison of present endwall data with correlation for slot injection on a flat plate and zero pressure gradient

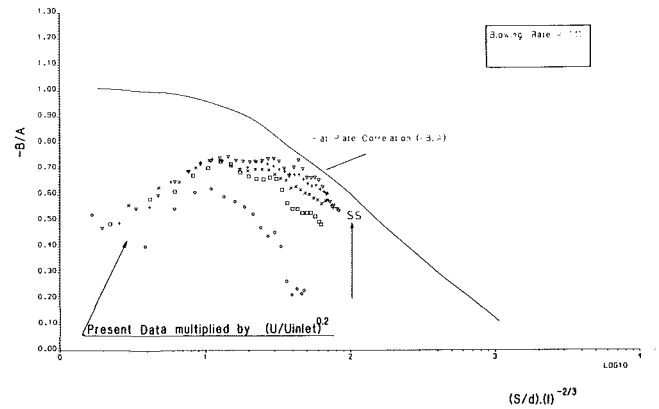

Fig. 12 Comparison of present endwall data with correlation for slot injection on a flat plate and zero pressure gradient

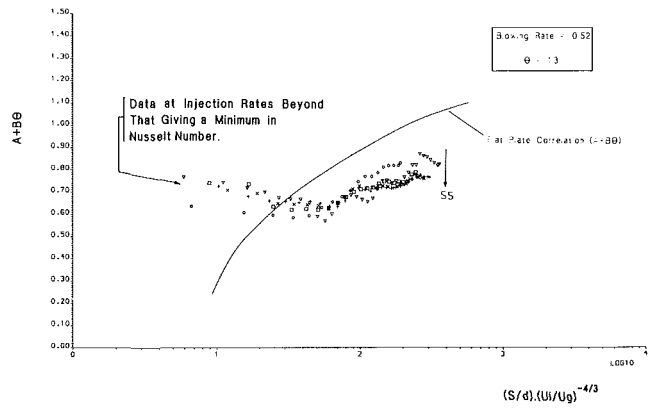

Fig. 13 Comparison of present endwall data with correlation for discrete hole injection on a flat plate/zero pressure gradient

(Jones et al., 1986). The slot wall jet correlation provides a functional relationship of the form:

$$\eta = -B/A = \Phi(S/d) \times (I)^{-2/3} \tag{5}$$

while the correlation for discrete hole cooling indicates that:

$$\left(\frac{\mathrm{Nu}}{\mathrm{Nu}_o}\right)_{cp} = A + B\theta = \Psi(S/d) \times (U_i/U_g)^{-4/3} \tag{6}$$

The present data are plotted against Eq. (5) in Figs. 9, 10, and 11 for blowing rates of 0.52, 0.83, and 1.11. The figures show that as the blowing rates are increased the cooling effectiveness approaches the flat plate correlation but that the agreement with the flat-plate result is very poor. This is to be expected because the comparison is between experimental data from discrete hole injection and a correlation representing slot injection. The present data are further complicated due to axial and cross-passage pressure gradients as well as secondary flows and the horseshoe vortex.

A correction was therefore made for the axial pressure gradient by multiplying the present effectiveness data by $(U/U_{\mathrm{inlet}})^n$ and plotting against Eq. (5). The result for a blowing rate of 1.11 is shown in Fig. 12, in this case $n = 0.2$. It can be seen that the data are now quite close to the slot wall jet parameter. The value of $n = 0.2$ was chosen by arguing that, usually, heat transfer coefficients may be put as functions of the Reynolds number (velocity) raised to the power 1/5th or 4/5th. Alternatively, it would be acceptable to multiply the correlation of Eq. (5) by $(U/U_{\mathrm{inlet}})^{-0.2}$ to achieve the same result. A similar approach has been evaluated by Hartnett et al. (1961) and found to be reasonably successful.

The results of the present investigation are also compared

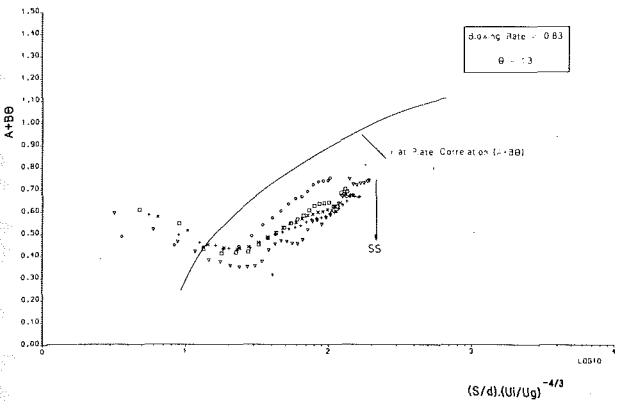

Fig. 14 Comparison of present endwall data with correlation for discrete hole injection on a flat plate/zero pressure gradient

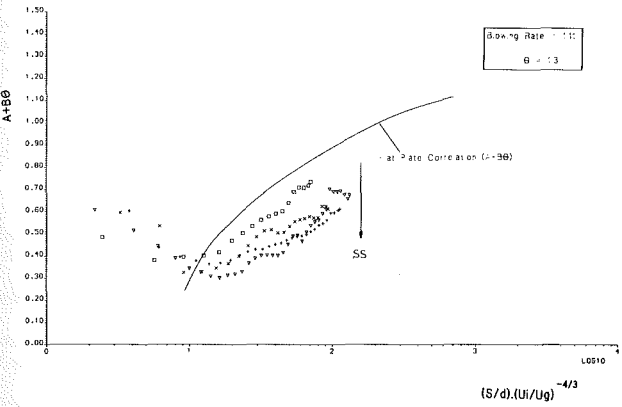

Fig. 15 Comparison of present endwall data with correlation for discrete hole injection on a flat plate/zero pressure gradient

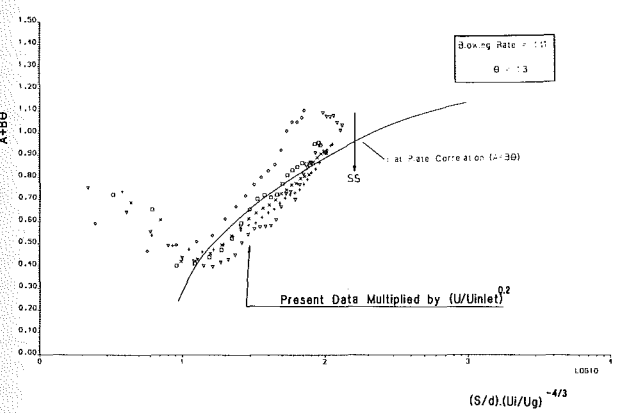

Fig. 16 Comparison of present endwall data with correlation for discrete hole injection on a flat plate/zero pressure gradient

with the discrete hole correlations (Eq. (6)) in Figs. 13, 14, and 15 for blowing rates of 0.52, 0.83, and 1.11, respectively. It can be seen that $(Nu/Nu_o)_{cp}$ for the present case lies below the correlation but is in closer agreement than for the slot-wall correlation as expected. This again is as expected due to the adverse effects on the present film cooling configuration of pressure gradients and secondary flow. The same approach for correcting for axial pressure gradient was applied to the case of $G = 1.11$ and replotted against Eq. (6) on Fig. 16. It can be seen that the correction has proved very successful and correlates the present data to within ± 11 percent of the flat-plate, zero pressure gradient function of Eq. (6). This has, in

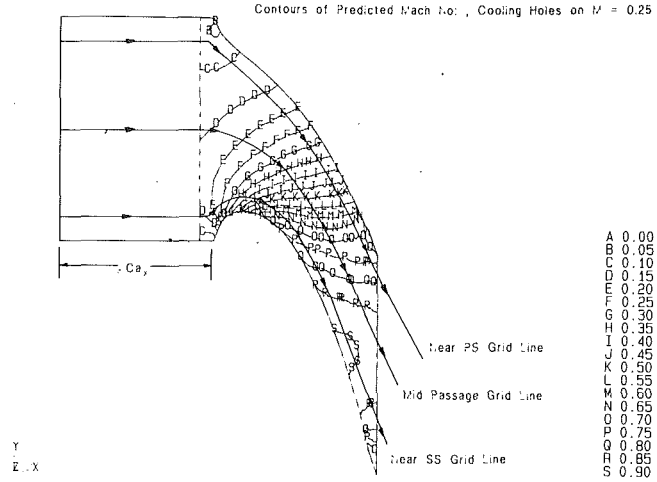

Fig. 17 Flat plate model for STANCOOL predictions

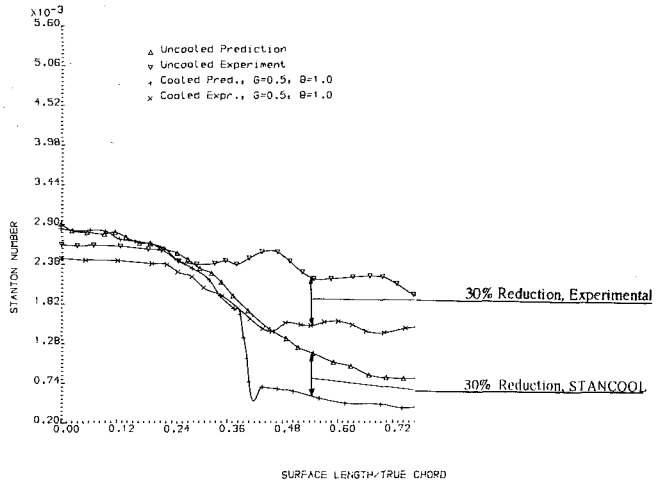

Fig. 18 Endwall Stanton numbers along midpassage gridline

effect, removed the streamwise pressure gradient effects from the data and Eq. (3) now merely represents the cross-passage variations of $(Nu/Nu_o)_{cp}$ along with the correlation of Eq. (6). It is considered that the ± 11 percent scatter in the correlations is due to the cross-passage pressure gradient effect.

Numerical Analysis. In order to evaluate the capability of available film cooling codes to tackle the present geometry, the STANCOOL program was utilized. It was recognized that the two-dimensional boundary layer approach used in STANCOOL would not be able to predict the present situation adequately. However, it is the only film-cooling code that is in the public domain.

The cooling configuration used as input to STANCOOl is shown on Fig. 17. The code was run in the fully turbulent mode and started with a Blasius profile at one axial chord upstream of the vane leading edge. Results are presented for the midpassage streamline (grid line) without allowing for any endwall flow skewing. The velocity boundary conditions are taken from the three-dimensional inviscid computations as presented in the companion paper by Harasgama and Burton (1992). The cooling was switched on when the midpassage grid line intersected the plane of cooling holes along the 0.25 iso-Mach line. The resulting computations are presented on Fig. 18. It can be seen that the computed Stanton numbers are approximately 50 percent below the experimental values for both the cooled and uncooled case. However, even though the absolute levels are in error, the code predicts the reduction in

heat transfer quite accurately at around 30 percent between uncooled and cooled cases. There also appears to be the possibility that the code is not running in the fully turbulent mode (Crawford, 1990) due to the damping functions used in the Van Driest model. It is evident that it may be possible to achieve closer agreement with experiment if the code is run along the skewed streamlines on the platform. Such an approach is possible by either using the flow-visualization performed on this configuration (Harvey, 1991) or by utilizing the secondary flow predicted by a three-dimensional viscous flow solver (Harasgama and Wedlake, 1991).

Conclusions

Heat transfer results in the presence of film cooling on the endwall of a fully annular nozzle guide vane cascade have been analyzed. The main conclusions may be summarized as follows:

- The superposition theory of film cooling has been successfully applied to the case of platform cooling. The present data follow the linearity of superposition and can therefore be extrapolated to other engine conditions operating at different coolant, gas, and wall temperatures.
- The data have been correlated with the slot-wall jet parameter and the discrete hole cooling parameter from flat-plate zero pressure gradients. It is shown that by correcting for axial pressure gradient, the present data can be correlated to within ± 11 percent of the flat-plate discrete hole parameter.
- Computations of endwall film cooling have been performed using the STANCOOL code. It is shown that the code can correctly predict the reduction in Stanton number between the uncooled and cooled cases. However, the code cannot accurately predict the absolute levels of endwall Stanton number with and without cooling. This is because the code is a purely two-dimensional boundary layer scheme, while the endwall cooling configuration is complicated by streamline skewing due to the passage secondary flow and horseshoe vortex.

This paper and its companion paper (Harasgama and Burton, 1992) provide a good quality data base for methods validation on film cooling of turbine platforms at engine representative aerothermal conditions. In addition, the analysis presented herein should enable the designer to utilize existing data bases and the present correlations to progress the science of film cooling in areas of severely three-dimensional flows.

References

Ammari, H. D., Hay, N., and Lampard, D., 1990, "The Effect of Density Ratio on the Heat Transfer Coefficient From a Film-Cooled Flat Plate," ASME JOURNAL OF TURBOMACHINERY, Vol. 112, pp. 444–450.

Bose, T. K., 1979, "Some Numerical Results for Compressible Turbulent Boundary Layer Heat Transfer at Large Free-Stream/Wall Temperature Ratios," in: *Studies in Heat Transfer*, Hemisphere, Washington, DC, pp. 69–81.

Choe, H., Kays, W. M., and Moffat, R. J., 1974, "The Superposition Approach to Film Cooling," ASME Paper No. 74-WA/HT-27.

Crawford, M. E., Kays, W. M., and Moffat, R. J., 1980, "Full Coverage Film Cooling on Flat, Isothermal Surfaces: A Summary Report on Data and Predictions," NASA-CR-3219.

Crawford, M. E., 1990, Private Communication.

Forth, C. J. P., Loftus, P. J., and Jones, T. V., 1985, "The Effect of Density Ratio on the Film Cooling of a Flat Plate," AGARD-CP-390.

Forth, C. J. P., and Jones, T. V., 1986, "Scaling Parameters in Film Cooling," *Proc. 8th Int. Heat Transfer Conference*, San Francisco, CA, Aug.

Goldstein, R. J., 1971, "Film Cooling," in: *Advances in Heat Transfer*, Vol. 7.

Harasgama, S. P., and Wedlake, E. T., 1991, "Heat Transfer and Aerodynamics of a High Rim Speed Turbine Nozzle Guide Vane Tested in the RAE Isentropic Light Piston Cascade (ILPC)," ASME JOURNAL OF TURBOMACHINERY, Vol. 113, pp. 384–391.

Harasgama, S. P., and Burton, C. D., 1992, "Film Cooling Research on the Endwalls of a Turbine Nozzle Guide Vane in a Short Duration Annular Cascade: Part 1—Experimental Technique and Results," ASME JOURNAL OF TURBOMACHINERY, Vol. 114, this issue, pp. 734–740.

Hartnett, J. P., Birkebak, R. C., and Eckert, E. R. G., 1961, "Velocity Distributions, Temperature Distributions, Effectiveness and Heat Transfer in Cooling of a Surface With a Pressure Gradient," *Proc. ASME Int. Heat Transfer Conf.*, Aug.–Sept.

Harvey, N. W., 1991, "Heat Transfer on Nozzle Guide Vane Endwalls," D Phil Thesis, Dept. of Eng. Science, Oxford University, United Kingdom.

Jones, T. V., Forth, C. J. P., Fitt, A. D., and Robertson, B. A., 1986, "Temperature Ratio Effects in Compressible Turbulent Boundary Layers," *Int. J. Heat Mass Transfer*, Vol. 29, No. 1.

Jones, T. V., and Forth, C. J. P., 1986, "The Scaling of Film Cooling, Theoretical and Experimental Results," VKI-LS-1986-06.

Ligrani, P. M., and Williams, W., 1990, "Effects of an Embedded Vortex on Injectant From a Single Film-Cooling Hole in a Turbulent Boundary Layer," ASME JOURNAL OF TURBOMACHINERY, Vol. 112, pp. 428–436.

Ligrani, P. M., Subramanian, C. S., Craig, D. W., and Kaisuwan, P., 1991, "Effects of Vortices With Different Circulations on Heat Transfer and Injectant Downstream of a Single Film-Cooling Hole in a Turbulent Boundary Layer," ASME JOURNAL OF TURBOMACHINERY, Vol. 113, pp. 433–441.

Metzger, D. E., Carper, H. J., and Swank, L. R., 1968, "Heat Transfer With Film Cooling Near Non-tangential Injection Slots," ASME *Journal of Engineering for Power*, Vol. 90, pp. 157–163.

Pietrzyk, J. R., Bogard, D. G., and Crawford, M. E., 1990, "Effects of Density Ratio on the Hydrodynamics of Film Cooling," ASME JOURNAL OF TURBOMACHINERY, Vol. 112, pp. 437–443.

Teekaram, A. J. H., Forth, C. J. P., and Jones, T. V., 1991, "Film Cooling in the Presence of Mainstream Pressure Gradients," ASME JOURNAL OF TURBOMACHINERY, Vol. 113, pp. 484–492.

The Influence of Density Difference Between Hot and Coolant Gas on Film Cooling by a Row of Holes: Predictions and Experiments

W. Haas[1]

W. Rodi

B. Schönung[2]

University of Karlsruhe,
Karlsruhe, Federal Republic of Germany

The two-dimensional boundary-layer procedure of Schönung and Rodi [1] for calculating film cooling by a row of holes was extended to account for density differences between hot gas and injected coolant gas. The extensions concern the injection model for leaping over the immediate blowing region in the boundary-layer calculation and also the dispersion model for taking into account three-dimensional effects. The extended model is tested for a density ratio of $\rho_j/\rho_e \approx 2$ for both flat-plate situations and film cooling on a model turbine blade. The predicted laterally averaged film cooling effectiveness is compared with measurements for these cases. Results for the flat-plate experiments were taken from the literature, while experiments for a model turbine blade are also described in this paper. For a fixed injection angle of 32 deg, the film cooling effectiveness was measured for various spacings and velocity ratios U_j/U_e. The density ratio $\rho_j/\rho_e \approx 2$ was achieved by adding Freon to the injection gas. The results are compared with those reported in [2] for negligible density difference. At the same blowing rate $M = U_j/U_e$, the film cooling effectiveness was found to increase with the density ratio ρ_j/ρ_e. In general, the influence of the density difference is well predicted by the model.

1 Introduction

The desire for higher thermal efficiency of gas turbines has led to higher and higher temperatures at the inlet of the turbine section. The temperatures have reached such high levels that the turbine blades need to be protected by efficient cooling. One of the most efficient cooling methods is film cooling by injection of cooling fluid through rows of holes, and this method is now widely used in practice. Already for one row of holes, for which the flow situation is shown in Fig. 1, a very complex flow develops with a wide variety of influence parameters such as the blowing angle α, the relative spacing s/D, the velocity ratio U_j/U_e, the density ratio ρ_j/ρ_e, and the state of the oncoming boundary layer. The cooling air tapped from the compressor causes a flow loss, and there are further losses associated with the injection itself. Under unfavorable conditions, the gain achieved by the film cooling can be used up by the flow losses, and hence the amount of cooling air must be kept at a minimum. This requires a delicate optimization of the film cooling design. As there are many influence parameters involved, optimization with the aid of experiments is not really feasible and a reliable prediction method is needed.

The flow field in the vicinity of injection holes is strongly three dimensional, and it is also associated with reverse flow, which is governed by elliptic equations rather than by parabolic boundary-layer equations. Hence, basically a three-dimen-

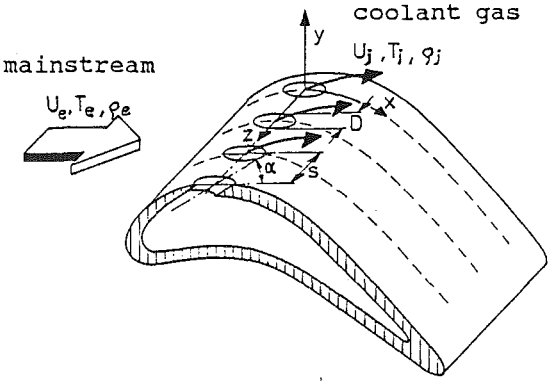

Fig. 1 Flow configuration

[1]Present address: Betriebsforschungsinstitut, Düsseldorf, Federal Republic of Germany.

[2]Present address: ABB Turbosystems, Baden, Switzerland.

Contributed by the International Gas Turbine Institute and presented at the 36th International Gas Turbine and Aeroengine Congress and Exposition, Orlando, Florida, June 3–6, 1991. Manuscript received at ASME Headquarters March 4, 1991. Paper No. 91-GT-255. Associate Technical Editor: L. A. Riekert.

sional elliptic calculation procedure is necessary for simulating the film cooling flow. Such methods are now available, but as the review of Schönung and Rodi [1] has shown, these methods are still too costly for carrying out parameter studies necessary for optimizing the film cooling design. Hence, much faster two-dimensional boundary-layer methods are highly desirable. Schönung and Rodi [1] have developed such a method, in which the elliptic reverse-flow region in the vicinity of the injection holes is passed over and new boundary-layer profiles are set up downstream of this region with an injection model, while the three-dimensional effects are simulated with the aid of dispersion terms appearing in the two-dimensional boundary-layer equations. Both the injection and the dispersion model were developed with the aid of systematic three-dimensional film cooling calculations covering a wide range of injection angles α, velocity ratios U_j/U_e, and relative spacings s/D. The two-dimensional boundary-layer method of Schönung and Rodi [1] covers the full range of these parameters of practical interest, and test calculations carried out for a wide variety of these parameters showed fairly good agreement with experiments in most cases. However, although the density is formally included as a variable in this model, the influence of density ratio of hot and coolant gas cannot be simulated realistically because the injection and dispersion models were based on three-dimensional calculations for a density ratio of 1. In this paper, therefore, the film cooling model of Schönung and Rodi is extended to include the effects of density ratio ρ_j/ρ_e. For verification purposes, experiments were carried out on a model turbine blade for a density ratio of $\rho_j/\rho_e = 2$ as an extension of the experiments with $\rho_j/\rho_e = 1$ reported in detail by Haas et al. [2]. These experiments are also reported in this paper, and the calculations are compared with these experiments as well as with experiments for flat-plate situations taken from the literature.

2 Film Cooling Model

2.1 Basic Flow Features. For the development of a film cooling model it is important to know the basic flow phenomena occurring in the vicinity of injection holes. Hence, a brief description of these phenomena is given by considering the injection of a single jet as sketched in Fig. 2. Two regions of the flow with three-dimensional behavior can be distinguished. In the immediate vicinity of the injection hole, pressure forces

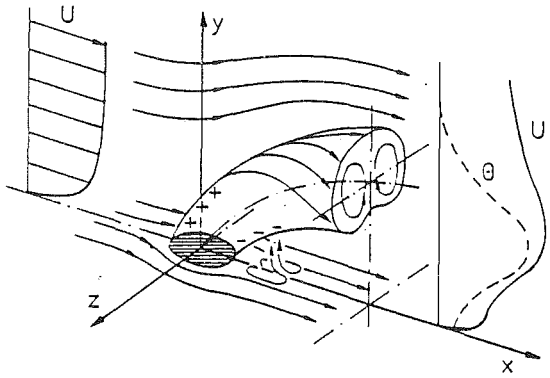

Fig. 2 Flow field in the vicinity of a single jet in a crossflow

are important that cause a bending-over of the injected jet due to the high upstream pressure and in certain cases also reverse flow behind the jet due to the low pressure in this region. Owing to the shearing of the bending-over jet by the crossflow, longitudinal vorticity is generated, which leads to the secondary motion sketched in Fig. 2 and consequently to the kidney shape of the bent-over jet. Simultaneously with the bending-over, mixing between the jet fluid and the oncoming fluid occurs, thereby reducing the excess or deficit velocity of the jet. The penetration of the jet depends mainly on the injection angle α and on the momentum ratio $I = (\rho U^2)_j/(\rho U^2)_e$ and can lead to strongly different characteristics behind the injection. For large α and I, the flow is of wake character and is similar to the flow past a solid cylinder placed on the wall. Downstream of the bending-over jet, a reverse-flow zone develops into which hot gas is mixed in from the side. Past the reverse-flow zone, the jet attaches on the blade surface. At small momentum ratios I, the jet bends over very quickly and attaches to the wall. When the injection angle is small, the jet also attaches quickly to the wall and at higher momentum ratios the flow develops wall-jet character.

When the bending-over of the jet is complete and the jet has attached to the wall, pressure forces are small and the flow development is mainly determined by turbulent mixing. The flow has regained its boundary-layer character, but it is still three dimensional and, as sketched in Fig. 2, the velocity and

Nomenclature

D = hole diameter
D_h, D_u, D_Θ = dispersion terms
h = static enthalpy
I = momentum, momentum ratio $= (\rho U^2)_j/(\rho U^2)_e$
ΔI = momentum difference between positions A and B (Fig. 4)
k = turbulent kinetic energy
M = blowing rate $= (\rho U)_j/(\rho U)_e$
P = pressure
ΔP = pressure difference between positions A and B (Fig. 4)
Re_1 = Reynolds number based on chord length and inlet conditions
s = hole spacing
T = temperature
Tu = free-stream turbulence level in percent
U = velocity component in x direction
y_{max}, y_{wen} = parameters in injection model for dimensionless temperature
y_{imin}, y_{imax}, y_{iend} = parameters in injection model for momentum
x, y, z = Cartesian coordinates
α = injection angle
δ = boundary-layer thickness
δ^* = boundary-layer displacement thickness $= \int_0^\delta (1 - \rho U/\rho_e U_e)dy$
ϵ = dissipation rate
$\bar{\eta}$ = laterally averaged cooling effectiveness
Θ = dimensionless temperature, tracer concentration $= (T - T_e)/(T_j - T_e)$
ρ = fluid density

Subscripts

a = adiabatic wall
A = value before injection region (Fig. 4)
B = value after injection region (Fig. 4)
e = free-stream (external) value
j = injection value
max = maximum
min = minimum
wall = value on the wall

temperature profiles differ strongly from those in developed boundary layers. In this region, the individual jets grow together so that after some distance the spanwise variations disappear and the flow becomes two dimensional. This process depends not only on the injection angle and the momentum ratio but also on the relative spacing. For large spacing and when the jets penetrate into the crossflow, the individual jets merge only at larger downstream distances.

The dependence of the phenomena described above on the various flow parameters must be described realistically by the film cooling model. In the present study, the injection angle α, the relative spacing s/D, the velocity ratio U_j/U_e, and the density ratio ρ_j/ρ_e (defining together the momentum ratio I) are in the foreground. Additional parameters that influence the film cooling characteristics are the state of the oncoming boundary layer (laminar or turbulent), the ratio of boundary layer thickness to injection hole diameter, the surface curvature, the longitudinal pressure gradient, and the free-stream turbulence level.

2.2 Basic Calculation Procedure. The two-dimensional boundary layer calculation procedure of Schönung and Rodi [1] formed the basis of the present work. The boundary layer equations, the low-Reynolds-number k–ϵ model used for simulating the turbulent momentum and heat transfer, and the marching-forward finite-volume method for solving the flow equations are described in [1]. The complex flow phenomena sketched in Section 2.1 can be simulated with a two-dimensional boundary layer procedure only when special measures are taken. This is done in the film cooling model of Schönung and Rodi [1] by introducing an injection model and a dispersion model, which will now be summarized briefly.

Injection Model. The region near the injection is passed over and new boundary layer profiles are set up at a certain distance behind the blowing region. These profiles take into account the characteristics of the oncoming boundary layer as well as of the injected jets.

Dispersion Model. Formal lateral averaging of the three-dimensional equations leads to two-dimensional equations with additional terms accounting for the lateral variation of the flow quantities and the additional lateral mixing. These so-called dispersion terms are modeled as additional source and sink terms in the two-dimensional boundary layer equations and cause a redistribution of the laterally averaged quantities in the y direction normal to the wall.

Both models are based on the results of three-dimensional elliptic calculations, which Demuren et al. [3] have carried out for 27 different film cooling configurations for the flat-plate situation. A detailed analysis of these results provided the necessary information for setting up the boundary layer profiles of the injection model and for the distribution of the dispersion terms in the dispersion model. The injection model contains 10 parameters that are used for generating boundary-layer profiles past the injection, and the dispersion model contains five parameters with which the three-dimensional effects are described. The values of these parameters are stored in the calculation procedure in the form of a coefficient matrix for 100 film cooling configurations depending on the injection angle α, the relative spacing s/D, and the velocity ratio U_j/U_e. By interpolation of the stored coefficient matrix, film cooling configurations can be calculated in the following ranges of the influence parameters:

$$0 \text{ deg} < \alpha \le 90 \text{ deg}$$
$$1.2 \le s/D \le 10.0$$
$$0 \le U_j/U_e \quad 4.0$$

As the three-dimensional calculations of Demuren et al. [3] were all for a density ratio $\rho_j/\rho_e = 1$, they provided no information on density effects, and the model was in fact found to produce unrealistic results when the density ratio was significantly different from 1. Hence, in the following section the injection and dispersion models are extended to account for the influence of significant density differences between hot and coolant gas.

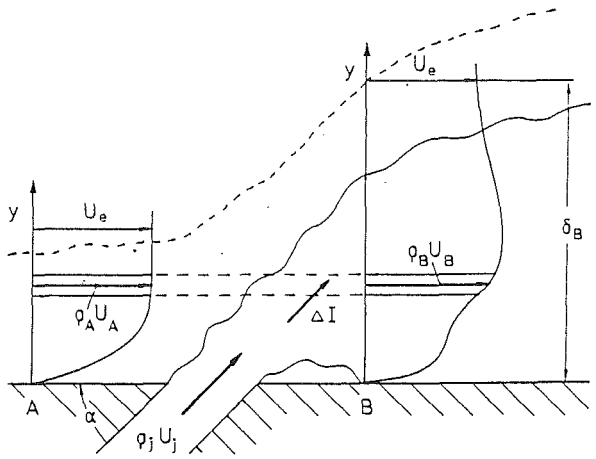

Fig. 3 Control-volume layer for one-dimensional momentum balance

2.3 Model Extension to Account for the Effect of Density Differences. The extension of the film cooling model was carried out step by step, starting with a revision of the correlations stored in the calculation procedure for generating the restart boundary-layer and the dispersion profiles. To this end, the parameters in the film cooling model were written in dimensionless form so that the influence parameters characterizing the film cooling configuration can be accounted for directly. This also simplified the physical interpretation of the basic mechanisms. The effect of the density ratio ρ_j/ρ_e was brought into the model with the aid of similarity considerations and with experimental information available from the literature. This revealed that the blowing rate $M = (\rho U)_j/(\rho U)_e$, which is often used in film cooling studies, is not so suitable for the film cooling model developed here. The blowing rate M is a measure of the mass flux injected into the boundary layer, but the dynamics of the flow field are better characterized by the momentum ratio

$$I = \frac{(\rho U^2)_j}{(\rho U^2)_e} \tag{1}$$

This ratio determines the penetration of the cooling jets into the hot-gas stream and is therefore relevant for the distribution of the injected cooling air in the near field of the injection holes. Hence, the momentum ratio I is used in the extended model as an additional parameter for generating the restart boundary-layer profiles. Further, by combining various parameters and by expressing some of the correlations in analytical form, the number of parameters stored in the calculation procedure could be reduced from 15 to 10. In the following, the extension of the film cooling model to account for the effect of density differences is briefly sketched; details of the model extension can be found in [4, 5].

2.3.1 Injection Model. The location B (see Fig. 3) at which the restart boundary-layer profiles are prescribed after the injection has been correlated with the aid of the three-dimensional results as described in [1]. The velocity profile at this location is determined with the aid of the one-dimensional momentum balance

$$\Delta I(y) = \underbrace{\rho_B(y)U_B^2(y)}_{I_B(y)} - \underbrace{\rho_A(y)U_A^2(y)}_{I_A(y)} = I_j(y) - \Delta P(y) \tag{2}$$

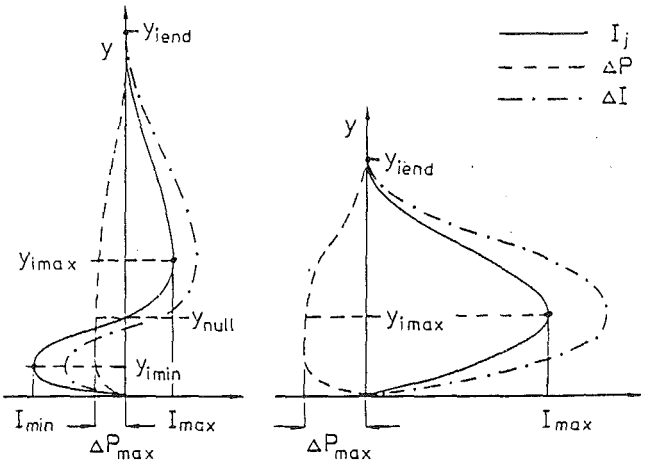

(a) Flow with wake character (b) Flow with wall-jet character

Fig. 4 Modeling of the momentum distribution

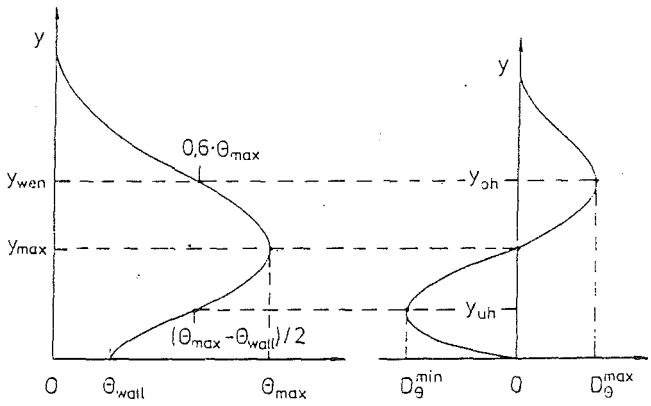

Fig. 5 Distributions of laterally averaged adiabatic temperature $\Theta_B(y)$ and dispersion term D_ϑ past the injection

for layers sketched in Fig. 3. In Eq. (2), $I_B(y)$ is the momentum distribution at location B downstream of the injection and $I_A(y)$ is the momentum distribution in the oncoming boundary layer, which follows from a normal boundary layer calculation upstream of the injection. The distribution of the injected momentum is described by $I_j(y)$ while $\Delta P(y)$ accounts for the pressure difference between locations A before and B after the injection. It should be noted that the pressure is not yet uniform at location B where the boundary layer profiles are set up.

Figure 4 shows two typical profiles of the injected momentum I_j, the pressure difference ΔP, and the difference ΔI between in-flowing and out-flowing momentum. The profiles in Fig. 4(*a*) correspond to a wake-flow situation as it occurs in most film cooling situations, so for $\alpha<30$ deg with small and medium velocity ratios U_j/U_e and for $\alpha>60$ deg when the velocity ratio is high. Only when α is small and $U_j/U_e>1$ is the flow downstream of the injection of wall-jet character, and the distributions in Fig. 4(*b*) are for this situation. As in the basic model, the excess momentum I_{max} is determined such that integration over the modeled injection momentum distribution $I_j(y)$ yields the total momentum discharged by the jet. The parameters y_{imin}, y_{imax}, and y_{iend} defining the distribution $I_j(y)$ are correlated with the injection angle α and the momentum ratio I but are virtually independent of the relative spacing s/D. The model relations for the other parameters were simplified somewhat over those in the basic model.

For determining the restart temperature distribution at location B, the laterally averaged adiabatic temperature

$$\Theta_B(y)=\frac{T_a(y)-T_e}{T_j-T_e} \tag{3}$$

is used. This corresponds to the temperature under adiabatic conditions and can be the considered as a tracer-concentration distribution with which the spreading of the cooling jets can be characterized. The realistic approximation of this distribution was very important for extending the film cooling model to situations with strong density differences. A typical profile of the adiabatic temperature is shown in the left part of Fig. 5. The parameters stored in the calculation procedure for generating this distribution are y_{max}, y_{wen}, and Θ_{wall}. The parameter y_{max}/D was correlated with U_j/U_e and the difference $(y_{wen}-y_{max})/D$ with the momentum ratio I. This modeling causes a widening of the tracer-concentration distribution normal to the wall when the density ratio ρ_j/ρ_e increases, thereby accounting for the larger input of mass and enthalpy. Immediately downstream of the injection, the adiabatic wall temperature Θ_{wall} correlates with the velocity ratio U_j/U_e and is independent of the density ratio ρ_j/ρ_e, as became obvious from the evaluation of measurements for different film cooling configurations [6–8]. However, this statement is valid only for sufficiently large momentum ratios. Below a limiting value of $I\approx 0.1$, the adiabatic wall temperature correlates with the momentum ratio I [8, 9].

Another important aspect of the model extension is the use of balance equations for tracer mass and enthalpy. The maximum value of the tracer distribution shown in Fig. 5, Θ_{max}, is calculated iteratively from the following balance equation:

$$\int_0^{y_e}(\rho U\Theta)_B dy=\frac{\pi D^2}{4s}\rho_j U_j \tag{4}$$

where the left-hand side is the tracer mass flux at location B and the right-hand side is the injected mass (note that the injected tracer concentration is 1 according to Eq. (3)). An estimated value of Θ_{max} needed for the first iteration is obtained from a correlation provided by the basic film cooling model.

The parameters for generating the tracer distribution are now known, and with this the temperature distribution $T_B(y)$ and also the density distribution $\rho_B(y)$ at location B downstream of the injection can now be determined. The corresponding velocity profile $U_B(y)$ is calculated iteratively with the aid of Eq. (2). For nonadiabatic walls, the temperature distribution $T_B(y)$ to be set up is not identical with the distribution of the adiabatic temperature, since the temperature distribution in the oncoming boundary layer has to be accounted for. This is achieved with the following relation:

$$T_B(y)=T_e+\Theta_B(y)\,(T_j-T_e)+\sigma[T_A(y)-T_e] \tag{5}$$

Here, $T_A(y)$ is the temperature profile at location A upstream of the injection, which follows from a normal boundary layer calculation. The parameter $\sigma=(1-D/s)$ takes account of the part of the oncoming boundary layer that extends to the region between the cooling jets in the vicinity of the injection holes. For generating the enthalpy distribution at location B, a balance equation analogous to Eq. (4) is used:

$$\int_0^{y_e}[(\rho Uh)_B-(\rho Uh)_A]dy=\frac{\pi D^2}{4s}\rho_j U_j(h_j-h_e) \tag{6}$$

Here, h_j-h_e is the difference in static enthalpy between the oncoming flow and the coolant. The profile of the static enthalpy $h_B(y)$ at location B is calculated from the temperature distribution $T_B(y)$ in the iterative process.

For setting up the restart profiles of turbulence quantities at location B, the distribution of turbulent energy in the cooling jets is superimposed to the energy distribution in the oncoming boundary layer. The boundary-layer measurements reported in [5] have shown that the distribution of the turbulent energy

due to the cooling jets can be described by a profile similar to that for the adiabatic temperature $\Theta_B(y)$. A maximum of this distribution is obtained with the aid of a correlation derived from measurements [5]. The dissipation rate ϵ is determined with the aid of a mixing-length model, in which the turbulent length scale of the oncoming boundary layer and of the injection jets is accounted for.

2.3.2 Dispersion Model. Dispersion terms representing three-dimensional effects are introduced into the two-dimensional equations for the velocity U, the adiabatic temperature Θ, and the enthalpy h. Dispersion terms for the turbulence quantities k and ϵ are considered negligible compared with the source and sink terms in the k and ϵ equations. A typical distribution of a dispersion term D_Θ for the adiabatic temperature Θ as determined from the three-dimensional calculations is shown on the right-hand side of Fig. 5 for a position just downstream of the injection. The principles of the dispersion model are now explained with the aid of this distribution. D_Θ is negative near the wall and positive in the outer part of the boundary layer, describing the lifting of the coolant jets by the lateral entrainment of hot gas near the wall. As can be seen from Fig. 5, the position of the maximum $D_\Theta^{\max}$ and the minimum $D_\Theta^{\min}$ and the zero crossing are closely related to the distribution of the adiabatic temperature Θ. The value of the near-wall minimum, $D_\Theta^{\min}$, is calculated with the aid of coefficients stored in the calculation procedure, and the decay of the dispersion terms with streamwise distance from the injection is described with the aid of exponential functions. The maximum value $D_\Theta^{\max}$ in the outer part of the boundary layer is calculated from the constraint that the integral over the dispersion distribution has to be zero since dispersion terms do not produce any net sources and sinks but only a redistribution of the quantity in question. For reasons of momentum conservation, the pressure difference introduced according to Eq. (2) must be removed farther downstream, and this is described by an additional source term in the dispersion model. As dispersion terms physically represent fluxes, the density effect is accounted for simply by multiplying the dispersion terms obtained without density variation with the local density ratio $\rho(y)/\rho_e$. The dispersion term for the enthalpy h calculated from the Θ-dispersion term is as follows:

$$D_h(y) = D_\Theta(y)[h_j - h_e - \sigma(h_A(y) - h_e)] \tag{7}$$

The term $h_A(y) - h_e$ represents the profile of the static enthalpy upstream of the injection. This term is multiplied with the factor $\sigma = (1 - s/D)$ in order to account in a similar way to Eq. (5) for the influence of the oncoming boundary layer, which penetrates between the coolant jets into a limited region downstream of the injection.

3 Measurements of Film Cooling Effectiveness on a Model Turbine Blade

In order to allow a realistic testing of the film cooling model, film cooling experiments were carried out on a model blade. These are an extension of the measurements described in [2] for a density ratio of $\rho_j/\rho_e \approx 1$. The experimental apparatus, the measurement blade, and the measurement techniques are described in detail in [2] and are only briefly sketched here. The measurements were carried out on an enlarged model of a relatively thin, highly curved turbine blade (see Fig. 6). The "cooling" gas was injected on the suction side through a row of holes at a relative surface distance of 25 percent and at an injection angle of $\alpha = 32$ deg. The hole diameter D was chosen such that the ratio δ/D assumes a value of about 0.3 typical for real turbine blades. In the measurements presented here, the relative spacing s/D and the blowing rate M were varied.

The Reynolds number based on the chord length (0.25 m) and the oncoming velocity was $\mathrm{Re}_1 \approx 1.4 \times 10^5$, and the turbulence level of the free stream was $Tu_1 = 6.2$ percent. The injected air was heated, and the laterally averaged film cooling effectiveness $\bar{\eta}$ was determined by measuring the adiabatic wall temperature. In real film cooling situations, the density ratio is $\rho_j/\rho_e \approx 2$, and this density ratio was achieved by adding Freon to the injected air. Measurements for the density ratio of $\rho_j/\rho_e \approx 1$ (without addition of Freon) were reported already in [2]. Because of heat transfer from the duct supplying the heated injection air placed in the front part of the blade (see Fig. 6), the conditions at the blade surface upstream of the injection were not adiabatic. A temperature boundary layer developed in this region, which had to be taken into account in the calculations. The measured distributions of the film cooling effectiveness are presented together with the calculation results in Section 4.2.

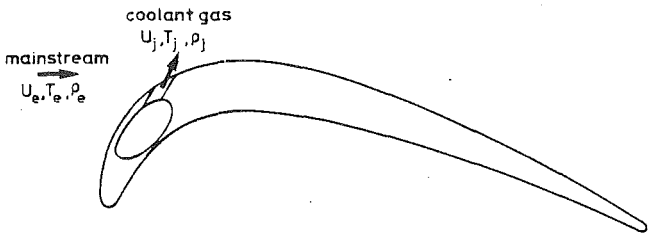

Fig. 6 Model turbine blade

4 Comparison of Predictions With Measurements

The extended film cooling model was tested first extensively for film cooling situations with small density differences. The results reported in [4, 5] demonstrate that, in general, the extended model leads to better agreement with measurements than the basic version. The present paper presents predictions for cases with density ratios occurring in practice, i.e., for $\rho_j/\rho_e \approx 2$. The model is tested first against measurements available in the literature for flat-plate situations and then against our own measurements on a model turbine blade described in Section 3. It should be mentioned here that the numerical uncertainty of the calculation procedure is very small; it is certainly negligible compared with the uncertainties introduced by the injection and dispersion models.

4.1 Film Cooling Effectiveness on Flat Plates. In the flat-plate experiments simulated, the density difference was achieved by injecting a Freon–air mixture and the film cooling effectiveness η was obtained from wall concentration measurements. Since the equations governing heat and mass transfer are the same, the density difference could be simulated in the calculations by the temperature difference.

The first set of experiments simulated were those of Pedersen et al. [9], who investigated film cooling for an injection angle of $\alpha = 35$ deg and a spacing of $s/D = 3$. The free-stream velocity was $U_e = 15.4$ m/s and the free-stream turbulence level $Tu_e = 0.4$ percent. The oncoming boundary layer was turbulent and its relative displacement thickness was $\delta^*/D = 0.16$. For various blowing rates, each of the following figures includes results for density ratios 1 and 2. While for $\rho_j/\rho_e = 1$, the velocity ratio U_j/U_e is identical with the blowing rate, the velocity and momentum ratio is only half for $\rho_j/\rho_e = 2$.

Figure 7 compares calculated and measured streamwise distributions of the laterally averaged film cooling effectiveness for $M = 0.5$. In the vicinity of the injection down to $x/D = 40$, the measured $\bar{\eta}$ values are higher for the larger density ratio, which is due to the faster reattachment of the cooling air jets at the smaller momentum ratio. In the far field, the film cooling effectiveness does not depend on the density ratio because the mixing is more or less complete so that the density difference has disappeared. The increase in cooling effectiveness by in-

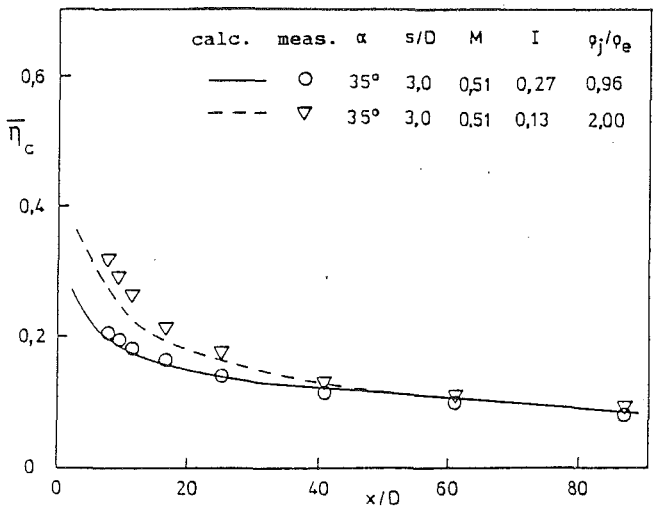

Fig. 7 Cooling effectiveness on flat plate at $M \approx 0.5$ and different density ratios; measurements of Pedersen et al. [9]

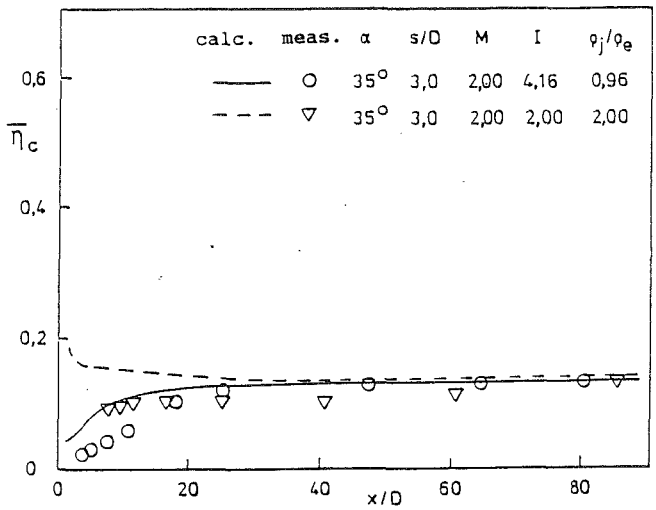

Fig. 9 Cooling effectiveness on flat plate at $M \approx 2$ and different density ratios; measurements of Pedersen et al. [9]

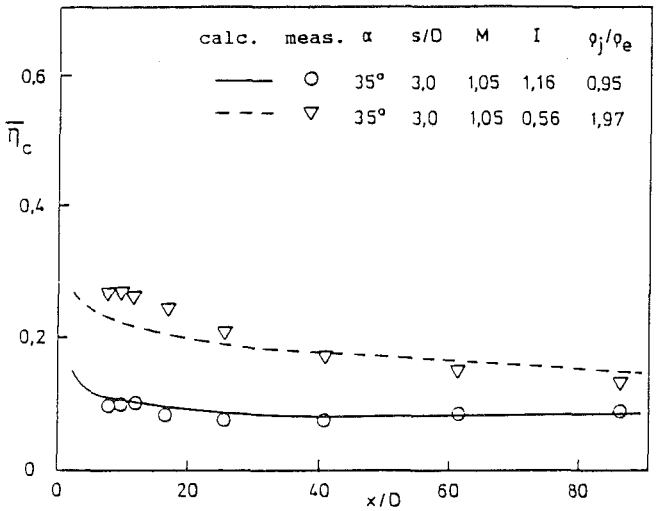

Fig. 8 Cooling effectiveness on flat plate at $M \approx 1$ and different density ratios; measurements of Pedersen et al. [9]

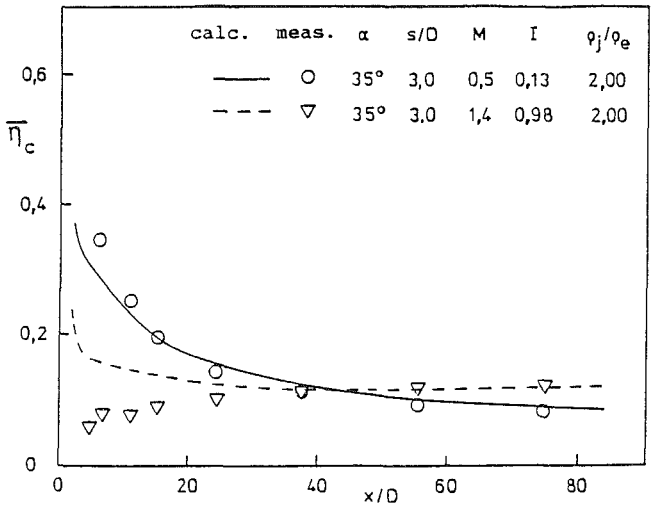

Fig. 10 Cooling effectiveness on flat plate at $\alpha = 35$ deg, $\rho_j/\rho_e = 2.0$, and different blowing rates; measurements of Foster and Lampard [10]

creasing the density ratio is much stronger in the case of $M \approx 1$ (Fig. 8). While the $\bar{\eta}$ distribution for $\rho_j/\rho_e \approx 1$ indicates a penetration of the cooling jets into the free stream, the variation and the higher values of $\bar{\eta}$ for $\rho_j/\rho_e \approx 2$ point to a wall-jet character of the flow. These differences in the flow character can also explain the large differences in $\bar{\eta}$ far downstream. This result is consistent with the general experimental observation that for similar spacings the best cooling effectiveness is always achieved at $U_j/U_e \approx 0.5$. At a blowing rate of $M = 2$ (Fig. 9) the measurements clearly indicate a detachment of the cooling jet from the wall. Since there is no difference in $\bar{\eta}$ in the far field, it may be concluded that the jet character is not influenced significantly by the density difference.

Except for fairly small deviations near the injection, the calculation procedure realistically describes the influence of the density ratio on the cooling effectiveness. In view of the complexity of the flow in the near field and of the simplicity of the model, the discrepancies in this region are not surprising. The good performance in the far field justifies the assumptions made in the model.

As further test cases, the experiments of Foster and Lampard [10] were simulated. The relative spacing was $s/D = 3$ and the injection hole diameter $D = 2.27$ mm. These experimenters investigated the cooling effectiveness for injection angles of $\alpha = 35$, 55, and 90 deg at blowing rates of $M = 0.5$ and $M = 1.4$. The free-stream velocity was 25 m/s. Foster and Lampard [10] do not report the free-stream turbulence level. Judging from their experimental setup, a value of $Tu_e = 1$ percent was assumed for the calculations. The oncoming boundary layer was also turbulent and had a relative displacement thickness of $\delta^*/D = 0.16$. For these experiments, different figures show results for different injection angles for both $M = 0.5$ and $M = 1.4$. Figure 10 displays the distribution of the film cooling effectiveness for $\alpha = 35$ deg. Both measurements and calculations show similar behavior as for the test cases of Pedersen et al. [9]. Figure 11 reports the results for $\alpha = 55$ deg. Due to the larger injection angle, the cooling effectiveness for $M = 0.5$ is reduced near the injection holes, while for $M = 1.4$ it increases. In the far field, the measurements approach the same level as in the case with $\alpha = 35$ deg. For $M = 0.5$, the calculation reproduces this behavior correctly, but for $M = 1.4$ it underpredicts the cooling effectiveness. The trend observed for $\alpha = 55$ deg continues when the injection angle is increased to $\alpha = 90$ deg and is reproduced correctly by the calculations (see Fig. 12). The increase in cooling effectiveness with increasing injection angle for $M = 1.4$ deserves special attention. It appears

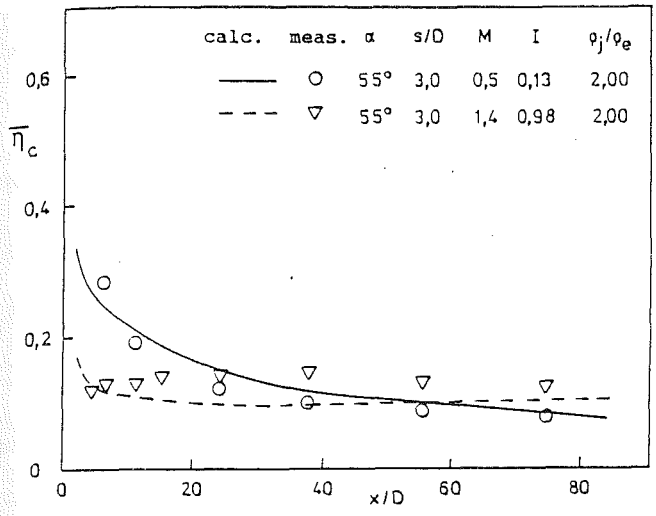

Fig. 11 Cooling effectiveness on flat plate at $\alpha = 55$ deg, $\rho_j/\rho_e = 2.0$, and different blowing rates; measurements of Foster and Lampard [10]

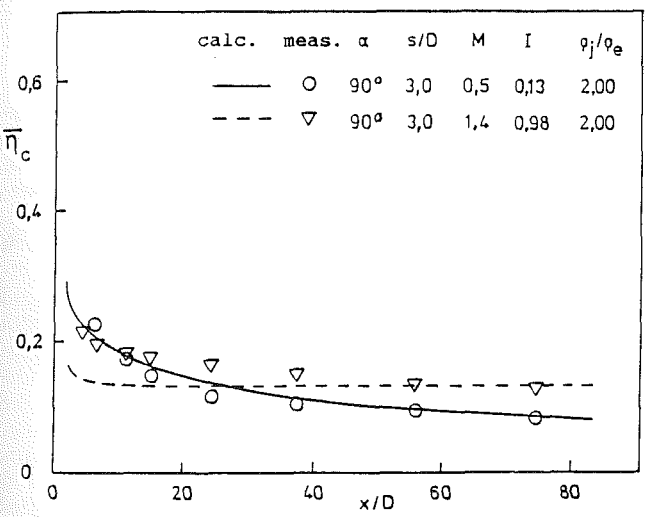

Fig. 12 Cooling effectiveness on flat plate at $\alpha = 90$ deg, $\rho_j/\rho_e = 2.0$, and different blowing rates; measurements of Foster and Lampard [10]

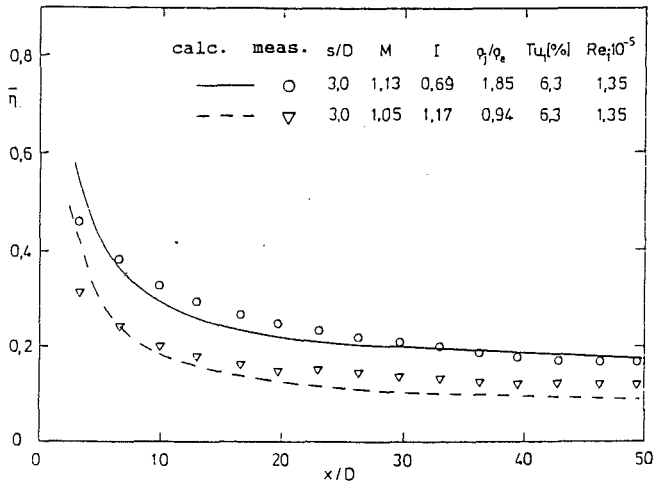

Fig. 13 Cooling effectiveness on model turbine blade at $s/D = 3.0$, $M \approx 1$, and different density ratios; our own measurements

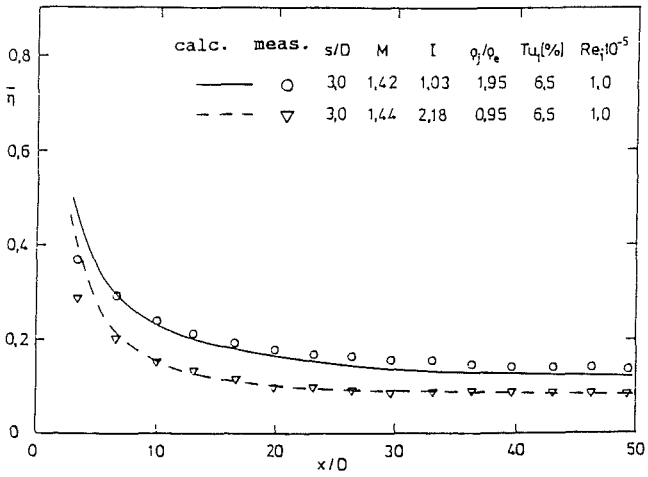

Fig. 14 Cooling effectiveness on model turbine blade at $s/D = 3.0$, $M \approx 1.4$, and different density ratios; our own measurements

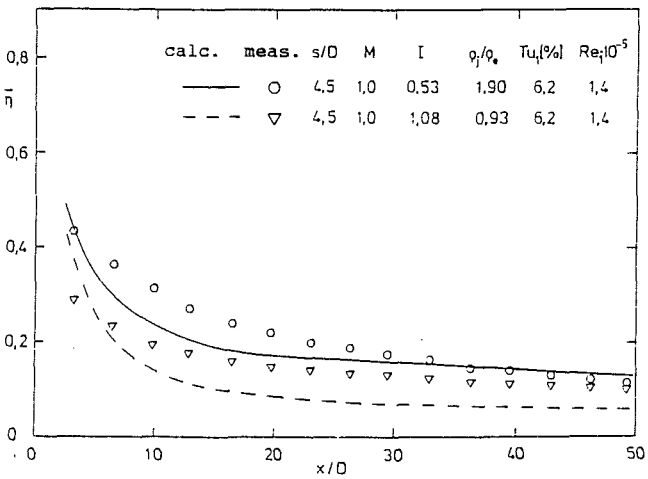

Fig. 15 Cooling effectiveness on model turbine blade at $s/D = 4.5$, $M \approx 1.0$, and different density ratios; our own measurements

that this behavior is caused by the faster lateral mixing of the injected jets, an effect that is simulated correctly by the calculation procedure. This points to good reliability of the dispersion model also for larger density differences.

4.2 Film Cooling Effectiveness on a Model Turbine Blade. In this section, film cooling on a model turbine blade (Fig. 6) investigated in the experiments of Section 3 was simulated. As was mentioned already, the development of a temperature boundary layer upstream of the injection had to be taken into account. To this end, the heat fluxes in the leading edge region of the blade were determined first by a separate boundary layer calculation, and these fluxes were then prescribed as boundary condition upstream of the injection in the calculation of the film cooling effectiveness. In contrast to the flat plate test cases, the oncoming boundary layer was laminar on the model turbine blade ($\delta^*/D = 0.06$). It was assumed that the injection would cause transition and hence turbulent injection profiles were set up as in the other cases.

The test cases for which results are presented in Figs. 13–16 show that, at the same blowing rate, the cooling effectiveness $\overline{\eta}$ is considerably higher for the larger density ratio $\rho_j/\rho_e \approx 2$ than for $\rho_j/\rho_e \approx 1$. This was to be expected and corresponds to the results for the flat-plate situations discussed in the previous section. This influence can be explained by the smaller momentum of the coolant jets at larger density ratio but at the same M. The smaller injection momentum causes a faster bending-over of the jets, which in turn leads to a higher cooling effectiveness. For $s/D = 3$ and $M \approx 1$ (Fig. 13), the calculated

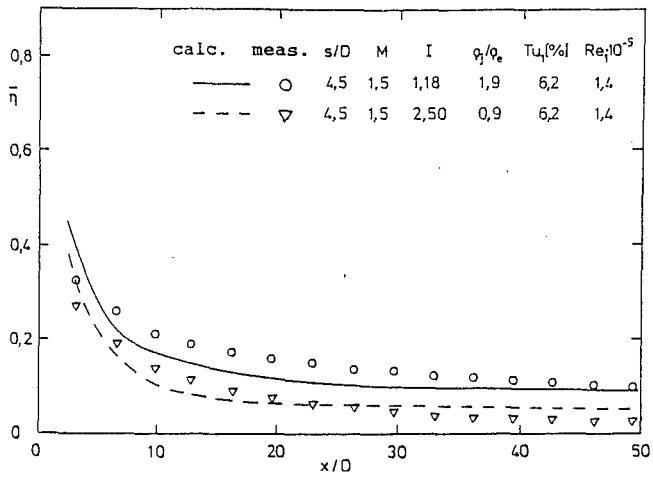

Fig. 16 Cooling effectiveness on model turbine blade at $s/D = 4.5$, $M \approx 1.5$, and different density ratios; our own measurements

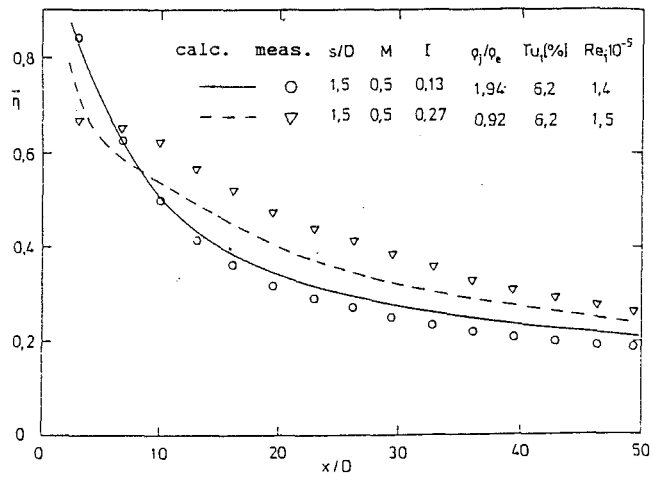

Fig. 17 Cooling effectiveness on model turbine blade at $s/D = 1.5$, $M \approx 0.5$, and different density ratios; our own measurements

$\bar{\eta}$ for $\rho_j/\rho_e \approx 1$ is somewhat lower than the measurements. This is presumably due to surface curvature effects, which are not accounted for in the calculation procedure. As shown in the work of Ito et al. [11], convex wall curvature causes a faster attachment of the jet (higher cooling effectiveness) at small blowing rates while it causes a deeper penetration of the jet into the free stream (lower effectiveness) at large blowing rates. For $\rho_j/\rho_e \approx 2$ the cooling effectiveness is underpredicted somewhat in the initial region, but the overall distribution is well simulated. In the case $s/D = 3$ and $M \approx 1.4$ (Fig. 14), the calculations are in good accord with the measurements.

Figures 15 and 16 show the corresponding $\bar{\eta}$ distributions for $s/D = 4.5$. The influence of the density ratio is similar to that for the spacing $s/D = 3$. The discrepancies between predictions and measurements are again stronger for $M = 1$ than for $M = 1.5$. This is consistent with the findings of Ito et al. [11] who correlate the influence of the wall curvature on film cooling with the parameter $I \cos^2 \alpha$. For higher momentum ratios I the curvature effect causes a deeper penetration of the jets into the free stream while for lower momentum ratios a faster attachment of the jets on the wall results. Hence the calculation, which does not account for any curvature effects, generally underpredicts the $\bar{\eta}$ values for large momentum ratios.

Figure 17 compares calculated and measured $\bar{\eta}$ distributions for the small spacing $s/D = 1.5$ and for the small blowing rate $M = 0.5$ (further measurements could not be carried out for this spacing). In this case, the cooling effectiveness is larger for $\rho_j/\rho_e = 1.9$ than for $\rho_j/\rho_e = 0.9$ only directly behind the injection, while downstream of $x/D = 7$ the situation is reversed and hence different from that discussed in Figs. 13–16. In the initial region, the faster bending-over of the jets again causes an increase in $\bar{\eta}$. Subsequently, a laterally coherent wall jet with a velocity deficit is formed at the small M and s/D values. The velocity deficit is larger for the larger injection density causing larger velocity gradients, which in turn cause an increased turbulence production and hence also an increased mixing with the outer stream. This explains the observed reduction in wall temperature and hence in $\bar{\eta}$. This behavior is different from that for the spacing $s/D = 3$ and 4.5 for which the individual jets penetrate into the boundary layer or even into the free stream. For $s/D = 1.5$, the flow has wall-jet character anyway, so that good cooling effectiveness is achieved already and a faster bending-over of the jets does not necessarily increase the cooling effectiveness. This behavior, which differs from that observed for the other situations, is reproduced correctly by the calculation procedure. Hence, it can be concluded that overall the calculation procedure reproduces fairly well the observed film cooling behavior and the influence of the density differences.

5 Conclusions

The film cooling model in the two-dimensional boundary-layer procedure of Schönung and Rodi [1] was extended to account for the influence of density differences between hot gas and injected coolant gas. The model consists of two components, namely an injection model for setting up new boundary-layer profiles downstream of the immediate injection region and a dispersion model for simulating three-dimensional effects. In the course of introducing density effects with the aid of similarity considerations and experimental information, both models were reoptimized. The number of parameters for generating the new boundary-layer and the dispersion-term profiles could thereby be reduced. The extended model covers the full range of the parameters injection angle, relative spacing, blowing rate, and density ratio of practical interest (see ranges given in Section 2.2). Also, the test calculations reported in [1] and here covered the following ranges of additional influence parameters: $0.05 \le \delta^*/D \le 0.25$, $1 \times 10^5 \le \mathrm{Re}_1 \le 3 \times 10^5$, $10^3 \le \mathrm{Re}_j = U_j D/\nu \le 4 \times 10^4$. The model was tested against flat-plate experiments and our own experiments on a model turbine blade. The measurements have shown that the laterally averaged film cooling effectiveness increases with increasing density ratio ρ_j/ρ_e at constant blowing rate. For the flat-plate cases, the predictions of the cooling effectiveness are in good agreement with the measurements except for small deviations near the injection. The film cooling effectiveness on the model blade is also generally predicted correctly. Only for configurations for which surface-curvature effects not accounted for in the model play an important role is the agreement not so good. However, in all cases the change in jet character due to the influence of density differences is simulated correctly. For constant-density cases, the model was shown in [1, 4, 5] also to predict satisfactorily the heat transfer coefficient. As there are hardly any experimental studies on the influence of the density ratio on the heat transfer, the model was not tested for such situations. There is no reason to presume that it would not predict this influence satisfactorily too, but test calculations have yet to be carried out. Future research should also concentrate on the modeling of curvature effects and on the extension to film-cooling situations with injection from more than one row of holes.

Acknowledgments

The research reported here was sponsored partly by the

Forschungsvereinigung Verbrennungskraftmaschinen e.V. The calculations were carried out on the Siemens 7881 computer of the University of Karlsruhe. The authors should like to thank Mrs. R. Zschernitz for preparing the typescript.

References

1 Schönung, B., and Rodi, W., "Prediction of Film Cooling by a Row of Holes With a Two-Dimensional Boundary-Layer Procedure," ASME JOURNAL OF TURBOMACHINERY, Vol. 9, 1987, pp. 579–587.

2 Haas, W., Rodi, W., and Schönung, B., "Filmkühlung von Turbinenschaufeln durch Ausblasung aus einer Lochreihe," *Zeitschrift für Flugwissenschaften und Weltraumforschung*, Vol. 12, 1988, pp. 159–172.

3 Demuren, A. O., Rodi, W., and Schönung, B., "Systematic Study of Film Cooling With a Three-Dimensional Calculation Procedure," ASME JOURNAL OF TURBOMACHINERY, Vol. 108, 1986, pp. 124–130.

4 Haas, W., and Schönung, B., "Erweiterte Version des Filmkühlmodells im Grenzschichtverfahren GRAFTUS/R zur Erfassung von Dichteunterschieden bei Filmkühlströmungen," Institut für Hydromechanik, Universität Karlsruhe, Bericht No. 662, June 1988.

5 Haas, W., "Experimentelle und theoretische Untersuchungen zur Filmkühlung von Gasturbinenschaufeln," Dissertation, Universität Karlsruhe, Germany, 1989.

6 Kruse, H., "Messungen zur Filmkühlung," Deutsche Forschungs- und Versuchsanstalt für Luft- und Raumfahrt, Köln, Bericht No. 352-74/9, 1974.

7 Kruse, H., and Metzinger, H., "Der Einfluß der Belochungsgeometrie auf die Filmkühlwirkung einer Lochreihe," *Deutsche Forschungs- und Versuchsanstalt für Luft- und Raumfahrt*, Köln, Interner Bericht IB 325-9-84, 1984.

8 Forth, C. J. P., Loftus, P. J., and Jones, T. V., "The Effect of Density Ratio on the Film Cooling of a Flat Plate," AGARD Conference Reprint No. 390, Heat Transfer and Cooling in Gas Turbines, Bergen, Norway, May 6–10, 1985.

9 Pedersen, D. R., Eckert, E. R. G., and Goldstein, R. J., "Film Cooling With Large Density Differences Between the Main Stream and Secondary Fluid Measured by the Heat Mass Transfer Analogy," ASME *Journal of Heat Transfer*, Vol. 99, 1977, pp. 620–627.

10 Foster, N. W., and Lampard, D., "The Flow and Film Cooling Effectiveness Following Injection Through a Row of Holes," ASME *Journal of Engineering for Power*, Vol. 102, 1980, pp. 584–588.

11 Ito, S., Goldstein, R. J., and Eckert, E. R. G., "Film Cooling of a Gas Turbine Blade," ASME *Journal of Engineering for Power*, Vol. 100, 1978, p. 476.

Computation of a Wall Boundary Layer With Discrete Jet Injections

P. Kulisa
Chargé de Recherches, C. N. R. S.

F. Leboeuf
Professor.

G. Perrin
Ph.D. Student.

Ecole Centrale de Lyon,
Laboratoire de Mecanique
des Fluides et d'Acoustique,
69131 Ecully Cedex—France

Cooling of turbine blades is often achieved with cold discrete jets introduced at the wall. In this paper, a new method for computation of a wall boundary layer with discrete jet interactions is presented. The jets are assumed to be arranged in rows and the flow is assumed locally periodic in the row direction. The conservation equations are spatially averaged between two jet orifices. The resulting equations look like two-dimensional boundary layer equations, but with three-dimensional jet source terms. The numerical method solves the boundary layer equations with a Keller box method. A strong interaction with inviscid flow is also introduced in order to avoid numerical difficulty in the jet region. Three-dimensional jet conservation equations are solved with an integral method, under the boundary layer influence. A coupling of the two methods is performed. Comparisons with low-speed experimental data are presented, particularly near the jet orifices. It is shown that the agreement between the results of computation and the experiments depends on the jet behavior very near the jet exit.

Introduction

The high temperatures reached in modern high-pressure turbines require the use of cooling techniques in order to protect the walls. As an example, cold flow may be introduced through holes drilled at the wall, thereby creating a film of discrete jets, which coalesce after some streamwise distance (Fig. 1). The difficulty of predicting this type of flow is connected to the great number of interacting phenomena. The flow in a turbine is strongly accelerated. As a consequence, the transition is spread out as the turbulence is partly inhibited; similarly, heat transfer at the wall is reduced, owing to the low level of turbulence. However, complications occur in real engines; for example, the flow may be locally decelerated, and thus separated, near the leading edge at off-design conditions, under the influence of shock-wave impingements or jet injections.

The behavior of discrete jets, introduced in a crossflow, has been the subject of many experiments. Although the various publications are not always fully detailed, they produce a rational picture of the jet and crossflow interactions, provided the jet-to-crossflow velocity ratio is sufficiently high. At first, for small length-to-diameter ratios of the injection holes, flow separation may be induced near the entrance of the tube. As a consequence, in the jet near the orifice, the turbulence is high and the jet velocity profile is also very uniform, as shown by Pietrzyk et al. (1989). This may be found even for low values of the blowing parameter, as low as 0.25. Just after the exit, the jet behaves like a flexible body whose structure becomes strongly three dimensional. On the upstream jet side, the outer flow decelerates as though in front of a solid body. On the downstream side, a low value of the static pressure may be measured (Moussa et al., 1977). As a consequence, a pressure force exists, directed toward the normal to the local jet trajectory at the orifice, which induces the jet to bend.

A set of vortices appears in the vicinity of the jet. Some of them have a low influence on the jet global behavior or shape, i.e., the Karman vortices in the wake (Moussa et al., 1977) or the horseshoe vortices that wrap around the upstream jet side (Andreopoulos and Rodi, 1984). However, the particular shape of the jet cross section is probably a direct consequence of the longitudinal counterrotating vortex pair induced by the interaction of the strong shear on the jet boundary. According to the computation performed by Sykes et al. (1986), this longitudinal vorticity exists immediately after the orifice, and is probably maximum in the immediate vicinity. As the jet bends downstream, dissipation of the vorticity is the prevailing phenomenon; positive production of the vorticity occurs according to the jet trajectory curvature, while a negative production appears when the jet velocity decreases. Carotte and

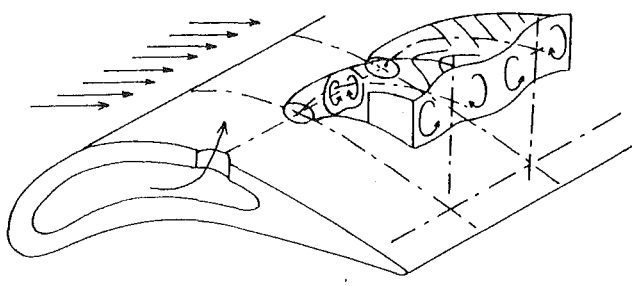

Fig. 1 Film cooling

Contributed by the International Gas Turbine Institute and presented at the 36th International Gas Turbine and Aeroengine Congress and Exposition, Orlando, Florida, June 3-6, 1991. Manuscript received at ASME Headquarters February 20, 1991. Paper No. 91-GT-143. Associate Technical Editor: L. A. Riekert.

Stevens (1988) also mention that the viscous crossflow, wrapping around the jet, induces a similar set of counterrotating vortices, which seems to dominate the bound vortex system some distance downstream in the case of multiple jet injection.

The neighboring jets, in the case of jet row injection, have a strong influence on the behavior of a particular jet in the row; Bario et al., (1990) have shown that the jet in a row is pushed closer toward the wall, in comparison with the single jet case. Similar behavior is also computed by Huang (1989), taking the velocity field induced by the counterrotating vortex system into account; however, only the case without mixing between jets was treated. In the multiple row configuration, the upstream row sees a thinner upstream viscous wall layer than the downstream rows; as a consequence, the downstream jets will deviate less toward the wall (Sinha et al., 1991). Similar behavior is observed for jets emerging from tubes introduced in a uniform flow. For that case, Huang (1989) has shown that this could be reproduced by taking the velocity field induced by the counterrotating vorticity into account.

Introduction of film cooling in a turbine also needs to take the high curvature of the walls into account. For low velocity ratios and owing to the pressure gradient normal to the wall, the lateral mixing of the jets increases on concave walls (Schwarz and Goldstein, 1989). For the same reason, the low-velocity jet is pushed toward the convex walls (Schwarz et al., 1990).

Detailed velocity and shear stress measurements, performed by Pietrzyk et al. (1988), indicate coincident peaks in the mean velocity gradient and the turbulent quantities. This points to the possible use of a turbulent viscosity model. However, computations realized with this model do not prove to be very efficient (Dibelius et al., 1990). The preceding description of the film cooling behavior emphasizes the need for a sophisticated computational method in order to take all the flow details into account. Besides analytical approaches, which are often used for heat transfer study, many numerical methods have been developed. Dibelius et al. (1990) use three-dimensional equations in an elliptic method of solution, which allows access to the flow inside the jet orifice. All the thermal effects inside the blade have to be taken into account to define properly the heat transfer at the blade wall (Camci, 1989). In order to avoid excessive computational time in the case of multiple jet injection, a two-dimensional boundary layer approach is also used (Herring, 1975; Miller and Crawford, 1984; Tafti and Yavuzkurt, 1990; Schönung and Rodi, 1987).

In this paper, we present a new method of computation for a wall boundary layer, with discrete jet injection. Starting with the Navier–Stokes equations, we first apply a spatial average in the direction of the row of jets, thereby forcing periodicity of the flow between two neighboring jets in the same row. A similar technique has already been used by Herring (1975). We thus obtain a set of two-dimensional equations with three-dimensional source terms. Boundary layer approximation is then applied in order to reduce the computational effort and to allow a better description of the flow near the wall. In order to allow the treatment of local flow separation, a strong interaction model has been added between the outer inviscid flow and the wall viscous layer (Kulisa et al., 1990). Compared to previous two-dimensional methods, we avoid the use of analytical laws for the description of the jet source terms. By contrast, we solve three-dimensional jet equations written in a curvilinear frame of reference, based on the local jet trajectory. An integral method is used for the solution of these equations. Closures are necessary for the description of the interactions between the jet and the outer flow. In the following, we shall describe the flow model and the interactions between the jet and the viscous wall layer. Then, the jet computation will be described. The complete computational method will there be described. Comparison with experimental results will be presented for a row of jets, introduced inside a low-speed boundary layer.

The Jet and Crossflow Computation

Basic Idea of the Modeling. As mentioned in the introduction, turbine film cooling is a complex phenomenon. Our objective is to build a method that allows most of these phenomena to be taken into account, if possible at a fine closure turbulent level, but with a reasonable computation effort; this last requirement implies that the use of Navier–Stokes equations for computation of the whole flow should be avoided.

Our flow model is based on an iterative exchange between a viscous wall layer and a three-dimensional jet computation. In the basic flow configuration, the discrete jets are assumed to be introduced through rows of orifices, located perpendicularly to the outer crossflow, along the z direction. Periodicity in the row direction is then assumed, over the distance G between two neighboring jets. As a consequence of this hypothesis, every flow quantity is separated in two terms:

$$q = \bar{q} + q'' \tag{1}$$

where $\bar{q}$ is the spatial average of q, defined as:

$$\bar{q}(x, y) = \frac{1}{G} \int_0^G q(x, y, z)\, dz \tag{2}$$

Therefore, $\bar{q}$ is a two-dimensional quantity that contains implicitly the jet effects. q'' is the spatial fluctuation of q; it is a three-dimensional quantity that expresses the lateral flow nonhomogeneity.

When this spatial averaging is applied to the flow conservation equations, a two-dimensional averaged problem results, whose unknowns are the space-averaged quantities. Nevertheless, additional terms also appear in the resulting equations, associated with their nonlinearity with respect to the basic flow

Nomenclature

H_t = stagnation enthalpy
K = curvature
P = static pressure
ST = jet source term
(s, n, b) = curvilinear coordinates linked to the jet trajectory
(u, v, w) = velocity components along (x, y, z), respectively
V = velocity modulus
x = crossflow streamwise coordinate
y = normal to the wall coordinate
z = in the wall, lateral coordinate
δq = mass flow defect
μ_t = turbulent eddy viscosity
ρ = static density
ϕ = jet diameter at the orifice

Superscripts

$-$ = space average along z
$''$ = space fluctuation along z
$'$ = turbulent fluctuation
$\wedge$ = crossflow
Δ = jet part
$\sim$ = turbulent average

Subscripts

e = inviscid flow
max = maximum value in the jet
o = condition at the orifice

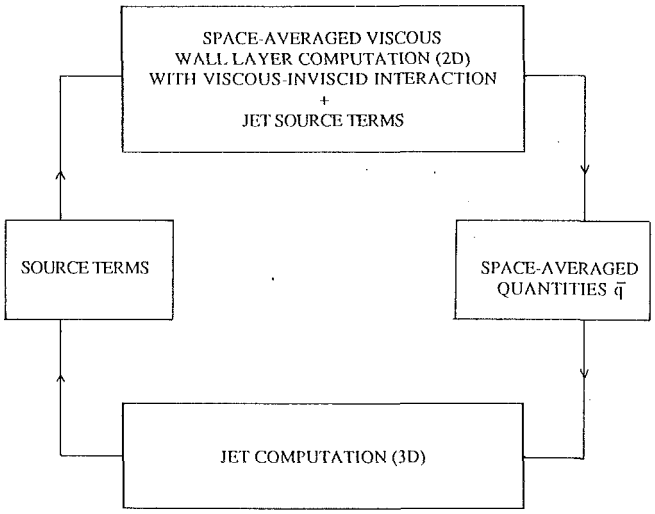

Fig. 2 Iterative procedure for the film cooling flow computation

variables (V, H_t). This is similar, but not equivalent, to the appearance of Reynolds stresses in the momentum equations when turbulent averaging is applied. In our case, these supplementary terms will be considered as source terms for the two-dimensional averaged problem, and will come from the three-dimensional jet computation. The jet model will be presented in the next paragraph.

In brief, the whole film cooling flow calculation leads to an information exchange between a thin wall layer computation, which includes a viscous–inviscid interaction as well as additional three-dimensional jet source terms, and a jet computation, which produces these source terms. From the numerical point of view, the thin wall layer computation uses a space marching procedure suited to the parabolic character of this approximated flow. The viscous–inviscid interaction reintroduces an elliptic effect, which is allowed for by repeating the space marching iteratively. After each upstream to downstream sweep, a jet computation is performed in order to update the three-dimensional source terms; these terms are computed on a three-dimensional mesh, and then averaged in the transverse Z direction. The iterative procedure is described on Fig. 2.

The Jet Computation. The behavior of the jet is defined in a curvilinear orthogonal coordinate system (s, n, b), the direction s being associated with the jet trajectory (Fig. 3), the third direction b being identical to z, and n is orthogonal to s and b; α_n is the angle between the direction s and the axial direction x.

Jet Computation Hypothesis. Various hypotheses allow the simplification of the problem. The s direction is located in the (x, y) plane. The transverse jet surface (n, b) is assumed to be flat. Along the directions n and b, the s-line radius of curvature is assumed great, compared to a characteristic jet width. The characteristic lengths of the jet in the transverse directions are small compared to crossflow length scales. The consequence of this is that the crossflow conditions are assumed constant over the jet transverse surface σ. The diffusion phenomenon along the direction s is neglected. Moreover, the static pressure gradient along s is governed by the crossflow. The last two hypotheses are typical of parabolized flow problems. In addition, the static jet density is also constant over σ and is computed from the crossflow static pressure and the average temperature in the section of the jet.

For convenience, we define the following notation: $\hat{o}$ will define a crossflow variable; $\Delta o = o - \hat{o}$ corresponds to the excess of o variable in the jet, by reference to the crossflow. Note that Δo is not necessary small, compared to o. The evolutions of ΔV_s and ΔT_t along the n and b directions are described by analytical laws; the ΔV_s and ΔT_t maxima are localized on the s line; on the jet boundary, the jet excess quantities ΔV_s and ΔT_t tend toward zero. ΔV_n and ΔV_b are neglected for the results presented in this paper; however, a complete formulation may be found from Leboeuf and Huang (1990). Similarly, heat fluxes and shear stress work are neglected on that boundary, in the jet computation.

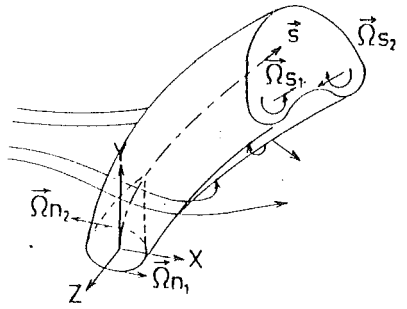

Fig. 3 Jet coordinate system

A potential core is assumed to exist at the jet orifice, according to the observations made by Pietrzyk et al. (1989) and Snel (1971). In this area, $\Delta V_{s,\max}$ and $\Delta T_{t,\max}$ are constant along s, although ΔV_s and ΔT_t are allowed to vary as the potential core disappears progressively. At the potential zone extremity, the jet cross section tends toward an ellipse.

Integral Formulation. For a steady, single-phase flow, we consider the conservation equations for mass, momentum, and energy. They are written in a conservative form, in a fixed frame of reference. These equations are expressed with respect to the curvilinear orthogonal coordinate system (s, n, b). Using the Leibnitz limit rule, the equations are integrated over the jet cross section (Huang, 1989). The integral equations are given below:

Defining the entrainment coefficient as:

$$E = \rho \hat{V}_s \frac{d\sigma}{ds} - \int\int_\sigma \rho \Delta V_n K_{sn} d\sigma - \oint_C \rho (\Delta V_n \mathbf{n} + \Delta V_b \mathbf{b}) \mathbf{dC} \quad (3)$$

the mass conservation equation gives:

$$\frac{d}{ds} \int\int_\sigma \rho V_s d\sigma = E + \rho\sigma \frac{d\hat{V}_s}{ds} \quad (4)$$

where C is the contour of the transverse surface σ. K_{sn} and K_{sb} are the curvatures of the jet s line. Equation (3) shows that the entrainment is a consequence of three effects: the growth of surface σ, a curvature effect, and the transverse jet induced velocity component.

For the momentum conservation equation, a deficit formulation with respect to the crossflow is used. According to the previous hypothesis, it is allowed to eliminate the static pressure term in the s component of the momentum equation. The s and n, components are given below:

$$\frac{d}{ds} \int\int_\sigma \Delta(\rho V_s^2) d\sigma - \frac{1}{C} \oint^C \Delta(\rho V_s^2) dC \frac{d\sigma}{ds} + 2 \int\int_\sigma \Delta\{(\rho V_s V_n) K_{sn}\} d\sigma + \oint_C \Delta\{(\rho V_s V_n)\mathbf{n}\} \mathbf{dC} - \oint_C \Delta t_s dC = 0 \quad (5)$$

$$\frac{d}{ds} \int\int_\sigma \Delta(\rho V_s V_n) d\sigma - \frac{1}{C} \oint_C \Delta(\rho V_s V_n) dC \frac{d\sigma}{ds} + \int\int_\sigma \Delta\{(\rho V_n^2) K_{sn}\} d\sigma$$

$$+\oint_C \Delta\{(\rho V_n^2)\mathbf{n}\}\mathbf{dC} - \int\int_\sigma \Delta(\rho V_s^2)K_{sn}d\sigma + \oint_C \Delta P\mathbf{n}\cdot\mathbf{dC} - \oint_C \Delta t_s dC = 0 \quad (6)$$

The viscous and turbulent forces appear in the Δt_s and Δt_n terms; the contributions of the shear stresses have been neglected in the curvature and in the $d\sigma/ds$ term.

The variation of the momentum excess is associated with various effects: The growth of the surface $d\sigma/ds$, a curvature effect, the momentum flux induced by the jet itself, pressure forces, viscous, and turbulent stresses.

For the conservative equation of energy, neglecting the heat flux in the s direction and the curvature terms, gives the following integral form as:

$$\frac{d}{ds}\int\int_\sigma \rho V_s H_t d\sigma = \frac{1}{C}\oint_C \rho V_s H_t dC\frac{d\sigma}{ds} - \int\int_\sigma \rho V_n H_t K_{sn} d\sigma - \oint_C \rho_t H_t V_n \mathbf{n}\mathbf{dC} - \oint_C (q_n\mathbf{n} + q_b\mathbf{b})\cdot\mathbf{dC} + \oint_C t_s V_s dC \quad (7)$$

On the jet boundary, the shear work is dominated by the contribution of the longitudinal velocity component V_s. The enthalpy transport in the s direction is created by the variation of σ, a curvature effect, the heat flux through the jet boundary $\hat{q}_n$, $\hat{q}_b$ and the friction power $t_s V_s$, associated with the viscous forces. The last two terms are usually neglected in the present computations, except for the condition on the wall.

The integral formulation has two consequences. It changes the parabolic nature of the previous equations to a hyperbolic type; this allows a marching process to be used from the jet exit to the downstream location. However, the averaging process must be associated with particular closure relationships, especially at the jet boundary.

Closure Relationships. According to the experimental results, the transverse jet section has a very particular shape, which may be observed far downstream of the exit; most of the preceding studies approximate this shape by a simple geometry. It seems that an ellipse is a good compromise. In the present model, the ratio of the major and minor axes (a_v/b_v) varies according to a linear relation:

$$\frac{a_v}{b_v} = -3K + C \quad (8)$$

where K allows us to introduce a potential core: $K = 1$ for a circle at the exit and $K = 0$ when the end of the potential region is reached; C varies usually between 2 and 4. Depending on particular injection conditions, a potential region may exist near the orifice. By hypothesis, we shall assume that, for a three-dimensional jet, the longitudinal velocity component is constant in the potential core and is equal to the injection velocity $V_{smax,o}$. In the potential region, the maximum jet velocity is then known, but the extent of the potential core is unknown. The previous equation system may then be used in order to calculate the length of the potential region.

According to the model, entrainment has two origins ($E_1 + E_2$): the diffusion effect E_1 and the lee side effect E_2. The turbulent diffusion effect is modeled as in a one-dimensional jet according to Herring (1975), but including the potential core:

$$E_1 = K_1\sqrt{\rho\hat{\rho}}V_{smax}\sqrt{\sigma}\sqrt{1-K^2} \quad (9)$$

with $K_1 = 0.14$.

For the E_2 part, we ignore the vorticity that appears in the jet wake, and take only the two counterrotating vortices on the lee side of the jet into account. Because these vortices do not induce any mass flow, we add a sink singularity on this lee side, according to Le Grivé's method (1977). Computing the velocity field induced by this sink singularity downstream of an assumed circular jet cross section, we get, in the frame of potential flow, the drag on the jet boundary ΔF_p with:

$$\Delta F_p = \oint_C \Delta P\, dC = E_2\hat{V}_n \quad (10)$$

where $\hat{V}_n$ is the crossflow velocity component in the cross sectional surface. Introducing a drag coefficient C_D:

$$\Delta F_p = \frac{a}{2} C_D\hat{\rho}\hat{V}_n^2 \quad (11)$$

a relationship is postulated between the lee side entrainment E_2 and the drag force:

$$E_2 = \frac{a}{2} C_D\hat{\rho}\hat{V}_n \quad (12)$$

In practice, the jet cross section is not circular but has a "bean" shape; however, this relation is assumed to be valid even when the cross section of the jet does not remain circular. As a consequence, the preceding formulas will be used with $C_D = 2.0$.

The momentum equations include a viscous force that we choose to compute in terms of the jet velocity excess as postulated:

$$\mathbf{\Delta t} = -C_T\rho(\mathbf{V} - \hat{\mathbf{V}})|\mathbf{V} - \hat{\mathbf{V}}|\sqrt{\sigma} \quad (13)$$

The negative sign in the above expression allows the momentum to be dissipated. A value $C_T = 0.3 \sim 0.6$ has been used for the present results.

Analytical laws have been used to describe the longitudinal velocity component and temperature distributions along the transverse directions. For the velocity distribution, we get:

$$\Delta V_s = \Delta V_{smax}\left(1 - \frac{b^2}{a_v^2} - \frac{n^2}{b_v^2}\right)^{5/2} \quad (14)$$

In the potential region, a constant value $\Delta V_{smax,o}$ is assumed in a core of similar shape as the jet cross section, but whose dimensions are reduced by the factor K (Eq. (8)); a expression (14) is retained for ΔV_s between the core and the jet boundary.

For the temperature distribution, we assume a Gaussian law:

$$\Delta T_t = \Delta T_{tmax}\exp^{-\beta\left(\frac{b^2}{a_v^2} + \frac{n^2}{b_v^2}\right)} \quad (15)$$

The diffusion coefficient β is defined so that $\Delta T/\Delta T_{max} = 1/10{,}000$ at the ellipse boundary.

The jet equation solution is obtained by using a Gauss–Newton method. The previous equations (4) to (7) are used to compute four main unknowns, which may be defined arbitrarily. We choose to compute a characteristic jet maximum velocity ΔV_{smax}, the transverse surface area σ, the angle α_n, and a jet maximum temperature ΔT_{tmax}. In the potential core region, as the maximum jet velocity is constant, we use the ratio of the potential core to the jet transverse area K, as one of the main variables; as a consequence, the potential core length drops out of the computation.

Jet Computations. The full jet model has been extensively tested for various jet injection conditions, including uniform as well as boundary layer crossflows (Huang, 1989; Leboeuf and Huang, 1990). We present here two examples of results obtained with the approximate model. Figures 4 and 5 give the evolution along the trajectory S of the ratio $\Delta T_{tmax}/\Delta T_{tmax,o}$, for a jet introduced perpendicularly in an uniform crossflow; comparisons are shown with the experimental results of Kamotani and Greber (1972) for two values of the jet and crossflow velocity ratio. Agreement between the results of computation and experiments is good when a potential core is introduced in the model.

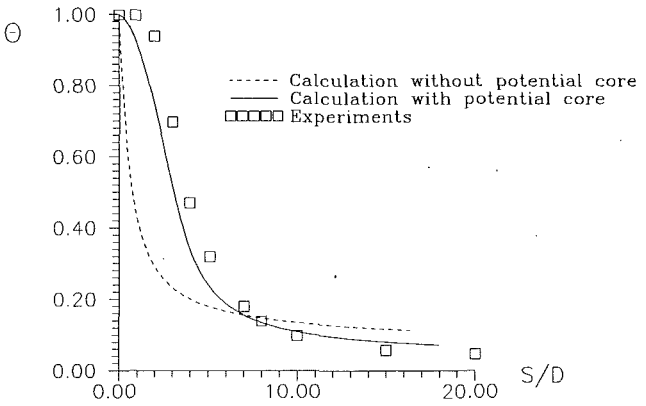

Fig. 4 Thermal evolution along the jet trajectory; velocity ratio 9.7; α_n = 90 deg

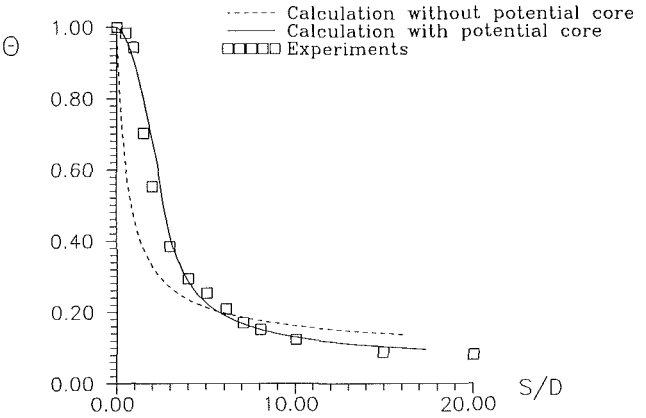

Fig. 5 Thermal evolution along the jet trajectory; velocity ratio 5.9; α_n = 90 deg

Figure 6 gives the evolution of the jet in a crossflow viscous wall layer (Bousgarbiès et al., 1991). The jet is introduced with an angle α_n = 45 deg, a jet-to-crossflow velocity ratio of 2/3. In that particular case, the crossflow velocity gradients near the orifice are very important, and our hypothesis of constant crossflow conditions over the jet cross section is no longer justified. For that purpose, a slightly modified form of the jet equations has been used, eliminating that particular hypothesis. The results show that the jet model is able to reproduce the growth of the jet cross section, and the trajectory of the jet, as defined from the maximum values of the jet velocity and temperature. Note a slight reduction of the jet crosswidth in the n direction, very near to the orifice; this is in fact connected to the bigger growth of the jet in the b direction, as a consequence of Eq. (8).

Space-Averaged Flow Computation

Basic Equations. We start from the Navier–Stokes equations. The conservation equation for the stagnation enthalpy is added to take the thermal effects into account.

In fact, as far as the average level of the film cooling problem is concerned, a dominant convection direction may often be found; however, the local flow has a strong three-dimensional behavior, which is influenced by the jet itself. As a consequence, the spatial averaging between neighboring jets must be applied before an introduction of a parabolization hypothesis, which will lead to the boundary layer model.

Applying first the spatial averaging, then we get for the x-momentum equation:

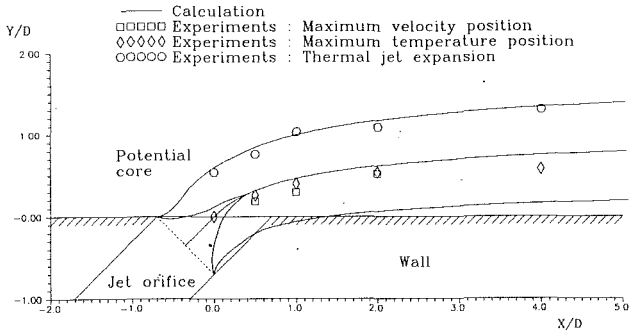

Fig. 6 Jet evolution experiments (Bousgarbiès et al., 1991); velocity ratio 2/3; α_n = 45 deg

$$\overline{\rho u}\frac{\partial \overline{u}}{\partial x}+\overline{\rho v}\frac{\partial \overline{u}}{\partial y}+\frac{\partial}{\partial x}\overline{(\rho u'' u'')}+\frac{\partial}{\partial y}\overline{(\rho v'' u'')}$$
$$+2K_X\overline{\rho u v}+2K_X\overline{\rho u'' v''}=-\frac{\partial P}{\partial x}+\frac{\partial \overline{\tau_{XX}}}{\partial x}+\frac{\partial \overline{\tau_{XY}}}{\partial y}+2K_X\overline{\tau_{XX}} \tag{16}$$

The stresses $\overline{\tau_{ij}}$ correspond both to laminar and turbulent contributions; K_x is the wall curvature, assumed constant in the z direction. Similar equations are obtained for the mass and energy conservation equations. These new equations present a similar form with and without jets; however, the $\overline{(\rho u'' u'')}$ and $\overline{(\rho u'' v'')}$ terms explicitly take the jet effects into account. It is interesting to remark that, following this averaging technique, first the Z derivatives have disappeared from these equations, second only the space-averaged stresses remain, and finally the momentum Z component is reduced to $D\overline{w}/Dt$ = 0; as a consequence, if the upstream flow is two dimensional and the jet trajectory is kept in the X–Y plane, then w is always zero.

The thin layer approximation may now be used in order to eliminate the diffusion terms in the X direction. We obtain:

$$\frac{\partial}{\partial x}\overline{\rho u}+\frac{\partial}{\partial y}\overline{\rho v}=0 \tag{17}$$

$$\overline{\rho u}\frac{\partial \overline{u}}{\partial x}+\overline{\rho v}\frac{\partial \overline{u}}{\partial y}+2K_X\overline{\rho u v}=-\frac{\partial \overline{P}}{\partial x}+\frac{\partial \overline{\tau_{XY}}}{\partial y}$$
$$-\frac{\partial}{\partial x}\overline{((\rho u)'' u'')}-\frac{\partial}{\partial y}\overline{((\rho v)'' u'')} \tag{18}$$

$$\overline{\rho u}\frac{\partial \overline{H_t}}{\partial x}+\overline{\rho v}\frac{\partial \overline{H_t}}{\partial y}=\frac{\partial}{\partial y}(\overline{\tau_{XY}}-\overline{q_Y}-\widetilde{(\rho v)' H_t'})$$
$$-\frac{\partial}{\partial x}\overline{((\rho u)'' H_t'')}-\frac{\partial}{\partial y}\overline{((\rho v'' H_t'')} \tag{19}$$

q_y is the heat flux component in the Y direction.

The unknowns are ($\overline{u}$, $\overline{v}$, $\overline{H_t}$); in the present computation, the density is computed according to the perfect gas law. The static pressure has been assumed constant in the Y direction. Although this a usual hypothesis in classical boundary layer approach, it is probably wrong when a high v velocity component exists under jet influence. As a consequence, the present computation must be seen as a first step only.

Although the static pressure P is identified with the inviscid value P_e, outside the film cooled layer, this inviscid static pressure is not prescribed as in the direct mode computation. On the contrary, it is a supplementary unknown of our problem. The P_e value is obtained from an equation that is a part of the strong coupling between the inviscid outer flow and the averaged film cooled layer. The main features of this coupling are briefly described in the following paragraphs.

Viscous–Inviscid Interaction and Numerical Method. The

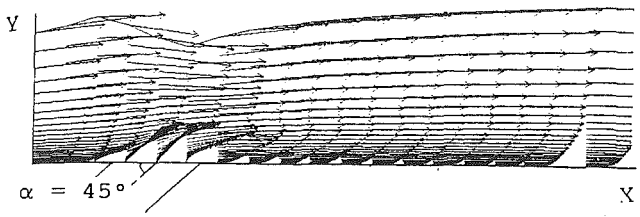

Fig. 7 Velocity vector evolution; $Z = 0$; CEAT experiments

coupling method between the inviscid and viscous wall flows has been described in detail by Kulisa et al. (1990). It is well known that the classical direct mode boundary layer approach fails near the separation area or when a strong perturbation occurs near the wall, because of jet injections for example. In order to stabilize the boundary layer computations, it is necessary to reintroduce an elliptic effect near the wall, which has been lost with the parabolic hypothesis. For that purpose, we solve a supplementary single equation, which simulates the inviscid response to the wall layer evolution. This technique has a few advantages. First, it allows us to solve the inviscid equation simultaneously with the viscous wall layer system, thereby allowing excellent stabilization of the computation without any relaxation requirement. Second, it avoids excessive computation as only that inviscid part, which is needed, is simulated.

We have developed an overlapping coupling method, in the sense that only one calculation domain is considered for the solution of viscous and inviscid equations. As a consequence, the inviscid flow close to the wall is a fictitious one. The two flows exchange information at the coupling boundary, which is located at the wall. This maintains the subcritical character of the wall layer, which behaves like a subsonic flow whatever the outer inviscid Mach number may be. The viscous–inviscid interaction is based on the use of the real flow mass defect δq with regard to the inviscid flow, defined as:

$$\delta q = \int_0^{\Delta} (\rho_e u_e - \rho u) dy \tag{20}$$

These defects δq are introduced in the inviscid flow at the wall, and induced curvatures of the streamlines. The correction of the inviscid axial velocity component may be derived then from Poincaré's formula (Kulisa, 1990); after some computation, we get:

$$\delta u_e(M) = -\frac{1}{\pi} \int_L \frac{1}{\rho} \frac{\dfrac{d}{dx}(\delta q) + (\rho v)_{y=0}}{(x - x_M)} dx \tag{21}$$

Equation (21) is called the "interaction system," and relates the velocity correction at a point M on the wall to the mass flow defect distribution, according to the required elliptic character. It takes the real flow injection into account through the $(\rho v)_{y=0}$ term.

The space-averaged flow Eqs. (17) to (19) are discretized according to the Keller box method, which is a second-order implicit scheme. The main feature of this scheme is to allow the treatment of first-order space derivatives only. As a consequence of the parabolized hypothesis, a space marching process is used. After discretization of Eq. (21), we extract that line of the resulting matrix that corresponds to the current computation station, and solved it with the system (17) to (19). The space marching procedure must be iteratively repeated in order to update downstream defect mass flow values δq.

Turbulence Model. For the present computations, the turbulence model is based on the Boussinesq hypothesis and uses the standard two-layer model of Cebeci-Smith (1974) with some modifications in order to take the jet injections into account. Mixing length models for film cooling applications have already been developed. Herring (1975) multiplies the two-dimensional turbulent viscosity by a factor that depends on the jet effects; however, as the inner law of μ_t tends toward zero at the wall, this model is unable to take the high level of turbulence encountered at the jet orifice into account. Yavuzkurt et al. (1980) has developed a mixing length model that is only suitable for computation in the mixing region of the jets, far downstream of the orifices.

In our model, the turbulent field is separated into a boundary layer part without injection μ_{tBL}, and a jet part μ_{tjet}, so that: $\mu_t = \mu_{tBL} + \mu_{tjet}$ and:

$$\mu_{tjet} = \rho l V_{Smax} \gamma;\ l^2 = \frac{1}{V_{Smax}} \int \int_{\sigma} \Delta V \, d\sigma \tag{22}$$

γ is the classical Van Driest function, which allows us to distribute μ_{tjet} on the jet section. Note that μ_{tjet} is a three-dimensional quantity, which is space averaged in the z direction.

Results of Computation

First, the code has been tested on various flows without injection; our purpose was to demonstrate the performance of the viscous–inviscid interaction method and to verify the stability of the code (Kulisa et al., 1990).

Now we pay attention to the description of the results obtained for the film cooled flow.

Experimental Configuration. We present here some results for an experimental configuration, which has been studied by Bousgarbiès et al. (1991). A flat plate is used, with a row of five holes. The injection holes have a diameter of 0.005 m, with a pitch (distance between two neighboring orifices) of 0.015 m. The boundary layer on that plate is turbulent, with a thickness of 0.010m. The jets are introduced in that flow with an injection rate of 2/3 and an angle of 45 deg with respect to the wall; the inviscid external velocity is 30 m/s. The jets are heated to a temperature of 340 K while the downstream flow has a temperature of 301 K. The test wall is warmed internally; a constant temperature of 310 K is fixed at $y = 0$, although variations have been observed experimentally, especially near the orifices of the jets.

Aerodynamic Aspect. First, the aerodynamic results are presented. The evolution of velocity vectors is shown in Fig. 7, for the spanwise position $z = 0$; the jet centerline is located in that (x, y) plan. The velocity vector field is presented here at convergence of the numerical process; it results from the superposition of the pitchwise spatial averages and jet fluctuations.

The computational mesh was constructed with 40 points in the Y direction; three stations of computation are located in the jet orifice; thus, the jet exit may be clearly seen from the strong deviation of the velocity vectors at the wall. Downstream of the jet orifice, a no-slip condition is recovered on the wall. Moreover, the jet influence is indicated by a "hump" in the velocity profiles at some distance from the wall. This moves off and is reduced progressively as it is displaced downstream. This is a direct consequence of the mixing of the jets and the crossflow; this mixing is expressed in the numerical method by the decrease of the source terms toward zero. In practice, this is obtained beyond five to six diameters. Moreover, the influence of the injection may be noticed upstream of the jet orifice. This is a typical elliptic effect, which is preserved by the inviscid interaction method. Qualitatively, the computation reproduces evolutions according to the experimental observations.

A more detailed comparison is presented in Fig. 8, concerning the streamwise component of the velocity profile. The results are given for the symmetry plane $z = 0$, and for several streamwise stations, $x = 0.5\phi$, $x = 1\phi$, $x = 2\phi$, $x = 4\phi$,

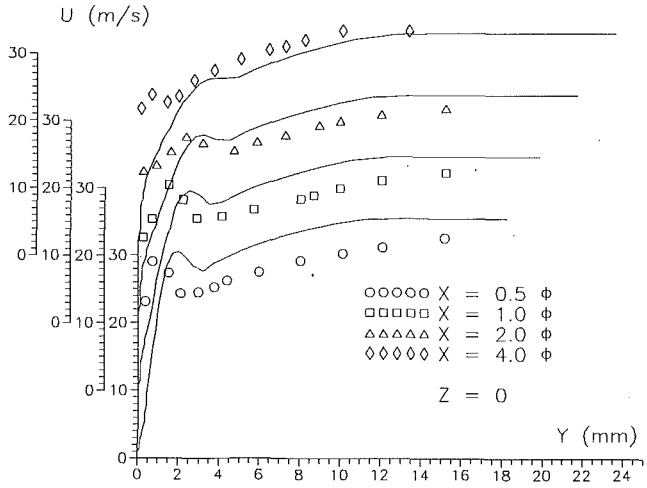

Fig. 8 Streamwise velocity profile; CEAT experiments

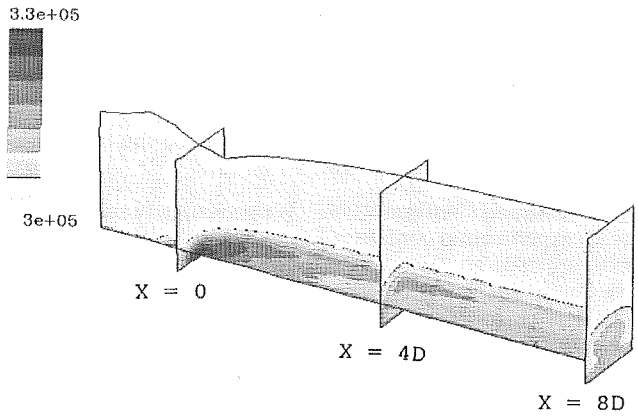

Fig. 9 Computed enthalpy distribution

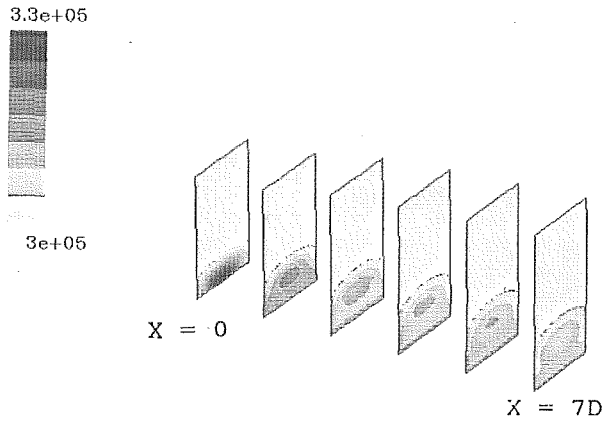

Fig. 10 Computed enthalpy distribution

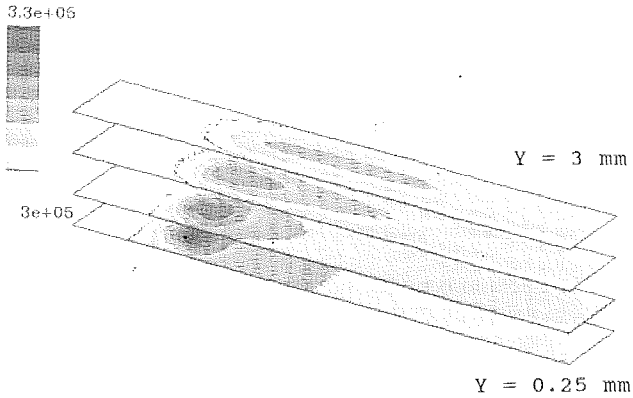

Fig. 11 Computed enthalpy distribution

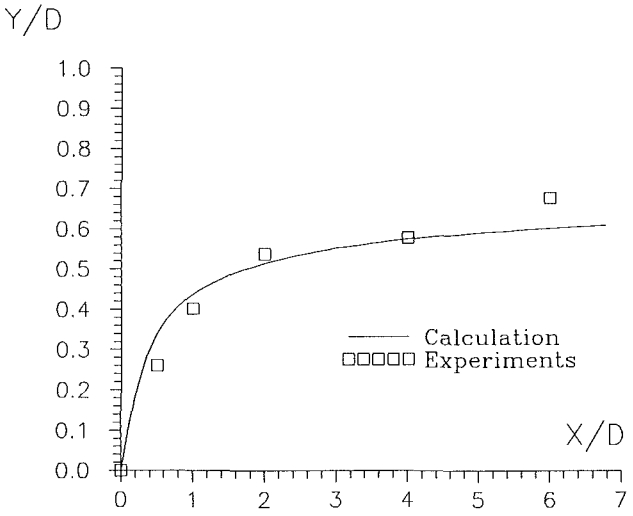

Fig. 12 Temperature maximum position; $Z = 0$; CEAT experiments

measured from the center of the hole. Note that the stations $x = 0.5\phi$ and $x = 1\phi$, in Fig. 8, are located in the hole. The calculated velocity at the wall is underpredicted in comparison with the expected injection velocity. The reason is that the velocity profile at the jet exit does not have a constant value as assumed in the potential core region. This is probably connected to deviation of the jet trajectory in the injection tube, before the orifice is reached (Dibelius et al., 1990; Charbonnier and Leblanc, 1990). On the whole, the velocity peak, which is associated with the jets, is calculated too far from the wall in the viscous layer. However, the width of this velocity peak seems to be well predicted. At the outer edge of the viscous layer, the computation shows a mass excess, which does not appear in the experiments. This effect must be connected with the viscous–inviscid interaction equation, which introduces an increase of the inviscid outer velocity U_e under the effect of the injections. This increase is reproduced on the complete layer thickness, according to the constant static pressure hypothesis in the Y direction. In practice, a static pressure gradient exists, and similarly an inviscid velocity gradient also, in the direction normal to the wall. Taking into account the previous remarks, we consider that the experimental evolutions are qualitatively well reproduced.

The spatial locations $x = 2\phi$ and $x = 4\phi$ indicate the mixing of the jets and of the viscous layer. The jet influence is clearly reduced. Now, the computed maximum velocity agrees with the experimental one. At these downstream locations, the jets are almost completely deflected and in line with the crossflow. The jet effects being less important, the influence of the interaction equation on the inviscid velocity U_e decreases and thus the outer edge velocity agrees with the experiments. However, the experimental results near the wall show a mass defect that is not reproduced by the computation. This is probably connected with an overestimation of the eddy viscosity.

Thermal Aspect. Now, we consider the thermal aspect. For the aerodynamic field, the thermal quantities may be determined over the whole domain, by reconstructing the complete three-dimensional field. The three-dimensional computed enthalpy evolution is shown in Fig. 9. Because of the periodicity of the flow in the z direction, the visualization around one jet only is presented. In the $x = 0$ station, the thermal effect, induced by the warm jet exit, may be seen. Downstream, Fig. 9 shows the mixing and the thermal diffusion of the jets.

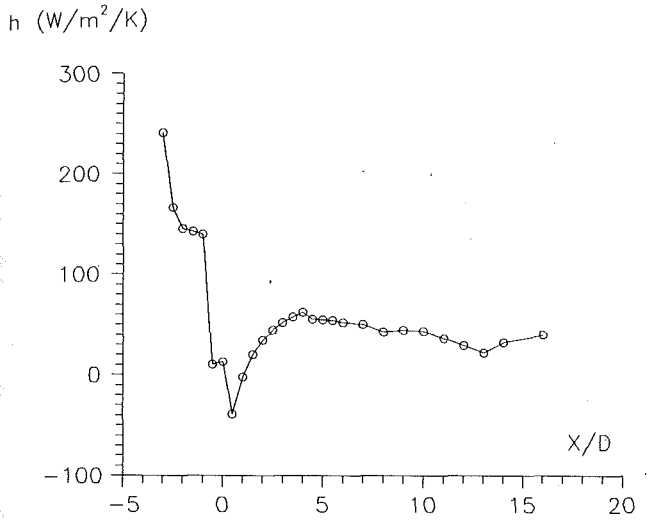

Fig. 13 Space-averaged heat transfer evolution

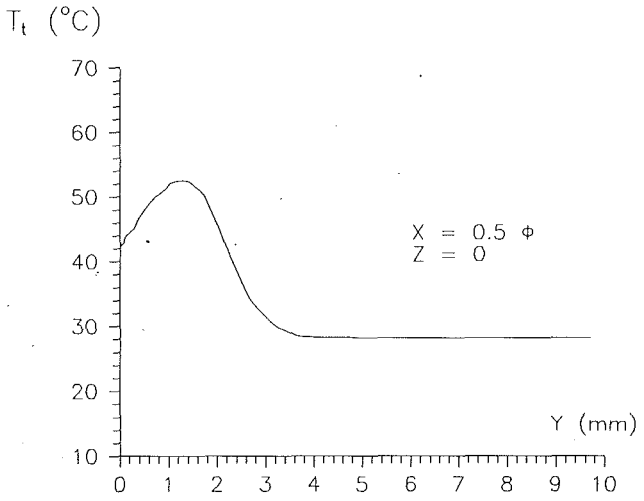

Fig. 14 Temperature profile

In Fig. 10, the spanwise planes (y, z) only are given, in order to illustrate all the phenomena in the z direction. Six equidistant surfaces are located from the orifice ($x = 0$) up to seven diameters downstream. We may note the elliptic shape of the enthalpy lines, which reproduce, in fact, the shape of the jet cross section. As before, the decrease of these elliptic regions is a consequence of the thermal diffusion.

Complementary views are presented in Fig. 11. Different areas (x, z), parallel to the wall, are located from $y = 0.00025$ m up to $y = 0.003$ m. Downstream diffusion may be observed for the closest plan to the wall. At $y = 0.003$ m, the downstream extension is a consequence of the jet bending. Although no experimental values were available at that time for this test case, it may be noted that the computed evolutions follow the general trends, observed by other authors.

Finally, the position of temperature maximum is given in Fig. 12, in the symmetric plan of a jet $z = 0$. The computed results agree well with the experimental one. The "thermal trajectory" of the jet is well predicted.

Figure 13 presents the evolution of the space-averaged heat transfer coefficient $\bar{h} = \bar{\Phi}/(\overline{T_y = 0} - \overline{T_e})$, where $\bar{\Phi}$ denotes the averaged heat flux density at $y = 0$. Up to $x/\phi = -1$, $\bar{h}$ decreases as the consequence of the growth of the wall layer, which is forced to flow over the downstream jets. Between $x/\phi = -0.7$ and 0.7, negative values of h occur; these stations are located inside the jet orifice. Downstream the orifice, the jet is in contact with the wall. Up to $x/\phi = 3.5$, the jet temperature is higher than at the wall (Fig. 14); as a consequence, negative h values will appear locally at the jet level; as we show here, for the space-averaged value $\bar{h}$ in Fig. 13, negative values only occur in the vicinity of the orifice; such behavior has already been observed by Camci and Arts (1985) and Dorignac (1990). The jet influence seems particularly important up to $x/\phi = 4$; downstream, the h evolution is mostly dominated by the wall itself.

Note that the stability of the numerical method, reinforced by the viscous–inviscid interaction equation, has been verified. In this case, five iterations between the viscous layer and the jet computations are necessary to obtain convergence of the complete procedure.

Conclusions

A method of modeling viscous flows on cooled turbine blades has been developed. Our approach is based on iterative information exchange between a viscous wall layer computation and a jet computation.

The viscous wall layer modeling uses a space-averaging technique, which allows the problem to be kept two dimensional. However, source terms appear in the equations. The parabolic nature of these viscous layer equations allows the use of a space-marching method. In order to ensure the stability of the method, a strong viscous–inviscid interaction method was introduced. The elliptic effect thus introduced requires the repetition of this space marching procedure.

The jet computation is a three-dimensional computation, using an integral method. The jet equations are solved on the jet trajectory, and closure relations are used. The jet computation results produce information necessary to determine the source terms, which are passed to the space-averaged viscous layer calculation.

Tests were performed on a film cooled flat plate. The aerothermal physical evolutions are well reproduced. Moreover, the numerical stability of the method was verified.

In order to apply this method to the computation of flow in a cooled turbine, more work is needed. First, the assumption of constant static pressure in the direction normal to the wall has to be eliminated; improvements in the jet computations are needed in particular to include the effects of the counter-rotating vortices; the turbulence also needs to be modified in order to include specific jet effects. Second, it is important to have access to good quality experimental data, including both aerodynamic and thermal informations.

Acknowledgments

We would like to thank SNECMA for the financial support of this study. The authors are also grateful to the staff and students of CEAT of Poitiers, which gives us access to experimental data, and especially Messrs. Leblanc, Bousgarbiès, and Vuillerme.

References

Andreopoulos, J., and Rodi, W., 1984, "Experimental Investigation of Jets in a Crossflow," *J. Fluid Mech.*, Vol. 138, pp. 93–127.

Bario, F., Leboeuf, F., Onvani, A., and Seddini, A., 1990, "Aerodynamics of Cooling Jets Introduced in the Secondary Flow of a Low Speed Turbine Cascade," ASME JOURNAL OF TURBOMACHINERY, Vol. 112, pp. 539–546.

Bousgarbiès, J. L., Deniboire, P., and Foucault, E., 1991, "Jet inclinés en écoulement transversal. Application au refroidissement de parois," presented at the A.V.M. 10 ème Congrès Français de Mécanique, Paris.

Camci, C., and Arts, T., 1985, "Short-Duration Measurements and Numerical Simulation of Heat Transfer Along the Suction Side of a Film-Cooled Gas

Turbine Blade," ASME *Journal of Engineering for Gas Turbines and Power*, Vol. 107, pp. 991–997.

Camci, C., 1989, "An Experimental and Numerical Investigation of Near Cooling Hole Heat Fluxes on a Film-Cooled Turbine Blade," ASME JOURNAL OF TURBOMACHINERY, Vol. 111, pp. 63–70.

Carotte, J. F., and Stevens, S. J., 1988, "Experimental Studies of Combustor Dilution Zone Aerodynamic," AIAA Paper No. 88-3274.

Cebeci, T., and Smith, A. M. O., 1974, "Analysis of Turbulent Boundary Layer," *Applied Mathematics and Mechanics*, Vol. 15.

Charbonnier, J. M., and Leblanc, R., 1990, "Preliminary Investigations in the Exit Region of a Jet in a Crossflow," presented at the First ISAIF, Beijing.

Dibelius, H. D., Pitt, R., and Wen, B., 1990, "Numerical Prediction of Film Cooling Effectiveness and the Associated Aerodynamic Losses With a Three-Dimensional Calculation Procedure," ASME Paper No. 90-GT-226.

Dorignac, E., 1990, "Contribution à l'Etude de la Convection Forcée sur une Plaque Plane en présence de Jets Pariétaux dans un Ecoulement Subsonique," PhD Thesis, University of Poitiers, France.

Herring, M. J., 1975, "A Method of Predicting the Behavior of a Turbulent Boundary Layer With Discrete Transpiration Jets," ASME *Journal of Engineering for Power*, Vol. 97, pp. 214–225.

Huang, P., 1989, "Modelisation et Calcul de Jets tridimensionnels en présence d'un Ecoulement Transversal," Thèse de Doctorat, Ecole Centrale Lyon, E.C.L. 89-007, France.

Kamotani, Y., and Greber, I., 1972, "Experiments on a Turbulent Jet in a Crossflow," *AIAA J.*, Vol. 10, pp. 1425–1429.

Kulisa, P., Leboeuf, F., Klinger, P., and Bernard, J., 1990, "Aerothermal Boundary Layer Computation Including Strong Viscous–Inviscid Flow Interaction," ASME Paper No. 90-GT-223.

Leboeuf, F., and Huang, G. P., 1990, "The Computation of Three-Dimensional Jets," presented at the First ISAIF, Beijing.

Le Grivés, E., 1977, "Mixing Process Induced by the Vorticity Associated With the Penetration of a Jet Into a Crossflow," presented at the Congress CIMAC, Tokyo, May.

Miller, K. L., and Crawford, M. E., 1984, "Numerical Simulation of Single, Double and Multiple Row Film Cooling Effectiveness and Heat Transfer," ASME Paper No. 84-GT-112.

Moussa, Z. W., Trischka, J. W., and Eskinazi, S., 1977, "The Near Field in the Mixing of a Round Jet With a Cross-Stream," *J. Fluid Mech.*, Vol. 80, Part 1, pp. 49–80.

Pietrzyk, J. R., Bogard, D. G., and Crawford, M. E., 1989, "Hydrodynamic Measurements of Jets in Crossflow for Gas Turbine Film Cooling Applications," ASME JOURNAL OF TURBOMACHINERY, Vol. 111, pp. 138–145.

Schönung, B., and Rodi, W., 1987, "Prediction of a Film Cooling by a Row of Holes With a 2-D Boundary Layer Procedure," ASME JOURNAL OF TURBOMACHINERY, Vol. 109, pp. 579–587.

Schwarz, S. G., and Goldstein, R. J., 1989, "The Two-Dimensional Behavior of Film Cooling Jets on Concave Surfaces," ASME JOURNAL OF TURBOMACHINERY, Vol. 111, pp. 124–130.

Schwarz, S. G., Goldstein, R. J., and Eckert, E. R. G., 1991, "The Influence of Curvature on Film Cooling Performance," ASME JOURNAL OF TURBOMACHINERY, Vol. 113, pp. 472–478.

Sinha, A. K., Bogard, D. G., and Crawford, M. E., 1991, "Gas Turbine Film Cooling: Flowfield Due to a Second Row of Holes," ASME JOURNAL OF TURBOMACHINERY, Vol. 113, pp. 450–456.

Snel, H., 1971, "A Semi-Empirical Model for the Development of a Round Turbulent Jet in a Crossflow," NRL TR 71107U.

Sykes, R. I., Lewellen, W. S., and Parker, S. F., 1986, "On the Vorticity Dynamics of a Turbulent Jet in a Crossflow," *J. Fluid Mech.*, Vol. 168, pp. 393–413.

Tafti, D. K., and Yavuzkurt, S., 1990, "Prediction of Heat Transfer Characteristics for Discrete Hole Film Cooling for Turbine Blade Applications," ASME JOURNAL OF TURBOMACHINERY, Vol. 112, pp. 504–511.

Yavuzkurt, S., Moffat, R. J., and Kays, W. M., 1980, "Full-Coverage Film Cooling. Part 1. Three-Dimensional Measurements of Turbulence Structure," *J. Fluid Mech.*, Vol. 101, Part 1, pp. 129–158.

Yavuzkurt, S., Moffat, R. J., and Kays, W. M., 1980, "Full-Coverage Film Cooling. Part 2. Prediction of the Recovery-Region Hydrodynamics," *J. Fluid Mech.*, Part 2, pp. 159–178.

A New Hue Capturing Technique for the Quantitative Interpretation of Liquid Crystal Images Used in Convective Heat Transfer Studies

C. Camci

K. Kim

The Pennsylvania State University,
Aerospace Engineering Department,
University Park, PA 16802

S. A. Hippensteele

NASA Lewis Research Center,
Internal Fluid Mechanics Division,
Cleveland, OH 44135

This study focuses on a new image processing based color capturing technique for the quantitative interpretation of liquid crystal images used in convective heat transfer studies. The present method is highly applicable to the surfaces exposed to convective heating in gas turbine engines. The study shows that, in single-crystal mode, many of the colors appearing on the heat transfer surface correlate strongly with the local temperature. A very accurate quantitative approach using an experimentally determined linear hue versus temperature relation is possible. The new hue-capturing process is discussed in detail, in terms of the strength of the light source illuminating the heat transfer surface, effect of the orientation of the illuminating source with respect to the surface, crystal layer uniformity, and the repeatability of the process. The method uses a 24-bit color image processing system operating in hue-saturation-intensity domain, which is an alternative to conventional systems using red-green-blue color definition. The present method is more advantageous than the multiple filter method because of its ability to generate many isotherms simultaneously from a single-crystal image at a high resolution, in a very time-efficient manner. The current approach is valuable in terms of its direct application to both steady-state and transient heat transfer techniques currently used for the hot section heat transfer research in air-breathing propulsion systems.

Introduction

The performance of present-day air-breathing propulsion systems can be significantly improved through a better understanding of heat transfer processes in the flow paths of the hot section components. Using surface-mounted liquid crystals in mapping temperature and heat transfer distributions has become a common practice. Steady-state and transient heat transfer techniques using liquid crystals require a careful quantitative interpretation of color patterns recorded from the heat transfer surfaces of hot section components. Cholesteric and chiral-nematic liquid crystals show a very interesting feature from a heat transfer point of view. They will progressively exhibit all colors of the visible spectrum as they are heated through the event temperature range. The phenomenon is reversible and repeatable, and the color can be accurately calibrated with temperature. Both the width of the temperature range and its location on the temperature scale can be controlled by selecting the appropriate cholesteric esters and proportions used in a given formulation. Liquid crystals are presently available for a temperature spectrum ranging from a few degrees below zero to several hundred degrees C. A mixture can be obtained with event temperature spans as small as 1°C to as large as 50°C. Excellent reviews of the application of liquid crystals in heat transfer measurements are given by Cooper et al. (1975), Simonich and Moffat (1984), and Hollingsworth et al. (1989). Hippensteele et al. (1983) used cholesteric liquid crystals in developing a liquid crystal sheet and electric heater composite. They used liquid crystals laid on a black plastic sealing material covered with a transparent Mylar layer. The lower layer of the composite was the heater sheet. As a result of an extensive study, they showed that the composite element is a relatively convenient, simple, inexpensive, and accurate device for high-resolution heat transfer measurements to be performed under laboratory temperature conditions. Local heat transfer measurements on a large-scale model turbine blade airfoil using a composite of heater element and liquid crystals is presented by Hippensteele et al. (1985). A transient liquid crystal technique for a heat transfer study in blade cooling geometries is presented by Ireland and Jones (1985). They used an initially heated heat transfer model in a transient wind tunnel with a mainstream at ambient temperature. A liquid crystal and heater element composite for quantitative and high-resolution heat transfer coefficients on a turbine blade was used by Hippensteele et al. (1987). Turbulence and surface roughness effects on heat transfer were also

Contributed by the International Gas Turbine Institute and presented at the 36th International Gas Turbine and Aeroengine Congress and Exposition, Orlando, Florida, June 3-6, 1991. Manuscript received at ASME Headquarters February 20, 1991. Paper No. 91-GT-122. Associate Technical Editor: L. A. Riekert.

included in the investigation. They calibrated the liquid crystal sheet in a temperature-controlled water bath. Yellow color provided the narrowest temperature band. They also pointed out the importance of the viewing angle. They indicated that the calibration drift could be minimized if the liquid crystal coated sheet is bonded to an air-tight surface. Another transient study focusing on the use of liquid crystals in wind tunnels is described by Jones and Hippensteele (1985). They used a transient heat transfer tunnel with a heated model in an air stream at ambient temperature. The emphasis in the experiments was to eliminate the initial surface temperature variations on the model surface.

In most of the studies summarized to this point, the images were processed for the existence of a yellow color region which appears at a very narrow temperature band. Visual detection of a single yellow contour in a majority of the experiments was the most quantitative description of a single isotherm that could be captured from a specific image. Baughn et al. (1988) described a visual method based on capturing the 0.7°C color band of a liquid crystal. Their method was for the investigation of pin fins with an experimental uncertainty of 4.7 percent on heat transfer coefficient. Wang et al. (1990) presented an imaging technique using an eight-bit black and white frame grabber. They marked the pixels for the appearance of a light intensity peak. By calibrating the intensity peak for the temperature, they were able to determine the isothermal line that represents a specific level of heat transfer coefficient at the specific time measured from the beginning of the transient experiment. Bunker et al. (1992) introduced another single color capturing technique using the chrominance-luminance description of color, which is widely used in commercial video applications. Their system was calibrated to capture a light blue liquid crystal color at a surface temperature of 38.4°C for the specific thermochromic liquid crystal. The chrominance determination was performed using the techniques developed by Hirsch (1987).

Numerous previous investigations performed during the last decade used mainly a single color mode, which provided a single isothermal contour per captured image based on the appearance of a very narrow precalibrated color band. There were also studies using multiple mixtures of liquid crystals to obtain a few isothermal lines per image. Another approach employed a number of optical filters to obtain more than one isothermal line from a given liquid crystal image. The current study presents and proves that the majority of the complete spectrum of colors appearing on a liquid crystal sprayed surface can be used to generate many isotherms simultaneously. A wide spectrum of colors from red to yellow, yellow to green, and finally from green to a wide blue zone can be calibrated very accurately to define extremely narrow multiple temperature bands. The method is very suitable for transient heat transfer studies. Having multiple (as many as 40) isotherms in each video frame reduces the total number of frames to be captured. The specific color capturing technique on a color image processor provides a highly automated heat transfer method, which reduces lengthy data reduction processes and significantly improves the spatial resolution of heat transfer measurements.

Interpretation of Color Vision Principles for Liquid Crystal Imaging Studies

Color may be defined as a psychophysical property of light, specifically, the combination of those characteristics of light that produce the sensations of hue, saturation, and intensity in a normal human observer. Color sensation from a liquid crystal covered surface is generated by a number of characteristics, such as the orientation of the crystals on the surface, the spectral characteristics of the light illuminating the liquid crystal covered surface, and the spectral response of the color-sensing component which may be a human eye or an imaging sensor used in a color camera. The orientation of liquid crystals is altered by the local temperature distribution on the heat transfer surface. Any temperature change at a given point on the liquid crystal covered surface results in a significant change

Nomenclature

c = specific heat
CCD = charge coupled device
CIE = Commission Internationale de L'Eclairage
D = jet exit diameter
E = power distribution of the illuminant
h = convective heat transfer coefficient $= \dot{q}/(T_{rec} - T_w)$
H = normalized hue
HSI = hue, saturation, intensity (normalized)
I = local intensity
k = thermal conductivity of air
l = the distance between the white point and the fully saturated color at a given ϕ
L = illumination length to heat transfer plate distance
m = slope of hue versus temperature relation
n = intercept of hue versus temperature relation
Nu = Nusselt number $= hD/k$
NTSC = National Television System Committee
$\dot{q}$ = heat flux
r = radius
R = reflectance characteristic of the colored surface
R, G, B = red, green, blue (normalized) local Reynolds number based on jet exit diameter and centerline velocity
R35C1W = chiral-nematic liquid crystal starting to respond at about 35 °C with an approximate bandwidth of 1 °C
S = saturation
t = time
T = temperature
TRS = total tristimulus value
Tu = turbulence intensity
U, V, W = three components of mean velocity
x, y, z = chromaticity coordinates
X, Y, Z = tristimulus values
x, y, z = standard psychophysical characteristics of human eye
α = thermal diffusivity of air $= k/(\rho c_p)$
β = nondimensional time $= h\sqrt{t}/\sqrt{\rho ck}$
δ = actual saturation distance between white point and the specific color at a given hue
θ = illumination angle (measured from the heat transfer surface)
λ = wavelength
ρ = density of air
ϕ = hue angle measured from red–white line in deg

Subscripts

∞ = free stream
i = initial
jet = jet centerline condition at the exit
rec = recovery
p = at constant pressure
w = local wall condition
λ = spectral local value

in the local spectral reflectivity of this point, and therefore a color change is sensed by the human eye or a visual sensor. Intensity of a color refers to the relative brightness of the color. This quantity represents a total sum of the spectral energy incoming to the sensor, emitted by the heat transfer surface at various wavelengths in the visible electromagnetic spectrum. Hue refers to that attribute of color that allows separation into groups by terms such as red, green, yellow, etc. In the visible spectrum, hue directly corresponds to the dominant wavelength of the color. Saturation refers to the degree to which a color deviates from a neutral gray of the same intensity, called pastel, vividness, etc. Saturation may also be defined as a color's purity or the amount of white contained in a specific color. By mixing a main hue (e.g., red) with white in different amounts, one can always generate less saturated colors (e.g., tones of pink). The amount of saturation is directly proportional to the amount of white added. Any color of the spectrum when highly desaturated should approach standard white color. These three characteristics, hue, saturation, and intensity, represent the total information necessary to define and/or recreate a specific color stimulus. Conceptually, this definition of color is highly convenient and appropriate for an image processing system to be used in the determination of convective heat transfer parameters from a liquid crystal sprayed surface, simply because the temperature of the point of interest is directly related to the hue value of the color displayed at that point. Since the orientation of the liquid crystal is the main controlling parameter for the color (hue, wavelength), a direct relation between the local temperature and the locally measured hue value can be established.

To determine specific parameters that describe a color on a heat transfer surface, three highly interrelated factors must be taken into account: (1) Spectral reflectivity of the surface being observed. (2) Spectral distribution of the light source illuminating the heat transfer surface. (3) Spectral sensitivity of the imaging sensor. Most of the available present day imaging sensors such as color CCD arrays simulate the spectral sensitivity of the "standard human eye." The main task of the presently developed image processing system hardware and algorithms is to bridge the perceived quantitative color information and the local temperature at a given point on a liquid crystal covered surface for heat transfer research purposes. The method assumes that perceived color changes due to slight changes in the illumination characteristics can be minimized and calibrated. The spectral response of the imaging sensor can also be taken into account during a typical hue versus temperature calibration procedure.

Color vision system uses a number of principles derived from a mathematical color matching model established by Grassman as described by Wyszecki and Stiles (1967) and Pritchard (1977). The basic principles used in modern tristimulus colorimetry are as follows:

1 The human eye can distinguish only three kinds of differences, which we now call hue (dominant wavelength), saturation, and intensity.

2 In a two-component color mixture, if one component is held constant and the other changed gradually, the color of the mixture will change gradually.

3 Lights of the same color (same dominant wavelength, saturation, and intensity) will produce identical effects in mixtures regardless of their spectral distribution.

4 The intensity produced by a mixture of several lights is equal to the sum of the intensities of the individual lights.

According to the trireceptor theory of vision, human eye translates radiant energy to visual stimuli by using three sets of cones and rods having individual response curves in the red, green, and blue portions of the visible spectrum.

The human eye detector evaluates the intensity of an image by summing the stimuli from the three receptors, while the chromatic attributes, hue and saturation, are determined by the ratios of the stimuli. Thus, light sources having widely different spectral distribution may give exactly the same visual color sensation as long as the amount and ratios of the total stimulation are the same. The intensity obtained by summing the stimuli from the three receptors is represented by a luminosity function. The details of the definitions are described in detail by Overheim and Wagner (1982), McIlwain and Dean (1956), Zworykin and Morton (1940), Fink (1955), Pearson (1975), and Bingley (1977). The basic principles and analysis given in these references state that only three independent quantities are required to specify a color and that color intensities add linearly. Therefore, a color specification system can be envisioned as involving a three-dimensional color space with any set of convenient coordinates, and these coordinates may be transformed mathematically into any other set for convenient measurement or analysis. Colorimetric coordinate systems that can be used include the intensities of three color primaries (R, G, B) or hue, saturation, and intensity (H, S, I), or intensity and two color difference signals (I, R-I, B-I). The fundamental quantities of tristimulus colorimetry as established by the CIE are as follows:

$$X=\int E_\lambda R_\lambda \bar{x} d\lambda \quad Y=\int E_\lambda R_\lambda \bar{y} d\lambda \quad Z=\int E_\lambda R_\lambda \bar{z} d\lambda \tag{1}$$

X, Y, and Z are the definitions of tristimulus values and the integrations are taken through the visible region of the spectrum. E_λ represents the spectral power distribution of the illuminant in which the colored object is viewed. The function R_λ represents the reflectance characteristic of the colored surface, that is, the proportion of incident light reflected, expressed as a function of wavelength. This quantity is strictly controlled by the liquid crystal response to local temperature. The three functions $\bar{x}$, $\bar{y}$, and $\bar{z}$ describe the standard psychophysical characteristics of a standard human eye.

Using the tristimulus values as fundamentals, other related quantities, called "chromaticity coordinates," may be defined as follows:

$$x=\frac{X}{X+Y+Z} \quad y=\frac{Y}{X+Y+Z} \quad z=\frac{Z}{X+Y+Z} \tag{2}$$

The quantity $\mathrm{TRS}=(X+Y+Z)$ is called the total tristimulus value. It may be written that

$$\mathrm{TRS}=(X+Y+Z)=\frac{X}{x}=\frac{Y}{y}=\frac{Z}{z} \tag{3}$$

The tristimulus values express the psychophysical assessment of a color by a standard observer whose characteristics have been established by a number of observers. The tristimulus values can also be transformed into a two-dimensional set of values describing the chromaticity values (hue and saturation), independent of intensity. In effect, x, y, and z represent the relative amounts of the three imaginary primaries required to match a particular color. Since $x+y+z=1$, once two of the three numbers x, y, z are given, the third is automatically determined. A graphic representation of x, y coordinates is shown in Fig. 1. Every (x, y) point on this diagram represents a unique color or chromaticity. It turns out that the chromaticities for all physically possible spectra are confined to a single region of the chromaticity diagram as shown in Fig. 1. This region is called "color locus." Chromaticities outside the color locus are impossible to achieve with any spectrum of light from the visible spectrum. The horseshoe-shaped outer boundary of the color locus represents the characteristics of all pure colors of the visible spectrum. The corresponding wavelengths are labeled around the periphery of this curve, which is also known as the spectrum locus as shown in Fig. 1. The lower portion of the locus is bounded by a straight line

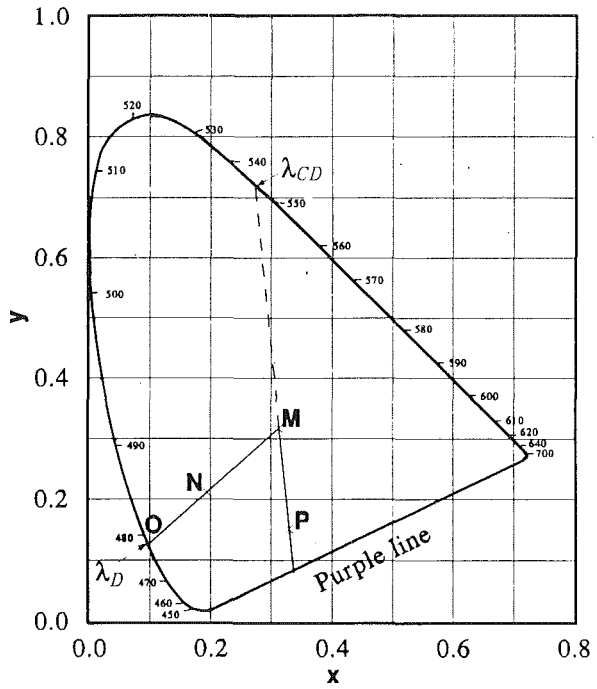

Fig. 1 Chromaticity diagram indicating all physically possible colors from the visible spectrum

that connects the blue and red ends of the spectrum locus. The straight line is known as the purple line. Hues along this line are not produced by any single wavelength of light, but rather result from the mixture of red and blue light. Points along the periphery of the color locus (along the spectrum locus and purple line) represent colors of the maximum saturation. As we move toward the center of the color locus, the saturation diminishes until, at the point $x=0.333$, $y=0.333$ the saturation becomes zero. This central point, labeled M in Fig. 1, represents equal energy white. The exact definition of the white point may vary slightly in different video standards.

The chromaticity diagram shown in Fig. 1 can be used to analyze color mixtures or determine dominant wavelength and saturation of a color. Point N in Fig. 1 represents the chromaticity of some spectrum of light. If a line is drawn from point M through N until the line strikes the spectrum locus at point O, point O will be located at a particular wavelength on the spectrum locus, λ_O. Thus, knowing λ_O gives an immediate idea of what kind of color N really is. The white point M is considered to have zero saturation while a pure color such as O is considered to be 100 percent saturated. Then saturation at point N expressed as a percent is given by:

$$S = (\text{length of } NM)/(\text{length of } OM) \tag{4}$$

Further details of RGB and HSI domain color operations are given by Ohta et al. (1980), Kender (1976), and Pratt (1978).

The Present Real Time Hue Capturing Scheme Using an Electronic Analog Circuit

The present real time hue capturing system operates using an NTSC standard 24-bit color image processing system. The system is capable of converting (R, G, B) information into (H, S, I) on each of the pixels in a 512×480 image, using a real time electronic hue converter. The imaging device used in this study has a high light sensitivity color CCD sensor consisting of about 632,000 pixels capable of generating red, green, and blue attributes. Thirty complete frames having a spatial resolution of about 512×480 can be scanned in one second. Red, green, and blue attributes are then multiplexed and sent to the image capturing board. The current system has the capability of either recording the image on a standard magnetic video tape or transferring the image data directly to the random access memory of the computer. The current computer and the image processor can transfer a complete color image captured in real time onto a hard disk approximately every two seconds. Direct digital recording on computer memory avoids a significant amount of noise that can be introduced when using standard video tapes. The present color image capturing board may either accept three individual R, G, B signals generated by a color camera or a multiplexed NTSC standard video signal. Three eight-bit video A/D converters generate digital signals before they are converted into an H, S, I signal for each pixel. The RGB–HSI conversion is performed on high-performance electronic circuitry in real time. Four individual frame buffers each having 256 kbytes of video memory are used for storing intensity, saturation, hue, and additional graphics and text information. There is also a second HSI–RGB converter at the output of the four frame buffers. This section provides a real time display of the contents of the buffers on typical RGB or NTSC color monitors. The buffer contents may be captured whenever needed and the storage process can be initiated by transferring the video image to the random access memory of the computer.

The RGB triangle used by the current system and the relation between HSI and RGB color coordinates is shown in Fig. 2. By knowing the red, green, blue attributes inside the RGB triangle, one can always generate the attributes hue, saturation, and intensity geometrically. The intensity attribute is dependent on the sum of the R, G, and B attributes. The chrominance attributes hue and saturation are based on the relative proportions of R, G, and B. Thus the relationships of red, green, and blue to the hue or saturation are highly nonlinear. A three-dimensional view of the HSI triangular model is also shown in Fig. 2. The intensity axis is perpendicular through the center of the RGB triangle. The present system uses three eight-bit video A/D converters, therefore each one of the R, G, B signals varies between 0 and 255. When they are converted into HSI values the new values are also normalized in such a way that they remain between 0 and 255. The definition of intensity is as follows;

$$I = (R+G+B)/3 \tag{5}$$

Saturation is defined as δ/I for the local point N as shown in Fig. 2. The lines connecting the R, G, and B points of the triangle carry the maximum available saturation of a given hue. Any movement from the maximum saturation line to the center of the HSI triangle makes this specific hue more desaturated. The point at the center of the triangle represents the color white. The saturation values around the periphery of the triangle are at a maximum value of 255. The hue is modeled as the angle (ϕ) rotating around the intensity axis with 0 deg at R, 120 deg at G, and 240 deg at B. In nondimensional form hue may be expressed as ($\phi/360$) for the point N. The normalized expressions of the saturation and hue values in eight-bit integer scale are as follows;

$$S = (\delta/I) * 255 \tag{6}$$

$$H = (\phi/360) * 255 \tag{7}$$

The (δ/I) and ($\phi/360$) can be calculated from the R, G, B attributes. The model resulting from the following expressions is based on an equal sided triangle with the white point located exactly on the center of gravity of the triangle. The conversions from R, G, B attributes are described in detail by Camci et al. (1991) and Berns (1989).

The Model

In order to validate the current hue capturing technique on

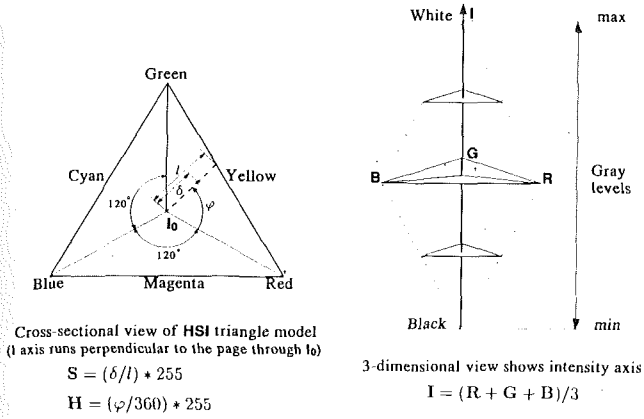

Cross-sectional view of HSI triangle model (I axis runs perpendicular to the page through I_0)

$S = (\delta/I) * 255$

$H = (\varphi/360) * 255$

3-dimensional view shows intensity axis

$I = (R + G + B)/3$

Fig. 2 RGB triangle used by the current system, geometric description of hue, saturation, and intensity, and a three-dimensional view of the present color model

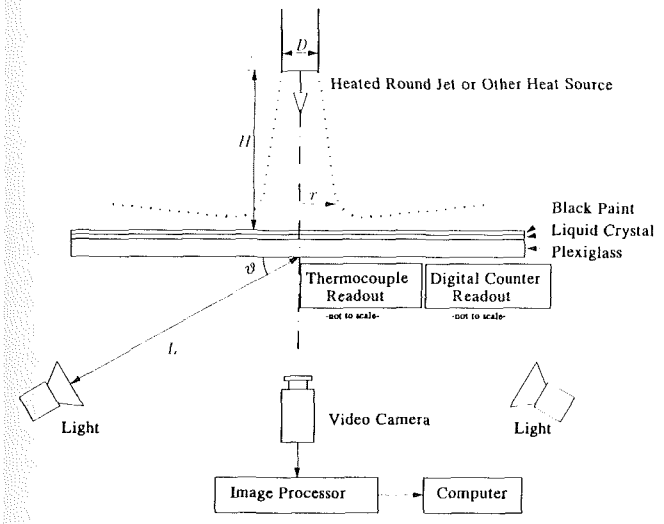

Fig. 3 Experimental setup, heated round jet, and heat transfer surface

a liquid crystal covered heat transfer surface, a 19.7-mm-thick flat plexiglass plate was manufactured. The plate had a total surface area of 1.0×1.0 m^2. One side of the plexiglass plate was coated with a chiral-nematic liquid crystal layer (R35C1W). The crystals used were encapsulated. After application of the crystal layer, a black coating was applied on top of the temperature-sensitive liquid crystal layer, as shown in Fig. 3. The top surface of the model was designated as a heat transfer surface. Convective heat flux was always applied from the top surface. However, the imaging camera was located at the bottom of the plexiglass model. This approach provided a viewing angle which was normal to the heat transfer surface. This configuration avoided a number of distortion corrections when viewing two-dimensional complicated images. The illumination system was also located on the camera side of the plate. The model was carefully covered in order not to damage the crystals from exposure to ultraviolet light. A direct exposure of the liquid crystal surface to sunlight was avoided. It was also expected that most of the ultraviolet light was going to be filtered during passage from laboratory windows and the thick (19.7 mm) plexiglass plate. Four fast response K-type thin foil thermocouples were flush mounted at separate locations on the heat transfer model for calibration purposes. The thermocouples had typical time response of about 2 milliseconds. The temperature measurement chain was carefully calibrated. The uncertainty of the temperature measurement

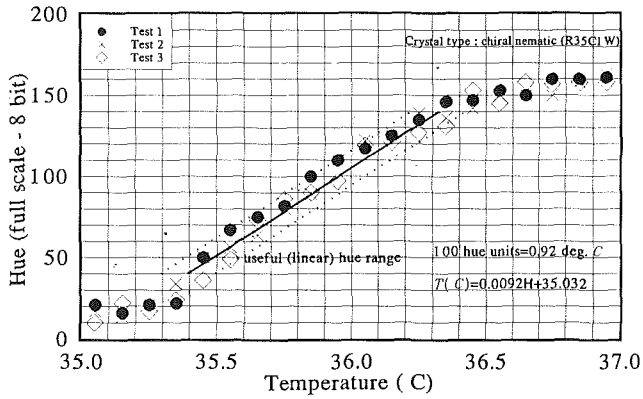

Fig. 4 Hue versus temperature relation for a typical pixel located on the heat transfer surface, (R35C1W)

with the foil thermocouple was expected to be within ∓ 0.15°C. Temperature recording was performed by using a 4 1/2 digit temperature readout made up of red seven-segment light emitting diodes. The readout was located on the camera side of the heat transfer plate. The video recordings of the liquid crystal image also carried the instantaneous temperature information at a local point. The time response of the whole temperature measurement chain was on the order of 100 Hz. This response guaranteed a correct temperature recording on each of the sequentially captured images, captured at a standard rate of 30 frames per second.

Experimental Results and Discussion

Hue Versus Temperature Relation. Hue versus temperature calibrations were performed locally in order to find out the dependency of liquid crystal color to temperature on the heat transfer surface. Hue values at a pixel located at the center of the plate were recorded at different local temperature values as shown in Fig. 4. The local temperature of the pixel was changed by applying a radiative heat flux from a temperature-controlled hot plate. A fast response thin foil thermocouple of K-type was flush mounted at the specific pixel location. Slowly varying color pattern and the measured temperature from the thermocouple were simultaneously recorded on a video tape. Figure 4 shows the variation of the local temperature measured by the thermocouple with respect to the color information captured by using a digital image processing system. The color information in the form of hue shows a very linear variation with respect to local temperature between 35.3°C and 36.3°C. The hue values smaller than 30 represent the black zone appearing just before red for the specific liquid crystal used (R35C1W). Very low intensity values are experienced in this zone. This area is the coldest zone on the heat transfer surface. The absolute value of the hue assigned to each color is strictly controlled by the calibration of the RGB to HSI analog conversion unit. Standard video calibration sources are needed to calibrate the color image capturing device. The hue range between 30 and 140 contained typical colors such as red, orange, yellow, green, and blue. This linear range was the most useful part of the hue versus temperature relation in terms of performing accurate temperature measurements using the color capturing technique. A complete spectrum of colors was located in an almost 1°C wide temperature band. The discrete data points shown in Fig. 4 showed an uncertainty band of less than ∓ 0.1°C in the hue range between 30 and 140. The hue values above 140 corresponded to the wide dark blue zone, which is very typical of liquid crystal images. The present color image processing system uses an eight-bit discretization for the hue capturing process. This feature allowed

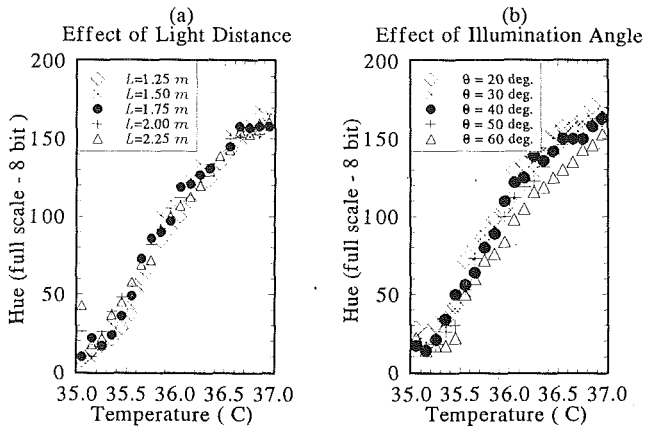

Fig. 5 Effect of light source distance and illumination angle on hue capturing process (R35C1W)

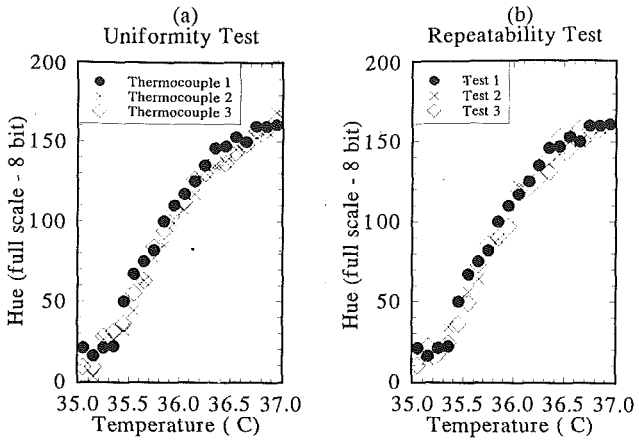

Fig. 6 Effect of liquid crystal layer uniformity and repeatability on hue capturing process (R35C1W)

division of the complete color range into 255 units. For the specific liquid crystal calibrated (R35C1W), the slope of the useful hue range suggested that a 0.1°C change in the local temperature corresponded to a relative hue change of 12 hue units.

Effect of Illumination Source to Model Distance. It is a known fact that color perception from a liquid crystal image is influenced by the type of liquid crystal applied, the amount of light illuminating the surface, spectral response of the color image sensing device, uniformity of the sprayed liquid crystal layer, in addition to the selective reflectivity of the surface, which is controlled by the liquid crystals in function of the local temperature. The effect of the amount of the light illuminating the heat transfer surface on the color capturing process is given in Fig. 5(*a*). An incandescent light source (500 W, 3200 K) contained in a reflector was used to illuminate the liquid crystal applied surface. The light source was kept at $\phi = 40$ deg to the surface for all of the experiments, unless otherwise stated. All of the experiments were performed during the night in complete darkness in order to eliminate the contribution of all other light sources, except the illuminating source. Figure 5(*a*) compares the results from five different experiments each with a different light source to model distance with the same source. The distances were varied from 1.25 m to 1.50, 1.75, 2.00, and 2.25 m. The figure shows that the change in captured hue values due to the varying amounts of illuminating light intensity was not very significant. When all of the points were compared, the uncertainty introduced by the light source distance variations was well within ∓0.08°C.

Effect of Illumination Angle. Figure 5(*b*) shows the influence of illumination angle on hue measurements. For the experimental results shown in this figure, the light source to model distance was always kept constant at 1.75 m. The illumination angle was measured from the flat heat transfer surface. At small angles ($\theta = 20$, 30, and 40 deg), the influence of the illumination angle was negligible as far as the linearity of the hue–temperature relation was concerned. However, after $\theta = 40$ deg, the deviation from the linear part of the hue versus temperature line became increasingly larger. At $\theta = 60$ deg, the temperature uncertainty increased to values as large as ∓0.20°C, especially for the temperature range above 36.0°C. The range below 35.0°C was not significantly influenced by the illumination angle variations. Figures 5(*a*) and 5(*b*) suggest that the color capturing process on a liquid crystal covered surface should always be performed with the same illuminating source, the same light distance, and the same illumination angle. The light source, distance, and angle should be kept the same both for the calibration and the actual experiment, in order to keep the temperature measurement uncertainty within ∓0.10°C. The camera conditions such as imaging sensor (circuit) gain, filter adjustment, diaphragm aperture, and optical adjustments (zoom, etc.) should also be kept unchanged for all the tests, including the hue versus temperature calibration process. The image processing system color capturing adjustments have to be locked during the calibration and actual testing efforts.

Spatial Distribution of Liquid Crystal Color Response and Repeatability of the Hue Capturing Technique. The chiral-nematic liquid crystal and binder mixture was sprayed by using a pressurized air brush as uniformly as possible. In order to check the spatial uniformity of the color response, three individual thin foil thermocouples were flush mounted at separate locations on the flat heat transfer surface. The hue versus temperature calibrations were repeated at each location individually using a number of local temperature levels. The results are presented in Fig. 6(*a*). The comparison of hue versus temperature curves at the three locations indicated that the liquid crystal color response provided a very consistent and reliable temperature measurement. The uncertainty band for the uniformity confirming experiments was better than ∓0.04°C.

Figure 6(*b*) presents the repeatability tests performed on three separate days at the same thermocouple location. The thin foil thermocouple located at the center of the plate was used for these tests. The exact same calibration procedure resulted in highly repeatable calibration curves as shown in Fig. 6(*b*). The maximum repeatability error was easily within ∓0.05°C in the linear portion of the hue versus temperature curve.

Hue Versus Intensity. The present color image processing technique provided simultaneous hue, saturation, and intensity values at each pixel location in real time. A very linear, reliable, and repeatable hue–temperature relation is shown in Fig. 4. The experiments in the present program showed that intensity information may also be used in processing liquid crystal data for quantitative heat transfer measurements. Figure 7 shows a high-resolution hue versus temperature relation from a few hundred discrete hue–temperature measurements using the present digital image processing system. A slowly varying temperature pattern on the thermocouple location was recorded on a video tape with its complete color image at a rate 30 frames per second. The image also consisted of the real time seven-segment LED display indicating the instantaneous thermocouple measurement. The details of the simultaneous hue and intensity measurements for a liquid crystal with a color play temperature of 42.8°C are given in Figs. 7, 8, and 9. The total bandwidth of the chiral-nematic liquid crystal was approximately 1.0°C (R42C1W). The experiments performed with

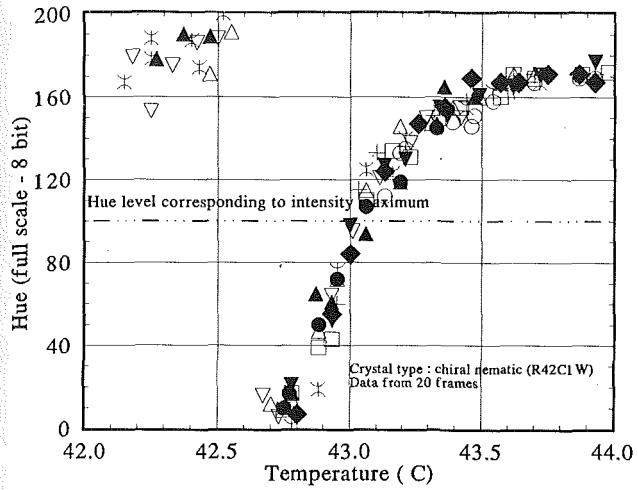

Fig. 7 High resolution hue versus temperature curve

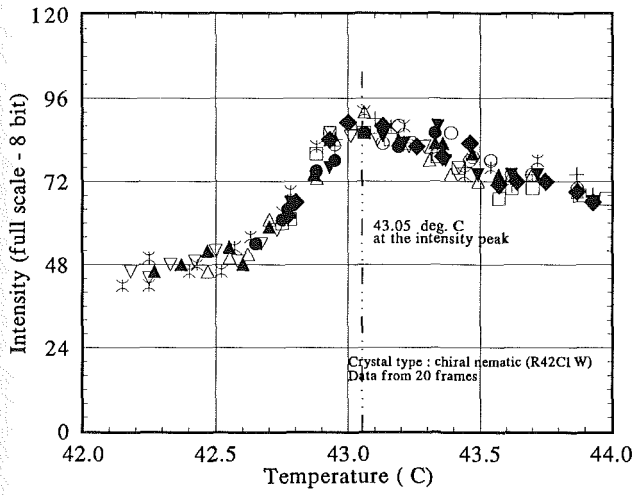

Fig. 8 Variation of local intensity with temperature

a high temperature resolution showed that there was always a very distinct intensity peak in the intensity versus temperature variation as presented in Fig. 8. The peak appeared at 43.05°C, corresponding to a very narrow color band that was mainly dominated by green. A close examination of Figs. 7 and 8 showed that the local temperature corresponding to the intensity peak may easily be determined. Figure 8 suggested that a single isotherm could be captured in a very accurate manner by carefully determining the peak intensity levels from a given image. For example, in an actual test under the same illumination conditions, the locus of intensity peak points may be associated with the isothermal line of 43.05°C occurring at a hue level of 109.5 hue units. Cross plotting hue and intensity is a very useful tool in setting up the illuminating system for a successful heat transfer experiment with well-defined hue points. It is a known fact that color image sensors do not respond in a healthy manner when the local intensity level is below a certain value. The illumination system should be adjusted in such a way that a typical hue distribution is obtained at reasonably high local intensity levels. Figure 9 shows a hue-intensity crossplot at the location of the calibration thermocouple. All the colors locally appearing from red to blue located themselves between hue levels of 0 and 170, on a slightly curved line. Figure 7 correspondingly showed that the hue levels above 140 are out of the linear portion of the calibration curve for the specific liquid crystal used (R42C1W). Above a hue value

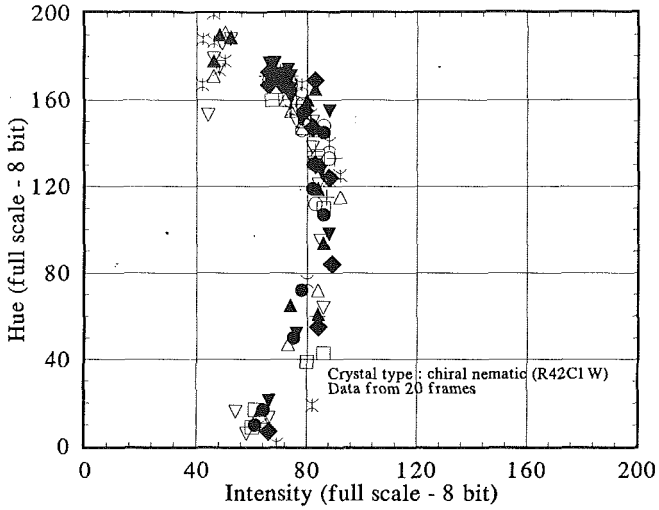

Fig. 9 Variation of local hue versus local intensity

of 140, the captured data points remained in the dark blue-black zone of the liquid crystal. Figure 9 indicated an overall intensity pattern smoothly varying in a range between 50 and 100. The experiments showed that the present hue capturing process worked very efficiently in an overall intensity range between 50 and 200. The hue versus intensity curve may be easily shifted to the right-hand side of the intensity scale (Fig. 9) by simply increasing the strength of the illuminating light source. It was found that the intensity levels above 200 affected the hue capturing method in a detrimental manner due to the saturation of the CCD sensor. It is also well known that very low overall illumination levels (e.g., intensity levels less than 50) make the hue capturing process unstable. Construction of a hue versus intensity chart using the intended illumination configuration (distance, angle, light source strength) provides a valuable and crucial check before the execution of an actual experimental program. Overall intensity levels between 50 and 200 (preferably between 100 and 200) were the typical levels for the hue capturing process performed on the color image processing system described in this study.

Further Implementation of the Method. The experimental calibration technique to convert color information into accurate temperature measurement was developed and tested at a local point having a fast response thermocouple flush mounted on the heat transfer surface. However, one of the final goals in this study was to obtain high-resolution distributions of temperature and convective heat transfer coefficients on surfaces with complex geometry or characteristic lines. In order to show the further applicability of the method, a baseline experiment was designed by using a heated round jet of air, stagnating on a flat wall. The heated jet originating from a round pipe was stagnated on a flat plate as shown in Fig. 3. The exit of the round pipe was square cut. The jet-to-plate distance was about 12 jet diameters and the jet exit velocity was measured to be 28 m/s at the centerline of the jet. The local temperature distribution on the liquid crystal covered model surface was known to be strongly affected from the geometry of the jet exit section. This effect was observed to be very strong at small jet-plane distances such as $x/D=4$. The round pipe was 5.08 cm in diameter, with a length of 55 cm. The pipe wall thickness was 0.4 cm. The air was heated using a 4 kW adjustable electric heater designed and built for this purpose. The heater was formed around a 50-cm-long refractory rod of 0.8 cm diameter. The heater rod was located along the centerline of the steel tube. This configuration provided a jet centerline temperature of 52.4°C with a typical variation of ∓ 0.15°C for a duration of at least 5 minutes.

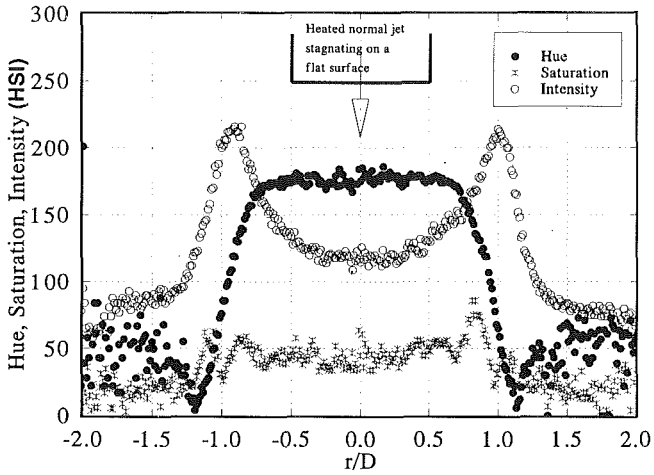

Fig. 10 A simultaneous representation of hue, saturation and intensity for a heated round jet stagnating on a flat plate (R35C1W)

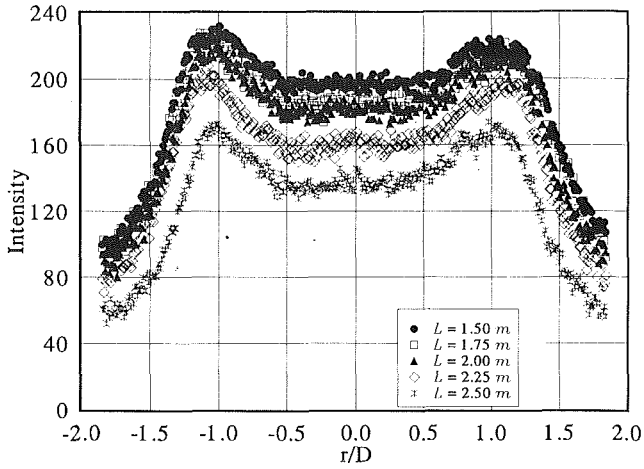

Fig. 11 Variation of local intensity values under strong illumination level changes along the radius (R35C1W)

The transient experiment was initiated with a cold jet. At this time the steadily flowing jet was deflected sufficiently far away from the flat heat transfer surface, by using a circular elbow section manually attached to the exit section of the pipe. Then, the heater was turned on to obtain a steady-state heated jet in terms of both velocity and temperature profiles at the exit. Special attention was paid in order not to disturb the flat heat transfer surface coated with liquid crystals in terms of its initial wall temperature uniformity. The liquid crystal surface was also carefully covered with a thermal barrier blanket, temporarily. The exit temperature distribution of the deflected jet reaches a steady state within the first 10 minutes of the heater start-up. The centerline temperature of the deflected jet was continuously monitored. The deflecting elbow was removed manually within a maximum of 60 milliseconds, which is much shorter than the time scale of the transient experiment. This initial period was checked by using a video camera and a display unit, which could accurately time stamp individual video frames. For this kind of impulsively starting heat transfer experiment, the definition of the beginning of the experiment and the elapsed time is needed in an accurate form in order to reduce the total uncertainty value on the convective heat transfer coefficient. The elapsed time was measured using an electronic counter operating at 30 Hz counting frequency to time stamp individual video frames. The video imaging system recorded at 30 frames per second. Figure 10 shows the distributions of hue, saturation, and intensity along the radius within the first two jet diameters radial distance. The circumferential uniformity of the jet flow was carefully checked and adjusted so that the information shown in Fig. 10 represented all of the circumferential positions for this nonswirling jet flow. The hue distribution provided a very wide color spectrum from red, yellow, green, and finally to blue. The hue values ranged from 0 to 170 between $r/D = 0.7$ and $r/D = 1.20$. The corresponding intensity values in the same radial band varied between 100 and 210. The peak intensity point corresponded to the radius at which a very narrow green color appeared, around a hue value of 90. The experiment presented in Fig. 10 and many other similar experiments run by the authors showed that the intensity peak is closely related to the green color observed on the surface. The saturation values obtained at each pixel location were not very helpful in obtaining accurate heat transfer results. Saturation of a color is strongly altered by the strength and by the geometric orientation of the illuminating system. The saturation values were almost at an overall flat level of 40 units for the pixels having local intensity value of greater than 100. The hue distribution shown in Fig. 10 can easily be converted into accurate temperature distribution by using the calibration curve provided in Fig. 4. The calibration showed that hue versus temperature relation was linear between hue values of 30 and 140. For the points having an r/D value greater than 1.25, hue capturing was not very successful due to relatively low intensity values generated by the "almost black" color, which shows the coldest zone on the heat transfer surface. The "almost black" color is an indication of a region out of the liquid crystal color response band. The term "almost black" was used here because any pure color may appear "almost black" under low-intensity, low-saturation conditions.

Robustness of Hue Capturing Technique Under Strong Illumination Variations. An experiment was designed to see the robustness of hue capturing process under different illuminating light strengths. An incandescent light source (500 W, 3200 K) oriented at $\theta = 40$ deg to the surface was used to generate different illuminating conditions on the same heat transfer image. The heated jet having a free-stream temperature of $T_{jet} = 52.4°C$ (at the exit) was located 12 jet diameters away from the wall. The jet exit velocity was measured to be 28 m/s at the centerline. A steady-state heat transfer pattern was reached by running the heated jet approximately 2 hours. The steady-state color pattern was then imaged when the light-to-model distance was at L = 1.50 m. A color video image was captured and processed for intensity and hue information useful for heat transfer studies. The data points in Fig. 11 also show the variation of local intensity values under strong illumination level changes. The light-to-model distance was changed from $L = 1.5$ m to 1.75, 2.00, 2.25, and finally to 2.50 m. A surface-mounted thin foil thermocouple monitored the surface temperature pattern at the center of the jet. No significant variation of wall temperature was observed at different light distances. It was found that the local intensity value was shifted from a value of 200 down to 135 when the same light source was moved from $L = 1.50$ m to $L = 2.50$ m (Fig. 11). However, the qualitative distribution of intensity remained almost the same.

The hue distributions corresponding to the light distance experiments given in Fig. 11 are shown in Fig. 12. An excellent feature of chiral-nematic liquid crystals of encapsulated type was observed as the extremely weak intensity dependency of surface hue distributions. Very strong local intensity variations created by moving the light source did not strongly alter the main color defining parameter "hue." This feature was expected because of the definition of the quantity hue. Hue is a direct measure of the dominant wavelength at which the electromagnetic light emission from the heat transfer surface oc-

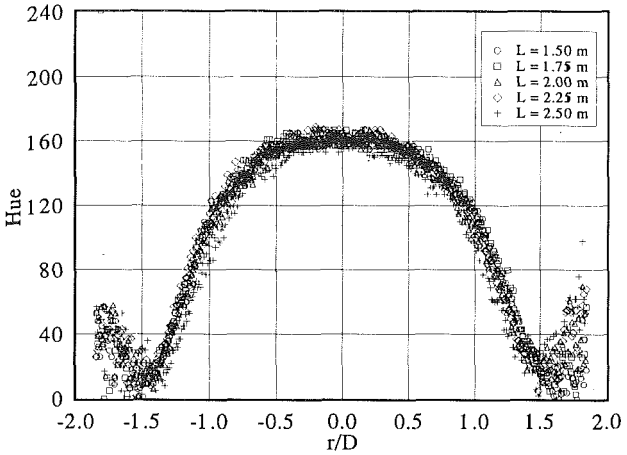

Fig. 12 Variation of local hue values under strong illumination level changes along the radius (R35C1W)

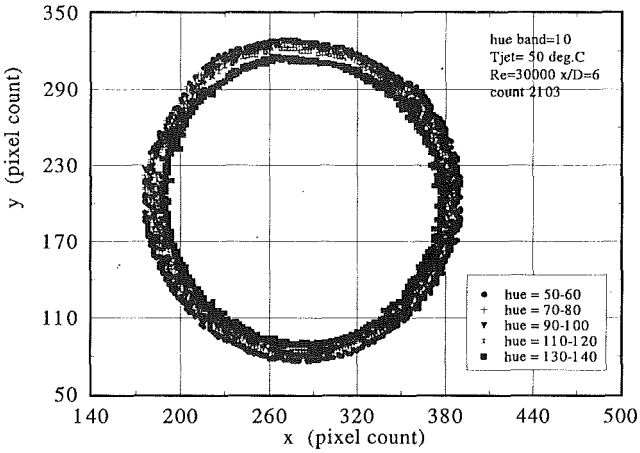

Fig. 13 Five discrete hue (isotherm) bands mapped using an image processor from a liquid crystal image (R35C1W)

curs. For the same light source located at several other distances, the only varying parameter is the amount of total energy incoming into the surface as electromagnetic energy. The variation of the incoming total electromagnetic energy results in strong variations in the amount of reflected light from the liquid crystal covered surface. However, the spectral character of the illuminating light source was always the same for all the experiments performed in this study. Therefore, it was expected that the spectral character of the reflected light from the heat transfer surface was not going to change if the surface temperature pattern was not altered by external means. A number of surface temperature checks also showed that thermal radiation contribution to the surface temperature pattern from the light source was quite negligible for all of the experiments presented in Fig. 12. The maximum local temperature variation at the center of the jet was within $\mp 0.10°C$ for all of the cases with different distances. It was concluded that by significantly changing the intensity of illuminating light, the local hue values did not vary in a strong manner. All of the measured hue points obtained at five separate light distances were within a hue band of $\mp$ 10 hue units. The corresponding temperature band was calculated as $\mp 0.08°C$ using the relation in Fig. 4. There are a few scattered data points with unexpected magnitudes, located at the extreme edges of the stagnation area on the surface. They were attributed to color capturing deficiencies of both the camera sensor and the RGB-HSI analog conversion process at very low local intensity levels, corresponding to "almost black" regions ($r/D > 1.25$). From a signal processing point of view, these are highly noisy parts of a typical liquid crystal image. The very slight variation in local hue values may include some thermal radiation effects due to varying distance or shape factors. In practice, model to light distance is most of the time unchanged from experiment to experiment. If one always uses the same illuminating source at the same angular position and distance for both the calibration process and actual experiments, very accurate quantitative measurements of local temperature may be obtained, as shown in Fig. 5 and 6.

Automatic Temperature Mapping Using the Present Hue Capturing Technique. The present color images from the stagnating heated jet experiment were sampled with a pixel resolution of 512×480, resulting in large data files containing 880 kbytes of digital information. At this resolution, in the useful (linear hue versus temperature) portion of the image, the temperature measurement resolution is much higher than the measurement techniques utilizing discrete sensors, such as thermocouples, resistance thermometers, thermistors, etc. A computerized process was shown to be very effective in extracting many distinct isothermal lines or very narrow temperature bands from a color image file containing 880 kbytes of digital image data. Figure 13 shows five hue bands each having a bandwidth of 10 hue units in an experiment having a jet exit temperature of 50.0°C, Re = 30,000, and $x/D = 6$. Solid circular symbols denote the hue values between 50 and 60, which corresponded to a temperature band of 0.08°C starting from 35.5°C (hue = 50). Solid square symbols show the maximum measurable temperature range. A solid symbol also indicates a temperature band of 0.08°C with a starting temperature of 36.3°C. The corresponding hue band was between 130 and 140. Five distinct temperature bands were located between 35.5 and 36.3°C. This kind of contouring was performed in a very time effective manner. A five-level contouring required a total of 45 seconds on the specific image processor described in this study.

Application of the Technique in Obtaining Convective Heat Transfer Coefficients. A very powerful application of the present method is the generation of convective heat transfer coefficients from time stamped color images, using transient heat transfer techniques. The transient technique used very frequently in the past required the elapsed time measured from the beginning of a transient experiment, local wall temperature, free-stream recovery temperature at the specific location, initial temperature of the model, and thermophysical properties of the model material (ρ, c_p, k) having the liquid crystal coating. The technique also assumed a one dimensional heat flow into a semi-infinite body. The convective heat transfer coefficients can be carefully evaluated if the elapsed time measurement is accurate enough, with a reasonably uniform initial wall temperature distribution. Knowing the free-stream recovery temperature distribution in an accurate form is also a crucial factor in reducing the uncertainties related to the convective heat transfer coefficient defined between the free-stream recovery temperature and the local wall temperature. Figure 14 shows the constructed convective heat transfer coefficients obtained using 16 individual color images sampled at different times. The results presented in Fig. 14 correspond to the flow conditions of the heated stagnating jet experiment described in Fig. 14. The measured recovery temperature distribution for the experiment having a Re = 30,000 and $x/D = 6$ is also presented in a nondimensional form in Fig. 14. The first image was captured at $t = 7.80$ s from the beginning of the transient experiment and the last image was taken at $t = 104.30$ s. The multiple temperature points corresponding to many of the colors that could be captured using the present technique improve the spatial resolution of the final heat transfer coefficient distribution greatly, compared to the previous techniques,

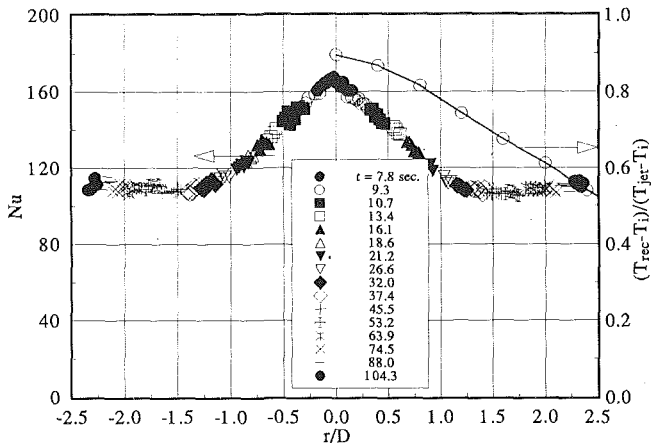

Fig. 14 Convective heat transfer coefficient and nondimensional recovery temperature distribution obtained using 16 individual color images sampled at different times (R35C1W) (heated round jet stagnating on a flat plate)

which provided only one single temperature point per video frame. The present method as shown in Fig. 14 provided more than 600 individual heat transfer coefficient measurements by using very accurately calibrated color information assigned to each pixel in the image. The initial wall temperature was uniformly distributed over the plate at ambient level. The initial wall temperature uncertainty was approximately $\mp 0.1°C$. The elapsed time measurement was performed by using an electronic counter. The time measurement uncertainty including the very initial transient flow establishment time was within $\mp$ 2 milliseconds. This is extremely small compared to the typical time scale of the experiment, which is on the order of seconds. The overall uncertainty of convective heat transfer coefficient was estimated to be around 5 percent using standard uncertainty prediction methods.

Conclusions

A new digital image processing technique based on a color capturing method was developed for the quantitative interpretation of liquid crystal images used in convective heat transfer studies. Quantitative color perception using a hue-saturation-intensity based description was proven to result in excellent results for surface temperature measurements using chiral-nematic liquid crystals.

It was shown that the local color play of the liquid crystal could be documented using a local hue quantity, which was a direct measure of the wavelength of the light selectively reflected from the liquid crystal surface. Since the selective reflection process was controlled by the liquid crystal as a natural response to local temperature, a hue versus temperature calibration was possible. A highly linear hue-temperature relationship was established by performing at least a few hundred local quantitative color-temperature measurements at a few calibration locations on the heat transfer surface.

The present technique allows the researcher to use many of the visible colors appearing on the liquid crystal coated surface, in contrast to many previous methods only utilizing a very narrow, distinct color band that formed a single isothermal line. It was concluded that the data density in a typical heat transfer coefficient distribution could be improved about 40 times with the present hardware, compared to the techniques using only a narrow color band as a single isotherm.

The new technique described was tested for the variations of illumination light strength. An excellent feature of chiral-nematic liquid crystals of encapsulated type was observed as the extremely weak intensity dependency of surface hue distributions. It was clearly shown that the variation of local light intensity captured from a pixel did not strongly alter the hue value, which is the direct measure of the local temperature. The uncertainty introduced by appreciable light source distance variations was well within $\mp 0.08°C$.

The effect of illumination angle was varied in a wide range from $\theta = 0$ deg to 60 deg. At small angles, the influence of the illumination angle was negligible as far as the linearity of the hue–temperature relation was concerned. However, after $\theta = 40$ deg, the deviation from the linear part of the calibration curve became increasingly larger. At $\theta = 60$ deg, the temperature uncertainty increased to values as large as $\mp 0.20°C$, especially for the temperature range above 36.0°C. It was concluded that the color capturing process should always be performed with the same illumination angle and the same illumination source fixed at a specific location for both the calibration process and actual experiments.

The camera conditions such as imaging sensor gain, filter adjustments, diaphragm aperture, and optical adjustments, (zoom, etc.) should be kept unchanged for all the experiments, including the calibration process. The image processing system color capturing adjustments have to be locked during the calibration and actual testing efforts.

The calibrations performed at discrete points on the heat transfer surface showed good spatial uniformity in terms of color response of the crystal layer. The uncertainty band for the uniformity confirming experiments repeated at discrete positions was better than $\mp 0.04°C$, in the linear part of the hue versus temperature curve.

Tests were also performed at the same location but at different times. The maximum uncertainty band for the repeatibility error was about $\mp 0.05°C$. The tests were performed to plot local intensities as a function of temperature. There was always an intensity peak at the location where the green color appeared dominantly. It was also shown that hue versus intensity curves could be utilized in improving the hue capturing process, by quantitatively checking the overall intensity distribution on the heat transfer surface.

The present technique was implemented for a heated round jet stagnating on a flat wall. High-resolution isothermal mapping was completed in a very time efficient manner. Five distinct isothermal lines in a range from 35.5°C to 36.3°C were computer generated in a total duration of 45 seconds, by processing 880 kbytes of digital color image data.

A very powerful application of the present liquid crystal method is the generation convective heat transfer coefficients with high resolution. The accurate temperature and elapsed time measurements performed on the liquid crystal covered surface were used in obtaining heat transfer coefficients. A transient method assuming one-dimensional heat flow into semi-infinite flat plate was employed. The color images captured at 16 different time steps measured from the beginning of the transient experiment, provided at least 600 discrete convective heat transfer coefficient measurements because of the multiple color processing capability of the present method. The pixel by pixel color capturing capability of the present method is extremely useful for two-dimensional processing of color information on more complex heat transfer surfaces. The overall uncertainty of convective heat transfer coefficient was estimated to be around ∓ 5 percent, using standard uncertainty estimation techniques.

References

Baughn, J. W., Ireland, P. T., Jones, T. V., and Saniei, N., 1988, "A Comparison of the Transient and Heated-Coating Methods for the Measurement of Local Heat Transfer Coefficients on a Pin Fin," ASME Paper No. 88-GT-180.

Berns, R. S., 1989, "Colorimetry for Electronic Imaging Devices," Tutorial Short Course Notes (T60), Center for Imaging Science/Rochester Institute of Technology, The International Society for Optical Engineering, OE/LASE '89.

Bingley, F. J., 1977, "Colorimetry in Color Television," *IEEE Transactions, Con. Electronics*, Vol. CE-23, pp. 467–478.

Bunker, R. S., Metzger, D. E., and Wittig, S., 1992, "Local Heat Transfer in Turbine Disk Cavities: Part I—Rotor and Stator Cooling With Hub Injection of Coolant," ASME JOURNAL OF TURBOMACHINERY, Vol. 114, pp. 211–220.

Camci, C., Kuisoon, K., and Hippensteele, S. A., 1991, "An Image Processing Based Liquid Crystal Technique Using a New Hue Capturing Method for Convective Heat Transfer Studies," NASA Technical Memorandum TM-xxxx, to be published.

Cooper, T. E., Field, R. J., and Meyer, J. F., 1975, "Liquid Crystal Thermography and Its Application to the Study of Convective Heat Transfer," ASME *Journal of Heat Transfer*, Vol. 97, pp. 442–450.

Fink, D. G., ed., 1955, *Color Television Standards—NTSC*," McGraw-Hill, New York.

Hippensteele, S. A., Russell, L. M., and Stepka, F. S., 1983, "Evaluation of a Method for Heat Transfer Measurements and Thermal Visualization Using a Composite of a Heater Element and Liquid Crystals," ASME *Journal of Heat Transfer*, Vol. 105, pp. 184–189.

Hippensteele, S. A., Russell, L. M., and Torres, F. J., 1985, "Local Heat-Transfer Measurements on a Large Scale-Model Turbine Blade Airfoil Using a Composite of a Heater Element and Liquid-Crystals," ASME *Journal of Engineering for Gas Turbines and Power*, Vol. 107, pp. 953–959.

Hippensteele, S. A., Russell, L. M., and Torres, F. J., 1987, "Use of a Liquid-Crystal, Heater-Element Composite for Quantitative, High-Resolution Heat Transfer Coefficients on a Turbine Airfoil, Including Turbulence and Surface Roughness Effects," NASA Technical Memorandum 87355.

Hirsch, C., 1987, "Aufbau und Inbetriebnahme eines Versuchsstandes zur instätionaren Wärmeübergangsmessung an rotierenden Scheiben beierzwungener Konvektion und Prallkühlung unter Nutzung thermochromer Flüssigkristalle als Temperaturindikatoren," Diplomarbeit No. 302, Institut für Thermische Strömungsmaschinen, Universität Karlsruhe, Germany.

Hollingsworth, D. K., Boehman, A. L., Smith, E. G., and Moffat, R. J., 1989, "Measurement of Temperature and Heat Transfer Coefficient Distributions in a Complex Flow Using Liquid Crystal Thermography and True-Color Image Processing," *Collected Papers in Heat Transfer*, ASME HTD-Vol. 123, pp. 35–42.

Ireland, P. T., and Jones, T. V., 1985, "The Measurement of Local Heat Transfer Coefficients in Blade Cooling Geometries," *AGARD Conference Proceedings on Heat Transfer and Cooling*, CP 390 Paper 28, Bergen.

Jones, T. V., and Hippensteele, S. A., 1985, "High-Resolution Heat-Transfer-Coefficient Maps Applicable to Compound-Curve Surfaces Using Liquid Crystals in a Transient Wind Tunnel," *Developments in Experimental Techniques in Heat Transfer and Combustion*, R. O. Warrington, M. M. Chen, J. D. Felske, and W. L. Grosshandler, eds., ASME HTD-Vol. 71.

Kender, J., 1976, "Saturation, Hue and Normalized Color: Calculation, Digitization Effects and Use," Technical Report, Department of Computer Science, Carnegie-Mellon University, Pittsburgh, PA.

McIlwain, K., and Dean, C. E., eds., 1956, *Principles of Color Television*, Wiley, New York.

Ohta, Y., Kanade, T., and Sakai, T., 1980, "Color Information for Region Segmentation," in: *Computer Graphics and Image Processing*, Academic Press, New York.

Overheim, R., and Wagner, D. L., 1982, *Light and Color*, Wiley, New York.

Pearson, D. E., 1975, *Transmission and Display of Pictorial Information*, Wiley, New York–Toronto.

Pratt, W. K., 1978, *Digital Image Processing*, Wiley-Interscience, New York.

Pritchard, D. H., 1977, "US Color Television Fundamentals—A Review," *IEEE Transactions, Con. Electronics*, Vol. CE-23, pp. 467–478.

Simonich, J. C., and Moffat, R. J., 1984, "Liquid Crystal Visualization of Surface Heat Transfer on a Concavely Curved Turbulent Boundary Layer," ASME *Journal of Engineering for Gas Turbines and Power*, Vol. 106, pp. 619–627.

Wang, Z., Ireland, P. T., and Jones, T. V., 1990, "A Technique for Measuring Convective Heat-Transfer at Rough Surfaces," ASME Paper No. 90-GT-300.

Wyszecki, G., and Stiles, W. S., 1967, *Color Science*, Wiley, New York.

Zworykin, V. K., and Morton, G. A., 1940, *Television*, Wiley, New York.

Convective Transport Phenomena on the Suction Surface of a Turbine Blade Including the Influence of Secondary Flows Near the Endwall

P. H. Chen[1]

R. J. Goldstein

Department of Mechanical Engineering,
University of Minnesota,
Minneapolis, MN 55455

A naphthalene sublimation technique is employed to study the mass transfer distribution on the suction (convex) surface of a simulated turbine blade. Comparison with a heat transfer study shows good agreement in the general trends in the region of two-dimensional flow on the blade. Near the endwall, local convective coefficients on the suction surface are obtained at 4608 locations from two separate runs. The secondary flows in the passage significantly affect the mass transfer rate on the suction surface and their influence extends to a height of 75 percent of the chord length, from the endwall, in the trailing edge region. The mass transfer rate in the region near the endwall is extremely high due to small but intense vortices. Thus, a large variation in the mass transfer distribution occurs on the suction surface, from a mass transfer Stanton number of 0.0005 to a maximum of 0.01. In the two-dimensional flow region, the mass transfer distributions at two different Reynolds numbers are presented.

Introduction

In modern aircraft gas turbine engines, the turbine inlet temperature has been steadily increased to at least 1780 K (Guenette et al., 1989). High temperatures and transient temperature response of engine components can produce large thermal stresses. The life of highly stressed components decreases significantly with increasing metal temperatures. Knowledge of the detailed heat transfer distribution is required to design such machines for thousands of hours of continuous operation without failure. In order to predict the service life of the engine, it is essential to have both local temperature levels of the hot gas and local temperature gradients from the hot gas to the components. After giving a brief summary of related studies, Graham (1979) and Dyban (1982) both listed several fundamental mechanisms that affected the heat transfer to gas turbine blades. These interrelated mechanisms include rotating effects, secondary flows, boundary layer transition, unsteady wakes, free-stream turbulence, surface curvature, injected coolant flow, flow separation, shock, etc. Taylor (1980) also suggested further studies on the combined effects of these parameters and the need to investigate specific problems to justify or to improve numerical predictions. The present state of the art in numerical predictions is generally not satisfactory for engine design due to difficulties in the prediction of boundary layer flows and heat transfer along a blade surface. More experimental work is needed to improve our understanding of the convective transport from the hot gas to turbine blades. The purpose of the present study is to obtain detailed mass transfer distributions on a (simulated) turbine blade under the influence of secondary flows. These measured mass transfer distributions can be used to validate and improve confidence in the accuracy of existing computational codes and through the heat/mass transfer analogy can be used to predict heat transfer to a blade.

For four decades, numerous studies have been conducted to investigate the external heat transfer processes from the hot gas to the blades. Smith (1948) reviewed early works conducted in the 1940s. The relation between the exit Reynolds number and the mean Nusselt number for five different blades was presented. He showed that the mean Nusselt number could change significantly for different blade profiles and increase with increasing exit Reynolds number for all blades. Wilson and Pope (1954) measured the local heat transfer along both surfaces of a heated blade over a wide range of inlet flow angle and exit Reynolds number. They presented many valuable observations. The transition from laminar to turbulent boundary layer flow can cause a steep rise on the heat transfer distribution on both surfaces. Higher mainstream turbulence as well as surface roughness result in a higher heat transfer rate.

More recently, turbine blade heat transfer has been inves-

[1]Presently at National Taiwan University, Department of Mechanical Engineering, Taipei, Taiwan.

Contributed by the International Gas Turbine Institute and presented at the 36th International Gas Turbine and Aeroengine Congress and Exposition, Orlando, Florida, June 3-6, 1991. Manuscript received at ASME Headquarters February 6, 1991. Paper No. 91-GT-35. Associate Technical Editor: L. A. Riekert.

tigated using a several new methods such as a shell blade technique, a transient technique (or a short duration measurement technique conducted in a shock tunnel), a naphthalene sublimation technique, and a liquid crystal technique. By applying the shell blade or similar technique, Turner (1971), Dyban and Glushchenko (1975), York et al. (1979), Mukherjee (1979), Bayley and Priddy (1981), Turner et al. (1985), and Priddy and Bayley (1985) reported blade heat transfer results. Bayley and Priddy (1981) showed the effect of free-stream turbulence intensity in the range of 0.5 to 32 percent and frequency of free-stream perturbation on the heat transfer rate to turbine blades. The heat transfer rate along both surfaces is slightly raised as the frequency of free-stream perturbation increased from 5 kHz to 10 kHz. On the suction (convex) surface, the laminar to turbulent transition was suppressed at $Tu \approx 17$ percent. The effect of surface roughness on the blade heat transfer rate was examined by Turner et al. (1985). Early transition and a fairly uniform increase of heat transfer are caused by the surface roughness. A discussion on the natural transition on both surfaces of several different blades was presented by Priddy and Bayley (1985). They concluded that the natural transition on the suction surface at low turbulence intensity commenced near separation of the laminar boundary layer and the empirical correlation of Abu-Ghannam and Shaw (1980) was not suitable to predict the onset of natural transition on the pressure (concave) surface.

In order to investigate the effect of high subsonic or supersonic Mach number on the heat transfer rate, Martin et al. (1978), Dunn and Stoddard (1979), Nicholson et al. (1984), Consigny and Richards (1982), Dunn and Hause (1982), Dunn et al. (1984a, 1984b), Arts and Graham (1985), and Guenette et al. (1989) applied transient methods using shock tunnel facilities or a blowdown turbine tunnel to study the turbine blade heat transfer distributions. These facilities provide well-defined flow conditions and the ability to simulate the test conditions of a real engine and to measure real-time heat transfer response. Typical outlet Mach number ranges from approximately 0.7 to 1.18. The shock wave induced on the suction surface has little effect on the local heat transfer rate for the high turbulent level case (Consigny and Richards, 1982). To simulate a full-scale engine, Dunn and Hause (1982) found the stator heat transfer rate for the full-stage case was about 20 percent higher than that for the stator-only case.

Hippensteele et al. (1985, 1987) applied the liquid crystal technique to measure the local heat transfer coefficient on a turbine airfoil. Their results showed some spanwise periodic temperature patterns on the suction surface, possibly caused by straw straighteners. From visualization results using yellow pigmented oil, they observed a laminar separation bubble formed on the pressure surface in the region just behind the leading edge. This separation bubble could be suppressed by increasing the flow inlet angle (Consigny and Richards, 1982).

Experimental measurements were conducted in long run-time cascade facilities, by Blair (1974), York et al. (1979), Graziani et al. (1980), and Nealy et al. (1984). Local heat transfer coefficients could be measured under steady-state conditions. Two studies by Sato and Takeishi (1987) and Sato et al. (1987) presented comprehensive local heat transfer results using electrically heated isothermal vanes in a low-speed wind tunnel. The effect of film cooling on the heat transfer process was also considered in these studies.

All of the studies noted above use heat transfer instrumentation. Kan et al. (1971) used a naphthalene sublimation technique to investigate the mass (heat) transfer from a turbine blade embedded in the two-dimensional flow region at different values of pitch-chord ratio, flow inlet angle, Reynolds number, and mainstream turbulence intensity. They showed that early transition occurred on the pressure surface when the flow inlet angle was small, but it became unclear where transition occurred when the flow inlet angle approached 40 deg. Chen and Goldstein (1988) also presented detailed mass transfer results on both surfaces of a turbine blade using the naphthalene sublimation technique. Both studies agree well in the trend of the mass transfer distribution.

Due to a low aspect ratio of the first-stage rotors or vanes, it is unrealistic to ignore the influence of the endwall on the flow field as well as the convective transport process. Sharma and Butler (1987) and Yamamoto (1987) proposed some numerical schemes to predict endwall losses and secondary flows in turbine cascades. Detailed experimental investigations of

Nomenclature

AC = axial chord length, see Fig. 2; $AC = 145.3$ mm in the present study
C = chord length of the test blade, see Fig. 2; $C = 169.1$ mm in the present study
c_p = specific heat, J/(kg K)
C_{ps} = static pressure coefficient = $(P_s - P_{1s})/(0.5\rho U_1^2)$
C_1 = an empirical constant, Eqs. (7) and (8)
d = diameter of the cylinder or the leading edge of the test blade; $d = 18.3$ mm in the present study
d_w = diameter of the trip wire, 1.59 mm and 3.76 mm for the cases of the thin and thick inlet boundary layers, respectively
D = diffusion coefficient of naphthalene in air, m^2/s; $D = 0.076$ m^2/s at 298.15 K and 0.1013 MPa
h = local heat transfer coefficient
h_m = local mass transfer coefficient, Eq. (1), m/s
H = shape factor of the approaching endwall boundary layer, δ_1/δ_2, measured 145 mm upstream of the leading edge of the test blade
k = thermal conductivity of air
L_{sb} = change in local naphthalene sublimation thickness during exposure in air stream, m
$\dot{m}$ = local naphthalene mass transfer rate per unit area, $kg/(m^2s)$
n = exponent in empirical correlations, Eqs. (7) and (8)
Nu = Nusselt number = hC/k
Nu_d = Nusselt number = hd/k
p = exponent in empirical correlations, Eqs. (7) and (8)
P = total pressure
P_s = static pressure measured on the blade surface
P_{1s} = static pressure upstream of the cascade
$P_{v,w}$ = local naphthalene vapor pressure at the test blade surface, N/m^2
Pr = Prandtl number = $\mu c_p/k$
R_{Vsc1} = reattachment line of the suction side corner vortex 1 (V_{sc1}), shown in Fig. 8
R_{Vsc2} = reattachment line of the suction side corner vortex 2 (V_{sc2}), shown in Fig. 8
R_{Vsh}/R_{Vp} = reattachment line of the passage vortex and the suction side horseshoe vortex, shown in Fig. 8
R_{2D} = reattachment line of the two-dimensional separation bubble on the suction surface of a turbine blade, shown in Fig. 8

the production and development of the secondary flows were presented in studies by Yamamoto (1987) and Bario et al. (1982). Sonoda (1985) used kerosene vapor to visualize the flows field in the blade passages. Although the approaching boundary layer flow in his study was laminar, the evolution of vortices was clearly captured. Hodson and Dominy (1987a) used a mixture of fluorescent powder and silicone oil to trace limiting streamlines on both suction and pressure surfaces of a low-pressure turbine blade. In their study, a two-dimensional separation bubble near the stagnation line was observed on both pressure and suction surfaces. Furthermore, the laminar boundary layer on the suction surface underwent separation, reattachment, and possibly transition, near the trailing edge, but this separation disappeared at higher inlet Reynolds numbers, Re_1. After studying the surface oil flow pattern, they concluded that the strengths and locations of the vortices were mainly affected by the approaching boundary layer and the blade loading instead of the inlet Reynolds number. By changing the incidence from +7.2 deg to −53.3 deg Yamamoto and Nouse (1988) showed the effect of incidence on the three-dimensional flows, blade loading at tip, and overall pressure loss in a linear rotor cascade. A detailed description of secondary flows in turbine blade passages can be found in a review of many earlier studies by Sieverding (1985).

Few studies are available on the effect of secondary flows on blade heat transfer. Walker and Markland (1965), Graziani et al. (1980), and Sato et al. (1987) showed that the heat transfer rate on the suction side was strongly affected by the secondary flows, especially in the region near the endwall. On the pressure surface, little effect of the secondary flow is observed. These measurements, however, were conducted using test blades with limited numbers of heat flux gages or thermocouples and might not present the whole picture of the heat transfer distribution.

Besides experimental studies, many computational codes have been proposed to evaluate the heat transfer rates to gas turbine blades. Daniel and Browne (1981) tested five different computer programs, which used different methods to model the turbulence quantities. The predictions are in good agreement with experimental data only in the laminar (leading edge) region and the fully turbulent region. Winstanley et al. (1981) used three different numerical schemes to predict the heat transfer distribution. Their results overestimated the surface heat transfer when compared with experimental data. Wang et al. (1985) incorporated a k–ϵ turbulence model with STAN5 to predict the heat transfer rate around turbine airfoils. Predicted results show a better agreement with the experimental data for the pressure surface than those for the suction surface. Some experimental studies, mentioned earlier, also compared numerical predictions with measured results. Two computational codes, two-dimensional parabolic boundary layer code (STAN5) and three-dimensional viscous code (NANCY), have been often used. Neither has achieved great success. This is attributed to inaccurate models for turbulence and the detailed flow conditions of the mainstream and blade surface boundary layer flow.

In the present study, a naphthalene sublimation technique is used to study the mass transfer coefficient instead of the heat transfer coefficient. Since the secondary flow over the suction surface is much more complex than that over the pressure surface, the present study only focuses on measuring the mass transfer distribution over the suction surface of a turbine blade. With the help of an automated data acquisition system, the mass transfer coefficient at several thousand locations over the test surface can be obtained for a single run and this can provide a detailed mass transfer distribution. This technique not only has high resolution, but also avoids heat conduction in the blade wall, which can mask out variations in convective transport. Values of the heat transfer coefficient can be evaluated from the measured mass transfer coefficient by applying the heat/mass transfer analogy.

Experimental Apparatus

Wind Tunnel and Test Section. The mass transfer experiments are conducted in the same open-circuit, low-speed wind tunnel that has been described in earlier film cooling studies (Ito et al., 1978). The configuration of the wind tunnel and the planar cascade is shown in Fig. 1. Three of seven threaded instrument holes ahead of the cascade are used to insert a total pressure tube, a static pressure tap, and a thermocouple. The approaching free-stream velocity, U_1, is measured at the third

Nomenclature (cont.)

q = heat flux
Re_d = Reynolds number = $U_1 d/\nu$ in the present study and $U_\infty d/\nu$ in earlier studies of a cylinder in a cross stream
Re = Reynolds number
Re_1 = inlet Reynolds number = $U_1 C/\nu$
Re_2 = exit Reynolds number = $U_2 C/\nu$
S_p = pressure (concave) side curvilinear distance from the stagnation line of the test blade, shown in Fig. 2; note that the stagnation line is determined from flow visualization results in the present study and $S_p/C = 1.06$ at the trailing edge
S_s = suction side curvilinear distance from the stagnation line of the test blade, shown in Fig. 2; note that the stagnation line is determined from flow visualization results in the present study and $S_s/C = 1.355$ at the trailing edge
S_{Vp} = separation line of the passage vortex, shown in Fig. 8
S_{Vsc1} = separation line of the suction side corner vortex 1 (V_{sc1}), shown in Fig. 8
S_{Vsc2} = separation line of the suction side corner vortex 2 (V_{sc2}), shown in Fig. 8
S_{Vsh} = separation line of the suction side horseshoe vortex, shown in Fig. 8
S_1–S_2 = separation line of the horseshoe vortex on the wall, shown in Fig. 7
S_{2D} = two-dimensional laminar separation line on the suction surface, shown in Fig. 8
Sc = Schmidt number = $\nu/D \approx 2.04$ for naphthalene at 298.15 K and 0.1013 MPa
Sh = Sherwood number = $h_m C/D$
St = heat transfer Stanton number = $h/\rho C_p U_1$
$\underline{St}_m$ = local mass transfer Stanton number = h_m/U_1
$\overline{St}_m$ = average mass transfer Stanton number over the whole curvilinear distance on the suction side = S_s
T = absolute temperature, K
T_w = temperature of wall, K
T_∞ = temperature of free stream, measured 145 mm upstream of the leading edge of the test blade, K
Tu = turbulence intensity in approaching free stream
U = free-stream velocity in the blade passage
U_1 = velocity upstream of the cascade, see Table 3
U_2 = velocity measured at the midspan of the exit of the cascade, see Table 3, m/s

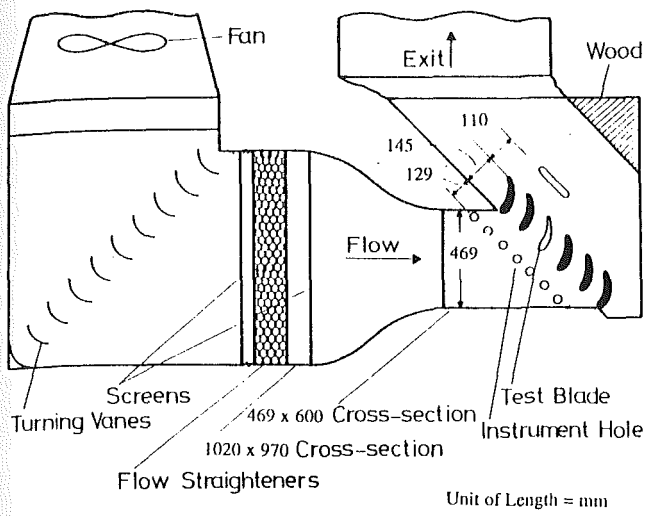

Fig. 1 A schematic view of the wind tunnel and cascade

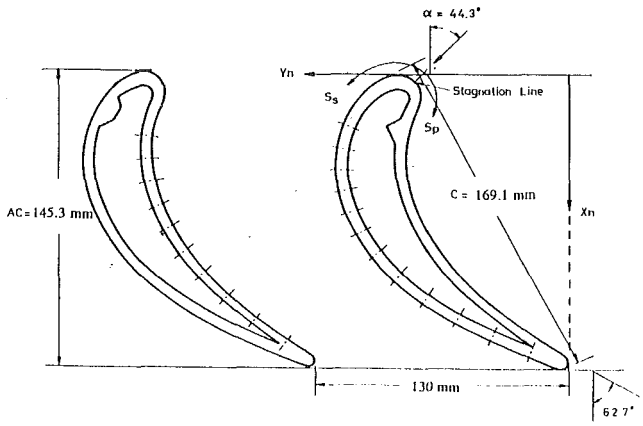

Fig. 2 Geometry of the turbine blade

threaded hole (at the right-hand side of the center hole), 145 mm upstream of the leading edge of the cascade. A slot in the top endwall located immediately after the cascade is used to install a total pressure tube and a static pressure tap for determining the cascade exit velocity, U_2.

The planar cascade consists of six scaled-up CF6-50 blades made of aluminum. Figure 2 shows the geometry of the blade. It has a chord length of 169.1 mm and its leading edge is an ellipse with a ratio of major to minor axis of 1.16. Coordinates of the surface profile of the test blade and parameters of the cascade geometry are given in Table 1 and Table 2, respectively. Each of the center two blades (the third and fourth blades counted from the top of the cascade in Fig. 1) of the cascade has three components: a bottom hollow section, a middle solid section, and a top supporting section. These three sections are held tightly together by two threaded bars. Lengths of the bottom, middle, and top sections are 600 mm, 171.5 mm, and 171.5 mm, respectively. During a mass transfer measurement, the middle solid section of the blade is replaced by the test piece, coated with naphthalene. Four dowel pins are used to ensure the same installation alignment for every mass transfer measurement.

Test Blade. The test blade consists of two smooth end pieces and a roughened piece in the middle. All three pieces are made of aluminum. The center part of the test blade, coated with solid naphthalene during a mass transfer measurement, has a span of 165.1 mm. Both end portions have the same contour as the blades of the cascade. The surface of the roughened section is approximately 1.63 mm deep as compared with the end pieces. Eleven grooves are also cut into each surface of the roughened blade in order to hold naphthalene better. Two thermocouples are installed at the central region of this roughened section, one on the pressure side and the other on the suction side.

Velocity and Pressure Measurement. The velocities at different streamwise locations over a turbine blade are determined by measuring the dynamic pressure between a total pressure tube located upstream of the cascade and static pressure taps on the blade. The value of the dynamic pressure is measured with a micromanometer, a Microtector made by Dwyer Com-

Nomenclature (cont.)

U_∞ = approach free-stream velocity for the study of a cylinder in a cross stream, m/s
V_p = passage vortex, shown in Fig. 7
V_{pc} = pressure side corner vortex, shown in Fig. 7
V_{ph} = pressure side horseshoe vortex, shown in Fig. 7
V_{pLc} = pressure side leading edge corner vortex, shown in Fig. 7
V_{sc1} = suction side corner vortex 1, shown in Fig. 7
V_{sc2} = suction side corner vortex 2, shown in Fig. 7
V_{sh} = suction side horseshoe vortex, shown in Fig. 7
V_{sLc} = suction side leading edge corner vortex, shown in Fig. 7
X = distance from the center of the rotary table on the horizontal plane and normal to the central line of the LVDT, cm, shown in Fig. 3
X_n = normalized dimension of the blade, shown in Fig. 2
Y = distance from the center of the rotary table on the horizontal plane and parallel to the central line of the LVDT, shown in Fig. 3
Y_n = normalized dimension of the blade, shown in Fig. 2
Z = vertical distance from the top wall of the test section
Z_r = direction along the central line of the rotating table, shown in Fig. 3
α = inlet flow angle of the cascade, deg, shown in Fig. 2
δ_1 = displacement thickness of the approaching endwall boundary layer, measured 145 mm upstream of the leading edge of the test blade
δ_2 = momentum thickness of the approaching endwall boundary layer, measured 145 mm upstream of the leading edge of the test blade
Δt = total time the test blade is exposed in the airstream, s
θ = angular direction of the rotating table, shown in Fig. 3
μ = dynamic viscosity of air
ν = kinematic viscosity of air
ρ_s = density of solid naphthalene, $\rho_s = 1145$ kg/m^3 at 298.15 K
$\rho_{v,w}$ = local naphthalene vapor density on the test blade surface
$\rho_{v,\infty}$ = naphthalene vapor density in the mainstream, zero in the present study

Table 1 Coordinates of the blade contour and locations of the pressure taps (see Fig. 2)

Concave Side			Convex Side		
X_n/AC	Y_n/AC	S_p/C	X_n/AC	Y_n/AC	S_s/C
			.01	.55	.007
			.000	.583	.037
.075	.521	.058	.005	.6147	.061
.15	.5478	.138	.045	.683	.133
.225	.565	.193*	.175	.7737	.270*
.3	.567	.257*	.25	.7948	.337*
.375	.555	.323*	.325	.7998	.402*
.45	.5306	.391*	.4	.7909	.467*
.525	.4928	.463*	.475	.768	.534*
.6	.4429	.540*	.55	.731	.606*
.675	.3775	.624*	.625	.6774	.686*
.75	.2948	.722*	.7	.6022	.777*
.825	.1953	.829*	.775	.5025	.884*
.9	.845	.944*	.84	.3912	.995*
.98	.0	1.045	.9	.2679	1.113*
			.96	.1302	1.242*
			1.0	.0220	1.341

* indicates locations of the pressure taps

Table 2 Cascade geometry

Number of blades	6
Chord length, C (mm)	169.1
Axial Chord, (mm)	145.3
Aspect Ratio	3.548
Pitch, (mm)	131.1
Inlet Angle	44.3^o
Exit Angle	62.7^o
Leading edge radius to chord ratio	0.054

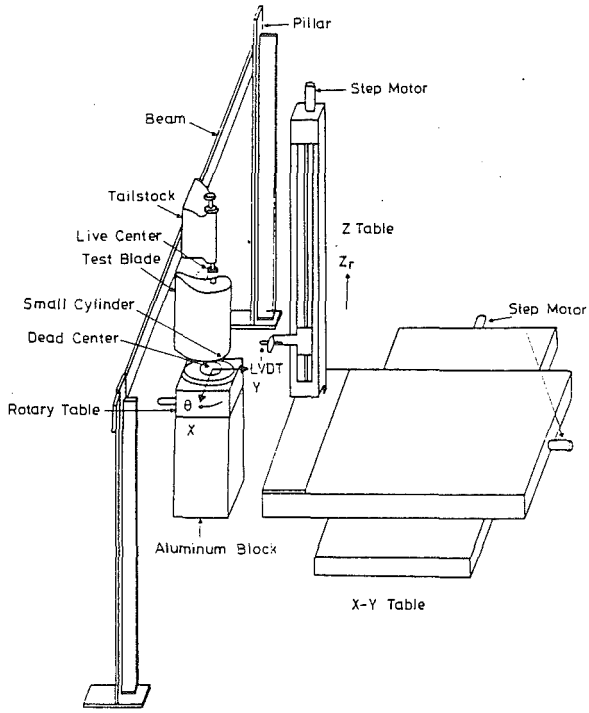

Fig. 3 The four-axis positioning stand

pany, which has resolution of 0.001 in. and a range of 2 in. water head.

The static pressure distribution over the blade surface is measured relative to a barometer pressure with the same micromanometer. Since the blades with pressure taps can be moved up and down through the walls, the pressure distribution at different elevations from the wall can be determined.

Data-Acquisition System. An automated four-axis data acquisition system is used to measure the sublimation depth over the test blade naphthalene surface. This system can fulfill many strict requirements of a mass transfer measurement, summarized as precise positioning, accurate surface elevation reading, and fast data acquisition (2500+ data points within a one hour period). It includes a four-axis positioning stand, a depth gage, an IBM-XT, and a motor-controller system. A detailed description of this system can be found in a study by Chen and Goldstein (1988).

The central part of the data acquisition system is a four-axis positioning stand, shown in Fig. 3. The probe (LVDT) can be moved independently in three directions, X, Y, and Z_r. The test piece can be rotated around an axis in the θ direction. The main function of this stand is to align the test piece and to move the depth gage accurately and quickly on the naphthalene surface (S_p–Z_r or S_s–Z_r). Since the local mass transfer rate is determined from the difference in naphthalene surface profiles at the same location measured before and after exposure to the flow, the test piece must be precisely installed on the positioning mechanism.

Procedure and Test Conditions

Experimental Procedure. After a smooth naphthalene layer is cast on the test blade, the naphthalene surface profile is measured at designated locations before the test blade is installed in the wind tunnel. Then the test blade is put into a sealed plastic box to prevent sublimation due to natural convection. It is placed in the wind tunnel and exposed to the airstream for a period of 30–45 minutes, depending on the test conditions. Meanwhile, the readings of the thermocouples are recorded. Since the naphthalene vapor pressure is susceptible to changes in temperature, it is important to keep a steady free-stream temperature. Finally, the test blade is removed from the wind tunnel and installed back in the positioning mechanism. Readings of the second surface profile are at the same locations as in the first measurement. The change in naphthalene thickness during exposure in the flow is determined from the difference of these surface profiles.

The mass transfer coefficient is evaluated from the measured naphthalene sublimation loss,

$$h_m = \dot{m}/(\rho_{v,w} - \rho_{v,\infty}) = L_{sb} \cdot \rho_s/[(\rho_{v,w} - \rho_{v,\infty})\Delta t] \quad (1)$$

In the free stream, $\rho_{v,\infty}$ is equal to zero and

$$h_m = L_{sb} \cdot \rho_s/(\rho_{v,w})\Delta t \quad (2)$$

The mass transfer coefficient can be nondimensionized as the mass transfer Stanton number

$$\mathrm{St}_m = h_m/U_1 \quad (3)$$

or the Sherwood number

$$\mathrm{Sh} = h_m C/D \quad (4)$$

where D is the diffusion coefficient of naphthalene in air. A discussion of the value of the diffusion coefficient is given in a study by Chen (1988).

To compare the present results with direct heat transfer measurements, a heat/mass transfer analogy is applied. The analogy between heat and mass transfer process was discussed by Eckert (1976). The definition of the heat transfer coefficient can be expressed as

$$h = q/(T_w - T_\infty) \quad (5)$$

Correspondingly, the mass transfer coefficient is defined as

$$h_m = \dot{m}/(\rho_{v,w} - \rho_{v,\infty}) \quad (6)$$

At the same flow conditions, the sublimation mass transfer system is equivalent to a heat transfer system with a constant wall temperature boundary condition. Empirical correlations are commonly applied to correlate the heat and mass transfer

Table 3 Test conditions

	Case 1	Case 2	Case 3
U_1(m/sec.)	10.45	7.33	10.45
U_2(m/sec.)	17.18	12.05	17.18
Re_1	104,000	73,000	104,000
Re_2	171,000	122,000	171,000
d_w(mm)	1.59	1.59	3.76
δ_1 (mm)	2.13	2.4	3.18
δ_2 (mm)	1.51	1.69	2.25
H	1.41	1.42	1.41
Tu(%)	1.31	1.27	1.31

coefficient when Sc and Pr are not equal. Often the power law relation is used,

$$\mathrm{Nu} = C_1 \mathrm{Pr}^n \mathrm{Re}^p \tag{7}$$

and

$$\mathrm{Sh} = C_1 \mathrm{Sc}^n \mathrm{Re}^p \tag{8}$$

For the same Reynolds number

$$\frac{\mathrm{Nu}}{\mathrm{Sh}} = \left[\frac{\mathrm{Pr}}{\mathrm{Sc}}\right]^n \tag{9}$$

If the Stanton number and the mass transfer Stanton number are to be used,

$$\frac{\mathrm{St}}{\mathrm{St}_m} = \left[\frac{\mathrm{Pr}}{\mathrm{Sc}}\right]^{n-1} \tag{10}$$

For air the Prandtl number is approximately 0.7 and the value of the Schmidt number by naphthalene in air is between 2.0 and 2.5, depending on the flow conditions and the temperature at the naphthalene surface. In Eqs. (9) and (10), n is an empirical constant; its value is taken as 1/3 in the present study. It should be noted that relationships such as Eqs. (7)–(10) are not required if only relative values are intended such as comparison of transport in the end-wall region to that on the blade in the two-dimensional flow.

Test Conditions. The test conditions established for the experiments are given in Table 3. For measurements in the two-dimensional flow region, the exit Reynolds number was either 122,000 or 171,000. When the effect of secondary flows was considered, the approaching displacement thickness on the endwall (measured 145 mm upstream of cascade) was changed from 2.13 mm (case 1) to 3.18 mm (case 3) at the same exit Reynolds number, $Re_2 = 171{,}000$. For the data run in the two-dimensional flow region, the active naphthalene area of the test blade extends from midspan of the test section to 131.3 mm from the endwall. For measurements in the three-dimensional flow region, the test blade is moved into the location at which 1.5 mm of naphthalene is embedded into the top endwall.

Based on the method proposed by Kline and McClintock (1963), the uncertainty in h_m of the present study is about 4.9 percent. A detailed discussion on the estimation of the uncertainty was presented by Chen and Goldstein (1988).

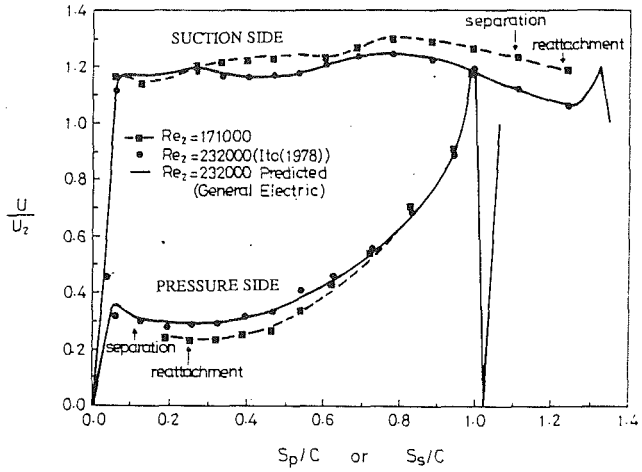

Fig. 4 Normalized velocity distribution along the blade surface

Results and Discussion

Velocity and Pressure Distribution. The variation of free-stream velocity, U/U_2, over both surfaces of the blade is presented in Fig. 4. Predicted values of U, supplied by General Electric, compare well with measured data (Ito et al., 1978). On the suction side, the velocity rapidly increases up to 1.15 U_2 at $S_s/C \approx 0.05$, indicating a strong acceleration. After the strong acceleration, the velocity is almost uniform along the whole suction surface. On the pressure surface, a strong rapid acceleration around the leading edge is followed by a region of deceleration until $S_p/C \approx 0.3$, following which the flow undergoes a strong acceleration as S_p increases further. In the accelerated region, the pressure gradient parameter $\frac{\mu}{\rho U^2}\frac{dU}{dS_p}$ is about 16×10^{-6}, which is considerably greater than the commonly accepted value (2×10^{-6}) above which relaminarization can occur. The difference between the present data and earlier results indicates that the normalized velocity distribution is slightly affected by a change in the exit Reynolds number. Note that the locations marked "separation" and "reattachment" on Fig. 6 were inferred from the mass transfer measurement.

Figure 5 shows contours of the static pressure coefficient on the suction surface at $Re_2 = 171{,}000$. The measurement area is from the endwall ($Z = 0$) up to $Z/C = 0.7$ and data at $Z/C = 0.7$ were used to obtain the free-stream velocity, U, shown in Fig. 4. Note that data near the leading edge are not available due to the absence of pressure taps. The effect of secondary flows is quite significant. A two-dimensional flow region can only be found in the region $Z/C > 0.6$. For the region $0.6 > Z/C > 0.3$, the flow accelerates from the leading edge toward a low-pressure zone ($C_{ps} = -2.9$) located near $S_s/C = 0.72$. After the low-pressure zone, a steep adverse pressure gradient causes a two-dimensional laminar separation, which is confirmed by the mass transfer measurements. The two-dimensional separation was also observed in several studies on different turbine blades (e.g., Hodson and Dominy, 1987a, and Hoheisel et al., 1987). In the region from $S_s/C \approx 0.2$ to 0.6, a pressure gradient in the spanwise direction drives both the suction side horseshoe vortex and the passage vortex upward, away from the endwall.

Flow Field. Measurements and flow visualizations have been extensively employed to study the flow field around a turbine blade. Although the flow field has a strong dependence on the incidence angle, flow inlet angle, Reynolds number, characteristics of the oncoming boundary-layer flow, and the blade profile, the qualitative trends are quite general. The boundary-layer flow in the two-dimensional flow region, shown

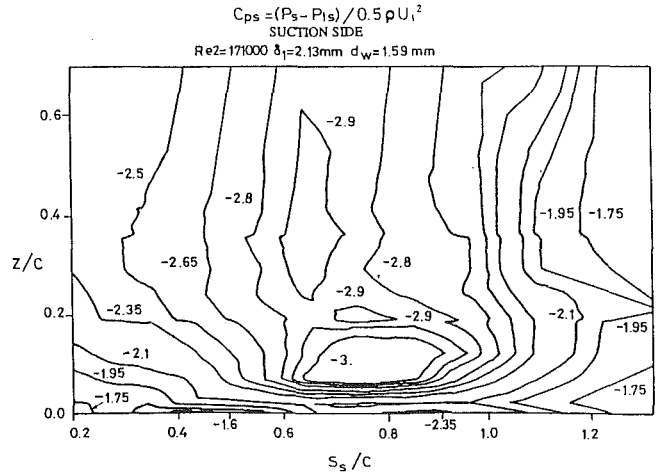

Fig. 5 Suction blade surface pressure coefficient contour

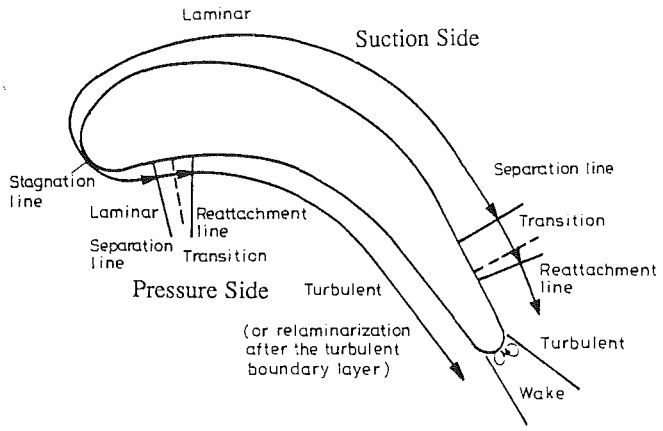

Fig. 6 Boundary layer over a turbine blade in the two-dimensional region

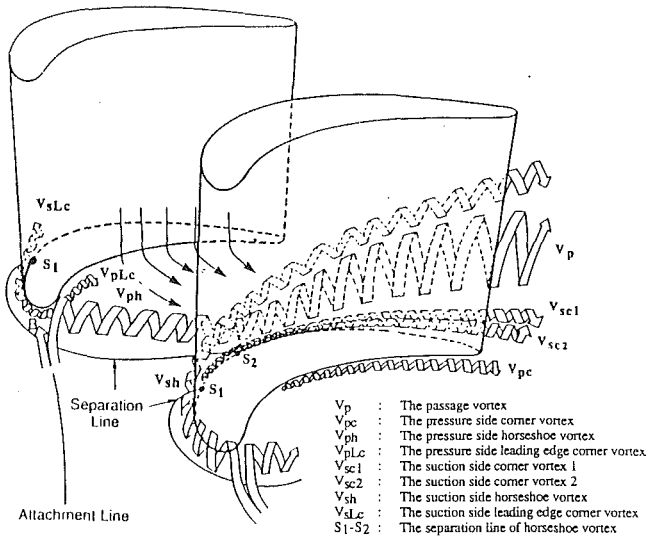

Fig. 7 Diagrams of turbine blade vortices

in Fig. 6, is summarized from studies conducted by Hodson and Dominy (1987b), Hoheisel et al. (1987), and Nicholson et al. (1982). On the suction side, a laminar boundary layer grows from the stagnation line. Hodson and Dominy (1987b) observed that the laminar boundary layer proceeds through separation, transition, and reattachment after which the flow becomes fully turbulent near the trailing edge. This separation bubble, near the trailing edge, is also indicated by the mass transfer measurement in the present study. Vortices shed from the trailing edge are present in the wake region. The flow field, on the pressure surface, is also indicated in Fig. 6. The laminar boundary layer develops from the stagnation line and a separation bubble forms near the leading edge. In the separation bubble, a transition occurs and develops into a fully turbulent boundary layer. The turbulent boundary-layer flow, subjected to a strong acceleration, might relaminarize.

Based on earlier studies, the secondary flows in the three-dimensional flow region within the blade passage are schematically presented in Fig. 7 from Goldstein and Spores (1988). When the incoming boundary layer on the endwall approaches the blade, it is subjected to an adverse pressure gradient and starts to roll up to form a horseshoe vortex. Ahead of the leading edge of the blade, S_1–S_2 is the separation line of the horseshoe vortex and the two legs of the horseshoe vortex are marked as vortices V_{sh} and V_{ph}. The leading edge corner vortex, driven by the horseshoe vortex, forms at the corner of the leading edge and rotates an opposite direction to the horseshoe vortex. Separating from the leading edge, the suction and pressure side leading edge corner vortices are marked as vortices V_{sLc} and V_{pLc}, respectively. A verification of this intense leading edge corner vortex from the mass transfer results will be shown in a later section.

The strong pressure gradient in the blade passage is the main driving force of the complex secondary flows. It affects the path of the low-momentum flow, on the endwall as well as the secondary flows in the passage. It is also responsible for the overall downflow (toward the endwall) on the pressure surface and upflow on the suction surface. When both the suction side leading edge corner vortex and horseshoe vortex enter the blade passage, they experience a strong transverse pressure gradient and both vortices are kept close to the suction surface.

As the suction side horseshoe vortex travels along the suction surface toward the trailing edge, it moves away from the endwall toward the midspan and downstream to the separation bubble. When the suction side horseshoe vortex moves away from the endwall, its separation line is at S_1, shown in Fig. 7. Hodson and Dominy (1987a) indicate that the direction of the rotation of the flow in the separation bubble is opposite to that of the suction side horseshoe vortex; as a result, the vorticity of this vortex decreases. As to the leading edge corner vortex, after it is forced toward the suction surface, its path is not easily traced nor do earlier studies have a clear view of it.

The pressure (concave) side horseshoe vortex leg, driven by the strong transverse pressure gradient, moves away from the pressure surface and toward the suction surface of the adjacent blade. During the transverse movement, it becomes a major component of the passage vortex (V_p) that entrains fluid from the endwall boundary layer, as well as the mainstream. After the passage vortex reaches the suction surface of the adjacent blade, it moves away from the endwall toward the midspan as it travels along the suction surface toward the trailing edge. The location, S_2, is shown in Fig. 7, and indicates the extrapolation of the separation line of the passage vortex at the suction surface.

Using the kerosene oil vapor to visualize the flow field, a pair of suction side corner vortices (V_{sc1} and V_{sc2}) were observed by Sonoda (1985). This observation was also indicated by Goldstein and Spores (1988) from regions on the endwall with high mass transfer rate, caused by these intense vortices. In the present study, the mass transfer results indicate one suction side corner vortex (V_{sc1}) starts behind the location of S_1 and another (V_{sc2}) forms behind the location S_2. Over the pressure

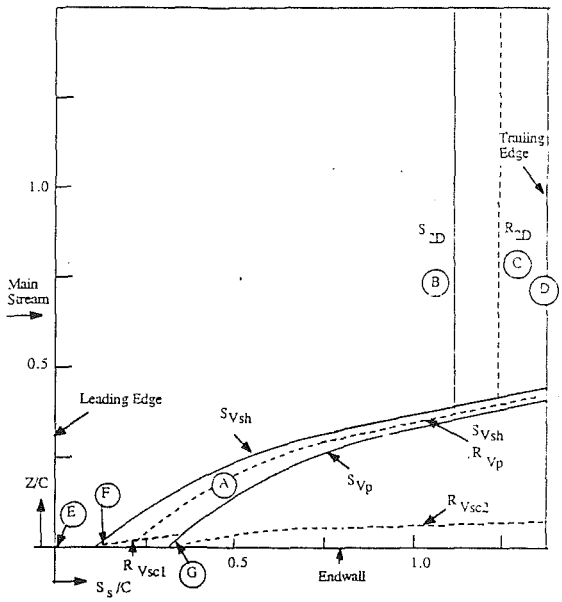

Fig. 8 Limiting streamline pattern on the suction surface of the test blade

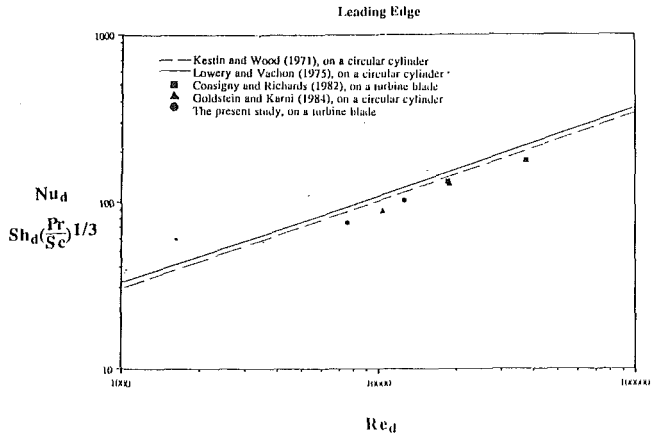

Fig. 9 A comparison of the leading edge heat transfer in the two-dimensional flow region

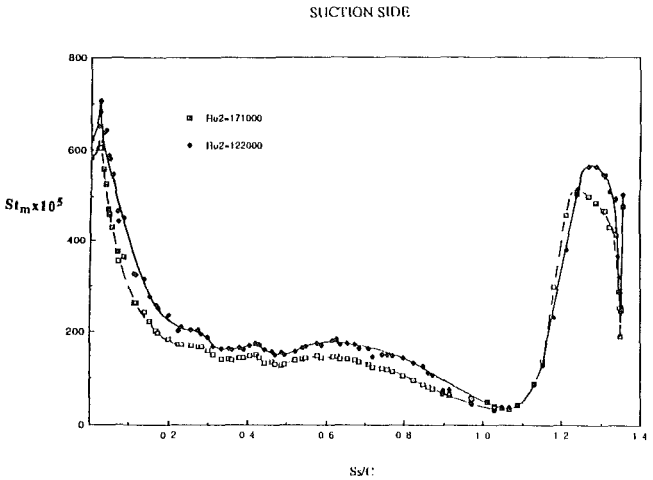

Fig. 10 A comparison of curvilinear distribution of the average mass transfer Stanton number on the suction surface between two different Reynolds numbers

surface, the flow is relatively simple. At the endwall/pressure-side corner, a pressure side corner vortex (V_{pc}) is formed due to the downflow on the pressure surface.

To help in identifying distinct regions affected by the secondary flows over the suction surface, Fig. 8 shows both the separation line and the reattachment line of the secondary flows. The path of these lines is determined from the mass transfer results. It has been reported that a low transfer rate is associated with the separation of the boundary layer and a high transfer rate with the reattachment of the flow (e.g., Consigny and Richards, 1982). As shown in Fig. 8, areas of interest are labeled A through G, interpreted from the mass transfer results in later sections, and the reattachment and separation lines of the flow are denoted by R and S, respectively. The separation lines (S_{Vsh} and S_{Vp}) indicate the evolution of the suction side horseshoe vortex and the passage vortex on the suction surface. Between these two separation lines, a reattachment line, R_{Vsh}/R_{Vp}, is observed (cf. Hodson and Dominy, 1987a). As the suction side horseshoe vortex moves toward the trailing edge, it encounters the two-dimensional separation bubble, which is defined by the lines S_{2D} and R_{2D}. The reattachment lines (R_{Vsc1} and R_{Vsc2}) associated with the suction side corner vortices are also shown.

Leading Edge Mass Transfer on a Turbine Blade. Figure 9 shows the blade stagnation Nusselt number in the two-dimensional flow region as a function of the Reynolds number, Re_d. Values of the Nusselt number from the present measurement are determined from the Sherwood number using the empirical correlation (Eq. 9) with $\mathrm{Pr}=0.7$ and $\mathrm{Sc}=2.04$. It should be noted that some recent (as yet unpublished) studies indicate a somewhat higher value of Sc.

The present measured results are compared, on Fig. 9, to two correlations for heat transfer from a circular cylinder in a cross flow from Kestin and Wood (1971) and Lowery and Vachon (1975). The values from these two correlations are calculated at $Tu=1.31$ percent, which is the turbulence level in the present study. Data points also include heat transfer results from Consigny and Richards's (1982) study for $Tu=0.8$ percent and mass transfer results from Goldstein and Karni's (1984) study for $Tu=0.43$ percent. These measured results are about 8 percent lower than values predicted by the Kestin and Wood (1971) correlation.

Mass Transfer Results in the Two-Dimensional Region. Figure 10 provides a comparison of the variation of the mass transfer Stanton number for two exit Reynolds numbers, 171,000 and 122,000. Although the values of mass transfer Stanton number are higher at smaller exit Reynolds number, the general trends of the mass transfer distribution is similar for the two flows. It is interesting to note, as shown in Fig. 10, that the maximum mass transfer does not occur at the stagnation line. This is also observed for flows over a heated ellipse (Ota et al., 1983) and in a study of the heat transfer over a turbine blade with an elliptic leading edge (Arts and Graham, 1985).

After the mass transfer reaches the peak value at $S_s/C\approx 0.01$, it drops off rapidly. This sharp drop ends approximately at $S_s/C\approx 0.27$; after that a varying mass transfer distribution, with two modest local peaks, at $S_s/C\approx 0.42$ and $S_s/C\approx 0.62$, is observed. The variation in curvature and the resulting pressure gradient along the suction surface apparently have a significant effect on the mass transfer distribution. At $S_s/C\approx 1.08$, the mass transfer rate reaches a minimum, probably due to laminar separation. The rapid increase of the mass transfer in the region from $S_s/C\approx 1.08$ to 1.18, after the separation, may indicate a progression through transition and reattachment. The exact location of the onset of transition within the laminar separation bubble cannot be determined from the mass transfer distribution.

Following reattachment, the mass transfer rate falls sharply. In the trailing edge zone, a rapid increase in the mass transfer

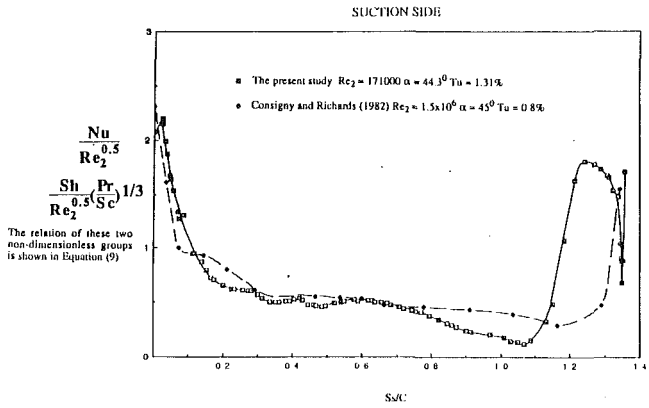

Fig. 11 A comparison of curvilinear distribution of the average Nusselt number on the suction surface between the present study and the study by Consigny and Richards (1982)

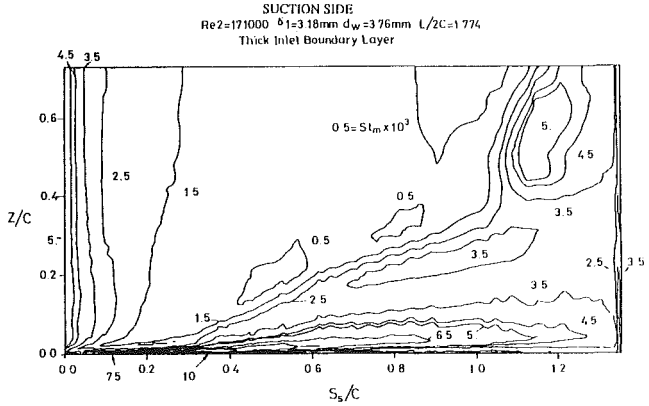

Fig. 12 Suction surface Stanton number contours for case 3 (see Table 3)

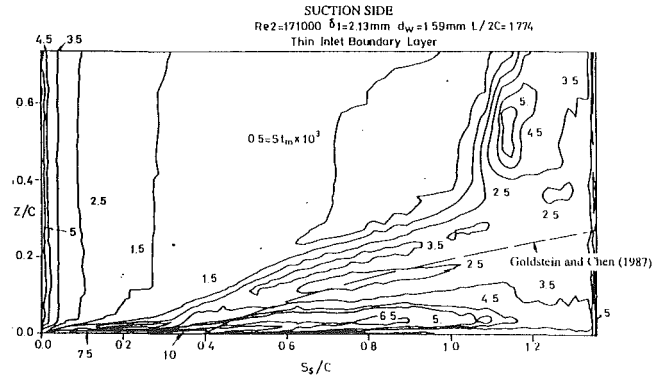

Fig. 13 Suction surface Stanton number contours for case 1 (see Table 3)

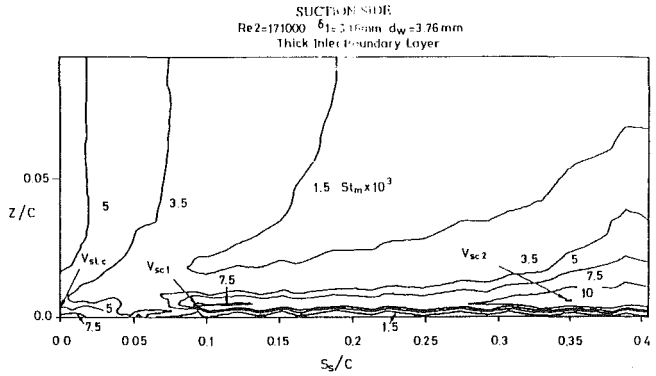

Fig. 14 Enlargement of Fig. 12 in the leading edge region near the endwall

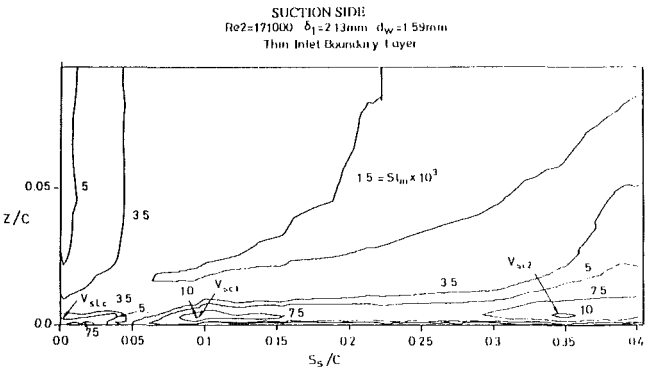

Fig. 15 Enlargement of Fig. 13 in the leading edge region near the endwall

rate to a value slightly less than that in the leading edge region is observed. The high transport rate is probably due to the vortices shed from the trailing edge. This implies that an effective cooling system must be applied in this region. A comparison with a heat transfer study by Consigny and Richards (1982) is presented in Fig. 11. Their exit Reynolds number 1.5×10^6 is much higher than Re_2 of the present study. The equivalent values of Nusselt number for the present study are evaluated from the Sherwood number using Eq. (9); $Nu/Re_2^{0.5}$ is plotted to allow a more reasonable comparison.

From Fig. 11, it is clear that the present technique is capable of showing more detail in the transport coefficient variation than a typical heat transfer experiment. Although the blade geometry is quite different in the two studies, the results of Consigny and Richards (1982) are qualitatively similar to those of the present work.

Mass Transfer Results in the Three-Dimensional Region. The influence of the endwall on the mass transfer rate along the suction surface is significant. The measurements are conducted at two values of the displacement thickness with the same free-stream velocity. The inlet displacement thickness, δ_1, is 3.18 mm and 2.13 mm for the "thick" and the "thin" boundary layers, respectively.

Stanton number contours for the two displacement boundary layer thicknesses are presented in Figs. 12 and 13, respectively. The difference between both contour plots is small. This indicates little influence of boundary-layer thickness on the blade mass transfer over the range studied. Enlargements of Figs. 12 and 13 in the region from $S_s/C = 0.0$ to 0.4 near the endwall are presented in Figs. 14 and 15, respectively.

Figures 12 and 13 show the strong three-dimensional flow field greatly influences the suction surface mass transfer except in the leading edge region, where three dimensionality is confined to a narrow region very close to the endwall. Near the stagnation line of a circular cylinder, Goldstein and Karni (1984) also observed that the horseshoe vortices only affect the mass transfer in the region very close to the endwall. Complex mass transfer patterns are observed and mass transfer levels are higher than two-dimensional values. In the region from $S_s/C \approx 0.9$ to the trailing edge ($S_s/C = 1.355$), the flow is essentially three dimensional over the whole measurement region ($Z/C < 0.77$).

The variation in mass transfer results is closely related to limiting streamline pattern, shown in Fig. 8. When the suction side horseshoe vortex lifts off the endwall as it moves toward the trailing edge, its separation line (S_{Vsh}), shown in Fig. 8,

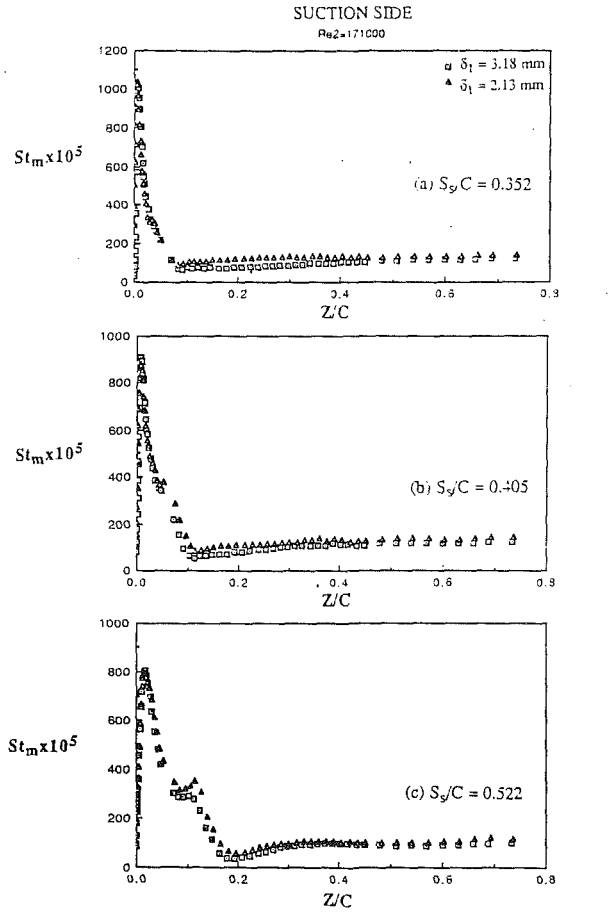

Fig. 16 A comparison of spanwise distribution of local Stanton number on the suction surface at selected curvilinear locations between cases of two different displacement thicknesses

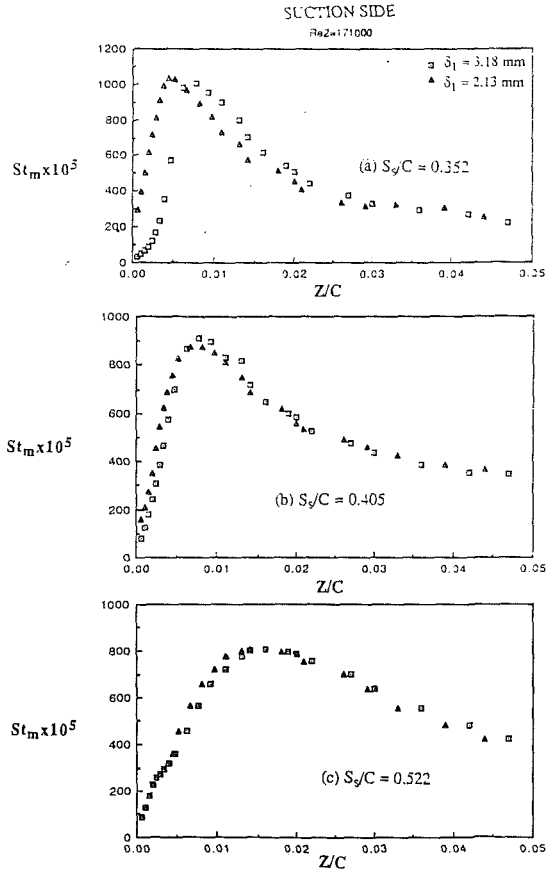

Fig. 17 Enlargement of Fig. 16 in the region near the endwall

can be traced approximately as a diagonal line, with a St_m of 0.0015 in the contour plots (Figs. 12 and 13). Underneath this diagonal line, the value of St_m increases from 0.0015 to 0.0035 along the spanwise direction (Z) and this increase is due to the reattachment line, R_{Vsh}/R_{Vp}, in Region A.

When the passage vortex moves away from the wall and travels toward the trailing edge, the separation line of the passage vortex (S_{Vp}) creates an area of low mass transfer with a Stanton number of 0.0025, shown in Fig. 12. Near the endwall, the contour lines are packed within a narrow region from the wall and most of them cannot be distinguished. This indicates the presence of larger gradients in the Stanton number occurring in this region, a result of the intense suction side leading edge corner vortex and the suction side corner vortices. The strip with $St_m = 0.0065$ is due to the effect of the reattachment line (R_{Vsc2}). Along the curvilinear direction (S_s) and farther away from the wall ($Z/C \approx 0.6$), the mass transfer drops sharply from $St_m = 0.005$ at the leading edge to 0.0005 at $S_s/C \approx 1.0$. The low mass transfer zone, Region B, is a result of the laminar separation. Farther downstream, the mass transfer increases up to a value of $St = 0.005$, indicating the reattachment of the boundary-layer flow (Region C). Downstream of the reattachment, the decrease in the mass transfer is expected as the boundary-layer flow becomes fully turbulent; and finally the mass transfer rate increases again up to a value of $St_m = 0.0035$ in the trailing edge region (Region D).

The dashed line, shown in Fig. 13, is the upper boundary of the unprotected region in which the coolant ejected from two rows of cooling holes located at $S_s/C \approx 0.208$ and 0.243 is absent as found by Goldstein and Chen (1987). Their conclusion that this unprotected region is due to the presence of the passage vortex is confirmed by the present mass transfer results measured in the same cascade. Figure 13 reveals that the dashed line passes through a low mass transfer zone with a value of $St_m = 0.0025$, which is caused by the separation line of the passage vortex.

Three peaks with values of $St_m = 0.0075$ or 0.01 can be seen in both Figs. 14 and 15. These peaks indicate the inception points of the leading edge corner vortex (at $S_s/C = 0.0$ (Region E)), the suction side corner vortex 1 (V_{sc1} at $S_s/C = 0.095$ (Region F)) and the suction side corner vortex 2 (V_{sc2} at $S_s/C = 0.35$ (Region G)). When the suction side horseshoe vortex moves away from the endwall at S_1 (see Fig. 7), it creates a low mass transfer zone between two contour lines with a value of $St_m = 0.0035$ near $Z/C \approx 0.005$ and $S_s/C \approx 0.05$, shown in Figs. 14 and 15. The suction side corner vortex 1 is formed as a result of the high angle of attack of the surface streamlines onto the suction surface (Hodson and Dominy, 1987a) and originates near the point where the suction side horseshoe vortex meets the suction surface. When the boundary-layer flow on the endwall of the blade passage is driven by the pressure gradient from the pressure surface toward the suction surface, the suction side corner vortex V_{sc2} is formed by both the separation of the boundary-layer flow near the suction surface and the high angle of attack of the passage vortex. This suction side corner vortex originates near the point S_2 (see Fig. 7) where the passage vortex encounters the suction surface.

Figure 16 shows the spanwise Stanton number distributions at three different values of S_s. Enlargements of Fig. 16 for locations near the endwall are presented at Fig. 17. In general, major trends of the Stanton number to both boundary layer cases are close enough that the St_m peaks occur at approximately the same values of Z/C. The dominant peak with

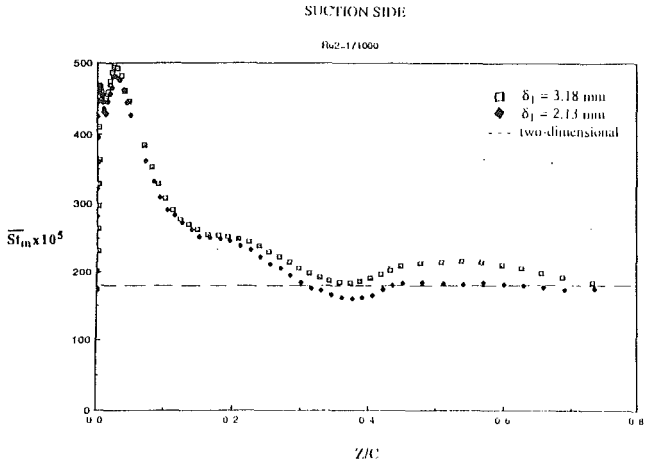

Fig. 18 *A comparison of spanwise distribution of the average mass transfer Stanton number on the suction surface between cases of two different displacement thicknesses*

$St_m \approx 0.01$ (Fig. 17(*a*)) is the highest on the suction surface. This peak is a result of the intense suction side corner vortex V_{sc2}. At the larger δ_1 studied, the dominant peak is slightly farther from the endwall. Figure 16(*c*) shows the secondary peak ($St_m \approx 0.0036$) at $Z/C \approx 0.12$ for large S_s/C; this is a result of the reattachment line (R_{Vsh}/R_{Vp}) between S_{Vp} and S_{Vsh}.

Figure 18 shows the spanwise variation of the curvilinear average (along curvilinear, S_s, direction) Stanton number over the whole chord from $S_s/C = 0$ to $S_s/C = 1.355$ at two different inlet boundary layer thicknesses. The average Stanton number from measured data points in the two-dimensional region is shown as the dashed line (it is independent of δ_1). The mass transfer rate is higher for the thicker boundary layer except in the region very close to the endwall. The average mass transfer rate ($\overline{St_m}$) near the endwall is much larger than that in the two-dimensional flow region.

Conclusions

Mass transfer distributions over the suction surface on a simulated turbine blade have been measured. In the two-dimensional flow region, the mass transfer rate is high in both the leading edge and the trailing edge regions. Along the suction surface, a steep rise following a sharp decrease of the mass transfer distribution indicates that the boundary layer undergoes a laminar separation, transition, and reattachment due to an adverse pressure gradient. The onset of the two-dimensional separation at $S_s/C \approx 1.1$ is insensitive to a change of the exit Reynolds number from 122,000 to 171,000.

In the three-dimensional flow region near the endwall, extremely high mass transfer occurs on the suction surface. This results from the existence of intense corner vortices, the leading edge corner vortex and the suction side corner vortices. The inception point of a particular vortex of the secondary flows can be inferred from the peak of either the spanwise variation or the curvilinear variation in the mass transfer distribution. In addition, the secondary flows inside the blade passage are apparently of sufficient strength to prevent separation of the suction surface boundary layer near the endwall, though separation does occur in the two-dimensional region. Due to the secondary flows and the two-dimensional laminar separation, large variations of the mass transfer occur on the suction surface from a minimum St_m of 0.0005 to a maximum St_m of 0.01.

The spanwise variation of the average mass transfer Stanton number on the suction surface reveals that this average mass transfer rate in the region near the endwall can be several times larger than that in the two-dimensional flow region. An increase of the displacement thickness of the approaching endwall boundary layer from 2.13 mm to 3.18 mm only has a small effect on the mass transfer pattern on the suction surface. Generally speaking, the average mass transfer rate is higher for the case of the thick boundary layer because the region away from the endwall, affected by the secondary flow, is wider for the case of the thick boundary layer.

It should be borne in mind that many particulars of the secondary flows described herein are inferred from the mass transfer distribution. Although these appear quite plausible, confirmation should be sought from direct measurements of the flow in the passage of the cascade including further flow visualization.

Acknowledgments

Support for this work was provided by the U.S. Air Force Office of Scientific Research. The insightful comments of the reviewers were helpful in improving the final manuscript.

References

Abu-Ghannam, B. J., and Shaw, R., 1980, "Natural Transition of Boundary Layers—The Effects of Turbulence, Pressure Gradient, and Flow History," *J. of Mech. Engr. Sci.*, Vol. 22, No. 5, pp. 213–228.

Ambrose, D., Lawrenson, I. J., and Sprake, C. H. S., 1975, "The Vapour Pressure of Naphthalene," *J. Chem. Thermodynamics*, Vol. 7, pp. 1173–1176.

Arts, T., and Graham, C. G., 1985, "External Heat Transfer Study on a HP Turbine Rotor Blade," AGARD-CP-390, *Heat Transfer and Cooling in Gas Turbine*, pp. 5-1 to 5-6.

Bario, F., Leboeuf, F., and Papailiou, K. D., 1982, "Study of Secondary Flows in Blade Cascades of Turbomachines," ASME *Journal of Engineering for Power*, Vol. 104, pp. 497–509.

Bayley, F. J., and Priddy, W. J., 1981, "Effects of Free-Stream Turbulence Intensity and Frequency on Heat Transfer to Turbine Blading," ASME *Journal of Engineering for Power*, Vol. 103, pp. 60–64.

Blair, M. F., 1974, "An Experimental Study of Endwall and Airfoil Surface Heat Transfer in a Large-Scale Turbine Blade Cascade," ASME *Journal of Heat Transfer*, Vol. 96, pp. 524–529.

Caldwell, L., 1984, "Diffusion Coefficient of Naphthalene in Air and Hydrogen," *J. Chem. Eng. Data*, Vol. 29, pp. 60–62.

Chen, N. H., and Othmer, D. F., 1962, "New Generalized Equation for Gas Diffusion Coefficient," *J. Chem. Eng. Data*, Vol. 7, No. 1, pp. 37–41.

Chen, P. H., 1988, "Measurement of Local Mass Transfer From a Gas Turbine Blade," Ph.D. Dissertation, U. of Minnesota, Minneapolis, MN.

Chen, P. H., and Goldstein, R. J., 1988, "Convective Transport Phenomena on a Turbine Blade," *Proceedings of the 3rd International Symposium on Transport Phenomena in Thermal Control*, Taipei; 1989, *Transport Phenomena in Thermal Control*, G.-J. Hwang, ed., Hemisphere Publishing Corporation, New York, pp. 267–293.

Consigny, H., and Richards, B. E., 1982, "Short Duration Measurements of Heat Transfer Rate to a Gas Turbine Rotor Blade," ASME *Journal of Engineering for Gas Turbines and Power*, Vol. 104, pp. 542–551.

Daniel, L. D., and Browne, W. B., 1981, "Calculation of Heat Transfer Rates to Gas Turbine Blades," *Int. J. Heat Mass Transfer*, Vol. 24, No. 5, pp. 871–879.

De Kruif, C. G., Kuipers, T., Van Miltenburg, J. C., Schaake, R. C. F., and Stevens, G., 1981, "The Vapour Pressure of Solid and Liquid Naphthalene," *J. Chem. Thermodynamics*, Vol. 13, pp. 1081–1086.

Dunn, M. G., and Stoddard, F. J., 1979, "Measurement of Heat-Transfer Rate to a Gas Turbine Stator," ASME *Journal of Engineering for Power*, Vol. 101, p. 275.

Dunn, M. G., and Hause, A., 1982, "Measurement of Heat Flux and Pressure in a Turbine Stage," ASME *Journal of Engineering for Power*, Vol. 104, pp. 215–223.

Dunn, M. G., Rae, W. J., and Holt, J. L., 1984a, "Measurement and Analyses of Heat Flux Data in a Turbine Stage: Part I—Description of Experimental Apparatus and Data Analysis," ASME *Journal of Engineering for Gas Turbines and Power*, Vol. 106, pp. 229–233.

Dunn, M. G., Rae, W. J., and Holt, J. L., 1984b, "Measurement and Analyses of Heat Flux Data in a Turbine Stage: Part II—Discussion of Results and Comparisons With Predictions," ASME *Journal of Engineering for Gas Turbines and Power*, Vol. 106, pp. 234–240.

Dyban, Ye.P., and Glushchenko, V. G., 1975, "Effect of the Mach Number Temperature Factor on Heat Transfer From a Gas to a Turbine Blade," *HEAT TRANSFER—Soviet Research*, Vol. 7, No. 2, pp. 17–21.

Dyban, Ye.P., 1982, "Heat Transfer in High-Temperature Gas Turbine," *HEAT TRANSFER—Soviet Research*, Vol. 14, No. 4, pp. 90–106.

Eckert, E. R. G., 1976, "Analogies to Heat Transfer Processes," *Measurement*

in Heat Transfer, E. R. G. Eckert and R. J. Goldstein, eds., Hemisphere Publishing, New York.

Fowler, C. E., Trump, W. N., and Vogler, C. E., 1968, "Vapor Pressure of Naphthalene: New Measurements Between 40° and 180°C," *J. Chem. Eng. Data*, Vol. 13, No. 2, pp. 209–210.

Goldstein, R. J., and Karni, J., 1984, "The Effect of a Wall Boundary Layer on Local Mass Transfer From a Cylinder in Crossflow," ASME *Journal of Heat Transfer*, Vol. 106, pp. 260–267.

Goldstein, R. J., and Chen, P. H., 1987, "Film Cooling on a Turbine Blade With Injection Through Two Rows of Holes in the Near-End-Wall Region," ASME JOURNAL OF TURBOMACHINERY, Vol. 109, pp. 588–593.

Goldstein, R. J., and Spores, R. A., 1988, "Turbulent Transport on the Endwall in the Region Between Adjacent Turbines Blades," ASME *Journal of Heat Transfer*, Vol. 110, pp. 862–869.

Graham, R. W., 1979, "Fundamental Mechanisms That Influence the Estimate of Heat Transfer to Gas Turbine Blades," ASME Paper No. 79-HT-43.

Graziani, R. A., Blair, M. F., Taylor, J. R., and Mayle, R. E., 1980, "An Experimental Study of Endwall and Airfoil Surface Heat Transfer in a Large Scale Turbine Blade Cascade," ASME *Journal of Engineering for Power*, Vol. 102, pp. 257–267.

Guenette, G. R., Epstein, A. H., Giles, M. B., Haimes, R., and Norton, R. J. G., 1989, "Fully Scaled Transonic Turbine Rotor Heat Transfer Measurements," ASME JOURNAL OF TURBOMACHINERY, Vol. 111, pp. 1–7.

Hippensteele, S. A., Russell, L. M., and Torres, F. J., 1985, "Local Heat-Transfer Measurements on a Large Scale-Model Turbine Blade Airfoil Using a Composite of a Heat Element and Liquid Crystals," ASME *Journal of Engineering for Gas Turbines and Power*, Vol. 107, pp. 953–960.

Hippensteele, S. A., Russell, L. M., and Torres, F. J., 1987, "Use of a Liquid-Crystal, Heater-Element Composite for Quantitative, High-Resolution Heat Transfer Coefficients on a Turbine Airfoil, Including Turbulence and Surface Roughness Effects," NASA-TM-87355, Washington.

Hodson, H. P., and Dominy, R. G., 1987a, "Three-Dimensional Flow in a Low-Pressure Turbine Cascade at Its Design Condition," ASME JOURNAL OF TURBOMACHINERY, Vol. 109, pp. 201–209.

Hodson, H. P., and Dominy, R. G., 1987b, "The Off-Design Performance of a Low-Pressure Turbine Cascade," ASME JOURNAL OF TURBOMACHINERY, Vol. 109, pp. 201–209.

Hoheisel, H., Kiock, R., Lichtfuss, H. J., and Fottner, L., 1987, "Influence of Free-Stream Turbulence and Blade Pressure Gradient on Boundary Layer and Loss Behavior of Turbine Cascades," ASME JOURNAL OF TURBOMACHINERY, Vol. 109, pp. 210–219.

Ito, S., Goldstein, R. J., and Eckert, E. R. G., 1978, "Film Cooling of a Gas Turbine Blade," ASME *Journal of Engineering for Power*, Vol. 100, pp. 476–480.

Kan, S., Miwa, K., Morishita, T., Munakata, Y., and Nomura, M., 1971, "Heat Transfer of a Turbine Blade," *Tokyo Joint Int. Gas Turbine Conference and Products Show*, JSME-30.

Kestin, J., and Wood, R. T., 1971, "The Influence of Turbulence on Mass Transfer From Cylinders," ASME *Journal of Heat Transfer*, Vol. 93, pp. 321–327.

Kline, S. J., and McClintock, F. A., 1953, "Describing Uncertainty in Single-Sample Experiments," *Mechanical Engineering*, Vol. 75, pp. 3–8.

Lowery, G. W., and Vachon, R. I., 1975, "The Effect of Turbulence on Heat Transfer From Heated Cylinder," *Int. J. Heat Mass Transfer*, Vol. 18, pp. 1229–1242.

Mack, E., Jr., 1925, "Average Cross-Section Areas of Molecules by Gaseous Diffusion Methods," *J. Am. Chem. Soc.*, Vol. 47, p. 2468.

Martin, B. W., Brown, A, and Garrett, S. E., 1978, "Heat Transfer to a PVD Rotor Blade at High Subsonic Passage Throat Mach Numbers," *Proc. Inst. Mech. Engr.*, Vol. 192, pp. 225–233.

Mukherjee, D. K., 1979, "Determination of Heat Transfer Coefficients Around a Blade Surface From Temperature Measurements," ASME Paper No. 79-GT-28.

Nealy, D. A., Mihelc, M. S., Hylton, L. D., and Gladden, H. J., 1984, "Measurements of Heat Transfer Distribution Over the Surfaces of Highly Loaded Turbine Nozzle Guide Vanes," ASME *Journal of Engineering for Gas Turbines and Power*, Vol. 106, pp. 149–158.

Nicholson, J. H., Forest, A. E., Oldfield, M. L. G., and Schultz, D. L., 1984, "Heat Transfer Optimized Turbine Rotor Blades—An Experimental Study Using Transient Techniques," ASME *Journal of Engineering for Gas Turbines and Power*, Vol. 106, pp. 173–182.

Ota, T., Aiba, S., Tsuruta, T., and Kaga, M., 1983, "Forced Convection Heat Transfer From an Elliptic Cylinder of Axis Ratio 1:2," *Bull. of the JSME*, Vol. 26, No. 212, pp. 262–267.

Priddy, W. J., and Bayley, F. J., 1985, "Effects of Free-Stream Turbulence on the Distribution of Heat Transfer Around Turbine Blade Sections," *Int. J. Heat and Fluid Flow*, Vol. 6, No. 3, pp. 181–192.

Sato, T., and Takeishi, K., 1987, "Investigation of the Heat Transfer in High Temperature Gas Turbine Vanes," ASME Paper No. 87-GT-137.

Sato, T., Aoki, S., Takeishi, K., and Matsuura, M., 1987, "Effect of Three-Dimensional Flow Field on Heat Transfer Problems of a Low Aspect Ratio Turbine Nozzle," presented at the 1987 Tokyo International Gas Turbine Congress, 87-TOKYO-IGTC-59.

Sharma, O. P., and Butler, T. L., 1987, "Predictions of Endwall Losses and Secondary Flows in Axial Flow Turbine Cascades," ASME JOURNAL OF TURBOMACHINERY, Vol. 109, pp. 229–236.

Sieverding, C. H., and Van Den Bosche, P., 1983, "The Use of Coloured Smoke to Visualize Secondary Flows in a Turbine-Blade Cascade," *J. of Fluid Mech.*, Vol. 134, pp. 85–89.

Sieverding, C. H., 1985, "Recent Progress in the Understanding of Basic Aspects of Secondary Flows in Turbine Blade Passages," ASME *Journal of Engineering for Gas Turbines and Power*, Vol. 107, pp. 248–257.

Smith, A. G., 1948, "Heat Flow in the Gas Turbine," *Proc. Inst. Mech. Engr.*, Vol. 159, pp. 245–254.

Sonoda, T., 1985, "Experimental Investigation on Spatial Development of Streamwise Vortices in a Turbine Inlet Guide Vane Cascade," ASME Paper No. 85-GT-20.

Taylor, J. R., 1980, "Heat Transfer Phenomena in Gas Turbines," ASME Paper No. 80-GT-172.

Turner, A. B., 1971, "Local Heat Transfer Measurements on a Gas Turbine Blade," *J. Mech. Eng. Sci.*, Vol. 103, No. 1, pp. 1–12.

Turner, A. B., Tarada, F. H. A., and Bayley, F. J., 1985, "Effect of Surface Roughness on Heat Transfer to Gas Turbine Blades," AGARD-CP-390, *Heat Transfer and Cooling in Gas Turbines*, pp. 9-1 to 9-10.

Van Ekeren, P. J., Jacobs, M. H. G., Offringa, J. C. A., and De Kruif, C. G., 1983, "Vapor-Pressure Measurements on Transdiphenylethene and Naphthalene Using a Spinning-Rotor Friction Gauge," *J. Chem. Thermodynamics*, Vol. 15, pp. 409–417.

Walker, L. A., and Markland, E., 1965, "Heat Transfer to Turbine Blading in the Presence of Secondary Flow," *Int. J. Heat Mass Transfer*, Vol. 8, pp. 729–748.

Wang, J. H., Jen, H. F., and Hartel, E. O., 1985, "Airfoil Heat Transfer Calculation Using a Low Reynolds Number Version of a Two-Equation Turbulence Model," ASME *Journal of Engineering for Gas Turbines and Power*, Vol. 107, pp. 60–67.

Wilson, D. G., and Pope, J. A., 1954, "Convective Heat Transfer to Gas Turbine Blade Surfaces," *Proc. Inst. Mech. Engr.*, Vol. 168, pp. 861–874.

Winstanley, D. K., Booth, T. C., and Dunn, M. G., 1981, "The Predictability of Turbine Vane Convection Heat Transfer," AIAA Paper No. AIAA-81-1435.

Yamamoto, A., 1987, "Production and Development of Secondary Flows and Losses in Two Types of Straight Turbine Cascades: Part 1—A Stator Case," ASME JOURNAL OF TURBOMACHINERY, Vol. 109, pp. 186–200.

Yamamoto, A., and Nouse, H., 1988, "Effects of Incidence on Three-Dimensional Flows in a Linear Turbine Cascade," ASME JOURNAL OF TURBOMACHINERY, Vol. 110, pp. 486–496.

York, R. E., Hylton, L. D., Fox, R. G., Jr., and Simonich, J. C., 1979, "An Experimental Investigation of the Heat Transfer to a Turbine Vane at Simulated Engine Conditions," ASME Paper No. 79-GT-23.

R. P. Taylor

J. K. Taylor

Thermal & Fluid Dynamics Laboratory,
Mechanical and Nuclear Engineering,
Mississippi State University,
Mississippi State, MS 39762

H. H. Hosni

Department of Mechanical Engineering,
Kansas State University,
Manhattan, KS 66506-5106

H. W. Coleman

Thermal and Fluid Dynamics Laboratory,
Mechanical and Nuclear Engineering,
Mississippi State University,
Mississippi State, MS 39762

Heat Transfer in the Turbulent Boundary Layer With a Step Change in Surface Roughness

Measurements of Stanton numbers, velocity profiles, temperature profiles, and turbulence intensity profiles are reported for turbulent flat plate boundary layer flows with a step change in surface roughness. The first 0.9 m length of the test surface is roughened with 1.27-mm-dia hemispheres spaced 2 base diameters apart in a staggered array. The remaining 1.5 m length is smooth. The experiments show that the step change from a rough to a smooth surface has a dramatic effect on the convective heat transfer. In many cases, the Stanton number drops below the smooth-wall correlation immediately downstream of the change in roughness. The Stanton number measurements are compared with predictions using the discrete element method with excellent results.

Introduction

In this paper, the effects of a step change in surface roughness on heat transfer and fluid flow in the turbulent boundary layer are investigated experimentally. The primary motivation for the work reported here is to gain insight into the use of smooth heat flux gages to measure the external heat transfer rate on otherwise rough gas turbine engine blades. Taylor (1990) measured and statistically classified the surface roughness on a number of first-stage in-service turbine blades from TF-39 and F-100 aeroengines. He found the blades to be very rough and to have a wide range in both height and character of the roughness at different points around the blades. The average roughness ranged from about 10 μm to about 1.5 μm. This is very rough considering that the thickness of the boundary layer is on the order of 1 mm. In a related work, Taylor (1989) reported roughness measurements on the Space Shuttle Main Engine (SSME) fuel-pump turbine blades. He found that the blades had rms roughness heights on the order of 15 μm, which resulted in a computed Stanton number increase of about 100 percent in the nominally 0.5-mm-thick boundary layer. Tests on these engine components are often conducted by installing small (about 1 mm in diameter) heat flux gages. These gages are usually much smoother than the surrounding rough surface.

Flows with step changes in roughness are also important in such applications as the land–sea interface and mountain ranges. Therefore, there is a large body of both theoretical and experimental work that is concerned with step changes in surface roughness in the planetary boundary layer. Good reviews of the literature on this subject are given by Tani (1968) and Smits and Wood (1985).

Important early experimental work on this subject was done in fully developed channel flows by Jacobs (1939). One of the most comprehensive data sets was presented for zero pressure gradient boundary layer flows by Antonia and Luxton (1971a, 1972). They presented extensive velocity and turbulent measurements for both smooth-to-rough and rough-to-smooth step changes in surface roughness. They used rib-roughened surfaces where the rib crests on the rough part of the surface were aligned with the smooth section of the surface. Antonia and Luxton (1971b) reported similar experiments where the test surface consisted of a smooth section followed by a rib-roughened section with the bases of the ribs aligned with the smooth surface. This resulted in a smooth-to-rough transition with an upstanding roughness. Schofield (1975) presented extensive flow measurements for step changes in surface roughness with adverse pressure gradient. Andreopoulos and Wood (1982) reported extensive measurements of velocity profiles, turbulence quantities, and skin friction distribution for flow over a smooth surface that was roughened in one narrow strip at about midplate using sandpaper. Their experiments modeled the effect of an impulse of roughness on the boundary layer flow.

Important theoretical contributions were made by Townsend (1965), who developed a theory for velocity and temperature profile development in the internal layer that develops after a step change in surface condition. Prediction methods based on numerical solutions of the boundary layer equations have been presented by Antonia and Wood (1975) and Andreopoulos and Wood (1982).

Contributed by the International Gas Turbine Institute and presented at the 36th International Gas Turbine and Aeroengine Congress and Exposition, Orlando, Florida, June 3-6, 1991. Manuscript received at ASME Headquarters March 4, 1991. Paper No. 91-GT-266. Associate Technical Editor: L. A. Riekert.

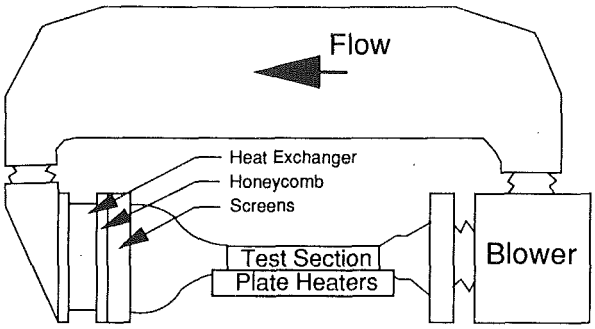

Fig. 1 Schematic diagram of the Turbulent Heat Transfer Test Facility (THTTF)

In this paper a set of heat transfer experiments are discussed where the test surface is composed of a rough section followed by a smooth section (a rough-to-smooth transition). The results of the experiments are compared with the results of boundary layer computations using the discrete element prediction method. In the following, the experimental apparatus and measurement procedures, the discrete element prediction method, and the results of the experiments and computations are presented and discussed.

Experimental Apparatus and Measurement Procedures

The experiments were performed in the Turbulent Heat Transfer Test Facility (THTTF), which is shown in Fig. 1. Complete descriptions of the facility and its qualification are presented by Coleman et al. (1988). This facility is a closed-loop wind tunnel with a free-stream velocity range of 6 to 67 m/s. The temperature of the circulating air is controlled with an air-to-water heat exchanger and a cooling water loop. Following the heat exchanger, the air flow is conditioned by a system of honeycomb and screens.

The bottom wall of the nominally 2.4 m long by 0.5 m wide by 0.1 m high test section consists of 24 electrically heated flat plates, which are abutted together to form a continuous flat surface. Each nickel-plated aluminum plate (about 10 mm thick by 0.1 m in the flow direction) is uniformly heated from below by a custom-manufactured rubber-encased electric heater pad. Design computations showed that, with this configuration, a plate can be considered to be an a uniform temperature.

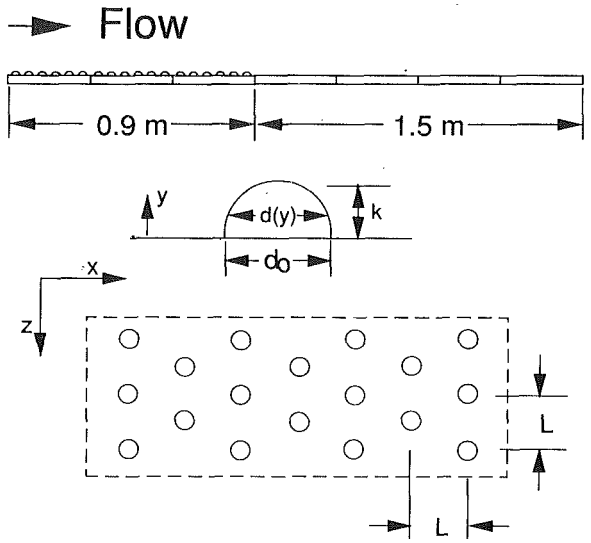

Fig. 2 Schematic diagram of the test surface and the roughness element layout

Figure 2 shows a schematic diagram for the test surface used in these experiments. The first 0.9 m of the test section surface was roughened with 1.27-mm-diameter hemispheres, and the remaining 1.5 m length was smooth. The roughness elements were spaced 2 base diameters apart in a staggered array as shown in the figure.

The measured average surface roughness on the "smooth" wall portion of the plates is less than 1.6 μm, and the allowable step (or mismatch) between any two plates is 0.013 mm. The

Nomenclature

A = plate plan surface area
C_D = roughness element drag coefficient
C_f = skin friction coefficient
C_p = specific heat
$d(y)$ = local roughness element diameter
H = enthalpy
H_0 = total enthalpy
k = roughness element height
K = thermal conductivity
L = roughness element spacing
l_m = mixing length
Nu_d = roughness element Nusselt number
P = pressure
Pr = Prandtl number
Pr_t = turbulent Prandtl number
q_c = conductive heat loss rate
q_r = radiative heat loss rate
r = recovery factor
Re_d = Reynolds number based on local roughness element diameter
Re_x = x-Reynolds number
St = Stanton number
T = local fluid static temperature
T_0 = free-stream total temperature
T_r = free-stream recovery temperature
T_R = roughness element temperature
T_{rail} = side rail temperature
T_w = wall temperature
$(UA)_{\mathrm{eff}}$ = overall conductance for q_c calculation
u = mean longitudinal velocity
$\overline{u'^2}$ = turbulent intensity factor
$\overline{u'v'}$ = Reynolds shear stress factor
U_∞ = free-stream velocity
v = mean normal velocity
$\overline{v'h'}$ = turbulent heat flux factor
w = plate width in flow direction
W = plate heater power
x = axial distance from nozzle exit
x_0 = lag model parameter
x_c = turbulent transition model parameter
y = coordinate normal to the wall
β_x = blockage factor
β_y = blockage factor
δ = boundary layer thickness
δ_0 = lag model parameter
Δ = thermal boundary layer thickness
ϵ = plate surface emissivity
η = lag model parameter
λ = lag model parameter
μ = dynamic viscosity
μ_t = turbulent eddy viscosity
μ_{t0} = lag model parameter
μ_{te} = lag model parameter
ν = kinematic viscosity
ρ = density
σ = Stefan–Boltzmann constant

heating system is under active computer control and any desired set of plate temperatures can be maintained within the limits of the power supply. To minimize the conduction losses, the side rails that support the plates are heated to approximately the same temperature as the plates.

The top wall can be adjusted to maintain a constant free-stream velocity. An inclined water manometer with resolution of 0.06 mm is used to measure the pressure gradient during top wall adjustment. Static pressure taps are located in the side wall adjacent to each plate. The pressure tap located at the second plate is used as a reference, and the pressure difference between it and each other tap is minimized. For example, the maximum pressure difference for the 43 m/s case was 0.30 mm of water.

The boundary layer is tripped at the exit of the 19:1 area ratio nozzle with a 1 mm × 12 mm wooden strip. This trip location is immediately in front of the heated surface.

Before proceeding with rough surface testing with the THTTF, a series of qualification tests (Coleman et al., 1988) were performed with a set of smooth test plates to insure the fitness of the test rig and the correctness of the instrumentation, data acquisition system, and data reduction procedures. Measurements in the nozzle exit plane showed the mean velocity to be uniform within about 0.5 percent and the free-stream turbulence intensity to be less than 0.3 percent. Measurements 1.1 m downstream of the nozzle exit showed the spanwise variation of momentum thickness to be less than ±5 percent. Profiles of mean temperature and velocity were in good agreement with the usual "laws of the wall." Stanton number data for the constant wall temperature cases were in excellent agreement with the data of Reynolds et al. (1958), which is the definitive data set on which the usual Stanton number correlations are based. The THTTF smooth wall data fall within the data scatter of this definitive data set.

Stanton Number Determination. The data reduction expression for the experimentally determined Stanton number is

$$\mathrm{St}=\frac{W-(UA)_{\mathrm{eff}}(T_w-T_{\mathrm{rail}})-\sigma\epsilon A(T_w^4-T_r^4)}{\rho C_p U_\infty A(T_w-T_o)} \tag{1}$$

The power, W, supplied to each plate heater is measured with a precision wattmeter. The radiation heat loss, q_r is estimated using a gray body enclosure model where the emissivity of the nickel-plated aluminum is estimated at $\epsilon = 0.11$. The conductive heat loss, q_c, is calculated using an experimentally determined effective plate conductance, $(UA)_{\mathrm{eff}}$, which includes both side rail and back losses. The conduction losses are minimized by actively heating the side rails. Both q_r/W and q_c/W are generally in the 0.5–1 percent range. The density and specific heat are determined from property data for moist air using the measured values of barometric pressure and wet and dry bulb temperatures in the tunnel. The free-stream velocity is measured using a Pitot probe and specially calibrated precision pressure transducers. The free-stream and plate temperatures are measured using specially calibrated thermistors. The free-stream total temperature, T_0, is computed using the measured free-stream recovery temperature, T_r and a recovery factor for the free-stream thermistor probe of $r = 0.86$ (Eckert and Goldstein, 1976). All fluid properties are evaluated at the free-stream static temperature.

The uncertainty in the experimentally determined Stanton number was estimated based on the ANSI/ASME Standard on Measurement Uncertainty (1986) following the procedures of Coleman and Steele (1989). For the Stanton number data in this paper, the overall uncertainty, as discussed in detail by Coleman et al. (1988) and Hosni et al. (1989), ranged from about ±2 percent to ±5 percent, depending on flow conditions.

Profile Measurements. The profiles of mean velocity and longitudinal velocity fluctuation, $\overline{u'^2}$, were taken with a horizontal hot wire. At each measurement position, 100 instantaneous anemometer output voltage readings 0.01 second apart were taken and converted into velocities using a fourth-order least-squares calibration equation. The mean of the 1000 velocities was used as the mean velocity at that location, and the variance was taken as $\overline{u'^2}$. According to Coleman et al. (1988) the overall uncertainties are ±2 percent for u and ±5 percent for $\overline{u'^2}$.

The mean temperature profiles were measured using a specially calibrated, butt-welded, chromel-constantan thermocouple probe. The overall uncertainty in the temperature measurement with this probe is quoted by Coleman et al. to be ±0.08 °C.

Discrete Element Method

The two basic categories in which calculation efforts have fallen are (1) the equivalent sandgrain approach and (2) the discrete element approach. While both methods require experimental input, the equivalent sandgrain approach may require experimental data on the particular surface under consideration. On the other hand, the discrete element approach incorporates more basic physics of the process and uses a more generalized empirical input. It is therefore applicable to a broader spectrum of rough surfaces without requiring surface-specific experimental data. Since the discrete element approach is used for computations reported in this paper, an overview of this method is presented next.

The discrete element approach considers the mass, momentum, and energy transport processes on the collection of individual roughness elements and the smooth surface between the elements. The basic idea is to formulate a system of partial differential equations that describes the mass, momentum, and energy transport for the flow over, around, and between the roughness elements. In this method, the roughness effects are taken as an integral part of the flow problem and not (as with the equivalent sandgrain approach) as some ill-defined boundary condition.

The discrete element method used in this work is formulated for roughness elements with three-dimensional shapes (as opposed to transverse ribs) for which the element cross section can be approximated as circular at every height y. Thus, the geometric description of the roughness element, $d(y)$, is easily included in this prediction scheme.

The steady (Reynolds-averaged), two-dimensional turbulent boundary layer equations presented here are for flow over a rough surface with roughness elements of uniform shape and spacing as derived by Taylor et al. (1984, 1985). The equations are:

$$\frac{\partial}{\partial x}(\rho\beta_x u)+\frac{\partial}{\partial y}(\rho\beta_y v)=0 \tag{2}$$

$$\beta_x\rho u\frac{\partial u}{\partial x}+\beta_y\rho v\frac{\partial u}{\partial y}=-\frac{\partial}{\partial x}(\beta_x P)+\frac{\partial}{\partial y}\left[\beta_y\left(\mu\frac{\partial u}{\partial y}-\rho\overline{u'v'}\right)\right]-\frac{1}{2}\rho C_D d(y)\frac{u^2}{L^2} \tag{3}$$

$$\beta_x \rho u \frac{\partial H}{\partial x} + \beta_y \rho v \frac{\partial H}{\partial y} = \frac{\partial}{\partial y}\left[\beta_y\left(\frac{K}{C_p}\frac{\partial H}{\partial y} - \overline{\rho v' h'}\right)\right] + u\frac{\partial}{\partial x}(\beta_x P) + \beta_y \frac{\partial u}{\partial y}\left(\mu\frac{\partial u}{\partial y} - \overline{\rho u' v'}\right) + \frac{1}{2}\rho C_D \frac{d(y)}{L^2} u^3 + \pi \frac{K \mathrm{Nu}_d}{L^2}(T_R - T) \quad (4)$$

Empirical models for $-\overline{\rho u' v'}$, $-\overline{\rho v' h'}$, the roughness element drag coefficient $C_D(y)$, and the roughness element Nusselt number $\mathrm{Nu}_d(y)$ are necessary for closure.

The blockage parameters β_x and β_y and the element shape descriptor $d(y)$ require no empirical fluid mechanics input as they are determined solely from the geometry of the rough surface. Taylor et al. (1984) have shown for uniform three-dimensional roughness elements with circular cross section that

$$\beta_x = \beta_y = 1 - \frac{\pi d^2(y)}{4L^2} \quad (5)$$

where for $y > k$, $d(y) = 0$ and both β_x and β_y become identically 1.0.

The boundary conditions for the discrete element approach for rough wall flows are identical to those for smooth wall flows. The wall location ($y = 0$) is the smooth surface on which the roughness elements occur. At $y = 0$, $u = v = 0$ and $H = H_w$. As $y \to \infty$, $u \to U_\infty$ and $H \to H_\infty$.

The numerical solution of the discrete element equations is obtained by finite difference solution of the transformed equations in the computational plane. The transformation, finite difference scheme, and program structure are described by Taylor et al. (1984). The streamwise derivative is approximated with a first-order backward difference. The surface normal derivatives are replaced with second-order approximations, which allow the spacing between grid points to vary with distance from the wall. This allows a concentration of nodes near the wall and below the crests of the elements. In this stretched grid the ratio of any two adjacent mesh lengths is a constant.

The solution is by an iterative marching, implicit method. The solution is known at station i and is sought at station $i + 1$. The implicit difference equations result in a tridiagonal coefficient matrix whose inverse is known and can be expressed algebraically (often referred to as the Thomas algorithm). Since the equations are nonlinear, the system must be solved by iteration. A relaxation scheme is employed with a required residual < 0.01 percent.

The solutions were obtained on finer and finer grids until differences were less than 1 percent in computed values of C_f and St. In the transformed coordinates there were typically 120 grid points across the boundary layer with approximately 20–30 grid points below the crests of the elements. The streamwise grid spacing was typically 1 cm.

In addition, the codes were verified by comparisons with known solutions of smooth-wall laminar and turbulent flows.

The "wall shear stress" is defined as the sum of the shear and drag forces on the wall in the mean flow direction divided by the plan area of the wall. The corresponding skin friction coefficient is then

$$C_f = \frac{(\beta_y)_w \mu \frac{\partial u}{\partial y}\Big|_w + \frac{1}{2}\frac{1}{L^2}\int_0^k (\rho d C_D u^2)\, dy}{\frac{1}{2}\rho_\infty U_\infty^2} \quad (6)$$

and the Stanton number is

$$\mathrm{St} = \frac{-(\beta_y)_w \frac{K}{C_p}\frac{\partial H}{\partial y}\Big|_w + \frac{\pi}{L^2}\int_0^k [K \mathrm{Nu}_d (T_R - T)]\, dy}{\rho_\infty U_\infty (H_w - H_{0,\infty})} \quad (7)$$

In order to solve Eqs. (2), (3), and (4), turbulence models for $-\rho u' v'$ and $\rho v' h'$ and roughness models for C_D and Nu_d are required. Because of its proven predictive capability for attached boundary layer flows over smooth surfaces, the Prandtl mixing length model with van Driest damping and a constant turbulent Prandtl number (Kays and Crawford, 1980) is used for turbulence closure. Thus

$$-\overline{\rho u' v'} = \rho l_m^2 \left(\frac{\partial u}{\partial y}\right)\left|\frac{\partial u}{\partial y}\right| = \mu_t \frac{\partial u}{\partial y} \quad (8)$$

where

$$l_m = 0.40 y[1 - \exp(-y^+/26)]; \quad l_m < 0.09\delta$$
$$l_m = 0.09\delta; \text{ otherwise,} \quad (9)$$

and

$$-\overline{\rho v' h'} = \frac{\mu_t}{\mathrm{Pr}_t}\frac{\partial H}{\partial y} \quad (10)$$

where $\mathrm{Pr}_t = 0.9$. Transition from laminar to turbulent flow is modeled using a streamwise intermittency factor

$$\frac{\mu_{\mathrm{eff}}}{\mu_t} = 1 - e^{-3.61(x/x_c - 1)^2} \quad (11)$$

where x_c is the specified point at which transition begins.

After the surface changes abruptly from rough to smooth, the turbulence will not immediately take on the new equilibrium values for the smooth surface. The turbulent flow "remembers" the upstream history. The mixing length model presented above does not account for this effect. Here, a fairly crude fix is adopted by using a lag model downstream of the step in roughness. This was done by taking a weighted average of the predicted local eddy viscosity, μ_{te}, with the eddy viscosity at some upstream location

$$\mu_t = \mu_{t0}(1 - \eta) + \mu_{te}\eta \quad (12)$$

$$\eta = 1 - e^{-(x - x_0)/\lambda} \quad (13)$$

where $\lambda = 10\delta_0$ with δ_0 being the boundary layer thickness at x_0, which was located 0.02 m upstream of the interface between the surfaces. This idea was taken from a boundary layer shock wave interaction model of Shang et al. (1976).

The roughness element C_D and Nu_d models are formulated as functions of the local element Reynolds number $\mathrm{Re}_d = u(y)d(y)/\nu$, which includes roughness element size and shape information through $d(y)$. As discussed by Taylor et al. (1984), the C_D model that gave the best overall agreement with experimental data was

$$\log_{10}(C_D) = -0.125 \log_{10}(\mathrm{Re}_d) + 0.375 \quad (14)$$

This model has been tested for values of Re_d up to 25,000 (Taylor et al., 1984; Scaggs et al., 1988) using many data sets. In particular, Scaggs et al. used eleven different rough surfaces, nine of which had uniform roughness elements and two of which were roughened nonuniformly. It was demonstrated that the roughness element drag coefficient model in the discrete element prediction approach gave excellent agreement with all of these data sets. Consequently, this model was used unchanged for the predictions presented in this work.

The roughness element energy transport model requires empirical input in the form of a Nusselt number, Nu_d. Hosni et al. (1989) developed the model

$$\mathrm{Nu}_d = 1.7\, \mathrm{Re}_d^{0.49}\mathrm{Pr}^{0.4} \quad (15)$$

used in this work. The model has been tested up to Re_d of about 2200. All of the experiments reported in this article have local element Reynolds numbers, Re_d, that fall within the ranges of calibration listed above.

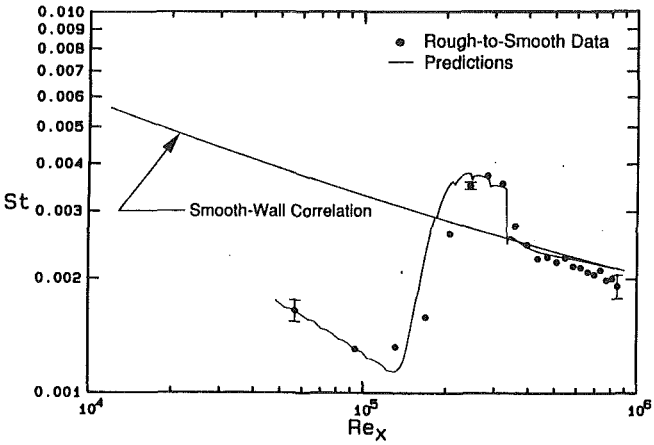

Fig. 3 Results of the Stanton number measurements and predictions for U_∞ = 6 m/s

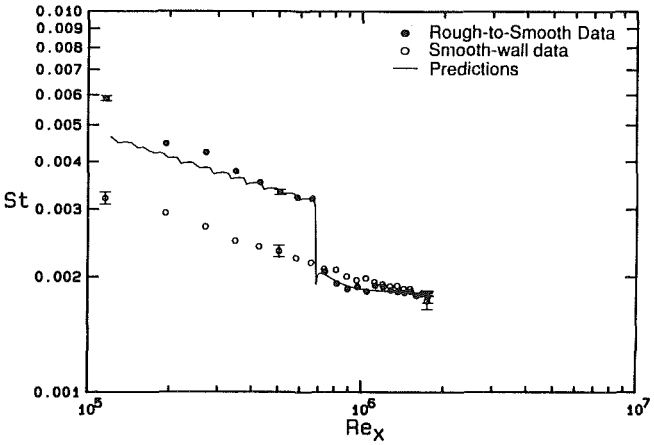

Fig. 4 Results of the Stanton number measurements and predictions for U_∞ = 12 m/s

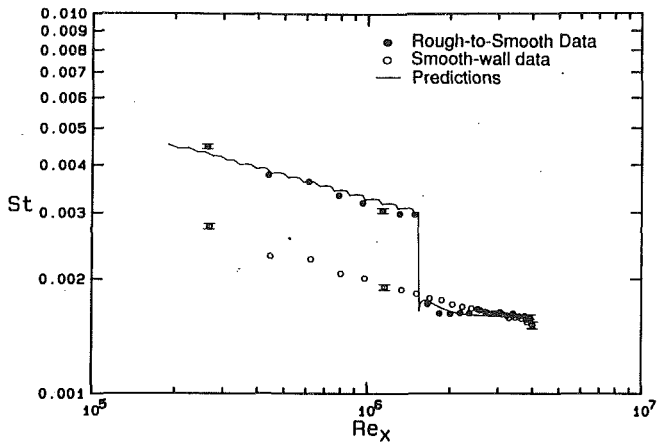

Fig. 5 Results of the Stanton number measurements and predictions for U_∞ = 27 m/s

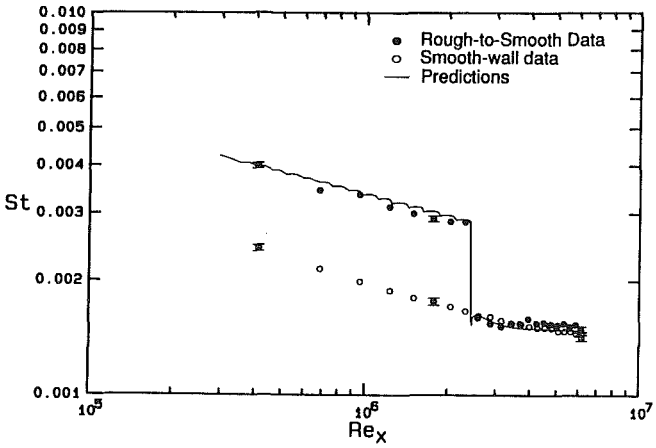

Fig. 6 Results of the Stanton number measurements and predictions for U_∞ = 43 m/s

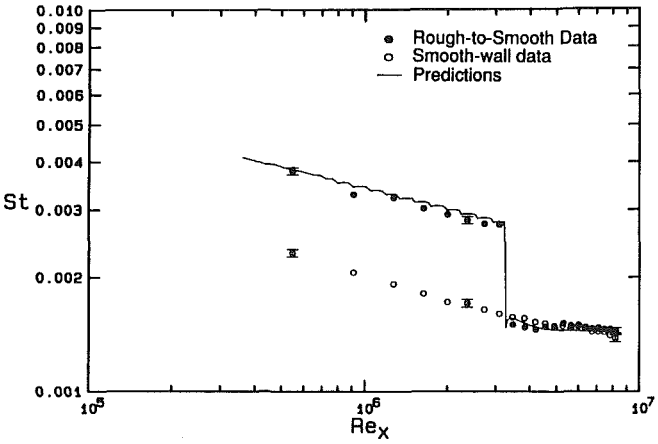

Fig. 7 Results for the Stanton number measurements and predictions for U_∞ = 58 m/s

Results

Stanton number data sets are presented for zero pressure gradient turbulent boundary layers with free-stream velocity of 6, 12, 27, 43, 58, and 67 m/s and constant wall temperature boundary conditions. According to Hosni et al. (1989), the 6 m/s case has a transitionally rough[1] boundary layer over the rough portion of the surface, and the 12, 27, 43, 58, and 67 m/s cases have fully rough boundary layers. These data are shown in Figs. 3–8. The data are compared with results obtained from the same facility using a smooth surface over the entire 2.4 m length. In the 6 m/s case, there was a considerable region of laminar flow as seen in Fig. 3. In this case, a line that represents the smooth wall correlation for turbulent boundary layers (Taylor et al., 1989)

$$\mathrm{St} = 0.185(\log_{10}\mathrm{Re}_x)^{-2.584}\mathrm{Pr}^{-0.4} \qquad (16)$$

was plotted for comparison since no smooth-wall data were taken for 6 m/s. In Figs. 4–8, the smooth wall correlation line is not shown since the smooth wall data are given; these data are in excellent agreement with the correlation (Taylor et al., 1989). In each of Figs. 3–8, the results of the predictions using the discrete element method outlined in the preceding section are plotted as a solid curve.

The experiments presented in this article roughly scale with full-size turbine engine tests. The x-Reynolds numbers range from 300,000 to 3,000,000 at the rough-to-smooth interface, and the boundary layer thickness is on the order of 0.025 m at the first smooth plate. Under these conditions a 0.1 m test plate roughly scales with a 1 mm heat flux gage in terms of plate width to boundary layer thickness ratio, δ/w (0.25 versus 0.5–1), roughness height to plate width, k/w (0.00635 versus

[1]Turbulent flows that are influenced by surface roughness are usually divided into three regimes. Aerodynamically smooth flows are those where the roughness effects are so small that the flow behaves as if the wall were smooth. Fully rough flows are those where the roughness so dominates the momentum transport to the wall that viscous effects are negligible. In turbulent pipe flow fully rough flows are those where the friction factor is no longer a function of the Reynolds numbers. Transitionally rough flows are those at Reynolds numbers between, where viscous and roughness effects are both significant.

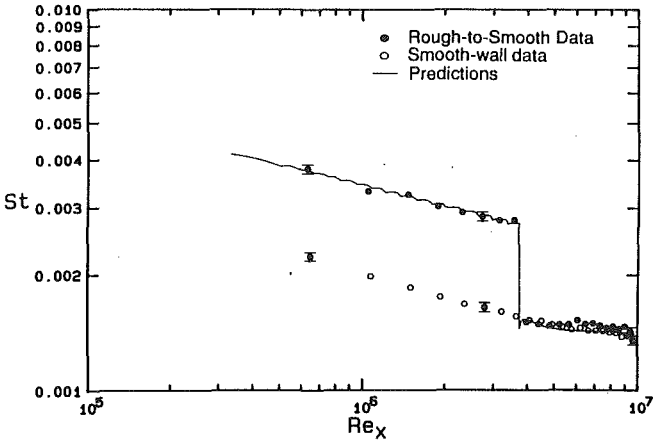

Fig. 8 Results for the Stanton number measurements and predictions for U_∞ = 67 m/s

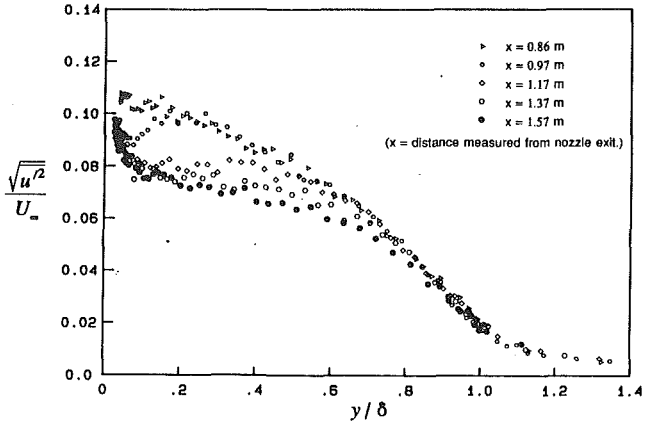

Fig. 9 Axial turbulence intensity profiles for U_∞ = 12 m/s

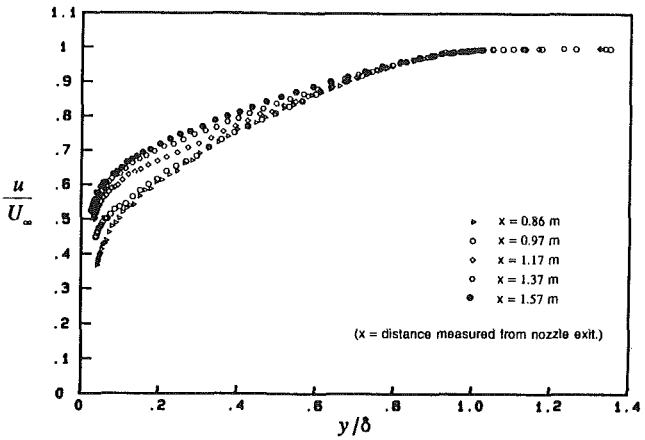

Fig. 10 Mean velocity profiles for U_∞ = 12 m/s

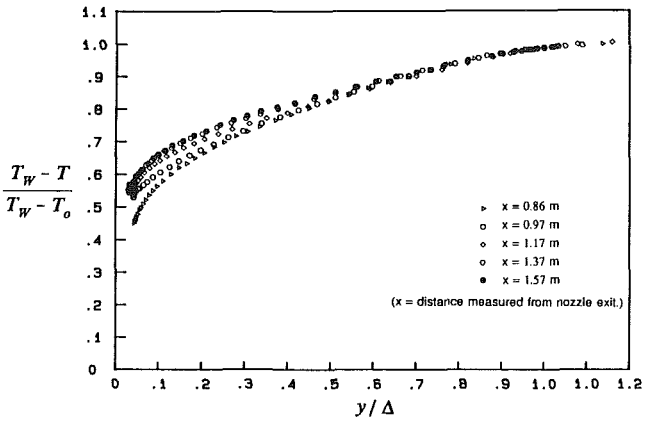

Fig. 11 Nondimensional temperature profiles for U_∞ = 12 m/s

0.0015–0.015), and roughness height to boundary layer thickness, k/δ (0.025 versus 0.003–0.03). Also, while all of the experiments reported in this article are for uniform arrays of hemispheres, we believe that the general trend of the heat transfer results would be the same for a randomly rough surface. Scaggs et al. (1988) found that pipes roughened with hemispheres had friction factor versus Reynolds number functions that were similar in trend to sandgrain-roughened pipes.

Figure 3 shows the plot for the case with U_∞ = 6 m/s. At these low Reynolds numbers the flow remains laminar for a considerable length in spite of the effects of the trip located at the nozzle exit. In this laminar region the roughness had almost no effect on the heat transfer. The figure also shows that the discrete element method does a good job of predicting St in this particular laminar flow even though it was not calibrated for this flow regime. At a Reynolds number of about 100,000, the flow undergoes transition to turbulent flow, and a transitionally rough turbulent boundary layer is established for a short distance, then the rough surface abruptly changes to a smooth surface. For this case, the Stanton numbers in the region between the rough-wall boundary layer and the new smooth-wall equilibrium decrease monotonically.

Figure 4 shows a similar plot for U_∞ = 12 m/s. For this case there is no appreciable laminar region since no transition from laminar to turbulent flow is observed as in Fig. 3. We also observe a different behavior after the step change in roughness. The Stanton number drops dramatically, undershooting the smooth-wall values and then increasing toward the new smooth-wall equilibrium values. Similar results have been observed by Antonia and Luxton (1972) and Andreopoulos and Wood (1982) for skin friction coefficient, C_f, downstream of a rough-to-smooth step change in roughness. Figures 5–8 show similar results for the higher speed flows. In all cases, the discrete element method predictions are seen to be in excellent agreement with the experimental data.

Figure 9 shows a plot of the turbulence intensity profiles at several x locations for a free-stream velocity of 12 m/s. The first x location (0.86 m) corresponds to the middle of the last rough plate, and the second one (0.97 m) corresponds to the middle of the first smooth plate. The other x locations show the development of the new smooth-wall equilibrium. The profile at x = 0.86 m shows typical behavior for a fully rough turbulent boundary layer. The turbulence intensity is elevated for much of the boundary layer and no near wall sharp peak in $\overline{u'^2}$ is seen. Over the first smooth plate the turbulence level over most of the boundary layer ($y/\delta > 0.2$) is identical to that over the last rough plate. However, near the wall ($y/\delta < 0.1$) the $\overline{u'^2}$ profile is seen to correspond closely with the usual smooth-wall behavior. The profiles farther down the test surface shown a slow adjustment of the middle region of the boundary layer to the new conditions. Figures 10 and 11 show the velocity and temperature profiles for $U_{\infty m}$ = 12 m/s. For a value of y/δ = 0.1, u/U_∞ = 0.5 over the first smooth plate as compared with u/U_∞ = 0.7 from the 1/7-power law velocity profile. A similar behavior is seen in Fig. 11 for the temperature profiles.

Summary

A step change in surface roughness from rough to smooth has been shown to have a dramatic effect on heat transfer in the turbulent boundary layer. For transitionally rough flow the Stanton number after the step change in roughness is seen to drop rapidly but monotonically to a new smooth-wall equi-

librium. On the other hand, for fully rough flows the Stanton number drops below the value for a smooth-wall boundary layer at the same x-Reynolds number then increases slightly before the new smooth-wall equilibrium is reached.

These results indicate that the use of smooth surface heat flux gages to measure the heat transfer rate on otherwise rough surfaces could yield erroneous results. We recommend that heat flux data taken in this fashion be used with caution.

Acknowledgments

This research was supported by the NASA Lewis Research Center, Grant #NAG 3 1116. The authors gratefully acknowledge the interest and encouragement of Mr. Kestutis Civinskas of Lewis Research Center.

References

ANSI, 1986, *Measurement Uncertainty*, ANSI/ASME PTC 19.1-1985 Part 1.

Andreopoulos, J., and Wood, D. H., 1982, "The Response of a Turbulent Boundary Layer to a Short Length of Surface Roughness," *J. Fluid Mech.*, Vol. 118, pp. 143-164.

Antonia, R. A., and Luxton, R. E., 1971a, "The Response of a Turbulent Boundary Layer to a Step Change in Surface Roughness, Part 1. Smooth to Rough," *J. Fluid Mech.*, Vol. 48, pp. 721-726.

Antonia, R. A., and Luxton, R. E., 1971b, "The Response of a Turbulent Boundary Layer to an Upstanding Step Change in Surface Roughness," ASME *Journal of Basic Engineering*, Vol. 93, No. 1, pp. 22-32.

Antonia, R. A., and Luxton, R. E., 1972, "The Response of a Turbulent Boundary Layer to a Step Change in Surface Roughness. Part 2. Rough-to-Smooth," *J. Fluid Mech.*, Vol. 53, pp. 737-757.

Antonia, R. A., and Wood, D. H,. 1975, "Calculation of a Turbulent Boundary Layer Downstream of a Small Step Change in Surface Roughness," *Aeronautical Quarterly*, Vol. 26, Part 3, pp. 202-210.

Coleman, H. W., Hosni, M. H., Taylor, R. P., and Brown, G. B., 1988, "Smooth Wall Qualification of a Turbulent Heat Transfer Test Facility," Report TFD-88-2, Mech. and Nuc. Eng. Dept., Mississippi State University.

Coleman, H. W., and Steele, W. G., 1989, *Experimentation and Uncertainty Analysis for Engineers*, Wiley, New York.

Eckert, R. G., and Goldstein, R. J., 1976, *Measurements in Heat Transfer*, 2nd ed., McGraw-Hill, New York.

Hosni, M. H., Coleman, H. W., and Taylor, R. P., 1989, "Measurement and Calculation of Surface Roughness Effects on Turbulent Flow and Heat Transfer," Report TFD-89-1, Mech. and Nuc. Eng. Dept., Mississippi State University.

Jacobs, W., 1939, "Unformung eines turbulenten geschwindigkeits Profiles," *Zeitschrift fur Angewandte Mathematic and Mechanik*, Vol. 19, No. 2, pp. 87-100 (also NACA TM 951).

Kays, W. M., and Crawford, M. E., 1980, *Convective Heat and Mass Transfer*, McGraw-Hill, New York.

Reynolds, W. C., Kays, W. M., and Kline, S. J., 1958, "Heat Transfer in the Turbulent Incompressible Boundary Layer, Part I, II, and III," NASA MEMO 12-1-58W, 12-2-58W, 12-3-58W.

Scaggs, W. F., Taylor, R. P., and Coleman, H. W., 1988, "Measurement and Prediction of Rough Wall Effects on Friction Factor-Uniform Roughness Results," ASME *Journal of Fluids Engineering*, Vol. 110, pp. 385-391.

Schofield, W. H., 1975, "Measurements in Adverse-Pressure-Gradient Turbulent Boundary Layers With Step Change in Surface Roughness," *J. Fluid Mech.*, Vol. 70, pp. 573-593.

Shang, J. S., Hankey, W. L., and Law, C. H., 1976, "Numerical Simulation of Shock Wave-Turbulent Boundary-Layer Interaction," *AIAA J.*, Vol. 14, pp. 1451-1457.

Smits, A. J., and Wood, D. H., 1985, "The Response of Turbulent Boundary Layers to Sudden Perturbations," *Ann. Rev. Fluid Mech.*, Vol. 17, pp. 321-358.

Tani, I., 1968, "Review of Some Experimental Results on the Response of a Trubulent Boundary Layer to Sudden Perturbations," *Proceedings Computation of Turbulent Boundary Layers—1968 AFOSR-IFP-Stanford Conference*, Stanford University, Calif., Aug. 18-25, pp. 483-495.

Taylor, R. P., Coleman, H. W., and Hodge, B. K., 1984, "A Discrete Element Prediction Approach for Turbulent Flow Over Rough Surfaces," Report TFD-84-1, Mech. and Nuc. Eng. Dept., Mississippi State University.

Taylor, R. P., Coleman, H. W., and Hodge, B. K., 1985, "Prediction of Turbulent Rough-Wall Skin Friction Using a Discrete Element Approach," ASME *Journal of Fluids Engineering*, Vol. 107, pp. 251-257.

Taylor, R. P., 1989, "Skin Friction and Heat Transfer Predictions for Turbulent Boundary Layer Flow Over Rough Surfaces," Mech. and Nuc. Eng. Dept., Mississippi State University.

Taylor, R. P., Coleman, H. W., Hosni, M. H., and Love, P. H., 1989, "Thermal Boundary Condition Effects on Heat Transfer in the Turbulent Incompressible Flat Plate Boundary Layer," *Int. J. Heat Mass Transfer*, Vol. 32, pp. 1165-1174.

Taylor, R. P., 1990, "Surface Roughness Measurements on Gas Turbine Blades," ASME JOURNAL OF TURBOMACHINERY, Vol. 112, pp. 175-180.

Townsend, A. A., 1965, "The Response of a Turbulent Boundary Layer to Abrupt Changes in Surface Conditions," *J. Fluid Mech.*, Vol. 22, pp. 799-822.

White, F. M., 1974, *Viscous Fluid Flow*, McGraw-Hill, New York.

Navier-Stokes Analysis of Turbine Blade Heat Transfer and Performance

D. J. Dorney
Associate Research Engineer.

R. L. Davis
Senior Research Engineer.

Theoretical & Computational Fluid Dynamics Group,
United Technologies Research Center,
East Hartford, CT 06108

A three-dimensional Navier–Stokes analysis of heat transfer and aerodynamic performance is presented for a low-speed linear turbine cascade. The numerical approach used in this analysis consists of an alternate-direction, implicit, approximate-factorization, time-marching technique. An objective of this investigation has been to establish the computational grid density requirements necessary to predict blade surface and endwall heat transfer accurately, as well as the exit plane aerodynamic total pressure loss and flow angle distributions. In addition, a study has been performed to determine the importance of modeling transition as well as a viable implementation strategy for the three-dimensional turbulence model in the turbine blade passage. Results are presented demonstrating that the present procedure can accurately predict three-dimensional turbine blade heat transfer as well as the absolute level and spanwise distribution of aerodynamic performance quantities.

Introduction

The accurate prediction of three-dimensional turbomachinery blade row heat transfer and aerodynamic performance, including total pressure loss and flow turning, remains a challenging task for most Navier–Stokes numerical procedures. The very large computational grid densities necessary to resolve the viscous flow physics accurately and properly convect the vorticity require computational resources that far exceed those available to most engineering facilities. Thus, in most instances, it has not been possible to produce grid-independent three-dimensional flow solutions for turbomachinery blade rows that ensure the accuracy required for reliable predictions.

The proper modeling of transition and turbulence within turbomachinery blade passages is also often compromised in order to reduce computational times to acceptable levels. The effects of turbulence in the flow are quite often modeled with an algebraic eddy viscosity correlation, which has its basis in two-dimensional boundary layer data, even though the flow in a blade row passage has strong secondary and occasional reversed flows. The modeling of transition in most Navier–Stokes approaches is practically nonexistent due to the lack of reliable correlations for three-dimensional internal blade row flows and due to the numerical instabilities caused by the unsteady movement of the transition region as the flow field develops. Unfortunately, it is unlikely that improvements in turbulence and transition modeling will improve beyond the current state of the art for three-dimensional turbomachinery flows until Navier–Stokes procedures can affordably and reliably produce grid-independent solutions. Only then will researchers be able to separate out the turbulence modeling effects on the flow from those caused by truncation error and numerical viscosity.

Several investigations have been made recently in which three-dimensional Navier–Stokes procedures have been used to predict the heat transfer and/or aerodynamic performance of the Langston linear turbine cascade (Langston et al., 1977; Graziani et al., 1980). Among these numerical investigations, Chan and Sheedy (1990) have used a pressure correction method with a two-equation (k–ϵ) turbulence model to predict the losses in the Langston cascade for a thick (3.3 cm) inlet boundary layer. Their predicted results indicate that the numerical procedure is very sensitive to spanwise computational grid density. Even the use of comparatively fine computational grids, however, was not adequate to achieve the flow field resolution needed to accurately predict aerodynamic performance quantities. Hah (1984, 1989) has also used a pressure correction technique with a two-equation (k–ϵ) turbulence model to predict endwall Stanton numbers (Hah, 1989) and losses as a function of axial distance (Hah, 1984) for the Langston cascade with a thick inlet boundary layer. The predicted endwall Stanton numbers show fair agreement with the experimental data, but it is unclear if a sufficiently fine computational grid was used to attain grid independent solutions. Moore and Ransmayr (1984) and Moore and Moore (1985) used a pressure correction method with an algebraic turbulence model to predict losses and secondary flows for the Langston cascade with a thick inlet boundary layer. Lee and Knight (1989) solved the thin layer Navier–Stokes equations using an approximate factorization technique and the two-equation (q–ω) turbulence model to study heat transfer for the Langston cascade with a thick inlet boundary layer. A portion of their investigation focused on the effects of different grid topologies (H- and O-

Contributed by the International Gas Turbine Institute for publication in the JOURNAL OF TURBOMACHINERY. Manuscript received by the International Gas Turbine Institute May 1991. Associate Technical Editor: L. S. Langston.

H grids) on the predicted heat transfer quantities. In their study, it was determined that grid topology, as well as computational grid density, can impact the predicted solutions.

The objective of the current investigation has been to provide guidance as to the computational grid density requirements that are necessary to produce reliable and accurate Navier–Stokes predictions of turbomachinery blade row flows. Simulations of transitional flow through the Langston cascade (Langston et al., 1977; Graziani et al., 1980) with a thin inlet boundary layer (0.41 cm) have been performed where the focus has been to conduct a computational grid refinement study to determine the computational grid density necessary to resolve surface heat transfer and aerodynamic performance quantities properly. As part of this investigation, a study was performed to determine a viable strategy for implementing an algebraic turbulence model for three-dimensional internal blade row flows and to determine the limitations of using an algebraic turbulent model on the accuracy of the exit plane distributions of total pressure loss and flow angle. Also, a brief study was conducted to demonstrate the importance of modeling laminar/turbulent transition for these flows.

Numerical Integration Procedure

The governing equations considered in this study are the time-dependent, three-dimensional Navier–Stokes equations:

$$U_t + (F_i + F_v)_x + (G_i + G_v)_y + (H_i + H_v)_z = 0 \tag{1}$$

where

$$U = \begin{bmatrix} \rho \\ \rho u \\ \rho v \\ \rho w \\ e_t \end{bmatrix} \tag{2}$$

$$F_i = \begin{bmatrix} \rho u \\ \rho u^2 + P \\ \rho uv \\ \rho uw \\ (e_t + P)u \end{bmatrix} \qquad F_v = - \begin{bmatrix} 0 \\ \tau_{xx} \\ \tau_{xy} \\ \tau_{xz} \\ \tau_{hx} \end{bmatrix} \tag{3}$$

$$G_i = \begin{bmatrix} \rho v \\ \rho uv \\ \rho v^2 + P \\ \rho vw \\ (e_t + P)v \end{bmatrix} \qquad G_v = - \begin{bmatrix} 0 \\ \tau_{yx} \\ \tau_{yy} \\ \tau_{yz} \\ \tau_{hy} \end{bmatrix} \tag{4}$$

$$H_i = \begin{bmatrix} \rho w \\ \rho uw \\ \rho vw \\ \rho w^2 + P \\ (e_t + P)w \end{bmatrix} \qquad H_v = - \begin{bmatrix} 0 \\ \tau_{zx} \\ \tau_{zy} \\ \tau_{zz} \\ \tau_{hz} \end{bmatrix} \tag{5}$$

where

$$\begin{aligned}
\tau_{xx} &= 2\mu u_x + \lambda(u_x + v_y + w_z) \\
\tau_{xy} &= \mu(u_y + v_x) \\
\tau_{xz} &= \mu(u_z + w_x) \\
\tau_{yx} &= \tau_{xy} \\
\tau_{yy} &= 2\mu v_y + \lambda(u_x + v_y + w_z) \\
\tau_{yz} &= \mu(v_z + w_y) \\
\tau_{zx} &= \tau_{xz} \\
\tau_{zy} &= \tau_{yz} \\
\tau_{zz} &= 2\mu w_z + \lambda(u_x + v_y + w_z) \\
\tau_{hx} &= u\tau_{xx} + v\tau_{xy} + w\tau_{xz} + \gamma\mu \mathrm{Pr}^{-1} e_x \\
\tau_{hy} &= u\tau_{yx} + v\tau_{yy} + w\tau_{yz} + \gamma\mu \mathrm{Pr}^{-1} e_y \\
\tau_{hz} &= u\tau_{zx} + v\tau_{zy} + w\tau_{zz} + \gamma\mu \mathrm{Pr}^{-1} e_z \\
e &= \frac{P}{(\rho(\gamma - 1))} \\
e_t &= \rho e + \frac{\rho(u^2 + v^2 + w^2)}{2}
\end{aligned} \tag{6}$$

For the present application, the second coefficient of viscosity is calculated using Stokes' hypothesis, $\lambda = -2/3\mu$. The equations of motion are completed by the perfect gas law.

The viscous fluxes are simplified by incorporating the thin layer assumption (Baldwin and Lomax, 1978). In the current study, viscous terms are retained in the direction normal to the hub surface (z direction) and in the direction normal to the blade surface (y direction). To extend the equations of motion to turbulent flows, an eddy viscosity formulation is used. Thus, the effective viscosity and effective thermal conductivity can be defined as:

$$\begin{aligned}
\mu &= \mu_L + \mu_T \\
\frac{k}{c_p} &= \frac{\mu_L}{\mathrm{Pr}_L} + \frac{\mu_T}{\mathrm{Pr}_T}
\end{aligned} \tag{7}$$

The turbulent viscosity, μ_T, is calculated using the Baldwin–Lomax (1978) algebraic turbulence model. The specific techniques used to implement this model for three-dimensional flows in turbomachinery blade rows will be described below.

The numerical procedure for the three-dimensional analysis

Nomenclature

a = speed of sound
c_p = specific heat ratio at constant pressure
e = specific energy
e_t = total energy
k = thermal conductivity
L = reference length = 2.54 cm
M = Mach number
P = static pressure
Pr = Prandtl number
P_T = stagnation pressure
q = heat flux
Re = free-stream inlet reference Reynolds number
T = static temperature
u = x component of velocity
v = y component of velocity
w = z component of velocity
λ = second coefficient of viscosity
μ = first coefficient of viscosity
ρ = density
τ = shear stress

Subscripts

i = inviscid
L = laminar quantity
t = stagnation quantity
T = turbulent quantity
v = viscous
x, y, z = first derivative with respect to x, y, or z
xx, yy, zz = second derivative with respect to x, y, or z
1 = inlet quantity
2 = exit quantity

consists of a time marching, implicit, third-order spatially accurate, upwind, finite difference scheme. The inviscid fluxes are discretized using a combination of central, forward, and backward differences depending on the local eigenvalues of the flux Jacobians according to the scheme developed by Roe (1981). The third-order upwind scheme was chosen because it has been shown to introduce little artificial diffusion and is capable of accurately predicting boundary layer quantities (Dorney and Davis, 1989). The viscous fluxes are calculated using standard central differences. The alternate direction, approximate-factorization technique of Beam and Warming (1977) is used to compute the time rate changes in the primary variables. An inner Newton iteration can be used to increase stability and reduce linearization errors. For all cases investigated in this study, one Newton iteration was performed at each time step. Further details of the three-dimensional numerical technique can be found from Rai (1988, 1989).

Grid Generation and Geometry

The three-dimensional Navier–Stokes analysis uses zonal grids to discretize the turbine flow field. A combination of O- and H-grid sections are generated at constant radial spanwise locations in the blade-to-blade direction extending upstream of the airfoil leading edge to downstream of the airfoil trailing edge. Algebraically generated H-grids are used in the regions upstream of the leading edge, downstream of the trailing edge, and in the interblade region. The O-grid, which is body-fitted to the surface of the airfoil and generated using an elliptic equation solution procedure, is used to resolve the viscous flow in the blade passages properly and to apply the algebraic turbulence model easily. Computational grid lines within the O-grid are stretched in the blade-normal direction with a fine grid spacing at the wall. The combined H- and O- overlaid grid sections are stretched in the spanwise direction away from the hub and shroud regions with a fine grid spacing located adjacent to the hub and shroud.

Boundary Conditions

The theory of characteristics is used to determine the boundary conditions at the passage inlet and exit. For subsonic inlet flow, the total pressure, v and w velocity components, and the downstream running Riemann invariant, $R_1 = u + 2a/(\gamma - 1)$, are specified while the upstream running Riemann invariant, $R_2 = u - 2a/(\gamma - 1)$, is extrapolated from the interior of the computational domain. For subsonic outflow the pressure ratio, P_2/P_{t1}, is specified while the v and w velocity components, entropy, and the downstream running Riemann invariant are extrapolated from the interior of the computational domain. Periodicity is enforced along the outer boundaries of the H-grids in the circumferential (θ) direction.

Dirichlet conditions, in which the time rate change in the vector U of Eq. (2) is set to zero, are imposed at the overlaid boundaries of the O- and H-grids. The flow variables of U at zonal boundaries are explicitly updated after each time step by interpolating values from the adjacent grid. Because of the explicit application of the zonal boundary conditions, large time steps may necessitate the use of more than one Newton iteration. The zonal boundary conditions are nonconservative, but for subsonic flow this should not affect the accuracy of the final flow solution. For flows containing discontinuities, conservative boundary conditions, such as those developed by Rai (1985) should be implemented into the procedure.

No-slip boundary conditions are enforced at the hub and shroud endwalls of the turbine passage and along the surface of the airfoil. In addition, a specified heat flux or wall temperature distribution is held constant in time along the solid surfaces. In the present investigation, a specified heat flux given by

$$q_{\text{wall}} = -k \frac{\partial T}{\partial n} \tag{8}$$

is prescribed over all solid surfaces at a level consistent with the experimental conditions. Upon discretizing Eq. (8) using a first-order backward difference, a Neumann boundary condition arises, which is held during the implicit sweep of lines normal to the surface. The implicit update of the solid boundary flow variables is followed by a second-order accurate explicit update. Further information describing the implementation of the boundary conditions can be found from Rai (1985, 1989) and Rai and Madavan (1988).

Turbulence/Transition Model

The Baldwin–Lomax (1978) two-layer algebraic turbulence model is used to represent the turbulent eddy viscosity in the flow field. This turbulence model is based upon two-dimensional boundary layer data, and as such, is not well suited for corner flows such as those at the blade/endwall juncture. Previously, the treatment used to implement this turbulence model in the corner regions was the technique proposed by Hung et al. (1978, 1984). In this technique, the Baldwin–Lomax turbulence model is computed separately for each endwall and the blade surface. The mixing length in the corner region depends on the computational indices of a given node. For instance, consider the case when the J = const computational lines run normal to the blade surface and the K = const lines run normal to the endwall. For any computational node whose J-wise index is less than its K-wise index, the "normal" distance is defined as the distance from the blade surface to the grid point and the "parallel" distance is defined as the distance from the endwall to the grid point. The mixing length for the inner region of the boundary layer is then calculated as

$$l = 2sn/(s + n + \sqrt{(s^2 + n^2)}) \tag{9}$$

where s is the parallel distance and n is the normal distance. The eddy viscosity is then based on the flow variables along a computational grid line from the airfoil surface (normal direction) to the grid point under consideration. Likewise, for any computational node whose J-wise index is greater than its K-wise index, the parallel distance is measured from the blade surface to the grid point and the normal distance is measured from the endwall to the grid point. The eddy viscosity is then based on the flow variables along a computational grid line from the endwall to the grid point. Two significant problems arise from this particular three-dimensional implementation of the Baldwin–Lomax turbulence model. First, the eddy viscosity distribution in the corner regions is discontinuous across the $J = K$ computational lines, which can cause large gradients to occur in the velocity field. Secondly, this particular blending is highly dependent upon the computational grid density and stretching in both computational directions. It was determined, based upon numerical simulations, that the steady-state solution in the blade/endwall region was extremely sensitive to changes in the computational grid structure.

In the present investigation, a blending function has been used to vary the eddy viscosity distribution smoothly between the blade and endwall. Separate eddy viscosity distributions are computed for the blade and endwall surfaces along the computational lines, which run normal to each surface, respectively. The eddy viscosity in the corner flow regions is then computed based upon the following blending function according to the work of Vatsa and Wedan (1988):

$$\mu_T = \frac{d_{ew}^2 \mu_{T_b} + d_b^2 \mu_{T_{ew}}}{d_b^2 + d_{ew}^2} \tag{10}$$

where d_b is the distance from the blade surface to a given node, d_{ew} is the distance from the endwall surface to the node, and

Table 1 Grid refinement study

Case	Grid Density stream×tang×span	Δy_{blade} (y^+)	$\Delta y_{endwall}$ (y^+)	Profile $\Delta P_T/P_{T_1}$	Total $\Delta P_T/P_{T_1}$	Profile β_2	Total β_2	Trns
1	H-70 × 31 × 25	0.00100	0.00300	0.20846	0.19065	27.96	27.34	yes
	O-101 × 31 × 25	(4.260)	(7.430)					
2	H-70 × 31 × 25	0.00010	0.00100	0.16102	0.18373	27.49	27.36	no
	O-101 × 31 × 25	(0.384)	(2.920)					
3	H-70 × 31 × 25	0.00010	0.00100	0.16100	0.18372	27.49	27.58	yes
	O-101 × 31 × 25	(0.379)	(2.781)					
4	H-70 × 31 × 51	0.00010	0.00010	0.14575	0.17271	27.67	27.38	yes
	O-101 × 31 × 51	(0.360)	(0.266)					
5	H-70 × 31 × 71	0.00010	0.00010	0.13898	0.17075	27.73	27.26	yes
	O-101 × 31 × 71	(0.351)	(0.266)					
6	H-70 × 31 × 91	0.00010	0.00010	0.13051	0.17064	27.75	27.25	yes
	O-101 × 31 × 91							
2-D	O-131 × 61	0.00002	—	0.12030	—	26.58		yes
	H-71 × 21	(0.059)	—					
EXPT	—	—	—	0.13000	0.17437	26.80	26.32	—

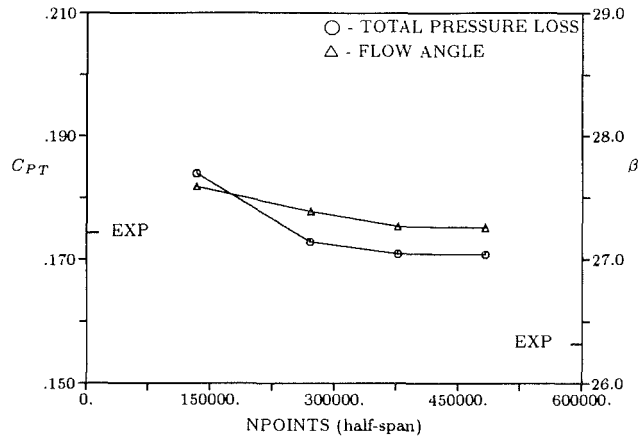

Fig. 1 Exit flow angle and total pressure loss as a function of grid point density

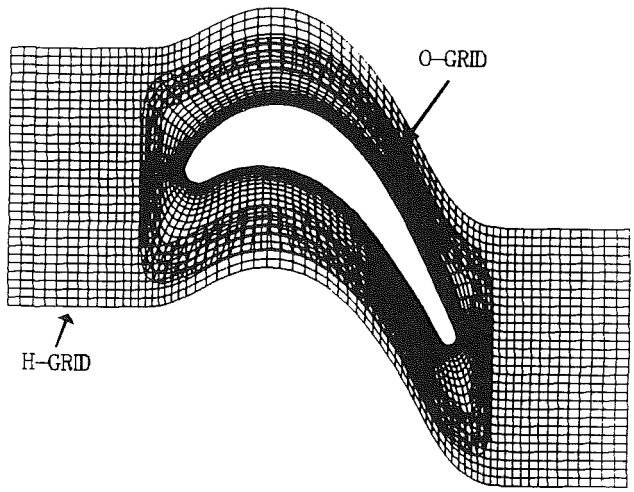

Fig. 2 Blade-to-blade computational grid for Langston cascade

μ_{T_b}, $\mu_{T_{ew}}$ are the eddy viscosities computed from the blade and endwall flows, respectively. This type of blending greatly reduces the dependence of the eddy viscosity distribution on the computational grid and creates a smooth eddy viscosity distribution in the corner regions.

As will be shown below, results from a number of computations demonstrate the importance of correctly modeling transition of the flow from laminar to turbulent on the blade surface. In the present investigation in which turbine blade heat transfer is being predicted, the modeling of transition is essential for the accurate prediction of Stanton number distributions. In this study, transition was modeled using a prescribed location for the onset of transition. The onset of transition was varied as a function of span, with the endwalls assumed to be fully turbulent, and midspan transition beginning at the 25 percent axial chord location on the suction surface according to the experimental data. Transition was assumed to occur as an instantaneous process. As will be discussed below, a means of accurately *predicting* transition, especially in turbine blade rows, clearly must be developed in order reliably and accurately to predict heat transfer.

Results

A set of viscous three-dimensional numerical simulations of flow through the Langston low-speed turbine cascade with a thin inlet boundary layer (0.41 cm), including heat transfer and transition, have been performed and the predicted results compared to experimental data (Langston et al., 1977; Graziani et al., 1980). The heat flux values at the endwall and airfoil surfaces were specified to be the same as in Graziani et al. (1980). The inlet Mach number was set to $M_1 = 0.0917$ and the inlet flow angle was specified to be $\beta_1 = 44.7$ deg. The inlet Reynolds number was set to $Re_1 = 25{,}590$ per cm and the ratio of the exit static pressure to the inlet total pressure was fixed at $P_2/P_{T_1} = 0.9847$ based on the experimental data.

A computational grid refinement study has been performed to establish the grid density required to produce essentially grid-independent solutions in both the blade-to-blade and spanwise directions. A combination of two- and three-dimensional simulations were performed to establish the required grid density and wall spacing in the blade-to-blade direction to predict turbine blade heat transfer accurately. As a result of the two-dimensional simulations, it was determined that a computational grid consisting of 70×21 grid points in the H-grid and 131×61 grid points in the O-grid with an average wall spacing of 0.00002 ($y^+ = 0.059$) produced grid-independent solutions. Once this was established, a similar grid topology and density were used in the blade-to-blade direction for the three-dimensional simulations. The wall spacing adjacent to the airfoil surface was then refined during a series of three-dimensional simulations to insure the accuracy of the three-dimensional blade-to-blade solution. Finally, the spanwise

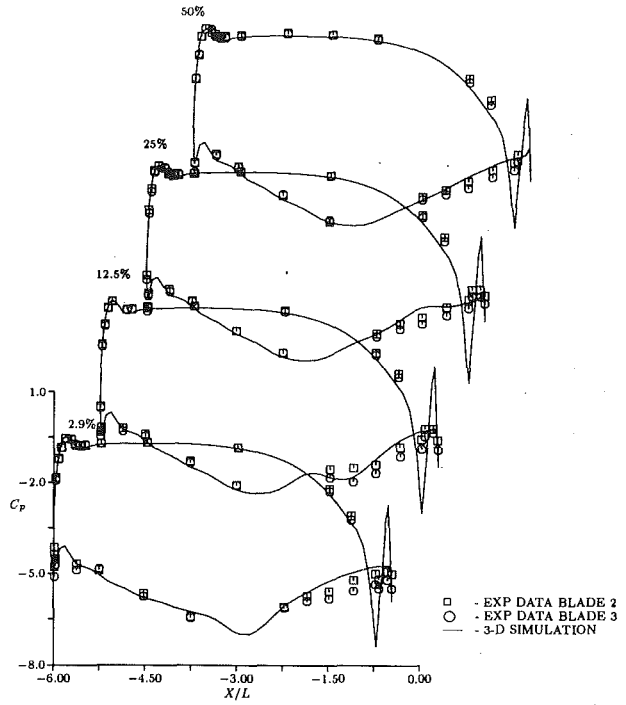

Fig. 3 Airfoil surface static pressure coefficient distributions

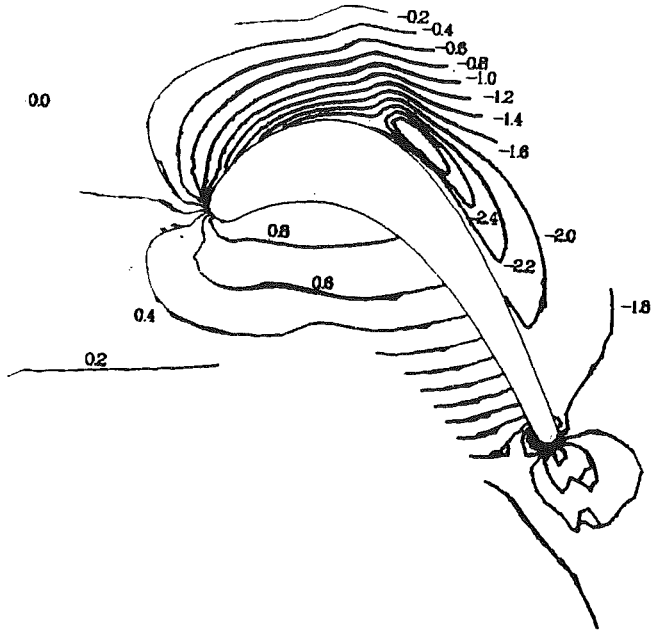

Fig. 4 Predicted three-dimensional endwall static pressure coefficient contours

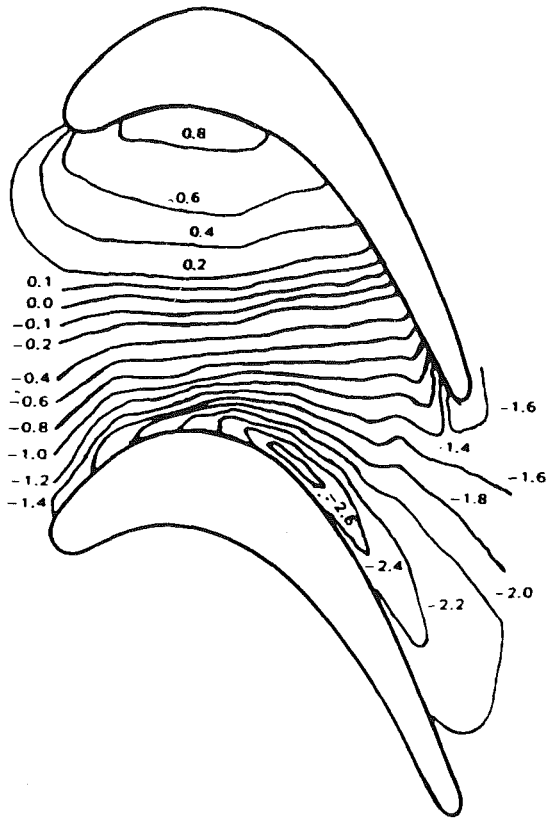

Fig. 5 Experimental three-dimensional endwall static pressure coefficient contours

computational grid was refined both in terms of endwall spacing and density until the exit total pressure loss and exit flow angle distributions remained unchanged and exhibited close agreement with the experimental data.

A summary of the cases executed during this investigation are given in Table 1. The columns labeled "Total" in Table 1 indicate area-averaged values in the spanwise direction, while the columns labeled "Profile" refer to midspan values. The area-averaged values were calculated using trapezoidal integration and only the computational grid points at the experimental data locations were included in the integration (a total of 13 locations for the half-span) in order to be consistent with the experimental area-averaged exit loss and flow angle values. The column labeled "Trns" indicates whether or not transition was modeled. Since the geometry was symmetric about the midspan, the numerical simulations were performed for only the half-span and a symmetry boundary condition was used along the symmetry plane. The spanwise grid densities given in Table 1 are for the half-span geometry. Figure 1, which illustrates the "Total" exit flow angle and total pressure loss (see Eq. (13)) values as a function of grid point density, demonstrates that a half-span grid-independent solution was obtained with approximately 450,000 grid points. Except where noted, the predicted results shown below are for this fine grid (Case 6) solution.

Figure 2 illustrates an example of the blade-to-blade computational grid used in the numerical simulations. Planes of blade-to-blade computational grids such as shown in Fig. 2 are stacked in the spanwise direction to create the discretized geometry. Computational grid lines are clustered adjacent to the airfoil surface and endwall to resolve the viscous flow properly.

Figure 3 illustrates the predicted fine grid (Case 6) and experimentally measured pressure coefficient distributions along the surface of the airfoil at the 2.9, 12.5, 25.0, and 50.0 percent span locations, where the pressure coefficient is defined as:

$$C_p = \frac{2(P - P_1)}{\rho U_1^2} \tag{11}$$

and U_1 is the total inlet velocity. Experimental data were taken on two separate blades in the cascade and both sets of data are presented for each spanwise location. There is close agreement between the predicted results and the experimental data for the entire span of the cascade. In both the predicted results (Cases 4–6 in Table 1) and the experimental data the effects of the endwall secondary flow on the pressure distribution are visible on the suction surface of the airfoil near the trailing edge at 12.5 percent span. This phenomenon was not present in the coarser grid calculations (Cases 1–3).

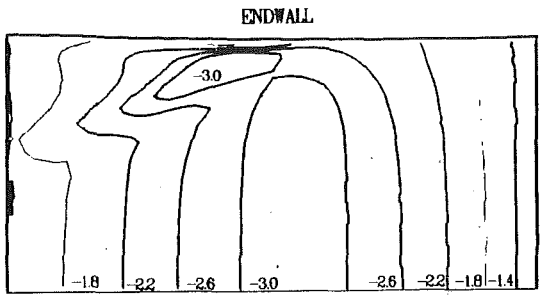

Fig. 6 Predicted suction surface static pressure coefficient contours

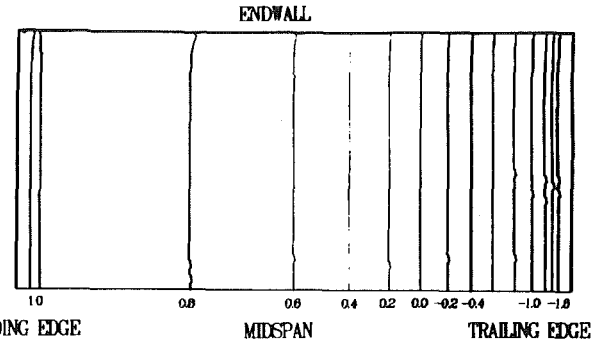

Fig. 7 Predicted pressure surface static pressure coefficient contours

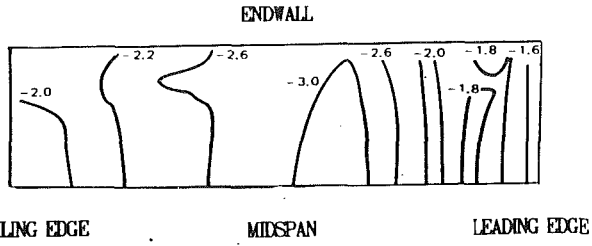

Fig. 8 Experimental suction surface static pressure coefficient contours

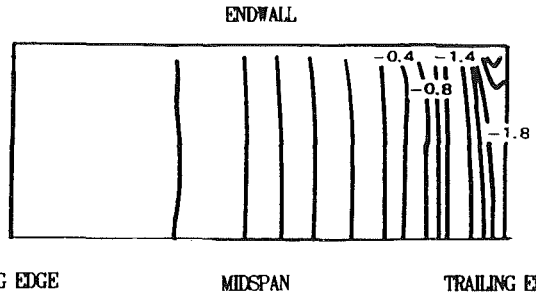

Fig. 9 Experimental pressure surface static pressure coefficient contours

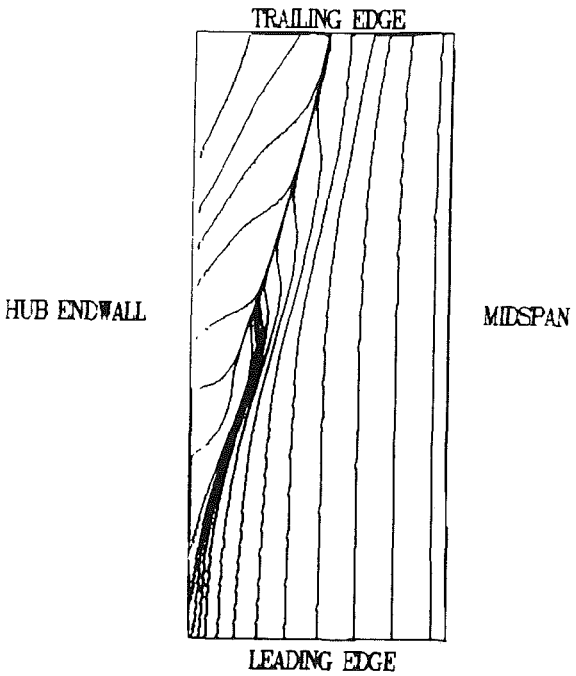

Fig. 10 Predicted suction surface limiting streamlines

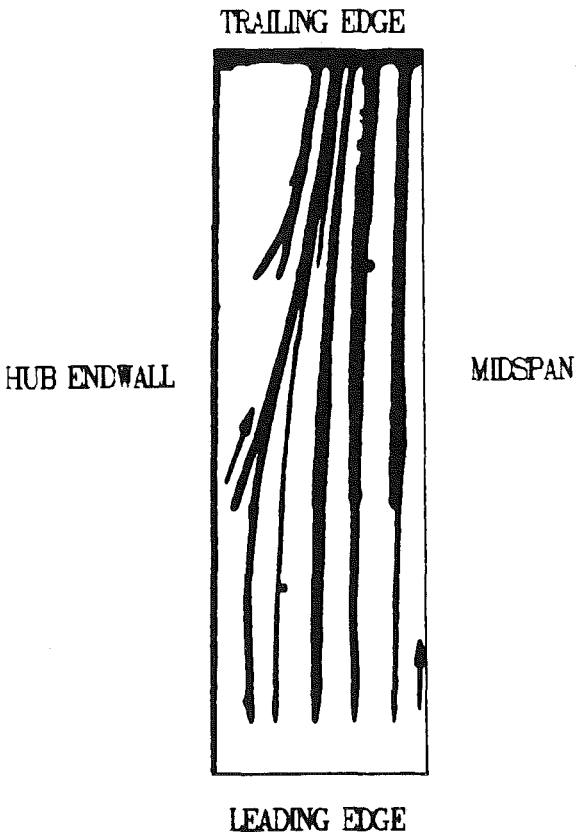

Fig. 11 Experimental suction surface limiting streamlines

The predicted and experimental (Graziani et al., 1980) endwall static pressure coefficient contours are illustrated in Figs. 4 and 5, respectively. Comparison of the two figures shows that the predicted results and experimental data agree very well. Both figures show a pressure "island," corresponding to the minimum pressure point, located on the suction surface at approximately 60 percent axial chord. The predicted results also exhibit the characteristic "footprint" of the endwall secondary flow on the suction side of the passage, similar to that observed in computational studies for a thick inlet boundary layer (Hah, 1984, 1989). This suggests that the boundary layer in the numerical procedure grows slightly faster than that observed experimentally. In the leading edge plane, the boundary

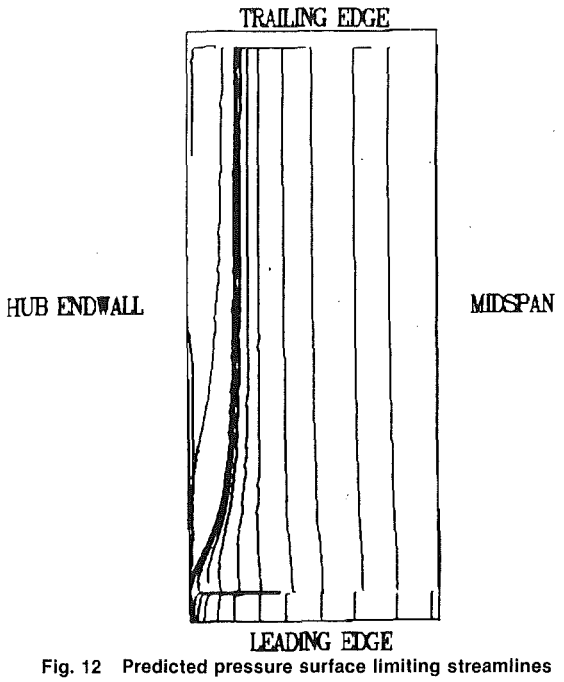

Fig. 12 Predicted pressure surface limiting streamlines

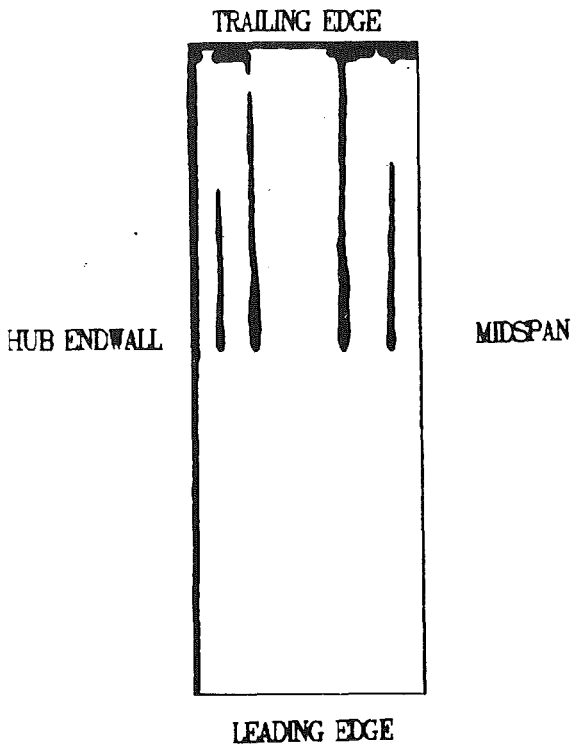

Fig. 13 Experimental pressure surface experimental limiting streamlines

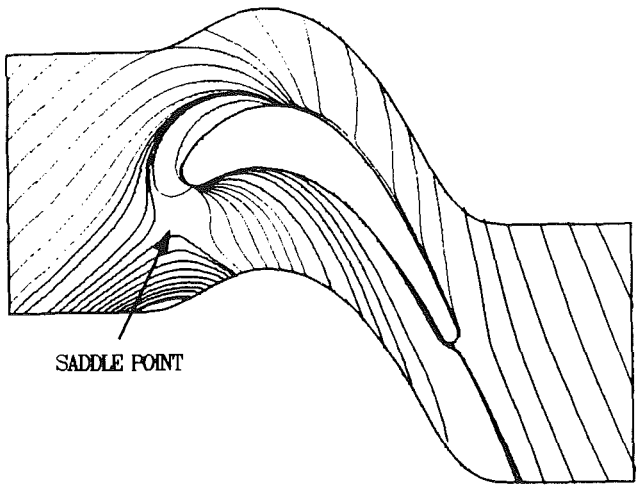

Fig. 14 Predicted endwall limiting streamlines

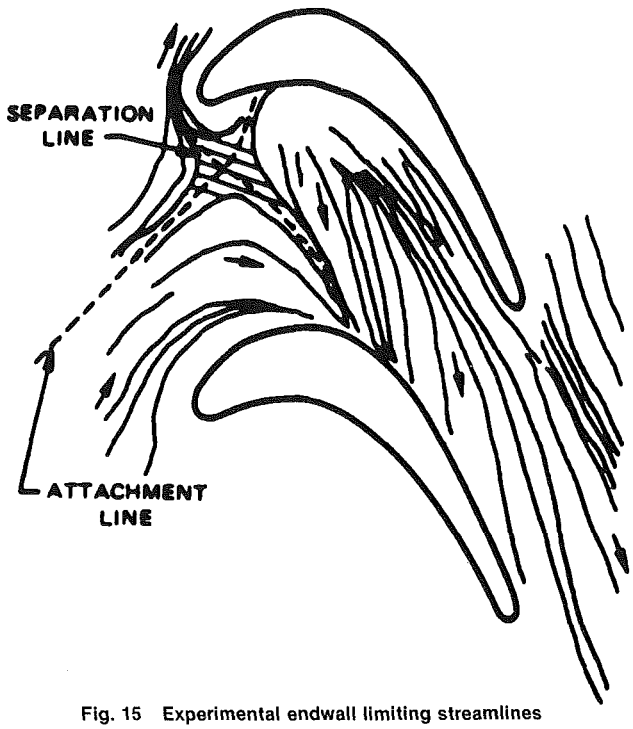

Fig. 15 Experimental endwall limiting streamlines

layer thickness predicted with the current numerical procedure is approximately 4 percent greater than that observed experimentally.

The predicted static pressure coefficient contours for the suction and pressure surfaces of the airfoil are shown in Figs. 6 and 7, while the experimental contours for both surfaces are shown in Figs. 8 and 9, respectively. It is important to note that Figs. 6 and 7 are three-dimensional renderings of the airfoil surface, while Figs. 8 and 9 are two-dimensional projections of the airfoil surface. There is good agreement between the predicted results and experimental data on both surfaces of the airfoil. The static pressure island associated with the minimum pressure point, located at 38 percent axial chord on the suction surface, is shown in both the predicted and experimental results. The effects of the endwall boundary layer are visible in Figs. 6 and 8 just downstream of the midaxial chord location. In both the predicted results and the experimental data, the static pressure changes very little for the first 50 percent axial chord of the pressure surface (see Figs. 7 and 9), then decreases very rapidly as the flow accelerates near the trailing edge.

The predicted limiting streamlines for the suction surface of the airfoil are shown in Fig. 10. Limiting streamlines obtained experimentally using surface flow visualization techniques are included for comparison in Fig. 11. The predicted limiting streamlines (Fig. 10) show close agreement with the experimental data. The flow in the midspan region of the suction surface is two-dimensional, while the flow in the endwall region is highly three-dimensional. A separation streamline forms at the airfoil leading edge in the endwall region and extends spanwise to approximately the 25 percent span position at the trail-

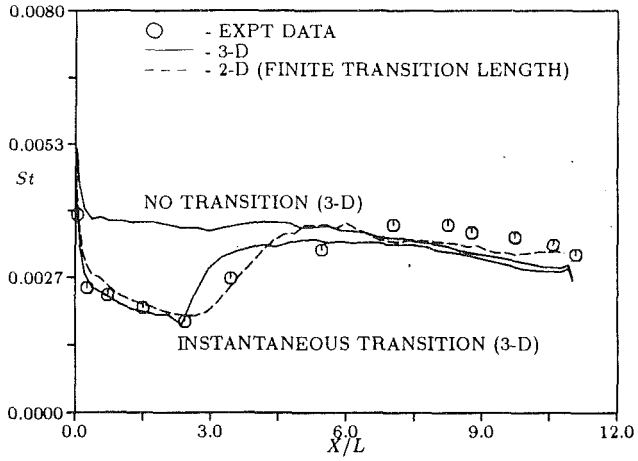

Fig. 16 Midspan suction surface Stanton number distributions

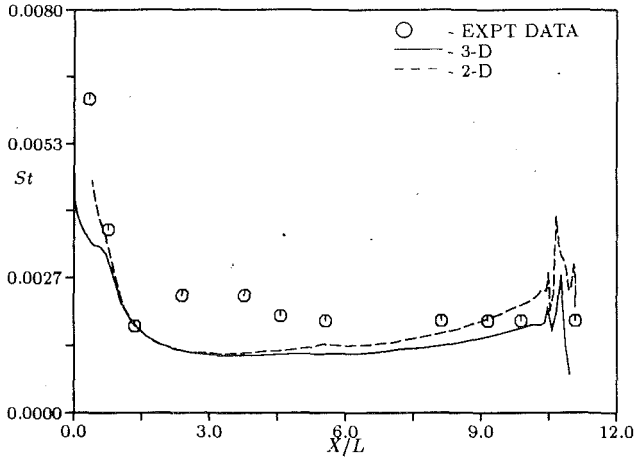

Fig. 17 Midspan pressure surface Stanton number distributions

ing edge. As the flow moves toward the exit of the blade passage, it is forced toward midspan by the endwall secondary flow. The predicted pressure surface limiting streamlines are shown in Fig. 12. The corresponding experimental pressure surface limiting streamlines are presented in Fig. 13. The leading edge stagnation line is well illustrated in Fig. 12 and it is evident from both the predicted and experimental limiting streamlines that the flow on the pressure surface is predominantly two dimensional in nature.

The predicted endwall limiting streamlines from the fine grid simulation are shown in Fig. 14, while the experimental endwall limiting streamlines are shown in Fig. 15. In both Figs. 14 and 15, a saddle point is evident near the pressure surface leading edge of the airfoil. In the numerical simulation, the saddle point location is predicted somewhat farther upstream than that observed in the experiment. This again indicates that the predicted endwall boundary layer is slightly too thick. In Graziani et al. (1980), it was demonstrated that the location of the saddle point moves upstream as the endwall boundary layer is thickened. In both Figs. 14 and 15, the flow in the leading edge region moves onto the suction side of the passage and intersects the suction surface near the minimum pressure point. The flow on the pressure side of the passage migrates toward the suction surface, intersecting it in the region downstream of the minimum pressure point.

To assess the ability of the present Navier–Stokes analysis to predict heat transfer, the Stanton number was calculated along the surface of the airfoil and compared with the experimental data of Graziani et al. (1980). The Stanton number is defined as:

$$\mathrm{St} = \left(\frac{\partial h}{\partial n}\right) / (\mathrm{RePr}(h_{aw} - h_w)) \qquad (12)$$

where n is the normal distance from the wall, h_{aw} is the adiabatic enthalpy at the wall, and h_w is the enthalpy at the wall. Figure 16 compares the predicted suction surface midspan Stanton number distributions obtained with and without transition, the predicted results from the two-dimensional simulation, and the experimental data. The fully turbulent calculation overpredicts the Stanton number in the first 25 percent of the axial chord, demonstrating the importance of modeling transition. As discussed earlier, midspan transition was prescribed, according to the experimental data, to be instantaneous at the 25 percent axial chord position. The effects of transition are evident from the rapid increase in the Stanton number at the 25 percent axial chord location. The Stanton number is predicted very well ahead of transition but is slightly underpredicted aft of the transition point. It has been found, based upon a number of two-dimensional simulations, that this small discrepancy is due to the instantaneous transition model currently used in the three-dimensional procedure. Very good agreement was found to exist between the predicted Stanton number distribution and the experimental data in the two-dimensional simulations when transition was modeled over a region extending between 25–60 percent axial chord (see Fig. 16).

A comparison of the predicted three-dimensional midspan pressure surface Stanton number distribution with the experimental data is presented in Fig. 17. The three-dimensional predicted results demonstrate only fair agreement with the experimental data. A series of two-dimensional simulations were performed to determine if the difference between the predicted Stanton number and the experimental data near the 25 percent axial chord location was due to transition, similar to the suction surface. The results from these two-dimensional simulations showed that transition had little effect on the pressure-side Stanton number distribution in this region of the flow. Further investigation is required to determine the contributing factors of these differences.

The predicted three-dimensional fine grid suction surface Stanton number contours are shown in Fig. 18. The experimental suction surface Stanton number contours are illustrated in Fig. 19. The predicted results demonstrate good quantitative agreement with the experimental data, except along the hub endwall downstream of the separation streamline, where the experimental data indicate increased amounts of heat transfer. In Fig. 18, the variation of the transition location with span is apparent in the leading edge endwall regions. Both the predicted results and the experimental data indicate enhanced heat transfer at the airfoil leading edge in the endwall regions and downstream of the endwall separation line.

Figures 20 and 21 illustrate the predicted fine grid and experimental Stanton number contours for the pressure surface. The predicted Stanton number distribution shows close agreement with the experimental data. Both the predicted results and the experimental data reveal much less heat transfer taking place on the pressure surface, as indicated by smaller values of the Stanton number.

Figures 22 and 23 present the predicted fine grid and experimental Stanton number contours for the endwall. In both the predicted results and the experimental data, the lowest values of the endwall Stanton number are located on the pressure surface, beginning just downstream of the saddle point and extending to the trailing edge. In both figures, a region of increased heat transfer is located near the suction surface leading edge and in the vicinity of the minimum pressure point on the suction surface. In the wake region, discrepancies exist between the predicted results and the experimental data. The

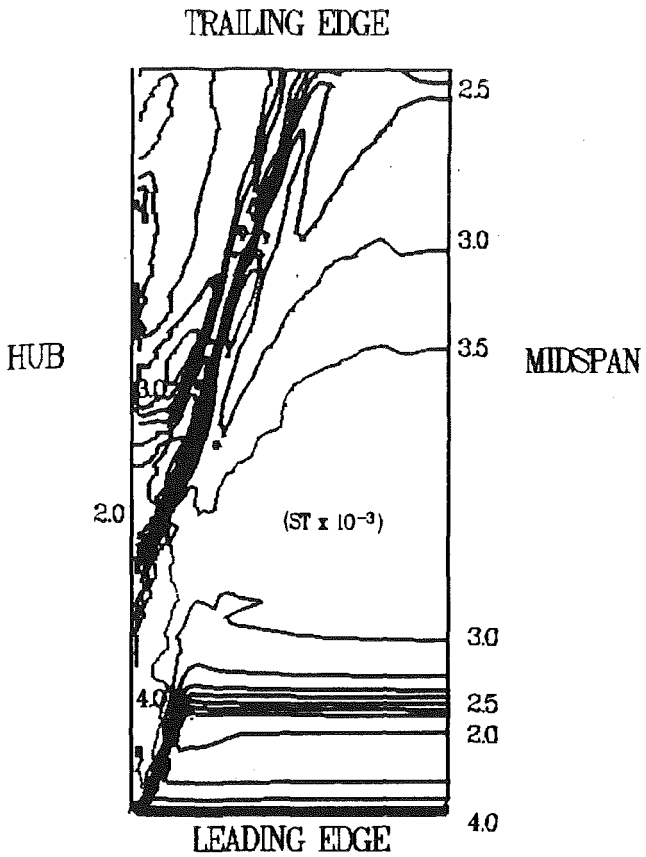

Fig. 18 Predicted suction surface Stanton number contours

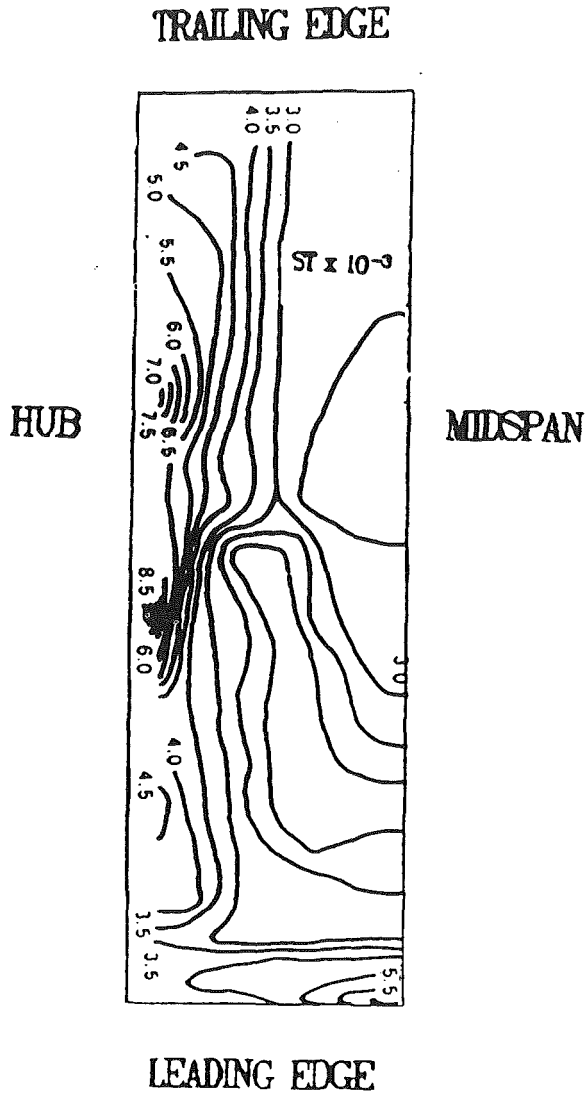

Fig. 19 Experimental suction surface Stanton number contours

predicted results indicate a small amount of heat transfer in the wake region, while the experimental data indicate larger amounts of heat transfer. These discrepancies may be partially due to the use of O-grids to discretize around the airfoil surface. In the wake region, the gradients used in the turbulence model are parallel, rather than normal, to the wake. A previous numerical study for a multistage compressor, however, has shown that this technique can be used to obtain accurate wake profile predictions (Gundy-Burlet et al., 1990). Other than in the wake region, the predicted results show good agreement with the experimental data.

The predicted spanwise distributions of the total pressure loss coefficient downstream of the trailing edge for all of the cases given in Table 1 are compared with the experimental data in Fig. 24. The total pressure loss coefficient is defined as:

$$C_{P_T}=\frac{2(P_T-P_{T_1})}{\rho U_1^2} \tag{13}$$

The midspan profile loss is accurately predicted using the fine grid, but overpredicted using the coarser grids. The predicted fine grid spanwise loss distribution shows features similar to the experimental data. The profile loss at midspan is predicted very well by the current procedure, but the peak loss region near the 25 percent span location is not being accurately predicted. The predicted loss in this region associated with the secondary flow is predicted to be lower and more toward midspan. The small rise in the predicted loss distribution in the endwall region (Cases 5 and 6) agrees well with the experimental data.

Table 1 provides the area-averaged total pressure loss for each of the curves shown in Fig. 24. These values of area-averaged loss were computed using C_{P_T} values at the experimental data locations in order to be consistent. Table 1 shows that for the finest grid solution, a 2 percent error exists between the predicted and experimental area-averaged losses. The primary source of this error is the underprediction of the secondary flow loss near the 25 percent span location as shown in Fig. 24. Since an essentially grid-independent solution was achieved using the finest grid (see Fig. 1), this error can be mainly attributed to the algebraic turbulence model and the transition model.

Figures 25 and 26 illustrate the predicted and experimental total pressure loss contours at the exit plane of the turbine passage. The effects of the passage vortex and endwall secondary flow on the total pressure loss distribution are accurately predicted by the numerical analysis. Both the predicted and the experimental total pressure loss contours indicate the existence of three peak loss regions. These peak loss regions may be associated with three separate vortices, which form a triangle bounded by the airfoil suction surface and the hub endwall. The largest vortex, associated with the secondary flow, is located at the apex of the triangle (Graziani et al., 1980). By examining the vorticity field, it was determined that the secondary flow vortex rotates in the clockwise direction (see Fig. 25). A slightly smaller vortex, which may possibly be associated with the suction side leg of the horseshoe vortex, rotates in the counterclockwise direction and is located more toward the midspan region than the secondary flow vortex (Graziani et al., 1980). The smallest vortex, which may be associated with the suction side corner vortex, also rotates in

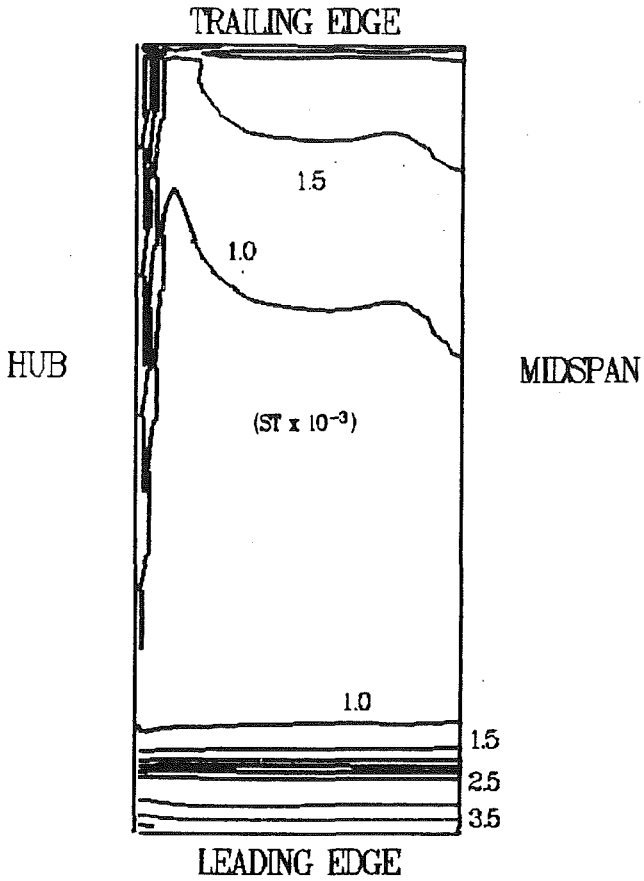

Fig. 20 Predicted pressure surface Stanton number contours

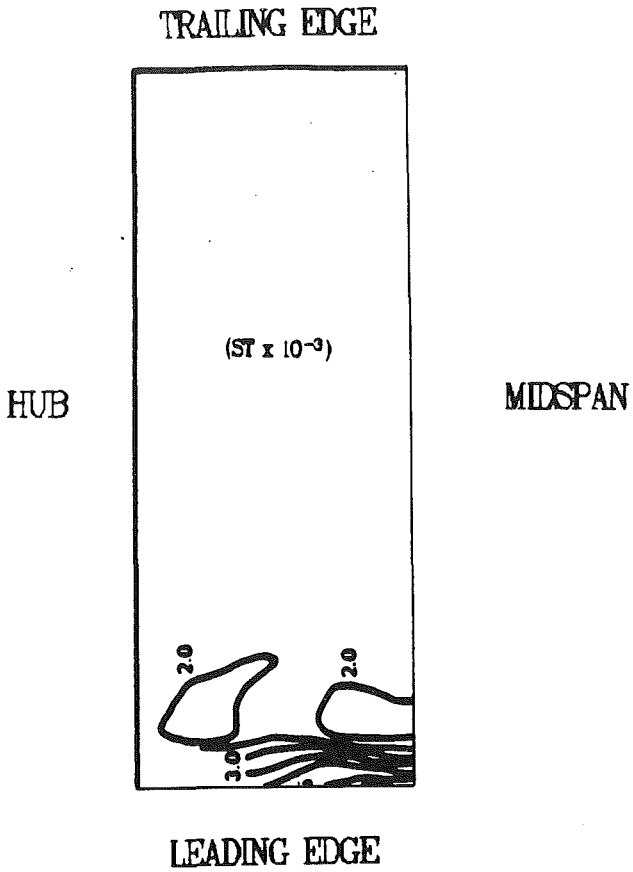

Fig. 21 Experimental pressure surface Stanton number contours

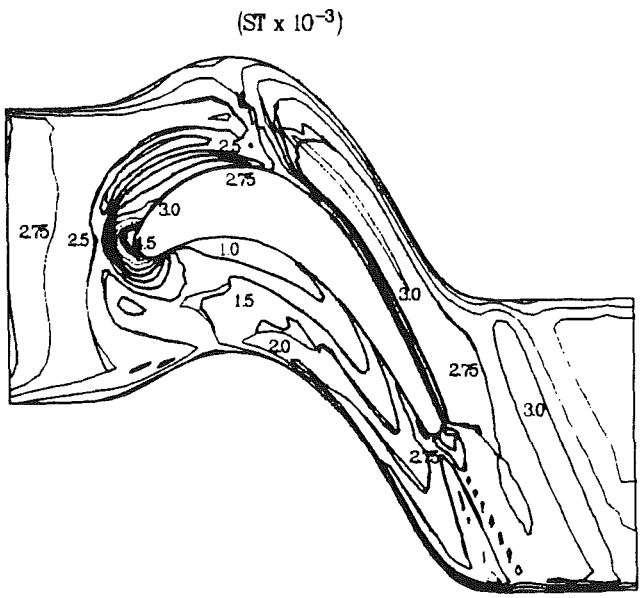

Fig. 22 Predicted endwall Stanton number contours

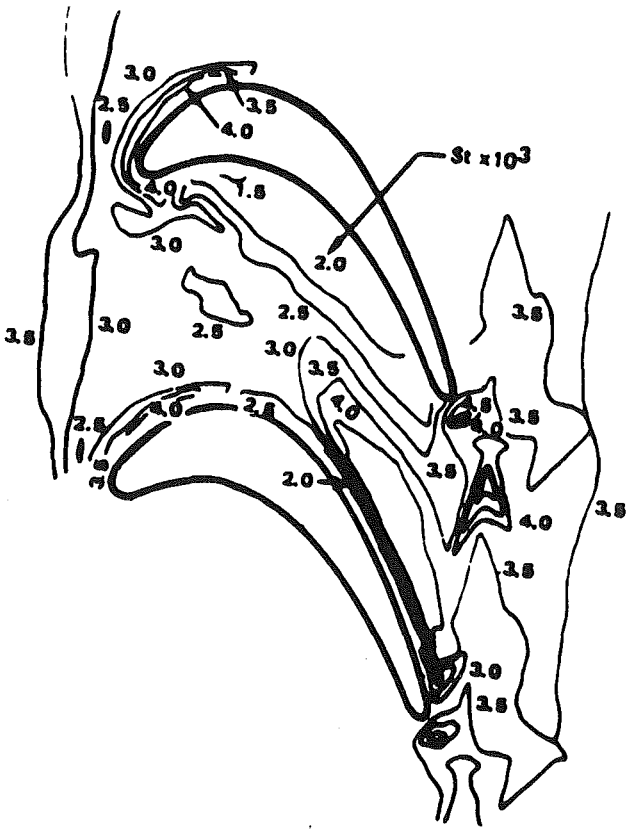

Fig. 23 Experimental endwall Stanton number contours

the counterclockwise direction and is located closer to the hub endwall than the other two vortices.

The predicted spanwise distribution of the gap-averaged flow angle (in the pitchwise direction) downstream of the trailing edge for the cases given in Table 1 are compared with the experimental data in Fig. 27. The shape of the predicted three-dimensional flow angle distribution demonstrates good qualitative agreement with the experimental data, but the numerical values are uniformly larger than the experimentally measured flow angles by approximately 1 deg. It should be noted that

the experimentally measured flow angles are generally accurate to within approximately 0.5 deg. As shown in Table 1, the exit flow angle changed very little with increasing grid density, indicating that grid dependence is not the cause of the discrepancy between the predicted and experimental flow angles. The 3.5 percent difference between the predicted area-averaged exit flow angle and the experimental data could possibly to be due to inadequacies in the modeling of transition and turbulence, and/or it could be due to a breakdown of the thin layer assumption in the secondary flow regions.

Conclusions

A three-dimensional, implicit, upwind Navier-Stokes procedure has been used to predict heat transfer and aerodynamic performance quantities in the Langston cascade for a thin inlet boundary layer. A grid resolution study has been performed that indicates that approximately 900,000 (full span) computational grid points are required for a typical single turbomachinery blade row to produce grid-independent solutions for flows at Reynolds numbers typical of those in gas turbine engines. While no general formula can be derived for determining the grid density needed for more complex flows (i.e., flows with tip clearance vortices, etc.), this study can serve as a useful guide in future investigations. In addition, this study has shown that overall aerodynamic turbomachinery blade row performance can be predicted within 2 percent using these fine computational grids with the Baldwin-Lomax algebraic turbulence model. Also, the importance of modeling transition from laminar to turbulent flow within the blade passage for the accurate prediction of heat transfer is demonstrated. Clearly, further progress in reducing the computational time required for three-dimensional Navier-Stokes procedures is required to enable reliable and affordable grid-independent solutions for turbomachinery blade row flows. This capability is required before major improvements in turbulence modeling can be made and three-dimensional heat transfer and aerodynamic performance quantities can be routinely and accurately predicted.

Acknowledgments

This work was supported by the Naval Air Systems Command under NAVAIR contract No. N00140-88-0677 from the office of George Derderian with Raymond Shreeve of the Naval Post Graduate School acting as technical monitor and the United Technologies Research Center under the Corporate Research Program. The three-dimensional simulations performed during this investigation were performed on the NAS Numerical Aerodynamic Simulation CRAY-2 supercomputer. The authors would like to thank Man Mohan Rai and Linda Haines of the NASA Ames Research Center for assistance in computational aspects of this investigation. The authors appreciate the helpful discussions with Om Sharma of Pratt & Whitney and Mike Blair and Bob Dring of the United Technologies Research Center concerning interpretation of the experimental results. The authors are also indebted to R. A. Graziani and J. R. Taylor of Pratt & Whitney, R. E. Mayle of Rensselaer Polytechnic Institute, and L. S. Langston of the University of Connecticut, all of whom helped create the extensive experimental data base that made this investigation possible. Results in this paper were first presented at the Ad-

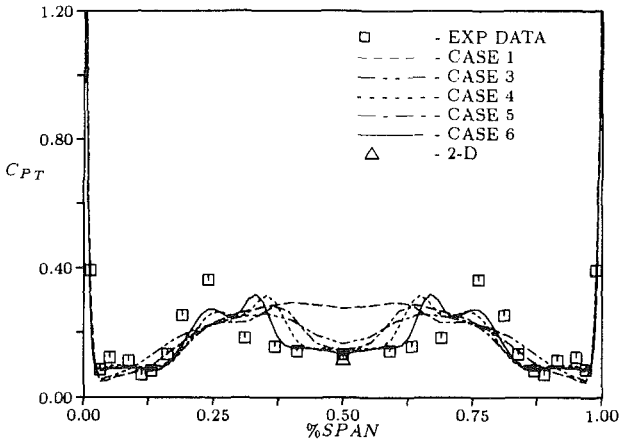

Fig. 24 Gap-averaged total pressure coefficient distributions

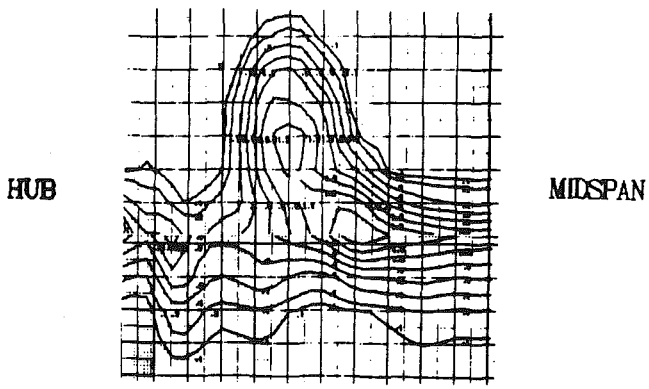

Fig. 26 Experimental total pressure loss coefficient contours at exit of turbine passage

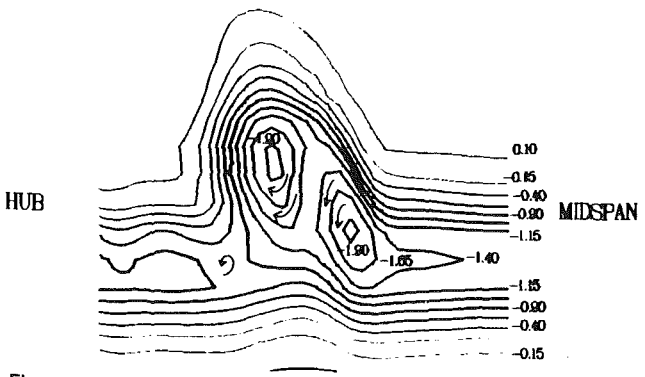

Fig. 25 Predicted total pressure loss coefficient contours at exit of turbine passage

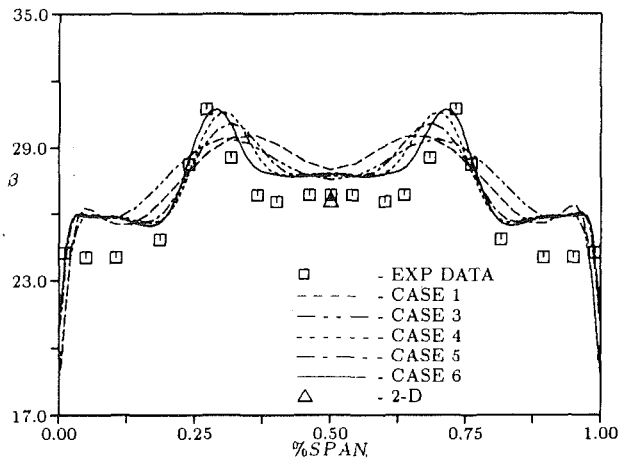

Fig. 27 Gap-averaged flow angle distributions

visory Group for Aerospace Research and Development, North Atlantic Treaty Organization (AGARD/NATO) PEP Symposium of CFD Techniques for Propulsion Applications, May, 1991.

References

Baldwin, B. S., and Lomax, H., 1978, "Thin-Layer Approximation and Algebraic Model for Separated Turbulent Flows," AIAA Paper No. 78-257.

Beam, R. M., and Warming, R. F., 1977, "An Implicit Factored Scheme for the Compressible Navier-Stokes Equations," AIAA Paper No. 77-645.

Chan, D. C., and Sheedy, K. P., 1990, "Turbulent Flow Modeling of a Three-Dimensional Turbine," AIAA Paper No. 90-2124.

Dhawan, S., and Narasimha, R., 1958, "Some Properties of Boundary Flow During Transition From Laminar to Turbulent Motion," *Journal of Fluid Mechanics*, Vol. 3, pp. 418–436.

Dorney, D. J., and Davis, R. L., 1989, "Investigation of Hot Streak Migration and Film Cooling Effects on the Heat Transfer in Rotor/Stator Interacting Flows," United Technologies Progress Report No. R89-957927-2.

Graziani, R. A., Blair, M. F., Taylor, J. R., and Mayle, R., E., 1980, "An Experimental Study of Endwall and Airfoil Surface Heat Transfer in a Large Scale Turbine Blade Cascade," ASME *Journal of Engineering for Power*, Vol. 102, No. 2, pp. 257–267.

Gundy-Burlet, K. L., Rai, M. M., Stauter, R. C., and Dring, R. P., 1990, "Temporally and Spatially Resolved Flow in a Two-Stage Axial Compressor, Part 2—Computational Assessment," NASA TM-102273.

Hah, C., 1984, "A Navier-Stokes Analysis of Three-Dimensional Turbulent Flows Inside Turbine Blade Rows at Design and Off-Design Conditions," ASME *Journal of Engineering for Gas Turbines and Power*, Vol. 106, pp. 421–429.

Hah, C., 1989, "Numerical Study of Three-Dimensional Flow and Heat Transfer Near the Endwall of a Turbine Blade Row," AIAA Paper No. 89-1689.

Hung, C. M., and MacCormack, R. W., 1978, "Numerical Solution of Three-Dimensional Wave and Turbulent Boundary Layer Interaction," AIAA Paper No. 78-161.

Hung, C. M., and Buning, P. G., 1984, "Simulation of Blunt-Fin Induced Shock Wave and Turbulent Boundary Layer Interaction," AIAA Paper No. 84-0457.

Johnson, D. A., and King, L. S., 1985, "A Mathematically Simple Turbulence Closure Model for Attached and Separated Turbulent Boundary Layers," *AIAA Journal*, Vol. 23, No. 11, p. 1684.

Langston, L. S., Nice, M. L., and Hooper, R. M., 1977, "Three-Dimensional Flow Within a Turbine Cascade Passage," ASME *Journal of Engineering for Power*, Vol. 99, pp. 21–28.

Lee, D., and Knight, C. J., 1989, "Evaluation of an O-H Grid Formulation for Viscous Cascade Flows," AIAA Paper No. 89-0207.

Moore, J., and Ransmayr, A., 1984, "Flow in a Turbine Cascade: Part I—Losses and Leading Edge Effects," ASME *Journal of Engineering for Gas Turbines and Power*, Vol. 106, pp. 400–408.

Moore, J., and Moore, J. G., 1985, "Performance Evaluation of Linear Turbine Cascades Using Three-Dimensional Viscous Flow Calculations," ASME *Journal of Engineering for Gas Turbines and Power*, Vol. 107, pp. 969–975.

Rai, M. M., 1985, "An Implicit, Conservative, Zonal-Boundary Scheme for Euler Equation Calculations," AIAA Paper No. 85-0488.

Rai, M. M., and Madavan, N. K., 1988, "Multi-airfoil Navier-Stokes Simulations of Turbine Rotor-Stator Interaction," AIAA Paper No. 88-0361.

Rai, M. M., 1989, "Three-Dimensional Navier-Stokes Simulations of Turbine Rotor-Stator Interaction," *Journal of Propulsion and Power*, Vol. 5, pp. 307–319.

Roe, P. L., 1981, "Approximate Riemann Solvers, Parameter Vectors, and Difference Schemes," *Journal of Computational Physics*, Vol. 43, pp. 357–372.

Vatsa, V. N., and Wedan, B. W., 1988, "Navier-Stokes Solutions for Transonic Flow Over a Wing Mounted in a Wind Tunnel," AIAA Paper No. 88-0102.

Prediction of Unsteady Rotor-Surface Pressure and Heat Transfer From Wake Passings

L. T. Tran
Sverdrup Technology, Inc.,
Lewis Research Center Group,
Brook Park, OH 44142

D. B. Taulbee
Department of Mechanical and
Aerospace Engineering,
University at Buffalo, SUNY,
Buffalo, NY 14260

The research described in this paper is a numerical investigation of the effects of unsteady flow on gas turbine heat transfer, particularly on a rotor blade surface. The unsteady flow in a rotor blade passage and the unsteady heat transfer on the blade surface as a result of wake/blade interaction are modeled by the inviscid flow/boundary layer approach. The Euler equations that govern the inviscid flow are solved using a time-accurate marching scheme. The unsteady flow in the blade passage is induced by periodically moving a wake model across the passage inlet. Unsteady flow solutions in the passage provide pressure gradients and boundary conditions for the boundary-layer equations that govern the viscous flow adjacent to the blade surface. Numerical solutions of the unsteady turbulent boundary layer yield surface heat flux values that can then be compared to experimental data. Comparisons with experimental data show that unsteady heat flux on the blade suction surface is well predicted, but the predictions of unsteady heat flux on the blade pressure surface do not agree.

Introduction

Unsteady flow effects are a concern in determining heat transfer and aerodynamics on a turbine blade surface. Flow unsteadiness arises from the relative motion between a stationary vane row and a rotating blade row. The sources of unsteadiness include shock wave passing, secondary vortices, potential flow interaction, and wake passing. In many cases, all of these sources of unsteadiness occur simultaneously. It is the purpose of the present work to study the wake effects on heat transfer to the blade surface.

Computational investigations of vane/blade interactions reported in the past concentrated on the aerodynamics of the blades and/or vanes, e.g., Erdos et al. (1976), Hodson (1985), Koya and Kotake (1985), Fourmeau (1986), Lewis et al. (1989), Giles (1988), Rai (1987), Jorgenson and Chima (1989), and Richardson (1990). With the exception of the last three methods, which solved the averaged Navier–Stokes equations, other methods cited above do not have the capability to calculate the surface heat transfer. In order to predict the heat transfer accurately using a Navier–Stokes solver, it is necessary to resolve the viscous layer adjacent to the wall. This requires an adequate number of grid points inside the boundary layer. Solution of the passage flow using the approach of solving the Navier–Stokes equations, including the boundary layer, is feasible but not practical at this time due to a large amount of computer time required. An alternate approach to the solution is described in the next paragraph.

Unsteady flow inside the blade passage can be viewed as a two-step process. First, the core flow consists of a throughflow with vane wakes passing from upstream and appears as unsteady flow in the rotor frame of reference. The passage core flow drives the surface boundary layer via pressure gradients. Second, the viscous layer flow reacts to the core flow, thus yielding the fine flow structure near the wall which determines the heat transfer. For the purpose of determining the blade surface unsteady heat transfer, the boundary layer approach can be followed, e.g., Krainer (1988), Cebeci and Platzer (1988), Taulbee and Tran (1989), and Jang et al. (1990). The focus of the current work is to combine the boundary layer solution with a realistic prediction of the unsteady pressure distribution.

Since the flow inside the blade passage is inviscid, the fluid motion is governed by the Euler equations. Flow unsteadiness in the blade passage is induced by periodically moving the wake model across the passage inlet. Time accurate solutions of the Euler equations subject to the appropriate boundary conditions yield the pressure distribution on the blade surface as functions of time and space needed for the unsteady boundary layer solutions. The viscous layer adjacent to the blade surface can be modeled by the unsteady boundary-layer equations, with the assumption that the viscous layer is thin compared to the blade dimension. The pressure gradients in the boundary-layer equations and conditions at the boundary-layer edge are obtained from the inviscid flow calculation. The turbulence flow in the viscous layer are modeled by a low Reynolds number k–ϵ model. Solutions of the boundary-layer equations yield the heat transfer at the surface.

Inviscid Flow Equations

In generalized coordinates the two-dimensional Euler equations are written in conservative form as:

Contributed by the International Gas Turbine Institute and presented at the 36th International Gas and Aeroengine Congress and Exposition, Orlando, Florida, June 3–6, 1991. Manuscript received by the ASME Headquarters March 4, 1991. Paper No. 91-GT-267. Associate Technical Editor: L. A. Riekert.

$$\frac{\partial \overline{\mathbf{D}}}{\partial t}+\frac{\partial \overline{\mathbf{E}}}{\partial \xi}+\frac{\partial \overline{\mathbf{F}}}{\partial \eta}=0 \tag{1}$$

where $\overline{\mathbf{D}}=\mathbf{D}/J$,

$$\overline{\mathbf{E}}=\frac{(\xi_x\mathbf{E}+\xi_y\mathbf{F})}{J},\quad \overline{\mathbf{F}}=\frac{(\eta_x\mathbf{E}+\eta_y\mathbf{F})}{J},\quad J=\frac{\partial(\xi,\eta)}{\partial(x,y)} \tag{2}$$

$$\mathbf{D}=\begin{pmatrix}\rho\\ \rho U\\ \rho V\\ e\end{pmatrix},\quad \mathbf{E}=\begin{pmatrix}\rho U\\ \rho U^2+P\\ \rho UV\\ (e+P)U\end{pmatrix},\quad \mathbf{F}=\begin{pmatrix}\rho V\\ \rho UV\\ \rho V^2+P\\ (e+P)V\end{pmatrix} \tag{3}$$

and ρ is the fluid density, U and V are the velocity components in x and y direction, respectively, e is the relative total energy and P is the static pressure. The pressure is related to the density, velocity, and energy via the equation of state

$$P=(\gamma-1)(e-\rho(U^2+V^2)/2) \tag{4}$$

There are many numerical schemes in the literature to solve the Euler equations. MacCormack's explicit scheme was used in this work because of its simplicity and the fact that it has been applied successfully in many flow situations. MacCormack's explicit scheme consists of two steps, namely predictor and corrector,

$$\overline{\mathbf{D}}^{\overline{n+1}}=\overline{\mathbf{D}}^{n}-\frac{\Delta t}{\Delta\xi}[\overline{\mathbf{E}}^{n}_{i,j}-\overline{\mathbf{E}}^{n}_{i-1,j}]-\frac{\Delta t}{\Delta\eta}[\overline{\mathbf{F}}^{n}_{i,j}-\overline{\mathbf{F}}^{n}_{i,j-1}] \tag{5}$$

$$\overline{\mathbf{D}}^{n+1}=\frac{1}{2}\left\{\overline{\mathbf{D}}^{n}+\overline{\mathbf{D}}^{\overline{n+1}}-\frac{\Delta t}{\Delta\xi}[\overline{\mathbf{E}}^{\overline{n+1}}_{i+1,j}-\overline{\mathbf{E}}^{\overline{n+1}}_{i,j}-\frac{\Delta t}{\Delta\eta}[\overline{\mathbf{F}}^{\overline{n+1}}_{i,j+1}-\overline{\mathbf{F}}^{\overline{n+1}}_{i,j}]\right\} \tag{6}$$

The superscripts n and $n+1$ represent the value of variables at time step n and $n+1$, respectively. Variables at time level n are used to evaluate the temporary variables $\overline{\mathbf{D}}^{n+1}$ in the predictor step. Next, the predictor $\overline{\mathbf{D}}^{n+1}$ is decoded to evaluate $\overline{\mathbf{E}}^{\overline{n+1}}$ and $\overline{\mathbf{F}}^{\overline{n+1}}$.

The boundary conditions involved are a combination of four types: inflow, outflow, solid wall, and periodic boundary conditions. For inviscid flow, the velocity at the wall is tangential to the wall surface. The periodic boundary conditions for unsteady flow in a blade passage present a challenge for calculating this flow. There are two types of periodic boundary conditions: spatial periodicity and temporal periodicity. The spatial periodicity appears when the blades and vanes have the same pitch. That is $P_r/P_s=1$, where P_r and P_s are the blade and vane pitches, respectively. In such cases, the periodic boundary conditions are enforced by requiring that flow conditions at one boundary be exactly the same as those at the other at the same time, that is: $\phi(x, y, t)=\phi(x, y+P_r, t)$. However, this is not the case where the pitches of the vanes and blades are different, that is $P_r/P_s\neq 1$. The spatial periodic boundary conditions can be enforced in this case by considering multiple passages, but it is not practical because large amounts of computer storage and time are often required to resolve the computational plane that spans many blade passages. Thus for the cases of $P_r/P_s\neq 1$ the temporal periodicity is useful since it can handle unsteady flow in a turbine stage with an arbitrary number of blades and vanes. This approach, called "phase-lagged," was first proposed by Erdos et al. (1976). The phase-lagged boundary condition is enforced by equating solutions at the exterior grid to those at the interior grid at an earlier time through appropriate phase relations, that is: $\phi(x, y, t)=\phi(x, y+P_r, t-\Delta t)$, where $\Delta t=(P_s-P_r)/V_r$ and V_r is the rotor speed. The "phase-lagged" approach has been used in many calculations of unsteady flow in a rotor passage. In practice, it would be simpler to have spatially periodic boundary conditions. The turbine engine geometry used in this study is the Garrett 731-2 HP, which has 78 blades and 41 vanes; thus the pitch ratio is 1.9, which for the purpose of this work was assumed to be sufficiently close to 2. Therefore, the computational plane includes two blade passages for every vane wake. The error introduced by this approximation is expected to be small because the time lag due to that approximation is small compared to the time that it takes for a wake to pass through the passage.

Computationally, the nodes on the periodic boundary are evaluated consistently with the interior nodes in predictor/corrector steps. For example, in the predictor step, nodes on the lower boundary ($j=1$) are evaluated using Eq. (5) where the values at $(j-1)$ are those of the interior row adjacent to the upper boundary $(J-1)$. After the corrector steps, values at the upper and lower boundaries are averaged so that their values are identical.

For unsteady flow, boundary conditions at the inlet and outlet of the rotor blade passage are time dependent. Following Giles' work (1988), the inlet conditions consist of two parts: a perturbation of the inlet flow condition due to wake/blade interaction, and a specified unsteady inlet flow given by a wake model. The wake model used in this study is the Gaussian wake model in which the wake flow is assumed to be parallel, with uniform static pressure and uniform relative total enthalpy. In the wake frame of reference, the density, velocity components, and static pressure can be expressed as:

$$P_{iw}=P_{is} \tag{7}$$

$$U_{iw}=q_{is}[1-f(\zeta)]\cos(\alpha_{is}) \tag{8}$$

$$V_{iw}=q_{is}[1-f(\zeta)]\sin(\alpha_{is}) \tag{9}$$

$$\rho_{iw}=\frac{\gamma}{\gamma-1}\frac{P_{is}}{\left[H_{is}-\frac{1}{2}(U^2_{iw}+V^2_{iw})\right]} \tag{10}$$

Nomenclature

c = speed of sound
C = axial blade chord
C_μ, C_1, C_2, σ = k–ϵ model parameters
D, W = wake deficit and wake width
e = relative total energy
f_μ, f_2 = low Reynolds number functions
H = relative total enthalpy
k = turbulent kinetic energy
P = static pressure
P_r, P_s = blade and vane pitches
Pr = Prandtl number
Pr_t = turbulent Prandtl number
t = time
Tu = turbulence intensity
U, V = velocity components in x and y direction
V_r = rotor speed
x, y = Cartesian coordinates
α = flow angle
ϵ = dissipation rate
γ = specific heat ratio
μ, μ_t = viscosity and turbulent viscosity
ξ, η = generalized coordinates
ρ = fluid density
τ = wake passing period
τ_w = shear stress at blade surface
$\bar{\omega}$ = $2\pi V_r/P_s\, C/U$ = reduced frequency
$\omega_{1,2,3,4}$ = characteristic variables
$(\ )_{\mathrm{inl}}$ = inlet condition in rotor frame
$(\ )_{\mathrm{is}}$ = steady condition in rotor frame
$(\ )_{\mathrm{iw}}$ = inlet condition in wake frame

where α_{is} is the wake flow angle, H_{is} is the relative total enthalpy, and q_{is} is the velocity magnitude. The subscript $(\,)_{iw}$ denotes values of variables in the wake frame of reference and the subscript $(\,)_{is}$ denotes steady-state values of variables (obtained from a prior calculation); $f(\zeta)$ is the Gaussian wake model

$$f(\zeta) = D\exp\left(-\frac{\zeta^2}{2W^2}\right) \tag{11}$$

where ζ is defined as $\zeta = [y - \tan(\alpha_{is})x]/P_s$; D and W are the wake deficit and wake width, respectively. The values of the Gaussian wake parameters $D = 0.15$ and $W = 0.04$ were estimated from the nozzle guide vane boundary layer calculations and the experimental data given by Raj and Lakshminarayana (1973) at a location $x/C = 0.2$ from the nozzle guide vane trailing edge. Note that the assumption of uniform total relative enthalpy could be replaced by a periodic function to account for the cooling of the portion of the fluid that has been in contact with nozzle guide vanes.

Giles (1988) assumed that the wake/rotor interaction generates outgoing pressure waves, which can be approximated by the perturbation of the inlet flow conditions. This involves the assumption that the perturbation waves have minimal variation in the circumferential direction, thus one-dimensional characteristic theory can be applied. The perturbation part of the inlet flow conditions can be expressed as (Giles, 1988):

$$\omega_1 = P - P_{\text{inl}} - c_{is}^2(\rho - \rho_{\text{inl}}) \tag{12}$$

$$\omega_2 = (V - V_{\text{inl}})\rho_{is}c_{is} \tag{13}$$

$$\omega_3 = P - P_{\text{inl}} + \rho_{is}c_{is}(U - U_{\text{inl}}) \tag{14}$$

$$\omega_4 = P - P_{\text{inl}} - \rho_{is}c_{is}(U - U_{\text{inl}}) \tag{15}$$

where the subscript $(\,)_{\text{inl}}$ denotes the inlet conditions in the rotor frame of reference described in the previous paragraph. Equation (13) arises from the perturbation of the normal velocity component. At the inlet, ω_1, ω_2, and ω_3 are set equal to zero to impose the condition that there is no other wave coming into the inlet boundary except the wave that has been incorporated into the wake model. ω_4 is the outgoing pressure characteristic and is extrapolated from the interior nodes. At the outlet boundary, a similar perturbation of the outlet flow conditions is applied. Here ω_4 is set equal to zero and values of ω_1, ω_2, and ω_3 are extrapolated from the interior nodes.

Inviscid Flow Results. Steady flow solutions in the TFE 731-2 HP rotor passage are obtained first since they are needed to initiate the unsteady flow calculations. A steady flow calculation was carried out in the rotor passage with a computational mesh of 21×151 nodes. The grid system employed is the H-type. The disadvantage in using the H-type grid system is that it cannot resolve the flow in the region of high surface curvature such as the leading and trailing edges of an airfoil unless a large number of grid points are concentrated in those regions. For the relatively small number of nodes in the x direction used in this study (151 nodes), solutions in the leading and trailing edges are not expected to be highly accurate. In addition, rapid changes of the surface slope at the leading and trailing edges result in large numerical errors; these errors eventually grow and destroy the calculation. Thus in generating the H-type grid for the Garrett 731-2 HP rotor passage, the leading and trailing edges of the blade were modified by fitting a wedge there.

Pressure distributions on the suction and pressure surfaces are shown in Fig. 1. The solid lines represent the present calculation results and the broken lines represent the results taken from Rae et al. (1988). The pressure has been normalized by the relative total pressure and the axial distance is normalized by the blade axial chord. There are no experimental pressure data available for this turbine blade to compare with the calculated results. However, it is seen that the present results agree reasonably with the results of Rae et al. for most of the pressure surface. For the suction surface, some discrepancies can be seen in the region of 65 percent $\leq x/C \leq$ 90 percent. It should be noted that the codes used in Rae et al. are the quasi-three-dimensional codes MERIDL and TSONIC, which are capable of predicting some features of three-dimensional flow. Thus discrepancies seen on the suction surface are probably due to three-dimensional flow effects that are not included in the present model.

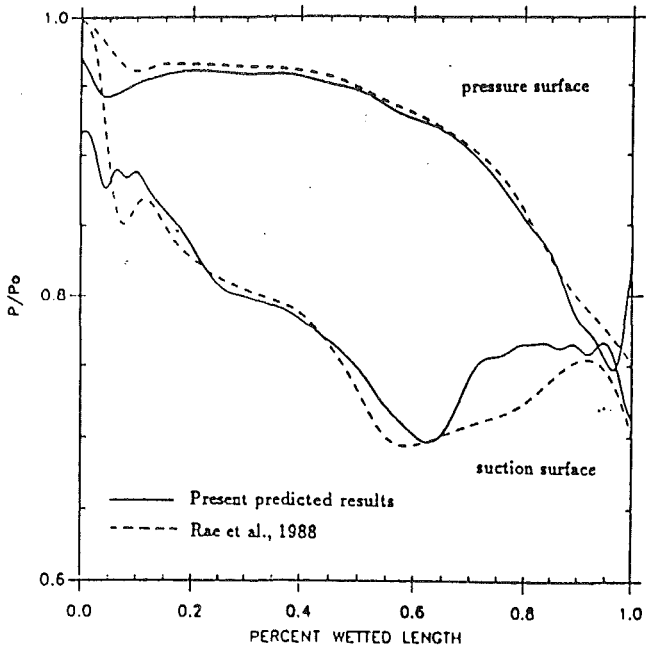

Fig. 1 Pressure distribution on the TFE 731-2 HP blade surface

As discussed earlier, unsteady flow calculations in the TFE 731-2 HP blade passage have to be carried out in two blade passages to model the wake/blade interaction realistically. Starting from a steady-state solution, the governing equations were integrated in time until the solution reached the periodic state. In this case, the time required for a periodic solution to develop is about 15 wake passing periods. A period is made up of about 300 time steps.

The wake is often characterized by the velocity defect whose minimum is identified as the wake centerline. For qualitative purposes, the velocity defect vectors are particularly helpful in identifying the wake regions in the blade passage. The velocity defect vectors, obtained by subtracting the steady-state velocity from the instantaneous velocity, are shown in Fig. 2 at five instants of a period, $t/\tau = 0.0$, 0.2, 0.4, 0.6, and 0.8. For the sake of clarity, only a quarter of the vectors in the x direction and half of the vectors in the y direction are shown.

In the entrance region, the wakes can be clearly identified as the banded concentrated vectors, which form an angle of 67 deg with the axial direction. This is the value of the nozzle guide vane exit angle. The size of the vector indicates the relative magnitude of the velocity defect, that is, large vectors inside the wake and small vectors outside of the wake. The region between two wakes is relatively calm, as shown by small vectors, although the vector directions are not in a common order. The motion of wakes moving in the entrance region can be seen by comparing the relative locations of the wakes in Fig. 2. At the blade leading edge, wakes are cut into segments and each segment finds itself in a different strain field from the other because of the inclination of the wake. Although the flow fields in the two blade passages at any instant in time are different, the one in the lower passage is exactly the same as the one in the upper passage at half a period later.

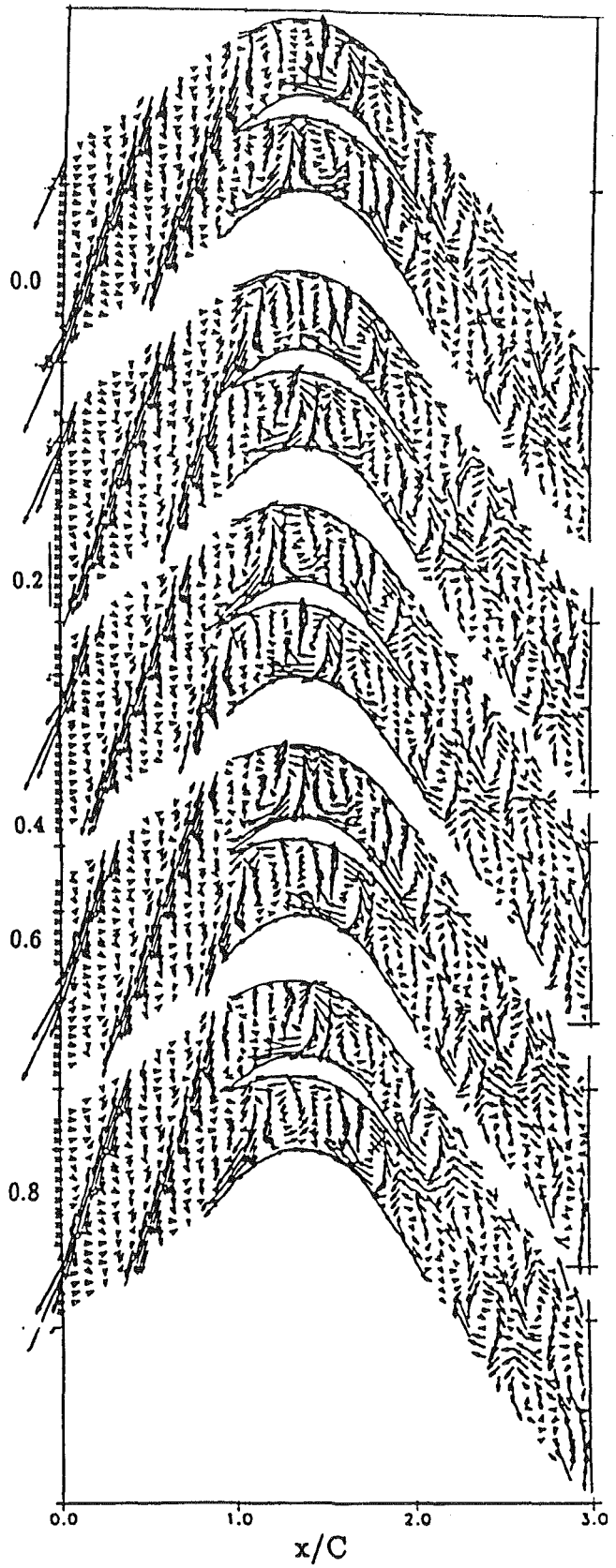

Fig. 2 Velocity defect vector in the TFE 731-2 HP blade passage, $t/\tau = 0.0$, 0.2, 0.4, 0.6, and 0.8

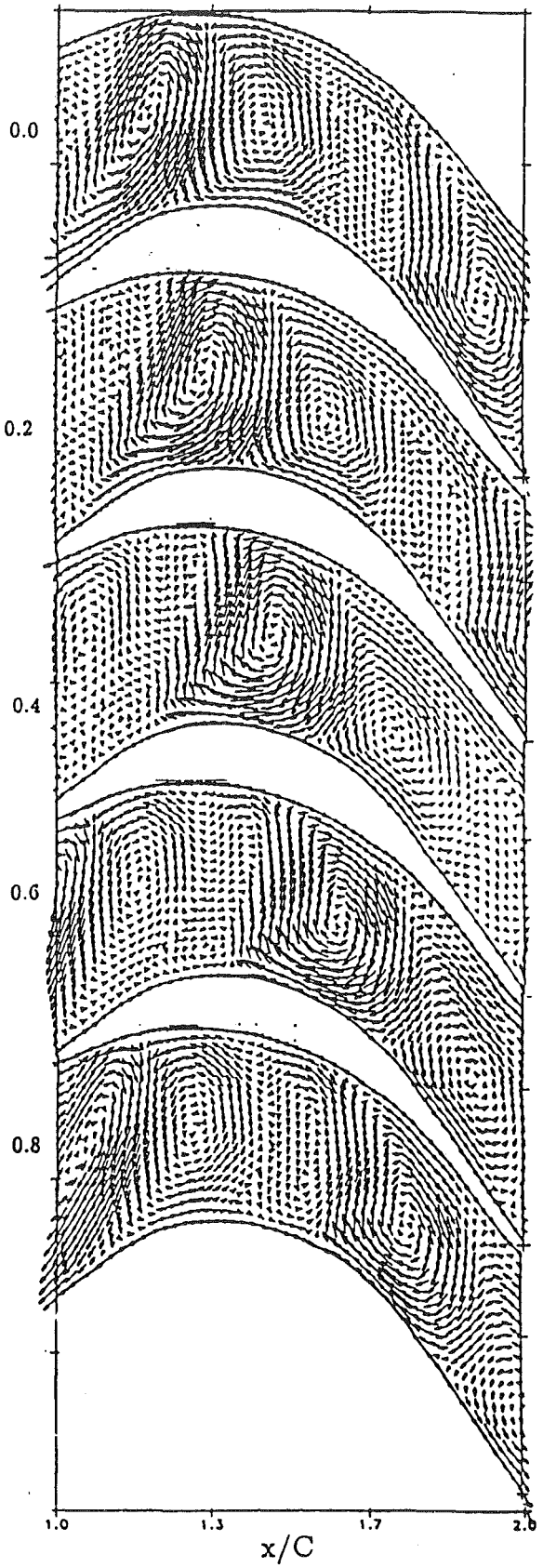

Fig. 3 Velocity defect vector in the TFE 731-2 HP blade passage, $t/\tau = 0.0$, 0.2, 0.4, 0.6, and 0.8

It is rather difficult to visualize the wake location and other flow activities inside the blade passage without a detailed enlarged plot. Therefore velocity defect vectors are replotted at all grid points inside the lower passage at five instants as shown in Fig. 3. Wake segments enter the blade passage at an angle, and their shapes are quickly deformed. As seen in Fig. 3

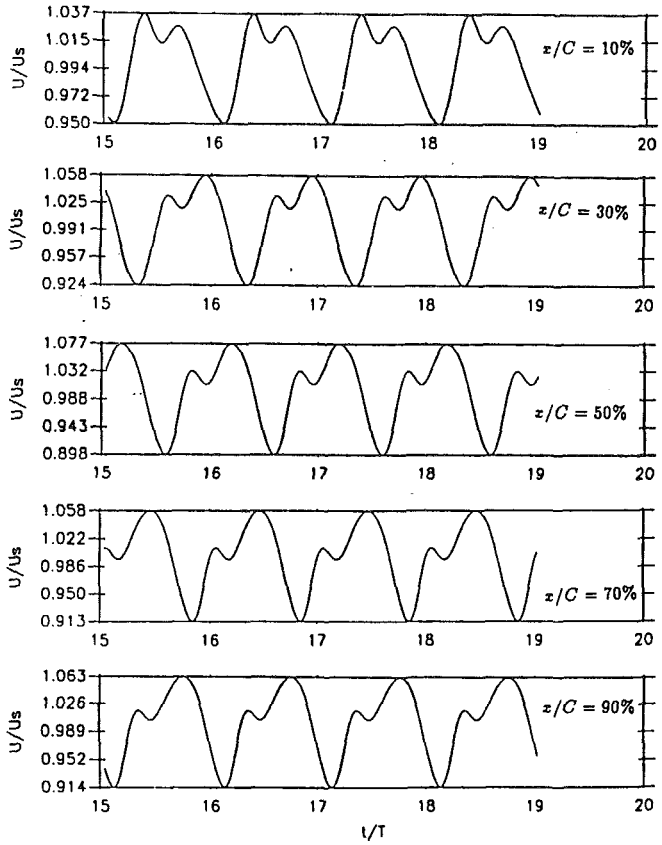

Fig. 4 Velocity variation at five locations on the suction surface

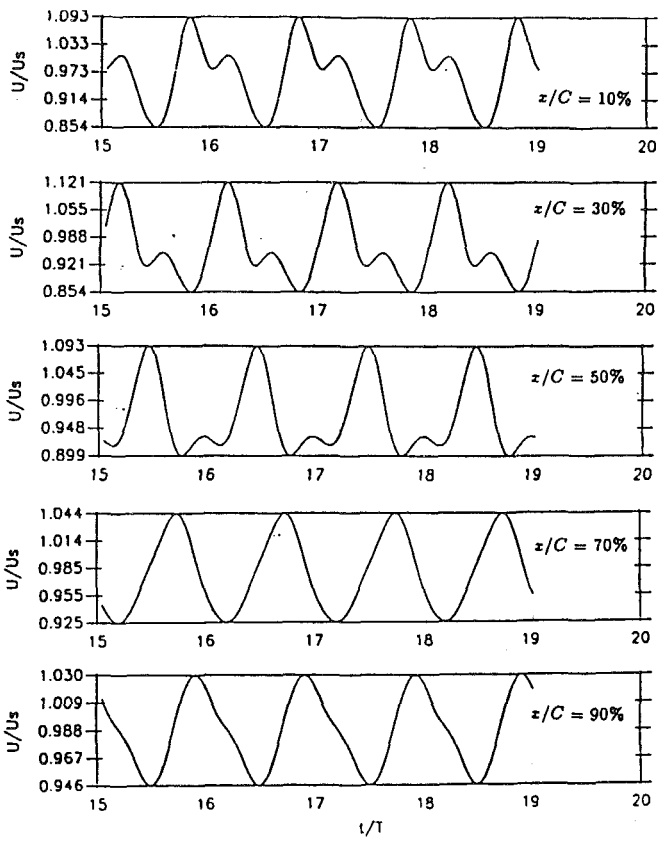

Fig. 5 Velocity variations at five locations on the pressure surface

($t/\tau = 0.6$), part of the segment near the pressure surface is narrowed down while the other part has not been affected by the surface. As the wake moves farther inside the blade passage ($t/\tau = 0.0$ and $t/\tau = 0.2$), the wake segment is nearly normal to the pressure surface but forms an angle with the suction surface. Farther downstream the wake angle near the pressure surface remains relatively unchanged until after approximately 2/3 of the axial distance from the blade leading edge, while the wake angle near the suction surface varies as it moves along the suction surface. Beyond that point, the wake shape cannot be visually recognized because it has been distorted so much due to strong acceleration near the pressure surface and deceleration near the suction surface ($t/\tau = 0.8$ and $t/\tau = 0.0$). However, the wake still causes large velocity and pressure variations on both surfaces, as will be seen later. The shape of the wake segment is also deformed by the variation of mean velocity across the blade passage. As a result, the wake is thin near the pressure surface and thick near the suction surface, as shown by the velocity defect vectors, which spread over few grid points on the pressure surface and over a quarter of the suction surface.

Two circulation regions are formed between the wake segments. The region immediately behind the wake rotates in clockwise direction, while the region in front rotates in the counterclockwise direction. These rotations help thin the wake segment at one end and thicken it at the other. The circulation regions also increase the instantaneous velocity on the surfaces in the vicinity of these regions, as indicated by arrows pointing in the streamwise direction. The number of wake segments, in this case equal to two, depends on the reduced frequency, which has the value of about 16 for the TFE 731-2 HP turbine stage. As reduced frequency increases, the relative distance between wake segments decreases and therefore decreases the size of the circulation regions, but increases their effects on the surfaces.

Unsteady velocities on the suction and pressure surfaces are plotted in Figs. 4 and 5, respectively. The velocity is normalized by its local undisturbed value and time is expressed in terms of the wake passing period. It is seen that the velocity has reached the periodic state solutions. The wake centerline at a location on a surface is indicated by the low dips in velocity waveform. On the suction surface, the second dip following the wake is caused by the unequal numbers of vane wake and rotor passage, as seen in Fig. 4. It is also seen that there are two wakes striking the suction surface within a wake passing period. The unsteady velocity varies about its undisturbed value ranging from 8 to 18 percent depending on location along the surface. The velocity decreases below its undisturbed value about 80 percent of the time in a period; therefore the time-averaged velocity is lower than the undisturbed velocity.

Velocity waveforms on the pressure surface are not similar to those on the suction surface. In the leading half surface the wake is followed by a little structure and this structure merges with the wake after about $x/C = 50$ percent. As a result the velocity waveform has a broader valley as seen in Fig. 5. The velocity magnitude variation about its undisturbed value is also higher than that on the suction surface. Here the variation ranges from 8 to 27 percent with the lower range being near the blade trailing edge. This is not unexpected since the undisturbed velocity on the pressure surface is lower than that on the suction surface. The time-averaged velocity on the pressure surface is also smaller than its undisturbed value.

Unsteady pressure variations on the suction and pressure surfaces are shown in Figs. 6 and 7. The axial locations where the pressure is shown are exactly the same as those shown in the unsteady velocity plots. In order to see the pressure changes due to wake passings, the unsteady pressure is normalized by its undisturbed value. It is seen that the pressure change on the suction surface varies from 1 to 2.5 percent. With an exception at $x/C = 90$ percent, pressure increases and decreases

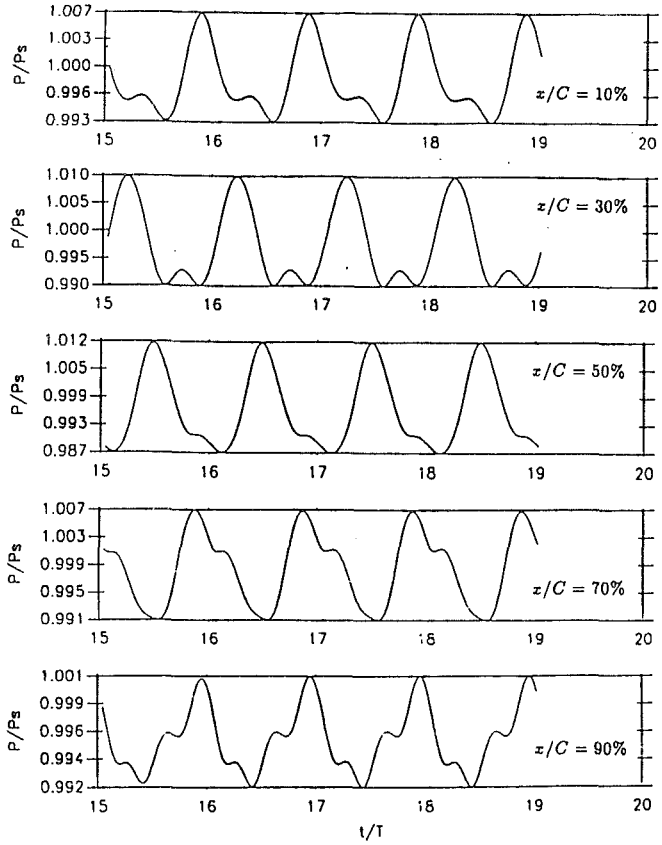

Fig. 6 Pressure variation at five locations on the suction surface

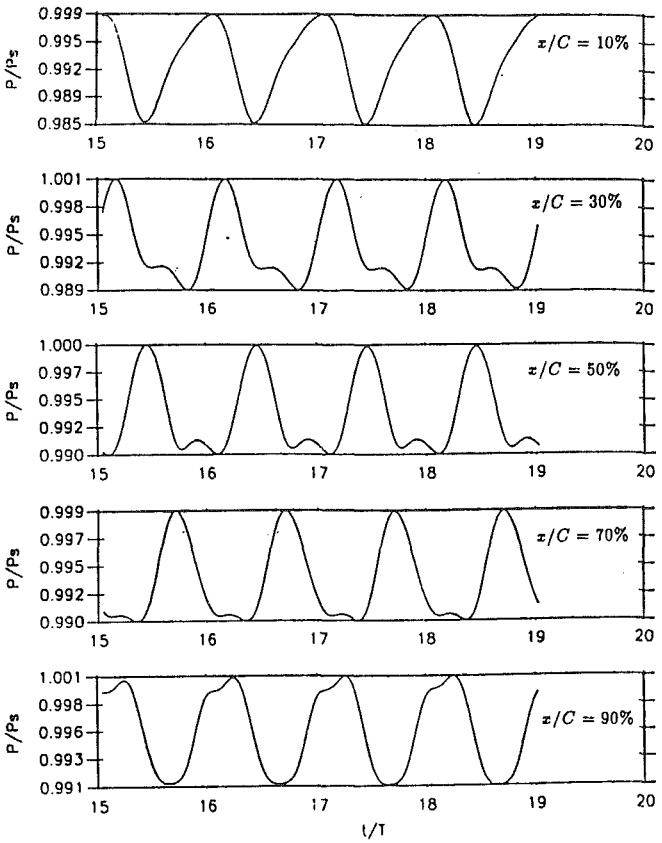

Fig. 7 Pressure variation at five locations on pressure surface

from its steady value the same amount, as shown in Fig. 6, whereas the pressure change is only in the negative direction on the pressure surface, i.e., the unsteady pressure decreases about 1 to 1.4 percent from its steady value. Pressure variation on the suction surface is higher than that on the pressure surface due to the lower steady-state pressure there.

The negative change of unsteady pressure on the pressure surface is a direct consequence of the fluid lifted off from the pressure surface as wake segments pass by. This can be seen by comparing the phases of the velocity and pressure waveforms in Figs. 5 and 7. It is seen that, with the exception at $x/C = 90$ percent, pressure and velocity are in phase. However, this is not true for the suction surface where the phase relationships between velocity and pressure are much more complicated. The positive pressure change is thought to be due to fluid impinging on the suction surface, and the negative change is a consequence of gaining momentum from the circulation leading the wake segment.

Turbulent Flow in Turbine Blade Passage. Turbulent flow within the blade passage originates from two different sources, namely, the background turbulence, and the turbulence from nozzle guide vane wakes. Therefore, the turbulent flow entering the blade passage can be modeled by a distribution function describing the turbulence wake and a uniform function describing the background turbulent flow which separates two wakes. The turbulent flow in the rotor blade passage is modeled using the turbulent kinetic energy/dissipation model. In Cartesian coordinates, the equations for turbulent kinetic energy k and dissipation ϵ can be written as:

$$\frac{\partial \mathbf{D}'}{\partial t}+\frac{\partial \mathbf{E}'}{\partial x}+\frac{\partial \mathbf{F}'}{\partial y}=\mathbf{S} \tag{16}$$

$$\mathbf{D}'=\begin{pmatrix}\rho k\\ \rho\epsilon\end{pmatrix},\quad \mathbf{E}'=U\mathbf{D}',\quad \mathbf{F}'=V\mathbf{D}',$$

$$\mathbf{S}=\begin{pmatrix}P_k-\rho_e\\ \epsilon/k\,(C_1P_k-C_2\rho\epsilon)\end{pmatrix} \tag{17}$$

where $P_k=-\rho\overline{u_iu_j}\,\partial U_i/\partial x_j$ denotes the production of turbulent kinetic energy and the turbulent stresses are calculated from

$$-\rho\overline{u_iu_j}=\frac{2}{3}\rho k\delta_{ij}-\mu_t\left(\frac{\partial U_i}{\partial x_j}+\frac{\partial U_j}{\partial x_i}\right) \tag{18}$$

where μ_t is defined as $\mu_t=C_\mu\rho k^2/\epsilon$. The model parameters C_1, C_2, and C_μ have the standard value of 1.44, 1.92, and 0.09, respectively, as given by Launder and Spaulding (1974).

With the exception of the source terms on the right-hand side of Eq. (16), the vector form of the turbulence variable equations is exactly the same as that of the mean flow. This suggests that the same numerical scheme can be applied to Eq. (16). Thus Eq. (16) was transformed into (ξ, η) coordinates and solved in the same manner as the mean flow.

At the inlet, the turbulence intensity is assumed to have the form $Tu=Tu_0+f(\zeta)$, where Tu_0 represents the background turbulence intensity and $f(\zeta)$ is the Gaussian function (Eq. (11)) representing the turbulence intensity within the wake. The turbulence wake width is assumed to be the same as the velocity wake width; thus $W=0.04$. Inconsistent with the results reported by Taulbee et al. (1989) and Taulbee and Tran (1989), Tu_0 is taken to be 6 percent. The value of D in Eq. (11) was estimated from the data of Raj and Lakshminarayana (1973) at a location corresponding to the distance at the blade leading edge along the wake path from the nozzle guide vane trailing edge. The centerline value of turbulence intensity is 13 percent for this location; therefore D is equal to 7 percent. The turbulent kinetic energy k and dissipation ϵ are then estimated from $k=1.5\,(TuV)^2$ and $\epsilon=k^{3/2}/\ell$ where V is the local velocity magnitude and ℓ is the turbulence length scale assumed to be one tenth of the wake thickness at the inlet passage. At

the exit and the wall boundaries, the turbulent kinetic energy and dissipation are simply extrapolated from the interior nodes. The periodic boundary conditions are applied in the usual manner. Solutions of the turbulent kinetic energy and dissipation equations on the blade surface will be used as boundary conditions for the boundary layer calculations reported later.

Boundary Layer Flow

It is the purpose of this section to calculate the unsteady heat transfer on the blade surface in the context of boundary layer theory. It is assumed that the relatively large viscous and thermal gradients that dictate the surface heat transfer are contained within the thin layers on blade surfaces. These boundary layers on the surfaces are disturbed by wake segments moving through the rotor passage. The convective wake segments result in disturbances in the inviscid flow field adjacent to the boundary layer. This effect can be incorporated via the boundary conditions of the unsteady boundary layer equations. The low Reynolds number kinetic energy/dissipation model is used to account for the turbulence effects.

The steady-state heat transfer on the vane and blade surfaces of the Garrett TFE 731-2 HP and the Teledyne 702 HP turbines were predicted with reasonable success by Taulbee et al. (1989) using the k–ϵ turbulence model. The same model is used in the presentation to calculate the unsteady boundary layer. Since the k–ϵ model is relatively unproven in unsteady boundary layer application, it must be assumed that it works adequately in this situation.

The continuity, momentum, thermal energy, turbulent kinetic, and dissipation equations for an unsteady compressible boundary layer are:

$$\frac{\partial \rho}{\partial t}+\frac{\partial(\rho U)}{\partial x}+\frac{\partial(\rho V)}{\partial y}=0 \tag{19}$$

$$\rho\frac{\partial U}{\partial t}+\rho U\frac{\partial U}{\partial x}+\rho V\frac{\partial U}{\partial y}=-\frac{\partial P}{\partial x}+\frac{\partial}{\partial y}\left[(\mu+\mu_t)\frac{\partial U}{\partial y}\right] \tag{20}$$

$$\rho\frac{\partial H}{\partial t}+\rho U\frac{\partial H}{\partial x}+\rho V\frac{\partial H}{\partial y}=+\frac{\partial}{\partial y}\left[\left(\frac{\mu}{\mathrm{Pr}}+\frac{\mu}{\mathrm{Pr}_t}\right)\frac{\partial H}{\partial y}\right]+\frac{\partial P}{\partial t}+\frac{\partial}{\partial y}\left\{\left[\mu\left(1-\frac{1}{\mathrm{Pr}}\right)+\mu_t\left(1-\frac{1}{\mathrm{Pr}_t}\right)\right]\mathrm{U}\frac{\partial \mathrm{U}}{\partial y}\right\} \tag{21}$$

$$\rho\frac{\partial k}{\partial t}+\rho U\frac{\partial k}{\partial x}+\rho V\frac{\partial k}{\partial y}=\frac{\partial}{\partial y}\left[(\mu+\mu_t)\frac{\partial k}{\partial y}\right]+\mu_t\left[\frac{\partial U}{\partial y}\right]^2-\rho\epsilon-D \tag{22}$$

$$\rho\frac{\partial \epsilon}{\partial t}+\rho U\frac{\partial \epsilon}{\partial x}+\rho V\frac{\partial \epsilon}{\partial y}=\frac{\partial}{\partial y}\left[\left(\mu+\frac{\mu_t}{\sigma}\right)\frac{\partial \epsilon}{\partial y}\right]+C_1\frac{\epsilon}{k}\mu_t\left(\frac{\partial U}{\partial y}\right)^2-C_2 f_2\rho\frac{\epsilon^2}{k}+E \tag{23}$$

where $\mu_t = C_\mu f_\mu \rho k^2/\epsilon$ is the turbulent viscosity, Pr and Pr_t are the Prandtl number and turbulent Prandtl number, taken to be 0.71 and 0.9, respectively.

For Chien's version (1982), the model parameters are: $C_\mu = 0.09$, $C_1 = 1.35$, $C_2 = 1.80$, $\sigma = 1.30$, $f_\mu = 1 - e^{-0.0115y^+}$, $f_2 = 1 - 0.22e^{-(R_T/6)^2}$, $D = 2\mu k/y^2$, and $E = -2\mu(\epsilon/y^2)e^{-0.5y^+}$. The turbulent Reynolds number and the nondimensional wall coordinate y^+ are defined as $R_T = k^2/(\nu\epsilon)$, $y^+ = yU_\tau/\nu$, and U_τ is the friction velocity, $U_\tau = \sqrt{\tau_w/\rho}$.

Equations (20)–(23) are solved subject to boundary conditions at the boundary layer edge and at the wall. At the boundary layer edge, velocity $U_e(x, t)$, total enthalpy $H_e(x, t)$, turbulent kinetic energy $k_e(x, t)$ and dissipation $\epsilon_e(x, t)$ were obtained in a prior unsteady inviscid flow calculation, as reported in the previous sections. The boundary conditions on the wall surface are: $U(x, 0, t) = 0$, $H(x, 0, t) = C_pT_w$, $k(x, 0, t) = 0$, $\epsilon(x, 0, t) = 0$, where T_w is the wall surface temperature.

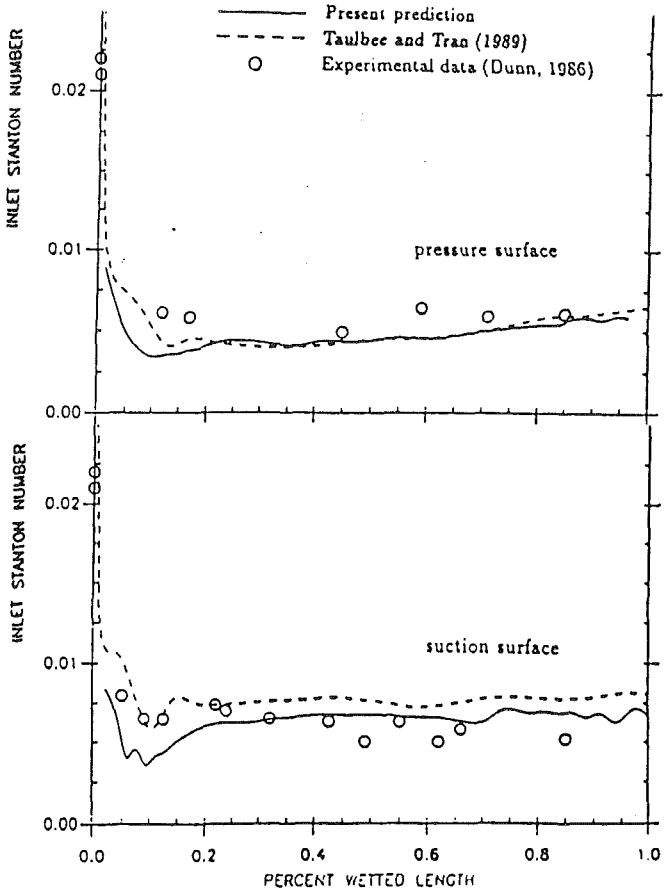

Fig. 8 Comparison of steady heat transfer on the TFE 731-2 HP blade surface

Equations (20)–(23) are backward differenced in time so that in effect a steady equation is solved at each instant in time. The solution is accomplished by marching down the surface solving a boundary value problem in the y direction at each x station, thus determining profiles for U, H, k, and ϵ. The density ρ is given by the perfect gas equation and the velocity component normal to the surface is determined from the continuity equation. The solution for the profiles at each station were converged via iteration. Three hundred grid points on a nonuniform grid were used across the boundary layer with the first node away from the surface set at $y^+ = 0.5$ to insure accuracy in the wall heat flux calculation. A total of 300 stations were calculated down the blade surface. Calculations were initiated at a station near the blade leading edge. Profiles at the initial station for the unsteady solution were obtained by multiplying the steady solution there by the ratio of the unsteady free-stream value to the steady free-stream value, i.e., $F(x_0, y, t) = F_s(x_0, y)[F_e(x_0, t)/F_e(x_0)]$. The unsteady solution was initiated from the steady-state solution.

Steady Heat Transfer. Steady boundary layer solutions were obtained by solving boundary layer Eqs. (19)–(23) without the time-dependent terms and with pressure gradient obtained from steady inviscid flow solutions. As pointed out earlier, calculations were initiated after the leading edge and terminated before the trailing edge of the blade due to the oscillations in predicted surface pressure there. Comparisons of the predicted Stanton number with the experimental data of Dunn (1986) are given in Fig. 8 for suction and pressure surfaces, respectively, of the TFE 731-2 HP turbine blade. Note that

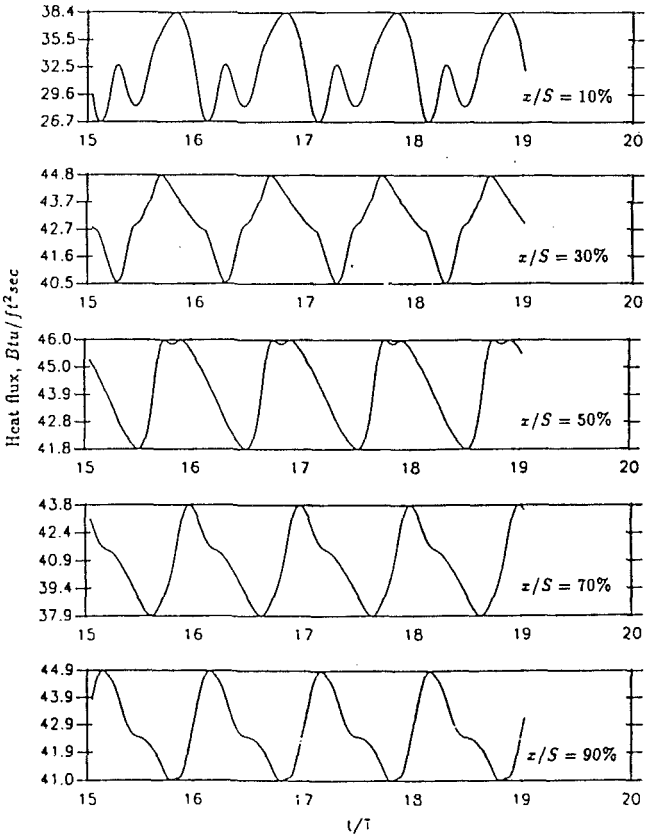

Fig. 9 Unsteady heat flux at five locations on suction surface

the Stanton number was evaluated consistently with the definition given by Dunn (1986) in which mass flux was based on the inlet flow rate and the inlet area.

The solid lines in Fig. 8 represent the present calculated results and the circles represent the experimental data of Dunn (1986). The calculated results underpredict the experimental data in the region of $5 \leq x/S \leq 20$ percent on the suction and pressure surfaces. This is probably due to the lack of a good initial profile near the leading edge to start the calculations. Farther down the surface the predicted Stanton number agrees reasonably well with the data. The oscillations near the trailing edge of the suction surface are due to oscillations of the predicted surface pressure there.

Shown in the same figure are broken lines, which represent the results taken from Taulbee and Tran (1989) in which calculations were initiated from the stagnation region where mean and turbulent flow quantities were obtained from stagnation point calculations (Taulbee et al., 1989). Those results in the leading edge regions were predicted reasonably well, as shown by the broken line. The present prediction of heat transfer in the leading edge region could be improved if solutions in the stagnation point region were obtained in the same way as in Taulbee et al. (1989). Unfortunately, the alteration of the leading edge geometry in the inviscid flow calculation prevented the pursuit of this approach. Overall, the present predictions of steady heat transfer on the surfaces are reasonably good.

Unsteady Heat Transfer. Unsteady boundary layer solutions were obtained by solving Eqs. (19)–(23) with the unsteady boundary conditions applied at the boundary layer edge. At each time step, calculations were started near the leading edge and marched down the surfaces in the same way as used in solving the steady boundary layer equations described earlier. Solutions at every grid point in the computational domain were stored so that time derivatives in the next time step could be estimated. Unsteady calculations started from steady-state solutions.

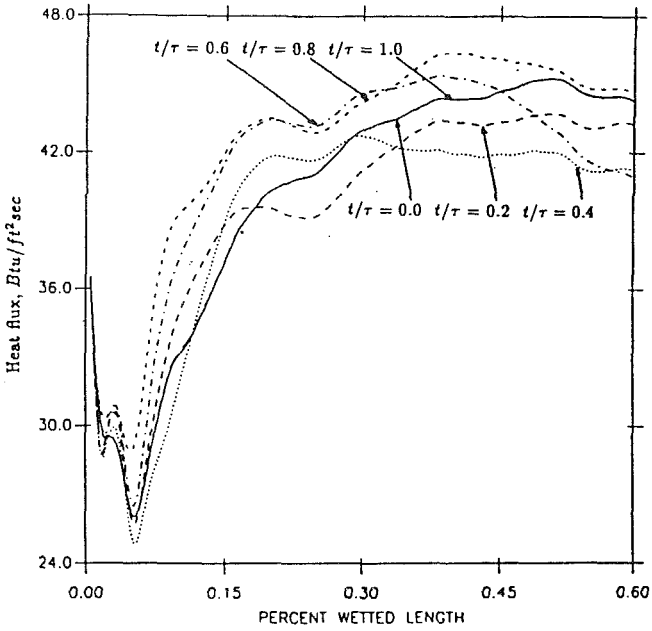

Fig. 10 Unsteady heat flux on suction surface

The unsteady heat flux at five locations on the suction surface is shown in Fig. 9 at various distances along the surface. The amplitude of the fluctuating heat flux is around 4 Btu/ft^2 sec for the locations shown, except at $x/S = 10$ percent, where a large heat flux variation occurred. This large variation of heat flux (about 11 Btu/ft^2 sec) is due to the boundary layer state, which is in transition between laminar and turbulent. As the wake segments move along the rotor blade surface, the transition region also moves along the surface. A point in this region would produce a laminar heat flux value if the boundary layer is laminar when flow passes through this point. Because of free-stream turbulence and/or pressure gradients, the same point would experience a turbulent state of the boundary layer at some later instant in the wake passing period. This turbulent boundary layer produces high heat flux compared to that from a laminar boundary layer. At any other time between those two instants this point would experience some transitional state of the boundary layer, which produces a heat flux value falling between laminar and turbulent values. A good portion of the blade surface would have large fluctuations in heat flux because the transitional boundary layer usually takes up a region of boundary layer on the surface. As seen on Fig. 9, other locations on the blade surface have about 4 Btu/ft^2 sec variation in heat flux because the boundary layer there has already passed the transitional state. At these locations, unsteadiness does not have much influence on the turbulent boundary layer, as indicated by a small variation of the heat flux. This observation is consistent with the experimental data of Doorly (1988) in which unsteady heat flux was measured in a turbulent boundary layer. Small variations of heat flux in a turbulent boundary layer are mainly due to unsteady pressure gradients. A good way to observe the variation of heat flux is shown in Fig. 10 for the leading half of the suction surface at six instants in a period. It is seen that for $10 \leq x/S \leq 20$ percent, the boundary layers is in a transitional state, as shown by large variation of heat flux. After $x/S \geq 20$ percent the heat flux change is about 4 Btu/ft^2 sec, as shown in Figs. 9 and 10.

The heat flux variation on the pressure surface is less profound; the variations are from 2 Btu/ft^2 sec to 9 Btu/ft^2 sec with highest variation near $x/C \simeq 15$ percent, as shown in Figs. 11 and 12. The same explanation given for the suction surface can also be applied here, except that transition of the boundary layer on the pressure surface is not clear. Thus large variations of heat flux are not predicted for pressure surface. Since the

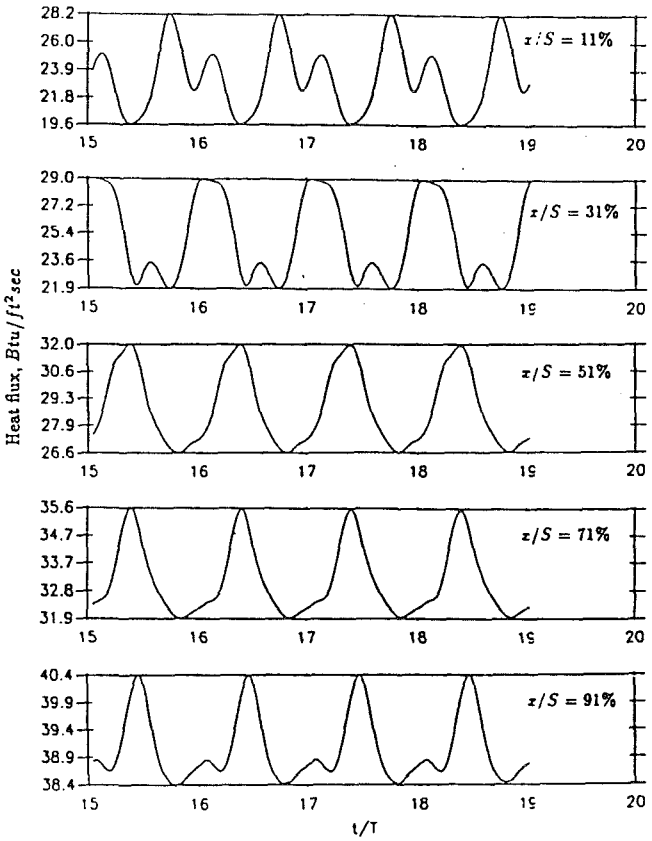

Fig. 11 Unsteady heat flux at five locations on pressure surface

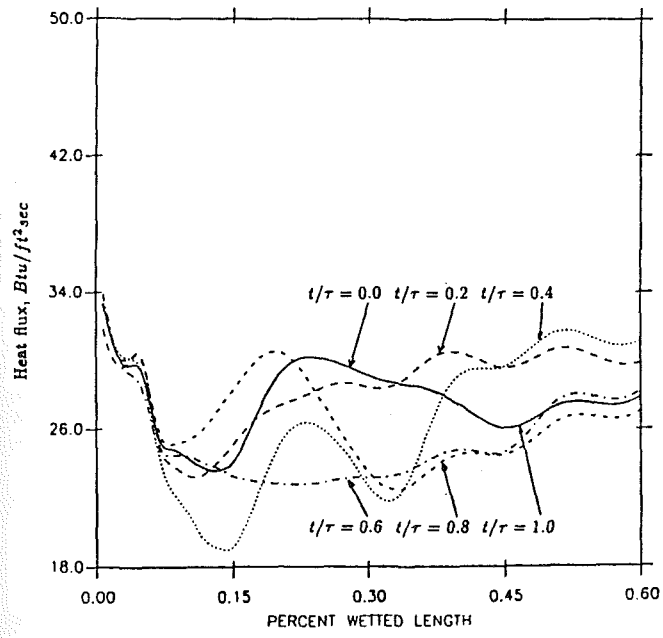

Fig. 12 Unsteady heat flux on pressure surface

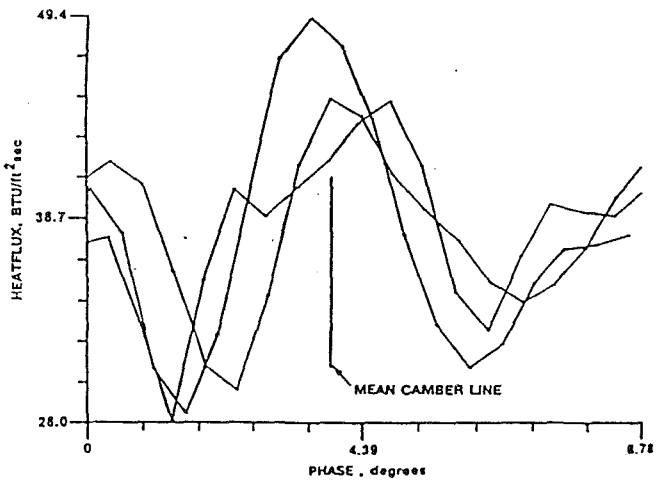

Fig. 13(*a*) Experimental data (Dunn, 1990)

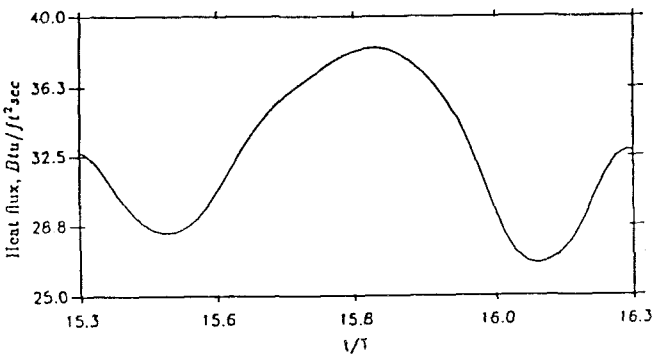

Fig. 13(*b*) Predicted heat flux

Fig. 13 Comparison of unsteady heat flux at $x/S = 10$ percent on suction surface

boundary layer on this surface does not go through transition, variations of heat flux are mainly due to unsteady pressure gradients and variations of inviscid flow boundary conditions.

A comparison of heat flux at two locations on the suction surface, $x/S = 10$ percent and $x/S = 85$ percent, is shown in Figs. 13 and 14. Figure 13(*a*) shows the experimental data taken from Dunn (1990) presented as a function of the phase angle, in which a wake passing period is equivalent to 8.78 deg for 41 vanes of the turbine stage. The three curves in Fig. 13(*a*), and also in subsequent figures, are the curves of actual data points taken from the digital sampled data record in three separate passages during one revolution. In Fig. 13(*b*) the beginning and end of a period are chosen arbitrarily so that the calculated phase is best matched with data. However, once this reference time is chosen, it will be fixed for other locations, as will be shown later. It is seen that the trend of the experimental data curve is well predicted at this location. The predicted heat flux varies from 27 Btu/ft^2 sec to 38 Btu/ft^2 sec, giving a total change of 11 Btu/ft^2 sec, which is close to the average of 13 Btu/ft^2 sec change in data heat flux.

Shown in Figs. 14(*a*) and 14(*b*) are the experimental data and predicted results, respectively, at $x/S = 85$ percent on the suction surface. It is seen that the experimental data have the same trend as the predicted curve. The two curves in Fig. 14(*a*) have a lower peak, which is not predicted in Fig. 14(*b*). The higher peak of the experimental heat flux is well predicted. If this peak is associated with wake passing, then it can be concluded that the predicted results are also very good at this location. The lower peak in the experimental data is probably due to effects that are not included in this model. The predicted profile seems to be shifted slightly to the right compared to the data, which is an indication of overpredicted convection velocity at this location. The averaged magnitude of the experimental heat flux varies from 27 Btu/ft^2 sec to 33 Btu/ft^2 sec whereas the prediction shows only 4 Btu/ft^2 sec variation, from 42 Btu/ft^2 sec to 46 Btu/ft^2 sec. Thus the variation of heat flux is reasonably predicted but not the magnitude. A higher prediction of heat flux magnitude is not unexpected,

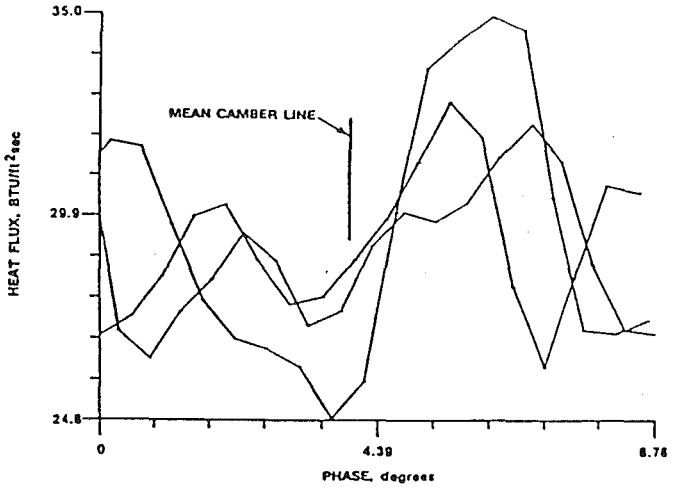

Fig. 14(*a*) Experimental data (Dunn, 1990)

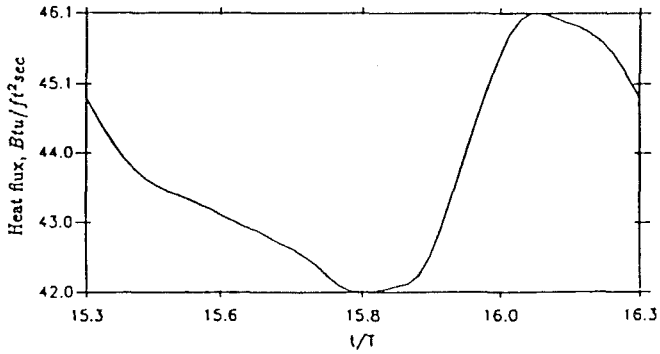

Fig. 14(*b*) Predicted heat flux

Fig. 14 Comparison of unsteady heat flux at $x/S = 85$ percent on suction surface

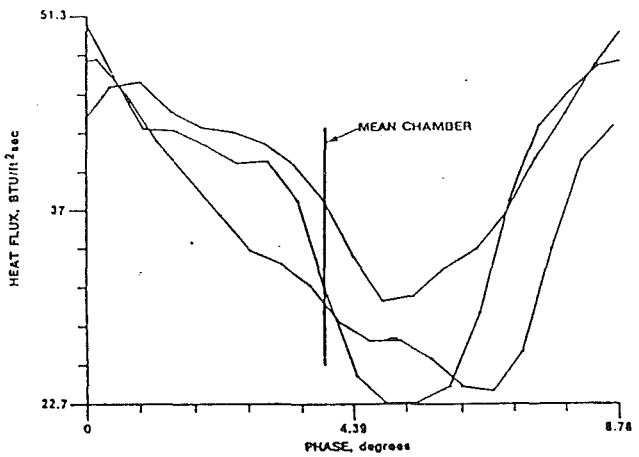

Fig. 15(*a*) Experimental data (Dunn, 1990)

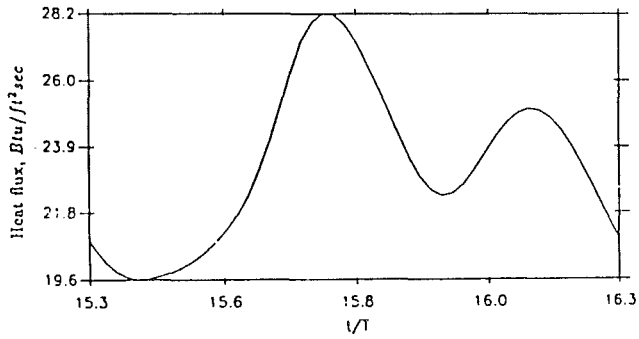

Fig. 15(*b*) Predicted heat flux

Fig. 15 Comparison of unsteady heat flux at $x/S = 11$ percent on pressure surface

since the steady-state flow prediction, presented earlier, also overpredicted the data.

A comparison of predicted heat flux with experimental data for $x/S = 11$ percent and $x/S = 85$ percent on the pressure surface is shown in Figs. 15 and 16. At $x/S = 11$ percent, the predicted heat flux variation is about 8 Btu/ft^2 sec compared to about 20 Btu/ft^2 sec for the data. Note that the times shown in Figs. 14, 15, and 16 are exactly the same period shown in Fig. 13. In that connection the phase in Fig. 15(*b*) does not agree with the data. Figure 15(*a*) shows a low heat flux at the midcycle, whereas the prediction shows a peak of heat flux there. Also, the predicted heat flux has a second peak that does not exist in the data. A similar observation can be made in Fig. 16, which shows the heat flux data and prediction at $x/S = 85$ percent on the pressure surface. At this location, the experimental data have a peak at the midcycle, whereas the prediction shows low heat flux. The prediction also shows a small variation of heat flux (about 2.5 Btu/ft^2 sec) whereas the experimental data show about 7 Btu/ft^2 sec variation. It should be pointed out that steady heat transfer predictions agreed reasonably well with the data on the pressure surface as shown earlier. It can be concluded that predictions of unsteady heat transfer on the pressure surface do not agree with the experimental data, both in phase and also in net variation.

These discrepancies in unsteady heat flux predictions are probably due to inaccurate prediction of the unsteady inviscid flow solutions, which appear in the boundary layer equations as the driving terms and boundary conditions. Discrepancies in predicting unsteady pressure on the pressure surface were also experienced in the Hodson (1985) calculations. It can be concluded that other flow phenomena happen on the pressure surface that cannot be predicted by the wake model alone. Another phenomenon that affects the unsteady blade surface heat transfer is wake cooling by the nozzle guide vanes. In the test for the TFE 731-2 HP turbine reported by Dunn (1990), air entered the turbine at 1006° whereas the vanes were at room temperature. Therefore, air in the boundary layers of the vanes was cooled and the wakes left the trailed edges with a thermal defect. The thermal defect is not included in the wake model used in this study. An including of the wake cooling effects can be achieved by replacing the uniform relative total enthalpy with a periodic function in the wake model. Another reason for discrepancies in unsteady heat transfer predictions is probably that potential flow interactions occur, which could modify the real flow substantially and are not included in the present study.

Summary

In summary, unsteady pressure and heat transfer on rotor blade surfaces due to wake passings were modeled using the inviscid/boundary layer flow approach. The calculation method combines the solutions of unsteady inviscid flow and solutions of viscous boundary layer flow. Unsteady flow in a rotor blade passage due to vane wake passings was modeled by solving the Euler equations with a wake model periodically passing across the passage inlet. Unsteady heat transfer was calculated using the boundary layer theory incorporating with a low Reynolds number k–ϵ model for the turbulent boundary layer on the blade surface. Unsteady heat flux on the suction surface is well predicted, both in phase and net variation. Large variations of heat flux are found in the transition region, which

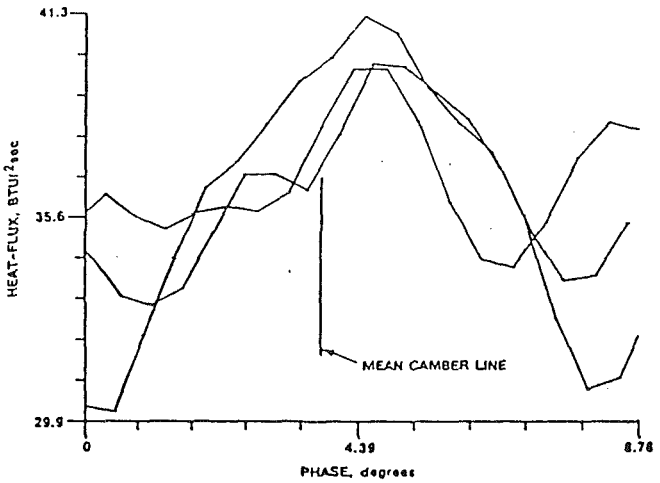

Fig. 16(*a*) Experimental data (Dunn, 1990)

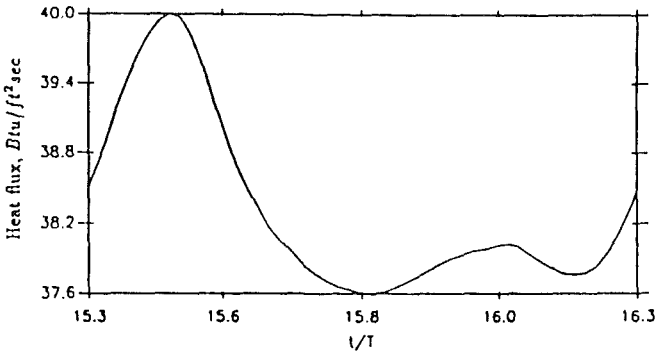

Fig. 16(*b*) Predicted heat flux

Fig. 16 Comparison of unsteady heat flux at $x/S = 85$ percent on pressure surface

constantly moves along some portion of the suction surface as a result of wake passing. Downstream from the transition region, the heat flux variation is fairly small, consistent with experimental data taken by Doorly (1988) on a turbulent boundary layer. On the pressure surface, the variation and the phase of unsteady heat flux do not agree with the data. This is probably due to inaccurate predictions of inviscid flow on the pressure surface, and/or neglect of potential flow effects which could be important on the pressure surface. Other flow mechanisms could contribute to the discrepancies, but have not been included in this model.

Acknowledgments

The authors wish to thank M. G. Dunn of Calspan and K. C. Civinskas of U.S. Army Research & Technology Activity—AVSCOM, Lewis Research Center for their advice during the course of this work. This work was supported under Grant No. NAG-3-581.

References

Cebeci, T., and Platzer, M. F., 1988, "A General Method for Unsteady Heat Transfer on Turbine Blades," NASA CR 4206.

Chien, K. Y., 1982, "Predictions of Channel and Boundary Layer Flows With a Low Reynolds Number Turbulence Model," *AIAA J.*, Vol. 20, No. 1, pp. 33–38.

Doorly, D. J., 1988, "Modeling the Unsteady Flow in a Turbine Rotor Passage," ASME JOURNAL OF TURBOMACHINERY, Vol. 110, pp. 27–36.

Dunn, M. G., 1986, "Heat Flux Measurements for the Rotor of a Full-Stage Turbine: Part 1—Time-Averaged Results," ASME JOURNAL OF TURBOMACHINERY, Vol. 108, pp. 90–97.

Dunn, M. G., 1990, "Phase and Time-Resolved Measurements of Unsteady Heat Transfer and Pressure in a Full-Stage Rotating Turbine," ASME JOURNAL OF TURBOMACHINERY, Vol. 112, pp. 531–538.

Erdos, J. I., Alzner, E., and McNally, W., 1976, "Numerical Solution of Periodic Transonic Flow Through a Fan Stage," AIAA Paper No. 76-369.

Fourmeau, A., 1986, "Unsteady Flow Calculation in Cascades," ASME Paper No. 86-GT-178.

Giles, M. B., 1988, "Calculation of Unsteady Wake/Rotor Interaction," *AIAA J. of Propulsion and Power*, Vol. 4, No. 4, pp. 356–362.

Hodson, H. P., 1985, "An Inviscid Blade-to-Blade Prediction of a Wake-Generated Unsteady Flow," ASME *Journal of Engineering for Gas Turbines and Power*, Vol. 107, pp. 337–344.

Jang, H. M., Ekaterinaris, J. A., Platzer, M. F., and Cebeci, T., 1990, "Essential Ingredients for the Computation of Steady and Unsteady Blade Boundary Layers," AIAA Paper 90-XXX.

Jorgenson, P. C. E., and Chima, R. V., 1989, "An Unconditionally Stable Runge-Kutta Method for Unsteady Flows," AIAA Paper No. 89-0205.

Koya, M., and Kotake, S., 1985, "Numerical Analysis of Fully Three-Dimensional Periodic Flows Through a Turbine Stage," ASME *Journal of Engineering for Gas Turbines and Power*, Vol. 107, pp. 945–952.

Krainer, A., 1988, "A Numerical Method for Computing Unsteady 2-D Boundary Layer Flows," NASA CR 4198.

Lewis, J. P., Delaney, R. A., and Hall, E. J., 1989, "Numerical Prediction of Turbine Vane-Blade Aerodynamic Interaction," ASME JOURNAL OF TURBOMACHINERY, Vol. 111, p. 387–393.

Rae, W. J., Taulbee, D. B., Civinskas, K. C., and Dunn, M. G., 1988, "Turbine-Stage Heat Transfer: Comparison of Short-Duration Measurements With State-of-the-Art Predictions," *AIAA J. of Propulsion and Power*, Vol. 4, No. 6, pp. 541–548.

Rai, M. M., 1987, "Navier-Stokes Simulations of Rotor-Stator Interaction Using Patched and Overlaid Grids," *AIAA J. of Propulsion and Power*, Vol. 3, No. 5, pp. 387–396.

Raj, R., and Lakshminarayana, B., 1973, "Characteristics of the Wake Behind a Cascade of Airfoils," *J. Fluid Mech.*, Vol. 61, Part 4, pp. 707–730.

Richardson, S., 1990, "Analysis of Unsteady Rotor-Stator Interaction Using a Viscous Explicit Method," AIAA Paper No. 90-0342.

Taulbee, D. B., Tran, L., and Dunn, M. G., 1989, "Stagnation Point and Surface Heat Transfer for a Turbine Stage: Prediction and Comparison With Data," ASME JOURNAL OF TURBOMACHINERY, Vol. 111, pp. 28–35.

Taulbee, D. B., and Tran, L., 1989, "Prediction of Unsteady Rotor-Surface Heat Transfer From Wake Passings," AIAA Paper No. 89-1692.

Comparison of Time-Resolved Turbine Rotor Blade Heat Transfer Measurements and Numerical Calculations

R. S. Abhari[1]

G. R. Guenette

A. H. Epstein

M. B. Giles

Gas Turbine Laboratory,
Massachusetts Institute of Technology,
Cambridge, MA 02139

Time-resolved turbine rotor blade heat transfer data are compared with ab initio numerical calculations. The data were taken on a transonic, 4-to-1 pressure ratio, uncooled, single-stage turbine in a short-duration turbine test facility. The data consist of the time history of the heat transfer distribution about the rotor chord at midspan. The numerical calculation is a time accurate, two-dimensional, thin shear layer, multiblade row code known as UNSFLO. UNSFLO uses Ni's Lax-Wendroff algorithm, conservative boundary conditions, and a time tilting algorithm to facilitate the calculation of the flow in multiple blade rows of arbitrary pitch ratio with relatively little computer time. The version used for this work had a simple algebraic Baldwin-Lomax turbulence model. The code is shown to do a good job of predicting the quantitative time history of the heat flux distribution. The wake/boundary layer and transonic interaction regions for suction and pressure surfaces are identified and the shortcomings of the current algebraic turbulence modeling in the code are discussed. The influence of hardware manufacturing tolerance on rotor heat transfer variation is discussed. A physical reasoning explaining the discrepancies between the unsteady measurement and the calculations for both the suction and pressure surfaces are given, which may be of use in improving future calculations and design procedures.

Introduction

The accurate prediction of heat transfer in high-pressure turbine stages has long been recognized as a key to improved gas turbine performance and engine life. To that end, a vast amount of engineering effort has been extended over the last forty years to provide accurate experimental measurements of the heat transfer distribution and to improve the accuracy by which that distribution can be predicted. This work has included the measurement of two-dimensional airfoil heat transfer in both steady-state (Turner et al., 1985) and transient cascades (Schultz et al., 1977) as well as stage measurements in short duration test rigs (Dunn et al., 1984; Guenette et al., 1989).

Progress in calculational techniques has been rapid over this same period. Two-dimensional steady viscous calculations of the flow in turbines is now commonplace and three-dimensional steady techniques are also being applied. More recently, unsteady multiblade row codes have been developed (Rai, 1985), including those capable of handling multiple blade rows with arbitrary blade counts (Giles, 1988).

It has long been observed that gas turbine engine rotor heat transfer experience often does not follow that to be expected from steady, two-dimensional cascade flows (Sharma et al., 1988, 1992). Rotor pressure side heat transfer may be the most different in this regard. Unsteadiness, three-dimensionality, and nonuniform inflow all may be contributors to this difference.

Unsteady effects in particular have been studied in some detail. Cascade experiments using rotating bars to simulate NGV wakes and shock waves (Doorly and Oldfield, 1985; Ashworth et al., 1985; Johnson et al., 1989a, 1989b) have shown that wake impingement on the rotor can trigger laminar to turbulent transition, increasing the time average heat transfer to a level between that of steady-state laminar and fully turbulent. Experiments on low-speed turbine rotors tend to confirm this observation (Blair et al., 1989; Dring et al., 1986; Sharma et al., 1988; Addison and Hodson, 1990a, 1990b). The interaction of shock waves with the blade boundary layers can also increase rotor heat transfer. Rigby et al. (1989) constructed a simple physical model explaining the unsteady heat transfer in terms of compressional heating in the boundary layer by the moving shock waves.

The intent of this work is to examine the time-resolved aerodynamics and heat transfer in a transonic turbine rotor with a particular emphasis on elucidating the difference between the unsteady flow and the time mean design intent. This is

[1]Current address: Textron Lycoming, Stratford, CT.

Contributed by the International Gas Turbine Institute and presented at the 36th International Gas Turbine and Aeroengine Congress and Exposition, Orlando, Florida, June 3-6, 1991. Manuscript received at ASME Headquarters March 4, 1991. Paper No. 91-GT-268. Associate Technical Editor: L. A. Riekert.

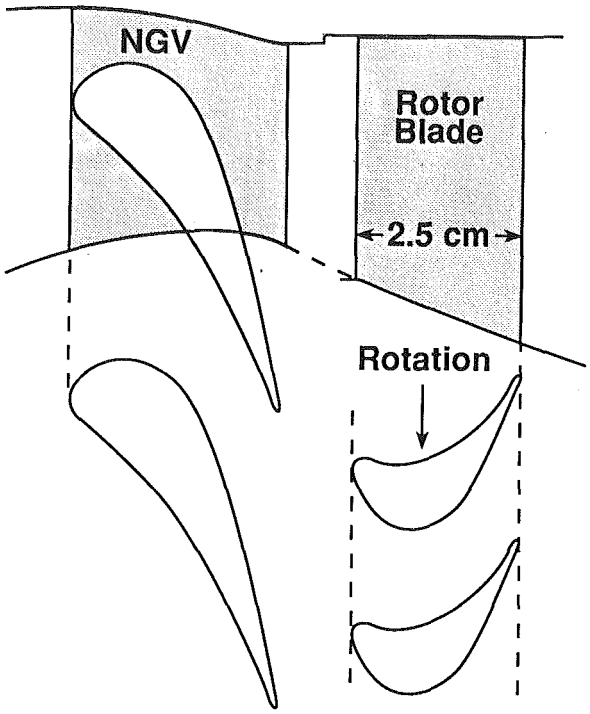

Fig. 1 Transonic turbine geometry investigated

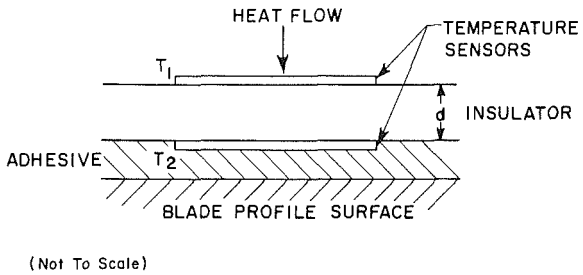

Fig. 2 Schematic of thin film multilayer heat flux gage; total thickness is about 25 μm

done by a detailed comparison between time-resolved measurements and a viscous, multiblade row numerical calculation.

Experimental Arrangement

The test article (Fig. 1) is a 4:1 pressure ratio single-stage, 0.5-m-dia, transonic turbine whose design parameters are given in Table 1. It was tested in the MIT Blowdown Turbine Facility. This is a short-duration (0.3 s test time) rig, which maintains real engine similarity of Reynolds number, Mach number, Prandtl number, gas-to-wall temperature ratio, and flow geometry (Table 2). Corrected speed and weight flow are maintained constant to better than 0.5 percent over the test time. The turbulent intensity at the NGV inlet is less than 1 percent for these tests. The stage results reported herein are for an uncooled geometry. More details may be found from Epstein et al. (1984) and Guenette et al. (1989).

Temperature and pressure rakes measure the flowfield at the inlet to the nozzle guide vanes (NGVs) and the outlet of the rotor. Shaft rotational speed, rotor torque, and various wall static pressures are recorded as well. Of interest here is the measurement of the time-resolved heat flux distribution about the rotor blade. This was done using thin film heat flux gages distributed about the blade profile. These transducers measure both the d-c and a-c components of heat flux. The heat flux gages consist of two thin film (140-nm-thick) nickel temperature transducers mounted on either side of a 25-μm-thick polyimide insulator (Fig. 2). The sensing area is rectangular (1.0 × 1.3 mm), oriented such that the longer dimension is in the chordwise direction. The insulator is adhesively bonded to, and completely covers, the blade profile (preventing thermal discontinuities). At low frequencies, the temperature drop across the insulator is a direct measure of the heat flux to the wall (the device is essentially a thermal shunt). This direct proportionality between heat flux and temperature difference extends from d-c to about 20 Hz, at which point the thermal waves within the insulator begin to damp. Above 1 kHz, however, the 25-μm-thick insulator appears infinitely thick to the top surface. Thus, above this frequency, a quasi-one-dimensional assumption can be used to infer the heat flux from the top surface temperature history (blade passing frequency is 3.6 kHz). Using a numerical data reduction technique, the entire frequency domain from d-c to 100 kHz is reconstructed. The gages were calibrated using a pulsed laser. The relative gage calibrations are accurate to better than 5 percent. Absolute calibration accuracy is about 10 percent. Uncertainty is evaluated for each transducer. Details of the gage theory, data reduction, and calibration may be found from Epstein et al. (1986).

For the data presented herein, the signals from the heat flux gages were digitized at a 200 kHz sampling rate. Unless otherwise specified, the digital signal was then ensemble-averaged for 360 vane passing periods (Guenette et al., 1989).

Table 1 Turbine design parameters

Turbine loading, $\Delta H/U^2$	-2.3
Total pressure ratio	4.2
Velocity ratio, C_x/U	0.63
Rotor aspect ratio	1.5
NGV exit Mach No.	1.18

Table 2 MIT blowdown turbine scaling

	Full Scale	MIT Blowdown
Fluid	Air	Ar-Fr 12
Ratio specific heats	1.28	1.28
Mean metal temperature	1118°K (1550°F)	295°K (72°F)
Metal/gas temp. ratio	0.63	0.63
Inlet total temperature	1780°K (2750°F)	478°K (400°F)
True NGV chord	8.0 cm	5.9 cm
Reynolds number*	2.7×10^6	2.7×10^6
Inlet pressure, atm	19.6	4.3
Outlet pressure, atm	4.5	1.0
Outlet total temperature	1280°K (1844°F)	343°K (160°F)
Prandtl number	0.752	0.755
Eckert number†	1.0	1.0
Rotor speed, rpm	12,734	6,190
Mass flow, kg/sec	49.0	16.6
Power, watts	24,880,000	1,078,000
Test time	Continuous	0.3 sec

* Based on NGV chord and isentropic exit conditions
† $(\gamma-1)M^2T/\Delta T$

The Numerical Procedure

The numerical procedure used to model this flow was a two-dimensional, Reynolds-averaged, unsteady multiblade row Navier–Stokes code, UNSFLO. This is a coupled viscous/inviscid code in which the thin shear layer Navier–Stokes equations are solved on a body-fitted boundary layer grid using an implicit algorithm, while the Euler equations are solved on an outer inviscid grid using an explicit algorithm. The interface between the two regions is handled in a conservative manner. The code utilizes an innovative space-time coordinate transformation,

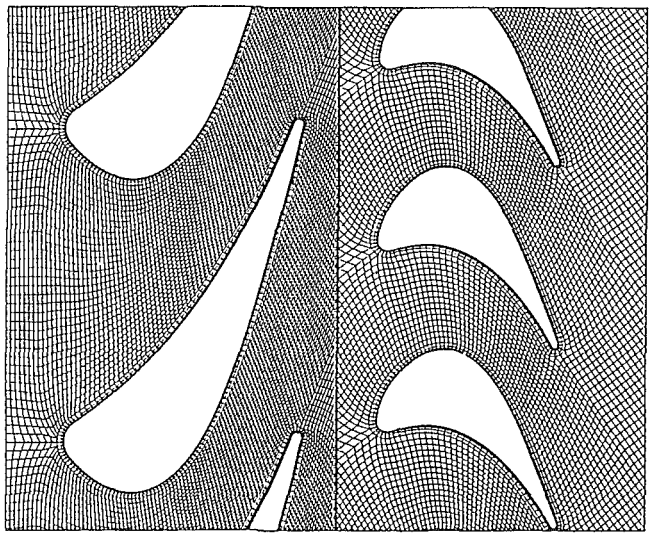

Fig. 3 Grid used in unsteady nozzle guide vane-rotor calculation

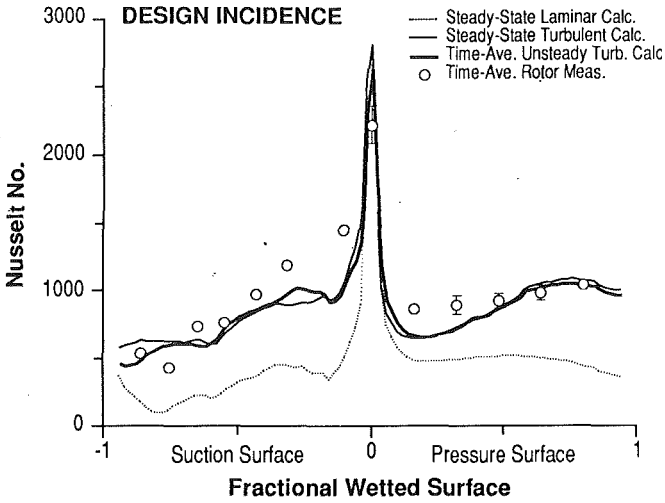

Fig. 5 Comparison of measured heat transfer with fully laminar and fully turbulent steady-state calculations, and the time average of the unsteady multiblade row calculation for the design point

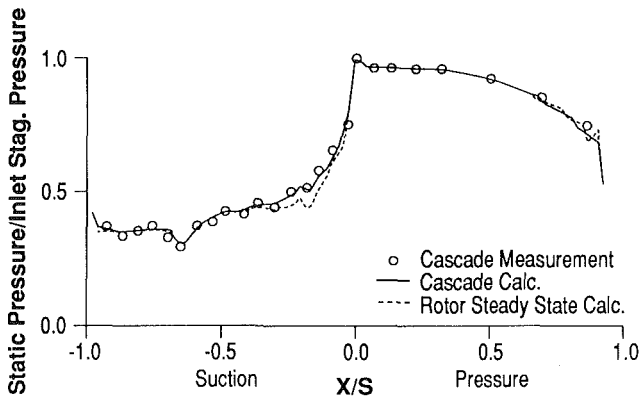

Fig. 4 Steady-state static pressure distribution calculations compared to cascade measurement; the stream-tube height differs between the rotor and cascade by about 3 percent

"time-tilting" (Giles, 1988), to permit arbitrary rotor–stator pitch ratios while incurring little penalty in computation time.

The viscous grid is an O-type mesh about each blade for which an ADI (alternating-direction-implicit) method with Roe's flux-difference splitting gives third-order upwinding for the residual operator and first-order upwinding for the implicit operator. An algebraic turbulence model is used. Quasi-three-dimensional effects are included through the specification of a stream-tube thickness in the third dimension (axial velocity density ratio, AVDR, or hade). The inviscid grid is an unstructured finite element type of mesh composed of an arbitrary mix of quadrilateral and triangular cells. Here, the Euler equations are solved using a generalization of Ni's Lax–Wendroff algorithm (Ni, 1981). Full second-order accuracy is achieved. The Baldwin–Lomax turbulence model used in the viscous part of the solution is not capable of predicting boundary layer transition. For the calculations presented herein, transition was assumed at the leading edge unless otherwise specified. Many more details on this code and its checkout may be found in a companion paper by Giles and Haimes (1991).

For the calculations done here, the O grid had 18 points across the boundary layer and a total of 16,000 were used throughout the domain, Fig. 3. Only the midheight geometry of the stage was modeled and the code was relatively fast, requiring approximately 20 CPU hours on a Stellar GS1000 workstation, equivalent to about 2 hours on a Cray XMP. The stream-tube height distribution through the stages (an input to the code) was derived from a streamline curvature calculation (Norton, 1988).

Although the static pressure distribution about the rotor was not measured in this series of experiments, Ashworth et al. (1985; also Ashworth, 1987) did measure it for the same blade profile in a cascade. The measured values are shown in Fig. 4, along with steady state calculations for the rotor and for the cascade installation (which has a slightly different stream-tube height distribution). The agreement is quite good except at the trailing edge, where natural instabilities such as vortex shedding are important but not resolved in this steady state solution. We infer from this comparison that the code in its steady-state version does a good job of calculating the mean static pressure distribution about the rotor profile.

Comparison of Steady-State Heat Transfer Predictions and Measurements

A comparison between the time average of the measured rotor heat transfer, the time average of the unsteady NGV-rotor calculation, and a steady-state solution for the rotor alone is shown in Fig. 5 for design point flow. The heat transfer coefficient is presented as Nusselt number, defined in terms of the rotor blade axial chord, inlet relative total minus local profile temperature, and thermal conductivity based on local temperature. The local profile temperatures used were those measured by the top sensors on the heat flux gages. Unless explicitly indicated, the relative uncertainties (± standard deviation) in the measurements are less than the size of the symbols. Surface length is defined with the axial leading edge tangential chord intersection as the zero reference.

There is relatively little difference between the steady-state turbulent and the time-averaged unsteady calculations. In general, the measured heat transfer is equal to or greater than the fully turbulent calculation. Integrated about the profile, the predicted heat transfer is 11 percent less than the measured value. (Note that the uncertainty in the absolute level of heat transfer in the measurement is 10 percent.) A similar trend can be seen in Fig. 6 for a different flow condition, −10 deg rotor incidence. Here, the predicted heat transfer is 12 percent lower than that measured. A comparison of the two flow conditions (Fig. 7) shows that the differences in the measurements are confined principally to the first part of the suction surface,

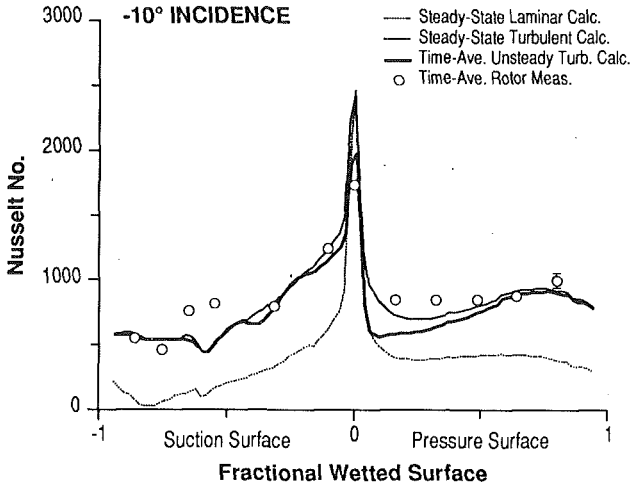

Fig. 6 Comparison of measured heat transfer with fully laminar and fully turbulent steady-state calculations, and the time average of the unsteady multiblade row calculation for – 10 deg incidence

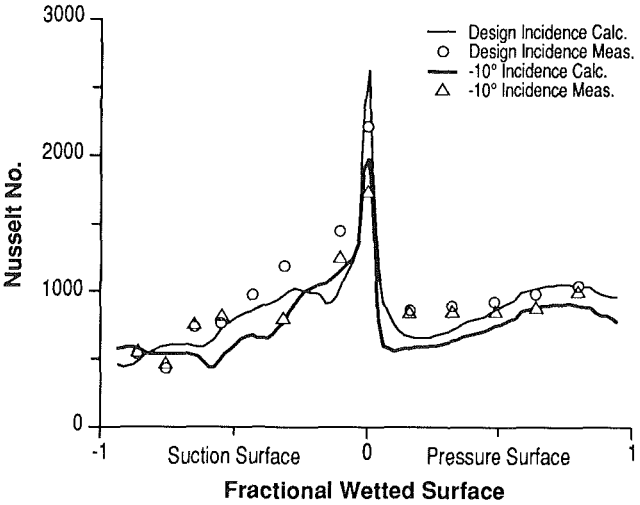

Fig. 7 Comparison between measurements and time-averaged unsteady calculations at design and – 10 deg incidence

while the difference in predicted heat transfer is spread along the blade. Both the predicted and measured heat transfer at – 10 deg incidence are reduced by some 11 percent under that for the design incidence.

The general picture these comparisons suggest differs significantly from cascade and low-speed rotor data in that the pressure side heat transfer does not lie between laminar and fully turbulent levels, but rather the data are above the pressure side turbulent prediction. This difference bears examination. The validity of the measurements was established earlier by Guenette et al. (1989) who showed that the midspan rotor measurements in the blowdown tunnel agreed closely with those made on the same profile in a cascade by Ashworth et al. (1985). This serves to both confirm the rotor measurements and suggest that flow in this midspan region is largely two dimensional. Rather than simply dismiss the calculations then as inaccurate (the calculational accuracy is really quite good for an *ab initio* effort; it is not sufficient, however, for realizing desired turbine life), we thought it instructive to examine in as much detail as possible the difference between the data and calculations in order to shed light on the modeling assumptions, test numerical approximations, and generally understand the flowfield. To do this, we shall start by looking at the unsteady flow.

Time-Resolved Data and Calculations

A comparison of the time-resolved heat transfer data and calculations is shown in Fig. 8 for the design point and for – 10 deg incidence flow. Along both the suction and pressure surfaces, the flow is highly unsteady in both the calculations and the measurements, which are in qualitative agreement. The exception to this is at the leading edge where calculation shows a much larger degree of unsteadiness than do the data. (Note that the calculational result was averaged over the same surface extent as is covered by the heat transfer gage.) The unsteadiness in the flow is a result primarily of two physical interactions between the blade rows: NGV wake impingement on the rotor and potential coupling, including moving shock patterns.

The complexity of the NGV-rotor shock pattern can be seen in Fig. 9, which is an animation of the time unsteady calculational results (the times correspond to those in Fig. 8). At any moment, as many as six shock waves may be moving through a single rotor passage—some traveling upstream, some down, some strengthening, some attenuating. Simultaneously, there are interactions between the NGV wakes and the rotor. This is illustrated in Fig. 10. The wake convection is such as to continuously keep an NGV wake along the rotor suction surface. The pressure surface, however, sees intermittent wake impingement. The overall complexity of the curved shock waves and convection of the wakes through the rotor are qualitatively similar to that observed in Schlieren photographs by Ashworth (1987), using rotating bars to simulate NGV wakes and shock waves upstream of a cascade of blades with the midspan rotor profile.

Although flow visualization is not available for the NGV-rotor flow, time-resolved heat transfer data are (Fig. 8). The calculational results can be used to help understand the flow structure evident in the measurements. For example, the three peaks in the heat transfer data on the crown of the suction surface (Fig. 8*c*) can be seen to be the result of a shock wave sweeping forward along the suction surface, Fig. 11. By using the calculational results in such a way, many of the features in the time-resolved heat transfer can be quantitatively explained.

Discussion of the Difference Between Calculation and Measurement

Inviscid Versus Viscous Flow Effects. In a practical sense, it is the differences between the calculation and measurements that are of the most interest since, if they were always in complete agreement, few experiments would need to be run.

One discrepancy is in the strength of the shock-induced heat transfer spike observed on the crown of the suction surface for the design point flow (Fig. 8*b*). The difference in the area under the calculated and measured spikes accounts for the difference in the time averages at that location observed in Fig. 5. This difference could conceivably be either from an inaccuracy in the inviscid flow (improper shock strength, for example) or a problem with the viscous boundary layer calculation. To explore this, we made use of a one-dimensional model of the shock heating process developed by Rigby et al. (1989), which explains the abrupt rise in surface heat flux as being primarily due to compressional heating of the inner sublayer. The modulation of heat transfer is given as

$$\frac{\mathrm{Nu}(t)-\mathrm{Nu}_0}{\mathrm{Nu}_0}=\left(\frac{P(t)}{P_0}-1\right)+\frac{\sqrt{\rho c_p/k}Cg(t)}{\mathrm{Nu}_0\left(\frac{T_g}{T_w}-1\right)} \qquad (1)$$

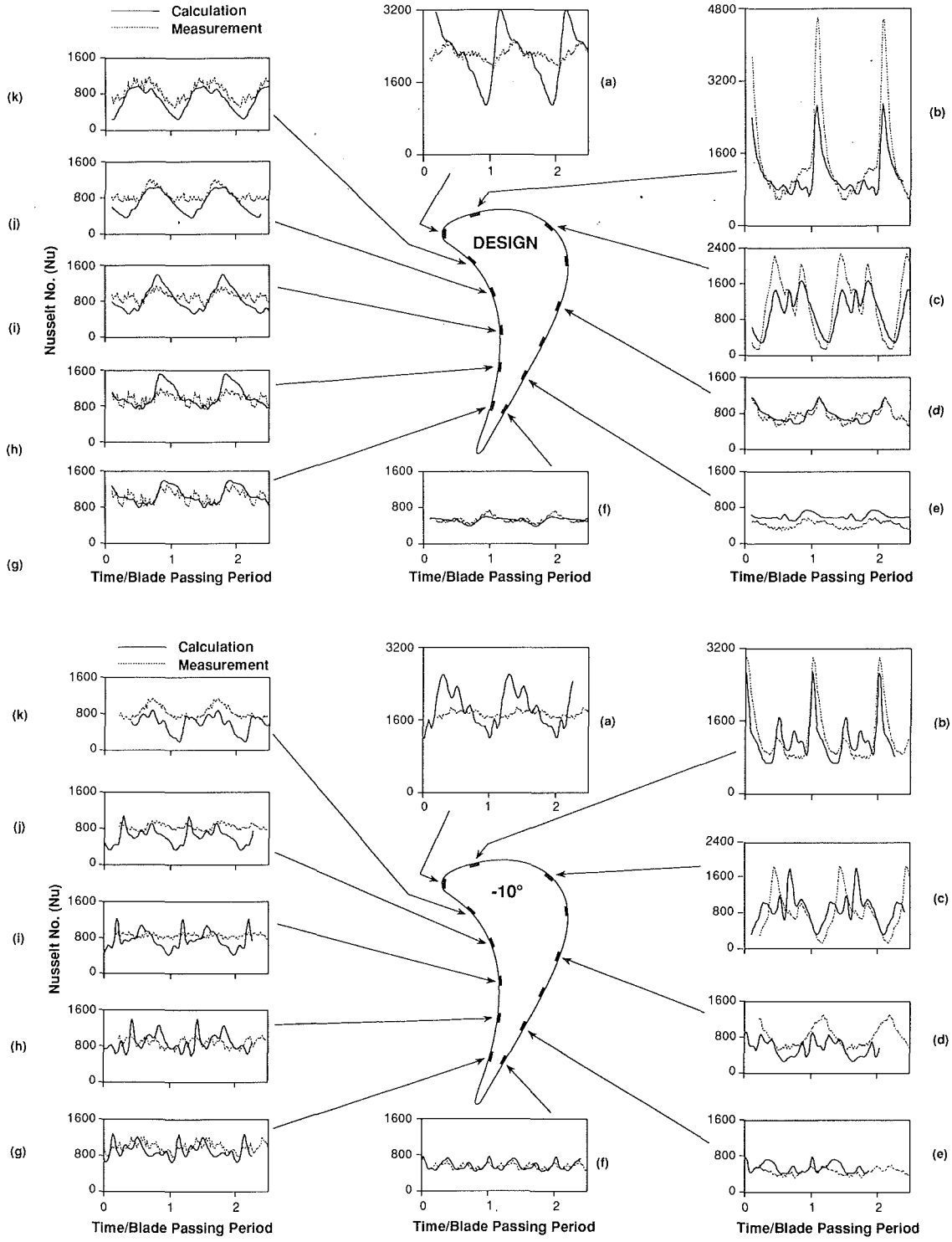

Fig. 8 Comparison of time-resolved measurements and calculations at the design point and at −10 deg incidence

where

$$g(s) = \mathcal{L}\{g(t)\} = s^{1/2}\mathcal{L}\left\{\left(\frac{P(t)}{P_0}\right)^{\frac{(\gamma-1)}{\gamma}} - 1\right\} \qquad (2)$$

The symbol s is the Laplacian operator and the subscript 0 corresponds to the steady-state values. P is the static pressure, T_g the gas temperature, T_w the wall temperature, ρ the density, c_p the specific heat, k the thermal conductivity, C the axial chord, and γ the ratio of specific heats. The first term on the right-hand side of Eq. (1) represents the compression, while the second term is the isentropic heating in the sublayer. Thus, the heat flux perturbation can be predicted from the static pressure history. This was done using the unsteady wall static pressure predicted by the computer code (Fig. 12) to evaluate Eq. (1). Figure 13 shows that Eq. (1) predicts the same perturbation in heat transfer as does the code. This implies that the problem with the code here lies in the prediction of the

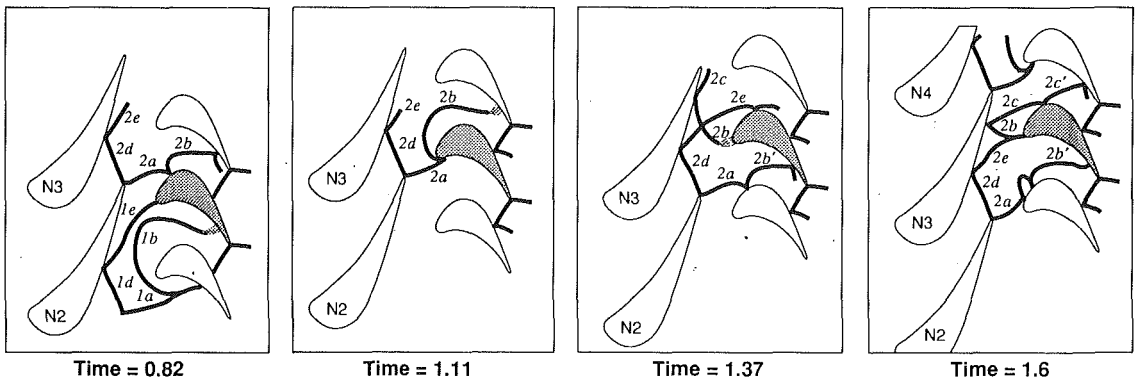

Fig. 9 Animation of the shock structure predicted by the time-resolved code at the design point; the times correspond to those of Fig. 8

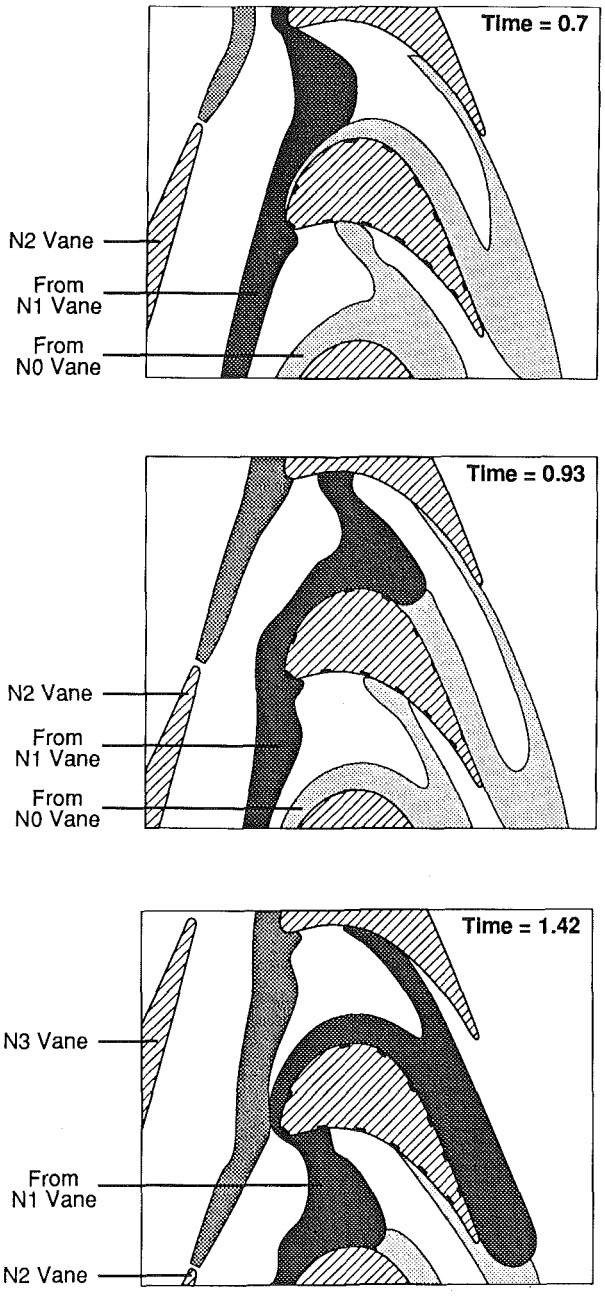

Fig. 10 Calculated wake trajectory at design point using entropy as a marker

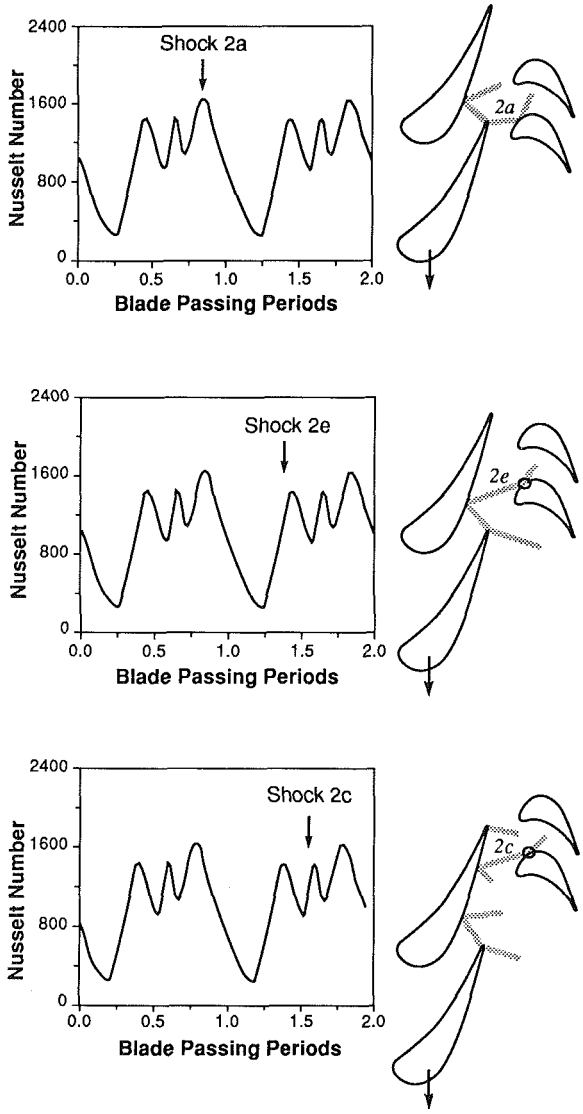

Fig. 11 Correlation of heat transfer measurement features with calculated shock motion for suction surface location corresponding to Fig. 8(c)

inviscid flow (the shock strength) rather than in the treatment of the viscous boundary layer.

Disagreement between the code and measurements takes a different form on the pressure side of the blade. Shock waves

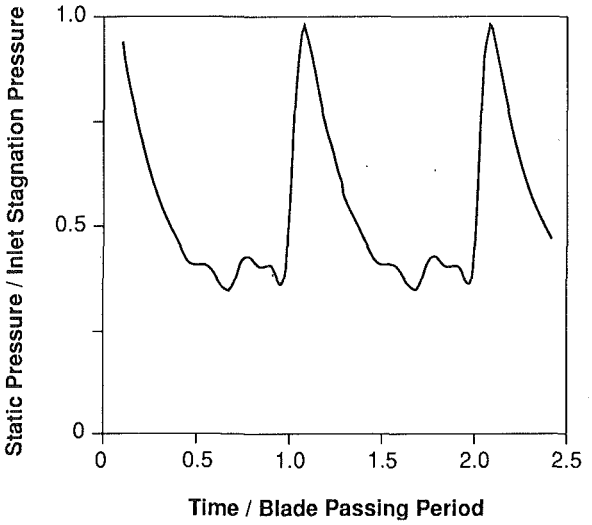

Fig. 12 Calculated static pressure history at suction surface location corresponding to Fig. 8(*b*)

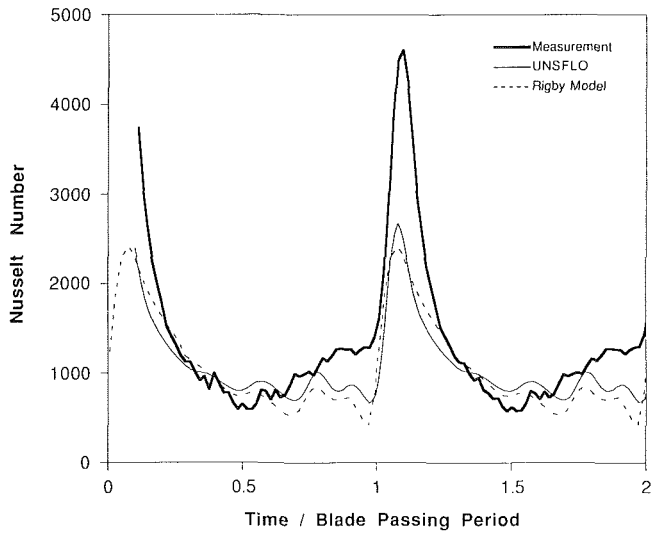

Fig. 13 Comparison of measured heat transfer, that calculated by the code, and that inferred from the calculated static pressure history using the shock compression model

do not reach the forward portion of the pressure surface and this is reflected in the more sinusoidal nature of the unsteady heat transfer. Wakes do periodically impinge on the pressure surface but this process is not well modeled by the code for two reasons. The first is that since this is a hybrid Navier–Stokes/Euler method, the inviscid part of the flowfield does not have an accurate way of representing the convection of the turbulence characteristics of the wakes. The second problem is that the algebraic turbulence model used in the viscous part of the flow does not transfer turbulence from the free stream to the boundary layer.

An example of how these modeling deficiencies may influence the solution can be seen with reference to Fig. 14(*a*), which replots the data-calculation comparison of Fig. 8(*j*). The instantaneous Mach number distribution through the boundary layer at two instants of time is also shown, as is the instantaneous ratio of turbulent to laminar viscosity predicted by the code at that location. At $t = 0.75$, the local Mach number is high, the turbulent viscosity high, and the heat transfer large. At $t = 1.1$, the calculation shows the local Mach number is reduced, the turbulent viscosity has dropped by an order of magnitude, and the heat transfer reduced by a factor of two. This behavior is consistent with the limitations of an algebraic turbulence model. On the pressure surface of a turbine rotor blade, the influence of the turbulence convected in by the wake is not modeled here. In the code, the boundary layer turbulence is only a function of the instantaneous local velocity, which fluctuates rapidly. In the physical flow, however, the turbulence has a physical time constant, which serves to keep the turbulence level more uniform with time, smoothing out the short-term response to inviscid flow variations such as those predicted by the code. This is less of a problem on the blade suction surface, where more of the turbulence is generated in the boundary layer.

Influence of Airfoil Geometric Variations. There is always a question in the numerical modeling of fluid flow as to whether the geometry modeled is an accurate representation of the physical device. This can often be important in turbomachinery since the design intent is not always realized at operating conditions and because of manufacturing tolerances. To examine the importance of NGV airfoil geometric variations in this turbine, the raw data were ensemble averaged over 30 rotor revolutions for *each* of the 36 NGV passages (phase lock averaging), yielding the time average flow in each passage. These data, shown in Fig. 15 for a transducer on the crown of the suction surface corresponding to Fig. 8(*b*), illustrate the spatial variation in heat transfer that a rotor blade sees during one revolution. The average passage heat flux (replotted from Fig. 8*b*) is shown next to the variation about the annulus. From

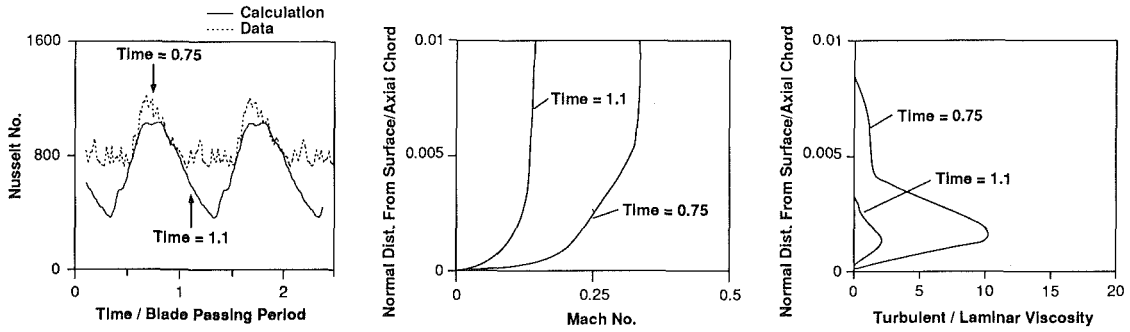

(a) Heat flux measurement and prediction

(b) Mach No. distribution through the boundary layer at t = 0.75 and t = 1.1

(c) Turbulent viscosity distribution through boundary layer at t = 0.75 and t = 1.1

Fig. 14 Algebraic turbulence model only responds to instantaneous velocity fluctuations overestimating the drop in heat transfer due to decreasing free-stream velocity on the rotor pressure surface

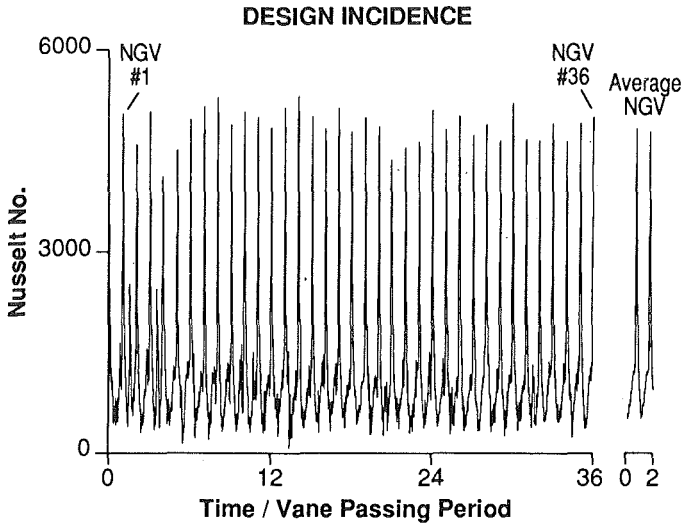

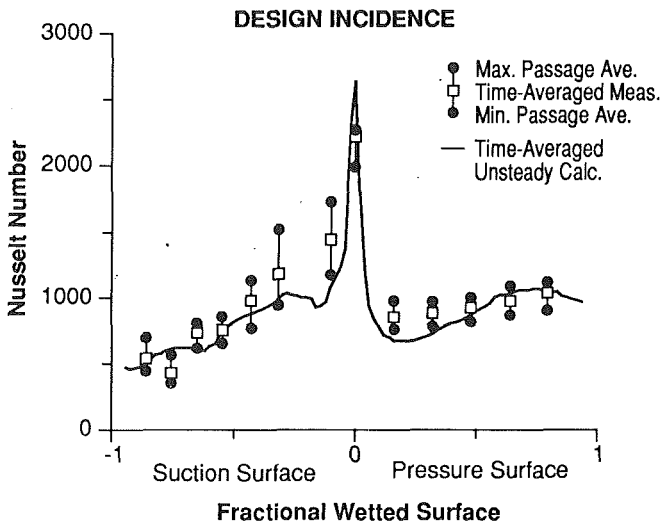

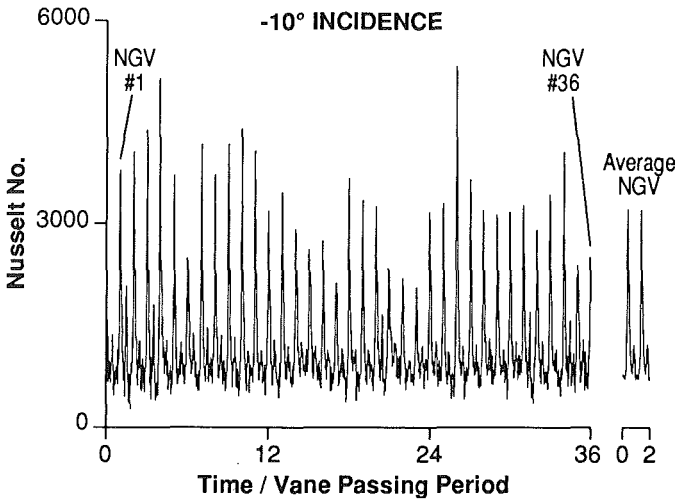

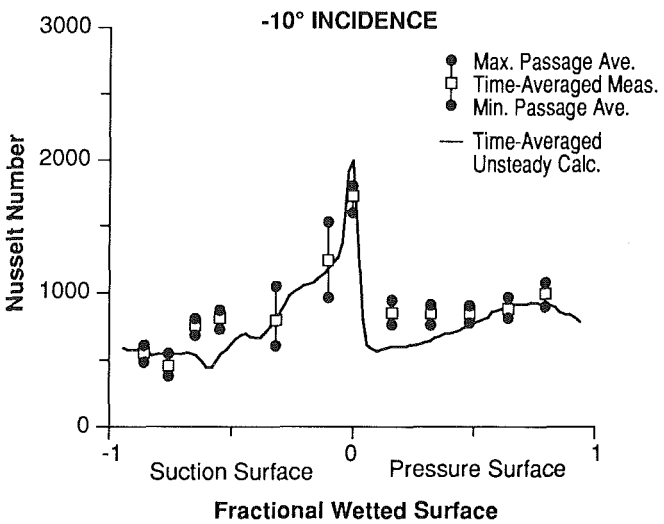

Fig. 15 Rotor blade heat flux distribution measured about the annulus on the suction surface crown (location as in Fig. 8*b*) compared to that for the average NGV passage. There are 36 NGVs in this turbine

Fig. 16 Time-averaged heat flux about the rotor blade showing the maximum and minimum average (d-c) value corresponding to the passages illustrated in Fig. 15

this figure, we note two things. The first is that the passage-to-passage variation in heat transfer due to shock impingement is quite noticeable, and the second is that there is a much wider variation at -10 deg incidence (± 65 percent of mean) than at design (± 14 percent). The mean (d-c) heat flux averaged over the passage varies by about ± 13 percent at both incidences. The magnitude of the passage variations about the rotor is shown in Fig. 16, where the average as well as the minimum and maximum heat flux averaged over each passage is delineated.

We have considered two simple mechanisms that could account for the observed heat flux variations. The first is a variation in NGV throat area, which would change both the mass flux (and thus the rotor Reynolds number) and the NGV exit Mach number (and thus shock strength, since the choked rotor flow makes this a two-throat problem). The influence of Reynolds number would not be much different at the two rotor incidence angles, however. A second source of heat flux variation could be differences in area ratio between the NGV throat and trailing edge. This would change the strength of the NGV trailing edge shock waves that impinge on the rotor and enhance the heat transfer. Both mechanisms will alter the rotor relative incidence angle.

Inspection of the NGV ring revealed a ± 4 percent variation in nozzle throat area. The area ratio could not be readily checked to the necessary accuracy, but a ± 3 percent variation would be within the manufacturing tolerances for this experimental blade set.

The influence of the throat area variation was examined by running UNSFLO with a 4 percent change in throat area (nozzle pitch). At -10 deg incidence, the predicted integrated heat transfer about the rotor changed by 5 percent. The height of the shock-induced heat flux spike on the suction surface crown (Fig. 15) changed by 8 percent. Since this is much less than the observed 13 percent change in integrated heat flux and 43 percent change in peak-to-peak shock-induced heat transfer, we conclude that NGV throat area variation alone is not responsible for the observed differences.

We have crudely estimated the magnitude of NGV area ratio effects as follows. From the one-dimensional continuity equation (Shapiro, 1953), the change in Mach number (M) can be related to the change in area (A) by

$$\frac{d\mathrm{M}^2}{\mathrm{M}} = \frac{2+(\gamma-1)\mathrm{M}^2}{\mathrm{M}^2-1}\frac{dA}{A} \tag{3}$$

The pressure change, ΔP, across a weak shock wave is

$$\frac{\Delta P}{P_1} = \frac{2\gamma}{\gamma+1}(M^2-1) \tag{4}$$

Combining Eqs. (3) and (4) gives

$$\frac{d\left(\frac{\Delta P}{P_1}\right)}{\left(\frac{\Delta P}{P_1}\right)} \cong \frac{M^2[2+(\gamma-1)M^2]}{(M^2-1)^2}\frac{dA}{A} \tag{5}$$

From Eq. (1), the change in heat transfer will be proportional to the change in shock pressure rise (assuming the shape of the pressure time history remains the same and just the magnitude changes), thus

$$\frac{d\left(\frac{\Delta Nu}{Nu}\right)}{\left(\frac{\Delta Nu}{Nu}\right)} \cong \frac{M^2[2+(\gamma-1)M^2]}{(M^2-1)^2}\frac{dA}{A} \tag{6}$$

Note that Eq. (6) implies that, for a given geometric variation (dA/A), the variation in peak heat transfer will be greater as the Mach number approaches one. At the design incidence, the design value of the NGV exit Mach number is 1.22, while at -10 deg incidence it is 1.13. Equation (6) quantitatively explains the larger fluctuations observed at -10 deg incidence. We can then use Eq. (6) to estimate the amount of blade-to-blade geometric variation required to account for the observed heat flux variations. For both incidences, about a 2 percent variation in NGV area ratio will account for the ± 10 to ± 43 percent variation in shock-induced heat transfer measured. Thus, it appears to us that the measured passage-to-passage variation in heat flux is fully explained as a combination of a variation in NGV throat areas and in NGV throat-to-exit area ratios. However, the variation does not explain any of the differences between calculation and measurement.

In production turbines, the total nozzle throat area is closely controlled since it establishes the engine working line. The individual blade passages, however, may vary by the several percent discussed above. Thus, we might expect production transonic turbine rotors to have concomitant annular variations in heat load (on the order of ± 10 percent). Since the phenomena we have discussed are approximately linear, the total heat load in a typical built-up turbine with geometric variation similar to the one studied here will be about the same as a geometrically uniform one. The built-up machine sees a once-per-revolution heat load fluctuation, which the uniform turbine does not, but we know of no reason why this should be detrimental since the thermal penetration depth at shaft frequencies is small. In other words, while academically interesting, we do not see any practical import to the observed passage-to-passage difference in heat flux.

Unresolved Influences and Further Work. It is clear from the preceding section that small geometry changes can have a large influence in the details of the heat transfer in a transonic turbine. This reinforces the importance of proper specification of the axial distribution of streamtube height (AVDR or hade) in a two-dimensional calculation like this. It would be surprising if the streamline curvature calculation used to prepare the inputs for the numerical calculations presented here was always accurate to better than the few percent level that caused the large variations in the measured flow from the NGV passages. Inaccurate specification of the streamtube height is, we believe, the principal reason for the observed differences in shock-induced heat transfer between the calculations and the measurements. A steady, three-dimensional inviscid code may provide an improvement over the streamline curvature approach in estimating the streamtube height distribution throughout the turbine stage.

Streamtube tube height variations may explain other differences between the code and measurements. At the leading edge, for example, the calculation predicts a considerable modulation of the heat transfer as a shock wave (shock 2*a* of Fig. 9) sweeps around from the suction surface. However, the measurements show little evidence of this modulation, implying either that the inviscid shock structure is calculated inaccurately here (i.e., unlike the calculation, the shock wave never reaches the leading edge in the turbine measurements) or that there is a problem with the boundary layer calculation near the stagnation point. We cannot otherwise explain the discrepancy at this time.

One of the more puzzling results to us is the relatively small difference between the steady fully turbulent rotor calculation and the time average of the unsteady calculation. It very much appears that, integrated over time, the unsteadiness plays a relatively small role in this highly loaded transonic turbine, even though both the calculations and data show the unsteadiness to be very large.

This is in many ways a progress report on an ongoing effort as the code continues to evolve. For example, true grid independence has not been rigorously demonstrated in the sense that the grid is continually refined in all directions until there are not changes in the calculated flowfield, although a finer boundary layer grid has been run with little change in the calculated heat transfer. Also, work is ongoing to move from an algebraic turbulence model to a more sophisticated one. Thus, many of the questions raised in this work will continue to be addressed.

Summary

Time-resolved heat transfer measurements and calculations have been compared at two operating points. In both cases, the code predicts about 90 percent of the measured integrated heat load to the blades. For one flow condition, the discrepancy is mainly on the first part of the suction surface and is thought to be due to an underestimation of the local shock strength. At the reduced loading conditions, the shock waves in the numerical solution are weaker and the predicted heat transfer more closely matches the measurements. At this -10 deg incidence flow condition, however, the heat transfer on the pressure surface is underpredicted. Examination of the time-resolved data showed ± 13 percent variations in average heat flux about the annulus. This was explained as due to 2 percent variations in NGV geometry. The importance of stream-tube height on the detailed heat transfer was emphasized.

Although this paper has focused on the differences between the calculational results and the measurements in order to assess the impact of various modeling assumptions and numerical approximations, it should be noted that, both overall and in detail, the agreement between the two is quite good. This good agreement using a quite unsophisticated turbulence model implies that accurate prediction of heat transfer in highly loaded turbines may be more sensitive than generally realized to details of the inviscid flow prediction than to the particulars of the turbulence model employed.

Clearly, a relatively fast and accurate two-dimensional unsteady multiblade row code is a useful tool both for interpreting experimental measurements and for elucidating the complex flow in unsteady turbomachinery.

Acknowledgments

The authors would like to thank Dr. R. J. G. Norton and Mr. R. Haimes for their useful comments and Mr. T. Shang for his help in running the code. This work was supported by Rolls Royce Inc., Mr. A. Veninger, Technical Monitor.

References

Addison, J. S., and Hodson, H. P., 1990a, "Unsteady Transition in an Axial Flow Turbine: Part 1—Measurements on the Turbine Rotor," ASME JOURNAL OF TURBOMACHINERY, Vol. 112, pp. 206–214.

Addison, J. S., and Hodson, H. P., 1990b, "Unsteady Transition in an Axial Flow Turbine: Part 2—Cascade Measurements and Modeling," ASME JOURNAL OF TURBOMACHINERY, Vol. 112, pp. 215–221.

Ashworth, D. A., LaGraff, J. E., Schultz, D. L., and Grindrod, K. J., 1985, "Unsteady Aerodynamics and Heat Transfer Processes in a Transonic Turbine Stage," ASME *Journal of Engineering for Power*, Vol. 107, No. 4, pp. XX–00.

Ashworth, D. A., 1987, "Unsteady Aerodynamics and Heat Transfer Processes in a Transonic Turbine Stage," D. Phil. Thesis, Oxford University, United Kingdom.

Blair, M. F., Dring, R. P., and Joslyn, H. D., 1989, "The Effects of Turbulence and Stator/Rotor Interactions on Turbine Heat Transfer: Part II—Effects of Reynolds Number and Incidence," ASME JOURNAL OF TURBOMACHINERY, Vol. 111, pp. 97–103.

Doorly, D. J., and Oldfield, M. J., 1985, "Simulation of the Effects of Shock Wave Passing on a Turbine Rotor Blade," ASME *Journal of Engineering for Gas Turbines and Power*, Vol. 107, No. 4, pp. 998–1006.

Dring, R. P., Blair, M. F., Joslyn, H. D., Power, G. D., and Verdon, J. M., 1986, "The Effects of Inlet Turbulence and Rotor Stator Interactions on the Aerodynamics and Heat Transfer of a Large-Scale Rotating Turbine Model, Vol. I—Final Report," NASA CR 4079, UTRC-R86-956480-1.

Dunn, M. G., Rae, W. J., and Holt, J. L., 1984, "Measurement and Analysis of Heat Flux Data in a Turbine Stage," ASME *Journal of Engineering for Gas Turbines and Power*, Vol. 106, pp. 229–240.

Epstein, A. H., Guenette, G. R., and Norton, R. J. G., 1984, "The MIT Blowdown Turbine Facility," ASME Paper No. 84-GT-116.

Epstein, A. H., Guenette, G. R., Norton, R. J. G., and Yuzhang, C., 1986, "High Frequency Response Heat Flux Gauge," *Review of Scientific Instruments*, Vol. 57, No. 4, pp. 639–649.

Giles, M. B., 1988, "Calculation of Unsteady Wake Rotor Interaction," *AIAA J. of Prop. and Power*, Vol. 4, No. 4, pp. 356–362.

Giles, M. B., and Haimes, R., 1991, "Validation of a Numerical Method for Unsteady Flow Calculations," ASME Paper No. 91-GT-XX.

Guenette, G. R., Epstein, A. H., Giles, M. B., Haimes, R., and Norton, R. J. G., 1989, "Fully Scaled Transonic Turbine Rotor Heat Transfer Measurements," ASME JOURNAL OF TURBOMACHINERY, Vol. 111, pp. 1–7.

Johnson, A. B., Rigby, M. J., Oldfield, M. L. G., Ainsworth, R. W., and Oliver, M. J., 1989a, "Surface Heat Transfer Fluctuations on a Turbine Rotor Blade Due to Upstream Shock Wave Passing," ASME JOURNAL OF TURBOMACHINERY, *Vol. 111, pp. 105–115.*

Johnson, A. B., Rigby, M. J., and Oldfield, M. L. G., 1989b, "Unsteady Aerodynamic Phenomena in a Simulated Wake and Shock Wave Passing Experiment," AGARD-CP-468, p. 9.

Ni, R.-H., 1981, "A Multiple Grid Scheme for Solving the Euler Equations," *AIAA Journal*, Vol. 20, No. 11, pp. 1565–1571.

Norton, R. J. G., 1988, Private Communication.

Rai, M. M., 1985, "Navier-Stokes Simulations of Rotor-Stator Interaction Using Patched and Overlaid Grids," AIAA Paper No. 85-1519.

Rigby, M. J., Johnson, A. B., Oldfield, M. L. G., and Jones, T. V., 1989, "Temperature Scaling of Turbine Blade Heat Transfer With and Without Shock Wave Passing," 9th International Symposium on Air Breathing Engines, Athens, Greece.

Schultz, D. L., Jones, T. V., Oldfield, M. L. G., and Daniels, L. C., 1977, "A New Transient Cascade Facility for the Measurement of Heat Transfer Rates," AGARD CP-227.

Shapiro, A., 1953, *Dynamics and Thermodynamics of Compressible Fluid Flow*, Vol. 1, Ronald Press.

Sharma, O. P., et al., 1988, "Rotor-Stator Interaction in Multi-stage Axial Flow Turbines," AIAA Paper No. 88-3013.

Sharma, O. P., Pickett, G. F., and Ni, R. H., 1992, "Assessment of Unsteady Flows in Turbines," ASME JOURNAL OF TURBOMACHINERY, Vol. 114, pp. 79–90.

Turner, E. R., Wilson, M. D., Hylton, L. D., and Kaufman, R. M., 1985, "Turbine Vane External Heat Transfer," NASA CR-174827.

K. Takeishi

S. Aoki

T. Sato
Takasago Research & Development Center.

K. Tsukagoshi
Takasago Machinery Works.

Mitsubishi Heavy Industries, Ltd.,
Takasago, Japan

Film Cooling on a Gas Turbine Rotor Blade

The film cooling effectiveness on a low-speed stationary cascade and the rotating blade has been measured by using a heat–mass transfer analogy. The film cooling effectiveness on the suction surface of the rotating blade fits well with that on the stationary blade, but a low level of effectiveness appears on the pressure surface of the rotating blade. In this paper, typical film cooling data will be presented and film cooling on a rotating blade is discussed.

Introduction

Relating to environmental pollution problems, high-efficiency thermal plants are presently attracting attention. Large LNG burning gas-steam combined cycle power plants with about $10 \sim 15$ percent higher efficiency than the latest turbine thermal plants have been in big demand. One of the most powerful means of achieving higher efficiency in industrial gas turbine engines is being satisfied by raising the turbine inlet temperature. For this reason, high-temperature heavy-duty gas turbines have been actively developed and the turbine inlet temperature of the latest model will reach a level of 1350–1400°C (Entenmann et al., 1991; Brandt, 1988).

In such a high-temperature gas turbine, the first vane and blade will be exposed to the most harsh thermal conditions. The latest sophisticated cooling scheme has been adopted to keep the metal temperature under the metallurgical limit temperature. In such cooling methods, film cooling is used to decrease the heat load from a high-temperature mainstream by blowing a coolant through discrete holes. Such a cooling scheme was adopted in the high heat flux region of the vane and blade where large thermal stress will be generated if only internal convection cooling is used. Film cooling might be applied to the first rotating blades, whose turbine inlet temperature is over 1300°C.

Film cooling on the rotating turbine blade is influenced not only by the cascade geometry but also the rotating effect and unsteady flow generated by nozzle wakes. To design a film-cooled turbine blade, it is very important to understand the rotation effect on film cooling effectiveness in addition to the data taken by the stationary cascade test.

There are, however, very few film cooling data on rotating blades presented because of the difficulty of direct measurement of film cooling effectiveness on the rotating blade. Only Dring et al. (1980) have successfully studied the film cooling effectiveness and trajectory of the coolant blowing through a single hole on a large-scale, low-speed rotor blade model. They noted that the result fitted well to the stationary cascade data of Ito et al. (1978) on the suction surface and the low level of efficiency on the pressure surface.

The present experimental work has been done to study the film cooling effectiveness on a rotating blade. The tests were carried out by a low-speed stationary two-dimensional cascade test and the high-speed air turbine test rig for which the same scaled model blades were applied. In this paper, typical film cooling test data are presented and film cooling on a rotating blade is discussed.

Experimental Apparatus

The turbine model airfoils used for the two-dimensional low-speed cascade test and air turbine test were typical first-stage blades for a high-temperature gas turbine. The blade is equipped with three-row shower head cooling, a single row of holes on the suction surface, and two film cooling holes with a single row on the pressure surface.

The geometry of the airfoil used for the two-dimensional low-speed cascade test is the scale model of the rotating blade for the air turbine test rig.

Low-Speed Cascade Test Rig. A low-speed, open two-dimensional cascade wind tunnel facility shown in Fig. 1 was constructed using five model blades. The blade chord length and the height are 230.2 mm and 300.0 mm, respectively, so the aspect ratio is $h/c = 1.30$. The cascade geometry is given in Table 1. The center blade was a film-cooled blade and the remaining four blades were solid with instrumented static pressure taps to measure aerodynamic conditions. The configuration and dimensions of the film cooling holes are shown in Fig. 2 and Table 2. The mainstream is room temperature with atmospheric conditions. The exit velocity was 40 m/s under typical test conditions. A turbulent grid was mounted 500 mm upstream of the cascade to increase the mainstream turbulence intensity and the turbulence intensity measured at a point 50 mm in front of the leading edge of center blade was 4 percent.

Contributed by the International Gas Turbine Institute and presented at the 36th International Gas Turbine and Aeroengine Congress and Exposition, Orlando, Florida, June 3–6, 1991. Manuscript received at ASME Headquarters March 4, 1991. Paper No. 91-GT-279. Associate Technical Editor: L. A. Riekert.

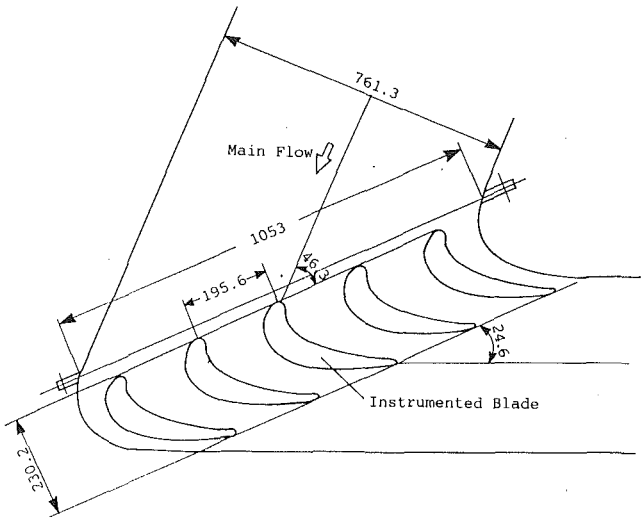

Fig. 1 Geometry of low-speed cascade test rig

Table 1 Cascade geometry

	2-D Low-Speed Cascade	Rotating Rig
Chord	230.2	35.02
Height	300	46.70
Pitch	195.6	26.4
Aspect Ratio (height/chord)	1.30	1.33
Air Inlet Angle	46.3	46.3
Air Exit Angle	65.4	65.4

Rotating Test Equipment. The film cooling effectiveness on the rotating turbine blade was measured by using the one-stage air turbine test rig. The schematic layout of the rotating rig is shown in Fig. 3. The main flow was compressed air from a centrifugal compressor driven by a 4000 kW electric motor. The turbine inlet mainstream temperature was kept constant by controlling the cooler exit temperature. The pressure ratio, rotating speed, and main flow rate were controlled by the flow control valve and water brake.

The experiment was carried out in a 559-mm-dia rotating rig with a one-stage turbine model. A cross section of the rotating test equipment is shown in Fig. 4. The first vane was constructed with 32 vanes. The first blade was constructed with 72 blades, whose measured sectional geometry is shown in Table 1. Two of the 72 blades, whose details will be mentioned below, were film cooled and instrumented blades and the remaining blades were solid.

The total temperature, the total pressure, and the static pressure were measured 100 mm ahead of the leading edge of the first vane, and at the exhaust duct.

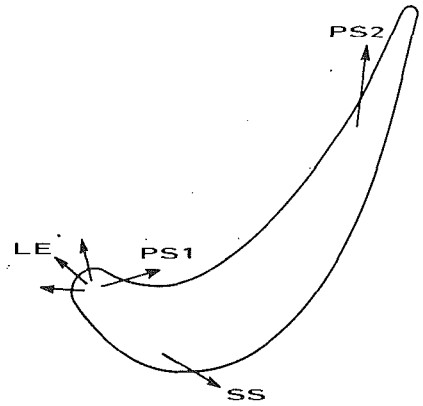

Fig. 2 Location of film cooling hole

Table 2 Film cooling hole dimensions

Location	Number of Row	Low Speed Cascade		Rotating Blade	
		Hole Diameter d[mm]	Pitch p[mm]	Hole Diameter d[mm]	Pitch p[mm]
LE	3	2.0	12.4	0.32	1.95
SS	1	2.6	9.2	0.41	1.41
PS1	1	2.6	9.2	0.41	1.41
PS2	1	2.0	6.68	0.32	1.00

Two model blades, shown in Fig. 5, were used to measure film cooling effectiveness. The reason two blades were used was to maintain a wide cross-sectional area of the internal flow path and to be able to test the additive nature of the film cooling effectiveness by controlling each film cooling flow rate.

Measuring Method

The film cooling effectiveness was defined by

$$\eta = \frac{T_{aw} - T_\infty}{T_2 - T_\infty} \tag{1}$$

Heated or cooled secondary fluid was injected through the film cooling holes and the adiabatic wall temperature T_{aw} was measured. In order to obtain local effectiveness, a large-scale model has to be used to decrease thermal conductivity error. It is a very difficult problem to adopt a large-size turbine blade made of a low thermal conductivity material for the air turbine test rig. So in this study, a mass-heat transfer analogy is applied to measure film cooling effectiveness. Local effectiveness η is defined as

$$\eta = \frac{C_x - C_\infty}{C_2 - C_\infty} \tag{2}$$

The analogy holds if the turbulent Lewis number and the molecular Lewis number are in unison (Ito et al., 1978; Ped-

Nomenclature

C = concentration of a tracer
C = blade chord
d = film cooling hole diameter
G = flow rate
h = blade height
M = mass flux ratio = $\rho_2 U_2/\rho_\infty U_\infty$
N = rotating speed
P = pressure
P = film cooling hole pitch
S = equivalent film cooling slot width = $\pi d^2/4P$ for SS, PSI, PS2 and 1.5 $\pi d^2/4P$ for LE
S = maximum surface distance
T = temperature
V = velocity
x = distance downstream of film cooling hole
z = distance from hole center normal to flow
η = film cooling effectiveness
π_T = turbine pressure ratio (ratio of inlet total pressure to exit static pressure)
ρ = density

Subscripts

aw = adiabatic wall
ex = exit
f = film cooling
x = local point
0 = film cooling hole exit
2 = secondary fluid
∞ = mainstream

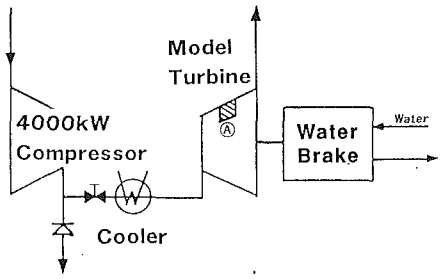

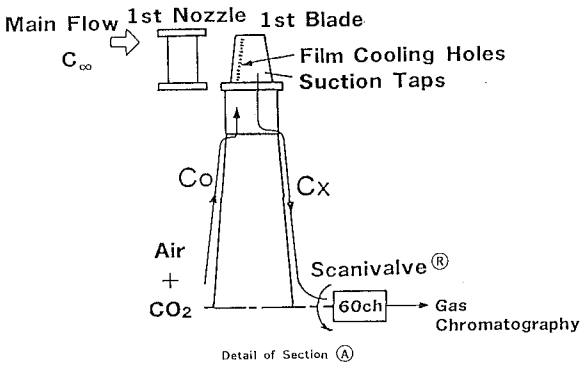

Fig. 3 Schematic layout of the rotating test rig

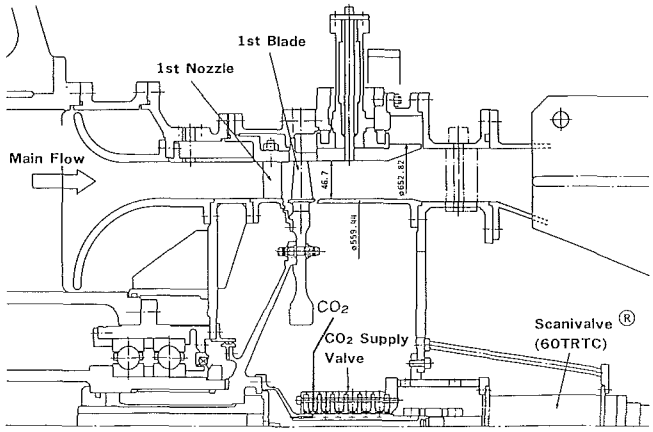

Fig. 4 Cross section of the rotating test equipment

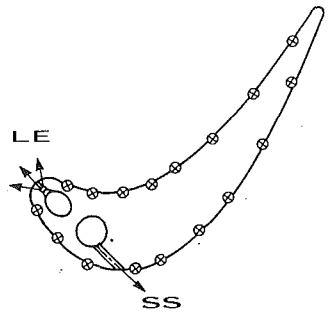

Model I

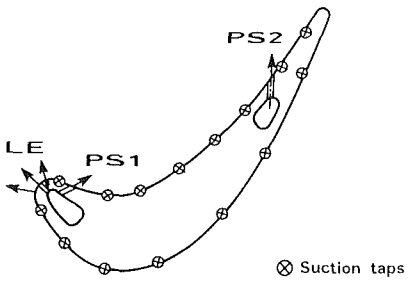

Model II

Fig. 5 Model blades to measure film cooling effectiveness

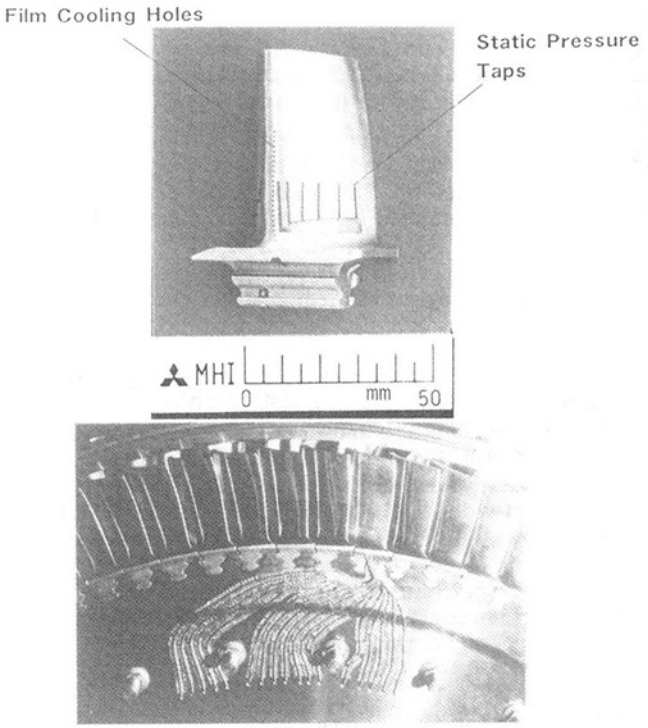

Fig. 6 Instrumented film cooled model 1 blade

ersen et al., 1977). In this study, carbon dioxide was used for the tracer. Much attention was paid to suction of the film cooling layer on the turbine airfoil. If the suction speed is too high, mainstream air will mix with the sucked-in air and cause large error. So first, examination was carried out by changing the suction speed and a suction speed where the effectiveness is constant was decided upon. The suction speed was kept under 10 m/s at each suction tap and the sucked-in air was accumulated in the air bag. Later, the concentration of carbon dioxide in the sucked-in air in the bag was analyzed by using gas chromatography. The sampling and measurement system is shown in Fig. 3.

The concentration of carbon dioxide was 3000 ppm, 70 ~ 90 ppm at the film cooling hole exit and mainstream, respectively. The effectiveness was calculated by the data, which were measured three times. The accuracy of the gas chromatography is ±1 percent. The film cooling air temperature is room temperature, so the density ratio ρ_2/ρ_∞ is about 1.0 at the low-speed cascade test and rotating test.

The suction taps on the stationary cascade blade are located three lines downstream of the film cooling holes as shown in Figs. 12–15. The stationary model blade is large enough to embed many suction taps; for example, to measure the film cooling effectiveness of SS, three taps ($Z/P=0$, $Z/P=1/4$, $Z/P=1/2$) at 23 locations ($X=5$, 10, 15, 20, 25, 30, 35, 40, 45, 50, 60, 70, 80, 90, 100, 120, 140, 160, 180, 200, 240, 280, 300 mm) are used.

The suction taps on the rotating blade are located as shown in Fig. 5. These taps are located downstream between the film cooling holes. Firstly, a channel was made by electric spark machining and 1.0 o.d., 0.5 i.d, stainless steel tubes were

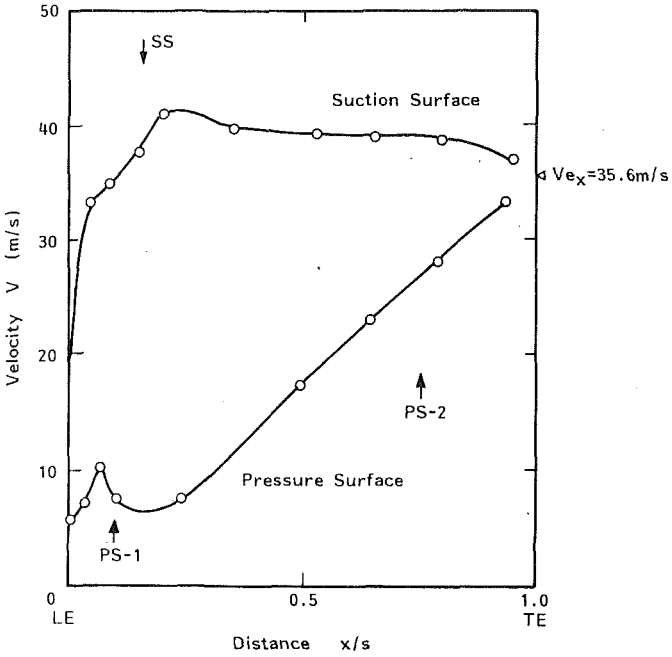

Fig. 7 Velocity distribution of the blade at low-speed cascade

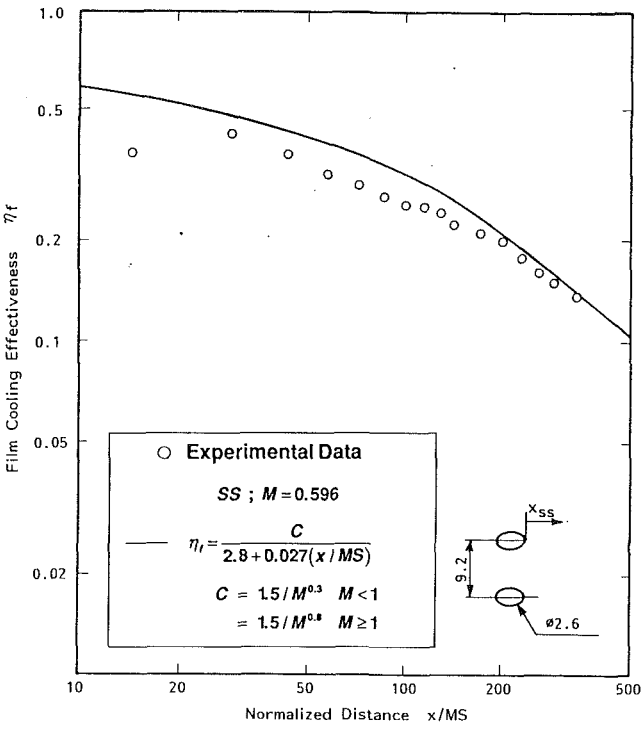

Fig. 9 Film cooling effectiveness blowing through SS

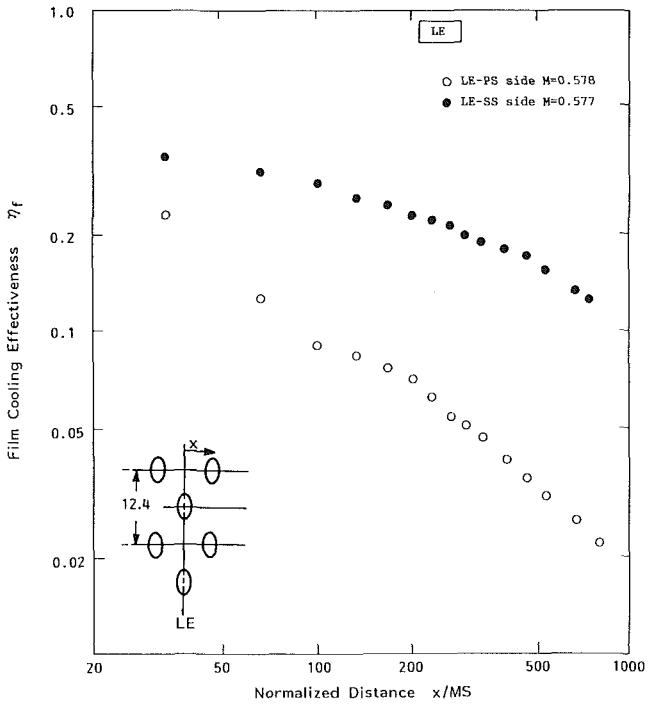

Fig. 8 Film cooling effectiveness blowing through LE

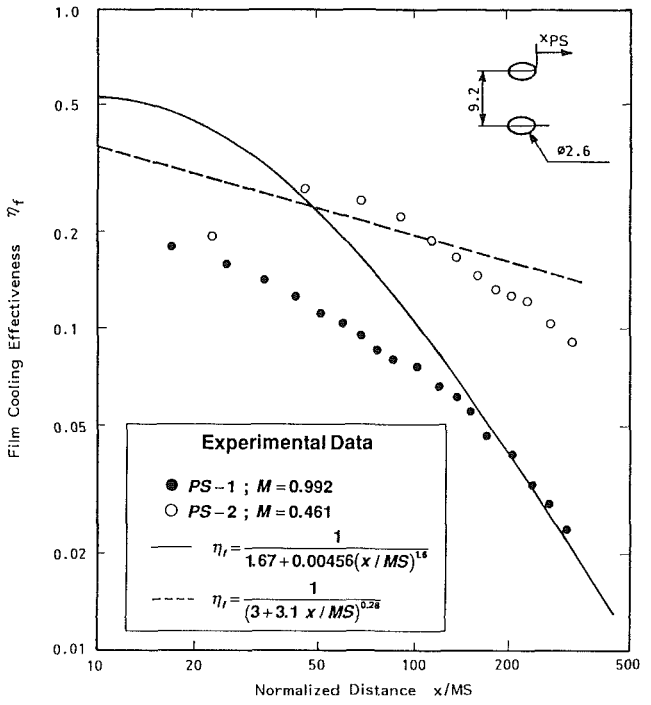

Fig. 10 Film cooling effectiveness blowing through PS1 and PS2

embedded. The gaps were silver welded and polished to reform the airfoil. 0.3 mm hole diameter suction taps were vertically machined to the surface, joining the cavity of the stainless steel tube by electric spark machining. The instrumented blade is shown in Fig. 6.

The film cooling air was supplied through rotating valves by which each film cooling air was supplied separately, and the sucked-in film air on the airfoil was delivered by 60 channel rotating Scanivalve® mounted at the end of the rotor axis as shown in Fig. 4.

Experimental Results and Discussion

Low-Speed Cascade Test. The velocity distribution around the airfoil, as shown in Fig. 7, was calculated by the static pressure distribution measured by using static pressure taps on the airfoil with the inlet total pressure. In Fig. 7, the location of the film cooling holes is indicated.

The measured averaged film cooling effectiveness blowing through each film cooling hole is shown in Figs. 8–10. The effectiveness data were arranged by using well-known non-dimensional distance x/MS, where x is the distance down-

stream of the film cooling hole, M is the mass flux ratio, and S is the equivalent film cooling slot width. The film cooling air flow separated at the leading edge was assumed to be even on the suction and pressure side, so the equivalent slot width was calculated by using 1 1/2 row of film cooling holes. The film cooling effectiveness of SS and LE on the suction side is the same level as shown in Figs. 8 and 9 even though that of LE on the suction side is a little lower than of SS. Also, the effectiveness of LE on pressure side is fitted very well with that of PS1 on the pressure side as is clear by comparing Figs. 8 and 10. The film cooling effectiveness of PS2 is higher compared with that of PS1. The reason the effectiveness of PS1 is lower is that the location of the PS1 film cooling location is situated at the velocity deceleration zone and the concave radius of curvature at PS1 is smaller than that of PS2. Especially the film cooling hole PS2 is located near the trailing edge and the curvature is almost flat. So the measured film cooling effectiveness was compared with Eq. (3) of Pedersen et al. (1977) on a flat plate and the result is shown in Fig. 10.

The effectiveness of PS2 roughly fits with Eq. (3).

$$\eta_f = \frac{1}{(3+3.1\ x/MS)^{0.28}} \tag{3}$$

The authors (Takeishi et al., 1990) presented Eqs. (4) and (5) by curve-fitting the film cooling test data measured by using the low-speed, full annular vane cascade rig.

Suction surface:

$$\eta = \frac{C}{2.8+0.027\ (x/MS)} \tag{4}$$

where $C=1.5/M^{0.3}$ $M<1.0$

$C=1.5/M^{0.8}$ $M\geq 1.0$

Pressure surface:

$$\eta = \frac{1}{1.67+0.00456\ (x/MS)^{1.6}} \tag{5}$$

The comparison of the film cooling effectiveness of SS with Eq. (4) is shown in Fig. 9. These data fit very well. The difference in the convex radius of curvature for the vane and blade has little effect on the film cooling effectiveness. Also, the effectiveness of PS1 was compared with Eq. (5). In this case, the effectiveness on the pressure surface of the blade is lower than that of the vane. This is estimated because the concave radius of curvature for the blade is smaller than that for the vane, producing a strong destabilizing situation along the blade pressure surface than is the case for the vane. Equations (3)–(5) will be applicable with some correction factor to design film cooled turbine blades.

The local film cooling effectiveness was measured along three lines downstream of the film cooling hole. Typical test data are shown in Figs. 12–15. The film cooling effectiveness measured along the centerline and off-centerline merge value at $x/d\approx 5$ from the film cooling hole exit on PS1 and at $x/d\approx 35$ on SS. Below these points a two-dimensional film cooling layer is achieved. The significant difference of the film cooling effectiveness between the concave surface and the convex surface depend on strong lateral mixing which causes fundamentally different roles of concave and convex curvature on boundary layer stability.

Rotating Test Results. The film cooling test to measure the film cooling effectiveness on the rotating blade was carried out under aerodynamically simulated conditions with an actual heavy-duty gas turbine. Therefore the rotating rig has simulated velocity triangles and pressure ratios. For each blowing site the coolant to mainstream mass flux ratio M covers the same value as actual engine conditions from 0.6 to 1.0, but the density ratio ρ_2/ρ_∞ is constant at 1.0. In actual engine conditions, the density ratio ρ_2/ρ_∞ is from 1.5 to 2.5 and

Table 3 Rotating test condition

Turbine Inlet Temperature	Tit°C	78.2
Turbine Inlet Total Pressure	Po ata	2.055
Turbine Exit Temperature	Tex°C	25.4
Turbine Exit Pressure	Pex ata	1.077
Pressure Ratio	π	1.908
Main Flow Rate	G kg/s	8.381
Rotating Speed	N rpm	6260

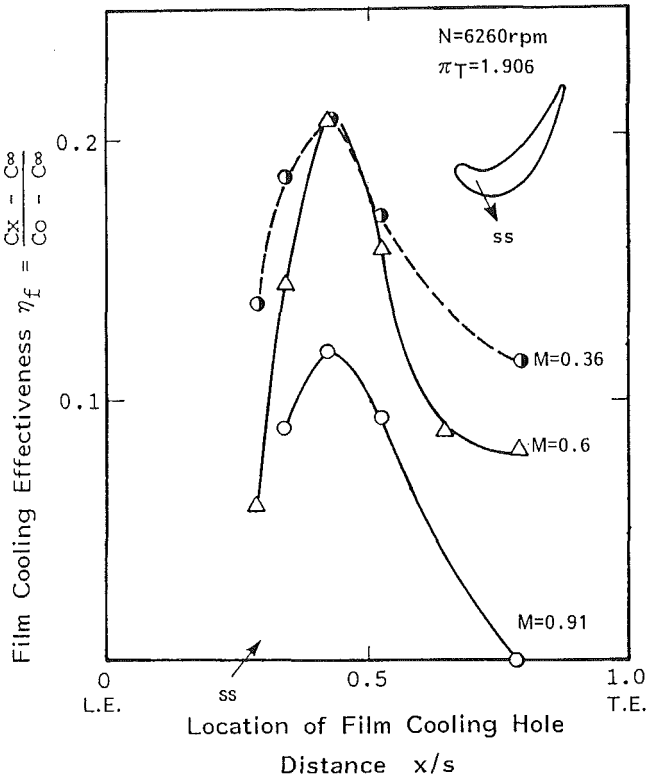

Fig. 11 Film cooling effectiveness at SS on suction surface

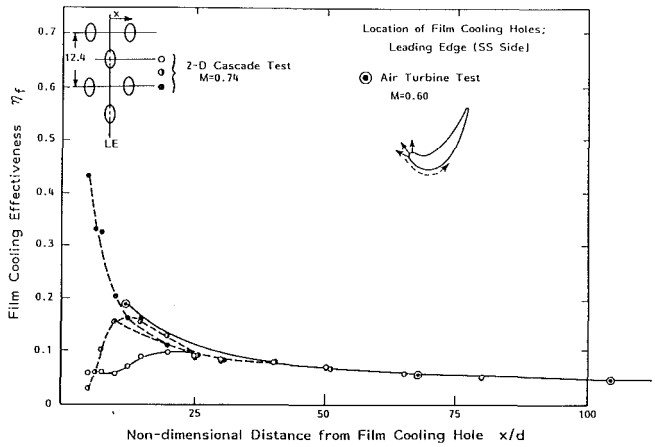

Fig. 12 Film cooling effectiveness of LE on suction surface

Pedersen et al. (1977) pointed out that the density ratio has a strong effect on the film cooling effectiveness. In this paper, we focused the rotation effect on film cooling effectiveness, and the tests were carried out at a density ratio ρ_2/ρ_∞ of nearly 1.0.

The typical test condition is shown in Table 3. The film

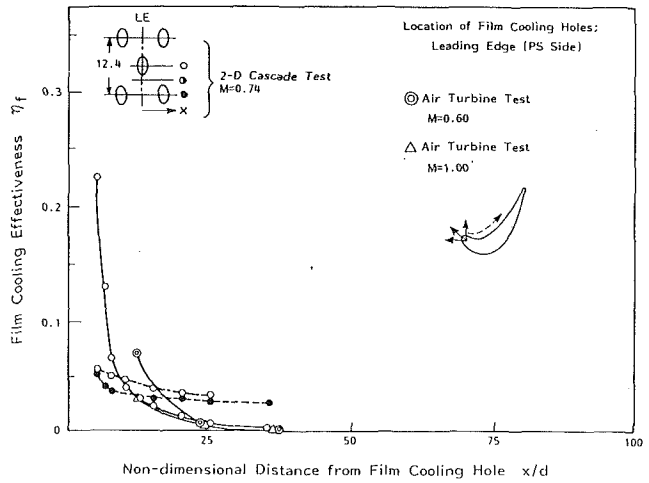

Fig. 13 Film cooling effectiveness of LE on pressure surface

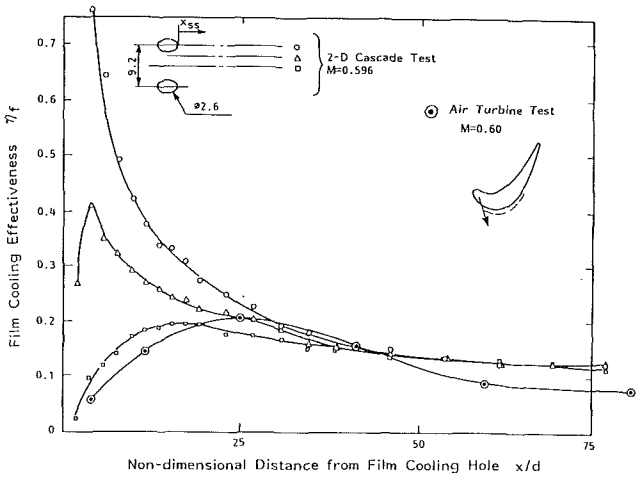

Fig. 14 Film cooling effectiveness of SS on suction surface

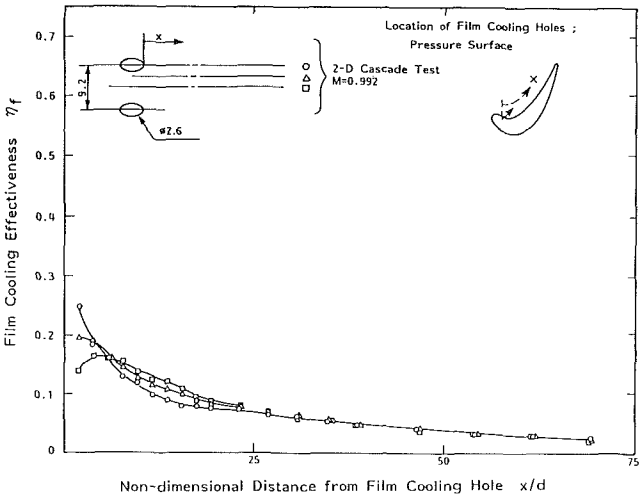

Fig. 15 Film cooling effectiveness of PSI on pressure surface

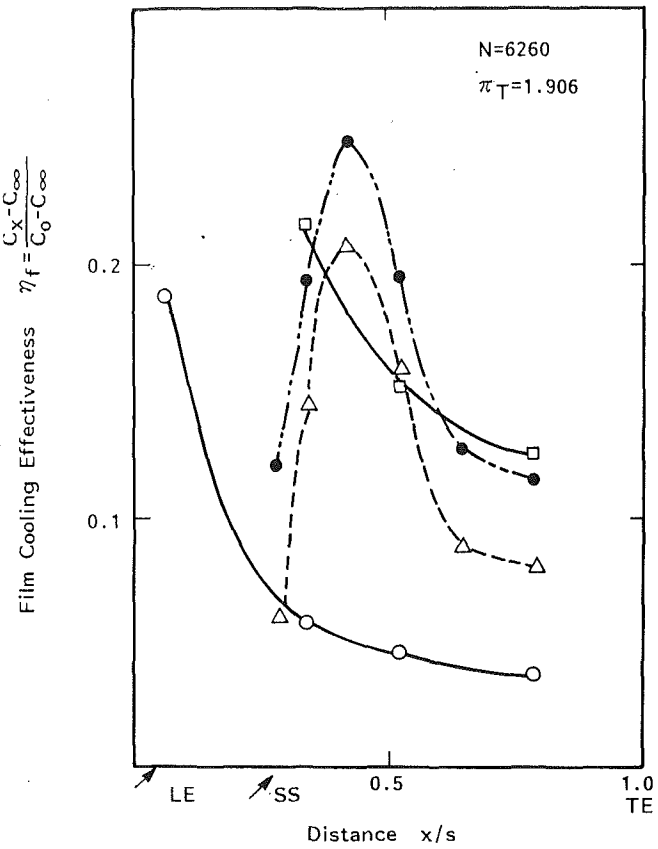

Symbol	Film Cooling
○	LE on Suction Side M=0.6
△	SS M=0.6
□	LE on Suction Side + M=0.6 SS M=0.6
●	Eq. (6)

Fig. 16 The additive nature of film cooling on suction surface

cooling effectiveness of SS on the suction surface is shown in Fig. 11 with the parameter of blowing flow rate M. In Figs. 11 and 16 nondimensional distance x/s (s is the maximum surface distance along the blade surface) is used because the film cooling hole diameter of the LE and the SS is different and the additive nature of film cooling can't be explained by using x/d. It is clear that the film cooling effectiveness decreases by increasing the blowing parameter M because at high M, the coolant penetrates to the mainstream and not enough film cooling layer is generated on the blade surface.

The film cooling effectivenesses of LE are shown in Figs. 12 and 13 with the comparison data of the low-speed stationary cascade. Much data can be measured by a stationary cascade test with the wide mass flux ratio M, but little data can be gotten with the air turbine test because much time has been used to measure accurate film cooling effectiveness. The mass flux ratio M of the air turbine test is controlled to be the same value as the actual engine condition.

The mass flux ratio M of the rotating test is not the same as that of the stationary cascade test, and the comparison is made at near M values in Figs. 12 and 13. It is clear from Fig. 12 that the effectiveness of LE on the suction surface fits very well with that of the low-speed cascade test. However, the film cooling effectiveness of LE on the rotating pressure surface decreases more rapidly than that on the stationary blade surface, as shown in Fig. 13. This tendency appeared in the low-speed rotating test carried out by Dring et al. (1980). This is

probably due to the effect of the radial flow and the strong mixing phenomena on the pressure surface.

The suction surface effectiveness data are shown in Fig. 14 compared with the low-speed stationary cascade test. In the rotating test, the suction taps were located downstream of the centerline between the film cooling holes. So the minimum film cooling effectiveness was measured on the rotating turbine blade. Comparing these minimum effectiveness data with the same data of low-speed cascade test, it appears that the film cooling effectiveness fits very well at the film cooling hole until about $x/d \approx 45$. However, over $x/d \approx 45$, the effectiveness on the rotating blade is about 30 percent lower than on low-speed stationary blade. This low film cooling zone is the two-dimensional film cooling region and is estimated due to high mixing with the divergent flow on the suction surface.

The pressure surface effective data are shown in Fig. 15. Some suction taps on the pressure surface were plugged after a long test time and enough data to evaluate film cooling of PS1 couldn't be measured, so the film cooling data on the rotating test rig were omitted from Fig. 15.

The additive nature of film cooling on the rotating blade was examined on the suction surface and the result is shown in Fig. 16. The additive film cooling effectiveness blowing through the two film cooling holes 1, 2 was calculated by Eq. (6) (Muska et al., 1976).

The independent effectiveness of LE on the suction surface and SS, and that of simultaneous blowing through LE and SS are shown in Fig. 16 compared with the calculated effectiveness by using Eq. (6).

$$\eta = \eta_1 + \eta_2 (1 + \eta_1) \tag{6}$$

From Fig. 16, the additive nature did not agree near the film cooling hole SS, where the three-dimensional film cooling effect is strong, but far downstream the measured effectiveness roughly fit the calculated one by Eq. (6). This is due to the two-dimensional boundary layer developed far downstream of the film cooling holes. The additive nature of film cooling was attained.

Conclusions

Measurements of the film cooling effectiveness were made by using the low-speed stationary cascade test and rotating test rig. The following conclusions were obtained through these results:

1 The film cooling effectiveness on the suction surface of the rotating blade fits well with that of the stationary blade but far downstream. The effectiveness is 30 percent lower than that of stationary cascade data.

2 The film cooling effectiveness on the suction surface can be estimated by Eq. (4), which was derived from the low-speed vane cascade test with some correction factor.

3 The leading edge film cooling effectiveness fits that on the suction and pressure surface of the low-speed cascade test.

4 A low level of effectiveness appears on the pressure surface of the rotating blade. This is due to the radial flow and high mixing motion that occur at the concave surface.

5 The additive nature of film cooling will not appear near the film cooling holes, but far downstream, where the two-dimensional film cooling layer is generated and the additive nature is attained at the rotating test rig.

Acknowledgments

The authors wish to express their indebtedness to Mitsubishi Heavy Industries, Ltd., for permission to publish this paper.

References

Brandt, D. E., 1988, "The Design and Development of an Advanced Heavy-Duty Gas Turbine," ASME *Journal of Engineering for Gas Turbines and Power*, Vol. 110, pp. 243–250.

Dring, R. P., Blair, M. F., and Joslyn, H. D., 1980, "An Experimental Investigation of Film Cooling on a Turbine Rotor Blade," ASME *Journal of Engineering for Power*, Vol. 102, pp. 81–87.

Entenman, D. T., North, W. E., Fukue, I., and Muyana, A., 1991, "Shop Test of the 501F—A 150 MW Combustion Turbine," ASME *Journal of Engineering for Gas Turbine and Power*, Vol. 113, pp. 488–494.

Goldstein, R. J., 1971, "Film Cooling," *Advances in Heat Transfer*, Vol. 7, Academic Press, New York, pp. 321–371.

Ito, S., Goldstein, R. J., and Eckert, E. R. G., 1978, "Film Cooling on a Gas Turbine Blade," ASME *Journal of Engineering for Power*, Vol. 100, pp. 476–481.

Muska, J. F., Fish, R. W., and Suo, M., 1976, "The Additive Nature of Film Cooling From Rows of Holes," ASME *Journal of Engineering for Power*, Vol. 98, pp. 457–467.

Pedersen, D. R., Eckert, E. R. G., and Goldstein, R. J., 1977, "Film Cooling With Large Density Difference Between the Mainstream and the Secondary Fluid Measured by the Heat Transfer Analogy," ASME *Journal of Heat Transfer*, Vol. 99, pp. 620–627.

Takeishi, K., Matsuura, M., Aoki, S., and Sato, T., 1990, "An Experimental Study on Heat Transfer and Film Cooling on Low Aspect Ratio Turbine Nozzles," ASME JOURNAL OF TURBOMACHINERY, Vol. 112, pp. 488–496.

Prediction of Turbulent Flow and Heat Transfer in a Radially Rotating Square Duct

C. Prakash

R. Zerkle

General Electric Company—
Aircraft Engines,
Cincinnati, OH 45215

The present study deals with the numerical prediction of turbulent flow and heat transfer in a rotating duct of square cross section. The axis of rotation is normal to the axis of the duct, and the flow is radially outward. The duct is smooth, of finite length, and the walls are isothermal at a temperature greater than the temperature of the incoming fluid. Both the Coriolis and the centrifugal-buoyancy effects are considered; the problem is three dimensional and fully elliptic. The predicted flow field is found to be quite complex, consisting of secondary cross-stream flows due to the Coriolis effects. Centrifugal buoyancy increases the radial velocity of the cooler fluid near the trailing face and decreases the radial velocity of the warmer fluid near the leading face; indeed, when the buoyancy effects are sufficiently strong, reverse radial flow may occur over the leading face. Rotation is found to increase the heat transfer over the trailing face, while, over the leading face, the heat transfer decreases near the inlet but increases further downstream. This finding agrees with the experimental observations. The quantitative agreement with the data is also satisfactory. The predictions are found to be quite sensitive to the inlet conditions, in particular, to the presence of rotational effects in the incoming stream. The effect of exit boundary conditions is examined by comparing the predictions for a single passage with those for a double-leg passage.

1 Introduction

1.1 The Problem Solved. The present study deals with the numerical prediction of turbulent flow and heat transfer in a rotating duct of square cross section. The problem schematics are shown in Fig. 1. The axis of rotation is normal to the axis of the duct and the flow is radially outward. The duct is smooth, of finite length, and the walls are isothermal at a temperature greater than the temperature of the incoming fluid. Further details of the problem will be provided in Section 2.

1.2 Motivation. Effective turbine blade cooling is necessary to enhance the efficiency of advanced aircraft engines. In general, film cooling is imposed on the external surface of the blades, while forced-convection cooling is used inside the blades by means of cooling passages as shown in Fig. 2. The internal cooling passages are connected at the ends, which leads to a serpentine flow path consisting of alternate channels of radial outflow and inflow. However, single-pass channels are also to be found near the leading and the trailing edges of the blades. To promote turbulence and enhance heat transfer, various kinds of turbulators are generally used on the walls of these internal passages.

Since the turbine undergoes high rotation, the flow in the internal blade cooling passages is strongly affected by the Coriolis and centrifugal forces. Consequently the flow, and hence, the heat transfer, in these rotating passages is quite different

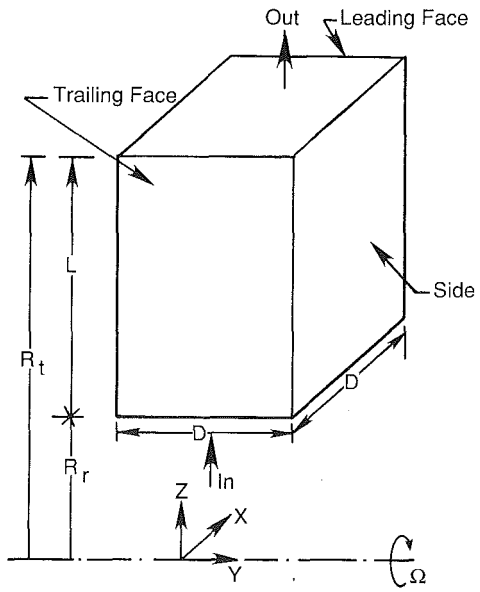

Fig. 1 Flow in a radially rotating duct

Contributed by the International Gas Turbine Institute and presented at the ASME Winter Annual Meeting, Atlanta, Georgia, December 1-6, 1991. Manuscript received by the International Gas Turbine Institute February 29, 1992. Associate Technical Editor: L. S. Langston.

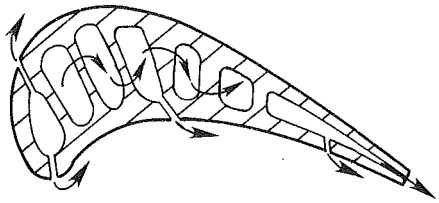

Fig. 2 Internal cooling passages in a turbine blade

as compared to that in stationary ducts. Indeed, serious errors may result if the correlations pertaining to stationary ducts are employed to predict heat transfer in rotating passages.

Clearly, comprehensive data bases, and accurate methods for predicting flow and heat transfer in rotating passages are necessary for turbine cooling design. This recognition provided the motivation for the present study.

1.3 Physical Features of the Problem. With regard to flow in rotating passages, two basic configurations are of much interest. The first, the so-called parallel axis rotating duct, pertains to a situation where the axis of rotation is parallel to the axis of the duct. The second configuration, called the radially rotating duct, refers to a case where the axis of rotation is normal to the axis of the duct. The present investigation deals with the second case, i.e., a radially rotating duct. The parallel axis rotating duct will not be discussed further.

Flow in a radially rotating duct is characterized by the following physical features:

(*a*) Coriolis forces produce a secondary flow in the cross-stream plane, which alters the distribution of the radial velocity and the temperature. Consequently, the friction and the heat transfer at the walls are modified as compared to a stationary passage. Generally, both these quantities increase with rotation.

For radial outflow in a rectangular duct, the Coriolis force leads to two symmetric cross-stream vortices, which are directed from the leading to the trailing face near the center and vice versa (trailing to leading) near the side walls. Since such a crossflow transports high-momentum fluid from the center to the trailing face, the wall friction increases over the trailing face and decreases over the leading face. The wall heat transfer is affected in a likewise manner.

(*b*) For an incompressible fluid, the centrifugal force does not affect the flow and only modifies the pressure. However, in all practical situations involving heat transfer, the dependence of density on temperature cannot be ignored and the centrifugal-buoyancy effects must be accounted for. Buoyancy affects the flow field primarily via the action on the radial velocity, since the magnitude of the force is greater on the cooler (heavier) fluid as compared to the warmer (lighter) fluid.

Consider the case of radial outflow in a rectangular duct with heated walls. As already mentioned, the Coriolis-induced secondary flow transports cooler fluid from the core to the trailing face. Thus, centrifugal buoyancy has the effect of increasing the radial velocity of the cooler fluid near the trailing face while decreasing the radial velocity of the warmer fluid near the leading face. As a result, friction and heat transfer at the trailing face are further enhanced while those at the leading face are further decreased.

(*c*) Rotation modifies the turbulent characteristics of the flow by two main mechanisms: (*i*) The Coriolis-generated secondary flow field, modified further by buoyancy effects, significantly alters the generation and distribution of the turbulent kinetic energy. (*ii*) The Coriolis force influences the basic stability of the turbulent boundary layers; thus, for rectangular ducts, turbulence is suppressed on the leading face and enhanced near the trailing face [1].

The problem is clearly quite complex, and development of a comprehensive model that takes account of all the physical processes listed above remains a challenging task. Nevertheless, there have been a number of experimental and theoretical studies of flow in rotating passages that have helped in the understanding of the various features of the problem. A brief review of these studies is provided below.

1.4 Literature Review. This review is limited to flow in radially rotating ducts. Also, unless otherwise noted, the flow is radially outwards. The term aspect ratio for rectangular ducts refers to the ratio a/b where a designates the width of the leading (trailing) face and b represents the width of the side walls.

1.4.1 Experimental. For fully developed laminar and turbulent flow in circular ducts, the friction factor was measured

Nomenclature

A, B, C = constants in the enthalpy ~ temperature relation
C_1, C_2, C_μ = turbulence model constants
c_p = specific heat
D = duct width
E = wall roughness parameter
G = rate of generation of turbulent kinetic energy
h = enthalpy
k = turbulent kinetic energy
L = duct length
$\dot{m}$ = total mass flow rate through the duct
Nu = local Nusselt number
Nu_∞ = Nusselt number for the fully developed flow in a stationary duct
P = the P function
p = pressure
Pr, Pr_t = laminar and turbulent Prandtl number, respectively
q = heat flux
R = gas constant
$R_r, R_t, \overline{R}$ = root, tip, and mean radius, respectively
Re = Reynolds number
Ro = rotation number
S = source term in the transport equations
s = friction coefficient
St = local Stanton number
T = temperature
u, v, w = velocity components in the x, y, z directions
V = tangential velocity close to a wall
x, y, z = coordinates
γ = heat transfer coefficient
δ = distance between the wall and the near-wall point
ϵ = rate of dissipation of turbulent kinetic energy
κ = von Karman constant
λ = thermal conductivity
μ, μ_t = laminar and turbulent viscosity, respectively
ν = laminar kinematic viscosity
ρ = density
$\sigma_k, \sigma_\epsilon$ = Prandtl numbers for k and ϵ, respectively
τ_w = shear stress at the wall
Ω = angular rotation speed

Subscripts

b = bulk
f = at the film temperature
i = at the inlet
ref = reference
w = at the wall

by Ito and Nanbu [2], and heat transfer by Mori et al. [3]. Both the wall friction and heat transfer are enhanced by rotation with the increase, relative to the stationary duct, being greater for laminar flow as compared to turbulent flow. Rotation is also found to enhance stability and delay the laminar–turbulent transition.

Wagner and Velkoff [4] made detailed measurements of radial and cross-stream velocity for developing turbulent flow in rectangular ducts of aspect ratio = 0.37. The presence of the two secondary vortices was confirmed.

Moore [5] studied developing turbulent flow in a 15-deg radial rectangular diffuser with a square inlet. The results indicate the formation of a large wake on the trailing side of the passage at high flow rates, and an eddy on the leading side at low flow rates.

Metzger and Stan [6] measured heat transfer for laminar developing flow in a circular duct. The results, obtained in the absence of entry swirl, showed that only a small rotational effect on heat transfer can be expected for relatively short cooling passages.

Morris and Ayhan [7] made heat transfer measurements for developing turbulent flow in a heated duct of circular cross section. It was demonstrated that Coriolis-induced heat transfer improvement may be nullified and even reversed by centrifugal buoyancy. This result is explained by noting that buoyancy increases the radial velocity of the cooler fluid in the core while reducing the radial velocity of the warmer fluid near the wall.

Morris et al. [8] measured local heat transfer on the leading and trailing surfaces of a heated square duct for developing turbulent flow. It was found that the Coriolis-induced secondary flow enhanced local heat transfer at the trailing face, while, on the leading face, little effect of rotation was detected over the range of experiments covered. Quite unlike the case of a circular duct [7], centrifugal buoyancy was found to increase the heat transfer at the trailing and the leading walls. This result points to the important effect of geometry on the interaction between various physical mechanisms.

Guidez [9] investigated turbulent developing flow in a rectangular duct of aspect ratio 2. It was found that rotation enhances heat transfer from the trailing face and reduces it over the leading face.

Wagner et al. [10, 11] have made detailed heat transfer measurements for developing turbulent flow in square ducts. The test section is a serpentine passage consisting of four legs (two upflow and two downflow) and three connecting 180-deg bends. Experiments were conducted under isothermal wall conditions. The first study [10] was limited to heat transfer mesurements in the first upflow leg. It was found that rotation increases heat transfer over the trailing face while, on the leading face, rotation was found to decrease the heat transfer near the inlet but increase it further downstream. In the second study [11], measurements were made in the first three legs (upflow, downflow, and upflow) and the connecting bends. It was found that the density ratio and rotation number cause large changes in heat transfer for radially outward flow and relatively small changes for radially inward flow.

1.4.2 Theoretical. With the the exception of Guidez [9], all the theoretical analyses listed below assume the fluid to be incompressible and hence neglect the centrifugal-buoyancy effects.

Ito and Nanbu [2] considered laminar fully developed flow in a circular pipe. By dividing the flow into two regions, an inviscid core and a boundary layer close to the wall, and by performing an analysis of the integral type, they obtained expressions for the flow resistance. The analysis was confined to high rotational speeds. Satisfactory agreement with the experimental data [2] was obtained. A similar analytical procedure was employed to analyze fully developed flow and heat transfer in circular ducts under laminar [12] and turbulent [3] conditions. Again, the analysis is valid only for high rotational speeds and resonable agreement with the the data [3] is obtained.

Moore [13] presented a simplified analysis, based on the strip integral method, to support his experiments on flow through a radial diffuser [5]. The model predicted the observed thickening of the trailing side boundary layer to form a large wake.

Skiadaressis and Spalding [14] numerically predicted laminar and turbulent developing flow in a circular duct. A three-dimensional parabolic procedure was employed, and turbulence was modeled using the two-equation (k–ϵ) model. The fully developed friction factor and Nusselt numbers agreed well with the data of Ito and Nanbu [2], Mori et al. [3], and Mori and Nakayama [12] for laminar flow; however, for turbulent flow, the predictions underestimated the heat transfer.

Majumdar and Spalding [15] employed a partially parabolic procedure to predict developing turbulent flow numerically in a rectangular duct. The case simulated corresponds to the experiments of Wagner and Velkoff [4]. Again, the k–ϵ model of turbulence was employed. The predicted secondary flows agree well with the experimental data.

Howard et al. [16] employed a parabolic procedure to predict developing turbulent flow numerically in rectangular ducts of varying aspect ratio. The k–ϵ model for turbulent was employed, but with three alternative modifications to account for the influence of Coriolis force on the turbulent kinetic energy. These modifications to the turbulence model reflected the observed effects that turbulence is suppressed near the leading face and enhanced near the trailing face. The modified turbulence model gave a better agreement with the data of Johnston [17] for high aspect ratio (>5) ducts where the flow is essentially two dimensional and the cross-stream flows are weak. However, for low aspect ratio ducts, the prediction showed little sensitivity to the Coriolis turbulence modification, which suggests that the secondary cross-stream flows are primarily responsible for the modification of wall shear and heat transfer in this case.

In support of his experiments, Guidez [9] made numerical predictions of turbulent flow in a rectangular duct using the mixing length model. However, only preliminary results were presented [9], which confirmed the expected presence of secondary crossflows. Further, although the density was assumed to be varying, the very limited results presented in [9] do not explain the separate roles of Coriolis and buoyancy effects.

Hwang and Jen [18] have numerically predicted fully developed laminar flow and heat transfer in rectangular ducts of varying aspect ratio (5 to 0.2). For low rotation, the Coriolis force produces two symmetric vortices in the cross-stream plane; however, at high rotation, four vortex solutions result. A comparison with experimental results was rendered difficult due to lack of fully developed data for rectangular ducts.

Iacovides and Launder [19] numerically predicted fully developed turbulent flow and heat transfer in square and rectangular (aspect ratio = 2) ducts. Except in the immediate vicinity of the wall, the standard k–ϵ model of turbulence was used; across the near-wall sublayer, the damping of turbulence is modeled by means of a low-Reynolds-number, one-equation model. As in [18], two-vortex solutions were noted at low rotational speeds, while four cross-stream vortices were found at higher rotation. Again, due to the presence of entrance and centrifugal-buoyancy effects in the available experimental data, a theory–data match was difficult.

1.5 The Present Contribution. The present study may be grouped with the numerical investigations of turbulent developing flow reported in [14–16]. The notable features of the

present investigation, which have not been considered in any previous analysis, are:

(*a*) Detailed examination of the centrifugal-buoyancy effects.

(*b*) Examination of the sensitivity of predictions to inlet conditions; in particular, the effect of rotation in the incoming stream.

(*c*) Examination of the effect of exit boundary conditions, i.e., a comparison between a single passage and a two-leg passage.

2 Analysis

2.1 Geometry and Thermophysical Data. To facilitate comparison, the geometric and thermophysical parameters are chosen similar to those used in [10].

Refer to Fig. 1. The duct width D, the root radius R_r, and the tip radius R_t, are taken equal to 1.27 cm, 53.21 cm, and 71.37 cm, respectively.

The working fluid is air, and the system pressure equals 10 atm.

Laminar viscosity, μ, is obtained using the Sutherland equation:

$$\mu = \mu_{\text{ref}}(T/T_{\text{ref}})^{0.636} \tag{1}$$

where T is the absolute temperature,

$$\mu_{\text{ref}} = 3.018 \times 10^{-7} \text{kg/(cm-s)}$$

and

$$T_{\text{ref}} = 600 \text{ K}$$

The density, ρ, is obtained using the ideal gas law, i.e.,

$$\rho = p/(RT) \tag{2}$$

We solve for the static enthalpy, h, and use the following $h \sim T$ relation:

$$T = A + Bh + Ch^2 \tag{3}$$

where

$$A = -4.4876 \text{ K}$$

$$B = 1.0403 \times 10^{-7} \text{K-s}^2/\text{cm}^2$$

$$C = -0.7478 \times 10^{-18} \text{K-s}^4/\text{cm}^4$$

From Eq. (3) the specific heat is obtained as:

$$c_p = 1/(B + 2Ch) \tag{4}$$

The laminar Prandtl number, Pr, is taken = 0.72.

2.2 The Governing Equations. The coordinate system shown in Fig. 1 rotates with the duct. In such a system, the flow is steady, but account must be taken of the Coriolis and centrifugal forces, which appear as additional source terms in the equations of motion. Further, as is common practice, we solve the time-averaged form of the turbulent flow equations in conjunction with a suitable turbulence model [20, 21]. The equations governing the mean flow variables are:

Continuity:

$$\text{div}(\rho \mathbf{u}) = 0 \tag{5}$$

x-Momentum:

$$\text{div}(\rho \mathbf{u} u) = -\frac{\partial p}{\partial x} - 2\,\rho\Omega w + \rho\Omega^2 x + \text{div}[(\mu + \mu_t)\text{grad}(u)] + S^u \tag{6}$$

y-Momentum:

$$\text{div}(\rho \mathbf{u} v) = -\frac{\partial p}{\partial y} + \text{div}[(\mu + \mu_t)\text{grad}(v)] + S^v \tag{7}$$

z-Momentum:

$$\text{div}(\rho \mathbf{u} w) = -\frac{\partial p}{\partial z} + 2\rho\Omega u + \rho\Omega^2 z + \text{div}[(\mu + \mu_t)\text{grad}(w)] + S^w \tag{8}$$

Enthalpy:

$$\text{div}(\rho \mathbf{u} h) = \text{div}\left[\left(\frac{\mu}{\text{Pr}} + \frac{\mu_t}{\text{Pr}_t}\right)\text{grad}(h)\right] + S^h \tag{9}$$

In the above, the symbols (div) and (grad) designate the divergence and the gradient operators. The variable μ_t represents the turbulent viscosity, and Pr_t designates the turbulent Prandtl number. The second and third terms on the right hand of Eqs. (6) and (8) arise due to the Coriolis and centrifugal forces, respectively. The terms S^u, S^v, S^w, and S^h include terms that have not been explicitly spelled out. Thus, S^h includes terms arising due to viscous dissipation and compression work, etc., while S^u, S^v, and S^w may include additional terms due to nonuniform density and viscosity. In addition, for boundary-fitted grids, where u, v, and w may represent contra- or co-variant velocity components, S^u, S^v, and S^w may include the terms arising due to grid curvature.

Even though the fluid properties (density, viscosity, etc.) are assumed to be varying, no additional turbulent correlations due to these property variations are taken into account in the mean flow equations. Thus, the property variations are acknowledged only in the mean sense.

2.3 Turbulence Model. To close the above system of equations, expressions need to be provided for the turbulence viscosity μ_t and the turbulence Prandtl number Pr_t.

The turbulent Prandtl number, Pr_t, is taken = 0.86.

The turbulent viscosity is obtained using the two-equation (k–ϵ) model [20, 21] where k and ϵ represent the turbulent kinetic energy respectively. μ_t is given as:

$$\mu_t = \rho C_\mu k^2/\epsilon \tag{10}$$

k and ϵ are obtained from the following transport equations.

$$\text{div}(\rho \mathbf{u} k) = \text{div}[(\mu_t/\sigma_k)\text{grad}(k)] + G - \rho\epsilon \tag{11}$$

$$\text{div}(\rho \mathbf{u} \epsilon) = \text{div}[(\mu_t/\sigma_\epsilon)\text{grad}(\epsilon)] + C_1\epsilon G/k - C_2\rho\epsilon^2/k \tag{12}$$

where

$$G = \mu_t \left\{ 2\left[\left(\frac{\partial u}{\partial x}\right)^2 + \left(\frac{\partial v}{\partial y}\right)^2 + \left(\frac{\partial w}{\partial z}\right)^2\right] + \left(\frac{\partial u}{\partial y} + \frac{\partial v}{\partial x}\right)^2 + \left[\frac{\partial u}{\partial z} + \frac{\partial w}{\partial x}\right]^2 + \left[\frac{\partial w}{\partial y} + \frac{\partial v}{\partial z}\right]^2 \right\} \tag{13}$$

The various constants above have the following values:

$$\sigma_k = 1.0; \quad \sigma_\epsilon = 1.314; \quad C_\mu = 0.09; \quad C_1 = 1.44; \quad C_2 = 1.92.$$

2.4 Modifications to the Turbulence Model. The turbulence model described above may be called the standard k–ϵ model. As already mentioned, rotation can affect the fundamental aspects (stability, etc.) of a turbulent flow. To account for these effects, some proposals have been made to modify the k–ϵ equations [16] and/or the constants in the wall functions [22] to be discussed in the next section.

In the present study, we do not make any modifications to the turbulence model and/or the wall function constants. Instead we simply use the standard model given above. The reasons are as follows:

(a) Howard et al. [16] found that whereas the Coriolis-induced modifications to the k equation improved predictions for high aspect ratio (>5) ducts, little effect of these modifications was noted for ducts of low aspect ratios. Thus, for the present case, with aspect ratio = 1, it is the large-scale secondary flow induced by the Coriolis and buoyancy forces that may be primarily responsible for altering the friction and the heat transfer at the walls.

(b) As the results will show, for a problem involving heat transfer, the centrifugal buoyancy effects are very important. Since buoyancy can also influence the basic structure of turbulent flow, a model that just accounts for the Coriolis effects on turbulent is clearly incomplete.

The present study may thus be regarded as a forerunner to future efforts focused on turbulence model enhancements. Our intent here is to see how well the standard k–ϵ model can do. The important effect of the inlet and the exit boundary conditions demonstrated in this study, as well as the uncertainty in the data, should be borne in mind in future model-development studies.

2.5 Near-Wall Treatment: Wall Functions. The k–ϵ equations provided above apply in fully turbulent regions away from the solid boundaries. Close to the walls, either (*i*) the k–ϵ equations must be modified to permit integration up to the wall or, (*ii*) the wall function treatment must be adopted where the boundary layer effects close to the wall are accounted for via the use of the logarithmic velocity profile etc. [21]. Since the present analysis is three dimensional and fully elliptic, the integration-to-the-wall approach is computationally prohibitive. Hence the wall function treatment is used here.

We use the generalized wall function treatment of Rosten and Worrell [23], details of which are provided in the appendix A. The following features of the method may be noted:

(*a*) The friction velocity, $u_\tau (= V\sqrt{s})$, is replaced by a velocity scale calculated from the local turbulent kinetic energy at the near wall point. Here s designates the friction coefficient, and V the magnitude of the tangential velocity at the near wall point.

(*b*) The kinetic energy at the near wall point is deduced from the regular transport equation with zero normal gradient condition at the wall. The generation term for the wall cells is calculated by an analytical integration based on the wall-shear stress.

(*c*) The dissipation rate for the near wall cells is fixed to an average obtained from analytical integration.

(*d*) The wall heat transfer is expressed using Jayatillika's [24] Stanton number correlation, which accounts for the thermal resistance of the viscous sublayer.

As already mentioned, the duct walls are taken to be isothermal. The wall temperature, T_w, was varied from 303 to 389 K for the different cases.

2.6 Inlet Conditions. Since the duct is short, and fully developed flow is not attained, the inlet conditions have strong influence on the predicted flow field. Therefore, to examine the effect of the inlet conditions, the following two limiting cases are examined:

(*a*) The first set of inlet conditions is intended to approximate fully developed flow in a nonrotating duct. Thus, the cross-stream velocities (u and v) are taken to be zero, and the radial velocity, w, is assigned a 1/7th profile in both the cross-stream directions, i.e.:

$$w = w_c(1 - |x|/(D/2))^{1/7}(1 - |y|/(D/2))^{1/7} \tag{14}$$

where w_c is the peak centerline velocity.

A uniform turbulent kinetic energy, based on 4 percent intensity [10], was prescribed at the inlet. Thus:

$$k = 3/2(0.04\ w_c)^2 \tag{15}$$

The dissipation rate at the inlet was also assumed uniform and set to:

$$\epsilon = C_\mu^{3/4}\frac{k^{3/2}}{l} \tag{16}$$

where the mixing length is taken as

$$l = 0.1(D/2) \tag{17}$$

(*b*) The second set of inlet conditions is intended to correspond to fully developed flow in a rotating duct; thus, the incoming fluid is assumed to contain the Coriolis-induced secondary flow. To simulate this inlet condition, the computational domain was extended to include a long ($\sim 30\,D$) unheated length before entering the main region of interest.

Most of the computations were made with the inlet condition (*a*). The condition (*b*) was used only for a few cases for comparison purposes.

For both the conditions listed above, the temperature at the inlet was taken uniform with a value $T = T_i = 300$ K.

2.7 Exit Conditions. The zero gradient ($d/dz = 0$), i.e., the outflow condition, was applied at the exit. Physically this implies that (*i*) diffusion is neglected at the exit, and (*ii*) the near-exit-cell values of all variables are convected in or out at the exit boundary. Use of such a treatment decouples the computational domain from the outside.

When the buoyancy effects are small, the flow leaves the computational domain everywhere at the exit boundary and the conditions are essentially parabolic there; hence, for such cases, the use of the outflow treatment is reasonable.

When buoyancy effects are significant, however, small reverse radial flows may occur near the leading face implying some entrainment of the fluid at the exit boundary. Under these conditions, the use of the zero gradient treatment at the exit is somewhat discomforting. To explore this issue, one case was rerun by extending the computational domain to include a 180-deg bend and a downflow leg so that the exit was far removed from the region of interest. The result of this comparison (see Section 3.7) indicated that the flowfield in the first upflow leg was not significantly altered by the presence of the bend and the second pass. Thus, the use of the zero gradient exit boundary treatment to limit the calculations to the first uppass appears reasonable.

2.8 Dimensionless Parameters. Since the density and viscosity are varying, the values corresponding to the inlet temperature are used for defining the dimensionless parameters. The primary dimensionless parameters are:

Duct height:	L/D
Mean radius:	$\overline{R}/D = 0.5(R_t + R_r)/D$
Prandtl number:	Pr
Reynolds number:	$\dot{m}/(\mu_i D) = \rho_i \overline{w}_i D/\mu_i$
Rotation number:	$\Omega D/\overline{w}_i$
Temperature ratio:	T_w/T_i

In the above, $\dot{m}$, $\overline{w}_i$, ρ_i, and μ_i, represent the total mass flow through the duct, the average radial velocity at the inlet, the density at the inlet, and the viscosity at the inlet, respectively. Ω designates the rotational speed.

In lieu of the temperature ratio, use is often made of the density ratio defined as:

$$\text{Density ratio: } (\Delta\rho/\rho)_i = (1 - \rho_i/\rho_w) = (1 - T_i/T_w)$$

In all of the present computations, the duct length (L/D) and the mean radius ($\overline{R}/D$) were kept fixed at 14.3 and 49, respectively, and the Prandtl number was kept fixed = 0.72 (see section 2.1). The Reynolds number, the Rotation number, and the density ratio were varied by varying $\dot{m}$, Ω, and T_w, respectively.

Note that other parameters in common use (Grashof number, Rayleigh number, buoyancy number, Grashof/Reynolds, etc.) can all be related to the primary variables listed above.

2.9 Numerical Details. The PHOENICS code [25], which embodies the control-volume-based finite-difference method described by Patankar [26], was employed in the present study.

Due to symmetry in the y direction, only half of the duct is considered. The computational domain was discretized by 10,000 cells arranged on a 20 × 10 × 50 grid along the x–y–z coordinates. The grid is nonuniform, with finer cells close to the duct inlet and the walls. The y^+ values were printed out as a part of the solution, and it was ensured that the near-wall cells had a $y^+ \sim 20$–50 so that the wall function treatment is applicable. Grid refinement studies, using up to 40,000 cells, ensured the 10,000 cell grid to be adequate. For the case involving two legs plus the 180 deg bend, the entire duct cross section had to be considered.

3 Results

3.1 Comments. The following comments apply to the results to be presented:

(*a*) Unless stated otherwise, the inlet conditions correspond to fully developed flow in a nonrotating duct (see Section 2.6; condition *a*).

(*b*) Heat transfer results are presented via the variation of the Nusselt number with radial distance. The Nusselt number is defined as follows:

Let q_t be the total heat flux at a face (leading, trailing, or side) at some radial location z. Then, the average heat flux, $\bar{q}$, is given by:

$$\bar{q} = q_t / D \tag{18}$$

Let h_b be the bulk enthalpy at the radial location z, defined as:

$$h_b = \frac{\iint \rho w h dx dy}{\dot{m}} \tag{19}$$

The bulk temperature T_b at z is obtained from h_b, using Eq. (3); thus:

$$T_b = A + Bh_b + Ch_b^2 \tag{20}$$

The local heat transfer coefficient, γ, for the face at the radial location z, is then taken as:

$$\gamma = \bar{q} / (T_w - T_b) \tag{21}$$

and the local Nusselt number, Nu, is defined as:

$$\mathrm{Nu} = \gamma D / \lambda_f \tag{22}$$

where λ_f is the thermal conductivity. The subscript f on λ indicates value at the local film temperature, T_f, which is defined as:

$$T_f = (T_w + T_b)/2 \tag{23}$$

Thus:

$$\lambda_f = \mu_f c_{pf} / \mathrm{Pr} \tag{24}$$

where μ_f and c_{pf} are the viscosity and the specific heat corresponding to the film temperature T_f. μ_f is obtained from Eq. (1); c_{pf} is obtained from Eq. (4) with $h = h_f$, where h_f is the enthalpy corresponding to the temperature T_f (Eq. (3) inverted).

(*c*) As is customary [10], instead of the Nusselt number, we present the Nusselt number ratio:

$$\mathrm{Nu}/\mathrm{Nu}_\infty$$

where Nu_∞ corresponds to fully developed flow in a nonrotating duct. As in [10], Nu_∞ is obtained using the textbook correlation [27] as:

$$\mathrm{Nu}_\infty = 0.022\ \mathrm{Re}_f^{0.8} \mathrm{Pr}^{0.6} \tag{25}$$

The Reynolds number Re_f uses the properties at the film temperature. Thus:

$$\mathrm{Re}_f = \dot{m} / (\mu_f D) \tag{26}$$

3.2 Flow Field. Illustrative flow fields, for a case corresponding to Re = 25,000 and Ro = 0.48, are shown in Figs. 3(*a*)–3(*c*). In each figure, the plot on the left corresponds to a low density ratio of 0.01, while the plot on the right corresponds to a higher density ratio of 0.13. For the low density ratio case, the buoyancy effects are small, and only the Coriolis effects are significant; for the higher density ratio case, however, both the buoyancy and the Coriolis effects are significant. A comparison of the low and high density ratio cases allows the influence of buoyancy to be inferred.

Figures 3(*a*)–3(*c*) display the projection of the velocity vectors (arrows), and the contours of the radial velocity (solid and dashed curves), on the cross-stream planes at increasing distance from the inlet. Due to symmetry in the y direction, only half of the duct cross section is shown. The solid curves correspond to positive values of w (radial outflow) while the dashed curves correspond to negative w (radial inflow). The velocity magnitudes shown in Figs. 3(*a*–3(*c*) may be put into perspective by comparing with the average velocity at the inlet, which, for this case, is = 324.8 cm/s.

The following features of the flow field may be noted from Figs. 3(*a*)–3(*c*).

(*a*) Coriolis force induces a secondary cross-stream flow, which is directed from the leading to the trailing face near the center of the duct and vice versa (trailing to the leading face) near the side wall. The sense of this motion may be understood from the Coriolis force term in the x-momentum equation (second term on right-hand side of Eq. (6)); as can be noted, this force is directed in the negative x direction and, being proportional to w, its magnitude is greater near the center as compared to the side walls.

(*b*) Near the duct inlet (Fig. 3(*a*)), the peak radial velocity occurs near the center of the duct. However, the Coriolis induced secondary flow transports the higher momentum fluid toward the trailing face, so that the location of the peak radial velocity is shifted toward the trailing face further downstream (Fig. 3(*b*)). At a large radial distance (Fig. 3(*c*)), peak radial velocity occurs near the trailing face–side wall corner.

(*c*) The Coriolis-induced secondary flow serves to transport cooler (heavier) fluid from the core to the trailing face. In comparison, the fluid near the leading face is warmer (lighter) since it got there after exchanging heat with the trailing and the side walls. As a result of this density variation, the centrifugal force is greater on the fluid near the trailing face and smaller on the fluid near the leading face; consequently, due to the imbalance of the force, the radial velocity of the fluid is increased near the trailing face and decreased near the leading wall. For small density ratios and/or small rotational speeds, this centrifugal-buoyancy effect is small. However, for high density ratio and/or high rotation, the centrifugal-buoyancy effect can be significant. Indeed, for situations involving large buoyancy, reverse radial flow can occur near the leading face. In Figs. 3(*a*)–3(*c*), buoyancy effects are small for the low-density ($\Delta\rho/\rho$ = 0.01) case. However, the buoyancy effects are very significant for the high density ratio case ($\Delta\rho/\rho$ = 0.13). Thus, higher radial velocity near the trailing face, and even reverse flow near the leading face, are found for the high density ratio case. Note that no reverse flow is found for the low-density ratio case.

Another perspective of the reverse radial flow near the leading face for the higher-density ratio case is provided by Fig. 4, which shows velocity projection on a plane parallel to, and just above, the leading face. As can be noted, the reverse flow penetrates quite deeply into the duct.

Reverse radial flows of the above kind were found only for a few cases. In most cases, involving a lower density ratio and/or lower rotation, the reverse radial flow was either absent or confined to a very small region near the leading wall-side wall corner close to the exit.

3.3 Basic Heat Transfer Variation

3.3.1 Trailing Face. The variation of the Nusselt number

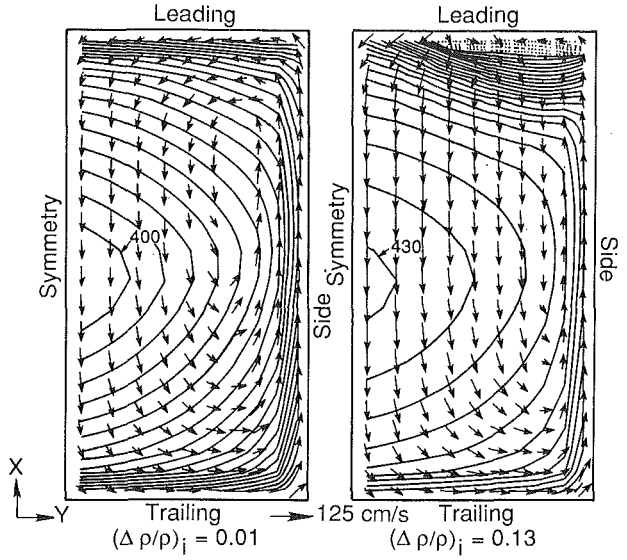

Fig. 3(*a*) Flow field at cross-stream plane at z = 54.2 cm, Re = 25,000 Ro = 0.48

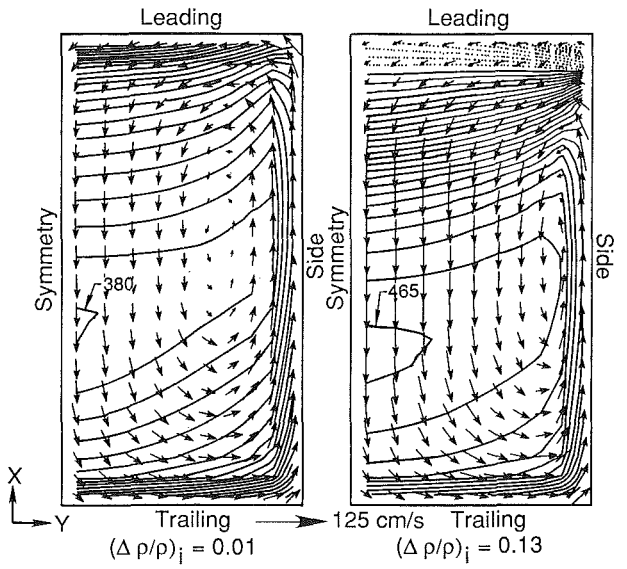

Fig. 3(*b*) Flow field at cross stream plane at z = 55.5 cm, Re = 25,000 Ro = 0.48

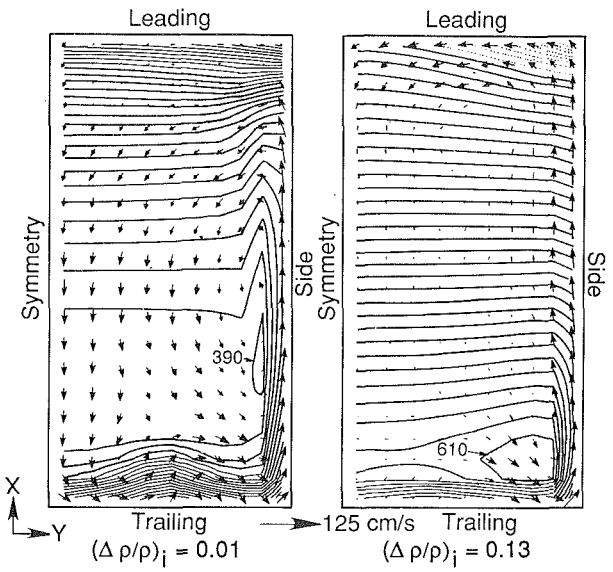

Fig. 3(*c*) Flow field at cross-stream plane at z = 66.7 cm, Re = 25,000 Ro = 0.48

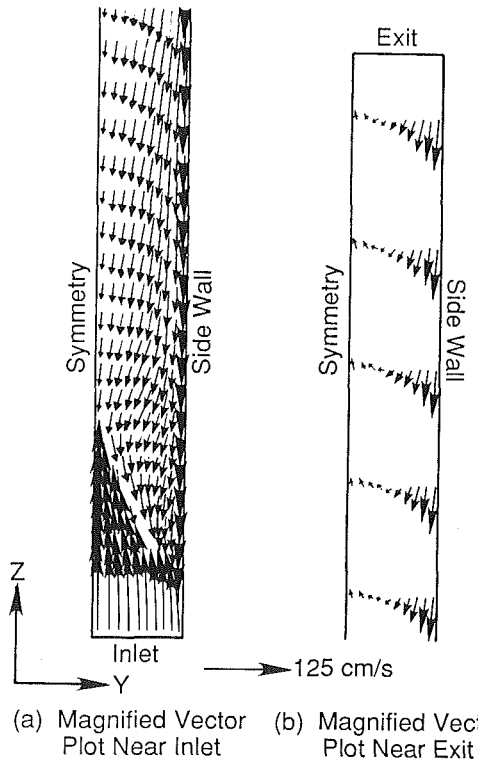

Fig. 4 Velocity field; Re = 25,000 Ro = 0.48, $(\Delta\rho/\rho)_i$ = 0.13 (the computational plane just above the leading surface)

over the trailing face is shown in Fig. 5(*a*). The parameters for this case are: Re = 25,000 and Ro = 0.24. A low density ratio case ($\Delta\rho/\rho$ = 0.01) is compared with a higher density ratio case ($\Delta\rho/\rho$ = 0.13). Again, for the lower density ratio, the buoyancy effects are small and only the Coriolis effects are active; however, for the higher density ratio, both the buoyancy and Coriolis effects are significant. Results for a stationary duct (no-rotation) are also presented.

Consider first the no-rotation case. The Nusselt number is high near the inlet due to thinner thermal boundary layers there; proceeding farther downstream, the Nusselt number decreases and asymptotically attains the fully developed value. This behavior is typical of entrance region flow in ducts. Note the the predicted fully developed value is slightly less than that

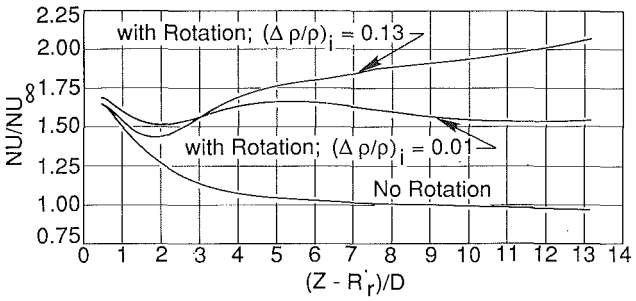

Fig. 5(*a*) Heat transfer over the trailing face: Ro = 0.24, Re = 25,000; inlet condition of fully developed flow in a nonrotating duct

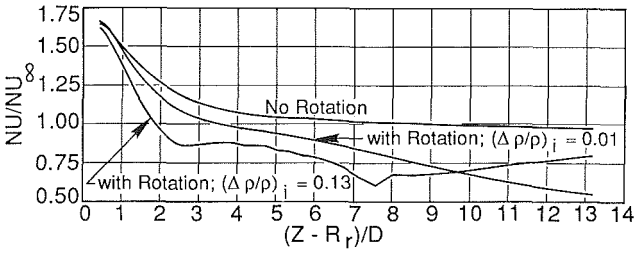

Fig. 5(*b*) Heat transfer over the leading face: Ro = 0.24, Re = 25,000; inlet condition of fully developed flow in a nonrotating duct

given by the correlations; this should not be alarming since the small difference could be due to the uncertainty of the empirical correlation, the k–ϵ model, the grid, and/or the property variation effects.

Consider next the effect of rotation on the heat transfer. Since it takes some distance for the Coriolis and centrifugal effects to be felt, the Nusselt numbers for the rotating case are close to those for the no-rotation case near the duct inlet. Farther downstream, however, rotation leads to an enhancement of the heat transfer at the trailing face. This increase is attributed to the following three reasons:

(*a*) The Coriolis-induced secondary flow transports cooler fluid from the core to the trailing face, which increases the temperature gradient at the wall.

(*b*) The secondary flow also transports the higher momentum fluid from the core to the trailing face, whereby the radial velocity, and hence the convective effects, are enhanced.

(*c*) The increase in the radial velocity near the trailing face leads to higher velocity gradients and, thereby, higher level of turbulent kinetic energy; thus, the conductance of the turbulent boundary layer (computed via the wall functions) is increased.

As already discussed, centrifugal buoyancy increases the radial velocity for the cooler fluid near the trailing face. Hence, for reasons (*b*) and (*c*) mentioned above, the Nusselt numbers are greater for the high density ratio case as compared to the low density ratio case.

Note that for the low density ratio case, the Nusselt number tapers off to a value corresponding to fully developed flow in a rotating duct. In contrast, for the high density ratio case, the Nusselt number continues to increase throughout the duct. This increase, it should be noted though, is not indefinite; if the duct were very long, the temperature variations (and hence the buoyancy effects) would eventually decrease and the Nusselt number would reduce to the fully developed value corresponding to the low density ratio (no buoyancy) case.

3.3.2 Leading Face. The variation of heat transfer at the leading face is shown in Fig. 5(*b*).

For the stationary duct, there is no distinction between a leading and a trailing face; hence, the Nusselt number shown are same as in Fig. 5(*a*) and no new discussion is warranted.

Rotation, as may be noted, leads to a decrease in the heat

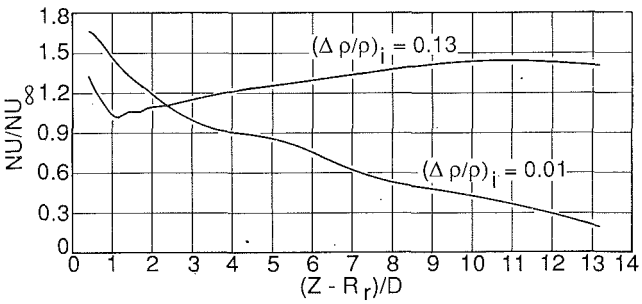

Fig. 6 Heat transfer at the leading face: Ro = 0.48, Re = 25,000; inlet condition of fully developed flow in a nonrotating duct

transfer all over the leading face for the low density ratio case. For the higher density ratio, the heat transfer decreases initially, but increases farther downstream.

The decrease in heat transfer at the leading face due to rotation is explained by the reverse of the reasons listed earlier while discussing the increase in the heat transfer at the trailing face. Thus, the heat transfer decrease occurs due to the following reasons:

(*a*) Due to the Coriolis-induced secondary flow, the fluid exchanges heat with the trailing and side walls before reaching the leading face. Thus, the fluid over the leading face is warmer and, hence, the temperature gradient is lower.

(*b*) For the same reason, the Coriolis-induced flow leads to a slower moving fluid (low radial velocity) over the leading face; thus convection is weaker.

(*c*) Due to reduced radial velocity, the velocity gradients, turbulent kinetic energy, and hence, conductance of the turbulent boundary layer, is also reduced at the leading face.

As already discussed, buoyancy reduces the radial velocity of the warmer fluid near the leading face. Hence, for reasons (*b*) and (*c*), the decrease in heat transfer is greater for the high density ratio case.

Consider the high density ratio case. An interesting feature of this case is the subsequent increase of the heat transfer at the leading face after the initial decrease. This behavior conforms with experimental data (included in the next section), and is believed to be caused, among other factors, by the buoyancy-induced reverse radial flow over the leading face, which leads to increased levels of mixing and turbulence. To examine this matter further, Fig. 6 is included, which shows the variation of heat transfer at the leading face for a higher rotation number of 0.48. Comparing Figs. 6 and 5(*b*), it can be noted that due to a stronger and more deeply penetrating reverse radial flow, the increase in the heat transfer with the radial distance starts sooner (lower z) for the higher rotation number case. This feature also conforms with the experimental data included in the next section. Note that even in Fig. 6, there is no increase in heat transfer for the low-buoyancy case ($\Delta\rho/\rho = 0.01$) for which the buoyancy effects are small and no reverse radial flows are found (recall Figs. 3(*a*)–3(*c*)).

3.4 Comparison With Data—Role of Buoyancy and Effect of Inlet Conditions. Figures 7(*a*) and 7(*b*) are similar to Figs. 5(*a*) and 5(*b*), respectively, except that they contain more information. Thus, (*i*) the experimental data of Wagner et al. [10] are included, and (*ii*) results are presented of the case where the inlet conditions correspond to fully developed flow in a rotating duct (Section 2.6; conditions *b*).

3.4.1 Trailing Face. Consider Fig. 7(*a*), which pertains to heat transfer variation over the trailing face.

As can be seen, the variation of the Nusselt number with the radial distance is correctly predicted. Thus, in agreement with the experimental data, the Nusselt number initially de-

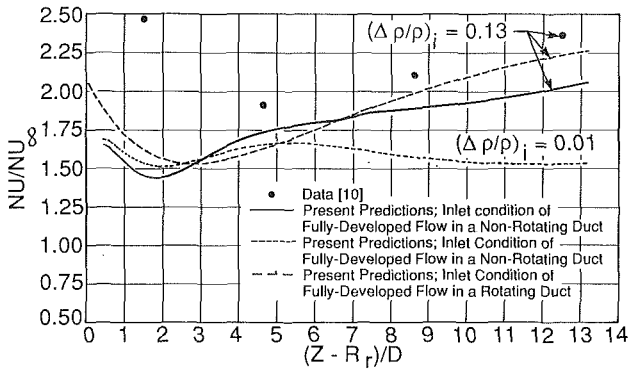

Fig. 7(*a*) Heat transfer at the trailing face: Ro = 0.24, Re = 25,000

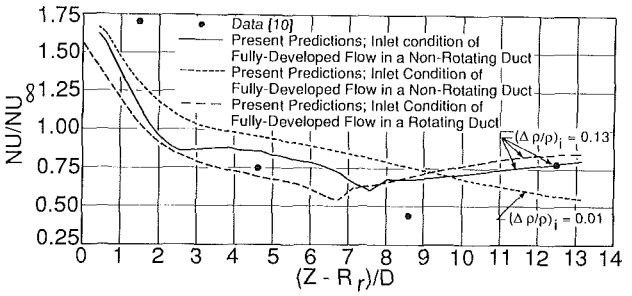

Fig. 7(*b*) Heat transfer at the leading face: Ro = 0.24, Re = 25,000

creases with the radial distance, followed by a continuous rise throughout the duct.

Except very close to the inlet, the quantitative agreement between the data and the predictions is also satisfactory. Compared with the data, the predicted Nusselt numbers are somewhat lower, with the underprediction, over most of the face, being ~ 10 percent.

It may be noted that good agreement between the predictions and the data occurs only when the buoyancy effects are taken into account ($\Delta\rho/\rho = 0.13$). If, however, the buoyancy effects are assumed small ($\Delta\rho/\rho = 0.01$), the predictions disagree markedly with the data both quantitatively and qualitatively. This observation clearly emphasizes the important role of buoyancy in the present problem.

It may also be noted that the predictions corresponding to the inlet condition of fully developed flow in a rotating duct agree better with the data as compared to inlet condition corresponding to flow in a nonrotating duct. This is expected; it is definite that the inlet conditions in the experiments of [10] were influenced by rotation. It may also be observed that the inlet conditions have an influence throughout the duct, which highlights the developing nature of the flow.

In the presence of rotation, the true inlet conditions for the test data of [10] are not known. However, appreciating the complexity of the experiments, it may be said that the inlet conditions in [10] could have some features that may explain the large discrepancy between the predictions and the data very close to the inlet.

The general underprediction of the Nusselt number could be attributed to a number of reasons, with the uncertainty in inlet conditions noted above, being one candidate. The other factor could be the effect of rotation on turbulence (recall Section 2.4) that has not been accounted for here; it is, however, comforting to note that had account been taken of this phenomenon, the predicted Nusselt numbers would only have been higher, and hence, in better agreement with data.

3.4.2 Leading Face. Heat transfer at the leading face is shown in Fig. 7(*b*).

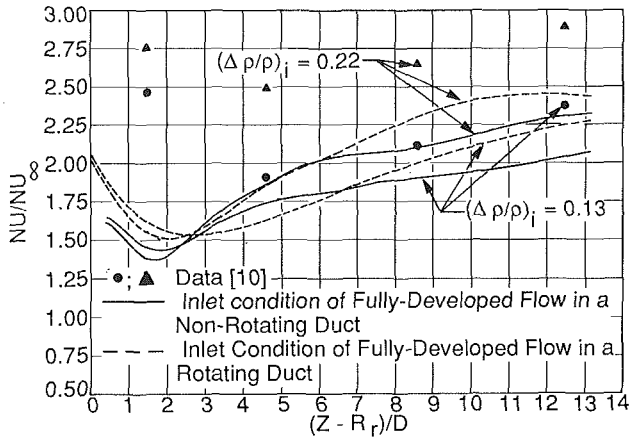

Fig. 8(*a*) Heat transfer at the trailing face: Ro = 0.24, Re = 25,000

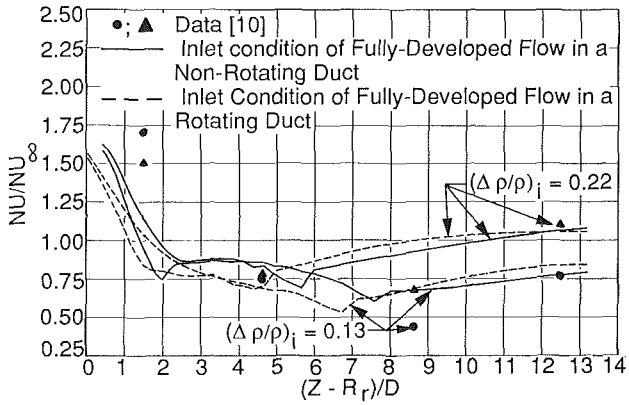

Fig. 8(*b*) Heat transfer at the leading face: Ro = 0.24, Re = 25,000

As may be noted, the variation of Nusselt number with the radial distance, vis-à-vis the initial decrease followed by an increase, is correctly predicted. Again, except very close to the inlet, the quantitative agreement with the data is also satisfactory; the predicted values are lower near the inlet and higher near the exit. Over most of the duct, the difference is in the 10 to 15 percent range. Compared to the trailing face (Fig. 7(*a*)) the heat transfer at the leading face is somewhat less sensitive to the inlet conditions; in general, however, the agreement with the data seems to be better with inlet conditions representing fully developed flow in a rotating duct.

The importance of buoyancy is again emphasized by comparing the results for the high and low buoyancy cases. For the low buoyancy situation (the $\Delta\rho/\rho = 0.01$ case) the Nusselt number continuously decreases throughout the duct, which is in clear disagreement with the data.

3.4.3 The Four Vortex Solutions. As already mentioned, the inlet condition of fully developed flow in a rotating duct was simulated by providing a long unheated length before entrance to the main test section. In such simulations, the Coriolis effects were found to produce four vortices in the cross-stream plane. This is in contrast with other cases (where the fully developed condition in a nonrotating duct was applied right at the inlet) in which only two symmetric vortices were found. It may thus be said here that four vortex solution reported by Iacovides and Launder [19] and Hwang and Jen [18] may not occur in short ducts where the flow is not fully developed.

3.5 Effect of Density Ratio. The role of buoyancy is highlighted again by Figs. 8(*a*) and 8(*b*), which show the effect of increasing the density ratio for a fixed rotation rate.

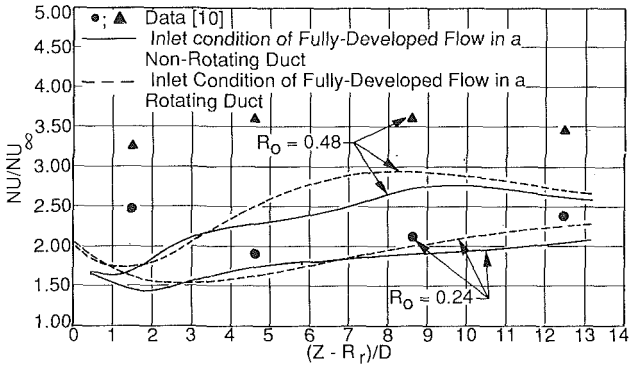

Fig. 9(*a*) Heat transfer at the trailing face: Re = 25,000, $(\Delta\rho/\rho)_i$ = 0.13

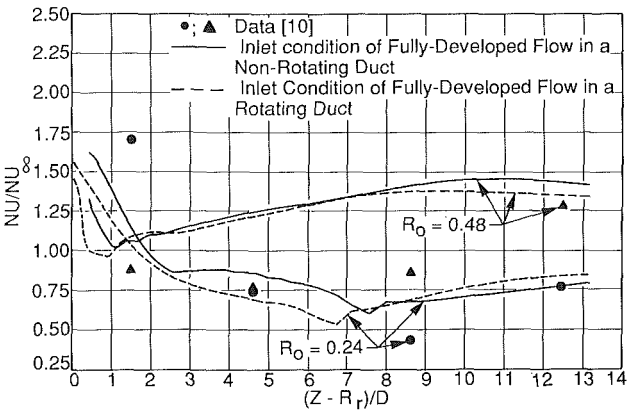

Fig. 9(*b*) Heat transfer at the leading face: Re = 25,000, $(\Delta\rho/\rho)_i$ = 0.13

At the trailing face, Fig. 8(*a*), the predicted Nusselt number increases with the density ratio, which is consistent with the data. The quantitative match with the data for higher density ratio is not as good as for lower density ratio case; the difference, except near the inlet, is now in the 20–25 percent range. Again, the agreement with the data is better for the inlet condition corresponding to fully developed flow in a rotating duct.

At the leading face, Fig. 8(*b*), an increase in the density ratio has the effect of decreasing the Nusselt number near the inlet but increasing if further downstream. This experimentally observed behavior is also displayed by the present predictions. Further, both the data and the predictions indicate that the increase of Nusselt number with the radial distance starts sooner (i.e., closer to the inlet) as the density ratio is increased.

3.6 Effect of Rotation Rate. Increasing the rotation rate increases both the Coriolis ($\sim\Omega$) and the centrifugal buoyancy effects ($\sim\Omega^2$). The effect of rotation on the heat transfer at the trailing and the leading faces is shown in Figs. 9(*a*) and 9(*b*), respectively. In agreement with the data, the predicted Nusselt number at the trailing face increase with rotation. At the leading face, the heat transfer is suppressed near the inlet but enhanced farther downstream; this behavior, observed in the data, is correctly predicted. The quantitative match with the data is not as good at the higher rotation rate (Ro = 0.48), with the discrepancy being in the 20–30 percent range. Again, the agreement with the data is better for the inlet conditions of fully developed flow in a rotating duct.

3.7 Effect of Exit Conditions. Due to the possibility of buoyancy-induced reverse radial flow near the leading face, a comparison was made of a single passage with a double pass duct shown in Fig. 10. The bend and the down-leg were taken to be insulated.

The region of reverse radial flow in a computational plane

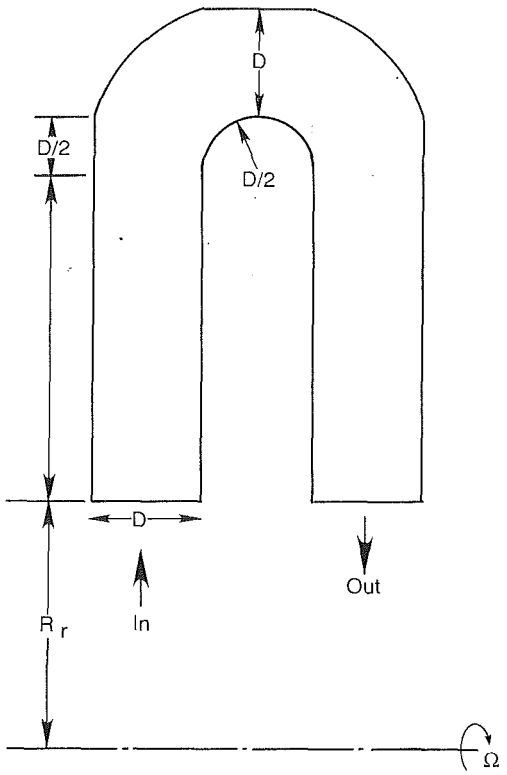

Fig. 10 A double-pass passage

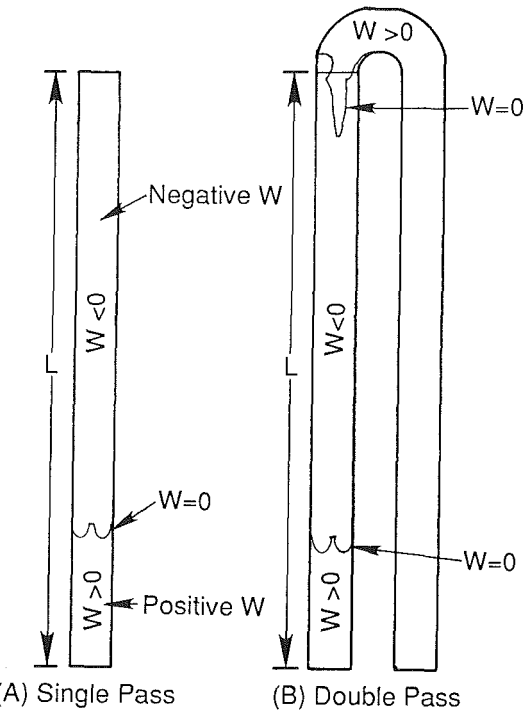

Fig. 11 Region of reverse flow in the computational plane just above the leading face: Re = 25,000 Ro = 0.48, $(\Delta\rho/\rho)_i$ = 0.13; a 10 × 10 × 40 grid is used for single-pass and a 10 × 10 × 100 grid for double-pass

just above the leading face is shown in Fig. 11. As can be noted, the presence of the bend and the downstream leg have only a small influence on the flow field in the first up-pass. The Nusselt number at the leading and the trailing face are compared in Fig. 12. Again, the predictions in the first up-pass are not altered much by the bend and the down-leg. Although not fully exhaustive, these results assure that the

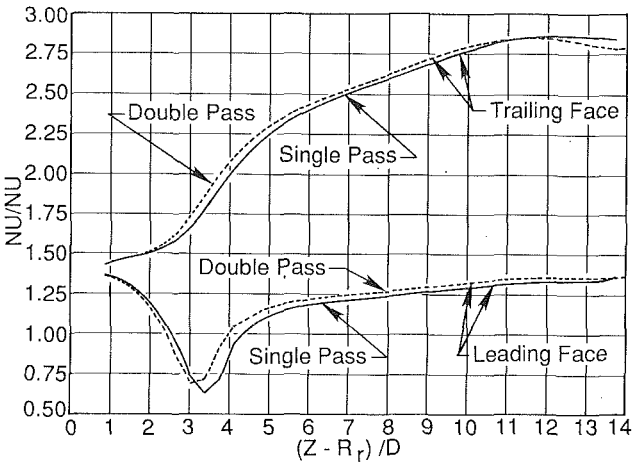

Fig. 12 Comparison of single and double pass: Re = 25,000 Ro = 0.48, $(\Delta\rho/\rho)_i$ = 0.13; a 10 × 10 × 40 grid is used for single-pass and a 10 × 10 × 100 grid for double-pass

findings of the single up-pass discussed so far will not be altered in a significant manner if the zero-gradient exit boundary condition is replaced by inclusion of multiple passes.

4 Conclusions

The present study has dealt with the numerical prediction of flow and heat transfer in a radially rotating square duct. The flow is turbulent and radially outward. The main findings of the present study may be summarized as follows:

(*a*) The Coriolis force induces a cross-stream flow, which is directed from the leading to the trailing face near the center of the duct, and vice versa near the side walls. Such a secondary flow transports cooler (and higher momentum) fluid from the center to the trailing face, and hence, serves to increase the heat transfer there; in contrast, the heat transfer at the leading face is decreased.

(*b*) Buoyancy increases the radial velocity of the cooler fluid near the trailing face while decreasing the radial velocity of the warmer fluid near the leading face. Thus, buoyancy further increases heat transfer at the trailing face while suppressing it at the leading face. The situation, however, gets more involved when buoyancy effects are very strong since, then, reverse radial flow can occur over the leading face; in such instances rotation enhances heat transfer at the leading face near the duct exit.

(*c*) Using the standard k–ϵ model, and including the buoyancy effects in the mean equations, all experimentally observed heat transfer variations are correctly predicted. Thus, on the trailing face, heat transfer increases with both rotational speed and density ratio. On the leading face, rotation suppresses heat transfer near the inlet but increases it farther downstream.

(*d*) The quantitative match with the data shows that the Nusselt numbers are underpredicted over the trailing face and near the inlet on the leading face. Midway and near the exit, heat transfer at the leading face is overpredicted. Except very close to the inlet, the difference between predictions and data ranges from 10 percent at low rotation speeds to about 30 percent at higher rotation. The possible causes of this difference, in the order of importance, are believed to be: (*i*) uncertainty in the data, (*ii*) specification of inlet conditions, and (*iii*) the needed modifications in the k–ϵ model to account for rotation and buoyancy effects.

(e) It is shown that inclusion of buoyancy is essential for correct predictions; if the buoyancy effects are neglected there is a marked disagreement, both qualitative and quantitative, between the predictions and the data.

Efforts intended to address some of the possible causes of theory–data mismatch are clearly the avenues for further research.

References

1 Johnston, J. P., "The Effects of Rotation on Boundary Layers in Turbomachine Rotors," NASA SP304, 1974, pp. 207–249.

2 Ito, H., and Nanbu, K., "Flow in Rotating Straight Pipes of Circular Cross-Section," ASME *Journal of Basic Engineering*, 1971, pp. 383–394.

3 Mori, Y., Fukada, T., and Nakayama, W., "Convective Heat Transfer in Rotating Radial Circular Pipe: 2nd Report," *Int. J. Heat Mass Transfer*, Vol. 14, 1971, pp. 1807–1824.

4 Wagner, R. E., and Velkoff, H. R., "Measurements of Secondary Flows in a Rotating Duct," ASME *Journal Engineering for Power*, Vol. 94, 1972, pp. 261–270.

5 Moore, J., "A Wake and an Eddy in a Rotating Radial-Flow Passage. Part 1: Experimental Observations," ASME *Journal of Engineering for Power*, Vol. 95, 1973, pp. 205–212.

6 Metzger, D. E., and Stan, R. L., "Entry Region Heat Transfer in Rotation Radial Tubes," AIAA Paper No. 77-189, 1977.

7 Morris, W. D., and Ayhan, T., "Observations on the Influence of Rotation on Heat Transfer in the Coolant Channels of Gas Turbine Rotor Blades," *Proc. Inst. Mech. Eng.*, Vol. 193, 1979, pp. 303–311.

8 Morris, W. D., Harasgama, S. P., and Salemi, R., "Measurements of Turublent Heat Transfer on the Leading and Trailing Surfaces of a Square Duct Rotating About an Orthogonal Axis," ASME Paper 88-GT-114, 1988.

9 Guidez, J., "Study of the Convective Heat Transfer in a Rotating Coolant Channel," ASME JOURNAL OF TURBOMACHINERY, Vol. 111, 1988, pp. 43–50.

10 Wagner, J. H., Johnson, B. V., and Hajek, T. J., "Heat Transfer in Rotating Passages With Smooth Walls and Radial Outward Flow," ASME Paper 89-GT-272, 1989.

11 Wagner, J. H., Johnson, B. V., and Kopper, F. C., "Heat Transfer in Rotating Serpentine Passages With Smooth Walls," ASME Paper No. 90-GT-331, 1990.

12 Mori, Y., and Nakayama, W., "Convective Heat Transfer in Rotating Radial Circular Pipes: 1st Report, Laminar Region," *Int. J. Heat Mass Transfer*, Vol. 11, 1968, pp. 1027–1040.

13 Moore, J., "A Wake and an Eddy in a Rotating, Radial-Flow Passage. Part 2: Flow Model," ASME *Journal of Engineering for Power*, Vol. 95, 1973, pp. 213–219.

14 Skiadaressis, D., and Spalding, D. B., "Heat Transfer in a Pipe Rotating Around a Perpendicular Axis," ASME Paper No. 77-WA/HT-39, 1977.

15 Majumdar, A. K., and Spalding, D. B., "A Numerical Investigation of Three-Dimensional Flows in a Rotating Duct by a Partially-Parabolic Procedure," ASME Paper No. 77-WA/FE-7, 1977.

16 Howard, J. H. G., Patankar, S. V., and Bordynuik, R. M., "Flow Prediction in Rotating Ducts Using Coriolis-Modified Turbulence Models," ASME *Journal of Fluids Engineering*, Vol. 102, 1980, pp. 456–461.

17 Johnston, J. P., Halleen, R. M., and Lezius, D. K., "Effects of Spanwise Rotation on the Structure of Two-Dimensional Fully Developed Turbulent Channel Flow," *J. of Fluid Mechanics*, Vol. 56, 1972, pp. 533–557.

18 Hwang, G. J., and Jen, T. C., "Convective Heat Transfer in Rotating Isothermal Ducts," Int. J. Heat Mass Transfer, Vol. 33, 1990, pp. 1817–1828.

19 Iacovides, H., and Launder, B. E., "Parametric and Numerical Study of Fully-Developed Flow and Heat Transfer in Rotating Rectangular Ducts," ASME Paper 90-GT-24, 1990.

20 Launder, B. E., and Spalding, D. B., *Mathematical Models of Turbulence*, Academic Press, New York, 1972.

21 Launder, B. E., and Spalding, D. B., "The Numerical Computation of Turbulent Flows," *Computer Methods in Applied Mechanics and Engineering*, Vol. 3, 1974, pp. 269–289.

22 Koyama, H., Masuda, S., Ariga, I., and Watanabe, I., "Stabilizing and Destabilizing Effects of Coriolis Force on Two-Dimensional Laminar and Turbulent Boundary Layers," ASME *Journal of Engineering for Power*, Vol. 101, 1979, pp. 23–31.

23 Rosten, H. I., and Worrell, J. K., "Generalized Wall Functions for Turbulent Flow," *PHOENICS Journal*, Vol. 1, 1988, pp. 81–109.

24 Jayatillika, C. L. V., "The Influence of the Prandtl Number and Surface Roughness on the Resistance of the Sub-layer to Momentum and Heat Transfer," *Prog. in Heat and Mass Transfer*, Vol. 1, 1969, pp. 193–329.

25 Rosten, H. I., and Spalding, D. B., "The PHOENICS Beginner's Guide," CHAM TR/100, 1987.

26 Patankar, S. V., *Numerical Heat Transfer and Fluid Flow*, Hemisphere Publishing Corp., New York, 1980.

27 Kays, W. M., and Perkins, H. C., "Forced Convection Internal Flow in Ducts," *Handbook of Heat Transfer*, W. M. Rohsenow and J. P. Hartnett, eds., McGraw-Hill, pp. 7–28 and 7–33, 1973.

APPENDIX

Generalized Wall Functions [23]

Consider Fig. A-1, which shows a near-wall grid point P located at a distance δ from the wall. Let V_p and k_p represent

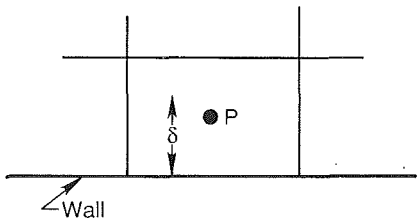

Fig. A-1 A near-wall grid point

the tangential velocity and the turbulent kinetic energy at the point P. The shear stress at the wall is obtained as:

$$\frac{\tau_w}{\rho} = sV_P^2 \tag{A1}$$

where s is the friction coefficient given by

$$s = \frac{\kappa C_\mu^{1/4} k_P^{1/2}}{V_P \ln (E\delta C_\mu^{1/4} k_P^{1/2}/\nu)} \tag{A2}$$

In the above,

κ = von Karman constant = 0.435

and

E = Wall roughness parameter = 9 (smooth wall)

The turbulent kinetic energy, k_p, is obtained via the differential equation for k with the zero-gradient condition imposed at the wall.

The generation rate of k at the point p is computed as:

$$G_p = \rho(sV_P^2)V_P/(2\delta) \tag{A3}$$

The dissipation rate at the point P is fixed as:

$$\epsilon_P = \frac{C_\mu^{3/4} k_P^{3/2} \ln (E\delta C_\mu^{1/4} k_p^{1/2}/\nu)}{\kappa(2\delta)} \tag{A4}$$

The heat flow at the wall is given by

$$q_w = (\mathrm{St}\rho V_P)(h_w - h_P) \tag{A5}$$

where h_w and h_p designate the enthalpy at the wall and the point P, respectively, and St is the Stanton number given by

$$\mathrm{St} = \frac{s}{\left[\mathrm{Pr}_t \left(1 + \frac{sPV_P}{C_\mu^{1/4}\sqrt{k_P}}\right)\right]} \tag{A6}$$

In the above, the P function is given by

$$P = 9\left(\frac{\mathrm{Pr}}{\mathrm{Pr}_t} - 1\right)\left(\frac{\mathrm{Pr}_t}{\mathrm{Pr}}\right)^{1/4} \tag{A7}$$

Heat Transfer in Rotating Serpentine Passages With Trips Normal to the Flow

J. H. Wagner

B. V. Johnson

United Technologies Research Center,
East Hartford, CT 06108

R. A. Graziani

Group Engineering,
Pratt & Whitney,
East Hartford, CT 06108

F. C. Yeh

NASA Lewis Research Center,
Cleveland, OH 44135

Experiments were conducted to determine the effects of buoyancy and Coriolis forces on heat transfer in turbine blade internal coolant passages. The experiments were conducted with a large-scale, multipass, heat transfer model with both radially inward and outward flow. Trip strips on the leading and trailing surfaces of the radial coolant passages were used to produce the rough walls. An analysis of the governing flow equations showed that four parameters influence the heat transfer in rotating passages: coolant-to-wall temperature ratio, Rossby number, Reynolds number, and radius-to-passage hydraulic diameter ratio. The first three of these four parameters were varied over ranges that are typical of advanced gas turbine engine operating conditions. Results were correlated and compared to previous results from stationary and rotating similar models with trip strips. The heat transfer coefficients on surfaces, where the heat transfer increased with rotation and buoyancy, varied by as much as a factor of four. Maximum values of the heat transfer coefficients with high rotation were only slightly above the highest levels obtained with the smooth wall model. The heat transfer coefficients on surfaces where the heat transfer decreased with rotation, varied by as much as a factor of three due to rotation and buoyancy. It was concluded that both Coriolis and buoyancy effects must be considered in turbine blade cooling designs with trip strips and that the effects of rotation were markedly different depending upon the flow direction.

Introduction

Advanced gas turbine airfoils are subjected to high heat loads that require escalating cooling requirements to satisfy airfoil life goals. The efficient management of cooling air requires detailed knowledge of local heat load and cooling air flow distribution for temperature and life predictions. However, predictions of heat transfer and pressure loss in airfoil coolant passages currently rely primarily on correlations derived from the results of stationary experiments. Adjustment factors are usually applied to these correlations to bring them into nominal correspondence with engine experience. This is unsatisfactory when blade cooling conditions for new designs lie outside the range of previous experience.

Knowledge of the local heat transfer in the cooling passages is extremely important in the prediction of blade metal temperatures, i.e., blade life. Rotation of turbine blade cooling passages gives rise to Coriolis and buoyancy forces, which can significantly alter the local heat transfer in the internal coolant passages due to the development of cross-stream (Coriolis), as well as radial (buoyant) secondary flows. Buoyancy forces in gas turbine blades are substantial because of the high rotational speeds and coolant temperature gradients. Earlier investigations (e.g., Eckert et al., 1953) with single pass co- and counterflowing stationary coolant passages indicated that there can also be substantial differences in the heat transfer when the buoyancy forces are aligned with or counter to the forced convection direction. A better understanding of Coriolis and buoyancy effects and the capability to predict the heat transfer response to these effects will allow the turbine blade designer to achieve cooling configurations that utilize less flow and that reduce thermal stresses in the airfoil.

An extensive analytical and experimental program was originated and sponsored by NASA at the Lewis Research Center, Cleveland, OH, as part of the Hot Section Technology (HOST) program. The objectives of this program were (1) to gain insight on the effect of rotation on heat transfer in turbine blade passages, (2) to develop a broad data base for heat transfer and pressure drop in rotating coolant passages, and (3) to improve computational techniques and develop correlations that can be useful to the gas turbine industry for turbine blade design. The attainment of these objectives become even more critical with the advent of the Integrated High Performance Turbine Engine Technology (IHPTET) initiative. As part of the IHPTET goal, the turbine would operate at near-stoichiometric (3500–4000°F) inlet temperatures, maintain efficiencies in the 88–94 percent range, and require total coolant flows of only 5 percent of the engine air flow rate. To attain these ambitious goals, a thorough understanding on the rotational effects of heat transfer and flow in turbine blade passages is mandatory.

Contributed by the International Gas Turbine Institute and presented at the 36th International Gas Turbine and Aeroengine Congress and Exposition, Orlando, Florida, June 3-6, 1991. Manuscript received at ASME Headquarters March 4, 1991. Paper No. 91-GT-265. Associate Technical Editor: L. A. Riekert.

Previous Studies. Heat transfer experiments in multiple-pass coolant passages with normal trips have been conducted in stationary models by several investigators to obtain a data base for the thermal design of gas turbine airfoils, e.g., Boyle (1984), Han et al. (1986), and Metzger et al. (1988). These data bases are directly applicable to the cooling designs of stationary vanes. However, the effects of Coriolis forces and buoyancy, due to the large rotational gravity forces (up to 50,000 g), are not accounted for.

The complex coupling of the Coriolis and buoyancy forces has prompted many investigators to study the flow field generated in unheated, rotating circular and rectangular passages without the added complexity of buoyancy, i.e., Hart (1971), Wagner and Velkoff (1972), Moore (1967), and Johnston et al. (1972). The effects of rotation on the location of flow reattachment after a backward facing step presented by Rothe and Johnston (1979) is especially helpful in understanding the effects of rotation on heat transfer in passages with trips. These investigators have documented strong secondary flows and have identified aspects of flow stability that produce streamwise oriented, vortexlike structures in the flow of rotating radial passages.

The effects of buoyancy on heat transfer without the complicating effects of Coriolis-generated secondary flow have been studied in vertical stationary ducts. Effects of buoyancy on heat transfer were reported by Eckert et al. (1953), Metais and Eckert (1964), and Brundrett and Burroughs (1967). Flow criteria for forced-, mixed-, and free-convection heat transfer were developed for parallel flow and counterflow configurations by Eckert et al. (1953) and Metais and Eckert (1964). Based on these experimental results, buoyancy forces would be expected to cause significant changes in the heat transfer in turbine blade coolant passages and to be strongly dependent on flow direction (radially inward versus radially outward).

The combined effect of Coriolis and buoyancy forces on heat transfer has been studied by a number of investigators. Heat transfer in rotating models has been reported by Wagner et al. (1991a, 1991b), Taslim et al. (1991), Guidez (1989), Clifford (1985), Iskakov and Trushin (1983), Morris (1981), Morris and Ayhan (1979), Lokai and Gunchenko (1979), Johnson (1978), and Mori et al. (1971). With the exception of Taslim and Clifford, all of the aforementioned work was conducted with smooth-wall models. Large increases and decreases in local heat transfer were found to occur by some investigators under certain conditions of rotation while other investigators showed lesser effects. Analyses of these results do not show consistent trends. The inconsistency of the previous results is attributed to differences in the measurement techniques, models, and test conditions.

Objectives. Under the NASA HOST program, a comprehensive experimental project was formulated in 1982 to identify and separate effects of Coriolis and buoyancy forces for the range dimensionless flow parameters encountered in axial flow, aircraft gas turbines. The specific objective of this experimental project was to acquire and correlate benchmark-quality heat transfer data for a multipass, coolant passage under conditions similar to those experienced in the blades of advanced aircraft gas turbines. A comprehensive test matrix was formulated, encompassing the range of Reynolds numbers, rotation numbers, and heating rates expected in a modern gas turbine engine.

The results presented in this paper are from the second phase of a three-phase program directed at studying the effects of rotation on a multipass model with smooth and rough wall configurations. The first phase utilized the smooth wall configuration. Initial results for outward flow in the first passage were previously presented by Wagner et al. (1991a). The effects of flow direction and buoyancy with smooth walls were presented by Wagner et al. (1991b). The present paper covers the phase with surface roughness elements oriented at 90 deg to the flow direction. Comparisons will be made with the results for smooth walls in the same model and with previous rotating and stationary experiments employing trips 90 deg to the flow direction. Results from the remaining phase of the program with trips oriented 45 deg to the flow direction will be discussed in a subsequent paper.

The facility, data acquisition, and data reduction techniques employed in this experiment were discussed in the Wagner et al. (1991a) paper and will not be repeated. However, the description of the model will be repeated for the convenience of the reader.

Description of Experimental Equipment

Heat Transfer Model. The heat transfer model was designed to simulate the internal multipassage geometry of a cooled turbine blade (Fig. 1). The model consists of three straight sections and three turn sections, which were instrumented followed by one uninstrumented straight section, as shown in Fig. 2. Data presented herein were obtained in the first, second, and third passages with radially outward, inward, and outward flow, respectively. The model passages are approximately square with a characteristic dimension of 0.5 in. (12.7 mm). Four elements form the walls of the square coolant passage at each streamwise location. The heated length of the first passage is 14 hydraulic diameters and is comprised of 16 heated copper elements at four streamwise locations. The heated copper elements at the first streamwise location were all smooth walls and were used as guard heaters. The two cross-sectional views shown in the figure show the orientation of the leading, trailing, and sidewall surfaces. Each copper element is heated on the side opposite the test surface with a thin film, 0.003 in. (0.1 mm), resistance heater. Each element is 0.150 in. (3.8 mm) thick and is thermally isolated from surrounding elements by 0.060 in. (1.5 mm) thick fiberglass insulators. The insulating material separating the copper elements at each streamwise location resulted in a 0.04 in. (1.0 mm) chamfer in the corners, which yielded a hydraulic diameter, D, in the straight sections of 0.518 in. (13.2 mm). The radius at the center of the heat transfer test sections with trips, i.e., average model radius,

Nomenclature

A = area of passage cross section
D = hydraulic diameter
e = trip height
Gr = rotational Grashof number
h = heat transfer coefficient
k = thermal conductivity
m = mass flow rate
Nu = Nusselt number = hD/k
P = trip spacing, i.e., pitch
R = radius
Re = Reynolds number = $(mD)/(\mu A)$
Ro = rotation number, $\Omega D/V$
T = temperature
V = mean coolant velocity
x = streamwise distance from inlet
μ = absolute viscosity
ν = kinematic viscosity
ρ = coolant density
$\Delta\rho/\rho$ = density ratio = $(\rho_b - \rho_w)/\rho_b$
Ω = rotational speed

Subscripts

b = bulk property
f = film property
i = inlet to model
w = heated surface location
∞ = fully developed, smooth tube

Superscripts

$-$ = average
$'$ = distance from beginning of second passage
$''$ = distance from beginning of third passage

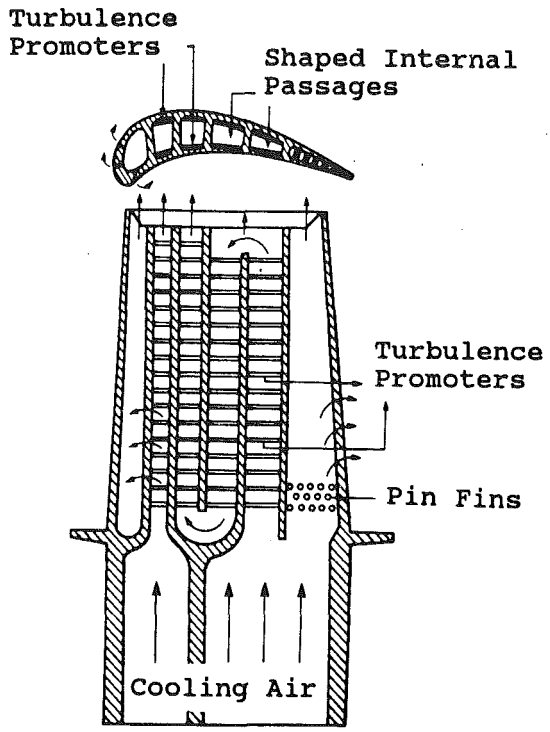

Fig. 1 Typical turbine blade internal convection cooling configuration (from Han et al., 1986)

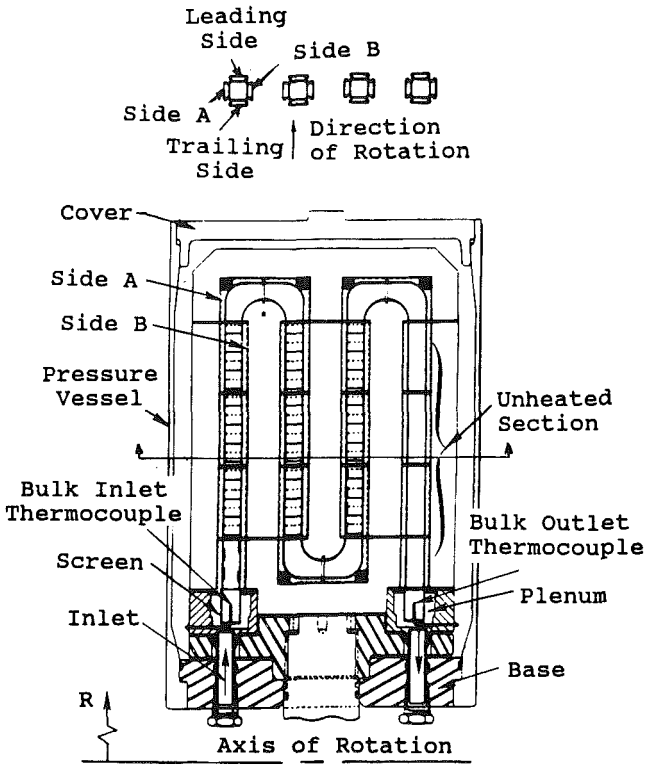

Fig. 2 Cross-sectional views of coolant passage heat transfer model assembly

was 26.1 in. (663 mm). The power to each element was adjusted to obtain an isothermal wall boundary condition. In practice, temperature differences less than 2°F (1°C) were achieved. The heat flux between elements with a 2°F (1°C) temperature difference was estimated to be less than 2 percent of a typical stationary heat flux.

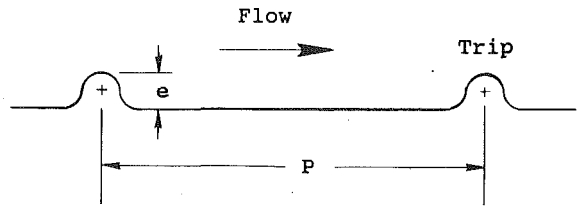

Fig. 3 Cross-sectional view of normal trip layout

Trip strips were machined in a staggered pattern on the leading and trailing surfaces of the 6 in. (152.4 mm) straight length of each passage. No trips were on the guard elements ($x/D<3$) in the first passage. The height, ($e/D=0.1$), shape (circular) and spacing ($P/e=10$) of the trips are shown in Fig. 3. These geometric parameters are typical of the trips cast on the coolant passage walls of turbine blades.

Testing was conducted with air at dimensionless flow conditions typical of advanced gas turbine designs. The required dimensionless rotation numbers were obtained with rotation rates of 1100 rpm or less by operating the model at a pressure of approximately 10 atm. The model inlet air temperature was typically 80°F (27°C) and the copper elements were held at 120°F, 160°F, 200°F, and 240°F (49°C, 71°C, 93°C, and 116°C) for coolant-to-wall temperature differences of 40°F, 80°F, 120°F, and 160°F (22°C, 44°C, 67°C, and 89°C). Temperatures of the copper elements were measured with two chromel-alumel thermocouples inserted in drilled holes of each element. Heat transfer coefficients were determined by performing an energy balance on each copper element to obtain the convected heat flux and the local coolant bulk temperature. The heat transfer coefficients were based on the projected area rather than the total heat surface area due to trip geometry. (The total heat transfer surface area was 1.11 times the projected area.) See Wagner et al. (1991a) for additional information about the data reduction procedure.

Nusselt numbers and Reynolds numbers were calculated for each element. The fluid properties in the Nusselt and Reynolds numbers were evaluated at the film temperature, i.e., $T_f=(T_w+T_b)/2$. All the heat transfer results presented herein have been normalized with a correlation for fully developed, turbulent flow in a smooth tube. The constant heat flux Colburn equation, adjusted for constant wall temperature, was used to obtain the Nusselt number for fully developed, turbulent flow in a smooth tube (Kays and Perkins, 1973). The resulting equation for the constant wall temperature condition with a Prandtl number equal to 0.72 is as follows:

$$Nu_\infty = 0.0176\ Re^{0.8}$$

An uncertainty analysis of the data reduction equations using the methods of Kline and McClintock (1953) showed that approximately 3/4 of the estimated uncertainty in calculating heat transfer coefficient was due to the measurement of temperatures in the model. The uncertainty of the heat transfer coefficient is influenced mainly by the wall-to-coolant temperature difference and the net heat flux from each element. Uncertainty in the heat transfer coefficient increases when either the temperature difference or the net heat flux decreases. For increasing x/D, the uncertainty increases because the wall-to-coolant temperature difference decreases. For low heat fluxes (i.e., low Reynolds numbers and on leading surfaces with rotation) the uncertainty in the heat transfer increased. Estimates of the error in calculating heat transfer coefficient typically varied from approximately ±6 percent at the inlet to ±30 percent at the exit of the heat transfer model for the baseline stationary test conditions. The uncertainty in the lowest heat transfer coefficient on the leading side of the third passage with rotation is estimated to be 40 percent, primarily due to the uncertainty in the calculated bulk temperature. Although

the uncertainty analysis was useful in quantifying the maximum possible uncertainty in calculating heat transfer coefficient, multiple experiments at the same test condition were repeatable within ranges smaller than those suggested by the analysis.

Results

Forward. Heat transfer in stationary experiments with augmentation devices on the passage walls is primarily a function of the Reynolds number (a flow parameter), the streamwise distance from the inlet, x/D (a geometric parameter), and the geometry of the augmentation device. However, when rotation is applied, the heat transfer is also strongly influenced by the coupled effects of Coriolis and buoyancy and becomes asymmetric around the passage. An unpublished analysis of the equations of motion by Suo (1980), similar to that of Guidez (1989), showed that the basic dimensionless fluid dynamic parameters governing the flow in a radial coolant passage were the Reynolds number, the rotation number, Ro, the fluid density ratio, $\Delta\rho/\rho$, and the geometric parameter, R/D. The same analysis of the equations of motion produces the rotational Reynolds number, $J=\Omega D^2/\nu$ as an alternate governing parameter. Note also that Ro equals J/Re. Note that the rotation parameter is reciprocal of the Rossby number, $V/\Omega D$, and governs the formation of cross-stream secondary flow. The rotation number, Ro, the fluid density ratio, $\Delta\rho/\rho$, and the geometric parameter, R/D, appear in the governing equation as a buoyancy parameter. This buoyancy parameter, $(\Delta\rho/\rho)(R/D)(\Omega D/V)^2$, is similar to Gr/Re^2 for stationary heat transfer. The difference between our rotational buoyancy parameter and the stationary Gr/Re^2 is that $\Delta\rho/\rho=(T_w-T_b)/T_w$ rather than $\beta\Delta T=(T_w-T_b)/T_b$. The difference between the parameters decreases as T_w approaches T_b. Thus, with rotation, the heat transfer is a function of three geometric parameters (surface roughness geometry, x/D, and surface orientation relative to the direction of rotation) and three flow parameters (Reynolds number, rotation number, and the buoyancy parameter).

Due to the vector nature of the equations of motion, it can be expected that flow direction can also have a significant effect on the coolant flow. In the parallel flow case, the flow is radially inward, coincident with buoyancy-driven flow for heated walls. For the counterflow case the flow is radially outward, opposite to the direction of the buoyancy-driven flow. Flow direction (i.e., radially inward or outward) and a fixed radially outward directed force field, created by the rotating reference frame, established the potential for parallel and counterflow situations as observed by Eckert et al. (1953) in their vertical tube experiments.

The references used in the text for low and high-pressure surfaces are consistent with the leading to trailing side, Coriolis-generated, pressure gradients. In general, high-pressure surfaces are expected to have normal components of flow toward the surface, while low-pressure surfaces are expected to have normal components of flow away from the surface. Therefore, trailing surfaces in the first passage with outward flow are on the high-pressure side of the passage. Similarly, leading surfaces in the second passage with inward flow are on the high-pressure side. In terms of turbine airfoils, the leading surfaces of the coolant passage are adjacent to the suction side of the airfoil and the trailing surfaces of the coolant passage are adjacent to the pressure side of the airfoil.

The format of this paper is to show the effects of each of the primary variables (x/D, rotation number, density ratio) on the heat transfer about a baseline flow condition to develop an understanding of the cause/effect relationships. The entire body of experimental results is then examined to determine the effects of the buoyancy parameter on the heat transfer in selected locations of the coolant passage.

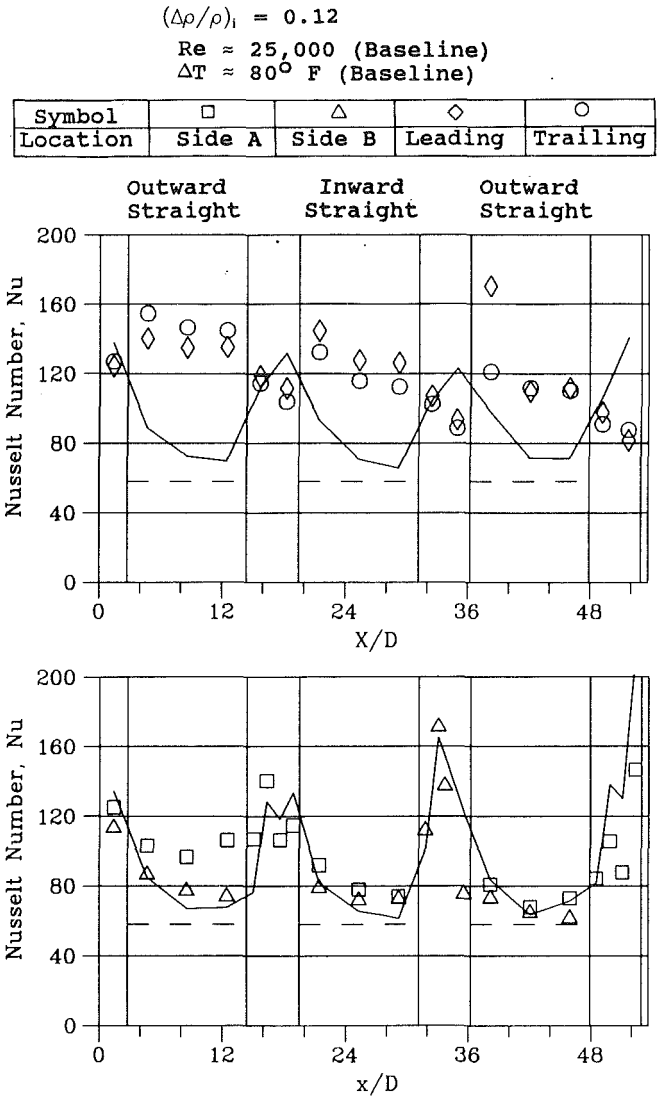

Fig. 4 Heat transfer results for stationary flow condition, ——— correlation for smooth-wall fully developed flow, ——— smooth-wall experiments (Wagner et al., 1991b)

Baseline Experiments. Two baseline experiments, one stationary and one rotating, were conducted to obtain data for comparison with all other data generated in this program. The stationary and rotating baseline experiments had dimensionless flow conditions, which consisted of a Reynolds number of 25,000 and an inlet density ratio, $(\Delta\rho/\rho)_i=(T_w-T_b)/T_w$, of 0.13. The rotating baseline experiment had a rotation number, $\Omega D/V$, of 0.24 and a radius ratio at the average model radius, R/D, of 49. These values were selected because they are in the central region of the operating range of current large aircraft gas turbine engines.

Stationary. Streamwise variations of Nusselt number for the stationary baseline test are shown in Fig. 4. The Nusselt number for fully developed, turbulent flow in a smooth tube with constant wall temperature and the results from the previous (Wagner et al., 1990) smooth wall experiments are shown for comparison.

The heat transfer from the walls with trips (denoted leading and trailing) in the first outward straight ($3<x/D<14$) passage has heat transfer coefficients more than twice that from the fully developed, smooth-wall correlation. Note that the heat transfer coefficients for the normal trips do not decrease significantly with x/D in each passage as they did for the smooth wall in the same model. Some differences in heat transfer are observed between the leading and trailing surfaces for this

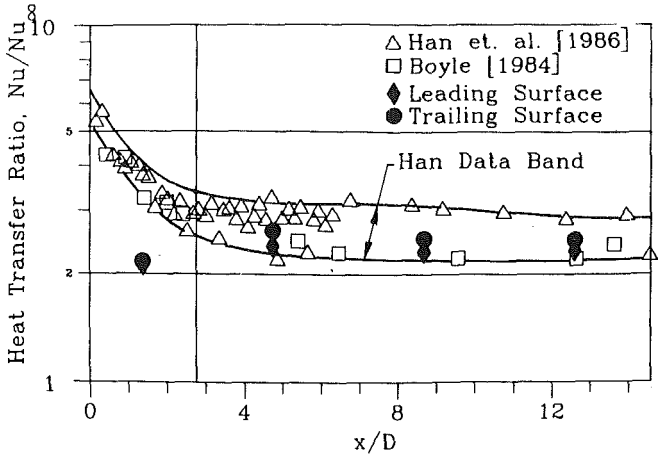

Fig. 5 Comparison of stationary heat transfer results from leading and trailing surfaces with results of Han et al. (1986)

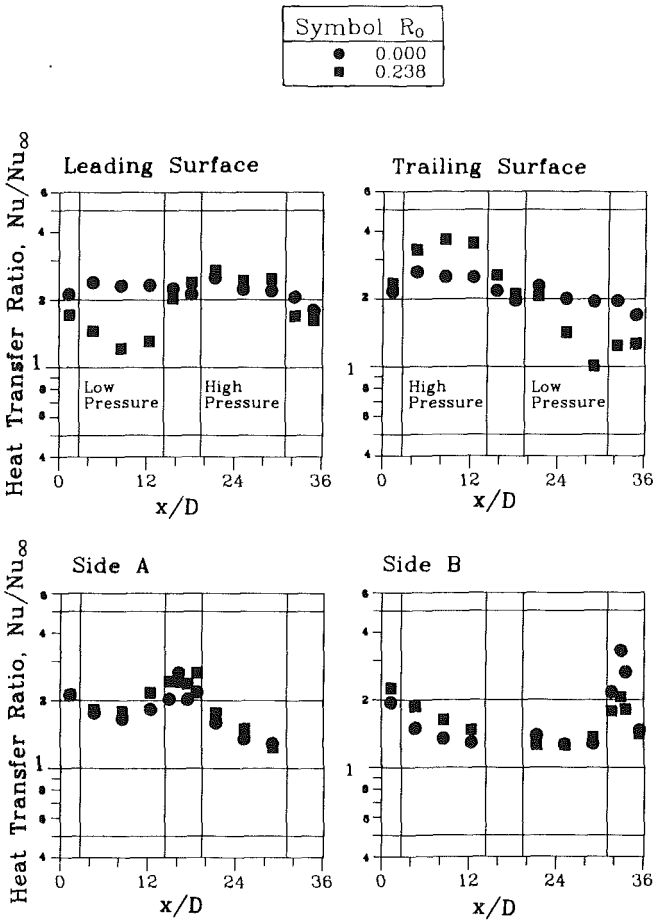

Fig. 6 Variation of heat transfer ratio with streamwise location for "rotating" baseline flow condition; Re = 25,000, $R_0 = 0.24$, $(\Delta\rho/\rho)_i = 0.13$

stationary baseline condition. The exact cause of the difference is not known but may be due to the staggering of the trips on the two surfaces. The heat transfer coefficients measured in the remaining two passages (i.e., $20 < x/D < 31$ and $36 < x/D < 48$) show similar characteristics. However, the greatest increase in heat transfer from the trips was less (i.e., 10 and 20 percent, respectively) than that obtained in the first outward straight section. This general reduction in heat transfer was attributed to the increased uncertainty in the bulk temperature for the model with the normal trips. The increased heat transfer compared to the smooth wall model causes the difference between bulk temperature and the wall temperature to decrease and hence the uncertainty of the heat transfer coefficient determined to increase.

The heat transfer in the turn regions was generally less for the present experiment than for the previous smooth wall experiments. These changes on the leading and trailing surfaces of the turn sections are attributed in part to the differences in the velocity profiles expected at the entrance to the turn regions. For the smooth wall flow condition, the velocities are expected to be high in the corners of the duct (e.g., Schlichting, 1968). For flow over normal trips, the velocity can be expected to peak in the center of the channel due to the large momentum losses at each trip. The changes in heat transfer on sides A and B (outside walls of turn sections) attest to the complexity of the flow structure in the turns and are not yet explained.

The results from the first outward straight coolant passage are compared with results from Boyle (1984) and Han et al. (1986) in Fig. 5. The present results in the region with trips, $3 < X/D < 14$, are almost identical with those from Boyle. The Boyle results were obtained for a constant heat flux boundary condition and sharp cornered trips, which are modest variations from the present experiment. Heat transfer ratios from the surfaces with trips are generally consistent with the data band for Han's measurements. Note that the heat transfer results from the present program for $x/D < 3$ are from the smooth-wall surfaces near the inlet of the first passage. However, in general, the levels of heat transfer augmentation due to the presence of the trips are consistent with those of Boyle and Han et al.

Rotating. The streamwise distributions of heat transfer ratio for the rotating baseline condition for the first two coolant passages are shown in Fig. 6. These results and those discussed in the following sections are shown as heat transfer ratio, Nu/Nu_∞. Nu_∞ is that expected from the Kays and Perkins (1973) correlation for fully developed, turbulent flow. The results will be shown in this manner to minimize effects of Reynolds number variations from test to test.

The most important feature of these results is the decrease in heat transfer on the "low pressure" sides shown for the leading surfaces for flow outward ($x/D < 14$) and the trailing surfaces for flow inward ($x/D < 31$). The lowest values of Nu/Nu_∞ are less than one-half the nonrotating values. The heat transfer on the high-pressure side of the coolant passage with flow outward (i.e., the trailing surfaces) increases about 50 percent compared to the stationary case. However, the heat transfer on the leading surface for flow inward does not increase noticeably. These results are qualitatively similar to those obtained for the smooth wall model. Further comparison with the smooth wall model results will be made in a later section.

The baseline results with rotation showed significant changes in the heat transfer in the first passage on the leading, trailing, and turn surfaces but relatively smaller changes on the sidewall surfaces. Therefore, the following discussion will focus on the heat transfer results from only the leading and trailing surfaces in the straight sections of the coolant passage with both inward and outward flow and will focus on the differences between inward versus outward flow. Discussion of effects of rotation on the heat transfer in the turn regions of the coolant passage are deferred to a subsequent paper.

Varying Rotation Number. The rotation number, $\Omega D/V$, was varied from 0 to 0.35 for this series of flow conditions. The Reynolds number, inlet density ratio, and radius ratio were held constant at the nominal values of 25,000, 0.13, and 49, respectively.

High Pressure Surfaces. Increasing the rotation rate causes significant increases in heat transfer on the trailing surfaces (Fig. 7*a*) of the first passage but relatively small increases

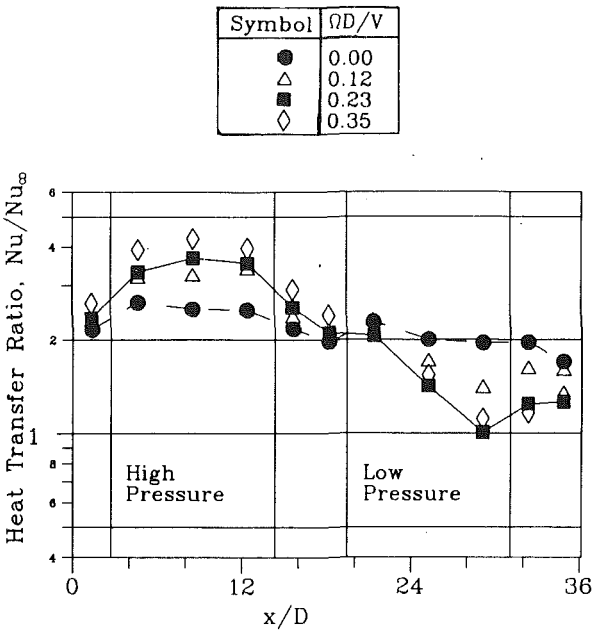

Fig. 7(*a*) Trailing surface

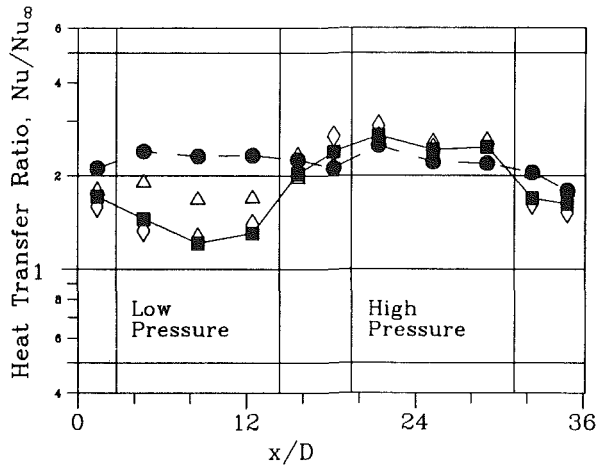

Fig. 7(*b*) Leading surface

Fig. 7 Effect of rotation number on heat transfer ratio; Re = 25,000, $(\Delta\rho/\rho)_i = 0.13$, $R/D = 49$

occurred on the leading surfaces in the second passage (Fig. 7*b*). Heat transfer in the first passage increased by more than 60 percent for the largest value of rotation parameter (0.35) compared to stationary heat transfer values. The substantial increases in heat transfer in the first passage are consistent with the results of Rothe and Johnston (1979). They found that as rotation rate was increased, the reattachment length after a step decreased. For the trip spacing of the present program ($P/e = 10$), this would translate into an increase in the effective heat transfer area between the trips with attached, turbulent flow, thereby causing an increase in the heat transfer. Compared to the stationary results, the heat transfer on the leading, high-pressure side of the second passage increased approximately 10 percent. The effects of heat transfer due to Coriolis-generated secondary flows and flow reattachment might be expected to be approximately the same for the first and second passages. The differences in heat transfer between the outward and inward flowing passages are therefore attributed to the different effects of buoyancy in the counterflowing first passage (radially outward flow) and the coflowing second passage (radially inward flow). In general, the trends noted above are compatible with those obtained for the smooth wall test surfaces in the same model (Wagner et al., 1991b).

The small increase in the heat transfer ratio on the high-pressure side of the second passage relative to the first passage is attributed to a reduction in the generation of near-wall turbulence. In the first passage, the near-wall buoyancy-driven flow was inward toward the axis of rotation and the coolant flow was outward. This counterflow is expected to generate additional near-wall turbulence due to the strong shear gradient. The large increases in heat transfer in the first passage are attributed to the destabilizing effects of the shear flow combined with the cross-stream secondary flows generated by Coriolis forces. However, when the flow and the buoyancy-driven near-wall flows are coincident, as in the second passage, the generation of near-wall turbulence may be diminished because of the relatively weaker near-wall shear layer. The expected lower near-wall turbulence and weaker shear flows may also contribute to increases in reattachment lengths following the trips. Therefore, the reduced effects of the buoyant and the cross-stream secondary flows coupled with possible increases in reattachment lengths in the second passage may have resulted in lesser changes in heat transfer. The magnitude of the buoyancy effect on the heat transfer is unclear in that the buoyancy effect on the heat transfer in the second passage may be zero (which implies a modest Coriolis dominated heat transfer increase) or negative (which implies a larger Coriolis dominated heat transfer increase which is offset by a reduction due to buoyancy). Future results from concurrent numerical simulations of these flow conditions are expected to assist in the understanding of this complex flow field.

Low-Pressure Surfaces. In contrast to the continual increase in heat transfer with increasing rotation number on the trailing side, the heat transfer ratio decreases with increasing rotation number on the leading side of the passage near the inlet, i.e., $x/D < 6$. For all of the remaining locations on the leading side of the passage, the heat transfer ratio decreases and then increases again with increasing rotation number. Heat transfer from the trailing, low-pressure surfaces of the second passage also had large decreases in heat transfer. Heat transfer in the first and second passages decreased to almost 50 percent of the stationary heat transfer levels. In both passages, the heat transfer decreased and then subsequently increased again as the rotation rate was increased.

The decrease in the heat transfer ratio are attributed to the cross-stream flow patterns as well as the stabilization of the near-wall flow on the leading side of the passage (e.g., Johnston et al., 1972). The cross-stream flows cause heated, near-wall fluid from the trailing and sidewall surfaces to accumulate near the leading side of the coolant passage resulting in reduced heat transfer. In addition, as described by Rothe and Johnston (1979), it can be expected that flow reattachment after trips on low-pressure surfaces occurs at larger distances from the trips with increasing rotation number. Longer reattachment lengths, due to the stabilizing effects, will decrease the effective heat transfer area between trips, thereby further reducing the turbulent transport of heat. The increase in the heat transfer ratio in the latter half of the coolant passage for the larger rotation numbers is attributed to buoyancy effects, possibly caused by buoyancy-enhanced flow in the recirculation cells downstream of the trips. Similar effects of rotation are noted for the low-pressure surfaces in both the first and second passages, with flow radially outward and radially inward, respectively. These results suggest that the decrease in heat transfer on low-pressure surfaces with trips is dominated by Coriolis-generated cross-steam flows, which cause a stabilization of the near-wall flows, and that the heat transfer on the high-pressure surfaces is affected by a combination of Coriolis and buoyant effects. Therefore, it can be expected that the correlations of local heat transfer data may be sub-

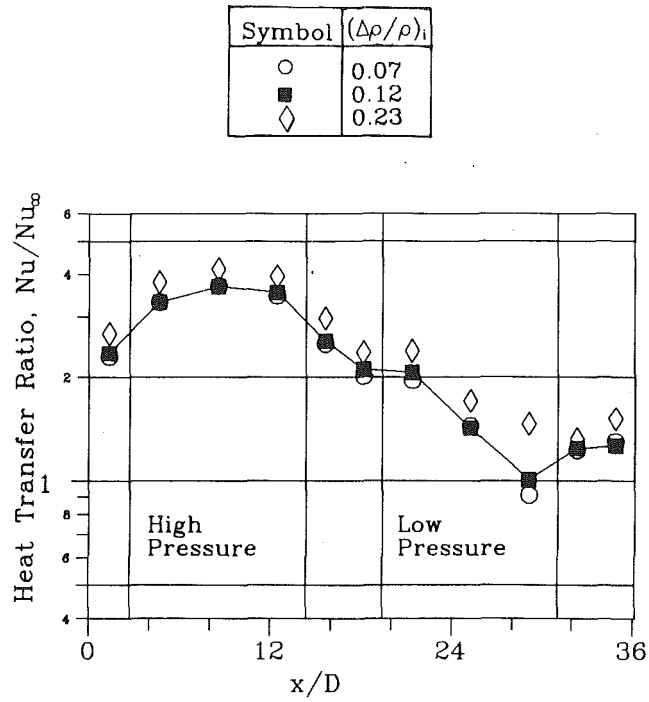

Fig. 8(a) Trailing surface

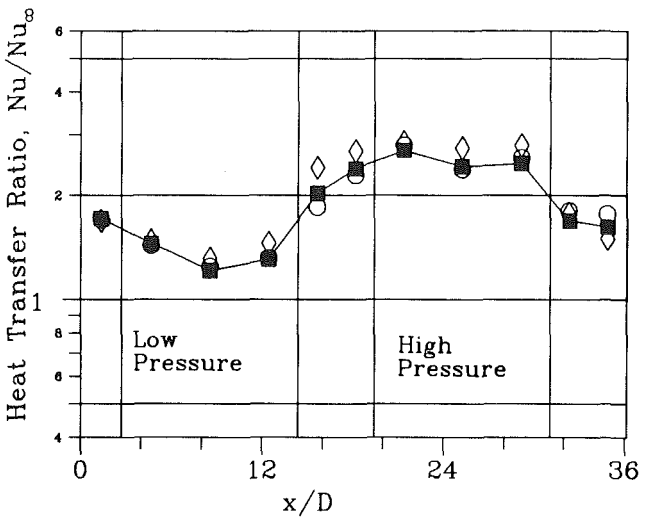

Fig. 8(b) Leading surface

Fig. 8 Effect of wall-to-coolant density difference on heat transfer ratio; Re = 25,000, $R_0 = 0.24$, $R/D = 49$

stantially different, depending on local flow conditions (i.e., due to differing near-wall shear gradients).

Varying Density Ratio. The inlet density ratio, $(\Delta\rho/\rho)_i$, was varied from 0.07 to 0.22 for this series of flow conditions. The Reynolds number, rotation number, and radius ratio were held constant at the baseline values of 25,000, 0.24, and 49, respectively. Heat transfer was obtained at a fixed rotation number and, therefore, conclusions can be obtained regarding the effects of buoyancy for flow conditions near the rotating baseline flow conditions.

Increasing the inlet density ratio (i.e., the wall-to-coolant temperature difference) from 0.07 to 0.22 causes the heat transfer ratio in the first passage to increase on all trailing surfaces by as much as 25 percent (Fig. 8*a*) and on the leading surfaces by as much as 20 percent (Fig. 8*b*). The exception to the general increase in heat transfer with increasing density ratio occurred near the inlet of the first passage on the leading side, where the heat transfer ratio is observed to be relatively unaffected by varying density ratio. Heat transfer in the second, inward flowing passage on the low-pressure side increased as much as 70 percent with increases in the temperature difference (Fig. 8*a*). (Larger effects of density ratio were obtained for a rotation number of 0.35.)

Varying Rotation Number and Density Ratio. Additional data from parametric variations of density ratio and rotation parameter were necessary to determine the effects of rotation and buoyancy over the range of interest. The inlet density ratio was varied from 0.07 to 0.23 for selected rotation numbers. Heat transfer results from these experiments were plotted versus inlet density ratio with rotation number as a secondary variable. The variation of heat transfer ratio with density ratio (not shown) was extrapolated for each value of the rotation number to obtain the value of the heat transfer ratio at a density ratio of 0.0 (i.e., limit as ΔT approaches 0.0). The heat transfer results obtained from the experiments plus the extrapolated values for a density ratio of 0.0 (dashed lines) are presented in Fig. 9 as the variation of heat transfer ratio with the rotation number with the density ratio as the secondary variable for three streamwise locations for the first and the second passage. The following discussion will concentrate on the differences in the heat transfer from the first and second passages.

High Pressure Surfaces. Heat transfer results from the high pressure side of the first and second passages is shown in Fig. 9(*a*) and 9(*b*) for ranges of rotation number and density ratio. Note that no effect of density ratio on the heat transfer ratio was expected (e.g., Wagner et al., 1991b) for a rotation number of 0 when film properties are used for the dimensionless heat transfer and flow parameters. Increasing the rotation number causes local increases in the heat transfer in the first passages by as much as 75 percent compared to the heat transfer for a rotation number of 0. Whereas the heat transfer ratios for the high-pressure surfaces in the first passage increase sharply with increases in either the density ratio or the rotation number, the heat transfer ratios in the second passage are less affected (increases of 30 to 35 percent) by variations of either parameter.

Low Pressure Surfaces. The heat transfer from the low-pressure surfaces from the first and second passages (Figs. 9*a* and 9*b*) is more complex than that from the high-pressure surfaces. The heat transfer ratio in the first passage decreases with increasing rotation number for low values of rotation number (i.e., $\Omega D/V < 0.25$ at the downstream location) and then increases with increases in rotation for larger values of rotation number depending on density ratio. The heat transfer ratio increases with increases in the density ratio, similar to the results obtained for the trailing surface of the first passage.

The effects of density ratio on the heat transfer ratio are larger in the second passage with radially inward flow than in the first passage (a factor of three for the second passage compared to a factor less than two for the first passage), for inlet density variations from 0.07 to 0.23. Note that the local density ratios in the second passage will be about half of the inlet values.

The more complicated heat transfer distributions on the low-pressure surfaces of the coolant passages are attributed to (1) the combination of buoyancy forces and the stabilization of the near-wall flow for low values of the rotation number; (2) the developing, Coriolis driven-secondary flow cells; (3) the increases in flow reattachment lengths after trips for the larger values of the rotation number. It is postulated that the relatively small effects from variations in density ratio near the inlet of the second passage and the large effects near the end of the second passage are due to the development of the near-wall thermal layers (i.e., thickening for the normal trip model compared to thinning for the smooth wall model). Near the inlet of the second passage, the thermal layers are postulated to be thin because of the strong secondary flows in the first turn

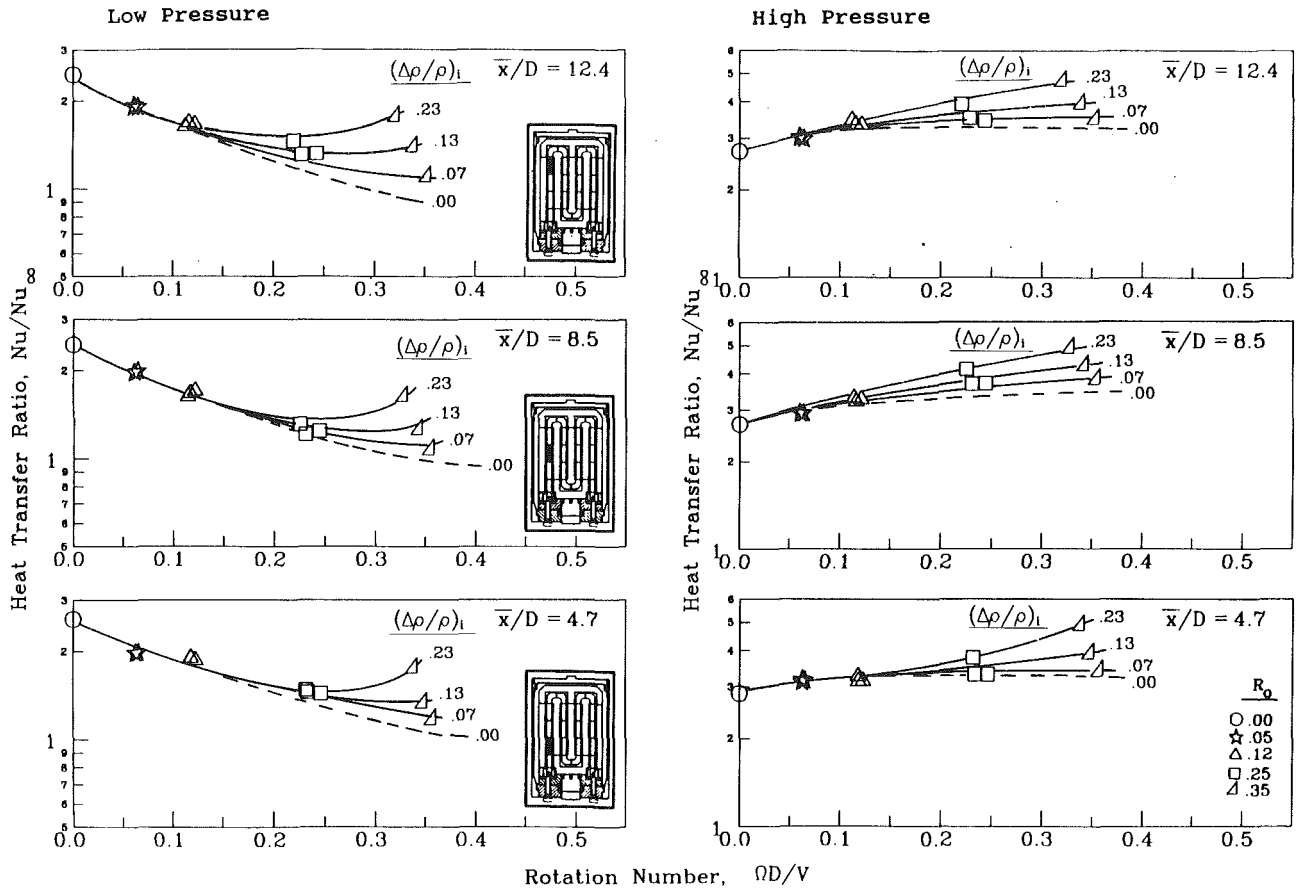

Fig. 9(*a*) Effect of rotation number and density ratio on heat transfer ratios in the first passage; Re = 25,000, *R/D* = 49

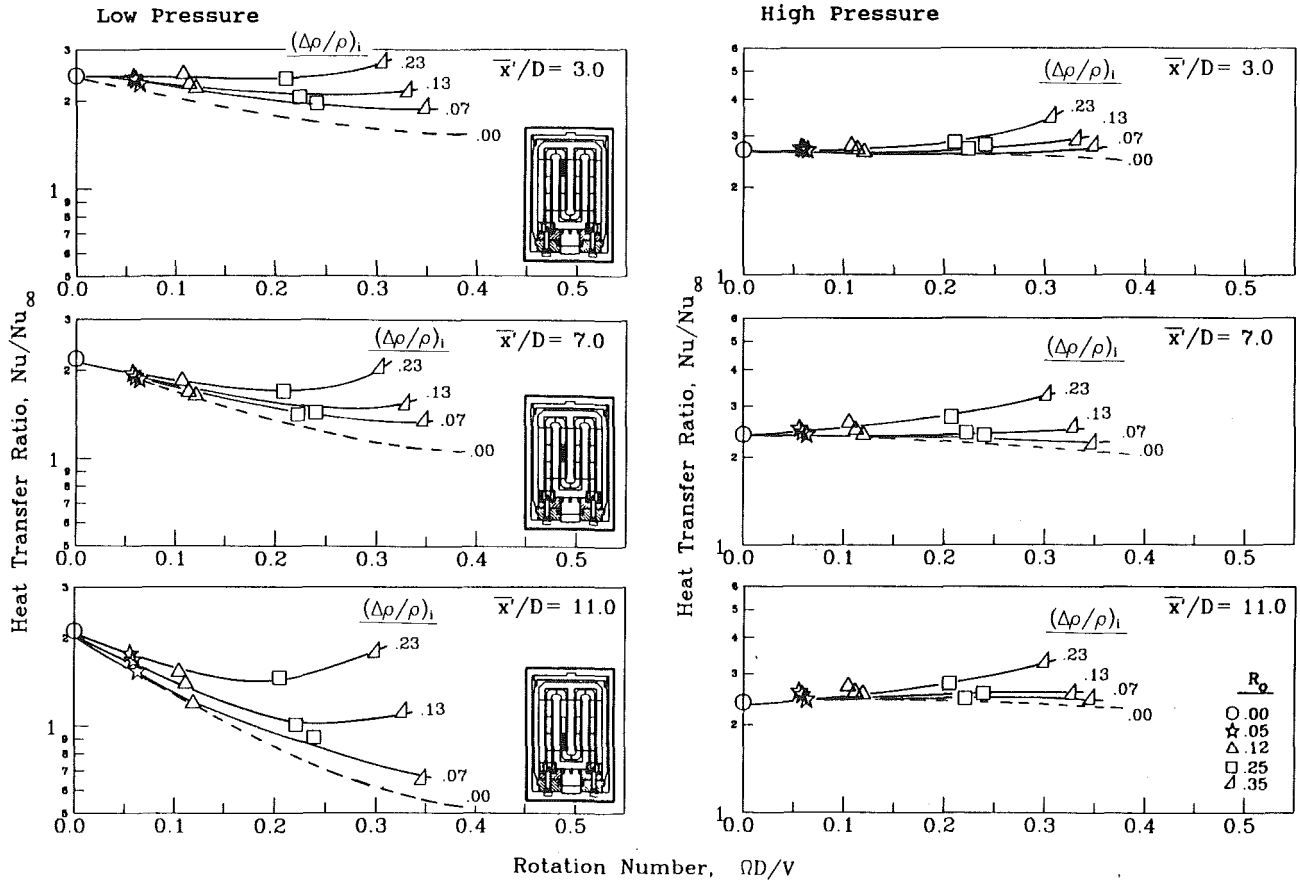

Fig. 9(*b*) Effect of rotation number and density ratio on heat transfer ratios in the second passage; Re = 25,000, *R/D* = 49

region. With increasing x/D, the turn-dominated secondary flows diminish and the counteracting effect of buoyancy and the Coriolis-generated secondary flow increases.

Correlating Parameters

The analysis of the equations of motion for flow in rotating radial passages by Suo (1980), discussed above, showed that (1) the cross-stream flows will be proportional to the rotation number, $\Omega D/V$, and (2) the buoyant flows will be proportional to the buoyancy parameter, $(\Delta\rho/\rho)\ (R/D)\ (\Omega D/V)^2$. The combined effect of the cross-stream flows and the buoyant flows is not easily ascertained from the equations of motion. The preceding discussions indicate that the combined effects are quite complex and are a strong function of flow direction. Therefore, the flow direction is also considered in the following paragraphs.

The buoyancy parameter, discussed previously, is similar to the ratio of the Grashof number (with a rotational gravitation term, $R\Omega^2$) to the square of the Reynolds number and has previously been used to characterize the relative importance of free- and forced-convection in the analysis of stationary mixed-convection heat transfer. Guidez (1989) used a similar analysis to establish appropriate flow parameters for the presentation of his results. These parameters, $\Omega D/V$ and $(\Delta\rho/\rho)\ (R/D)\ (\Omega D/V)^2$, will also be used in the present discussion of the effects of Coriolis and buoyancy forces on the heat transfer for inward and outward flow directions.

The data were analyzed to determine the effects of flow direction (radially inward or radially outward) on the heat transfer characteristics and to determine the differences between the first passage with outward flow downstream of an inlet, the second passage with inward flow downstream of a 180 deg turn, and the third passage with outward flow downstream of a 180 deg turn. The variations of heat transfer ratio with buoyancy parameter for the heated surface at the most downstream location from the inlet or a turn for each of the three passages are shown in Fig. 10 with heat transfer ratios obtained in the same model with smooth surfaces.

The data presented in Fig. 9 showed that the effects of Coriolis and buoyancy forces are coupled in the first two passages through the entire operating range investigated. The results from Fig. 9 are presented in Fig. 10 as the variation of the heat transfer ratio with the buoyancy parameter based on the local density ratio and radius, R. Thus, the range of the buoyancy parameter decreases with increasing values of x/D (i.e., decreasing temperature difference with increasing x). The temperature differences, $T_b - T_w$, at the end third passage were only one-third of the inlet value.

Heat transfer distributions from the low-pressure surfaces of each of the three passages exhibit a similar relationship with the buoyancy parameter. Heat transfer for all values of $(\Delta\rho/\rho)_i$ decreases with increasing values of buoyancy between 0.0 and 0.15. Heat transfer subsequently increases again with increasing values of buoyancy. Heat transfer on the low-pressure surfaces of rotating coolant passages is governed by complex relationships of streamwise location, rotation number, and buoyancy parameter.

The heat transfer results from the high-pressure surfaces in the first passage are better correlated by the buoyancy parameter. The second passage with radially inward flow had different heat transfer characteristics than the first and third passages with radially outward flow. Whereas the heat transfer

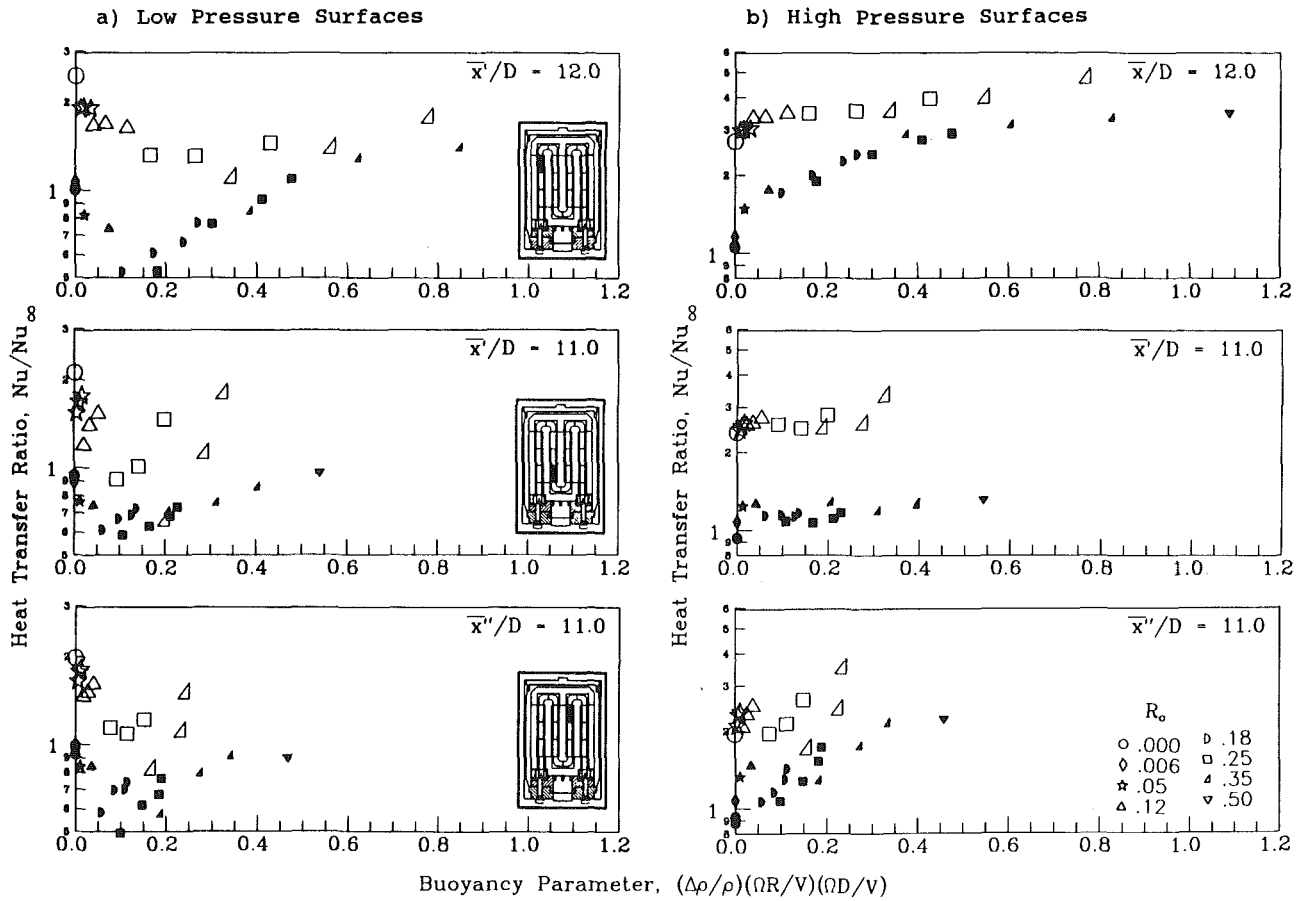

Fig. 10 Comparison of heat transfer ratios on the first, second and third passages; open symbols—normal trip data, solid symbols—smooth wall data

ratios for conditions of large density ratios for the high-pressure surfaces of the first and third passages generally increased with the buoyancy parameter, the heat transfer in the second passage was relatively less affected by buoyancy parameter for values of buoyancy greater than 0.05. These results for coflowing and counterflowing buoyancy effects on the high pressure surfaces are generally consistent with the stationary combined free- and forced-convection experiments of Eckert et al. (1953). They measured decreased levels of heat transfer for the coflowing condition (i.e., similar to that of radially inward flow in rotating systems).

The heat transfer results for surfaces with trips show trends that are similar to those observed for the same model with smooth surfaces. It is also interesting to note that the levels of heat transfer augmentation obtained in the first passage of the model with trips are only 10 to 30 percent greater than those for the smooth model for values of the buoyancy parameter greater than 0.4. The difference would be even less if the heat transfer coefficient were based on the total surface area (i.e., including trip area) instead of the projected surface area.

Comparison with Previous Rotating Experimental Results

Results from this study have shown that rotational and buoyancy forces strongly influence turbulent heat transfer in rotating passages with trips normal to the flow for conditions found in gas turbine blades. The heat transfer results from stationary models with similar geometries agree quite well with the present work, i.e., Boyle (1984), Han et al. (1986), and Metzger et al. (1988). The heat transfer results from rotating models are more difficult to compare because of differences in the geometries and the buoyancy conditions. However, the heat transfer results of Clifford (1985) and Taslim et al. (1991) obtained with rotation will be related to the present results.

Clifford (1985) obtained heat transfer coefficients in a multipass model with trips normal to the flow using transient measurement techniques. Direct comparison with Clifford's results is not possible due to the lack of specific model geometry and precise test conditions. Clifford observed increases in heat transfer of 36 percent on the pressure side of the model and decreases of 24 percent of the suction side of the first passage. Clifford's trends are in general agreement with the present results. However, the effects of rotation measured by Clifford are somewhat less than those measured in the present experiment. Clifford's heat transfer data from the second, inward flowing passage were generally consistent with the present results.

Taslim et al. (1991) also obtained heat transfer results in a rotating square passage with trips normal to the flow for several trip heights. Trips were square-edged and were mounted on two opposing walls (one heated). The remaining smooth walls and one of the walls with trips were unheated. Although all of the heat transfer results with rotation measured by Taslim were greater than the stationary value for $Re_d = 24{,}800$ and $e/D = 0.133$, the leading side heat transfer coefficients with rotation decreased with increasing rotation rate. This effect is similar to that observed by Clifford and in the present results. Taslim also measured increases in heat transfer, for most Reynolds numbers, on the trailing side of the model with increases in rotation rate for low values of rotation rate followed by relative decreases for further increases in rotation. The observations of Taslim on the trailing side of the passage are inconsistent with the present experiment where heat transfer was observed to increase with increases in rotation rate for a similar range of rotation number. The differences in the measured effects of rotation on the trailing side heat transfer are attributed to the differences in trip geometry ($e/D = 0.1$ and round trips for the present work and $e/D = 0.133$ and square trips for Taslim) and to the differences in the wall boundary conditions ($T_w = \text{const}$ for the present work and $q_w = \text{const}$ on one wall for Taslim). Additional work is necessary to determine the effects of model geometry and thermal boundary conditions with rotation.

Concluding Comments

Results from the present experiments with normal trips in rotating, radial, square coolant passages show that Coriolis forces and buoyancy effects can strongly influence heat transfer. The heat transfer coefficients on surfaces with trips were especially sensitive to rotation and buoyancy, decreasing as much as to one-third the stationary value due to rotation and increasing by a factor of 2.5 due to buoyancy. These effects were greater than measured previously for a smooth wall model. The maximum heat transfer coefficients on the pressure side of the coolant passage at the highest values of the buoyancy parameter were not much greater than obtained for a smooth wall model. The conclusion from this second observation is that some trips in the coolant passage can be relatively ineffective for certain combinations of coolant passage geometries and rotating flow conditions.

The comparison of results from the present experiments with previous results show that flow and heat transfer in rotating coolant passages can be complex, especially when no single flow mechanism dominates the heat transfer process. The present results were obtained for normal trips with values of trip pitch to trip height ($P/e = 10$) and trip height to coolant passage width ($e/D = 0.1$), typical of those used in coolant passages. This trip geometry generally produces heat transfer coefficients two times those obtained for smooth wall passages. The wide range of heat transfer coefficients obtained (0.65 to 4.5 times the values for fully developed flow in smooth passages) indicates that it is prudent to have a data base available for the design of specific coolant passages used in rotating turbine blades.

This paper has presented an extensive set of experimental data from heat transfer experiments in a rotating square passage with trips normal to the flow direction. Following are observations regarding the effects of forced convection, Coriolis forces, buoyancy, and flow direction on the heat transfer:

1 Changes in either the density ratio or the rotation number caused large changes in the heat transfer coefficients in passages with trips for flow radially outward or for flow radially inward.

2 The heat transfer ratio is a complex function of buoyancy parameter and density ratio on the low-pressure surfaces of the coolant passages, regardless of flow direction.

3 The heat transfer ratio on the high-pressure surfaces was significantly affected by flow direction. The heat transfer was a strong function of the buoyancy parameter for the high-pressure surfaces in the first and third passages with flow radially outward. However, the heat transfer was relatively unaffected by the buoyancy parameter for flow radially inward.

4 Increasing the density ratio with high rotation numbers generally caused an increase in heat transfer. However, the increase in heat transfer for the inward flowing passage was generally greater than that for outward flow.

5 The maximum increases in heat transfer in passages with normal trips with increases in density ratio were greater than the maximum increases measured from the same model with smooth surfaces.

6 Heat transfer ratios from rotating passages with normal trips at the highest rotation numbers and buoyancy parameters were not significantly greater than the heat transfer ratios measured in the same model with smooth surfaces for the same parameters.

Acknowledgments

The work published in this paper was supported by the NASA/Lewis Research Center under the HOST Program, Contract No. NAS3-23691 to the Pratt and Whitney Commercial Engine Business/Engineering Division, and by the United Technology Corporation's independent research program. The heat transfer models used in this program were furnished by the Pratt and Whitney Commercial Products Division. The experimental portion of the program was conducted at the United Technologies Research Center. The authors gratefully acknowledge the assistance of Ms. S. Orr (UTRC) and Mr. J. Minguy (UTRC) in the performance of this program. The authors are appreciative of the support and guidance by the HOST management team at NASA/Lewis Research Center, and by their colleagues at P&W and UTRC.

References

Boyle, R. J., 1984, "Heat Transfer in Serpentine Passages With Turbulence Promoters," ASME Paper No. 84-HT-24; NASA Technical Memorandum 83614.

Brundrett, E., and Burroughs, P. R., 1967, "The Temperature Inner-Law and Heat Transfer for Turbulent Air Flow in a Vertical Square Duct," *Int. J. Heat Mass Transfer*, Vol. 10, pp. 1133–1142.

Clifford, R. J., 1985, "Rotating Heat Transfer Investigations on a Multipass Cooling Geometry," AGARD Conference Proceedings No. 390: Heat Transfer and Cooling in Gas Turbines, May 6–10.

Eckert, E. R. G., Diaguila, A. J., and Curren, A. N., 1953, "Experiments on Mixed-, Free- and Forced-Convective Heat Transfer Connected With Turbulent Flow Through a Short Tube," NACA Technical Note 2974.

Guidez, J., 1989, "Study of the Convective Heat Transfer in Rotating Coolant Channel," ASME JOURNAL OF TURBOMACHINERY, Vol. 111, pp. 43–50.

Han, J. C., Park, J. S., and Ibrahim, M. Y., 1986, "Measurement of Heat Transfer and Pressure Drop in Rectangular Channels With Turbulence Promoters," NASA Contractor Report 4015.

Hart, J. E., 1971, "Instability and Secondary Motion in a Rotating Channel Flow," *J. Fluid Mech.*, Vol. 45, Part 2, pp. 341–351.

Iskakov, K. M., and Trushin, V. A., 1983, "Influence of Rotation on Heat Transfer in a Turbine-Blade Radial Slot Channel," *Izvestiya VUZ. Aviatsionnaya Tekhnika*, Vol. 26, No. 1, pp. 97–99.

Johnson, B. V., 1978, "Heat Transfer Experiments in Rotating Radial Passages With Supercritical Water," *ASME Heat Transfer*, bound proceedings from 1978 ASME Winter Annual Meeting.

Johnston, J. P., Halleen, R. M., and Lezius, D. K., 1972, "Effects of Spanwise Rotation on the Structure of Two-Dimensional Fully Developed Turbulent Channel Flow," *J. Fluid Mech.*, Vol. 56, Part 3, pp. 533–557.

Kays, W. M., and Perkins, H. C., 1973, "Forced Convection, Internal Flow in Ducts," *Handbook of Heat Transfer*, W. M. Rohsenow and J. P. Hartnett, eds., McGraw-Hill, pp. 7–28 and 7–33.

Lokai, V. I., and Gunchenko, E. I., 1979, "Heat Transfer Over the Initial Section of Turbine Blade Cooling Channels Under Conditions of Rotation," *Therm. Engng.*, Vol. 26, pp. 93–95.

Metais, B., and Eckert, E. R. G., 1964, "Forced, Mixed, and Free Convection Regimes," ASME *Journal of Heat Transfer*, Vol. 64, pp. 295–296.

Metzger, D. E., Fan, C. S., and Plevich, C. W., 1988, "Effects of Transverse Rib Roughness on Heat Transfer and Pressure Losses in Rectangular Ducts With Sharp 180 Degree Turns," AIAA Paper No. 88-0166.

Moore, J., 1967, "Effects of Coriolis on Turbulent Flow in Rotating Rectangular Channels," M.I.T. Gas Turbine Laboratory Report No. 89, Cambridge, MA.

Mori, Y., Fukada, T., and Nakayama, W., 1971, "Convective Heat Transfer in a Rotating Radial Circular Pipe (2nd Report)," *Int. J. Heat Mass Transfer*, Vol. 14, pp. 1807–1824.

Morris, W. D., and Ayhan, T., 1979, "Observations on the Influence of Rotation on Heat Transfer in the Coolant Channels of Gas Turbine Rotor Blades," *Proc. IMechE*, Vol. 193, pp. 303–311.

Morris, W., 1981, *Heat Transfer and Fluid Flow in Rotating Coolant Channels*, Research Studies Press.

Rothe, P. H., and Johnston, J. P., 1979, "Free Shear Layer Behavior in Rotating Systems," ASME *Journal of Fluids Engineering*, Vol. 101, pp. 117–120.

Schlichting, H., 1968, *Boundary-Layer Theory*, McGraw-Hill, New York, 6th ed., p. 575.

Suo, M., 1980, Unpublished Notes, United Technologies Research Center.

Taslim, M. E., Rahman, A., and Spring, S. D., 1991, "An Experimental Investigation of Heat Transfer Coefficients in a Spanwise Rotating Channel With Two Opposite Rib-Roughened Walls," ASME JOURNAL OF TURBOMACHINERY, Vol. 113, pp. 75–82.

Wagner, J. H., Johnson, B. V., and Hajek, T. J., 1991a, "Heat Transfer in Rotating Passages With Smooth Walls and Radial Outward Flow," ASME JOURNAL OF TURBOMACHINERY, Vol. 113, pp. 42–51.

Wagner, J. H., Johnson, B. V., and Kopper, F. C., 1991, "Heat Transfer in Rotating Serpentine Passages With Smooth Walls," ASME JOURNAL OF TURBOMACHINERY, Vol. 113, pp. 321–330.

Wagner, R. E., and Velkoff, H. R., 1972, "Measurement of Secondary Flows in a Rotating Duct," ASME *Journal of Engineering for Power*, Vol. 94, pp. 261–270.

An Attempt to Uncouple the Effect of Coriolis and Buoyancy Forces Experimentally on Heat Transfer in Smooth Circular Tubes That Rotate in the Orthogonal Mode

W. D. Morris
Professor and Head of Department of Mechanical Engineering.

R. Salemi
Research Assistant.

University College of Swansea, Singleton Park, Swansea, SA2 8PP, United Kingdom

This paper reports the results of an experimental investigation of the combined effect of Coriolis and buoyancy forces on forced convection in a circular tube that rotates about an axis orthogonal to its centerline. The experiment has been deliberately designed to minimize the effect of circumferential conduction in the tube walls by using material of relatively low thermal conductivity. A new correlating parameter for uncoupling the effect of Coriolis forces from centripetal buoyancy is proposed for the trailing and leading edges of the tube. It is demonstrated that enhanced heat transfer on the trailing edge occurs as a result of rotation. On the leading edge significant reductions in heat transfer compared to the zero rotation case can occur, but with possible recovery at high rotational speeds.

Introduction

For over a decade the quest for improved aero gas turbine power and fuel economy has stimulated much research interest in the design of high-performance cooling systems for rotor blade airfoil sections. Current state-of-the-art cooling systems require complex air flow passages to be incorporated inside the rotating airfoil section. These passages, channeling compressor-bled air in a spanwise direction along the blade, may have a variety of smooth or artificially roughened cross-sectional shapes with interconnecting bends if the coolant flows in a multipass manner.

The internal airways constrain the cooling air to spin with the blade. Consequently, as the coolant flows through the blade, it experiences Coriolis and centripetal forces, which combine to change the nature of the flow field relative to the nonrotating case and therefore the cooling performance.

Because the blade airways tend to channel the coolant in a spanwise direction from the root of the blade toward its tip (or indeed vice versa in the case of multipass cooling geometries), a great deal of interest has been focused on studying the nature of flow and heat transfer in straight ducts rotating about a perpendicular axis, as illustrated in Fig. 1. Although a duct of circular cross section is shown, other cross-sectional shapes are of practical interest.

The theoretical and experimental investigations that have been reported in the technical literature (see, for example, [1–23]) have confirmed the following general flow features of this rotating geometry. Coriolis forces generate a cross-stream secondary motion by which fluid in the vicinity of the centerline of the duct is driven toward the trailing edge, as shown in Fig. 1. To preserve continuity, a return flow in the near-wall cir-

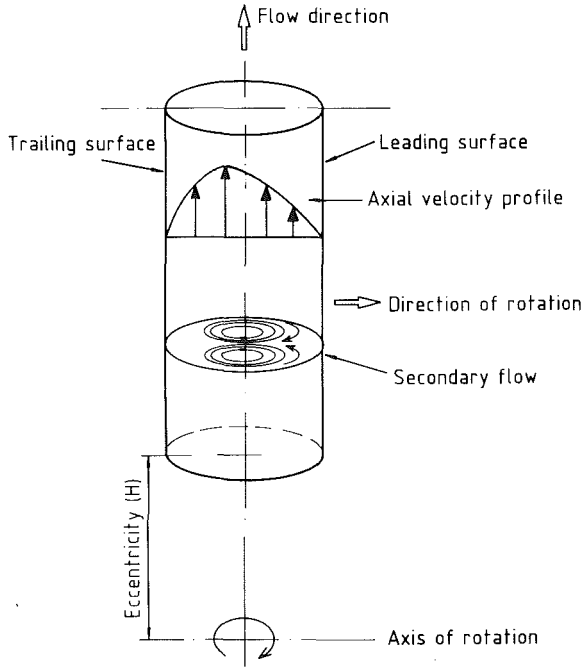

Fig. 1 Fundamental flow geometry with orthogonal-mode rotation

Contributed by the International Gas Turbine Institute and presented at the 36th International Gas Turbine and Aeroengine Congress and Exposition, Orlando, Florida, June 3–6, 1991. Manuscript received at ASME Headquarters January 25, 1991. Paper No. 91-GT-17. Associate Technical Editor: L. A. Riekert.

cumferential direction occurs, taking fluid toward the leading edge. Additionally, the axial velocity profile distorts and departs from a condition of axisymmetry with the point of maximum velocity moving toward the trailing edge, as again shown in the figure. The net effect of the Coriolis force is to sustain a double helix type of flow structure. There is also evidence to suggest that the nature of the turbulent structure of the flow is dependent on rotation; see Johnston et al. [5].

The flow structure outlined above influences convective heat transfer at the interfacing surface of the duct and the fluid when duct wall heating is present. The secondary flow tends to "wash" the trailing edge region with central core fluid that is relatively cool, thus promoting better cooling in relation to the leading edge surface.

Additionally with heated flow, density gradients interact with the centripetal acceleration field experienced by the fluid to produce a buoyancy effect. This rotationally induced free convection motion encourages the warmer and less dense fluid to move toward the axis of rotation.

The complex three-dimensional flow structure created by the combination of externally generated pressure gradients along the tube axis with the Coriolis forces and the centripetal buoyancy gives rise to circumferential as well as axial variations in the local heat transfer at the inside surface of the tube. A number of research publications have experimentally confirmed the relative enhancement of local heat transfer on the trailing edge of the tube in relation to the leading edge. However, the leading edge heat transfer has been shown either to experience no change in comparison with nonrotating forced convection or, in some cases, a reduction. Theoretically a reduction in leading edge heat transfer would be expected due to the Coriolis-driven return secondary flow along the wall from the trailing edge region (see Fig. 1).

If the tube wall material used for experimental studies of the effect of rotation is metallic, then the asymmetric heat transfer around the circumference will tend to be smoothed out due to wall conduction. Thus the relative difference of heat transfer around the girthwise direction will be functionally related to the tube wall characteristics in some way. This will be an important point in relation to the turbine blade application. Also the comparison of experimental data from different sources will need to take account of this feature.

The present paper reports the results of an experimental study using smooth circular tubes having low wall conductivity to suppress deliberately the smoothing influence of high conductivity walls on the rotationally driven circumferential variation of heat transfer. It is interesting to note that this style of heat transfer experiment is more analogous to the naphthalene mass transfer simulation of heat transfer technique used by some authors (i.e., Mori and Nakayama [2]) since, by definition, wall conduction does not occur with a uniform wall temperature boundary condition.

The main objective of the present investigation was to acquire good quality data, not bedeviled by the wall conduction effect mentioned above, with which to examine the possibility of empirically uncoupling the combined influence of Coriolis forces and centripetal buoyancy and hence the generation of design-type correlations. Additionally the data were planned to be used to aid the validation of a finite element CFD code being developed in parallel with the experimental program.

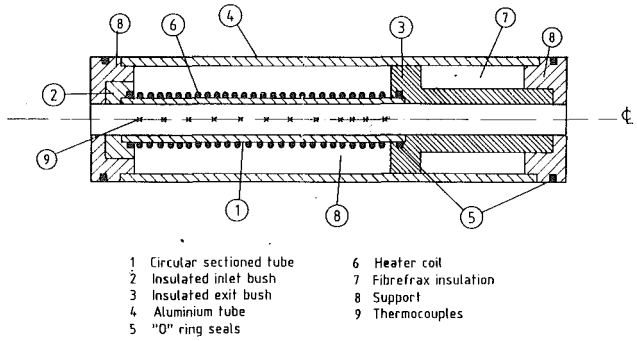

Fig. 2 Test section construction

Apparatus

The constructional details of test section used are shown in Fig. 2. The actually heated circular sectioned tube (1) used was 10 mm in diameter, nominally 143 mm long with a 1.5 mm wall thickness, and made from a bar of machinable ceramic glass having a thermal conductivity of 1.3 W/mK. This tube was held between inlet and exit insulated support bushes, (2) and (3) respectively, to give an actively heated test length of 130 mm. The support bushes and test section were enclosed in an aluminum tube (4) fitted with external "O" ring seals (5) at both ends.

Twelve type K thermocouples were attached, at a depth of 1 mm below the outer diameter, to each of two diametrically opposed edges of the test section to form, when fitted into the rotating test facility described below, the leading and trailing edges of the tube. The axial location of these thermocouples is shown in Fig. 2. Similar thermocouples, with their sensing beads located on the duct axis in the inlet and exit bushes, permitted the air temperature rise to be assessed.

The tube was electrically heated with Nichrome resistance wire spirally wound into a screw thread machined on the outer surface of the tube. All thermocouple and heater cables were brought from the test assembly through holes machined in the exit support bush. The space between the outer surface of the glass tube and the inner surface of the encapsulating sheath was filled with Fiberfrax thermal insulation to minimize external heat loss from the module.

The mechanical layout of the rotating test facility into which the test module was fitted is shown in Fig. 3. A hollow air delivery plenum chamber (1) was bolted to a shaft (2), which itself was supported between two Plummer block bearings (3). The shaft/plenum chamber assembly was driven by means of a controllable electric motor (4) via a toothed belt drive pulley system (5). The right-hand side of the shaft, as viewed in the figure, was bored to permit the passage of air to the plenum chamber and hence to the actual instrumented test geometry (6) used. The test geometry could be fitted into the plenum at a specified eccentricity to the axis of rotation. A rotary seal (7), fitted over the extreme right-hand end of the shaft assem-

Nomenclature

Bu = buoyancy parameter
c_p = constant-pressure specific heat
d = tube diameter
H = eccentricity
k = thermal conductivity
n = buoyancy gradient
Nu = local Nusselt number
Pr = Prandtl number
$\dot{q}$ = heat flux
Re = Reynolds number
Ro = Rossby number
T_B = local fluid bulk temperature
T_W = local wall temperature
w = mean axial velocity
z = axial location
Z = nondimensionalized axial location
β = volume expansion coefficient
ϵ = eccentricity parameter
μ = absolute viscosity
ρ = density
Φ = functional relationship
ω = angular velocity

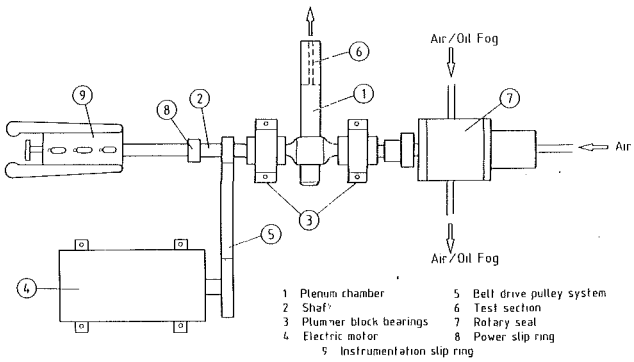

Fig. 3 Test facility

bly, permitted pressurized air to be fed to the plenum chamber and hence through the test section assembly, finally exhausting to atmosphere.

An electrical two channel power slip ring (8) permitted current from a Variac transformer supply to be fed to the heater section with the heater power consumption being measured with a conventional wattmeter.

A silver/silver-graphite multichannel instrumentation slip ring (9) was used to take the thermocouple signals from the rig to a Solatron System 35 data recording and processing system and a magnetic encoder and timer counter fitted to this slipring permitted the speed of the rotor to be measured.

The instrumented test module was actually fitted into the rotating plenum chamber to give an eccentricity, measured at the commencement of the actively heated test section, of 270 mm.

Pressurized dry and oil free air from a central laboratory facility could be fed to the rotary seal inlet and monitored via an Annubar differential pressure flow meter. Valves located upstream of the rotating facility permitted the control of the air flow through the test section.

Method of Data Processing and Presentation

Experiments were conducted with flow rates giving Reynolds numbers of 15,000, 20,000, 25,000, and 30,000, respectively, based on inlet conditions to the test section. Adjustments to flow rates were made to ensure these values were preserved to within ± 1 percent. The rotational speeds used were 0, 1000, 2000, and 2700 rpm, respectively, and for each speed/Reynolds number combination five heater power settings were examined.

For any test, owing to various losses, the power dissipated by the heater is not entirely transferred to the fluid. Axial heat conduction along the tube walls (although relatively small for the glass–ceramic test section) together with external loss from the exterior surface of the module account for these losses. The external heat loss is dependent on the rotational speed and this was estimated from a series of calibration tests undertaken prior to the main experimental program.

By dividing the test section into a number of axial elements, it was possible to estimate the heat flux to the fluid by assuming the energy generated by the heating element was balanced against that which entered the fluid, that which was axially conducted, and that which was externally lost.

The axial conduction was estimated from the known axial wall temperature measurements and the external loss by assuming the loss to be proportional to the locally prevailing difference in temperature between the wall and the outside ambient temperature. The implied proportionality constant was determined from the earlier performed calibration tests mentioned above.

Once the axial distribution of heat flux had been determined, the bulk temperature variation along the test section was calculated via a simple enthalpy balance. A one-dimensional correction to the measured wall temperatures was made in order to specify the actual inner surface temperature. Finally the known flux, wall, and fluid bulk temperatures permitted calculation of the local heat transfer coefficient distribution along the test section on either the leading or trailing edges. Unaccountable energy losses with this method of data reduction were found to be less than 10 percent in all cases.

As outlined above, the customary forced convection mechanism present in the tube is modified due to the presence of Coriolis forces and centripetal buoyancy. The Coriolis effects may be expressed nondimensionally in terms of a Rossby number, Ro, defined as:

$$\mathrm{Ro} = w/\omega d \quad \text{(Rossby number)} \tag{1}$$

and the centripetal buoyancy via a buoyancy parameter, Bu, defined as

$$Bu = \beta(T_W - T_B) \quad \text{(buoyancy parameter)} \tag{2}$$

together with an eccentricity parameter, ϵ, defined as

$$\epsilon = H/d \quad \text{(eccentricity parameter)} \tag{3}$$

where all symbols are as defined in the Nomenclature section.

The net result of including these additional groups into the well-known nondimensional heat transfer relationships for forced convection in ducts is an equation, which may be applied to any circumferential location on the tube wall, having the structure

$$\mathrm{Nu} = \Phi(\mathrm{Re}, \mathrm{Pr}, \mathrm{Ro}, Bu, \epsilon, Z) \tag{4}$$

where

$$\mathrm{Nu} = \dot{q}d/k(T_W - T_B) \quad \text{(Nusselt number)} \tag{5}$$

$$\mathrm{Re} = wd\rho/\mu \quad \text{(Reynolds number)} \tag{6}$$

$$\mathrm{Pr} = \mu c_p/k \quad \text{(Prandtl number)} \tag{7}$$

and

$$Z = z/d \quad \text{(downstream parameter)} \tag{8}$$

with all symbols again defined in the Nomenclature.

The results of all tests undertaken were evaluated on a local basis using the nondimensional groups described above. All property values needed were calculated at the loyally prevailing bulk temperature of the fluid. An assessment of the interaction of the Coriolis force and centripetal buoyancy with normal ducted forced convection is given in the next section.

Results and Discussion

Experiments with zero rotational speed were undertaken initially and the results from these tests demonstrated that the wall temperatures measured individually on the leading and trailing edges were indistinguishable for the entire range of Reynolds numbers and heater power settings used. The processed local Nusselt numbers along the test section were consistent with a conventional forced convection behavior in circular tubes. An initial high local Nusselt number, in the immediate entry region, decayed toward a fully developed value consistent with the well-known Dittus–Boelter [24] recommendation for fully developed turbulent flow. As is well known with forced convection ducted flow experiments, the final 20 percent of the active length of the test section is affected by exit loss effects and for this reason this zone has been excluded from further analysis.

It was also noted that tests undertaken at specified values of Reynolds number, but with various heater power settings, gave extremely similar local Nusselt number profiles along both instrumented edges of the test section. This confirmed that temperature-induced property variations were being adequately taken into account by the normal processes of nondimensionalization. This point will be raised in more detail later when the detailed analysis of the effect of rotation is presented.

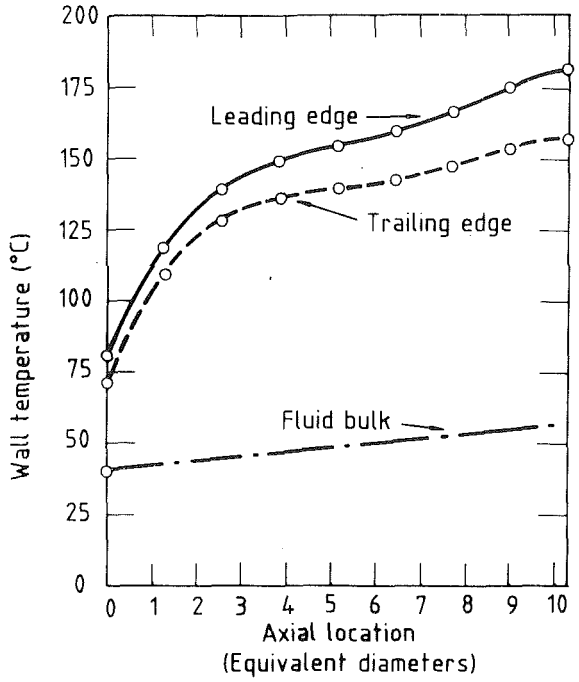

Fig. 4 Typical leading and trailing edge wall temperature distributions (nominal Reynold's number = 25,000; rotational speed = 2700 rpm; nominal mean heat flux = 18,300 W/m²)

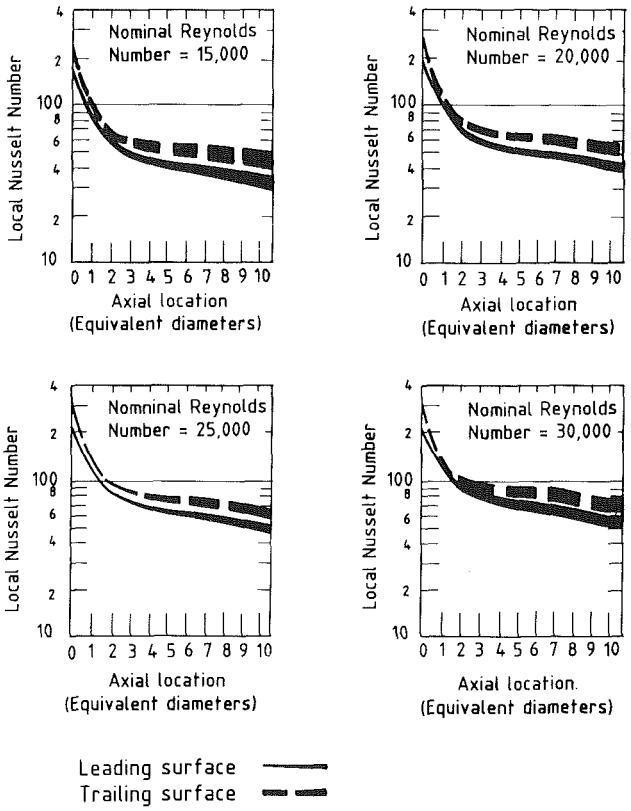

Fig. 5 Typical effect of rotation on leading and trailing edge heat transfer at 2700 rpm

Figure 4 shows the typical form of the measured wall temperature on the leading and trailing edges when rotation was introduced. The trailing edge was consistently confirmed to run at a significantly lower temperature than its leading counterpart. Indeed the level of difference was noted to be greater

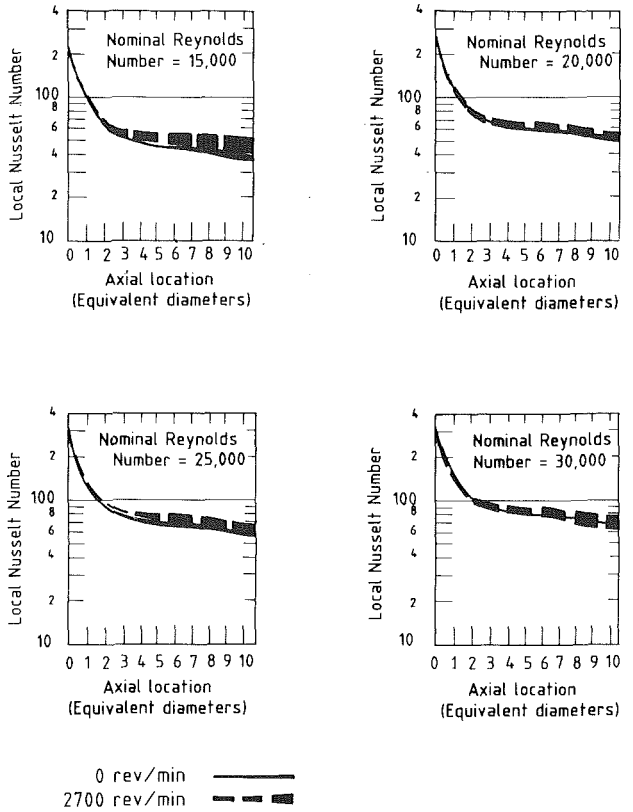

Fig. 6 Comparison of effect of rotation on trailing edge heat transfer in comparison with zero speed

than those experienced with other similar tests undertaken within the present overall research program (see [14, 18, 20], for example) but with metallic walls. This appears to add confirmation to the problem that motivated the present series of tests, namely that wall conduction seems to equalize out secondary flow created circumferential variations in heat transfer.

The local Nusselt numbers along the test section were evaluated and Fig. 5 illustrates, for a rotational speed of 2700 rpm, the very significant relative difference in leading and trailing edge response to rotation. The trailing edge is far better cooled at all Reynolds number values. This relative difference is mainly driven by the Coriolis-induced secondary flow described earlier, but it is important to note the band widths of the individual groups of results shown in Fig. 5. Each band of data corresponds to a specified Reynolds number and rotational speed and this is tantamount to fixing the Rossby number simultaneously with the Reynolds number. The individual lines in each band reflect the heater power setting used. Thus the normal property variations due to temperature are not taken into account by the process of nondimensionalization as was seen at zero speed. This confirms that the additional mechanism of centripetal buoyancy is clearly modifying the response of both leading and trailing edges.

From the viewpoint of design it is important to compare the results obtained with rotation with those that might be expected with a stationary tube and corresponding Reynolds numbers values. This is demonstrated in Figs. 6 and 7 for the trailing and leading edges, respectively. We see from Fig. 6 that the trailing edge heat transfer is increased relative to the zero speed case. The effect of buoyancy is also clearly illustrated in this figure, where the zero speed tests at various heater power settings are shown to collapse more closely onto quite tight bands. This collapsing tendency is definitely not present when the test section is rotating.

A similar comparison for the leading edge, shown in Fig. 7, demonstrated a severe tendency for the local heat transfer to be reduced in comparison to the zero speed case. This is a very important point from the viewpoint of predicting airfoil internal heat transfer, for if rotation is not adequately taken into account, local hot spot regions could develop in the leading edge regions of the cooling channels used. Similar trends as regards the influence of centripetal buoyancy are evident on the leading edge.

For turbulent flow in square and rectangular sectioned ducts rotating in the orthogonal mode, Morris et al. [18] and Morris and Ghavami-Nasr [20] have attempted to isolate the effect of Coriolis forces by assuming that the direct influence of forced convection may be taken into account by means of a 0.8 power of the Reynolds number. Thus, by plotting $Nu/Re^{0.8}$ against the reciprocal of the Rossby number, they were able to demonstrate the trend of the likely influence of Coriolis force. However, for both geometries studied there were noticeable wall conduction effects present. For this reason the reduction in leading edge heat transfer due to the Coriolis secondary flow has probably been suppressed to some extent in their results. To exemplify a slightly impaired leading edge, heat transfer response was detected with the rectangular duct and zero response with the square duct leading edge. In both cases, however, enhanced trailing edge heat transfer resulted from the rotation. Nevertheless this same technique has been adopted here, in the first instance, to illustrate the Coriolis effect on local heat transfer on the leading and trailing edges of the circular tube.

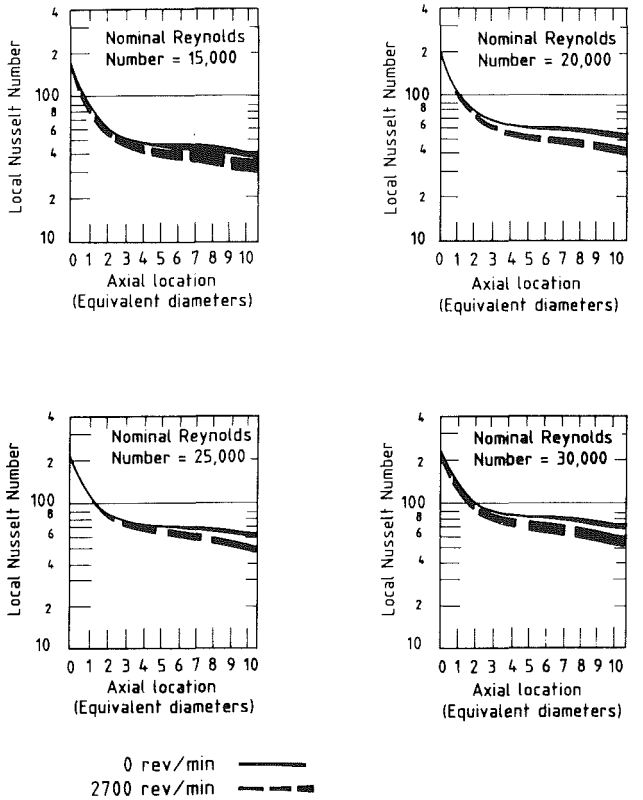

Fig. 7 Comparison of effect of rotation on leading edge heat transfer in comparison with zero speed

Figure 8 shows the effect of Coriolis forces on local heat transfer on both leading and trailing edges for all data points collected in the present investigation. The enhancements and impediments on the trailing and leading edges in relation to the zero speed condition are readily seen. Note that the use of the reciprocal of the Rossby number permits zero speed data to be conveniently plotted with those obtained with rotation. Although these plots do show the broad effect of Coriolis forces, there is clear evidence of the data spread caused by centripetal buoyancy at each cluster of Reynolds/Rossby points. However the increase in the relative heat transfer between the leading and trailing edges as the rotational speed is increased is clearly evident.

The centripetal buoyancy-driven data spread, mentioned above, was examined at each Reynolds/Rossby set, and Fig. 9 typifies the buoyancy trends found. In this figure the local Nusselt number at an axial location deemed to span the best approach to fully developed flow conditions are plotted against the buoyancy parameter for the trailing edge results obtained at 2700 rpm. At each Reynolds number there is a systematic tendency for the Nusselt number to increase with increasing buoyancy parameter values. The gradient, n, of each individual Reynolds number line does, however, decrease with Reynolds number. This makes physical sense since one would expect the forced convection contribution to heat transfer to dominate at the higher Reynolds number values. For the entire range of test undertaken, Fig. 10 shows the variation of the gradient, n, with Rossby number. As a result of numerical experimentation with the data, it was found that this particular plot seemed to give the most unique behavior. Thus the slope seems related to the Rossby number without the need for a family of Reynolds/Rossby lines as was originally expected. The decay of the influence of centripetal buoyancy as the Rossby number

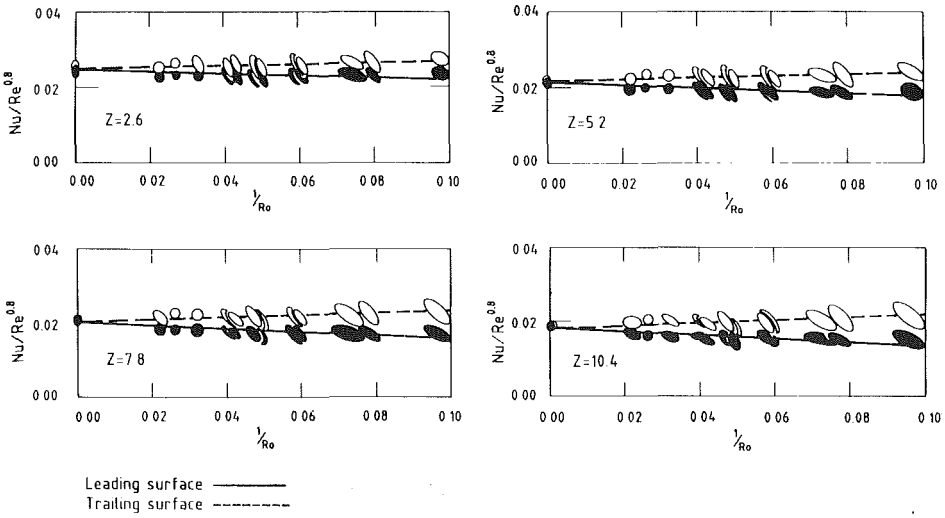

Fig. 8 Effect of Coriolis forces on local leading and trailing edge heat transfer

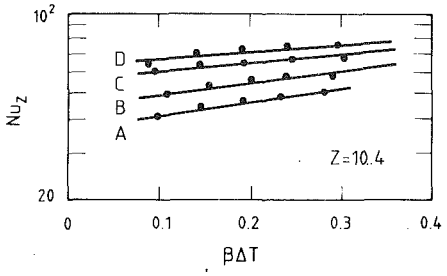

Legend	Reynolds number
A	15,000
B	20,000
C	25,000
D	30,000

Fig. 9 Typical effect of buoyancy on trailing edge heat transfer at 2700 rpm

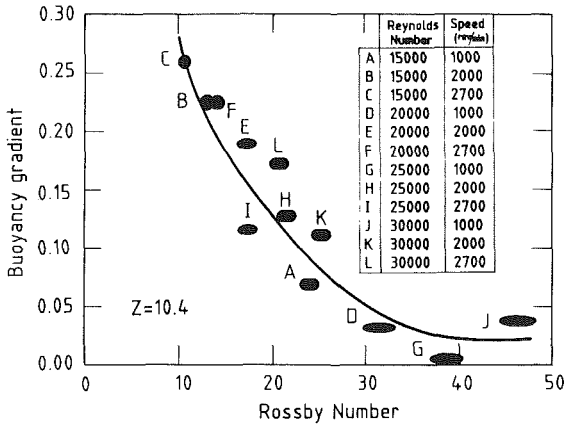

Fig. 10 An indication of the importance of buoyancy on trailing edge heat transfer

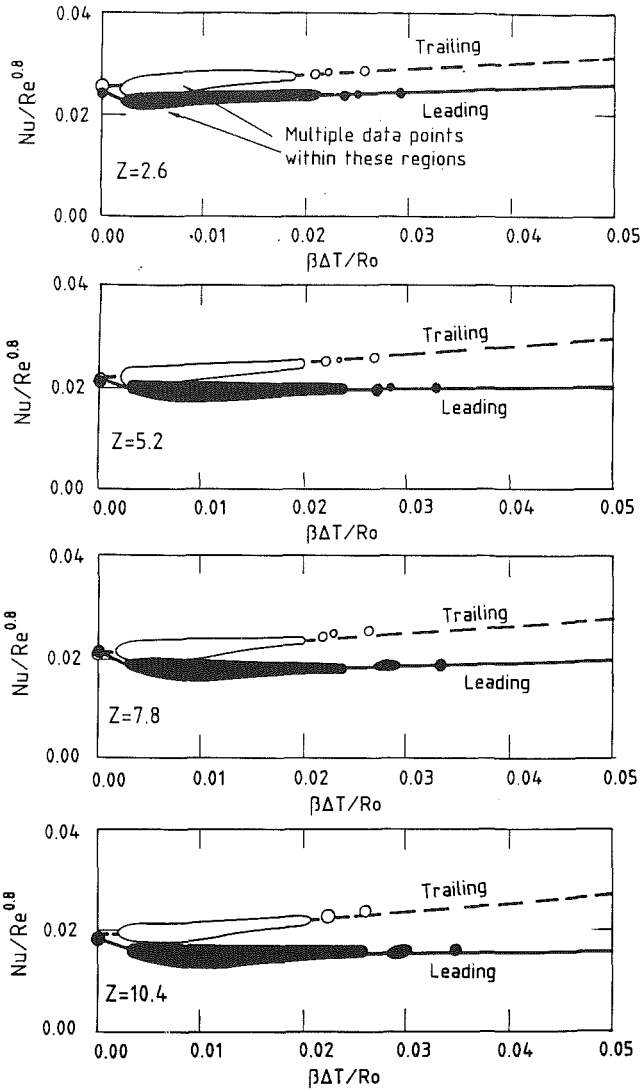

Fig. 11 Overall effect of Coriolis and buoyancy forces on leading and trailing edge heat transfer

increases is clearly seen in the figure. For Rossby numbers greater than about 40 the influence of buoyancy has effectively decayed away.

As a result of the trends illustrated by Figs. 8 and 10, an attempt was made to examine the possibility of defining an empirical correlating parameter that would permit the two rotational mechanisms described to be quantified simultaneously. Two features led to the following observations. First, the assumption that ordinary forced convection was related to the customary 0.8 power of the Reynolds number seemed to have some substance when the Coriolis effect was examined initially. Second, when considering the effect of buoyancy, this effect could be shown to depend broadly on the Rossby number without any additional need for a Reynolds number dependency. These observations led the authors to examine the possibility of using a correlating parameter involving the product of the inverse Rossby number with simple functions of the buoyancy parameter. Although numerous ideas were examined, a simple product of the inverse Rossby number with the buoyancy parameter itself proved to be highly successful in collapsing all data obtained into a unique set of curves for the trailing and leading edges. For four axial locations in the downstream direction relative to the inlet plane of the duct, Fig. 11 shows the result of plotting the quotient of the local Nusselt number and the 0.8th power of the Reynolds number with this new proposed overall rotational parameter. For convenience property values were evaluated at the bulk fluid temperature. The following interesting features emerge.

As the Rossby number is increased, implying low rotational speeds, the influence of buoyancy has been shown to become less important (see Fig. 10). Also centripetal buoyancy is not present by definition at zero rotational speed. Thus as the rotational parameter approaches zero, the experimental data for both leading and trailing surfaces should approach an asymptote of a zero gradient condition.

We note from Fig. 11 that the local heat transfer on the trailing edge increases steadily over the range covered as the rotational parameter is increased. This suggests that, for a specified Rossby number, the local heat transfer increases with increases in the buoyancy parameter, *Bu*, over the entire range.

On the leading edge, the local heat transfer was found initially to decrease with increases in the rotational parameter, giving reduced heat transfer in relation to the stationary case. This decreasing heat transfer was subsequently found to flatten off with a subsequent tendency for the local heat transfer to recover, although still lower than the stationary counterpart. Although the heat transfer on the leading edge can be significantly lower than the zero speed condition, the trend of Fig. 11 suggests the possibility of a recovery situation at higher levels of the rotational parameter.

The shape of the leading edge response in Fig. 11 gives a possible explanation why some workers have reported that buoyancy can either increase or decrease the Nusselt number at a given Rossby number value. We note from the figure that increases in the buoyancy parameter, *Bu*, at a specified Rossby number could be on the negative or positive slope region de-

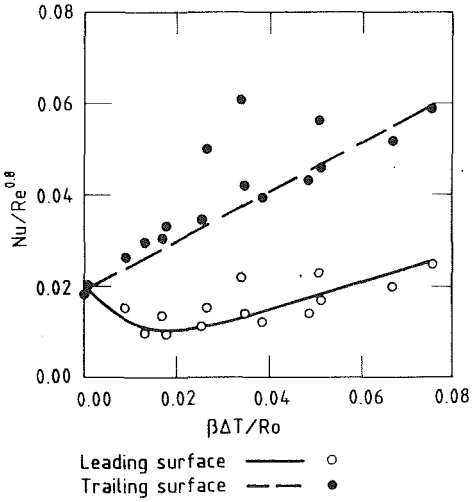

Fig. 12 Examination of experimental data of Wagner et al. [19] in relation to the proposed correlating parameter

pending on the combined operating condition. This, as far as the present authors are aware, is the first time that this possibility has been explicitly demonstrated.

An examination of the results reported by Wagner et al. [19] for a square sectioned duct has been found to demonstrate similar tendencies when plotted in terms of the rotational parameter. This is shown in Fig. 12. It should be noted that whereas our own data have been plotted on a local basis in Fig. 11, the buoyancy parameter has been based on the difference in wall to inlet temperature in Fig. 12. This was due to the manner in which information was presented in the paper of Wagner et al. Nevertheless, the general trends described above are identical. This adds considerable support for the use of the overall rotational parameter as a means of simultaneously accounting for the combined influence of Coriolis forces and centripetal buoyancy with this particular rotating geometry.

Closure

The salient conclusions resulting from the present paper may be highlighted as follows.

Coriolis forces, via the generation of a strong cross-stream secondary flow, can create circumferential variations in local heat transfer with a tendency to improve the heat transfer on the trailing edge of the tube in relation to the leading edge.

On the leading surface, local heat transfer can be reduced in relation to that which may be expected from Reynolds number controlled forced convection acting alone.

On the trailing surface, centripetal buoyancy has been shown to increase the local heat transfer further in comparison to that which is caused by the Coriolis-driven secondary flow.

A new correlating parameter, involving the product of the inverse Rossby number with the buoyancy parameter, has been shown to demonstrate a good tendency to uncouple the combined effects of Coriolis forces and centripetal buoyancy for this rotating geometry.

This new overall rotational parameter suggests that, on the leading edge, buoyancy can possibly impair or improve local heat transfer depending on the relative value of the new parameter itself. At high values of this new parameter, the possibility of an improvement in leading edge heat transfer in relation to the stationary case appears possible and this effect needs further investigation.

Acknowledgments

The authors wish to express their appreciation to the Ministry of Defence, the Science and Engineering Research Council, and Rolls Royce, Plc. for their encouragement and financial support.

References

1 Barua, S. N., "Secondary Flow in a Rotating Straight Pipe," *Proc. Roy. Soc., A.*, Vol. 227, 1955, p. 133.

2 Mori, Y., and Nakayama, W., "Convective Heat Transfer in Rotating Radial Circular Pipes (1st Report—Laminar Region)," *Int. J. Heat Mass Transfer*, Vol. 11, 1968, p. 1027.

3 Benton, J. S., and Boyer, D., "Flow Through a Rapidly Rotating Conduit of Arbitrary Cross-Section," *J. Fluid Mech.*, Vol. 26, Part I, 1969.

4 Ito, H., and Nanbu, K., "Flow in Rotating Straight Pipes of Circular Cross-Section," ASME *Journal of Basic Engineering*, Vol. 93, 1971, p. 383.

5 Johnston, J. P., Halleen, R. M., and Lezius, D. K., "Effects of Spanwise Rotation on the Structure of Two-Dimensional Fully Developed Turbulent Channel Flow," *J. Fluid Mech.*, Vol. 56, 1972, pp. 537–557.

6 Lokai, V. I., and Limanski, A. S., "Influence of Rotation on Heat and Mass Transfer in Radial Cooling Channels of Turbine Blades," *Izvestiya VUZ, Aviatsionnya Tekhnika*, Vol. 18, 1975, p. 69.

7 Metzger, D. E., and Stan, R. L., "Entry Region Heat Transfer in Rotating Radial Tubes," presented at the AIAA 15th Aerospace Sciences Meeting, Los Angeles, CA, Paper No. 77-189, 1977.

8 Skiadaresis, D., and Spalding, D. B., "Heat Transfer in a Pipe Rotating about a Perpendicular Axis," ASME Paper No. 77-WA/HT-39, 1977.

9 Zysina-Molozken, L. M., Dergach, A. A., and Kogan, G. A., "Experimental Investigation of Heat Transfer in a Radially Rotating Pipe," *HGEEE High Temp.*, Vol. 14, 1977, p. 988.

10 Morris, W. D., and Ayhan, T., "Observations on the Influence of Rotation on Heat Transfer in the Coolant Channels of Gas Turbine Rotor Blades," *Proc. IMechE*, Vol. 193, 1979, p. 303.

11 Morris, W. D., *Heat Transfer in Rotating Coolant Channels*, Research Studies Press, Wiley, New York, 1981.

12 Morris, W. D., and Ayhan, T., "Experimental Study of Turbulent Heat Transfer in a Tube Which Rotates About an Orthogonal Axis," *Proc. XIV ICHMT Symposium on Heat and Mass Transfer in Rotating Machinery*, Dubrovnik, Yugoslavia, Aug. 30–Sept. 3, 1982.

13 Clifford, R. J., Morris, W. D., and Harasgama, S. P., "An Experimental Study of Local and Mean Heat Transfer in a Triangular-Sectioned Duct Rotating in the Orthogonal Mode," ASME *Journal of Engineering for Gas Turbines and Power*, Vol. 106, 1984, pp. 661–667.

14 Morris, W. D., and Harasgama, S. P., "Local and Mean Heat Transfer on the Leading and Trailing Surfaces of a Square Sectioned Duct Rotating in the Orthogonal Mode," presented at Heat Transfer and Cooling in Gas Turbines, AGARD-CP-390, Bergen, Norway, May 6–10, 1985.

15 Clifford, R. J., "Rotating Heat Transfer Investigations on a Multi-pass Cooling Geometry," presented at Heat Transfer and Cooling in Gas Turbines, AGARD-CP-390, Bergen, Norway, May 6–10, 1985.

16 Iskakov, K. M., and Trushin, V. A., "The Effect of Rotation on Heat Transfer in the Radial Cooling Channels of Turbine Blades," *Teploenergetika*, Vol. 32, 1985, pp. 52–55.

17 Wagner, J. H., Kim, J. C., and Johnson, B. V., "Rotating Heat Transfer Experiments With Turbine Airfoil Internal Passages," ASME Paper No. 86-GT-133, 1986.

18 Morris, ,W.D., Harasgama, S. P., and Salemi, R., "Measurements of Turbulent Heat Transer on the Leading and Trailing Surfaces of a Square Duct Rotating About an Orthogonal Axis," ASME Paper No. 88-GT-114, 1988.

19 Wagner, J. H., Johnson, B. V., and Hajek, T. J., "Heat Transfer in Rotating Passages With Smooth Walls and Radial Outward Flow," ASME Paper No. 89-GT-272, 1989.

20 Morris, W. D., and Ghavami-Nasr, G., "Heat Transfer Measurements in Rectangular Channels With Orthogonal Mode Rotation," ASME Paper No. 90-GT-138, 1990.

21 Medwell, J. O., Morris, W. D., Xia, J. Y., and Taylor, C., "An Investigation of Convective Heat Transfer in a Rotating Coolant Channel," ASME Paper No. 90-GT-329, 1990.

22 Iacovides, H., and Launder, B. E., "Parametric and Numerical Studies of Fully-Developed Flow and Heat Transfer in Rotating Rectangular Passages," ASME Paper No. 90-GT-24, 1990.

23 Wagner, J. H., Johnson, B. V., and Kopper, F. C., "Heat Transfer in Rotating Serpentine Passages With Smooth Walls," ASME Paper No. 90-GT-331, 1990.

24 Dittus, F. W., and Boelter, L. M. K., Univ. Calif. Publs., Engng., Vol. 2, 1930, p. 443.

Comparison of Heat Transfer Measurements With Computations for Turbulent Flow Around a 180 deg Bend

D. L. Besserman

S. Tanrikut

Pratt & Whitney,
Group Engineering and Technology,
East Hartford, CT 06040

Results of detailed heat transfer measurements are presented for all four walls of a 180 deg 1:1 aspect ratio duct. Experiments using a transient heat transfer technique with liquid crystal thermography were conducted for turbulent flow over a Reynolds numbers range of 12,500–50,000. Computational results using a Navier–Stokes code are also presented to complement the experiments. Two near-wall shear-stress treatments (wall functions and the two layer wall integration method) were evaluated in conjunction with k–ϵ formulation of turbulence to assess their ability to predict high local gradients in heat transfer. Results showed that heat transfer on the convex and concave walls is a manifestation of the complex flow field created by the 180 deg bend. For the flat walls, the streamwise average Nusselt number increases to approximately two times the fully developed turbulent flow value. Ninety degrees into the bend, the importance of the cross-stream gradients is evident with the Nusselt number varying from approximately one to three times the fully developed turbulent flow value. The numerical predictions with two-layer wall integration k–ϵ turbulence model show very good agreement with the experimental data. These results reinforce the need to predict local heat transfer rates accurately in cooling passages of advanced turbine airfoils to enhance the durability of these components.

Introduction

In order to increase the efficiency of gas turbine engines, current trends include increasing the combustor exit temperature as well as minimizing the coolant flow rate to the internal turbine blade passages. As a result, detailed knowledge of heat transfer associated with internal cooling passages is necessary to prevent local "hot spots" and achieve acceptable turbine airfoil metal temperatures and life.

A square cross-sectioned duct with a 180 deg bend, which is representative of a turbine blade internal coolant passage, has been studied (Wagner et al., 1991a, 1991b; Fan and Metzger, 1987) in both stationary and rotating environments. In these investigations, data were acquired with models in which a single copper element was used to measure the heat transfer for each side wall. Although the copper elements were segmented in the streamwise direction, the flat surface of the 180 deg bend was fabricated from either one or two copper segments. Therefore, both large streamwise and cross-stream gradients could not be resolved with these models. However, the importance of the secondary flow fields generated in the duct was demonstrated. In all cases the heat transfer coefficients were approximately a factor of two greater in the bend as compared to fully developed turbulent pipe flow.

More detailed heat transfer measurements have been made in 180 deg bends by Baughn et al. (1986) for circular ducts and by Johnson and Launder (1985) for square cross-sectioned ducts. Baughn et al. (1986) reported that the maximum heat transfer occurred 90 deg into the bend with the variation from the inside to the outside of the bend ranging from one to three times the turbulent pipe flow value. The classical double-cell secondary vortex that is created causes the slow-moving fluid near the duct wall to move toward the inside of the bend and the cooler faster-moving fluid near the plane of symmetry to "impinge" on the outside of the bend. In addition, streamline curvature tends to increase turbulent mixing on the outside of the bend. Therefore, the large increases in heat transfer on the outside of the bend were attributed to both the secondary flow and to increased turbulent mixing. Johnson and Launder (1985) also reported maximum heat transfer 90 deg into the bend where the heat transfer on the concave walls was 2.2 times larger than the convex walls for Re = 56,000. Larger variations between the concave and convex walls were reported for lower Reynolds numbers.

To date, computations have focused on predicting the flow field within ducts with a 180 deg bend. Monson et al. (1989) solved the Navier–Stokes equations for an incompressible fluid

Contributed by the International Gas Turbine Institute and presented at the 36th International Gas Turbine and Aeroengine Congress and Exposition, Orlando, Florida, June 3–6, 1991. Manuscript received at ASME Headquarters January 18, 1991. Paper No. 91-GT-2. Associate Technical Editor: L. A. Riekert.

using a Prandtl mixing length zero-equation turbulence model. Comparisons between experimental measurements and the numerical solution indicate that the mean flow was well predicted in the first half of the bend since the flow field is mainly driven by the pressure field. However, the separation bubble measured on the inner wall near the end of the bend was not accurately predicted and the boundary layer thicknesses were overpredicted.

A series of modeling refinements were incorporated by Choi et al. (1989) in an effort to predict the flow more accurately. Replacement of wall functions by a fine grid used to resolve the buffer and viscous sublayers and replacement of the standard k–ϵ turbulence model by an algebraic second-moment closure provided significant improvements in the agreement between predictions and measurements. However, Choi et al. (1989) suggest that accurate predictions of the primary flow may be dependent on the ability to predict secondary flow, which may require the use of a turbulent transport model in the viscous sublayer.

Significant durability improvements in turbine airfoil designs beyond current state-of-the-art are dependent upon both an increased understanding of the heat transfer occurring within an internal cooling passage and the ability to predict these heat transfer coefficients accurately. Therefore, the current work included obtaining detailed heat transfer measurements in the turn region of a square cross-sectioned duct with a 180 deg bend, as well as numerically predicting the heat transfer associated with this geometry. The numerical predictions incorporated a k–ϵ turbulence model with the wall shear stress computed via either wall functions or the two-layer wall integration method. It was the goal of this work to compare the experimental results with the computations to assess the predictive capability of the Navier–Stokes code in the high gradient regions.

Experimental Method

A schematic diagram of the geometry used in the current investigation is shown in Fig. 1. The apparatus was designed with 29.7 mm (1.17 in.) radius of curvature on the convex wall. Since the concave wall has a smaller radius of curvature (27.4 mm, 1.08 in.), the model has a flat surface at the 90 deg location. The channel features were machined from a nominally 25.4 mm (1 in.) thick sheet of clear acrylic. The square cross-section duct was formed by sandwiching this piece between two other sheets. Since the acrylic was not exactly 25.4 mm thick, the resulting height and width of the channel were 24.4 and 25.4 mm (0.96 in. and 1 in.), respectively. This yielded a hydraulic diameter of 25.1 mm (0.99 in.).

A transient technique described by Metzger and Larson (1986) was used to measure the heat transfer in the model shown in Fig. 1. Unlike copper model data, which would yield average values for each element, this technique provided a means to obtain true local measurements. Heat transfer coefficients were obtained by solving the one-dimensional transient conduction equation for a semi-infinite wall subject to a convective heat transfer boundary condition. For each location in which the heat transfer coefficient was obtained, the time required for the wall to reach a specified temperature was recorded by observing the color change of liquid crystals applied to the surface of interest. An iterative solution scheme was employed to determine the heat transfer coefficients from these time–temperature pairs.

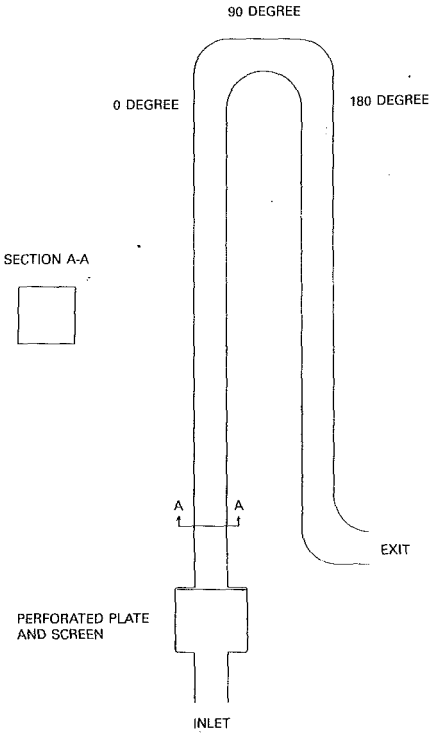

Fig. 1 Schematic diagram of square cross-sectioned duct with 180 deg turn

Inherent in the problem formulation is the assumption that the convective heat transfer coefficient is constant with time. Since $Gr/Re^2 \ll 1$ for these experiments, the results are independent of the wall-to-fluid temperature difference ($T_w - T_f$) and so the above assumption is believed to be valid. Due to the low thermal conductivity of acrylic (k = 0.19 W/m K) and the 25.4 mm wall thickness of the model, the semi-infinite wall assumption was valid. It was estimated that two-dimensional conduction effects within the acrylic affected the results by less than 3 percent (Vendula and Metzger, 1988).

A perforated plate and screen were placed in the small inlet plenum shown in Fig. 1. The velocity profile was surveyed three hydraulic diameters down-stream of the screen, which indicated a variation of 20 percent between the maximum and average velocity at this location. The distance from exit of the inlet plenum to the entrance to the turn was 14 hydraulic diameters. As a result, the velocity profile entering the bend

Nomenclature

D = hydraulic diameter
g = gravitational constant
Gr = Grashof number = $(g\beta(T_w - T_f)D^3)/\nu^2$
h = heat transfer coefficient
k = thermal conductivity
m = mass flow rate
Re = Reynolds number = $m^*D/\mu/A$
T = temperature
u_τ = friction velocity = $\sqrt{\tau_w/\rho_w}$
V = velocity
V_m = mean coolant velocity
x = streamwise distance
y = coordinate normal to solid surface
y^+ = dimensionless distance to solid surface = (yu_τ/ν_w)
β = volumetric thermal expansion coefficient
μ = absolute viscosity
ν = kinematic viscosity
ρ = density
τ = shear stress

Subscripts

f = film property
in = inlet
w = heated surface locations
∞ = fully developed, smooth tube

Superscripts

$\overline{\ }$ = average

was partially developed and is representative of the flow conditions present in turbine airfoil internal passages.

The model was sprayed with 1.1°C (2°F) temperature band chiral nematic liquid crystals. A thin misting of black paint (thickness less than 0.025 mm) was sprayed on top of the liquid crystals to provide a sharp contrast for viewing the color changes. The effect of conduction through this paint on the results was assumed to be negligible.

To initiate the test, heated air at 121°C (250°F) was diverted from a bypass line through the initially isothermal, 21°C (70°F) model. The time responses of liquid crystal color changes were recorded on video tape. The air flow rate was measured with a venturi and the inlet and exit air temperatures at the channel centerline were recorded with thermocouples. At each streamwise location, the centerline temperature was linearly interpolated from these measured temperatures. The local mixed mean fluid temperature was then calculated by assuming a 1/7 power law temperature profile using the local centerline and wall temperatures. The outside wall surface temperature was also monitored throughout the test to insure that the semi-infinite wall assumption was not violated. Data were acquired for flow rates corresponding to Reynolds numbers based on hydraulic diameter of 12,500, 25,000, and 50,000. Principle emphasis was placed on the case with Re = 25,000.

Due to the plane of symmetry about the centerline of the duct, results are presented for only one of the two flat surfaces. Henceforth, this surface shall be referred to as the top surface. In the turn region of the top surface, data were reduced at six degree intervals, in the streamwise direction, with seven equally spaced grid points across the width of the duct. This level of resolution provided a detailed mapping of the heat transfer coefficients that could be compared with the numerical predictions. The heat transfer coefficients on the concave and convex surfaces of the bend were determined at selected streamwise locations with five equally spaced data points across the width of these surfaces.

Numerical Procedure

The governing equations of continuity, momentum, and energy were solved using the Navier–Stokes code of Rhie (1986) for the same geometry used in the experiments. This is a pressure-based implicit procedure, which solves the full Navier–Stokes equations in general coordinates, thus allowing use of body-fitted coordinate systems.

In Rhie's approach, the preliminary velocity field is first obtained from the momentum equations with a preliminary pressure field. Since this preliminary velocity field does not satisfy the continuity equation, pressure correction equations are solved to establish a new velocity and pressure field, which does satisfy the continuity equation. The momentum and continuity equations are coupled through this pressure correction procedure. Then, the energy and turbulent scalar equations are solved in turn. To date, the procedure has been used in a wide variety of applications including two- and three-dimensional viscous and inviscid flows showing good comparison with experimental data (e.g., Rhie, 1986).

Two near-wall shear-stress treatments were evaluated in conjunction with the two-equation k–ϵ formulation of turbulence to assess their ability to predict high local gradients in heat transfer. In one case, the governing equations near the wall were solved by employing generalized wall functions, which assume that the boundary layer velocity profile has the universal "law-of-the-wall" profile (Launder and Spaulding, 1974). The turbulent kinetic energy (TKE) adjacent to the walls was computed from the TKE conservation equation. In the other case, the two-layer wall integration method was used in which the governing equations are solved to the wall (Dash et al., 1983). Near the wall, the classical Van-Driest mixing length formulation was used. This region was patched with a two-equation k–ϵ turbulence model at $y^+ = 50$.

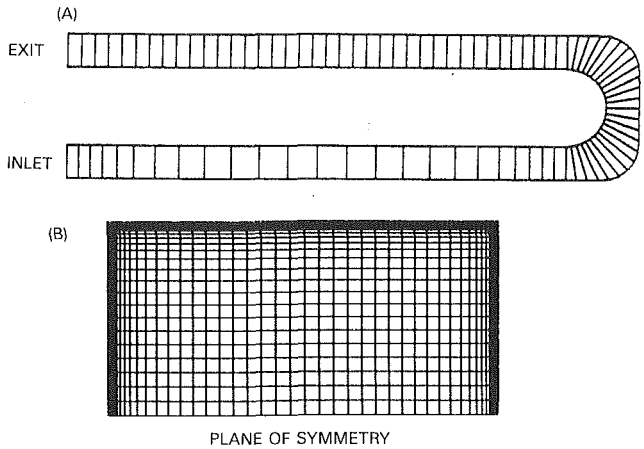

Fig. 2 Computational grid: (A) streamwise grid locations; (B) cross-stream grid for wall integration simulation

For the wall function simulation, a uniform grid of 30 × 30 was used for each cross-stream plane. The streamwise grid locations are shown in Fig. 2(*a*). In order to resolve the viscous and buffer sublayers, a nonuniform grid was employed for the two-layer wall integration simulation. The plane of symmetry in the duct was exploited in this case with a cross-stream grid of 59 × 30 as shown in Fig. 2(*b*).

A no-slip boundary condition was applied to the surfaces of the duct for the momentum equations and a constant-temperature boundary condition was used for the energy equation. A flat inlet velocity profile was specified for the computations presented below. Simulations with wall functions were performed with both a flat inlet velocity profile and using the velocity profile obtained from LDV measurements three hydraulic diameters downstream of the inlet plenum. These predictions indicated that the streamwise velocity profiles entering the bend were within 8 percent of the measurements for both inlet velocity profiles, within the experimental error of the measurements.

Discussion of Results

To aid in the understanding of the duct heat transfer characteristics, the flow fields predicted within the duct are discussed first. Liquid crystal data, numerical predictions, and previous copper model data are then compared for the top, outer (concave), and inner (convex) surfaces of the duct. Finally, detailed comparisons between the data and the predictions are highlighted with attention focused on the high gradient regions.

Flow Patterns. As flow approaches the bend, the velocity profile is characteristic of developing flow with a constant velocity in the core region of the flow. At the entrance of the bend, the peak velocity occurs near the inside of the bend, which would be anticipated from inviscid flow theory. The predicted streamwise velocity profiles are shown in Fig. 3 for the plane of symmetry and parallel planes, at the 90 deg location. For both near-wall shear-stress treatments, the maximum streamwise velocity has shifted toward the outside wall at the plane of symmetry (Fig. 3A). However, the predictions in which the turbulent shear stress is integrated to the wall show a larger variation across the width of the duct. With increasing depth into the duct, the peak velocity shifts toward the inside (convex) wall.

These peaks in the streamwise velocity profile can be understood by observing the secondary flow field which develops within the duct at this location. Shown in Fig. 4, a classical single-cell vortex has developed in the region from the symmetry plane to the top surface of the duct. The secondary

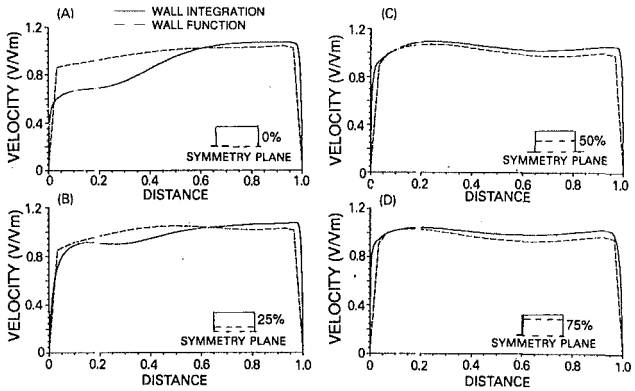

Fig. 3 Streamwise velocity profiles: (A) symmetry plane; (B) 25 percent depth; (C) 50 percent depth; (D) 75 percent depth

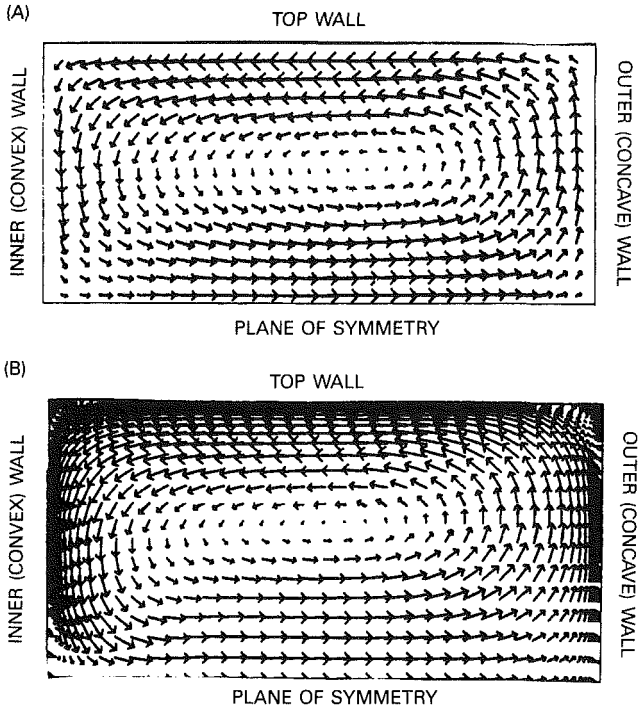

Fig. 4 Secondary flow patterns at 90 deg plane: (A) wall functions; (B) wall integration

motion indicates that the flow migrates from the inner wall toward the outer wall near the symmetry plane. This motion results in an increase in the streamwise velocity near the outer (concave) wall and a corresponding decrease near the inner (convex) wall. Likewise, near the top wall, streamwise velocity increases near the inner (convex) wall due to the effect of the secondary flow. The nonuniform grid associated with the wall integration method was able to resolve small corner vortices (Fig. 4B).

As the flow progresses around the turn, the single-cell vortex is transformed into a more complex secondary flow structure (Fig. 5). In both simulations, two large circulation cells are generated at the 180 deg location in the top half of the duct (a total of four main circulation cells develop within the duct). However, a more complex flow structure is again predicted with the wall integration model.

Flow visualization tests, utilizing fluorescent dye, indicated the same overall flow features. Specifically, two and four recirculation cells were observed at the 90 and 180 deg locations, respectively. These results indicated that both sets of computations predicted the overall flow structure.

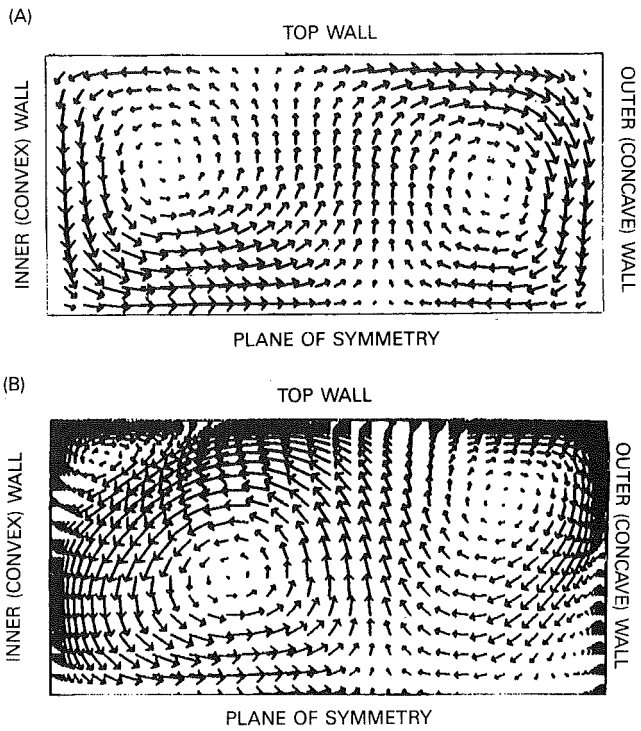

Fig. 5 Secondary flow patterns at 180 deg plane: (A) wall functions; (B) wall integration

Heat Transfer Data. Liquid crystal data were taken for three coolant flow rates corresponding to a Re range of 12,500–50,000. In all cases, the highest heat transfer, on the top surface, occurred along the outside edge near the 90 deg location. With increasing Reynolds number, the peak shifted toward the entrance of the bend. However, the peak always occurred in the region where the outside wall is straight.

Since the current investigation used the same geometry as that used by Wagner et al. (1991a), a direct comparison of the results can be made. In Fig. 6, the liquid crystal data, for the top surface, has been averaged across the width of the duct and is shown versus dimensionless streamwise distance (x/D). Copper model data (Wagner et al., 1991a) are shown as straight line segments, which correspond with the length of the copper segments. The Nusselt number for fully developed turbulent flow in a smooth tube with constant wall temperature is noted in the figure for reference (Kays and Crawford, 1980). The correlation used to obtain Nu_∞ is $Nu_\infty = 0.021\ Pr^{0.5}\ Re^{0.8}$.

The liquid crystal data indicate a large increase in heat transfer from the 0 to 90 deg locations and a gradual decline in the second half of the turn. The copper model data indicate an increase in heat transfer throughout the turn, which is consistent with the gradual decline in heat transfer obtained in the current study from the 90 to 180 deg locations. In order to make valid comparisons between the copper model data and the liquid crystal data, the liquid crystal results have been spatially averaged over regions corresponding to the copper model sections. In the turn region, $\overline{Nu}$ measured with the liquid crystal technique was lower than the copper model data by approximately 25 percent for Re = 12,500 and by 10 percent for Re = 50,000. Comparison of copper model data with the fully developed turbulent pipe flow value prior to the bend entrance indicates that for Re = 12,500 and Re = 50,000 $\overline{Nu}$ was approximately 20 percent higher than the correlations would predict. On the other hand, the liquid crystal data were lower than pipe flow by 9 percent for Re = 12,500 and higher than pipe flow by 8 percent for Re = 50,000.

For Re = 25,000, the Nusselt numbers of the liquid crystal data, copper model data, and the fully developed pipe flow

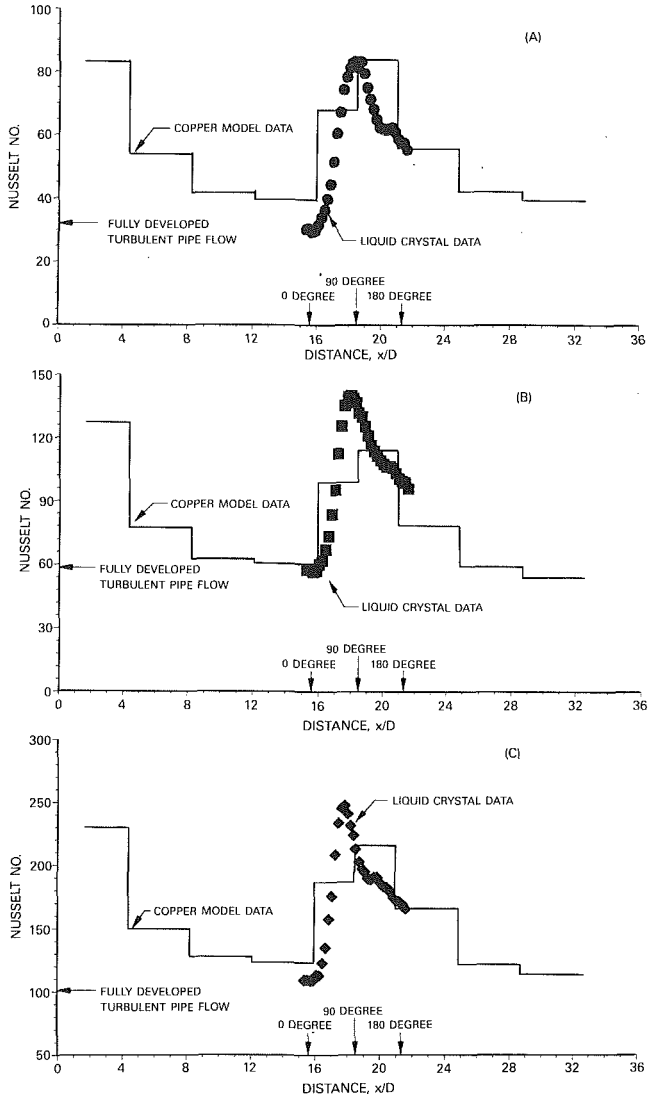

Fig. 6 Comparison of spanwise average liquid crystal and copper model data (Wagner et al., 1991a) for the top surface: (A) Re = 12,500; (B) Re = 25,000; (C) Re = 50,000

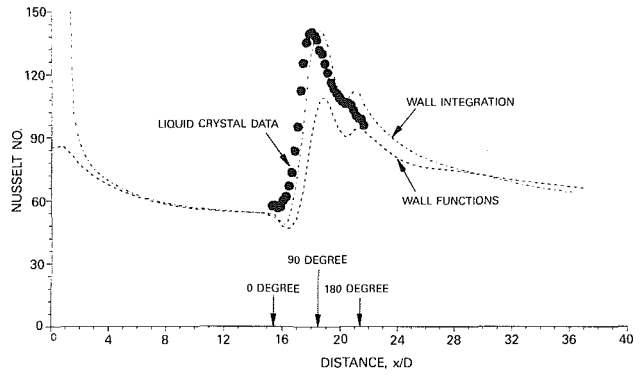

Fig. 7 Comparison of spanwise-averaged liquid crystal results with predictions for top surface and Re = 25,000

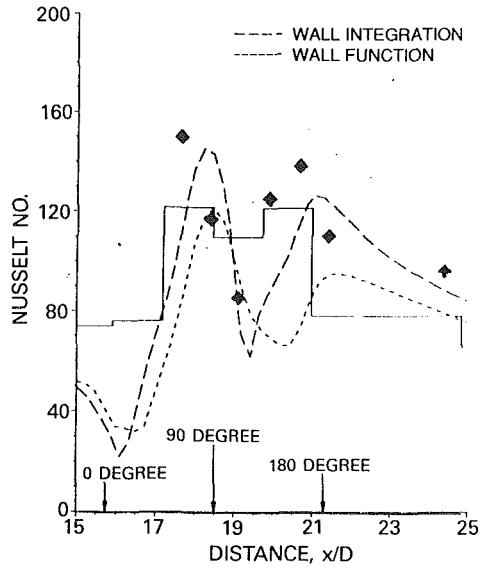

Fig. 8 Comparison of spanwise-averaged liquid crystal results with predictions and copper model data (Wagner et al., 1991a) for outside surface and Re = 25,000

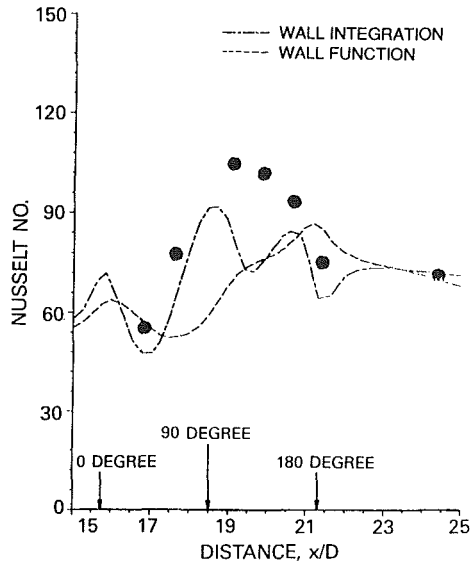

Fig. 9 Comparison of spanwise-averaged liquid crystal results with predictions for inside surface and Re = 25,000

value were within 5 percent prior to the bend. As a result, excellent agreement was obtained for this case in the turn region with a difference of less than 3 percent between the current measurements and those of Wagner et al. (1991a). Thus, the level of agreement between the liquid crystal and copper model data in the turn region is directly related to the agreement prior to the bend.

Predictions from the numerical simulations have been compared with the liquid crystal data in Fig. 7 for the top surface. Excellent agreement was obtained between the Nusselt number prediction with wall functions and that with wall integration prior to the bend where the flow is characteristic of almost fully developed turbulent flow. In the turn region, both predictions exhibit the same characteristic $\overline{Nu}$ curve shape with streamwise location. The minimum heat transfer was predicted to occur where the flow enters the bend and can be attributed to the reduced heat transfer associated with the separation of flow from the concave (outer) wall. The maximum heat transfer was predicted at the 90 deg location with a secondary peak at the 180 deg location. The simulation that employed the wall integration turbulence model accurately predicted the streamwise-averaged Nusselt numbers with less than 2 percent difference between the maximum values. However, the wall

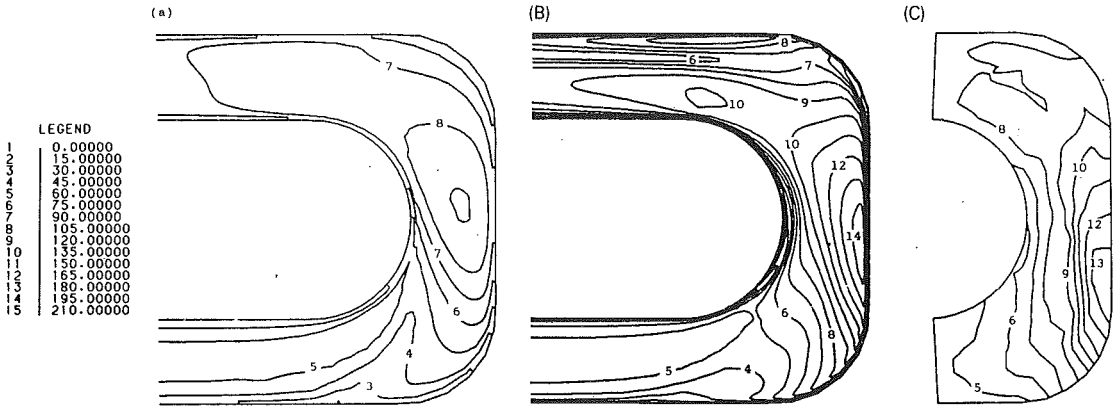

Fig. 10 Nusselt number contours: (A) wall functions; (B) wall integration; (C) liquid crystal data

function simulations underpredict heat transfer in the high gradient regions associated with the entrance of the duct and the turn region. For this case, $\overline{Nu}$ was underpredicted by approximately 20 percent in the turn.

The spanwise-averaged results for the outside (concave) wall indicate large variations with streamwise location around the turn (Fig. 8). At the 90 deg location, the flow impinges on the outside wall, which results in the first peak in heat transfer. The subsequent reduction is attributed to separation at approximately 135 deg. The increase in heat transfer beyond the separation region is characteristic of the high heat transfer associated with reattachment of the flow. This figure also demonstrates that the simulation with wall functions predicted smaller gradients in heat transfer than either the predictions with wall integration or the liquid crystal measurements. In this case, copper model data of Wagner et al. (1991a) provide accurate information regarding the average heat transfer for each copper segment but fail to provide information regarding the large variations that occur in the streamwise direction.

Spanwise average data for the inside (convex) surface are presented in Fig. 9. Both simulations underpredict the liquid crystal data in the turn region. (No data were acquired in this region with the copper model of Wagner et al., 1991a.) The variation of Nusselt number with streamwise distance is different between the simulations. The reason for this discrepancy has yet to be determined. It should be noted that data reduction was difficult in this region due to the curvature of the wall and the obscured view through the outside wall.

A contour plot of the local distribution of the Nusselt number on the top surface of the channel provides the final comparison between liquid crystal measurements and the numerical predictions (Fig. 10). Streamwise averages indicated that wall functions were underpredicting the heat transfer in the turn region (Fig. 6). This inability of wall functions to predict the heat transfer accurately in the high gradient regions is again highlighted in the contour plots. For this case, the variation between the maximum heat transfer and the value corresponding to fully developed turbulent pipe flow is approximately 2:1 with the peak heat transfer predicted in the central region of the top wall. Although good agreement exists between the spanwise-averaged wall integration simulation and the liquid crystal data, the local comparison shows some differences. Both the liquid crystal measurements and the predictions employing the wall integration model indicate that the maximum heat transfer is three times the fully developed turbulent flow value ($Nu_\infty = 58$). In addition, both the measurements and this prediction indicate that the peak heat transfer occurs on the outside edge of the channel. At the 90 deg location, the cross-stream velocity vectors indicate that the fluid moves from the center of the duct toward the outside wall and then along the top surface. This rolling of the fluid tends to increase heat transfer on the top surface near the outside edge.

Comparison of liquid crystal data and wall integration predictions indicates some differences in the second half of the turn. The large variations across the width of the duct predicted with wall integration turbulence model can be understood by examining the secondary flow field at the 180 deg location (Fig. 5). Heat transfer near the outside wall is enhanced by the impingement of the flow from the recirculation cell near the corner. The subsequent reduction can be attributed to the relatively slow-moving warm fluid associated with the interaction of the two recirculation cells near the outside wall. Heat transfer near the inside wall has been enhanced beyond the fully developed turbulent pipe flow value by the impingement and acceleration of the secondary flow on the top surface in this region. The secondary flow fields predicted by the simulations employing wall functions do not seem to affect the local heat transfer distribution. (Formulation of an anisotropic turbulence model may improve the local predictions in this region.)

Conclusions

Comparisons between predictions and measurements of the flow field and heat transfer within a duct with a 180 deg bend have yielded the following results and observations:

1 Both turbulence model near-wall treatments adequately predict the overall and secondary flow features.

2 Liquid crystal data indicate that large streamwise and cross-stream gradients in heat transfer exist in the turn region of a duct with a 180 deg bend.

3 Although a coarser mesh can be used with wall functions (which would reduce computational time), these predictions failed to predict the heat transfer accurately in the high gradient regions.

4 Predictions that solve the governing equations to the wall show very good agreement with liquid crystal data.

5 Further analysis of the turbulence model is necessary to resolve the differences between the predictions and the measurements on the convex surface.

Acknowledgments

The authors gratefully acknowledge Pratt & Whitney for permission to publish the results of this study. The plexiglass model used to acquire the liquid crystal data was borrowed from United Technologies Research Center. The authors gratefully acknowledge Scott Marquis and Glenn Bartkowski for their assistance in the data reduction. The authors are appreciative of the support and guidance provided by their colleagues at Pratt & Whitney and United Technologies Research Center.

References

Baughn, J. W., Iacovides, H., Jackson, D. C., and Launder, B. E., 1986, "Local Heat Transfer Measurements in Turbulent Flow Around a 180-deg Pipe Bend," ASME Paper No. 86-GT-53.

Becker, W. J., and Steiner, A. L., 1990, "The Application of 3D Navier-Stokes Codes to Turbine Internal Cooling Flow Problems," AIAA Paper No. 90-2267.

Choi, Y. D., Iacovides, H., and Launder, B. E., 1989, "Numerical Computation of Turbulent Flow in a Square-Sectioned 180 deg Bend," ASME *Journal of Fluids Engineering*, Vol. 111, pp. 59–68.

Dash, S. M., Beddini, R. A., Wolf, D. E., and Sinha, N., 1983, "Viscous/Inviscid Analysis of Curved Sub or Supersonic Wall Jets," AIAA Paper No. 83-1679.

Fan, C. S., and Metzger, D. E., 1987, "Effects of Channel Aspect Ratio on Heat Transfer in Rectangular Passage Sharp 180-deg Turns," ASME Paper No. 87-GT-113.

Johnson, B. W., and Launder, B. E., 1985, "Local Heat Transfer Behavior in Turbulent Flow Around a 180 deg Bend of Square Cross Section," ASME Paper No. 85-GT-68.

Kays, W. M., and Crawford, 1980, *Convective Heat and Mass Transfer*, McGraw-Hill, New York.

Launder, B. E., and Spaulding, D. B., 1974, "The Numerical Computation of Turbulent Flows," *Computer Methods in Applied Mechanics and Engineering*, Vol. 3, pp. 269–289.

Metzger, D. E., and Larson, D. E., 1986, "Use of Melting Point Surface Coatings for Local Convection Heat Transfer Measurements in Rectangular Channel Flow With 90-deg Turns," ASME *Journal of Heat Transfer*, Vol. 108, pp. 48–54.

Monson, D. J., Seegmiller, H. L., and McConnaughey, P. K., 1989, "Comparison of LDV Measurements and Navier-Stokes Solutions in a Two-Dimensional 180-Degree Turn-Around Duct," AIAA Paper No. 89-0275.

Rhie, C. M., 1986, "A Pressure Based Navier-Stokes Solver Using the Multigrid Method," AIAA Paper No. 86-0207.

Vedula, R. J., and Metzger, D. E., 1988, "Effects of Lateral and Anisotrpic Conduction on the Determination of Local Convection Heat Transfer Characteristics With Transient Tests and Surface Coatings," Arizona State University Technical Report ERC-R-89009.

Wagner, J. H., Johnson, B. V., and Hajek, T. J., 1991a, "Heat Transfer in Rotating Passages With Smooth Walls and Radially Outward Flow," ASME JOURNAL OF TURBOMACHINERY, Vol. 113, pp. 42–51.

Wagner, J. H., Johnson, B. V., and Kopper, F. C., 1991b, "Heat Transfer in Rotating Serpentine Passages With Smooth Walls," ASME JOURNAL OF TURBOMACHINERY, Vol. 113, pp. 321–330.

Influence of Surface Heat Flux Ratio on Heat Transfer Augmentation in Square Channels With Parallel, Crossed, and V-Shaped Angled Ribs

J. C. Han
Professor.
Fellow ASME

Y. M. Zhang
Research Associate.
Mem. ASME

Turbine Heat Transfer Laboratory,
Department of Mechanical Engineering,
Texas A&M University,
College Station, TX 77843

C. P. Lee
Senior Staff Engineer,
General Electric Company,
Cincinnati, OH 45215
Mem. ASME

The effect of wall heat flux ratio on the local heat transfer augmentation in a square channel with two opposite in-line ribbed walls was investigated for Reynolds numbers from 15,000 to 80,000. The square channel composed of ten isolated copper sections has a length-to-hydraulic diameter ratio (L/D) of 20. The rib height-to-hydraulic diameter ratio (e/D) is 0.0625 and the rib pitch-to-height ratio (P/e) equals 10. Six ribbed side to smooth side wall heat flux ratios (Case 1—$q''_{r1}/q''_s = q''_{r2}/q''_s = 1$; Case 2—$q''_{r1}/q''_s = q''_{r2}/q''_s = 3$; Case 3—$q''_{r1}/q''_s = q''_{r2}/q''_s = 6$; Case 4—$q''_{r1}/q''_s = 6$ and $q''_{r2}/q''_s = 4$; Case 5—$q''_{r1}/q''_s = q''_{r2}/q''_s = \infty$; and Case 6—$q''_{r1}/q''_s = \infty$ and $q''_{r2}/q''_s = 0$) were studied for four rib orientations (90 deg rib, 60 deg parallel rib, 60 deg crossed rib, and 60 deg V-shaped rib). The results show that the ribbed side wall heat transfer augmentation increases with increasing ribbed side to smooth side wall heat flux ratios, but the reverse is true for the smooth side wall heat transfer augmentation. The average heat transfer augmentation of the ribbed side and smooth side wall decreases slightly with increasing wall heat flux ratios. Two ribbed side wall heating (Case 5—$q''_{r1}/q''_s = q''_{r2}/q''_s = \infty$) provides a higher ribbed side wall heat transfer augmentation than the four-wall uniform heating (Case 1—$q''_{r1}/q''_s = q''_{r2}/q''_s = 1$). The effect of wall heat flux ratio reduces with increasing Reynolds numbers. The results also indicate that the 60 deg V-shaped rib and 60 deg parallel rib perform better than the 60 deg crossed rib and 90 deg rib, regardless of wall heat flux ratio and Reynolds number.

Introduction

Casting turbulence promoters/ribs inside cooling channels is an effective method to increase the heat transfer rate inside turbine airfoils. The ribs break up the laminar sublayer and create local wall turbulence due to flow separation from the ribs and reattachment between the ribs. Therefore, the heat transfer rate is greatly enhanced. The effects of rib configurations (rib height, spacing, angle of attack) and flow Reynolds numbers on the average heat transfer and pressure drop in the fully developed region of a uniformly heated square duct with two opposite ribbed walls were systematically studied (Han, 1984; Han et al., 1985). The effects of the above parameters on the local heat transfer and pressure drop in entrance and downstream regions of foil heated, ribbed rectangular ducts with five different aspect ratios were investigated (Han, 1988; Han and Park, 1988; Han et al., 1989). The results show that the parallel angled ribs (the ribs on two opposite walls of the cooling ducts are in parallel orientation) give a higher heat transfer rate than the transverse ribs, and the narrow aspect ratio ducts (near the leading edge of the airfoil) perform better than the wide aspect ratio ducts (near the trailing edge of the airfoil). The parallel angled ribs provide a better heat transfer performance than the transverse ribs because of the rib angle induced secondary flow, the laminar sublayer interruption, and the wall turbulence generation. The rib angle induced secondary flow effect diminishes in the wide aspect ratio ducts because the ribs on the two opposite wall are too close to each other. The effect of rib angle orientation on the local, regionally averaged heat transfer distributions and pressure drop in a ribbed square duct was recently re-examined (Han et al., 1991). The results show that the V-shaped angled rib performs slightly better than the parallel angled rib and, subsequently, better than the crossed angled rib (the ribs on two opposite walls of the cooling duct are in crossed orientation) and the transverse rib. The V-shaped angled rib produces the highest heat transfer augmentation and the greatest pressure drop increment, while

Contributed by the International Gas Turbine Institute and presented at the 36th International Gas Turbine and Aeroengine Congress and Exposition, Orlando, Florida, June 3-6, 1991. Manuscript received at ASME Headquarters January 18, 1991. Paper No. 91-GT-3. Associate Technical Editor: L. A. Riekert.

the crossed angled rib gives the lowest heat transfer enhancement and the smallest pressure drop penalty. This is because, in addition to breaking the laminar sublayer and creating the wall turbulence, the V-shaped angled rib induces a four-cell secondary flow while the parallel angled rib produces a two-cell, but the crossed angled rib has only a one-cell secondary flow.

The above studies consistently indicate that the rib angle induced secondary flow is responsible for high heat transfer augmentation in a square duct with two opposite in-line ribbed walls. These data were taken under the thermal boundary conditions of the ribbed side wall heat flux at 1.5 to 2 times the smooth side wall heat flux and the local ribbed side wall temperature were about the same as the local smooth side wall temperature. It is common, in the real turbine airfoil, that the ribbed side wall heat flux can be 1 to 10 times the smooth side wall heat flux and the local ribbed side wall temperature can be 1 to 1.2 times the smooth side wall temperature. The heat flux on the pressure side ribbed wall can also be different from that on the suction side ribbed wall. It is of interest whether the different wall heat flux levels can affect the heat transfer performance in cooling passages with angled rib promoters and whether the heat transfer augmentation can be further enhanced or reduced due to the different amount of heat inputs from the ribbed side wall and smooth side wall. The reason is that as the rib angle induced secondary flow cells move around the ribbed side wall and smooth side wall, the hot and cold fluid may be bouncing back and forth between the ribbed side wall and smooth side wall because the heat flux of the ribbed side wall is quite different from the smooth side wall.

The objective of this study is to investigate the effect of wall heat flux ratio on the local heat transfer augmentation in a square duct with two opposite in-line ribbed walls (see Fig. 1) for Reynolds numbers 15,000 to 80,000. Four typical rib configurations were studied (see Fig. 2(*a*)): 90 deg, 60 deg parallel, 60 deg crossed, and 60 deg V-shaped. Six ribbed side to smooth side wall heat flux ratios were employed (see Fig. 2(*b*) and Table 1): Case 1—$q''_{r1}/q''_s = q''_{r2}/q''_s = 1$; Case 2—$q''_{r1}/q''_s = q''_{r2}/q''_s = 3$; Case 3—$q''_{r1}/q''_s = q''_{r2}/q''_s = 6$; Case 4—$q''_{r1}/q''_s = 6$ and $q''_{r2}/q''_s = 4$; Case 5—$q''_{r1}/q''_s = q''_{r2}/q''_s = \infty$; and Case 6—$q''_{r1}/q''_s = \infty$ and $q''_{r2}/q''_s = 0$. The square channel has ten isolated copper sections in the axial direction. The regionally averaged heat transfer coefficients on both the ribbed side and smooth side walls of the duct are determined from the duct entrance to the downstream region. The duct averaged heat transfer coefficients are obtained and the heat transfer versus pressure drop performances are compared for the four rib configurations with six wall heat flux ratios. The semi-empirical heat transfer correlations are developed to account for the effect of the wall heat flux ratio.

Experimental Apparatus

To obtain the true average heat transfer coefficients for turbine cooling design, it is better to have a test section that can determine the regionally averaged heat transfer coefficients in the duct streamwise flow direction. The regionally averaged heat transfer method has been used previously (Burggraf, 1970; Metzger and Sahm, 1986; Han et al., 1991). The same technique is employed in this study.

The test duct is divided into ten short copper sections as seen in Fig. 1(*a*). Each copper section is composed of four copper plates 10.16 cm (4 in.) long, 0.63 cm (0.25 in.) thick and has an inner cross section of 5.08 cm by 5.08 cm (2 in. by 2 in.). Thin wooden strips (0.159 cm thickness) are attached along the periphery contact surface between copper sections as insulation to prevent possible heat conduction. The square test duct length-to-hydraulic diameter ratio (L/D) is 20. The local wall temperature of the test duct is measured by 80 copper-constantan thermocouples distributed along the length and across the span of the copper plates. There is an unheated entrance duct (not shown in Fig. 1(*a*)) that has the same cross section and length as that of the test duct, although the entrance duct is of plexiglass plates. This entrance duct serves to establish hydrodynamically fully developed flow at the entrance to the test duct. Figure 1(*b*) shows a schematic of the rib

Nomenclature

A = heat transfer surface area
D = square channel width or height
e = rib height
e^+ = roughness Reynolds number, Eq. (7)
f = friction factor in a channel with two opposite ribbed walls
f_o = friction factor in fully developed tube flow
f_r = friction factor for four-side ribbed channel
G = heat transfer roughness function; also mass velocity ρv
$\overline{G}$ = average heat transfer roughness function
g_c = conversion factor
h = heat transfer coefficient
K = thermal conductivity of air
L = channel length
Nu = Nusselt number = hD/K
Nu_o = Nusselt number in fully developed tube flow
Nu_r = ribbed side wall Nusselt number
Nu_s = smooth side wall Nusselt number
$\overline{\mathrm{Nu}}$ = average Nusselt number of ribbed side and smooth side wall
P = rib pitch
Pr = Prandtl number of air
ΔP = pressure drop across the entire test duct
q = heat generation rate from foils, W
q_{loss} = heat loss rate through insulation, W
q''_{r1} = heat flux from the left-hand side ribbed wall, W/m^2
q''_{r2} = heat flux from the right-hand side ribbed wall, W/m^2
q''_s = heat flux from the top smooth walls; also heat flux from the bottom smooth wall, W/m^2
R = friction roughness function
Re = Reynolds number = $\rho DV/\mu$
St = Stanton number = Nu/RePr
St_o = Stanton number in fully developed tube flow
St_r = ribbed side wall Stanton number
St_s = smooth side wall Stanton number
$\overline{\mathrm{St}}$ = average Stanton number of ribbed side and smooth side wall
T_b = local bulk mean temperature, °C
Tr_1 = local wall temperature of the left-hand side ribbed wall, °C
Tr_2 = local wall temperature of the right-hand side ribbed wall, °C
Ts_1 = local wall temperature of the top smooth wall, °C
Ts_2 = local wall temperature of the bottom smooth wall, °C
T_w = local wall temperature °C
V = average velocity of air
X = axial distance from heated channel inlet
μ = average dynamic viscosity of air
ρ = average density of air

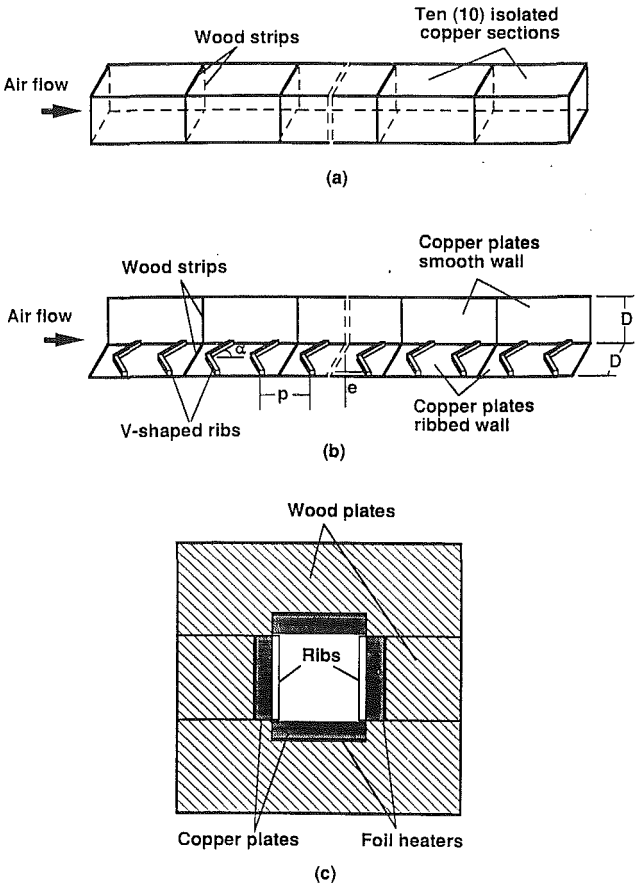

Fig. 1 (*a*) Test duct composed of ten copper sections; (*b*) V-shaped rib orientation; (*c*) cross section of the test duct

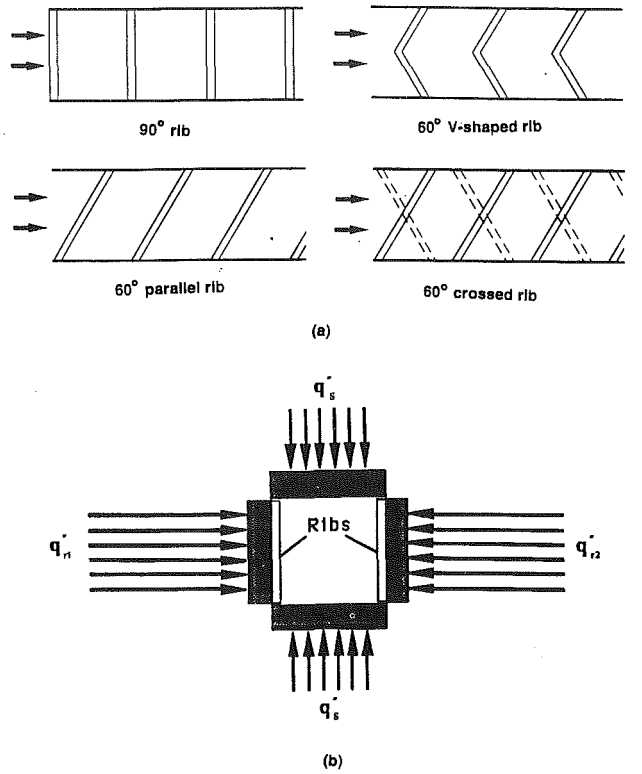

Fig. 2 (*a*) Top view of studied four rib orientations; (*b*) schematic of studied six wall heat flux ratios

Table 1 Six wall heat flux ratios studied

CASE NO.	WALL HEAT CONDITIONS	q''_{r1}/q''_s	q''_{r2}/q''_s
1	four walls uniform heat	1	1
2	non-uniform heat (two ribbed walls greater than two smooth walls)	3	3
3	non-uniform heat (two ribbed walls greater than two smooth walls)	6	6
4	non-uniform heat (two ribbed walls different but greater than two smooth walls)	6	4
5	two ribbed walls heated and two smooth walls unheated	∞	∞
6	one ribbed wall heated and other three walls unheated	∞	0

geometry. The ribbed wall was made by gluing copper ribs of square cross section to the copper plates in a required distribution and orientation. The glue thickness is less than 0.0127 cm. The rib height-to-hydraulic diameter ratio (e/D) is 0.063; the rib pitch-to-height ratio (P/e) equals 10 for the four rib configurations studied.

Figure 1(*c*) shows the cross section of the test duct. The test duct orientation is such that the two opposite ribbed walls of the square cross sections are vertical and the two opposite smooth walls horizontal. The foil heaters are uniformly cemented between the copper plate backface and a wood plate to insure good contact. Each of the four duct walls has one foil heater with each heater independently controlled by a variac transformer. Each heater provides a controllable uniform heat flux for each duct wall. The smooth side walls are isolated from the ribbed side walls to eliminate heat conduction (see Fig. 1(*c*)). The entire heated test duct is insulated by fiberglass material.

Data Reduction

A micromanometer connected to pressure taps measures the pressure drop across the test duct. The friction factor was calculated from the pressure drop across the test duct and the mass velocity of air as:

$$f = \Delta P/[4(L/D)(G^2/2\rho g_c)] \quad (1)$$

Based on the heating levels of this study, it was experimentally determined that the friction factor with heating is about 1–3 percent higher than that without heating. Therefore, the friction factor f is based on the isothermal conditions (tests without heating). The maximum uncertainty in the friction factor is estimated to be less than 8 percent for Reynolds numbers greater than 10,000 by using the uncertainty estimation method of Kline and McClintock (1953). To reduce the effect of flow Reynolds number on the friction factor increment, the friction factor f of the present study was normalized by the friction factor for fully developed turbulent flow in smooth circular tubes ($10^4 < \mathrm{Re} < 10^6$) proposed by Blasius as:

$$f/f_o = f/[0.046\mathrm{Re}^{-0.2}] \quad (2)$$

The local heat transfer coefficient was calculated from the local net heat transfer rate per unit surface area to the cooling air, the local wall temperature on each copper plate, and the local bulk mean air temperature as:

$$h = (q - q_{\mathrm{loss}})/[A(T_w - T_b)] \quad (3)$$

Equation (3) was used for the local ribbed side wall and smooth side wall heat transfer coefficient calculations. The local net heat transfer rate was the electrical power generated from the

foil heaters minus the heat loss outside the test duct. The electrical power generated from the foil was determined from the measured foil resistance and voltage on each wall of the test duct. The effect of the local wall temperature variation on the local foil resistance was estimated to be very small and negligible. The effect of axial wall conduction between copper sections on the local net heat transfer rate was small but included in the data reduction. The foil provided a nearly uniform heat flux on each wall of the test duct. The heat loss from the test duct was determined separately under a no-flow condition. The maximum heat loss from the ribbed side wall and smooth side wall was estimated to be less than 3 and 4 percent, respectively, for Reynolds numbers greater than 10,000.

Note that the ribbed side wall heat transfer area increases by adding ribs. The area increment depends upon the rib spacing and rib angle of attack but is independent of the wall heat flux ratio studied. For the present study of $P/e = 10$, the ribbed side wall heat transfer area with the 90 deg ribs increases by 20 percent compared with the smooth wall, while the heat transfer area with the 60 deg ribs (parallel, crossed, or V-shaped) increases by 23 percent. To place the results on a common basis, the heat transfer area used in Eq. (3) was always that of a smooth wall. The local wall temperatures used in Eq. (3) were read from the thermocouple output of each copper plate. Note that each copper plate on both smooth side walls had one thermocouple, and each copper plate on both ribbed side walls had three thermocouples with one at the center and two off center. It was found that these three thermocouples read the same temperature. This means that the temperature is uniform in the spanwise direction because of the high thermal conductivity of the copper plate. The bulk mean air temperatures entering and leaving the test duct were measured by thermocouples. The local bulk mean air temperature used in Eq. (3) was calculated from the measured inlet air temperature and the net heat input to the air. The total net heat transfer rate from the test duct to the cooling air agreed with the cooling air enthalpy rise along the test duct. The inlet bulk mean air temperature was 30° to 33°C depending on the test conditions. The maximum uncertainty in the Nusselt number was estimated to be less than 8 percent for Reynolds numbers larger than 10,000 by using the uncertainty estimation method of Kline and McClintock (1953).

To reduce the influence of flow Reynolds number on the heat transfer augmentation, the local Nusselt number of the present study was normalized by the Nusselt number for fully developed turbulent flow in smooth circular tubes correlated by Dittus-Boelter/McAdams as:

$$\mathrm{Nu}/\mathrm{Nu}_o = (h \cdot D/K)/[0.023\mathrm{Re}^{0.8}\mathrm{Pr}^{0.4}] \tag{4}$$

The friction data for turbulent flow in a square duct with two opposite ribbed walls can be correlated by the following equations (Han, 1988):

$$R(e^+) = (f_r/2)^{-1/2} + 2.5 \ln (2e/D) + 2.5 \tag{5}$$

where

$$f_r = 2f - f_o \tag{6}$$

$$e^+ = (e/D)\ \mathrm{Re}(f_r/2)^{1/2} \tag{7}$$

The heat transfer data for fully developed turbulent flow in a square duct with two opposite ribbed walls can be similarly correlated by the following equations (Han, 1988):

$$G = [(f_r/2)^{1/2}]/\mathrm{St}_r + 2.5 \ln(2e/D) + 2.5 \tag{8}$$

and

$$\overline{G} = [(f_r/2)^{1/2}]/\overline{\mathrm{St}} + 2.5 \ln(2e/D) + 2.5 \tag{9}$$

where

$$\overline{\mathrm{St}} = (\mathrm{St}_r + \mathrm{St}_s)/2 \tag{10}$$

Table 2 Tabulated data for the 60 deg parallel ribs at Re = 30,000

a) $q''_{r1}/q''_s = q''_{r2}/q''_s = 1$

X/D	T_b	T_{r1}	T_{r2}	T_{s1}	T_{s2}	q''_{r1}	q''_{r2}	q''_s
1	34.7	49.6	48.9	55.2	52.9	1727	1727	1686
3	35.4	51.6	50.3	58.5	58.1	1719	1719	1683
5	36.1	52.9	51.2	58.8	58.6	1719	1719	1681
7	36.8	51.9	51.2	58.6	58.4	1719	1719	1682
9	37.6	53.0	52.9	59.3	57.9	1719	1719	1679
11	38.3	57.5	54.3	60.3	60.0	1716	1716	1674
13	39.0	56.3	55.9	62.1	62.0	1713	1713	1674
15	39.7	59.8	57.5	61.9	64.3	1711	1711	1669
17	40.5	60.6	59.4	63.5	64.3	1709	1709	1667
19	41.2	60.6	59.4	63.5	64.3	1709	1709	1667

b) $q''_{r1}/q''_s = q''_{r2}/q''_s = 6$

X/D	T_b	T_{r1}	T_{r2}	T_{s1}	T_{s2}	q''_{r1}	q''_{r2}	q''_s
1	34.4	49.0	48.0	37.7	38.6	1770	1770	226
3	34.9	50.8	49.1	41.3	40.5	1765	1765	223
5	35.6	51.9	49.9	42.2	40.9	1764	1764	222
7	36.2	50.4	49.2	42.5	41.0	1763	1763	222
9	36.8	50.9	50.7	42.7	41.2	1763	1763	222
11	37.4	54.8	51.4	43.5	42.2	1762	1762	218
13	38.0	53.3	52.3	44.7	43.6	1759	1759	218
15	38.6	55.9	54.0	45.2	44.8	1758	1758	215
17	39.2	55.6	55.3	45.9	45.6	1757	1757	214
19	39.9	55.6	55.3	45.9	45.6	1757	1757	214

In the present data reduction program, Eqs. (5)-(10) were used to calculate the friction roughness function R and the heat transfer roughness function G and $\overline{G}$.

Experimental Results and Discussions

Regionally Averaged Heat Transfer Data. Figure 2(*a*) shows the top view of the studied four rib orientations: 90 deg rib, 60 deg parallel rib, 60 deg crossed rib, and 60 deg V-shaped rib. Six ribbed side to smooth side wall heat flux ratios are reported for each of four rib configurations (see Fig. 2(*b*) and Table 1): The heat flux on each of four walls is uniform (Case 1—$q''_{r1}/q''_s = q''_{r2}/q''_s = 1$); the heat flux on the two ribbed walls is higher than that on the two smooth walls (Case 2—$q''_{r1}/q''_s = q''_{r2}/q''_s = 3$; Case 3—$q''_{r1}/q''_s = q''_{r2}/q''_s = 6$); the heat flux on two ribbed walls is not the same and higher than the two smooth walls (Case 4—$q''_{r1}/q''_s = 6$ and $q''_{r2}/q''_s = 4$); the two ribbed walls are heated and the two smooth walls unheated (Case 5—$q''_{r1}/q''_s = q''_{r2}/q''_s = \infty$); one of the two ribbed walls is heated and the other three walls unheated (Case 6—$q''_{r1}/q''_s = \infty$ and $q''_{r2}/q''_s = 0$).

The local, regionally averaged heat transfer results are presented as the axial distributions of a normalized Nusselt number ratio. To observe the trend of the raw data, Table 2 provides a sample set of data for the 60 deg parallel ribs with Re = 30,000 for the uniform wall heat flux (Case 1—$q''_{r1}/q''_s = q''_{r2}/q''_s = 1$) and for the nonuniform wall heat flux (Case 3—$q''_{r1}/q''_s = q''_{r2}/q''_s = 6$) including local wall temperatures, heat fluxes, and bulk temperatures. Figures 3 and 4 show the effects of the wall heat flux ratio on the ribbed side wall and smooth side wall Nusselt number ratio distributions for Re = 30,000. The results show that, in general, the local ribbed side wall Nusselt number ratio increases with increasing the ribbed side to smooth side wall heat flux ratio for each of the four rib orientations studied. The reverse is true for the local smooth side wall Nusselt number ratio. The colder fluid moves from the smooth side wall with a lower heat flux toward the ribbed side wall and enhances the ribbed side wall heat transfer coefficient. Meanwhile, the hotter fluid moves from the ribbed side wall with a higher heat flux toward the smooth side wall to reduce the smooth side wall heat transfer coefficient. For

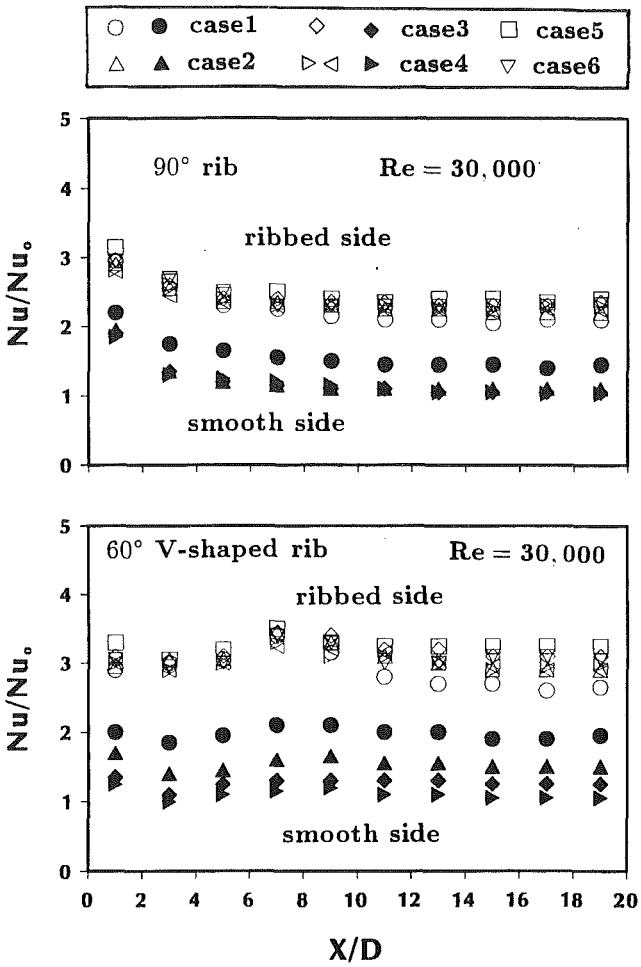

Fig. 3 Effect of wall heat flux ratio on local Nusselt number ratio distributions for 90 and 60 deg V-shaped ribs at Re = 30,000

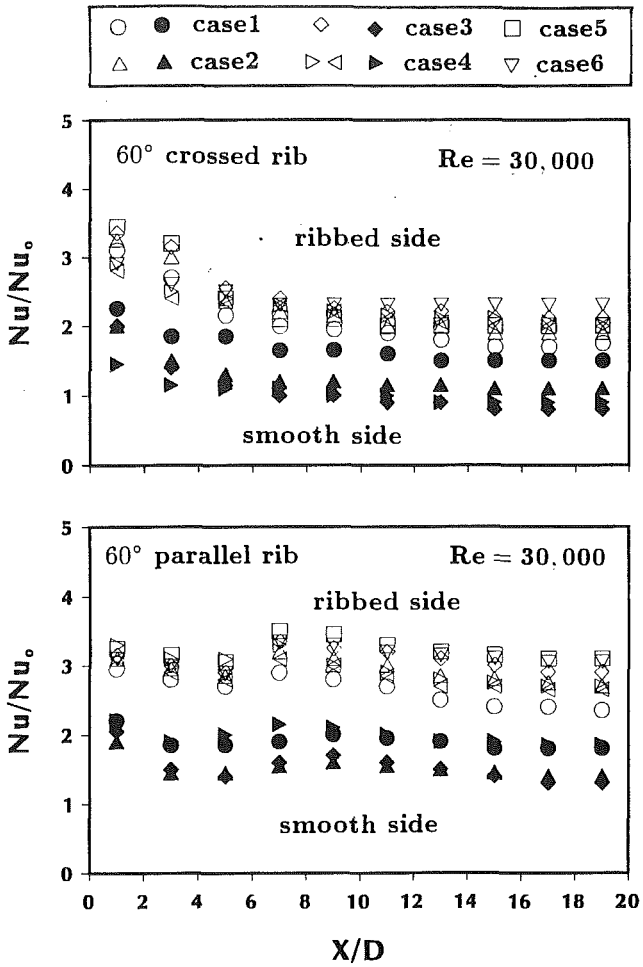

Fig. 4 Effect of wall heat flux ratio on local Nusselt number ratio distributions for 60 deg parallel and 60 deg crossed ribs at Re = 30,000

the cases of 90 deg rib and 60 deg crossed rib, the Nusselt number ratio (ribbed side and smooth side) decreases while increasing the axial distance, and reaches a constant value in the fully developed region at a given wall heat flux ratio. For the cases of 60 deg parallel rib and 60 deg V-shaped ribs, however, the Nusselt number ratio (ribbed side and smooth side) decreases to reach a minimum value at X/D around 4 and then increases to reach a maximum value at X/D around 8, due to the secondary flow induced by the rib orientation. The Nusselt number decreases again after the maximum value in the further downstream region. The results for other Reynolds numbers show similar trends as for Re = 30,000. The lower heat transfer coefficients obtained with crossed ribs as opposed to parallel ribs are similar to those reported by Metzger and Vedula (1987) in a triangular cross-sectional duct with two ribbed walls, and also reported in the previous studies (Han and Zhang, 1991; Han et al., 1991). It is conjectured that the 60 deg crossed ribs induce a single corotating cell of secondary flow, whereas the 60 deg parallel ribs produce a pair of counterrotating cells. The 60 deg V-shaped ribs may create similar counterrotating cells along each divergent axis of V-shaped ribs and cause a higher heat transfer. These secondary flow effects diminish at the downstream region of the flow channel. The conjectured secondary flow induced by the angled ribs will be verified through the flow visualization technique and by the velocity profile measurements in a separate project. This investigation focuses on the effect of wall heat flux ratio on the heat transfer augmentation with the angled ribs.

Channel-Averaged Heat Transfer and Pressure Drop Data. Figures 5 and 6 show the Nusselt number ratio (ribbed side and smooth side) versus Reynolds numbers for different wall heat flux ratios. The ribbed side wall Nusselt number ratio is the average value of the entire ribbed side wall Nusselt number from the channel inlet to the outlet. Similarly, the smooth side wall Nusselt number ratio is the average value of the entire smooth side wall Nusselt number from the inlet to the outlet of the heated channel.

The results show that the Nusselt number ratio decreases with increasing Reynolds numbers for the four rib orientations and six heat flux ratios studied. In general, the ribbed side wall Nusselt number ratio increases with increasing ribbed side to smooth side wall heat flux ratio whereas the smooth side wall Nusselt number ratio decreases with increasing ribbed side to smooth side wall heat flux ratio. For the case of uniform wall heat flux (Case 1), the ribbed side wall heat transfer coefficient is the lowest but the smooth side wall heat transfer coefficient is the highest. For the cases of one ribbed wall (Case 6) or two ribbed wall heating (Case 5), the ribbed side wall heat transfer coefficient is the highest. The results also indicate that the effect of wall heat flux ratio gradually reduces with increasing Reynolds numbers. At Re = 15,000, the ribbed side wall Nusselt number ratio increases by 25–30 percent and the smooth side wall Nusselt number ratio decreases by 20–60 percent. At Re = 80,000, the Nu_r/Nu_o increases by 10 percent and the Nu_s/Nu_o decreases by 20–40 percent depending upon the rib orientation. It is worthy to mention that, in the real

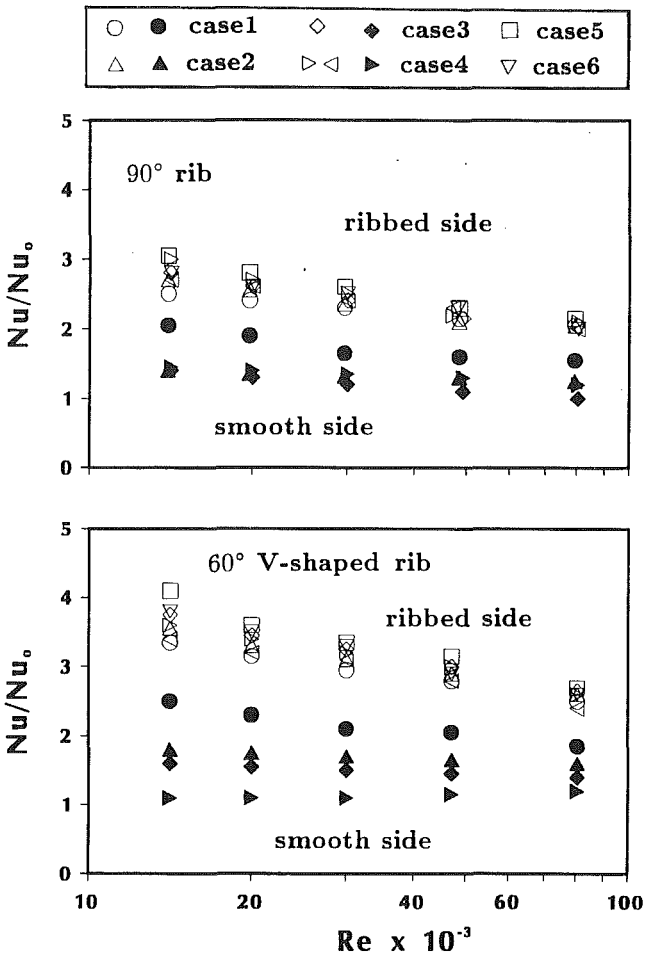

Fig. 5 Effect of wall heat flux ratio on Nusselt number ratio for 90 deg and 60 deg V-shaped ribs over a range of Reynolds numbers

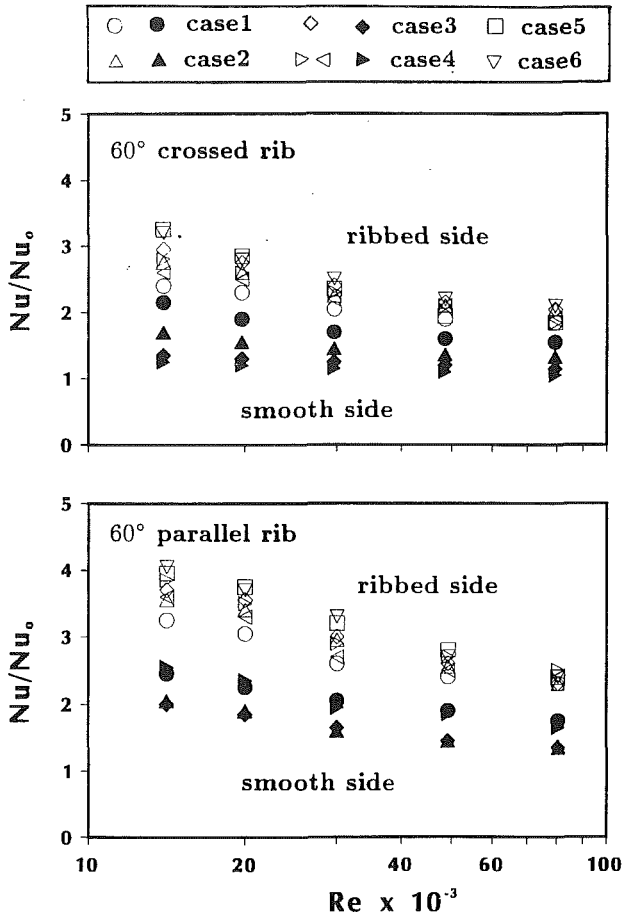

Fig. 6 Effect of wall heat flux ratio on Nusselt number ratio for 60 deg parallel and 60 deg crossed ribs over a range of Reynolds numbers

turbine airfoil, the ribbed side wall heat flux can be 1 to 10 times the smooth side wall heat flux and the heat flux on the pressure side ribbed wall can be different from the suction side ribbed wall. It is imperative from this study that the effect of wall heat flux ratio on the ribbed side wall and the smooth side wall heat transfer coefficient augmentation should be considered.

Figure 7 shows the effect of wall heat flux ratio on the average heat transfer augmentation of the ribbed side and smooth side wall. The results show that the average Nusselt number ratio of ribbed side and smooth side wall decreases slightly with increasing wall heat flux ratios (Cases 1, 2, 3, and 4). This is because the ribbed side wall heat transfer increment is smaller than the smooth side wall heat transfer reduction as discussed earlier.

Figure 8 compares the friction factor ratio for four rib orientations. The pressure drops across the test duct were measured at the unheated flow conditions. The results show that the friction factor ratio increases with increasing Reynolds numbers. The 60 deg V-shaped rib provides higher friction factor ratios than those of the 60 deg parallel rib, 90 deg rib, and 60 deg crossed rib. Note that the 60 deg crossed rib produces both the lowest heat transfer coefficient augmentation and the smallest pressure drop penalty compared to other rib orientations.

Heat Transfer Performance Comparison. Figure 9 shows the channel-averaged Nusselt number ratio (ribbed side or smooth side) versus the friction factor ratio for three different wall heat flux ratios over a range of studied Reynolds numbers. The three different wall heat flux ratios are: Case 1—uniform

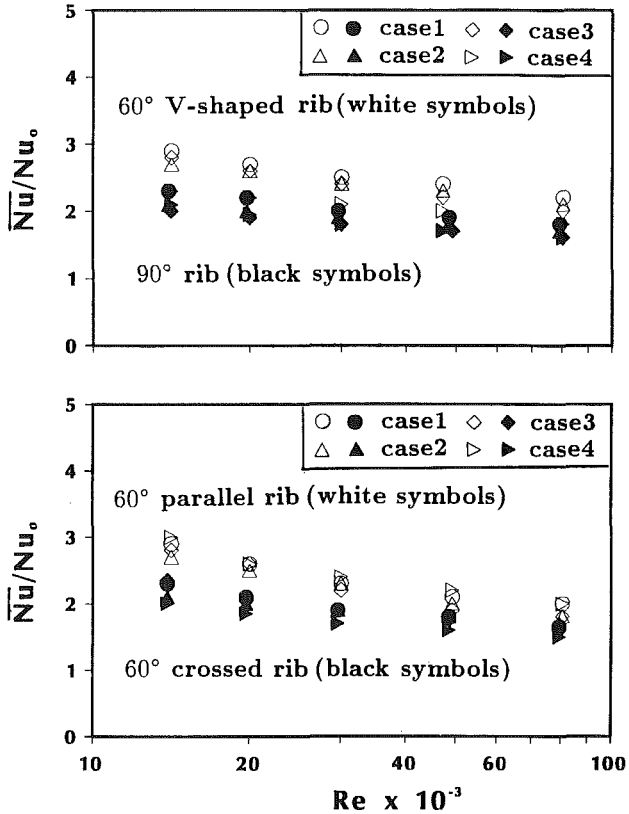

Fig. 7 Effect of wall heat flux ratio on average Nusselt number ratio for the four rib configurations studied over a range of Reynolds numbers

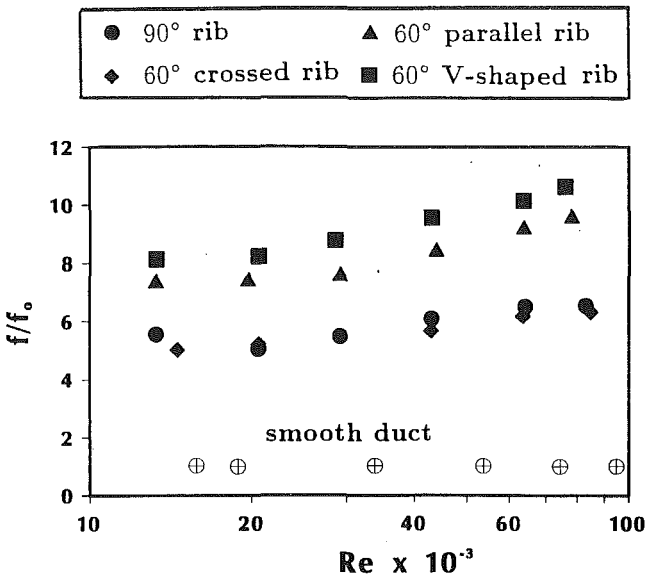

Fig. 8 Friction factor ratio versus Reynolds number for studied four rib orientations

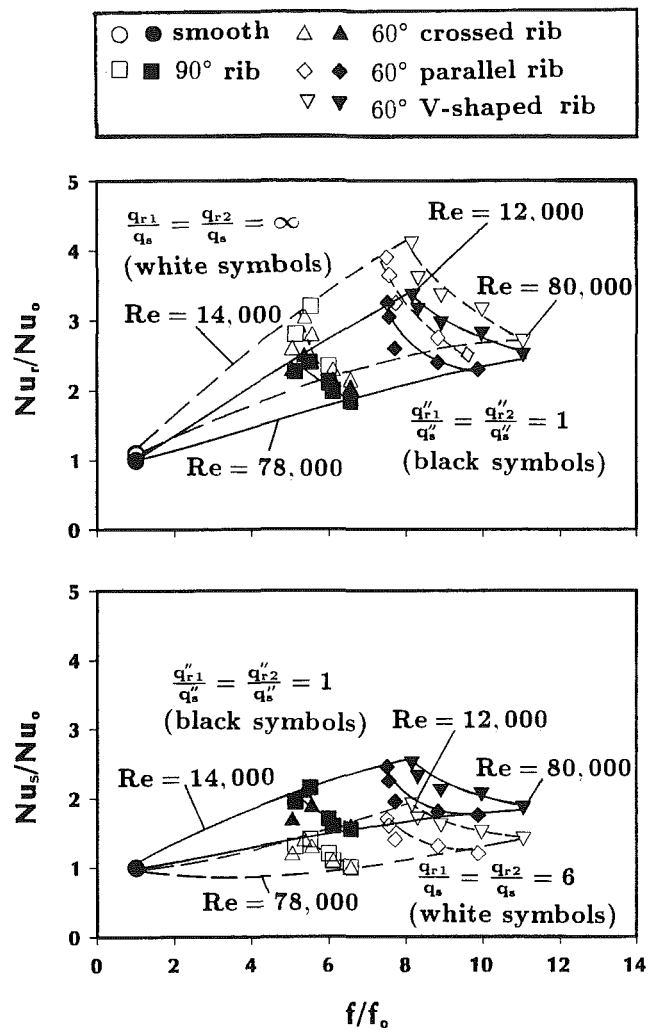

Fig. 9 Nusselt number ratio versus friction factor ratio for studied four rib orientations

wall heat flux, Case 3—two ribbed wall heat flux is six times two smooth wall, and Case 5—two ribbed wall heating but two smooth wall unheating. The results show that, in general,

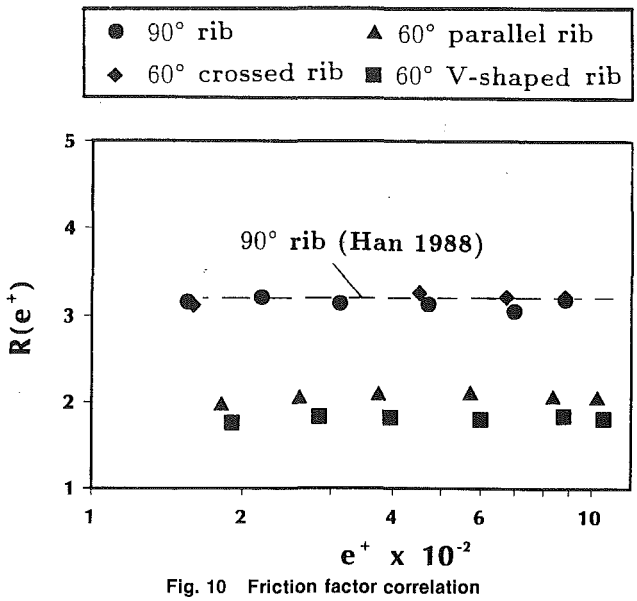

Fig. 10 Friction factor correlation

the ribbed side wall Nusselt number ratio with two ribbed wall heating (Case 5) is higher than that with four uniform wall heating (Case 1). However, the smooth side wall Nusselt number ratio with four wall uniform heating is higher than that with four wall nonuniform heating (Case 3). The Nusselt number ratio decreases but the friction factor increases with increasing Reynolds numbers as discussed in the previous section. This means that the heat transfer performance decreases with increasing Reynolds numbers. The results also show that the effect of wall heat flux on the heat transfer performance decreases with increasing Reynolds numbers. The heat transfer performance for the 60 deg V-shaped rib is slightly higher than the 60 deg parallel rib and higher still for the 60 deg crossed rib and 90 deg rib regardless of the wall heat flux ratio. The effect of wall heat flux ratio on the four-side smooth channel heat transfer results is also included in Fig. 9 for comparison. Note that the Nusselt number ratio is only enhanced by 3–5 percent for Case 5 compared with Case 1 (white circular symbols to black circular symbols) and no change for Case 3 compared with Case 1 (white and black circular symbols coincide). This confirms that the wall heat flux has an effect on the ribbed channel but none on the smooth channel.

Heat Transfer and Friction Correlations. Figure 10 represents the friction roughness function (R) versus the roughness Reynolds number (e^+) for four rib orientations over a range of studied Reynolds numbers. The roughness functions for 90 deg ribs and 60 deg crossed ribs are about the same and corresponded with previous correlations developed for the 90 deg rib (Han, 1988). The 60 deg V-shaped rib and 60 deg parallel rib have lower roughness functions, which implies higher pressure drops according to Eq. (5). The roughness function is almost independent of the roughness Reynolds number for all rib orientations studied, which implies in the fully rough regime. Table 3 provides the coefficients and exponents in this function for the four rib orientations studied. For a given rib configuration and flow Reynolds number, the friction factor can be predicted from the roughness function (R) read from Table 3. Note that the friction roughness function (R) shown in Fig. 10 is a universal result for each rib geometry independent of e/D. This has been verified for $0.021 \le e/D \le 0.063$ (Han, 1984).

Figure 11 shows the heat transfer roughness function (G) versus the roughness Reynolds number (e^+) with the effect of wall heat flux ratio for the four rib orientations over a range of Reynolds numbers studied. Similar plots for the average heat transfer roughness function ($\overline{G}$), based on the average

Table 3 Coefficients and exponents for friction and heat transfer roughness functions

	$R = a(e^+)^b$	
	a	b
90° rib	3.18	0
60° crossed rib	3.18	0
60° parallel rib	2.05	0
60° v-shaped rib	1.72	0

	$G = a(e^+)^b$							
	90° rib		60° crossed rib		60° parallel rib		60° v-shaped rib	
	a	b	a	b	a	b	a	b
Case 1	1.61	0.42	1.82	0.41	1.04	0.48	1.01	0.47
Case 2	1.23	0.46	0.91	0.51	0.53	0.57	0.87	0.48
Case 3	1.07	0.48	0.72	0.53	0.46	0.60	0.72	0.51
Case 4	0.9	0.51	1.18	0.48	0.7	0.53	0.75	0.52
Case 5	0.86	0.51	0.5	0.6	0.42	0.60	0.61	0.53
Case 6	1.05	0.50	0.69	0.55	0.43	0.59	0.54	0.56

	$\bar{G} = a(e^+)^b$							
	90° rib		60° crossed rib		60° parallel rib		60° v-shaped rib	
	a	b	a	b	a	b	a	b
Case 1	2.94	0.35	1.90	0.42	1.14	0.48	1.63	0.42
Case 2	2.12	0.42	2.27	0.40	1.48	0.45	1.86	0.41
Case 3	2.56	0.40	2.30	0.41	1.38	0.47	2.17	0.39
Case 4	2.27	0.42	1.89	0.43	1.31	0.47	2.03	0.40

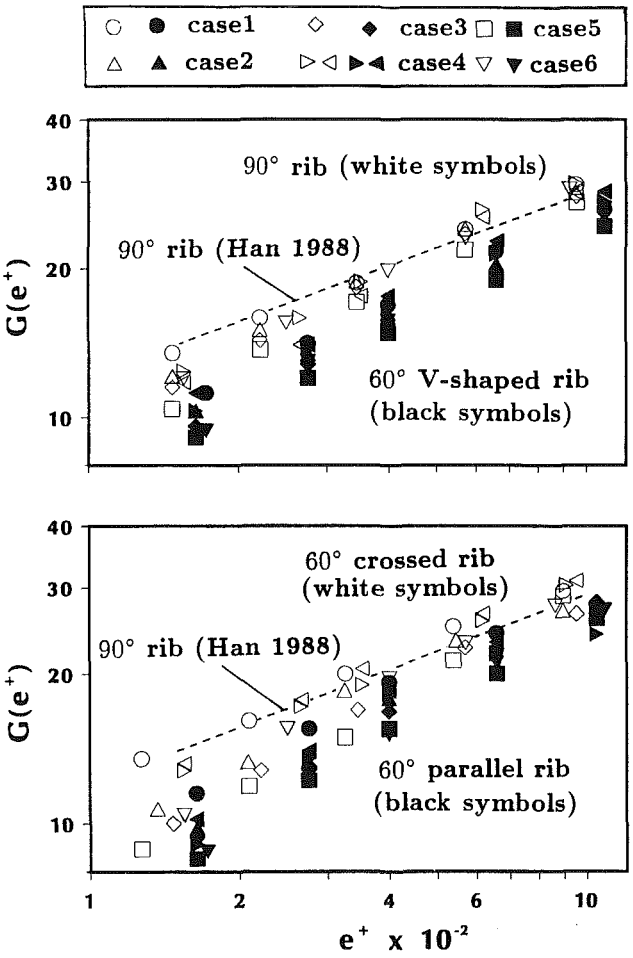

Fig. 11 Effect of wall heat flux ratio on the heat transfer correlation

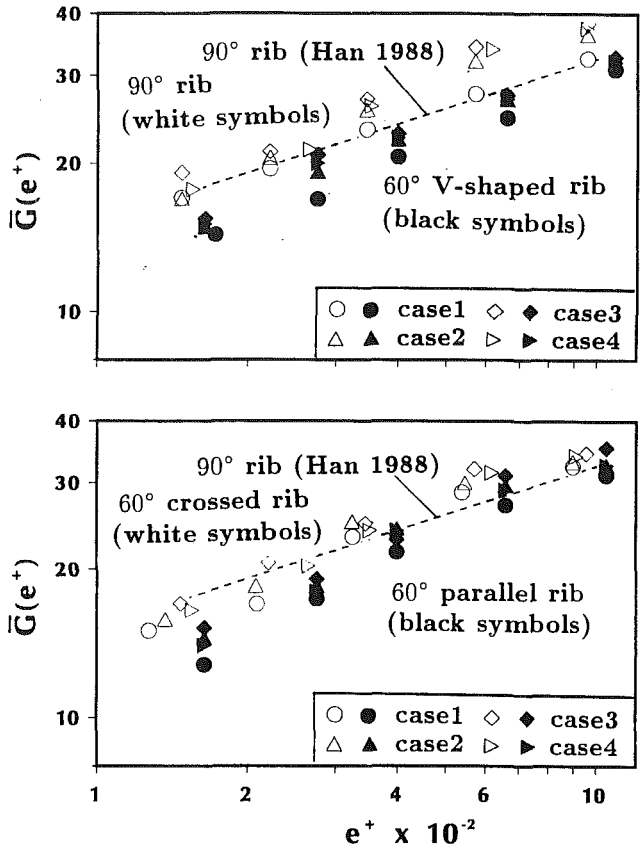

Fig. 12 Effect of wall heat flux ratio on the average heat transfer correlation

value of the ribbed side and smooth side wall heat transfer coefficients ($\overline{St}$), are shown in Fig. 12. The heat transfer roughness functions for 90 deg ribs are about the same as the previous correlations developed for the 90 deg rib (Han, 1988). The heat transfer roughness function increases with increasing roughness Reynolds number for all studied rib configurations regardless of the wall heat flux ratio. The heat transfer roughness functions for the one ribbed wall and two ribbed wall heating are lower than the four wall uniform heating (see Fig. 11), which implies higher heat transfer coefficients according to Eq. (8). The average heat transfer roughness functions ($\bar{G}$) for the nonuniform wall heating are higher than the four wall uniform heating (see Fig. 12), which means lower heat transfer coefficients according to Eq. (9). The effect of wall heat flux ratio on the average heat transfer roughness function ($\bar{G}$) is not as distinct as the heat transfer roughness function (G). Table 3 provides the coefficients and exponents in this function for the four rib orientations studied. For a given rib configuration and flow Reynolds number, the Stanton number can be predicted from the heat transfer roughness function (G or $\bar{G}$) and friction roughness function (R) read from Table 3.

Concluding Remarks

The influence of wall heat flux ratio on heat transfer augmentation in square channels with parallel, crossed, and V-shaped ribs has been performed for Reynolds numbers from 15,000 to 80,000. The main findings of the study are:

1 The 60 deg V-shaped rib provides a slightly better heat transfer performance than the 60 deg parallel rib. The 60 deg V-shaped rib and the 60 deg parallel rib perform much better than the 60 deg crossed rib and the 90 deg rib, which have about the same performance. For the four rib orientations studied, the heat transfer augmentation decreases with Reyn-

olds numbers while the pressure drop increment increases with Reynolds numbers.

2 The Nusselt number ratio for the 90 deg rib and the 60 deg crossed rib decreases by increasing the axial distance, and reaches a constant value several ribs from the channel entrance. For the 60 deg V-shaped rib and 60 deg parallel rib, however, the Nusselt number ratio decreases to a minimum and then increases to a maximum value downstream due to the rib angle induced secondary flow effect.

3 The ribbed side wall Nusselt number ratio increases with increasing ribbed side to smooth side wall heat flux ratio but the reverse is true for the smooth side wall. The wall heat flux effect decreases with increasing Reynolds numbers.

4 Two ribbed wall heating provides a higher ribbed side wall heat transfer augmentation than that of the four wall uniform heating. Nonuniform wall heating gives a lower smooth side wall heat transfer augmentation than that of the four wall uniform heating.

5 The average Nusselt number ratio of the ribbed side and smooth side wall decreases slightly with increasing wall heat flux ratios.

6 The semi-empirical correlations of the friction factor and Stanton number are developed for four rib configurations including wall heat flux ratio effect that can be used for turbine cooling design.

Acknowledgments

The investigation was supported by the General Electric Company.

References

Burggraf, F., 1970, "Experimental Heat Transfer and Pressure Drop With Two-Dimensional Turbulence Promoter Applied to Two Opposite Walls of a Square Tube," *Augmentation of Convective Heat and Mass Transfer*, A. E. Bergles and R. L. Webb, eds., ASME New York, pp. 70–79.

Han, J. C., 1984, "Heat Transfer and Friction in Channels With Two Opposite Rib-Roughened Walls," ASME *Journal of Heat Transfer*, Vol. 106, pp. 774–781.

Han, J. C., Park, J. S., and Lei, C. K., 1985, "Heat Transfer Enhancement in Channels With Turbulence Promoters," ASME *Journal of Engineering for Gas Turbines and Power*, Vol. 107, pp. 629–635.

Han, J. C., 1988, "Heat Transfer and Friction Characteristics in Rectangular Channels With Rib Turbulators," ASME *Journal of Heat Transfer*, Vol. 110, pp. 321–328.

Han, J. C., and Park, J. S., 1988, "Developing Heat Transfer in Rectangular Channels With Rib Turbulators," *International Journal of Heat and Mass Transfer*, Vol. 31, pp. 183–195.

Han, J. C., Ou, S., Park, J. S., and Lei, C. K., 1989, "Augmented Heat Transfer in Rectangular Channels of Narrow Aspect Ratios With Rib Turbulators," *International Journal of Heat and Mass Transfer*, Vol. 32, pp. 1619–1630.

Han, J. C., Zhang, Y. M., and Lee, C. P., 1991, "Augmented Heat Transfer in Square Channels With Parallel, Crossed, and V-Shaped Angled Ribs," ASME *Journal of Heat Transfer*, Vol. 113, pp. 590–596.

Han, J. C., and Zhang, P., 1991, "Effect of Rib-Angle Orientation on Local Mass Transfer Distribution in a Three-Pass Rib-Roughened Channel," ASME JOURNAL OF TURBOMACHINERY, Vol. 113, pp. 123–130.

Kline, S. J., and McClintock, F. A., 1953, "Describing Uncertainties in Single-Sample Experiments," *Mechanical Engineering*, Jan., pp. 3–8.

Metzger, D. E., and Sahm, M. K., 1986, "Heat Transfer Around Sharp 180 deg Turns in Smooth Rectangular Channels," ASME *Journal of Heat Transfer*, Vol. 108, pp. 500–506.

Metzger, D. E., and Vedula, R. P., 1987, "Heat Transfer in Triangular Channels With Angled Roughness Ribs on Two Walls," *Experimental Heat Transfer*, Vol. 1, pp. 31–44.

Computation of Laminar Flow and Heat Transfer Over an Enclosed Rotating Disk With and Without Jet Impingement

Y. Nakata

J. Y. Murthy

D. E. Metzger

Department of Mechanical and Aerospace Engineering,
Arizona State University,
Tempe, AZ 85287

Convection heat transfer phenomena on rotating disks are of general interest in relation to turbomachineray design. In gas turbine engines, for example, knowledge of the temperature distribution on turbine disks that are bounded by a fluid cavity is required to predict stresses and durability. Cooling air is generally provided by the compressor section and routed to the turbine disk cavities where it is utilized for cooling both the rotating and stationary components. Since the production and pumping of the compressed cooling air imposes performance penalties on the engine cycle, a goal of the designer is always to minimize cooling air consumption. This requirement produces a need for accurate and detailed knowledge of the convection heat transfer and flow characteristics associated with disk cavity flows for a large variety of possible cooling configurations. In the past, most reliable information on disk cavity flow and heat transfer has been derived from empirical studies, but the large range of possible geometries and flow conditions precludes a complete coverage by experiment alone. In the future, it should be possible to supplement disk cavity flow experiments with numerical computations both to aid in interpretation of and to extend empirical results. The present numerical study of laminar flow cases is intended to complement previous experimental information for disk convection with jet impingment. The computational method is described and applied first to a baseline case of a rotating disk in an enclosure where results are found to compare favorably with the experiments of Daily and Nece. The two-dimensional approach used to model the inclusion of an impinging jet is described, and the computational method is applied to predict both flow and heat transfer characteristics in the vicinity of the interaction between impinging jet and rotating disk. The computed results partition into impingment-dominated and rotational-dominated regimes similar to the findings of prior experimental studies.

Introduction

Heat transfer phenomena on rotating disks are of quite widespread interest in relation to turbomachinery design. In most such applications, it is important to have knowledge of and the ability to control disk temperature. In gas turbine engines, for example, knowledge of the temperature distribution on turbine disks is required to predict stresses and durability. Cooling air is generally provided by the compressor section and routed to the turbine disk cavities, where it is utilized for cooling the rotating and stationary components. Usually this air also serves to pressurize the cavities to protect the rotating disks and adjacent stationary components from the radial ingress of the hot combustion gases. Since the production and pumping of the compressed cooling air imposes performance penalties on the engine cycle, a goal of the designer is always to minimize cooling air consumption. However, the use of too little cooling air may cause durability problems or thermal-related structural damages to the turbine section. For this reason, the designer must have accurate and detailed knowledge of the convection heat transfer and flow characteristics associated with the disk cavity flow.

One method of cooling turbine disks is to supply the coolant locally to structurally critical regions through use of jet impingement. Figure 1 shows schematically a cross section of a typical configuration of impingement disk cooling. An advantage associated with this scheme is the possibility of providing high cooling rate concentrations at the locations of greatest need, with overall reduction in the total cooling air requirement. A possible disadvantage is local overcooling, producing locally large temperature gradients and high stresses. For confident design, much more information is needed on the heat transfer characteristics of jets impinging on rotating surfaces.

Efforts to acquire detailed heat transfer information on rotating surfaces started with, among others, the analysis of von

Contributed by the International Gas Turbine Institute and presented at the ASME Winter Annual Meeting, Atlanta, Georgia, December 1-6, 1991. Manuscript received by the International Gas Turbine Institute April 26, 1992. Associate Technical Editor: L. S. Langston.

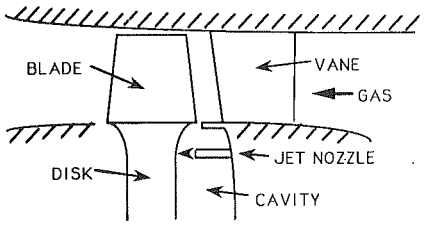

Fig. 1 Turbine disk impingement cooling

Karman (1921), and the experiments of Cobb and Saunders (1956) and Kreith et al (1959). A concise review of literature addressing both the fluid mechanics and heat transfer aspects of the subjects up to 1982 is provided by Owen (1984). Most of the published work deals with investigation of the flow aspects of the problem through experimental approaches, e.g., Daily and Nece (1960) and Bayley and Owen (1970). The analytical solution of the flow field is available only for the simplest case of a radially infinite rotating disk without a shroud. The acquisition of heat transfer data has been slow and is incomplete because of the expense and complexity involved with making local heat transfer measurement on rotating surfaces. Some experiments were conducted to acquire local data for heat transfer between a rotating disk and impinging jets for the case of free and unenclosed disks by Metzger and Grochowsky (1977), Metzger et al. (1979), and Bogdan (1982). Most recently Metzger et al. (1989) reported successful local heat transfer data acquisition for the case of an enclosed disk/stator cavity utilizing thin liquid crystal surface coatings together with a thermal transient test procedure. One of the first numerical studies of flow in a rotating cavity was that of Pao (1970), who considered the flow generated by rotating one of the disks with the other surface held stationary. Pao and other workers have used a variety of different methods to solve finite difference equations for laminar flow, experiencing convergence difficulties in cases with high disk Reynolds numbers. The finite element method has also been applied to a variety of different laminar flows by Bar-Yoseph et al. (1981). The main advantage of this method over finite difference techniques appears to be its versatility in accounting for complex boundary shapes. The problem of convergence at high disk speed remains. Chew (1984) indicated that the slow convergence of numerical solutions is associated with instabilities in the physical flows, and improved the convergence rate by giving better resolution in the Ekman layer, the boundary layer formed on the rotating surface, and by some improvement on the pressure correction method in the SIMPLE algorithm. Most recently Morse (1987) presented numerical predictions of turbulent flow in a rotating cavity and indicated that the SIMPLER algorithm achieves convergence more easily than SIMPLE because the pressure correction procedure employed is more effective.

All previous numerical efforts at prediction have investigated only disk-cavity flows without jet impingement. In the prior experimental heat transfer studies with jet impingement, some characteristic features have been observed that are thought to be associated with the interaction of the jet with the disk boundary layer. At low relative jet flow rates, the jet appears to be effectively deflected by the pumped boundary layer, and the convection heat transfer at the impingment radius remains dominated by the disk boundary layer. At higher flow rates the jet is better able to influence the surface heat transfer, and the transition between these rotationally dominated and impingement dominated flow regimes is quite abrupt in both laminar and turbulent situations. The present primary objectives are numerically to acquire details of a laminar flow field in the disk cavity and accompanying local heat transfer coefficients on the rotating disk surface enclosed by a stationary shroud, including situations designed to provide better understanding of interactions between a rotating flow and impinging jet. To this end, two cases have been modeled in the

Nomenclature

A_D = rotating disk area
A_{ex} = exit area, Eq. (15)
A_j = source jet area at the origin, Eq. (16)
c = specific heat of fluid
d_j = width of the source jet origin, Fig. 4
h = heat transfer coefficient
$\bar{h}$ = averaged heat transfer coefficient, Eq. (25)
$h(r)$ = local heat transfer coefficient, Eq. (23)
k = thermal conductivity of the fluid
K = ratio of angular velocity of fluid core and of rotating disk = β/Ω
$\mathrm{Nu}(r)$ = local Nusselt number, Eq. (22)
Nu_{ave} = averaged Nusselt number, Eq. (24)
$\overline{\mathrm{Nu}}_\delta$ = averaged Nusselt number, Eq. (27)
p = fluid pressure
p'' = dimensionless pressure, Eq. (6)
Pr = Prandtl number
q = heat flux
Q_j = mass flow rate of source jet, Eq. (13)
Q_p = disk pumping flow rate based on the von Karman solution, Eq. (14)
r_j = equivalent jet radius, Eq. 12)
R_D = rotating disk radius, Fig. 2
R_j = radial distance from centerline to the lower limit of source jet, Fig. 4
R_{ex} = exit radius, Fig. 4
Re_d = disk Reynolds number, Eq. (6)
Re_j = jet Reynolds number, Eq. (11)
T = fluid temperature
T_H = constant specified temperature on the rotating disk
T_C = constant specified temperature in the stationary shroud or source jet temperature
w_j = fluid velocity at the origin of source jet
Z_C = cavity depth, Fig. 2
Z_j = axial distance from the rotating disk surface to the origin of source jet, Fig. 4
r, ϕ, z = cylindrical coordinate system
u, v, w = velocity componets of respective cylindrical coordinates
U, V, W = dimensionless velocity components, Eq. (6)
α = underrelaxation factor
β = angular velocity of the fluid core
δ_r = Ekman layer thickness based on the von Karman solution, Eq. (28)
μ = dynamnic viscosity of fluid
ν = kinematic viscosity of fluid
ρ = density of fluid
Ω = constant specified angular velocity of rotating disk

present study. The first is cavity flow without jet impingement and the second introduces an impinging jet imposed as source inside the cavity.

Formulation of the Mathematical Model

General Assumptions. The following assumptions are made in the present study to reduce the Navier-Stokes equations to the form employed in the computations:

1 The cavity flow is enclosed by a plane rotating disk with constant rotational speed and a stationary, plane, shroud.
2 The geometry of rotating disk surface and shroud surface are circumferentially uniform.
3 The impinging jet velocity is constant; the inlet port width is circumferentially uniform.
4 The rotation speed and jet velocity are slow enough to consider that entire flow field is laminar, incompressible, and Newtonian, but the flow is fast enough to neglect buoyancy effects in the entire field.

In addition to these flow characteristics, the following assumptions are imposed as temperature boundary conditions to assess heat transfer characteristics on the rotating surface:

5 Uniform high temperature all over the rotating disk surface.
6 Completely insulated shroud.
7 Uniform low temperature at the outlet of impinging jet.
8 Zero heat transfer across the center line.
9 Constant fluid properties within the entire region.

With these considerations and assumptions, the flow and temperature fields can be assumed to be axisymmetric and steady. The Navier-Stokes equations are simplified to two-dimensional elliptic equations, and the momentum and energy equations are decoupled.

Conservation Equations. For laminar steady flow, with assumption of axisymmetry and constant fluid properties, the three momentum equations, the energy equation, and the continuity equation can be written nondimensionally as:

$$\frac{1}{R}\frac{\partial(RU^2)}{\partial R}+\frac{\partial(UW)}{\partial Z}=-\frac{\partial p''}{\partial R}+\frac{1}{\mathrm{Re}_d}\left[\frac{1}{R}\left(\frac{R\partial U}{\partial R}\right)+\frac{\partial^2 U}{\partial Z^2}-\frac{U}{R^2}\right]+\frac{V^2}{R} \quad (1)$$

$$\frac{1}{R}\frac{\partial(RUV)}{\partial R}+\frac{\partial(VW)}{\partial Z}=\frac{1}{\mathrm{Re}_d}\left[\frac{1}{R}\frac{\partial}{\partial R}\left(\frac{R\partial V}{\partial R}\right)+\frac{\partial^2 V}{\partial Z^2}-\frac{V}{R^2}\right]-\frac{UV}{R} \quad (2)$$

$$\frac{1}{R}\frac{\partial(RUW)}{\partial R}+\frac{\partial W^2}{\partial Z}=-\frac{\partial p''}{\partial Z}+\frac{1}{\mathrm{Re}_d}\left[\frac{1}{R}\frac{\partial}{\partial R}\left(\frac{R\partial W}{\partial R}\right)+\frac{\partial^2 W}{\partial Z^2}\right] \quad (3)$$

$$\frac{1}{R}\frac{\partial(RU\Theta)}{\partial R}+\frac{\partial(W\Theta)}{\partial Z}=\frac{1}{\mathrm{PrRe}_d}\left[\frac{1}{R}\left(\frac{R\partial\Theta}{\partial R}\right)+\frac{\partial^2\Theta}{\partial Z^2}\right] \quad (4)$$

$$\frac{1}{R}\frac{\partial(RU)}{\partial R}+\frac{\partial W}{\partial Z}=0 \quad (5)$$

where:

$$R=\frac{r}{\mathrm{R}_D},\ Z=\frac{z}{\mathrm{R}_D},\ U=\frac{u}{R_D\Omega},\ V=\frac{v}{\mathrm{R}_D\Omega},$$

$$W=\frac{w}{R_D\Omega},\ \Theta=\frac{T-T_C}{T_H-T_C},\ p''=\frac{p}{\rho R_D^2\Omega^2},$$

$$\mathrm{Re}_d=\frac{\rho\Omega R_D^2}{\mu},\ \mathrm{Pr}=\frac{\mu c}{k} \quad (6)$$

and (u, v, w) is the velocity relative to the cylindrical coordinate system (r, ϕ, z).

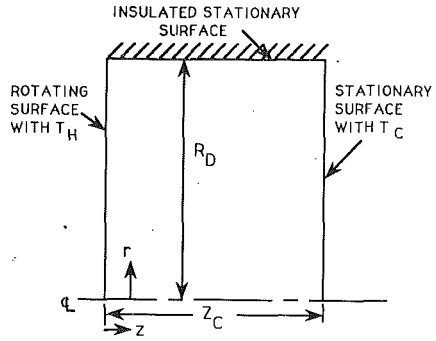

Fig. 2 Configuration without impingement

Cavity Flow Modeling Without Jet Impingement. The configuration modeled in this case is scehematically shown in Fig. 2. The rotating surface and the stationary shroud surface are considered nonslip boundaries, and the centerline is assumed to be the axis of symmetry. To investigate the steady-state heat transfer characteristics, a constant temperature T_H is specified over the entire rotating disk surface and a constant lower temperature is given to the stationary shroud facing the rotating disk. The aspect ratio of the cavity (Z_C/R_D) is set to be 0.2 throughout the present study.

The dimensionless boundary conditons for this case may be written as:

$$Z=0, 0<R<1;\ U=0,\ V=R,\ W=0,\ \Theta=1 \quad (7)$$

At the stationary surface facing the rotating disk:

$$Z=0.2,\ 0<R<1;\ U=0,\ V=0,\ W=0,\ \Theta=0 \quad (8)$$

At the symmetry line:

$$R=0,\ 0<Z<0.2;\ U=0,\ \partial V/\partial R=0\ \partial W/\partial R=0,\ \partial\Theta/\partial R=0 \quad (9)$$

At the stationary surface at the cavity rim:

$$R=1,\ 0<Z<0.2;\ U=0,\ V=0,\ W=0,\ \partial\Theta/\partial R=0 \quad (10)$$

Cavity Flow Modeling With Jet Impingement. A crucial element in the present study is the physical and mathematical modeling that was selected for this case, chosen from among numerous alternatives. A straightforward modeling of the situation would be that shown in Fig. 3(*a*). The jet originates at the stationary wall facing the rotating surface and the flow exits at the rim of the rotating disk. This approach, however, leads to an obvious problem in dealing with the exit condition. The most commonly used exit condition for numerical schemes is the Neumann condition with Peclet number at the exit very large so that there is no effect of downstream conditions. In an actual turbine setting, mainstream air flows outside the cavity and generally does affect the cavity outflow condition, including the possible radial inflow into the cavity. Therefore, to execute the modeling implied in Fig. 3(*a*) properly, it is necessary to expand the calculation domain to include the outside flow condition. If the Neumann condition is simply imposed on the exit in this setting, the condition near the exit is influenced by the artificially introduced exit area and may directly affect the flow condition around the rotating surface under the influence of impinging jet. A further and major difficulty with this approach is that with the two-dimensional jet modeling, the jet constitutes a flow barrier at its injection radius, dividing the cavity into inner and outer zones and preventing proper communication between the two.

An alternative modeling to minimize the influence of the exit condition uncertainties is to relocate the exit from the disk rim to near center line of the stationary shroud as shown in Fig. 3(*b*). In some actual applications, a portion of the cavity cooling may be routed in this manner. However, again the jet

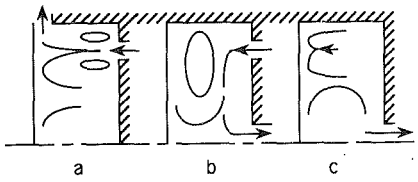

Fig. 3 Flow dependence on boundary conditions with impingement

constitutes a barrier at its injection radius, and the jet may be deflected well before reaching the rotating surface due to the relative pressure build-up between the inner and outer zones. The modeling applied in the present study is shown in Fig. 3(*c*). A flow source is located axially between the rotating disk and stationary shroud surfaces. The flow deflected upward after impinging on the rotating surface can go around the outer edge of the cavity and down behind the flow source. The exit area is located at the inner radius to remove the exit condition as far as possible from the jet-disk interaction, and by allowing an exit area large enough to suppress the outflow velocity, the influence of pressure near the exit on the entire flow field can be minimized. By applying this modeling, the jet-disk interaction investigated should be close to actual applications, and generic information about the interacting flow details and local heat transfer can be obtained.

The detailed configuration considered in this case is schematically shown in Fig. 4. The rotating and stationary shroud surfaces are set nonslip and the centerline is assumed to be an axis of symmetry. The circular exit is located at the center of the stationary shroud and the Neumann condition is prescribed. The exit area is adjusted based on the total mass flow added (as the impinging jet) to the calculation domain in order not to cause excessive outflow velocity and resultant low pressure, which may affect the entire flow field. The flow source is added at a specified position in the cavity to create a ring-shaped jet directed perpendicular to the disk surface. A uniform temperature T_H is prescribed over the entire rotating disk surface and a uniform lower temperature T_C is given at the origin of the jet. Stationary shroud surfaces are assumed to be thermally insulated. The location of flow source and the total mass flow rate introduced as the source jet are considered as parameters in the investigation. The cavity aspect ratio, Z_C/R_D is again maintained constant at 0.2, and the exit area A_{ex} is $\pi R_{ex}^2 = fn\ (w_j, d_j)$. In this case a jet Reynolds number Re_j and the mass flow ratio Q_j/Q_p are introduced as additional parameters, defined as:

$$\mathrm{Re}_j = \rho w_j r_j/\mu \tag{11}$$

where

$$r_j = \sqrt{A_j/\pi}, \text{ an equivalent jet radius} \tag{12}$$

$$Q_j = \rho A_j w_j \tag{13}$$

$$Q_p = 0.885\pi R_D^3 \Omega \mathrm{Re}_d^{1/2} \text{ (von Karman solution)} \tag{14}$$

The exit area is

$$A_{ex} = \pi R_{ex}^2 = fn(w_j, /d_j) \tag{15}$$

and for the source jet

$$Z_j,\ Z_C,\ R_j/R_D, \text{ and } A_j = \pi dj(2Rj + dj) \tag{16}$$

are variable parameters. The base source configuration is set at

$$Z_j/Z_C = 0.5,\ R_j/R_D = 0.8, \text{ and } d_j/R_D = 0.002 \tag{17}$$

The dimensionless boundary conditions for this case are:

At the rotating surface: the same as for Case 1

At the source jet:

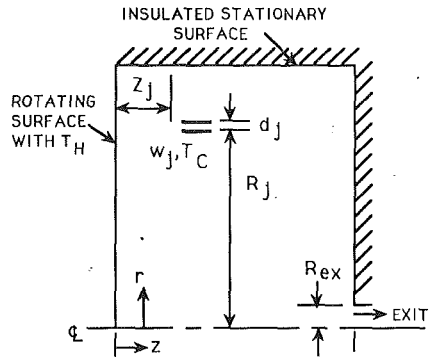

Fig. 4 Configuration with impingement

$$Z = (Z_j/R_D),\ (R_j/R_D) \le R \le ((R_j + R_D)/R_D) w = w_j/R_D\Omega, \Theta = 0 \tag{18}$$

At the exit:

$$Z = 0.2,\ 0 < R \le (R_{ex}/R_D); \text{ Neumann condition (grid Peclet number} = \infty) \tag{19}$$

At the stationary surface facing the rotating disk:

$$Z = 0.2,\ (R_{ex}/R_D) < R < 1;\ U = 0,\ V = 0,\ W = 0,\ \partial\Theta/\partial Z = 0 \tag{20}$$

At the symmetry line: the same as for Case 1

At the stationary surface at the tip: the same as for Case 1

Solution of the Equations. The derivation of the discretization equations used in the present study follows exactly the standard method described by Patankar (1980), using a staggered grid where velocity components are computed for points lying on the control volume faces and all other variables, including pressure, are calculated at the grid intersection points. The particular iterative method used for solution is the SIMPLER algorithm of Patankar (1981). Specific computational details for the various cases solved are given in the following section along with the results.

Results and Discussion

Computational Details for Cavity Flow Withour Jet Impingement. The solution algorithm and detailed problem settings were implemented in FORTRAN 77 and run on an IBM3090 using double precision. The discretization of the governing differential equations was carried out on a grid with 47 points in the z direction and 45 points in the r direction. The grid points are packed closely near the rotating surface and stationary shroud surface. The grid points near the centerline ($r = 0$) are packed sparsely. Computation at $\mathrm{Re}_d = 12{,}500$ for a grid system employing a 50 percent increase in the number of grids in each direction and with half-grid interval near the centerline indicated a change of less than 1 percent in the overall Nusselt numbers calculated, so the 47 × 45 grid was considered to be adequate.

A standard criterion is used to determine whether or not the solution has converged, based on residuals for each conservation equation. The residuals are calculated from the relation

$$\mathrm{Res} = \Sigma |a_p\Phi_p - \Sigma a_{nb}\Phi_{nb} - b| \tag{21}$$

where the first summation is carried out over all points P of the finite difference grid. As the residuals should be equal to zero for the exact solution, the computation may be stopped if the residuals all fall below some prescribed value. In all of the present study, it was found that a suitable cutoff value that always gives reasonable convergence and does not lead to excessive computing time was difficult to define. A very slow

velocity field in the r–z plane inside the fluid core mentioned in the next section sometimes caused sustained flucutations in residuals. In effect the residuals were used as a guide to see whether the solution is improving, and computations were stopped when further reduction in the residual appeared to produce only small changes in the velocity and pressures near the position of interest such as inside the Ekman layer.

Owing to the nonlinearity and the coupling of the governing equations, the iterative scheme used does not always converge. The solution sometimes oscillates or diverges, resulting in an overflow error on the computer. As Gosman and Spalding (1970) and Chew (1984) have previously reported, provision of good initial velocity and pressure estimates and a gradual increase in the disk Reynolds number helped to avoid these instabilities. No general rule is known for estimating the optimal underrelaxation factor α, and the behavior of the solution was very sensitive to this factor, especially when the disk Reynolds number is high. In the present case, α was selected to be 0.7 for lower disk Reynolds number $\mathrm{Re}_d < 12{,}500$ and approximately 200 iterations were necessary to get converged solutions. However, it was apparent from the computations that, as the disk Reynolds number was increased, convergence of the iterative solution method became more and more difficult to obtain and more computing time was required. In the present case the solution was safely obtained up to the disk Reynolds number of 25,000 with the appropriate underrelaxation factor α. Over $\mathrm{Re}_d = 20{,}000$, the underrelaxation factor α had to be reduced to 0.5 and more than 1000 iterations were required. With the disk Reynolds number at more than 25,000, the solution began to oscillate or diverge even with the underrelaxation factor $\alpha = 0.5$. To a limited extent it may be possible to get a solution over $\mathrm{Re}_d = 25{,}000$ by using very good initial velocity and pressure estimates and very heavy initial underrelaxation followed by increasing α to acceptable levels. However, it was found that with the underrelaxation factor less than 0.4 for the initial 500 iterations, a converged solution was obtained using the very good initial estimates, but the solution easily oscillated or diverged in this range of disk Reynolds number after increasing the underrelaxation factor to 0.5 or 0.6. This behavior of the solution may indicate that the physical flow is actually unsteady and/or unstable in this range of disk Reynolds number.

Discussion of the Computed Results for Cavity Flow Without Jet Impingement. The results obtained for this case are intended to serve as a baseline since the geometry conforms to the classic configuration investigated experimentally by Daily and Nece (1960). They investigated the fluid mechanics associated with the disk rotation within a right-cylindrical chamber both experimentally and theoretically. They describe four basic flow regimes in the axial gap between the disk and shroud, the existence and extent of which are governed by Reynolds number-axial spacing combinations. One of the regimes they investigated (laminar flow, separated boundary layers) correspond to the configuration in the present study.

Typical computed streamlines of the cavity flow in this case for a disk Reynolds number of 25,000 are shown in Fig. 5. The figure indicates a well-developed fluid core with thin boundary layers near the walls. Figures 6(*a–c*) show details of the local velocity distributions. The existence of the core is clear for this combination of disk Reynolds number and cavity configuration. The flow pattern corresponds to that categorized by Daily and Nece as Regime II: Laminar Flow, Separate Boundary Layers. As seen in Fig. 6, the radial velocity (*a*) in the fluid core is near zero and the circumferential velocity (*b*) is nearly constant. Axial velocity (*c*) is also near constant and very small compared with the circumferential velocity. The fluid core extends radially as shown in Fig. 7, and the radial velocity at $z/Z_C = 0.003$ corresponds to the peak radial velocity

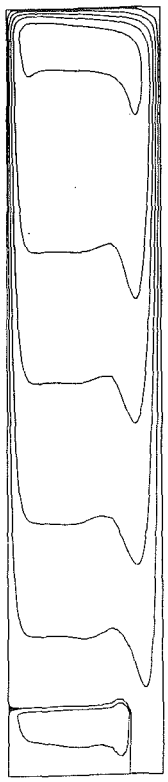

Fig. 5 Typical streamlines without impingement

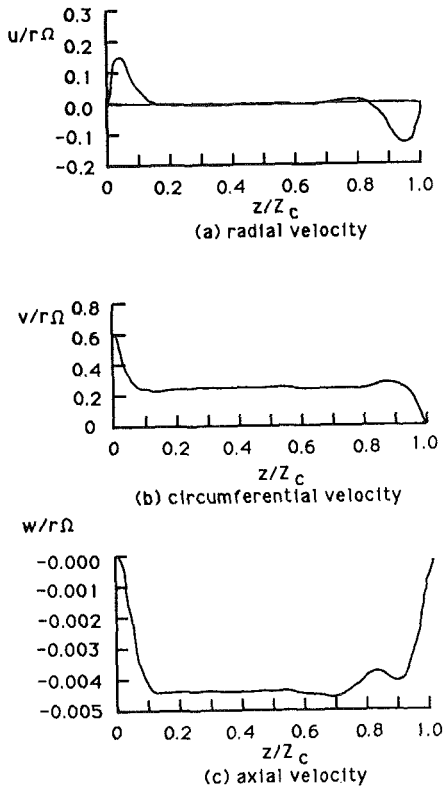

Fig. 6 Velocity profiles at $\mathrm{Re}_d = 25{,}000$, $r/R_D = 0.8$

of the Ekman layer, $z/Z_C = 0.42$ corresponds to the center of the fluid core, and $z/Z_C = 0.947$ corresponds to the peak radial velocity of the boundary layer on the stationary shroud. The effect of the rim shroud is confined to a very small radial

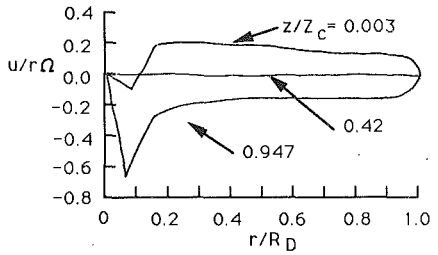

Fig. 7 Radial velocity profiles at Re = 25,000

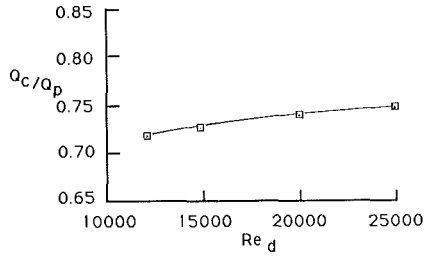

Fig. 8 Comparison of disk pumping flow

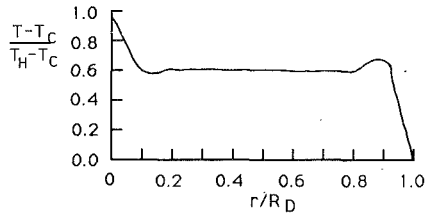

Fig. 9 Axial temperature profile at Re_d = 25,000

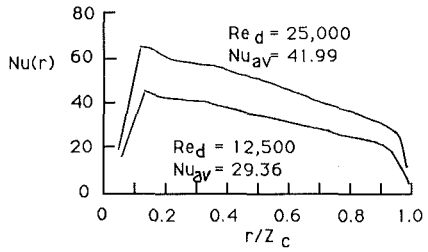

Fig. 10 Radial distribution of local Nusselt number

extent of the Ekman layer and the velocity profile in the Ekman layer does not change much radiually. The negative value near the centerline for $z/Z_C = 0.003$ corresponds to the recirculation near the axis shown in the stream lines in Fig. 5.

The ratio of angular velocity of fluid core to that of the rotating disk, $K = \beta/\Omega$, obtained here is 0.377, and this agrees quite well with the experimental result of 0.36 found by Daily and Nece for the corresponding cavity aspect ratio. The calculation limit in disk Reynolds number (over Re_d = 25,000) is found to be in the transition region from laminar to turbulent flow experimentally observed by Daily and Nece. Therefore it is plausible that convergence difficulties presently encountered for high disk Reynolds numbers may be associated with physical instabilities in the flow.

It is important to note that the effect of the rim shroud on the distribution of radial velocity is limited to a very small radial extent, and that the velocity profiles shown in Fig. 6 within the axial extent $0 \le z/Z_C \le 0.4$ are very similar to those of the free disk similarity solution of von Karman. Figure 8 shows the ratio of mass flow rate pumped radially outward by the rotating disk to that corresponding to the von Karman solution, where the pumping flow rate Q_c in the present case is obtained by numerical computation; Q_p is calculated from Eq. (14). Although this ratio is smaller when disk Reynolds number is small due to the effect of thicker boundary layer on the stationary wall, approximately 75 percent of the pumping flow indicated by von Karman is pumped and recirculated in this case. The 25 percent reduction in the pumping flow rate is considered to be a consequence of friction on the stationary wall. The slight reduction in the ratio as Reynolds number is reduced is probably associated with the corresponding thickening of the stationary wall boundary layer.

The axial distribution of temperature at $r/R_D = 0.8$ is shown in Fig. 9. Temperature changes only in the thermal boundary layers and temperature is axially near uniform inside the fluid core.

The radial distribution of local Nusselt number on the rotating disk is shown in Fig. 10, with local Nusselt number defined as:

$$\mathrm{Nu}(r) = \frac{h(r)R_D}{k} \tag{22}$$

where

$$h(r) = \frac{-k\left(\dfrac{\partial T}{\partial z}\right)}{T_H - T_C} \tag{23}$$

The negative slope of the local Nusselt number is due to the cooling effect at the stationary wall. Fluid is cooled while traveling near the low-temperature wall and is entrained by the Ekman layer near the centerline and gradually warmed in flowing along the high-temperature rotating disk.

The average Nusselt number is also shown in Fig. 10 for each disk Reynolds number, defined as:

$$\mathrm{Nu}_{\mathrm{ave}} = \frac{\bar{h}R_D}{k} \tag{24}$$

with the average heat transfer coefficient $\bar{h}$ defined by

$$\bar{h} = \frac{1}{R_D}\int_0^{R_D} h(r)dr \tag{25}$$

Figure 11 shows a strong correlation between the average Nusselt number and the square root of the disk Reynolds number. This relation can be expressed as:

$$\frac{\mathrm{Nu}_{\mathrm{ave}}}{\sqrt{\mathrm{Re}_d}} = \frac{\bar{h}\left(\dfrac{\nu}{\Omega}\right)^{1/2}}{k} = 0.264 \tag{26}$$

A corresponding relation was derived for the von Karman solution by Sparrow and Gregg (1959), where the constant is 0.396. The average heat transfer coefficient derived here is 33 percent lower than the uniform local heat transfer coefficient of the von Karman solution. This reduction in heat transfer coefficient is plausible considering the flow retardation by the stationary wall and the warm fluid enterainment by the Ekman layer because of the recirculation.

Computational Details for Cavity Flow With Jet Impingement. In this case, two-dimensional jet impingement is added to the basic cavity flow investigated in the previous section. The variation of flow pattern and heat transfer characteristics on the rotating surface was systematically investigated with changes in disk and jet Reynolds numbers and the ratio of source to calculated pumped flow. The discretization of the governing equation for this case is carried out on a grid of size

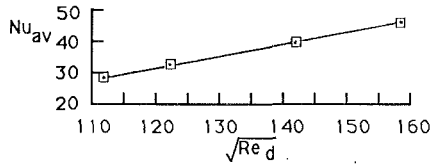

Fig. 11 Heat transfer characteristics without impingement

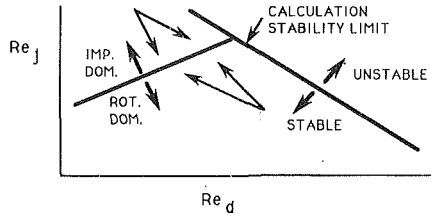

Fig. 12 Computational technique for initial estimates

49 × 46. In addition to the area near the wall boundary layer, grid points are also packed closely downstream of mass source jet. With the variation of source jet configuration, the grid distribution was adjusted so that abrupt volume changes in control volumes did not occur, while maintaining the total number of grid points. The area around the impingement point was packed closely until the decay of the source jet was sufficiently resolved. Based on this and the previous grid dependence check, the grid size of 49 × 46 was considered adequate.

Mass source is added to four control volumes whose west faces correspond to the specified dimensions (Z_j, R_j, and d_j) so that the jet velocity w_j and jet temperature T_C are the desired values. At the exit near the centerline, the Neumann condition is prescribed. Exit area is adjusted based on the total mass flow rate introduced as the source jet so that exit velocity does not change due to the change of source flow rate, which could affect the entire velocity field. The exit radius R_{ex} must be much larger than the radial extent of the source jet d_j because the circumferential extent for unit angle in the ϕ direction is longer for longer radius. As large exit radius also affects the entire velocity field as well as high exit velocity, a compromise was necessary for choosing the exit radius R_{ex}.

As indicated in the previous case, residuals did not decay rapidly after reaching a certain small value due to very small velocities inside the fluid core. Therefore, the residuals in effect were used as a guide to judge solution improvement, and computations were stopped when the velocities and pressures at the impingement area near rotating disk ceased to change significantly.

With introduction of the source jet, convergenece difficulties occurred at lower disk Reynolds numbers than in the cases without a source jet. To improve the convergence behavior, both disk and jet Reynolds numbers were increased gradually and smaller underrelaxation factors were applied. However, the final underrelaxation factor was set to more than 0.5 to assure that a false solution was not obtained because of excessive suppression by strong underrelaxation. As discussed in the following section, there are two distinct flow regimes, termed rotation-dominated and impingement-dominated, and a gradual increase in disk or jet Reynolds number did not always provide good initial estimates for velocity and pressure. A technique to provide a good initial estimate for each flow regime was to first obtain a solution with high jet Reynolds number and low disk Reynolds number and then gradually increase disk Reynolds number with lower jet Reynolds number to approach the lower limit of the impingement-dominated flow regime (and vice versa to approach the upper limit of the rotation-dominated flow regime) as shown schematically in Fig. 12. In addition to this technique, underrelaxation factors were carefully adjusted where both the boundary of flow regimes and the calculation limit due to instability came close. In this range, underrelaxation factors were set about 0.2 initially and gradually increased at least up to 0.5, monitoring the behavior of residuals.

Discussion of the Computed Results for Cavity Flow With Jet Impingement. Because of the complexity of flow patterns due to the combination of rotating flow and the jet imposed as source, velocity profile and/or streamlines are of little help in grasping actual flow patterns. Velocity vector plots help better describe the flow patterns in these cases. Figure 13 shows a typical velocity vector plot and the corresponding grid and control volume system.

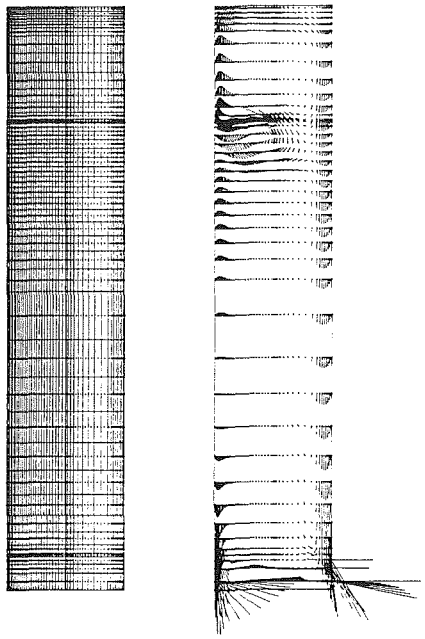

Fig. 13 Grid system and vector plot with impingement

In the velocity vector plot, the dot represents the grid point, the length of the bar represents the absolute value, and the angle represents the direction of the velocity vector. In Fig. 13, the source jet is imposed at $r/R_D = 0.8$ and $z/Z_C = 0.5$ and is directed perpendicular to the rotating disk. Because of the high jet velocity and relatively slow rotation ($Re_j = 453$, $Re_d = 10{,}000$), fluid goes both radially inward and outward after impingement. The fluid deflected outward after impinging on the rotating disk goes around the cavity rim and is partially entrained by the jet with the rest flowing down to the exit along the stationary shroud. The fluid deflected inward is pushed back by the rotating flow induced by the rotating disk, then is partially entertained by the jet with the rest entrained by the boundary layer on the stationary shroud going to the exit. Near the centerline, inward flow can be seen even on the rotating disk surface. This is due to low pressure near the exit and a relatively small centrifugal force at the small radius. Even with the high rate of mass source introduced as in the case shown in Fig. 13, the region affected by the exit condition is limited to locations near the centerline. This affected region is considered to be sufficiently far from the impingement region, which is the main interest of the present study. This type of flow pattern displayed in Fig. 13 in the impingement region is categorized as an impingement-dominated flow regime, and appears qualitatively similar to the impingement-dominated regime observed and defined by

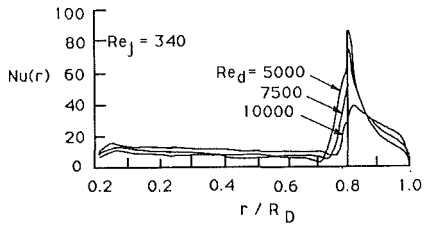

Fig. 14 Local Nusselt number for impingement-dominated flow regime

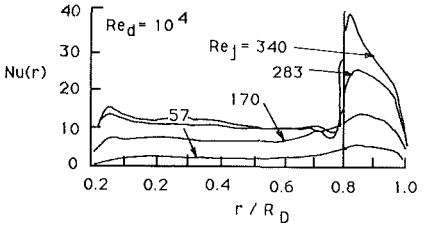

Fig. 15 Local Nusselt number for rotation-dominated flow regime

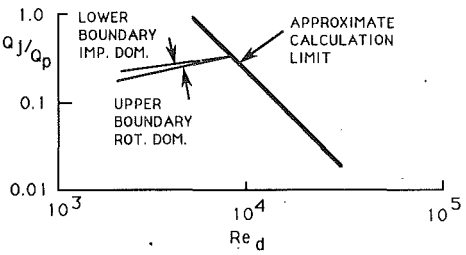

Fig. 16 Flow regime boundary and calculation limit

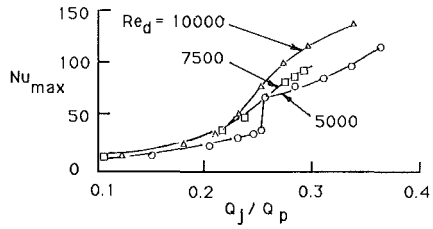

Fig. 17 Peak Nusselt number versus mass flow ratio

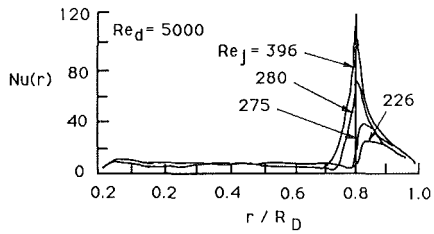

Fig. 18 Local Nusselt number at Re$_d$ = 5000

Metzger and Grochowsky (1977). As the rotation speed of the disk is increased or as the jet velocity is decreased, the rotating flow becomes strong enough to push the impinging jet and does not allow it to deflect inward, resulting in a jet that is deflected entirely outward. Then the flow pattern is categorized as rotation-dominated.

These distinct flow regimes can also be characterized by the radial distribution of local Nusselt number on the rotating disk. Radial Nusselt number distributions for various disk Reynolds number with fixed jet Reynolds number are shown in Fig. 14 for the impingement-dominated flow regime. When the jet Reynolds number is sufficiently high relative to the disk Reynolds number the cool impinging jet penetrates the Ekman layer and the peak Nusselt number is located right in front of the radial position of impinging jet origin. A high heat transfer region extends both inward ($r/R_D < 0.8$) and outward ($r/R_D > 0.8$). As the disk Reynolds number is increased, the inner high heat transfer region is diminished and the peak Nusselt number is drastically reduced and shifted radially outward at a given disk Reynolds number, indicating that the flow regime shift to rotation-dominated at a disk Reynolds number of approximately 10,000 in this case.

When the disk Reynolds number is sufficiently high relative to the jet Reynolds number, cool air does not fully penetrate the Ekman layer and the jet cool fluid is effectively deflected outward, thus the peak Nusselt number locates radially further out the jet origin as shown in Fig. 15. When the jet velocity is very low compared with the disk Reynolds number the cool fluid is simply smoothly entrained by Ekman layer.

In the present study, if the radial velocity is all positive near the rotating disk, the flow regime is judged to be rotation-dominated. Likewise, a negative velocity near the rotating disk indicates that an inward flow component is present and the flow regime is judged to be impingement-dominated. Based on this criterion, flow pattens were investigated for various combination of rotation speed and jet flow ratio for the base source jet configuration. The result is summarized in Fig. 16, and it was found that the flow regime transition occurs at approximately $Q_j/Q_p = 0.2$ to 0.3 for various disk Reynolds numbers up to 10,000. With the disk Reynolds number more than 10,000, it became increasingly difficult to get the steady-state solution because of the convergence difficulties.

The transition process between the two-flow regime may be characterized by the behavior of the peak local Nusselt number because the peak value reflects how far the impinging jet penetrates the Eckman layer. Behavior of the peak Nusselt number at fixed disk Reynolds numbers is plotted for various mass flow ratios in Fig. 17. A shift in the peak Nusselt number can be seen around mass flow ratios of 0.2 to 0.3, and it was found that the transition process is not identical for various disk Reynolds numbers. At a disk Reynolds number of 5000 the preak Nusselt number abruptly changes with a small change in mass flow ratio whereas the peak values more gradually shift for the other Reynolds number values investigated. A similar difference in transition process was reported by Metzger and Grochowsky (1977) based on their experiments.

Figure 18 shows the radial distribution of local Nusselt number where an abrupt change in the Peak Nusselt number was observed at disk Reynolds number $Re_d = 5000$. With a small change in jet Reynolds number ($Re_j = 275$ to 280), the profiles are quite different and each profile corresponds closely to typical profiles for the respective flow regimes.

Corresponding velocity vector plots are shown in Figs. 19(*a*) and 19(*b*). Here it is clear that the inner recirculation is strongly attenuated for the smaller jet Reynolds number. This abrupt change may indicate that the pressure balance between the outward-moving Ekman layer and the inner deflected jet is sustained, and the impinging jet penetrated the Ekman layer until inner recirculation is finally corrupted in this particular configuration, while the pressure balance is easily broken and the impinging jet is not allowed to penetrate completly to the rotating disk even when inner recirculation is maintained for other combination of disk rotation and jet flow rate.

At a higher disk Reynolds number ($Re_d = 10{,}000$) transition occurs gradually and no abrupt change in radial distribution of local Nusselt number occurs, as can be seen in Fig. 20. With the identical interval in jet Reynolds number, the local Nusselt number profile changes smoothly. Here velocity vector plots

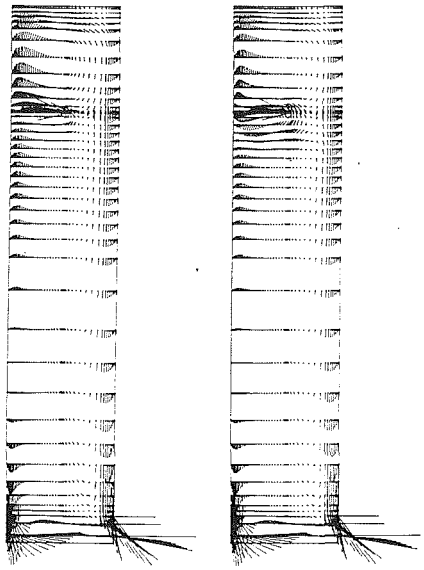

Fig. 19 Vector plots at Re_j = 275 (*a*) and 280 (*b*)

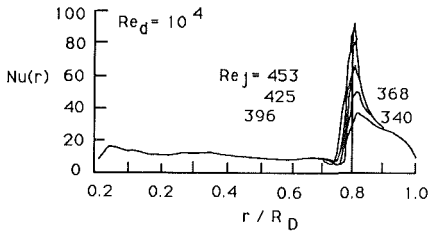

Fig. 20 Local Nusselt number at Re_d = 10,000

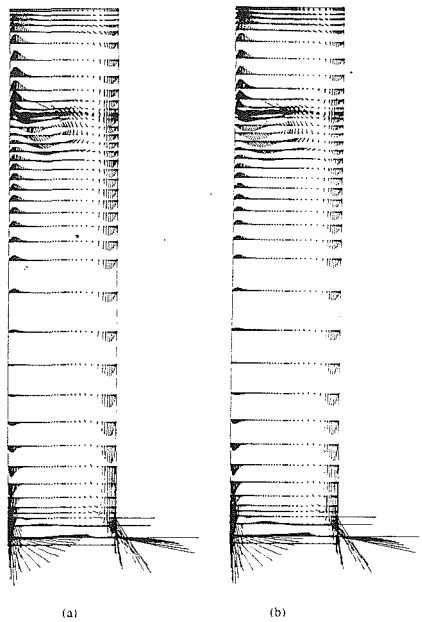

Fig. 21 Vector plots at Re_j = 396 (*a*) and 453 (*b*)

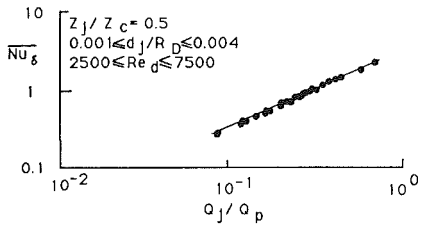

Fig. 22 Heat transfer characteristics with impingement

(shown in Fig. 21) indicate that the impinging jet does not completely penetrate the Ekman layer even though an inner recirculation is formed. At very close to the rotating disk the radial velocities remain positive while the impinging jet is deflected inward and the entire flow pattern is much like the impingement-dominated flow regime as can be seen in Fig. 21(*a*).

Finally, a relationship between averaged Nusselt number and mass flow ratio has been established. Figure 22 shows the relationship between averaged Nusselt number with the reference length based on the Ekman layer thickness and the mass flow ratio for various combination of disk Reynolds number and source jet configurations. The averaged Nusselt number introduced here is defined as

$$\overline{\mathrm{Nu}}_\delta = \mathrm{Nu}_{\mathrm{ave}}\frac{\delta_r}{R_D} = \frac{\bar{h}\delta_r}{k} \tag{27}$$

where $\mathrm{Nu}_{\mathrm{ave}}$ is the averaged Nusselt number define in Eq. (24), and δ_r is the Ekman layer thickness from the von Karman solution:

$$\delta_r = 5.0\mathrm{Re}_d^{-1/2} \tag{28}$$

In this combination of variables every computed point correlates very closely to a curve expressed as:

$$\overline{\mathrm{Nu}}_\delta = 3\left(\frac{Q_j}{Q_p}\right)^{0.87} = 3\left(\frac{w_j A_j}{0.885 A_D \nu^{1/2}\Omega^{1/2}}\right)^{0.87} \tag{29}$$

This average Nusselt number can also be expressed in terms of the combination of nondimensional parameters as below:

$$\overline{\mathrm{Nu}}_\delta = 3.34\left(\frac{A_i}{A_D}\right)^{0.435}\mathrm{Re}_d^{-0.435}\mathrm{Re}_j^{0.87} \tag{30}$$

In more general form, averaged Nusselt number of the rotating disk with the impingement of cooling air can be expressed as:

$$\frac{\mathrm{Nu}_{\mathrm{ave}}}{\left(\frac{A_j}{A_D}\right)^{0.435}\mathrm{Re}_d^{0.065}\mathrm{Re}_j^{0.87}} = 0.67 \tag{31}$$

Summary and Conclusions

The major findings of the present study are summarized as follows:

Cavity Flow Without Jet Impingement

1 The flow patterns obtained corresspond to those categorized as "laminar flow, separate boundary layers" in the experimental results by Daily and Nece. At the center of the cavity, a fluid core with near solid rotation is formed and is surrounded by the boundary layers. The Ekman layer formed on the rotating disk surface is separate from the other boundary layers formed on the stationary shroud.

2 The effect of the cavity rim is limited to a very small radial extent, and the flow pattern near the rotating disk is similar to the free disk similarity solution of von Karman. The pumping flow rate is about 75 percent of the von Karman solution value. The difference is plausibly attributed to fluid shear at the stationary shroud.

3 Average heat transfer coefficients are found to be proportional to the square root of disk rotating speed Ω, as in the case for the von Karman solution where local heat transfer coefficient is uniform over the radius. The average computed

heat transfer coefficient in the present case is about 67 percent of the von Karman value. The difference is plausibly attributed to the warm fluid entrainment by the Ekman layer associated with recirculation as well as to fluid shear at the stationary shroud.

4 The disk Reynolds number at which convergence difficulty occurred in the present study has been found to be in the range of transition from laminar to turbulent flow regime experimentally observed by Daily and Nece.

Cavity Flow With Jet Impingement

1 Detail cavity flow patterns were acquired and two distinct flow regimes previously identified in experimental studies as rotation-dominated and impingement-dominated have been observed and characterized by vector plots and local Nusselt number profiles.

2 It has been found that the transition from one regime to the other occurs when the mass flow ratio $Q_j/Q_p \approx 0.2$ to 0.3 for the base source jet configuration. This compares quite favorably with experimental observations. The transition process has been found to be different at different combinations of the primary parameters such as disk and jet Reynolds number. At Reynolds number of 5000, transition occurred abruptly, while more gradual transitions were observed for the other disk Reynolds numbers. This too is consistent with previous experimental observations.

3 The introduction of the source flow corresponded to appearance of convergence difficulties at smaller disk Reynolds numbers in comparison to Case 1. It is possible that introduction of jet impingement into the rotating flow promotes flow instabilities in the cavity.

4 Finally, a relation between averaged Nusselt number and the governing nondimensional parameters such as area ratio (A_j/A_D), disk and jet Reynolds number (Re_d, Re_j) had been established.

References

Bar-Yoseph, P., Blech, J. J., and Solan, A., 1981, "Finite Element Solution of the Navier-Stokes Equations in Rotating Flow," *International Journal of Numerical Methods in Engineering*, Vol. 17, pp. 1123–1146.

Bayley, F. J., and Owen, J. M., 1970, "The Fluid Dynamics of a Shrouded Disk System With a Radial Outflow of Coolant," ASME *Journal of Engineering for Power*, Vol. 92, p.335.

Bogdan, Z., 1982, "Cooling of a Rotating Disk by Means of an Impinging Jet," *Proceedings, 7th International Heat Transfer Conference*, U. Grigull et al., eds., Hemisphere Publishing Corp., Washington DC, Vol. 3, pp. 333–336.

Chew, J. W., 1984, "Development of a Computer Program for the Prediction of Flow and Heat Transfer in a Rotating Cavity," *Int. J. Num. Methods in Fluids*, Vol. 4, p. 667.

Cobb, E. C., and Saunders, O. A., 1956, "Heat Transfer From a Rotating Disk," *Proceedings of the Royal Society*, Vol. A236, p. 343.

Daily, J. W., and Nece, R. E., 1960, "Chamber Dimension Effects on Induced Flow and Frictional Resistance of Enclosed Rotating Disks," ASME *Journal of Basic Engineering*, Vol. 82, pp. 217–232.

Gosman, A. D., and Spalding, D. B., 1970, "Computation of Laminar Flow Between Shrouded Rotating Discs," Department of Mechanical Engineering, Imperial College, University of London, Report NO. EF/TN/A/30.

Kreith, F., Taylor, J. H., and Chong, J. P., 1959, "Heat and Mass Transfer From a Rotating Disk," ASME *Journal of Heat Transfer*, Vol. 81, pp. 95–105.

Metzger, D. E., and Grochowsky, L. D., 1977, "Heat Transfer Between an Impinging Jet and a Rotating Disk," ASME *Journal of Heat Transfer*, Vol. 99, pp. 553–667.

Metzger, D. E., Mathis, W. J., and Grochowsky, L. D., 1979, "Jet Cooling at the Rim of a Rotating Disk," ASME *Journal of Engineering for Power*, Vol. 101, pp. 68–72.

Metzger, D. E., Bunker, R. S., and Bosch, G., 1989, "Transient Liquid Crystal Measurement of Local Heat Transfer on a Rotating Disk With Jet Impingement," ASME Paper No. 89-Gt-XX.

Morse, A. P., 1987, "Numerical Prediction of Turbulent Flow in Rotating Cavities," ASME Paper No. 87-GT-74.

Owen, J. M., 1984, "Fluid Flow and Heat Transfer in Rotating Disc Systems," *Heat and Mass Transfer in Rotating Machinery*, D. E. Metzger and N. H. Afgan, eds., Hemisphere Publishing Corporation, Washington, DC, pp. 81–103.

Pao, H. P., 1970, "A Numerical Computation of a Confined Rotating Flow," ASME *Journal of Applied Mechanics*, Vol. 91, p. 480.

Patankar, S. V. 1980, *Numerical Heat Transfer and Fluid Flow*, McGraw-Hill, New York.

Panankar, S. V., 1981, "A Calculation Procedure for Two-Dimensional Elliptic Situtations," *Numerical Heat Transfer*, Vol. 4, pp. 409–425.

Schlichting, H., 1979, *Boundary Layer Theory*, McGraw-Hill, New York, pp. 102–107, 647–652.

Soo, S. L., 1958 "Laminar Flow Over an Enclosed Rotating Disk," *Trans. ASME*, Vol. 80, pp. 287–296.

Sparrow, E. M., and Gregg, J. L., 1959, "Heat Transfer From a Rotating Disk of Fluids of Any Prandtl Number," ASME *Journal of Heat Transfer*, Vol. 81, pp. 249–251.

von Karman, T., 1921, "Uber Laminare und Turbulence Reibung," *Z. Angew. Math. Mech.*, Vol. 1, p. 233.

White, F. M., 1974, *Viscous Fluid Flow*, McGraw-Hill, New York.

Hydrodynamic and Thermal Measurements in a Turbulent Boundary Layer Recovering From Concave Curvature

M. D. Kestoras

T. W. Simon

Mechanical Engineering Department,
University of Minnesota,
Minneapolis, MN 55455

The behavior of a boundary layer on a flat wall downstream of sustained concave curvature is documented. Experiments are conducted with negligible streamwise pressure gradient and a low free-stream turbulence intensity (0.6 percent). The turbulent boundary layer has a moderate strength of curvature ($\delta/R = 0.024$) at the entry to the recovery section. Results show that the skin friction coefficient, which increases over the concave wall, decreases rapidly at first over the recovery wall, then slowly approaches flat-wall values. Stanton number values decrease rapidly, undershooting expected flat-wall values. A discussion of this behavior, supported by profile measurements, is given. Effects include destabilization in the concave-curved flow and rapid streamline readjustment (acceleration) at the end of the curved section. Goertler vortices established on the curved wall persist onto the recovery wall; however, their effects weaken.

Introduction

The purpose of this study is to document the manner in which momentum and thermal boundary layers recover from sustained concave curvature on a downstream flat wall. Questions to be resolved include whether and where straight-wall relationships, including turbulence models, can be applied downstream of a curved section. The study is conducted with a negligible streamwise pressure gradient and a low free-stream turbulence intensity in order to isolate the curvature effect. The information provided is expected to be valuable in understanding the flow over regions of streamwise-varying curvature, including the latter parts of the pressure side of a turbine blade.

The importance of the effect of curvature on the boundary layer has been known for over 25 years. Bradshaw (1973) suggested that curvature causes a structural change in the turbulence of the boundary layer which reflects large effects on mean quantities. The topic has been the focus of intensive research over the last three decades and has been a topic of study at the University of Minnesota for the last 10 years (e.g., Wang and Simon, 1987; You et al., 1986; Kim et al., 1991).

It is now well known that concave curvature increases the rate of growth of the boundary layer, accompanied by increases in the skin friction coefficient, C_f, and Stanton number, St. These important effects of curvature are observed even for relatively weak curvature $\delta/R < 0.04$ (Meroney and Bradshaw, 1975; Ramaprian and Shivaprasad, 1977; Hoffmann et al., 1985). In addition, certain investigators have reported spanwise nonuniformities resulting in 100 percent variation in boundary layer thickness (So and Mellor, 1975) when $\delta/R = 0.1$, and 20 percent variation in skin friction coefficients (Meroney and Bradshaw, 1975) when $\delta/R = 0.01$. On the contrary, other investigators (e.g., Ramaprian and Shivaprasad, 1977; Jeans and Johnston, 1982) reported no spanwise nonuniformities. In an attempt to explain these apparently conflicting results. Barlow and Johnston (1988) conducted Laser Induced Fluoresence (LIF) flow visualization studies in a water channel. Their results showed that large-scale inflows and outflows appear in the boundary layer over a concave wall. These inflows and outflows, however, wandered about, appearing and disappearing randomly.

Barlow and Johnston did obtain stationary Goertler-like vortices when vortex generators were used to induce a fixed array of longitudinal roll cells. Based on skin friction coefficient observations, they proposed that the concave boundary layer be treated as two-dimensional, provided that an accurate prediction of the spanwise-averaged values is achievable. Similar conclusions were reached by Simonich and Moffat (1982) in a heat transfer study.

Kim et al. (1991), while investigating boundary layer transition on a concave wall, reported stable longitudinal vortices in both laminar and turbulent boundary layers for cases of low free-stream turbulence intensity. They concluded that preferred vortex locations were established in the laminar boundary layer preceding the turbulent flow.

The recovery of a boundary layer from curvature is important; it is believed that its documentation will be useful in

Contributed by the International Gas Turbine Institute and presented at the ASME Winter Annual Meeting, Atlanta, Georgia, December 1-6, 1991. Manuscript received by the International Gas Turbine Institute April 26, 1992. Associate Technical Editor: L. S. Langston.

understanding the underlying principles of production, diffusion, and decay of turbulence. You et al. (1986) studied the relaxation from convex curvature and reported a slow recovery of skin friction coefficients from the reduced values in the convex-curved flow toward flat-wall values. The Stanton number data showed a fast initial response to the removal of convex curvature, recovering about 30 percent of the drop seven boundary layer thicknesses downstream. The remaining recovery was slow.

In a similar study, Alving and Smits (1986) reported comparable results, but, interestingly enough, they also reported an overshoot above the flat-wall skin friction values by the end of the recovery wall.

Smits et al. (1979) studied the recovery of turbulent boundary layers downstream of short regions of convex and concave curvature. They also reported a slow recovery of the skin friction to flat-wall values and the persistence of Goertler-like vortices on the recovery wall downstream of sharp concave curvature.

The present study, to the best of the authors' knowledge, is the first to document the recovery of the momentum and thermal boundary layers downstream of sustained concave curvature and the first to document recovery of concave flows rich in coherent, naturally formed, streamwise (Goertler) vortices.

Test Facility and Instrumentation

The experiments are conducted in an open-circuit, blown-type wind tunnel (Fig. 1). Details of the flow delivery section are given by Wang (1984). The test channel is rectangular, 68 cm wide, 11.4 cm deep, and 284 cm long. The velocity at the exit of the nozzle, uniform to within 0.3 percent, is nominally 17.2 m/s. The free-stream turbulence intensity in the tunnel, based on all three components of the velocity vector, is 0.6 percent. The nozzle exit flow temperature is uniform to within 0.1°C.

The three test wall segments (flexible, intermediate, and recovery) are of a similar, composite structure. For example, the recovery wall consists of a layer of fiberglass insulation, a sheet of Plexiglas®[1], a heater, a spacer, and a layer of liquid crystal. Thermocouples embedded into the spacer layer are distributed in both the streamwise and spanwise directions.

[1] Plexiglas is a registered trademark of Rohmhaas Company.

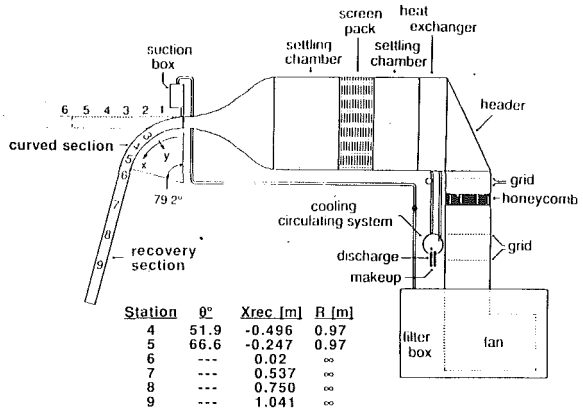

Station	θ°	Xrec [m]	R [m]
4	51.9	-0.496	0.97
5	66.6	-0.247	0.97
6	---	0.02	∞
7	---	0.537	∞
8	---	0.750	∞
9	---	1.041	∞

Fig. 1 Schematic of the wind tunnel test facility

The walls are designed and built to provide an instrumented, hydrodynamically smooth and uniformly heated surface.

The concave wall has a length of 1.38 m and is bent to a radius of curvature of 0.97 m. The recovery wall is 1.452 m long and is tangent to the concave wall. The outer wall is adjusted to provide negligible streamwise pressure gradient 2 cm from the test wall, along the entire test section (static pressure coefficients, C_p, are within 3 percent). An array of static taps is provided for this adjustment. The most upstream static pressure tap, 2 cm from the test wall, is used to reference C_p values.

The measured Reynolds numbers at the leading edge of the recovery wall, based on streamwise distance, and on displacement and momentum thicknesses, are 1.5×10^6, 3300, and 2600, respectively.

A personal computer was used for data acquisition and processing. Velocity measurements were made both with a pitot tube and a single-sensor hot-wire. The pitot tube was of 0.72 and 0.394 mm outside and inside diameter, respectively. The Young and Maas (1936) shear effect correction and the MacMillan (1954) wall effect correction were applied, as appropriate, to all the pitot tube measurements. The uncertainty in the pitot tube measurements was less than 1.5 percent. A constant-temperature anemometer bridge (TSI-IFA-100) was used to drive the hot wire. Mean and fluctuating components of streamwise velocity were measured with a single-wire probe (TSI 1218-T1.5). The probe was of the boundary layer configuration; thus, interference with the flow was minimal. Nor-

Nomenclature

C = constant of the velocity logarithmic law of the wall
C_f = skin friction coefficient
C_p = constant-pressure specific heat
C_p = static pressure coefficient $= (P - P_{ref})/(0.5\rho U_{pw}^2)$
k = thermal conductivity
K = acceleration parameter
Pr = Prandtl number
P_{ref} = reference static pressure
q_w = convective heat flux at the wall
r = radial distance from the wall
R = radius of curvature
$Re_{\delta 2}$ = Reynolds number based on momentum thickness
St = Stanton numbers $= q_w/(\rho C_p(T_w - T_\infty)U_{pw})$
T = temperature
T^+ = temperature in wall units $= ((T_w - T)/(T_w - T_\infty))\sqrt{C_f/2}/\mathrm{St}$
T_w = wall temperature
T_∞ = free-stream temperature
U_{pw} = velocity of the potential flow extrapolated to the wall
U = mean streamwise velocity
U_p = potential flow velocity
u' = RMS of the streamwise fluctuating velocity component
u^+ = velocity in wall coordinates
U_τ = shear velocity
V = cross-stream mean velocity
v' = RMS of the cross-stream velocity component
x = streamwise distance from the leading edge
y = normal distance from the wall
y^+ = normal distance from the wall in wall coordinates
y_{cl} = conduction layer thickness
z = spanwise coordinate
Δ = Clauser thickness $= \int_0^\infty U_p - U/U_\tau \, dy$
$\delta_{99.5}$ = momentum boundary layer thickness based on 99.5 percent of the free-stream velocity
δ_1 = displacement thickness
δ_2 = momentum thickness
$\Delta_{99.5}$ = thermal boundary layer thickness based on 99.5 percent of the wall to free-stream temperature difference
κ = von Karman constant
ν = kinematic viscosity

mally, the average sampling time was 40 seconds. Hot-wire calibrations were performed in the tunnel core flow against the pitot tube. The uncertainty of mean velocity was 2 percent and of the fluctuation velocity, 5 percent.

Pressure measurements were made with a variable-reluctance type (Validyne DP45) pressure transducer and carrier demodulator (Validyne CD-15) calibrated against a micromanometer of ± 0.06 mm H_2O resolution. The accuracy of the pressure transducer was 0.5 percent full scale (8.9 cm of H_2O). Output analog signals were digitized using an HP3437A system voltmeter. The uncertainty of C_p was 5×10^{-4}.

The test walls were heated to a nominal heat flux of 193 W/m^2. This provided a wall-to-free-stream temperature difference of nominally 5.5°C. The surface heat flux over each heater was uniform to within 1 percent (Wang, 1984); an electric circuit was built to equalize the heat flux dissipated by each of the four heaters, within 1 percent. Heat transfer measurements were performed using a series of chromel-constantan thermocouples of 76.2 μm diameter. The uncertainty of the thermocouple readings was 0.1°C (Wang, 1984). The thermocouples were installed on the center span of the test walls at streamwise spacings over the curved and recovery walls of 2.54 cm and 5.08 cm, respectively. Thermocouples were also distributed in the spanwise direction, with a spacing of 5.08 cm, at several streamwise stations to check two dimensionality.

Mean temperature profiles were taken using a thermocouple probe constructed following the design of Blackwell and Moffat (1975). Temperature and velocity profiles were taken using a traversing mechanism capable of 10 μm spatial resolution in the direction normal to the wall. The exact wall location was determined by stepping away from the wall; the wall position for velocity profiles was identified by searching for the step in slope of the hot-wire voltage. The distance of the wall was checked by testing against, and if necessary adjusting for agreement with the viscous sublayer equation, $u^+ = y^+$. A similar procedure is used with the thermocouple probe at the centerspan locations, where a thermocouple is embedded. For spanwise locations, other than the centerspan location, no thermocouple is embedded in the wall. For these spanwise locations, the y-correction is assumed to be the same as the correction applied at the centerspan temperature profile of the same streamwise distance. Then, the temperature of the wall, T_w, is determined from the near-wall profile. Velocity and temperature profiles were taken at three spanwise locations for each streamwise station, test wall centerspan and upwash and downwash sites of the Goertler vortices. Spanwise travel of the probes was achieved by a micrometer of 10 μm resolution.

The potential velocity of the wall, U_{pw}, was obtained over the curved section by extrapolation of least-square fits of radial velocity distributions measured in the irrotational core of the flow. The radius of curvature obtained by this method differed from the nominal value of the radius of curvature (97 cm) by less than 8 percent.

Boundary layer parameters such as displacement, momentum, and enthalpy thicknesses were determined using definitions that account for the presence of curvature (Honami, 1980). Least-square linear fits of the core velocities were used to supply the potential velocities in these definitions.

The wall surface temperatures were obtained from the embedded thermocouple values by correcting for the temperature drop across the interposed layers. The thermal resistances of appropriate layers for each of the three walls were determined by separate experiments and also by the use of foil thermocouples, which were mounted on the surface of the test walls. Notice that the correction thus obtained for the curved wall is much higher than that for the recovery wall, due to the different wall designs necessitated by the need for flexibility of the curved wall. With this correction, the uncertainty of wall temperature was 0.2°C over the concave wall and 0.1°C over the recovery wall. In evaluating Stanton numbers, air properties were determined at the mean film temperature at each streamwise location. The heat flux was calculated by performing an energy balance on the test wall, taking into account radiation, back heat loss and streamwise conduction within the test wall. The uncertainty in Stanton numbers is 6 percent.

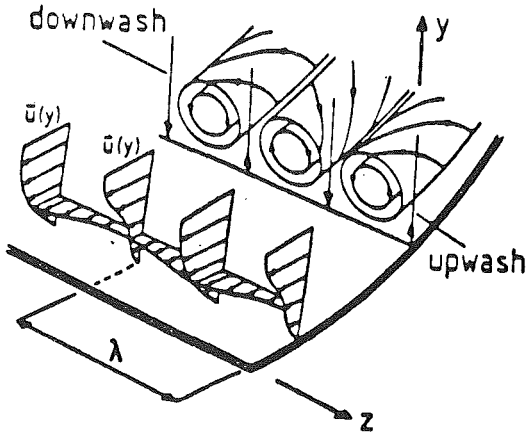

Fig. 2 Schematic of the diagram of Goertler vortices (from Crane and Sabzvari, 1984)

A liquid crystal sheet over the test wall provided an additional test of two dimensionality. It also supplied information about the onset, development, and decay of Goertler-like vortices over the test wall. These coherent structures are a series of longitudinal counterrotating vortices, which tend to appear over concave surfaces (Fig. 2).

The base case study was conducted with the flexible (later to become concave) wall in the straight configuration. Stanton numbers showed good agreement with TEXSTAN (Crawford and Kays, 1976) predictions. A balance between heat transfer through the wall and convected energy in the boundary layer, in the straight and curved configurations, closed to within 8 and 5 percent, respectively.

Results and Discussion

Important parameters of the study and a summary of the experimental results are shown in Table 1.

Static pressure profiles over the concave wall decreased linearly with radial distance, effected by centrifugal forces. Remarkably, a flat radial profile was observed only 1.4 cm downstream of the end of the curved section. There is evidence that this fast recovery of the static pressure may have a lasting influence on the structure of the boundary layer.

The presence of Goertler vortices was evidenced by streamwise color streaks appearing on the liquid crystal at preferred spanwise locations. The cold and hot streaks are believed to be the loci of the downwash and upwash sites of the Goertler vortices (Fig. 2), respectively. Goertler-like vortices persist on the recovery wall; however, their liquid crystal traces are not as clearly visible as those on the concave wall. Rather, they develop fuzzy and relatively wide boundaries while maintaining the size of the boundary layer thickness. It is believed that the vortices tend to lift off the surface at the beginning of the recovery wall. This claim seems to be supported by Barlow and Johnston (1988) who reported that the roll cells move closer to the solid surface as they pass from a flat to a concave wall. There will be evidence of this reported below.

The evolution of the Goertler vortices is documented by spanwise profiles of indicated velocity taken with a pitot tube traversed in the spanwise direction while touching the test wall (Fig. 3). As expected, the profiles exhibit maxima and minima resulting respectively from high-momentum fluid thrusted by

Table 1 Summary of boundary layer parameters: Downwash, centerline, and upwash are denoted by (DW), (CL), and (UW), respectively

	Station 4			Station 5			Station 6			Station 7			Station 8			Station 9		
	DW	CL	UW	DW	CL	UW	DW	CL	UW	DW	CL	UW	DW	CL	UW	DW	CL	UW
x(m)	0.878	0.878	0.878	1.127	1.127	1.127	1.394	1.394	1.394	1.911	1.911	1.911	2.124	2.124	2.124	2.415	2.417	2.417
z(cm)	-0.3	0.0	0.76	-0.2	0.0	0.6	-1.1	0.0	0.6	-0.55	0.0	0.883	-0.7	0.0	1.0	-1.2	0.0	0.9
R(cm)	97	97	97	97	97	97	∞	∞	∞	∞	∞	∞	∞	∞	∞	∞	∞	∞
U_{pw}(m/s)	17.56	17.22	17.38	17.03	16.21	17.15	17.34	17.37	17.49	17.55	17.42	17.57	16.95	17.12	17.03	16.72	17.23	17.48
Free-stream T.I.		0.647	0.539	0.615	0.664	0.590	0.600	0.610	0.569	0.628	0.593	0.631	0.598	0.653	0.636	0.635	0.657	0.667
$\delta_{99.5}$(cm)	1.574	1.529	1.714	2.243	2.32	2.352	2.839	2.968	3.324	3.772	3.694	4.110	4.112	4.307	4.394	4.471	4.490	4.552
δ_1(mm)	1.679	1.823	2.507	2.442	2.562	3.541	2.722	3.038	3.980	3.849	4.125	5.159	4.666	5.110	5.892	5.045	5.737	6.233
δ_2(mm)	1.289	1.396	1.857	1.926	2.023	2.657	2.183	2.452	3.137	3.022	3.213	3.932	3.597	3.933	4.425	3.893	4.374	4.675
y/δ_{995} (y^+=10)	0.012	0.013	0.012	0.009	0.009	0.009	0.007	0.007	0.007	0.006	0.008	0.006	0.005	0.005	0.005	0.005	0.005	0.005
$Re_x \times 10^5$	9.604	9.388	9.506	11.92	11.13	13.32	15.02	15.05	14.85	20.42	20.62	20.44	22.38	22.79	22.54	25.08	26.26	26.51
$Re_{\delta 1}$	1836	1949	2714	2583	2528	3789	2927	3275	4241	4112	4451	5519	4917	5484	6254	5240	6234	6839
$Re_{\delta 2}$	1409	1493	2010	2037	1997	2844	2348	2643	3344	3229	3467	4206	3791	4220	4697	4043	4752	5130
H	1.303	1.306	1.35	1.268	1.266	1.332	1.247	1.239	1.268	1.273	1.284	1.312	1.297	1.299	1.332	1.296	1.312	1.333
$C_f \times 10^3$	4.88	4.75	4.13	4.61	4.80	3.83	4.00	4.00	3.73	3.89	3.95	3.45	3.56	3.54	3.26	3.63	3.40	3.19
$\Delta_{99.5}$(cm)	1.772	1.769	1.916	2.742	2.563	2.598	3.192	3.365	3.426	3.892	3.951	4.450	4.595	4.859	4.643	4.956	5.114	5.095
Δ_2(mm)	1.589	1.698	1.957	2.245	2.418	2.547	2.326	2.724	2.980	2.920	3.067	3.540	3.332	3.711	3.718	3.818	4.025	4.130
T_∞	29.84	29.72	29.75	30.16	30.04	30.08	29.84	29.77	29.96	30.33	30.16	30.21	30.54	30.51	30.45	30.59	30.56	30.59
T_w	34.07	34.05	34.28	34.45	34.47	34.69	34.68	34.63	34.99	35.36	35.30	34.54	35.67	35.77	35.79	35.85	35.97	36.09
$Re_{\Delta 2}$	1705	1788	2078	2336	2396	2668	2447	2874	3158	3126	2262	3793	3441	3871	3857	3886	4222	4393
St $\times 10^3$	2.049	2.000	1.910	2.006	1.941	1.865	1.869	1.860	1.798	1.680	1.643	1.585	1.673	1.631	1.606	1.620	1.575	1.548

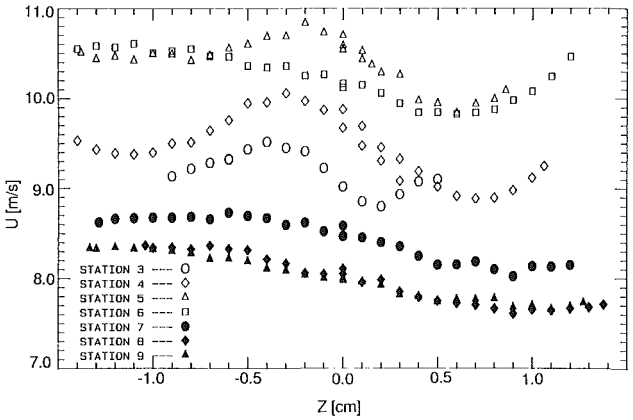

Fig. 3 Spanwise velocity profiles over the concave and recovery walls (y = 0.36 mm)

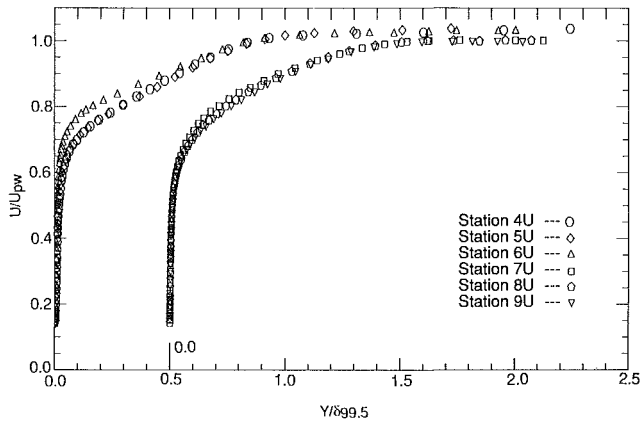

Fig. 4 Nondimensional velocity profiles in the upwash region

the vortices toward the wall (downwash site) and low-momentum fluid lifted from the wall (upwash site). The time invariability of the location of the vortices is shown in the data of station 4 (Fig. 3), which were taken during different runs. Liquid crystal observations support these measurements.

Nondimensionalized velocity profiles at the upwash positions are in Fig. 4. Intense mixing over the concave wall causes very sharp gradients near the wall and, thus, flattening of the outer portions of the profiles. The near-wall gradients become steeper with streamwise distance, consistent with the results of other researchers (Ramaprian and Shivaprasad, 1977; Barlow and Johnston, 1988).

The near-wall velocity profiles become drastically steeper at station 6, the first station on the recovery wall, while the outer parts show a flattened profile. This is effected by the fast recovery of the static pressure of the profiles; streamwise pressure gradients are created locally, which accelerate the fluid near the wall and decelerate the fluid in the core of the flow. Notice that these pressure gradients are effected by changes in curvature and are always present when the curvature varies. Although the acceleration is local, some of the near-wall features of the modified shape of station 6 persist downstream.

The velocity profiles have changed shape noticeably by station 7. The near-wall profile relaxes somewhat, allowing the far field gradients to increase slightly, but still remain quite flat. Stations 8 and 9 show self-similarity in these coordinates, throughout the boundary layer.

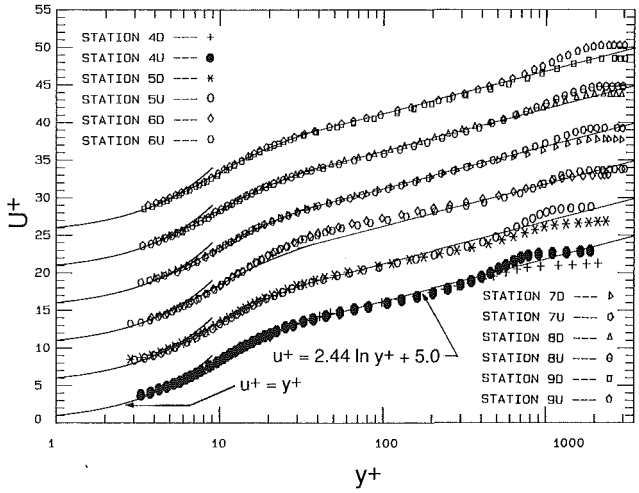

Fig. 5 Recovery of velocity profiles in wall coordinates: downwash and upwash regions

Figure 5 shows mean velocity profiles in wall units. The profiles are least affected near the wall, with the universality of the log law holding out to y^+ of 60. The effect of concave curvature is most pronounced in the outer parts of the boundary layer where the simple strain rate $\partial U/\partial y$ is small. This

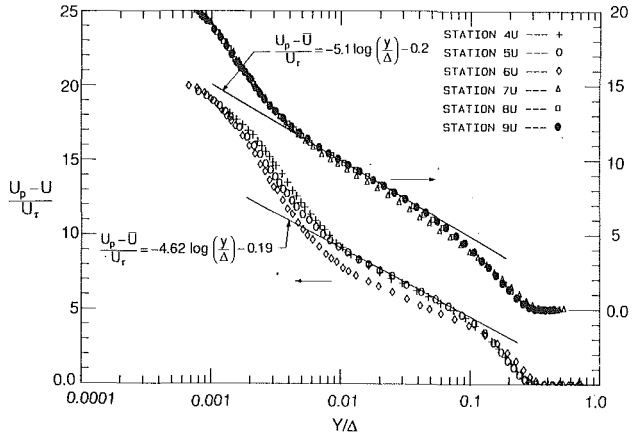

Fig. 6 Upwash velocity profiles in outer coordinates

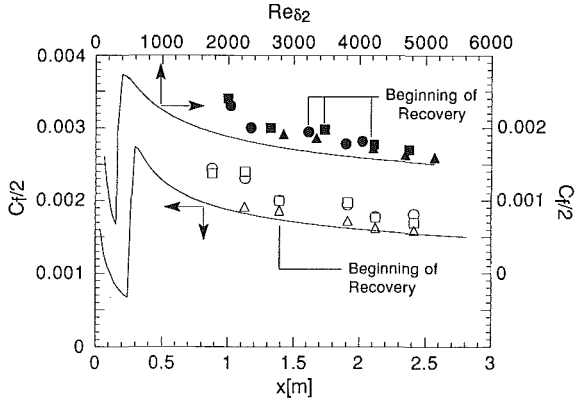

Fig. 7 Recovery of skin friction coefficients; □, ■: centerline; ○, ●: downwash; △, ▲: upwash

maximizes the strength of curvature as given by the relative magnitude of the extra rate of strain $(\partial V/\partial x)/(\partial U/\partial y)$. The extent of the logarithmic region in y^+ is reduced by curvature. For values of $y^+ > 80$, the data for the curved wall exhibit a lower slope than the standard law-of-the-wall behavior. This is a result of the intensified turbulent mixing effected by instabilities of concave-curved flow. The extra mixing by concave curvature was documented by Barlow and Johnston (1988): for $y^+ > 40$, energy spectra exhibited more energetic large-scale motions than over a flat wall. Thus, wake regions are suppressed by curvature. Coherent Goertler-like vortices have an additional effect on the wake: They force negative wakes over downwash sites and positive (but suppressed below flat-plate), wakes at the upwash sites.

Figure 6 shows velocity profiles plotted in outer coordinates, i.e., $(U_p - U)/U_\tau$ versus y/Δ, where Δ is the "Clauser thickness" defined by

$$\int_0^\infty \frac{U_p - U}{U_\tau} dy.$$

If the boundary layer of the present study is in equilibrium, it should obey outer-wall similarity. Indeed the profiles for stations 4 and 5 (concave wall) do. Asymptotic behavior is also observed over the recovery wall. Remarkably, however, self-similarity extends throughout the boundary layer.

The linear regions of the upwash and downwash profiles over the concave wall are best fitted by $(U_p - U)/U_\tau = -4.62$ log $(y/\Delta) - 0.19$ and $(U_p - U)/U_\tau = -4.4$ log $(y/\Delta) - 1.05$, respectively. The values of 4.62 and 4.4 are lower than 5.6, the flat-wall value, as expected due to the intensified mixing. The least-square fit equations of the linear region over the recovery wall are given by $(U_p - U)/U_\tau = -5.7$ log (y/Δ) 2.1

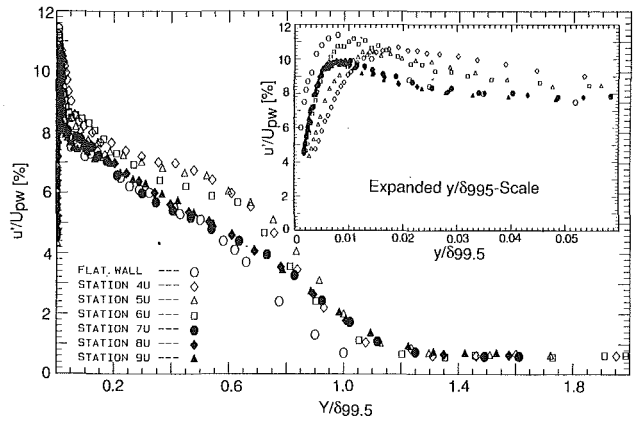

Fig. 8 Recovery of turbulence intensity for the upwash profiles

and $(U_p - U)/U_\tau = -5.1$ log $(y/\Delta) - 0.2$ for downwash and upwash profiles, respectively. The slope of the equations of the logarithmic linear region over the recovery wall approach the flat-wall value, revealing a less intense mixing.

Figure 7 shows the friction coefficients determined from velocity profiles by fitting the near-wall data to the Couette flow theory (see Fig. 5). The upper curve is $C_f/2$ versus X and the lower curve is $C_f/2$ versus $Re_{\delta 2}$. As expected, the intensified mixing of the boundary layer over the concave wall results in higher skin friction coefficients than those expected on a flat wall. Contrary to the results of So and Mellor (1975), who reported no spanwise variation in skin friction coefficient, but in agreement with Meroney and Bradshaw (1975) and Barlow and Johnston (1988), the current results show a variation as high as 20 percent.

The response of the skin friction coefficient to the withdrawal of curvature is abrupt at first and slow thereafter. Notice that on the recovery wall the difference in friction coefficient between the downwash and upwash sites diminishes to about 9.2 percent. Skin friction coefficients for upwash, downwash, and centerspan positions over the recovery wall (but not over the concave wall) seem to collapse in $C_f/2$ versus $Re_{\delta 2}$ coordinates. This suggests that the boundary layer at an upwash site is similar in structure to the boundary layer at a downwash site, only more mature. Nevertheless, skin friction coefficients over the recovery wall remain above flat-wall values.

Turbulence intensity profiles based upon the streamwise component of velocity (u'/U_{pw}) show that concave curvature increases turbulence intensity above flat-wall values throughout most of the boundary layer (see $y/\delta_{99.5} = 0.2$–0.8 in Fig. 8), as reported by Barlow and Johnston (1988). The flat-wall turbulence intensity profile reported by Klebanoff (1954) is shown for reference. This augmentation of turbulence is more pronounced with the upwash profiles (downwash profiles are not shown in Fig. 8), which exhibit an increase over flat-wall values of as high as 45 percent (at $y/\delta_{99.5} \sim 0.6$). Downwash profiles show an enhancement over flat-wall profiles of 13.6 percent.

Removal of curvature returns the turbulence intensities to the flat-wall values for most of the boundary layer. However, for $y/\delta_{99.5} < 0.02$ the values of turbulence intensities remain below the flat-wall values. Removal of curvature also brings the upwash and downwash profiles closer together, although their differences near the wall $(y/\delta_{99.5} < 0.006)$ persist (see Figs. 9 and 10). In the text below it is claimed that, upon removal of curvature, the Goertler vortices lift off the wall a bit, thus moving their effect into the wake region. The turbulence intensity behavior shown in Figs. 8–10 does not contradict this claim. Sharp gradients near the wall allow efficient mixing even when the near-wall vorticity is reduced, while the shallow gradients in the enhanced vorticity core inhibit mixing. Notice

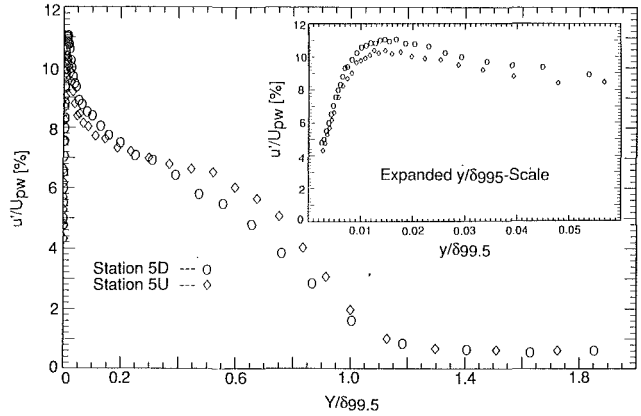

Fig. 9 Comparison of the upwash and downwash turbulence intensity profiles; station 5: within curve

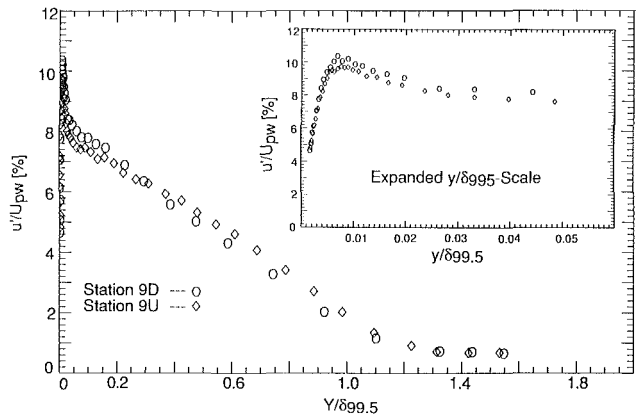

Fig. 10 Comparison of the upwash and downwash turbulence intensity profiles; station 9: on recovery wall

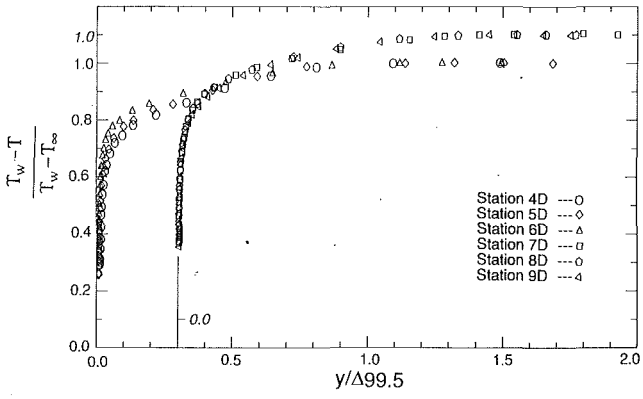

Fig. 11 Nondimensional temperature profiles: downwash and upwash regions

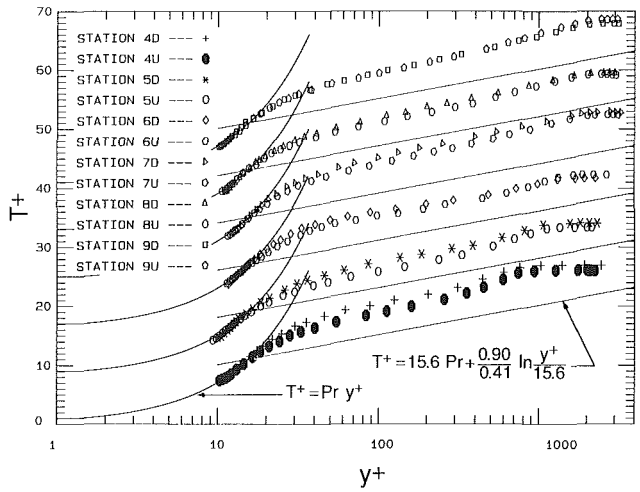

Fig. 12 Recovery of temperature profiles in wall coordinates: downwash and upwash regions

that at station 9, the downwash and upwash profiles agree for $y/\delta_{99.5}$ values as high as 0.005, indicating that the effect of the vortices has moved away from the wall.

The behavior of the turbulence intensities can be explained with the help of the production term of the shear stress transport equation (dominant terms only),

$$\left(1+\frac{y}{R}\right)v'^2\frac{\partial U}{\partial y}-(2u'^2-v'^2)\frac{U}{R}$$

(Bradshaw, 1973). The first term, dominant in the boundary layer, is proportional to the gradient of the mean velocity profile. Therefore, the sharpening of the near-wall velocity gradient would tend to increase turbulent shear stresses, which, in turn, would result in increased turbulence intensities. Similarly, away from the wall, the resulting shallow gradients lead to reduced turbulence intensities. Notice that the self-similarity exhibited by turbulence intensities at stations 8 and 9 (Fig. 8) follows the behavior of the nondimensional velocity profiles (Fig. 4).

The streamwise evolution of nondimensional temperature profiles at the downwash sites of the Goertler-like vortices is shown in Fig. 11. For ease of viewing, the profiles over the recovery wall are shifted on both axes. Over the concave wall, similar to their velocity counterparts, the temperature profiles show sharper near-wall gradients with downstream distance. The near-wall temperature gradient is sharpest at station 6, the first station of the recovery wall, partially due to local acceleration. Over the recovery wall the nondimensional temperature profiles show a self-similarity, which holds throughout the boundary layer. The temperature profiles clearly show a concentration of higher thermal resistance near the wall.

Temperature profiles in wall coordinates are shown in Fig. 12. The standard thermal law of the wall with conduction layer thickness of 15.6 and turbulent Prandtl number of $Pr_t = 0.90$ is also shown. Over the concave wall the data are above the thermal law of the wall, casting doubt on its validity over a concave surface. Pauley and Eaton (1988) reported that for a pair of counterrotating, spanwise-separated vortices over a flat wall, T^+ profiles increase at the downwash sites and decrease at the upwash sites. The present data show an increase in T^+ values for both spanwise locations, however, suggesting that the rise above the standard "law" is primarily caused by concave curvature effects. Violation of the law is also observed on the recovery wall. A possible explanation for the violation of the "law" over the curved and recovery walls is that the skin friction coefficient is inappropriate to use in the nondimensionalization of temperature profiles since heat transfer and momentum transfer behave differently in both cases.

Midspan temperature profiles (not shown) collapse with the downwash profiles at all stations, in agreement with Pauley and Eaton (1988) and Barlow and Johnston (1988), who reported that upwash regions are narrower than their downwash counterparts.

Stanton numbers are plotted in Fig. 13 against the streamwise distance from the leading edge (lower curve), and against $Re_{\Delta 2}$ (upper curve). Also shown is a TEXSTAN (Crawford and Kays, 1976) computation initiated at the leading edge (transition to turbulence is tripped at the location indicated by the data and turbulence closure is with the mixing length model—

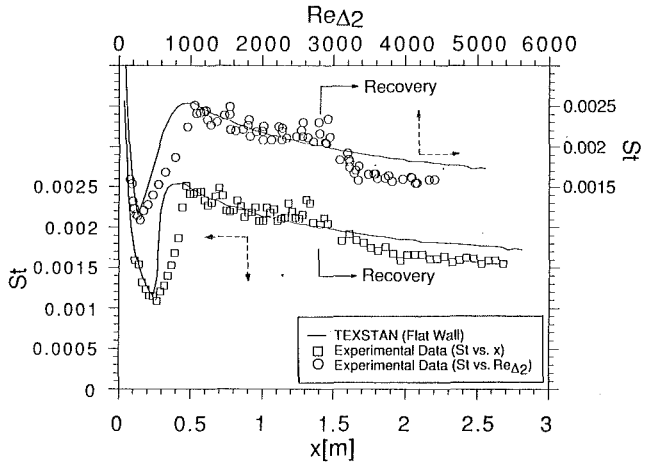

Fig. 13 Recovery of Stanton numbers

no curvature correction). The turbulent flow measurements over the concave wall show values that are above the TEXSTAN predictions with the difference increasing as the boundary layer continues to grow on the concave wall. By comparison with Fig. 7, one sees that Stanton numbers respond more slowly than skin friction coefficients to curvature.

On the recovery wall, Stanton numbers fall abruptly and undershoot the flat-wall predictions. After the initial drop upon removal of curvature, the data reach a near-constant value, and approach the prediction very slowly. This is apparent in the plot of St against $Re_{\Delta 2}$ (upper curve).

The difference in the behavior of Stanton numbers and skin friction coefficients is partially due to the local acceleration of the boundary layer at the end of the curve, as the flow adjusts to an abrupt change in radius of curvature. This acceleration is most intense very near the wall. Acceleration reduces Stanton numbers because it thickens the viscous sublayer (Kays and Crawford, 1980). The computed acceleration parameter,

$$K = \frac{\nu}{U_{pw}^2} \frac{dU_{pw}}{dx},$$

was 1.03×10^{-6} at the end of curvature. This is a strongly accelerated flow. In fact, Kays and Crawford (1980) state that "laminarlike" heat transfer behavior results when $K > 1 \times 10^{-6}$. The "laminarlike" heat transfer argument is further supported by Fig. 12, which clearly shows that station 6 temperature profiles tend to follow the conduction layer equation $T^+ = \mathrm{Pr}\, y^+$ to higher y^+ values than do profiles over the concave wall. Also, over the recovery wall, near-wall ($y/\delta_{99.5} < 0.02$) turbulence intensities, like their counterparts over the concave wall, remain below the flat-wall values, further supporting the "laminarlike" behavior. This would suggest that the reduced turbulence intensities in the viscous sublayer over the concave wall may also be responsible for the "laminarlike" behavior over the recovery wall.

The "laminarlike" heat transfer starting at the beginning of the recovery wall would explain why Stanton numbers show very slow recovery toward flat-wall values. Observation of the temperature profiles in wall units (Fig. 12) show that the thickened conduction layer persists over the whole recovery wall even though the boundary layer is only locally accelerated at the end of curvature. This is possibly due to the mild slopes of the velocity and temperature profiles generated in the curved section and the lifting of large-scale eddies away from the wall upon recovery. Thermal resistance remains concentrated near the wall. As indicated by the self-similarity of the temperature profiles over the recovery wall, the region of high resistance is growing with $\Delta_{99.5}$. Self-similarity is also observed in the velocity profiles of stations 8 and 9, where friction coefficients remain constant. Notice that skin friction coefficients lag Stanton numbers in reaching equilibrium. The acceleration effect, which affects the heat transfer differently than the momentum transfer, may have a major role here.

Conclusions

This study has shown some characteristics of the response of a boundary layer to the removal of concave curvature. In this case Goertler vortices were established naturally in the curved laminar flow, which subsequently passed through transition. By the end of the curve, the flow was a turbulent boundary layer with a coherent vortex pattern. The recovery behavior can be described as follows:

1 The Goertler-like vortices, once established on the concave wall, persist on the recovery wall. However, on the recovery wall, their effect diminishes, probably because they lift off the wall moving to the boundary layer core where shallow gradients render their mixing less effective. The result is that on the recovery wall, there are smaller spanwise nonuniformities in velocities, skin friction coefficients, Stanton numbers, turbulence intensities, and wall temperatures than on the curved wall.

2 Skin friction coefficients drop abruptly at first over the flat recovery wall, followed by a further, but slower, decrease toward flat-wall values. By the end of the recovery wall, C_f appears to have reached a near-constant value, possibly due to the reduced mixing of the inner boundary layer.

3 Remarkably, Stanton number values fall below flat-wall values upon removal of curvature. Subsequently, Stanton numbers level off and slowly tend toward flat-wall values from below. Nevertheless, by the end of the test section, 33 boundary layer thicknesses downstream of the beginning of recovery, the Stanton numbers have not reached flat-wall values.

4 The undershoot of the flat-wall values by the Stanton numbers over the recovery wall may be due to the reduced turbulence intensities in the near-wall region ($y/\delta_{99.5} < 0.005$) over the concave wall, which persist over the recovery wall, and due to the thickening of the viscous sublayer initiated by the step in local acceleration caused by the curvature discontinuity. The literature shows that this acceleration is high enough to cause "laminarlike" heat transfer behavior.

5 Profiles of turbulence intensity show a sharp and sudden drop of near-wall turbulence over the concave wall which persists over the recovery wall. The turbulence intensity reaches an asymptotic shape about 17 boundary layer thicknesses[2] downstream of the beginning of the recovery wall, consistent with the streamwise location where the Stanton numbers level off.

6 Full recovery is not expected until after the boundary layer has become fully turbulent again, replacing the large-scale turbulence structure residing in the outer flow as remnants of the curved flow with structure formed by turbulent wall bursting. This may require a considerable streamwise distance.

Acknowledgments

This work was supported by the Air Force Office of Scientific Research. The project (grant number AF/F49620-89-C-0060) monitors are Capt. H. Helin and Maj. D. Fant. The authors would like to thank R. Volino for assisting in the data collecting process and P. Tuma for working on the figures of this paper.

References

Alving, A. E., and Smits, A. J., 1986, "The Recovery of a Turbulent Boundary Layer From Longitudinal Curvature," Paper No. AIAA-86-0435, 24th Aerospace Sciences Meeting, Reno, NV.

[2] $\delta_{99.5}$ at entry of the recovery wall.

Barlow, S. R., and Johnston, J. P., 1988, "Structure of a Turbulent Boundary Layer on a Concave Surface," *J. Fluid Mech.*, Vol. 191, pp. 137–176.

Blackwell, B. F., and Moffat, R. J., 1975, "Design and Construction of a Low Velocity Boundary Layer Temperature Probe," ASME *Journal of Heat Transfer*, Vol. 97, No. 2, pp. 313–315.

Bradshaw, P., 1973, "Effects of Streamline Curvature on Turbulent Flow," AGARDOgraph No. 169.

Crane, R. I., and Sabzvari, J., 1984, "Laser-Doppler Measurements of Goertler Vortices in Laminar and Low-Reynolds-Number Turbulent Boundary Layers," *Laser Anemometry in Fluid Mechanics*, R. J. Adrian et al., eds., LADOAN-Instituto Superior Technico, Lisbon, pp. 19–35.

Crawford, M. E., and Kays, W. M., 1976, "STAN5 (TEXSTAN version)—A Program for Numerical Computation of Two-Dimensional Internal and External Boundary Layer Flow," NASA CR-2742.

Hoffmann, P. H., Muck, K. C. B., and Bradshaw, P., 1985, "The Effect of Concave Curvature on Turbulent Boundary Layers," *J. Fluid Mech.*, Vol. 161, pp. 371–403.

Honami, S., 1980, "New Definition of Integral Thickness on the Curved Surface," Internal Lab. Report IL-26, Thermosciences Division, Dept. of Mech. Engrg., Stanford University, CA.

Jeans, A. H., and Johnston, J. P., 1982, "The Effects of Streamwise Concave Curvature on Turbulent Boundary Layer Structure," Rept. MD-40, Thermosciences Division, Dept. of Mech. Engng., Stanford University, CA.

Kays, W. M., and Crawford, M. E., 1980, *Convective Heat Transfer*, 2nd ed., McGraw-Hill, New York.

Kim, J., Simon, T. W., and Russ, S. G., 1992, "Free-Stream Turbulence and Concave Curvature Effects on Heated, Transitional Boundary Layers," ASME *Journal of Heat Transfer*, Vol. 114, No. 2, pp. 338–347.

Klebanoff, P. S., 1954, NACA Tech. Note No. 3178.

MacMillan, F. A., 1954, "Viscous Effects on Pitot Tubes in Shear Flow," Aeronautical Research Council, Reports and Memoranda, No. 3028.

Meroney, R. N., and Bradshaw, P., 1975, "Turbulent Boundary Layer Growth Over a Longitudinally Curved Surface," *AIAA J.*, Vol. 13, No. 11, pp. 1448–1453.

Pauley, W. R., and Eaton, J. K., 1988, "The Fluid Dynamics and Heat Transfer Effects of Streamwise Vortices Embedded in a Turbulent Boundary Layer," Thermosciences Division, Dept. of Mech. Engrg., Stanford University, CA, Report MD-51.

Ramaprian, B. R., and Shivaprasad, B. G., 1977, "Mean Flow Measurements in Turbulent Boundary Layers Along Mildly Curved Surfaces," *AIAA J.*, Vol. 15, No. 2, pp. 189–196.

Simonich, J. C., and Moffat, R. J., 1982, "Local Measurements of Turbulent Boundary Layer Heat Transfer on a Concave Surface Using Liquid Crystals," Rept. HMT-35, Thermosciences Division, Dept. of Mechanical Engineering, Stanford University, CA.

Smits, A. J., Young, S. T. B., and Bradshaw, P., 1979, "The Effect of Short Regions of High Surface Curvature on Turbulent Boundary Layers," *J. Fluid Mech.*, Vol. 94, No. 2, pp. 209–242.

So, R. M., and Mellor, G. L., 1975, "Experiment on Turbulent Boundary Layers on a Concave Wall," *The Aeronautical Quarterly*, Vol. 26, pp. 25–40.

Wang, T., 1984, "An Experimental Investigation of Curvature and Freestream Turbulence Effects on Heat Transfer and Fluid Mechanics in Transition Boundary Layer Flows," PhD Thesis, University of Minnesota, Minneapolis, MN.

Wang, T., and Simon, T. W., 1987, "Heat Transfer and Fluid Mechanics Measurements in a Boundary Layer Undergoing Transition on a Convex-Curved Wall," ASME JOURNAL OF TURBOMACHINERY, Vol. 109, No. 3, pp. 443–452.

You, S. M., Simon, T. W., and Kim, J., 1986, "Boundary Layer Heat Transfer and Fluid Mechanics Measurements on a Mildly-Curved Convex Wall," *Proc. 8th Int. Heat Transfer Conf.*, Vol. 3, pp. 1089–1094.

Young, A. D., and Maas, J. N., 1936, "The Behavior of a Pitot Tube in a Transverse Total Pressure Gradient," Aeronautical Research Council Reports and Memoranda, No. 1770, London.